

**NASA TECHNICAL  
MEMORANDUM**

NASA TM X- 64652

**HIGH ENERGY ASTRONOMY OBSERVATORY  
MISSION C  
PHASE A FINAL REPORT**

**Volume II – Preliminary Analyses and Conceptual Design**

(NASA-TM-X-64652-Vol-2) HIGH ENERGY  
ASTRONOMY OBSERVATORY, MISSION C, PHASE A.  
VOLUME 2: PRELIMINARY ANALYSES AND  
CONCEPTUAL DESIGN Final Report (NASA)  
Jan. 1972 724 p

N72-21283

By Program Development

Unclas  
CSCL 14B G3/11 23554

January 1972



**NASA**

*George C. Marshall Space Flight Center  
Marshall Space Flight Center, Alabama*

# TABLE OF CONTENTS

## VOLUME I — EXECUTIVE SUMMARY

## VOLUME II — PRELIMINARY ANALYSES AND CONCEPTUAL DESIGN

- Chapter I — Introduction
- Chapter II — Baseline Experiments for HEAO-C Phase A Study
- Chapter III — Mission Analysis
- Chapter IV — Observatory Baseline Design
- Chapter V — Structural Analysis
- Chapter VI — Thermal Control System
- Chapter VII — Attitude Sensing and Control System
- Chapter VIII — Electrical System
- Chapter IX — Communication and Data Handling System
- Chapter X — Space Shuttle Launch and Retrieval of HEAO-C

## VOLUME III — APPENDICES

- Appendix A — Alternate Experiments for HEAO-C
- Appendix B — Mission Analysis and Launch Vehicle
- Appendix C — Alternate Observatory Configurations
- Appendix D — Thermal Control Trade Studies and Supporting Analyses
- Appendix E — Attitude Sensing and Control Analyses
- Appendix F — Electrical Systems
- Appendix G — Reliability Analysis

1. REPORT NO. <b>TM X- 64652</b>		2. GOVERNMENT ACCESSION NO.		3. RECIPIENT'S CATALOG NO.	
4. TITLE AND SUBTITLE <b>High Energy Astronomy Observatory, Mission C, Phase A Final Report Volume II – Preliminary Analyses and Conceptual Design</b>			5. REPORT DATE <b>January 1972</b>		6. PERFORMING ORGANIZATION CODE
			7. AUTHOR(S) <b>Program Development</b>		
9. PERFORMING ORGANIZATION NAME AND ADDRESS <b>George C. Marshall Space Flight Center Marshall Space Flight Center, Alabama 35812</b>			10. WORK UNIT NO.		11. CONTRACT OR GRANT NO.
			12. SPONSORING AGENCY NAME AND ADDRESS <b>National Aeronautics and Space Administration Washington, D.C. 20546</b>		
			14. SPONSORING AGENCY CODE		
15. SUPPLEMENTARY NOTES <b>Prepared by the Preliminary Design Office, Program Development. This document is one of three volumes.</b>					
16. ABSTRACT <p>In response to a request from the Office of Space Science, a Phase A study of the High Energy Astronomy Observatory Mission-C (HEAO-C) was undertaken by the George C. Marshall Space Flight Center. Results of this study are reported in three volumes, Volume I containing an executive summary, Volume II containing the preliminary analyses and conceptual design of a baseline mission and spacecraft, and Volume III containing supporting technical data and experiment and spacecraft alternatives.</p> <p>The HEAO-C is the third of four planned missions in the High Energy Astronomy Program. The primary objective of the first two missions, HEAO-A and -B, is a scanning survey of the celestial sphere to study X rays, gamma rays, and cosmic rays, and to map locations of high energy sources; the primary objective of HEAO-C is a detailed study of the more interesting high energy sources, using grazing-incidence X-ray telescopes and a spacecraft pointing accuracy of <math>\pm 1</math> arc minute.</p> <p>A principal design goal for the HEAO-C spacecraft was to maximize commonality with the spacecraft designed for Missions A and B; technical transfusion between the designs required the Phase A study to be accomplished in parallel with the Phase B definition of the precursor spacecraft. Plans call for a HEAO-C launch between 1 and 1½ years after the launch of HEAO-B.</p> <p>The HEAO-C will be launched from ETR on the Titan IIID and placed into a 270 nautical mile circular orbit with a 28.5 degree inclination; the Phase A baseline concept weighs under 16 000 pounds, provides the required <math>\pm 1</math> arc minute pointing accuracy, carries three grazing-incidence X-ray telescopes with multiple focal plane experiments plus several supporting experiments, and is designed for a two year operational life. The HEAO-C is a candidate for early satellite retrieval with the Space Shuttle.</p>					
17. KEY WORDS <b>High Energy Astronomy Observatory Scientific Satellite High Energy Space Physics Conceptual Satellite Design Unmanned Spacecraft</b>			18. DISTRIBUTION STATEMENT <b>STAR Announcement</b>  <b>Erich E. Goerner Director, Preliminary Design Office</b>		
19. SECURITY CLASSIF. (of this report) <b>Unclassified</b>		20. SECURITY CLASSIF. (of this page) <b>Unclassified</b>		21. NO. OF PAGES <b>691</b>	22. PRICE <b>\$9.00</b>

## ACKNOWLEDGMENTS

Phase A program management was assigned to the Space Physics Group in the Mission and Payload Planning Office of Marshall Space Flight Center's Program Development Organization. Program Development's Preliminary Design Office was assigned responsibility for the Phase A technical analyses and engineering design; the Program Planning Office assisted with cost analyses and trades; and Program Development's HEAO Task Team (now Program Management's HEAO Office) provided the required liaison with the Phase B contractors for HEAO missions A and B.

Science and Engineering's Laboratories gave valued consultation and support in many technical areas; of special note was the assistance of the Space Sciences Laboratory in the area of experiment requirements and the Astronautics Laboratory and Product Engineering and Process Technology Laboratory in the area of materials selection.

Grateful acknowledgment is made of the excellent efforts of MSFC's support contractor team. Teledyne Brown Engineering, under Contract NAS8-20073, made substantial contributions throughout the study and much of their design and analysis effort is incorporated in this final report.

The Physics and Astronomy Division of OSS worked closely with MSFC in establishing appropriate mission objectives and requirements and assigned the experiment complements to be investigated — both for the baseline concept and the candidate alternatives.

The following MSFC personnel were principal contributors to the study in the areas noted:

Overall Study Management	Mr. John M. Butler, Jr.	PD-DO-SI
	Mr. Carroll C. Dailey	PM-HE-X
	Mr. James W. Heyer	PD-DO-DIR
HEAO-C Experiments (Chapter II and Appendix A)	Mr. Carroll C. Dailey	PM-HE-X
	Mr. Stephen O. Larson	PD-MP-S
	Mr. Harold S. Manning	PD-DO-MT
	Mr. Richard A. Potter	PD-MP-S

Mission Analysis (Chapter III and Appendix B)	Mr. Rodney Bradford	PD-DO-PM
	Mr. Von L. Burton	PD-DO-PA
	Mr. Thomas C. French	PD-DO-PM
	Mr. John L. Fults	PD-DO-PA
	Mr. Richard I. Gold	PD-DO-PM
	Mr. Elbert L. Sullivan	PD-DO-PA
	Mr. Tommy J. Wheeler	PD-DO-PM
	Mr. Archie C. Young	PD-DO-PM
Observatory Design (Chapter IV and Appendix C)	Mr. D. Henry Black	PD-DO-SL
	Mr. Josef F. Blumrich	PD-DO-SL
	Mr. John M. Butler, Jr.	PD-DO-SI
	Mr. Carl E. Colley	PD-DO-SA
	Mr. Jerry A. Peoples	PD-DO-SI
	Mr. Jay D. Willard	PD-DO-SL
Structures (Chapter V)	Mr. Carl E. Colley	PD-DO-SA
Thermal Control (Chapter VI and Appendix D)	Mr. Carl G. Fritz	PD-DO-MT
	Mr. Gustav W. Mordan	PD-DO-MT
Attitude Sensing and Control (Chapter VII and Appendix E)	Mr. Billy G. Davis	PD-DO-ES
	Mr. Onis C. Green	PD-DO-ES
	Mr. William B. Price	PD-DO-MP
	Mr. David M. Schultz	PD-DO-ES
Electrical Power (Chapter VIII and Appendix F)	Mr. Richard J. Boehme	PD-DO-EP
	Mr. Robert W. Rood	PD-DO-EP
Communications and Data Handling (Chapter IX)	Mr. Edward C. Hamilton	PD-DO-EC
Reliability (Appendix G)	Dr. James W. Steincamp	PD-DO-ES

Space Shuttle Launch and Retrieval  
(Chapter X)

Mr. D. Henry Black PD-DO-SL  
Mr. Josef F. Blumrich PD-DO-SL  
Mr. John M. Bütler, Jr. PD-DO-SI

Technical Editor

Mrs. Frances M. Andrews PD-DO-DIR

## LIST OF ACRONYMS

ABR	analog bay rack
ACN	Ascension Island
AD	aspect detector
A/D	analog-to-digital
AGC	automatic gain control
AGE	automatic ground equipment
ASCS	attitude sensing and control system
AS&C	attitude sensing and control (system)
AS&E	American Science and Engineering
ATA	automatic threshold adjust (cell)
ATM	Apollo Telescope Mount
BCD	binary code digital
bdc	brushless dc
BDX	Bendix Aerospace Corporation
BECO	Teledyne Brown Engineering
B/Ep	boron/epoxy
BER	bit error rate
BOL	beginning-of-life
B/S/L	ball joints, shock mounts, and linkages (baseline bench mounting concept)

## LIST OF ACRONYMS (Continued)

CCS	curved crystal spectrometer
C&DH	communication and data handling (system)
CFD	coarse flare detector
CG	center of gravity
CINDA	Chryster Improved Numerical Differencing Analyzer (computer program)
CIU	cable interface unit
CMD	command
CMG	control moment gyro
COMM	communication (system)
COTA	circle of total access
CP	central processor
CRA	celestial reference assembly
CRO	Carnarvon
CSM	command and service module
CYI	Canary Island
D/A	digital-to-analog
DBR	digital bay rack
DCU	digital computer unit
DHS	data handling system

## LIST OF ACRONYMS (Continued)

DOD	depth-of-discharge
DSS	digital sun sensor
ECA	electrical control assembly
EDCS	electrical distribution and control subsystem
EIA	electrical integration assembly
EMI	electromagnetic interference
EOM	end-of-mission
EPS	electrical power system
ERTS	Earth Resources Technology Satellite
ESE	electrical support equipment
ESM	estimated secular momentum
ETR	Eastern Test Range
EVA	extravehicular activity
FCS	flat crystal spectrometer
FFD	fine flare detector
FHST	fixed-head star tracker
FOV	field of view
FST	fixed star tracker
FW	full width

## LIST OF ACRONYMS (Continued)

FWHM	full width half maximum
FWHR	filter wheel high resolution (telescope)
FWLA	filter wheel large area (telescope)
FWLE	filter wheel low energy (telescope)
GAC	Grumman Aerospace Corporation
GEP	Goddard Experiment Package
g.g.	gravity gradient
Gr/Ep	graphite/epoxy
GSE	ground support equipment
GSFC	Goddard Space Flight Center
GST	gimbal star tracker
GWM	Guam
HAW	Hawaii
HEAO	High Energy Astronomy Observatory
HR	high resolution (telescope)
HRID	HR Imaging detector
I/O	input/output
IRIG	inertial rate-integrating gyro
ITL	integrate-transfer-launch

## LIST OF ACRONYMS (Continued)

ITT	International Telephone and Telegraph
JPL	Jet Propulsion Laboratory
KSC	Kennedy Space Center
LA	large area (telescope)
LAI	large area image detector
LBD	low background detector
LE	low energy (telescope)
LHCP	left-hand circular polarization
LMSC	Lockheed Missiles and Space Company
LON	lines of nodes
LOS	line of sight
LSI	large scale integration
MC	maximum contribution (CMG steering law)
MIB	minimum impulse bit
MIT	Massachusetts Institute of Technology
MOCC	missions operation control center
MPC	monitor proportional counter
MSFC	Marshall Space Flight Center
MSFN	Manned Space Flight Network

## LIST OF ACRONYMS (Continued)

MTBF	mean time before failure
MUX	multiplexer
NAD	Naval Ammunition Depot (Crane, Ind.)
NEA	noise equivalent angle
NRZ	non-return-to-zero (pulse recording)
OAM	orbit adjust module
OAS	orbit adjust stage
ODC	optical data corrector
OG	objective grating
OU	optical unit
PCM	(1) pulse code modulator (encoder) (2) phase change materials
PEP	perpendicular to the ecliptic plane
PI	principal investigator
PLF	payload fairing
POP	perpendicular to the orbital plane
PRN	pseudo random noise
PSD	position sensitive detector
PSI	Pressure Systems Incorporated
PSK	phase shift keyed (demodulator)

## LIST OF ACRONYMS (Continued)

RCM	reaction control module
RCS	reaction control system
REA	reaction engine assembly
REM	reaction engine module
RF	radio frequency
RFI	radio frequency interference
RGA	reference gyro assembly
RHCP	right-hand circular polarization
ROM	read-only memory
rss	root-sum-square
RTG	radioisotope thermoelectric generator
RZ	return-to-zero (pulse recording)
SΦM	split phase mark
SAN	Santiago
S/C	spacecraft
SCS	Satellite Control Section
SEC	secondary electron conduction (vidicon)
S/L	shock/link (concept)
SMAB	Solid Motor Assembly Building

## LIST OF ACRONYMS (Concluded)

SPG	single-point ground
SRM	solid rocket motor
SSD	solid state detector
STADAN	Space Tracking and Data Acquisition Network
STPAN	Stiffened Panels (computer program)
STRESS	Structural Engineering Systems Solves (computer program)
SUVT	small ultraviolet telescope
TA	transfer assembly
TACS	thruster attitude control simulation
TCA	(1) thrust chamber assembly (2) tank control assembly (electrical system)
TCV	thrust chamber valve
TEX	Texas
TRW	TRW Systems, Inc.
UV	ultraviolet
VFC	voltage to frequency converter
VGP	vehicle ground point
WASS	wide angle sun sensor

# CHAPTER I. INTRODUCTION

## A. Mission Description

The High Energy Astronomy Observatory Mission C (HEAO-C) is the third of four planned satellite missions in the National Aeronautics and Space Administration's High Energy Astronomy Program. The overall objective of this program is to obtain high quality, high resolution data on cosmic rays, gamma rays, and X rays throughout the celestial sphere; data will include information on the structure, spectra, polarization, and, where applicable, source location.

The primary objective of the first two missions, HEAO-A and HEAO-B, is to accomplish a scanning survey of the celestial sphere, with emphasis on identifying and mapping source locations and investigating emitted energy to the extent possible within the constraints of both time and experiment detector capability. Thus, the first two satellites will operate primarily in a scanning mode and only limited time will be available for the inertial or "pointing" mode, this percentage of time increasing for the second mission as compared to the first. Both spacecraft will be capable of a pointing accuracy of  $\pm 1$  degree, or better.

The HEAO-C mission will follow the HEAO-B mission by 1 to 1 1/2 years and will be devoted entirely to the "pointing" mode, with a spacecraft pointing capability of  $\pm 1$  arc minute, or better. Principal scientific instruments on board will be the grazing-incidence X-ray telescopes, with multiple experiments (detectors) positioned into and out of the focal point region. Thus, HEAO-C will operate in a manner similar to a ground-based observatory in that various experiments will time-share the telescopes. In addition, several stationary experiments will be rigidly mounted to the optical bench alongside the telescopes to fill out the experiment complement and to provide background measurements.

## B. Study Objective and Approach

The objectives of the Phase A study were to determine mission feasibility, to study several alternative experiment complements, to investigate promising spacecraft alternative concepts, and to study a baseline experiment and spacecraft concept to sufficient depth to establish hardware feasibility.

The principal design goal for the HEAO-C spacecraft was to maximize commonality with the HEAO-A/B spacecraft in order to maintain cost effectiveness throughout the HEAO program.

The Phase A study of HEAO-C was initiated soon after the start of the Phase B definition contracts for the HEAO-A/B missions and spacecraft and progressed concurrently with them. Technical transfusion between the in-house Phase A study and the Phase B definition contracts influenced both design approaches and achieved the desired cost-effective commonality. This was reflected in design decisions incorporated in the Request for Proposal issued by MSFC for the HEAO Phase C/D for Missions A and B.

Technical effort on the Phase A study was concluded prior to receipt of the Phase C/D proposals and, consequently, does not reflect the exact manner in which the most recent version of the HEAO-A/B spacecraft will evolve through modification to accomplish the HEAO-C mission. Continuing study and design iteration will be required by the Phase C/D contractor, with special emphasis given to the experiments in order to incorporate improved definition of both requirements and hardware.

## C. Conclusions

Results of the Phase A study indicate that modifications to the HEAO-A/B spacecraft to accomplish the HEAO-C mission are entirely feasible; in general, spacecraft components which must be different result from the more stringent requirements for accuracy, higher reliability, and longer operational life, and the different experiment mounting and accommodation requirements.

Study results are reported in three volumes, Volume I containing an executive summary, Volume II containing the preliminary analyses and conceptual design of the HEAO-C baseline mission and spacecraft, and Volume III containing supporting technical data and experiment and spacecraft alternatives.

TABLE OF CONTENTS

	Page
A. X-Ray Observations of Space . . . . .	II- 1
B. Experiments . . . . .	II- 3
1. List of Baseline Experiments . . . . .	II- 3
2. Diagrams of Interrelations of Experiment Components . . . . .	II- 3
3. Experiment Parameters . . . . .	II- 8
4. Description of Experiments and Scientific Objectives . . . . .	II- 8
a. Nature of Sources and Observations. . . . .	II- 8
b. Description of Mirrors . . . . .	II-12
c. High Resolution Telescope Experiments . . . . .	II-13
d. Large Area Telescope Experiments. . . . .	II-16
e. Low Energy Telescope . . . . .	II-17
f. Experiments Without Telescopes. . . . .	II-18
g. Aspect and Computer Systems . . . . .	II-21
C. General Experiment Information. . . . .	II-24
1. South Atlantic Anomaly Effects . . . . .	II-24
2. Gas Purges and Quenching Gas Quantities Required . . . . .	II-27
3. Calibration of Experiments . . . . .	II-29
4. Launch Environment Tolerated by Experiments . . . . .	II-31
5. Spacecraft Degraded Mode Operation . . . . .	II-32
D. Relationship of HEAO-A and -B to HEAO-C . . . . .	II-32
E. Recommendation for Phase B Study . . . . .	II-37
References . . . . .	II-38

## LIST OF ILLUSTRATIONS

Figure	Title	Page
II-1.	Interrelations of experiment components for HEAO-C. . . . .	II- 6
II-2.	HEAO-C baseline experiment layout . . . . .	II- 7
II-3.	High resolution and large area telescope mirror concepts . . .	II-14
II-4.	X-ray telescope focal plane experiments . . . . .	II-15
II-5.	Flat crystal (iron line) spectrometer — 500 cm <sup>2</sup> . . . . .	II-19
II-6.	Monitor proportional counter — 620 cm <sup>2</sup> . . . . .	II-20
II-7.	Coarse flare detector . . . . .	II-22
II-8.	Proton flux contours for E greater than 5 MeV at an altitude of 270 nautical miles . . . . .	II-25
II-9.	Electron flux contours for E greater than 0.5 MeV at an altitude of 270 nautical miles . . . . .	II-26
II-10.	Proton flux in the South Atlantic Anomaly . . . . .	II-28
II-11.	Mission data worth versus time . . . . .	II-36

## LIST OF TABLES

Table	Title	Page
II-1.	Baseline Experiments and Abbreviations . . . . .	II- 4
II-2.	Experiment Energy Ranges . . . . .	II- 5
II-3.	Experiment Power, Weight, Size and Field of View . . . . .	II- 9
II-4.	Requirements and Specifications of the Baseline Telescope Packages . . . . .	II-10
II-5.	X-ray Source Intensity Distribution . . . . .	II-12
II-6.	Purging and Quenching Gas Quantities Required . . . . .	II-29
II-7.	Calibration Sequences . . . . .	II-31
II-8.	HEAO-C Operational Experiment Time . . . . .	II-33
II-9.	HEAO-C Telescope Experiment Operational Time . . . . .	II-34
II-10.	Scientific Worth Lost Due to Malfunction . . . . .	II-35
II-11.	Comparison of HEAO-A and -B to HEAO-C . . . . .	II-35

## CHAPTER II. BASELINE EXPERIMENTS FOR HEAO-C PHASE A STUDY

### A. X-Ray Observations of Space

Although the first celestial X-ray source was discovered less than 10 years ago, X-ray astronomy has already proven itself as an important and interesting field. It appears destined to become a major branch of astronomy, and it may well be more fruitful than radio astronomy.

Many of the known X-ray sources have unexpected and interesting properties. All of those which can be detected by existing instruments are extremely luminous. In the 10 keV range, for example, the known galactic X-ray sources appear brighter than the sun in that range, in spite of the fact that their radiation is diminished by an inverse-square distance factor of about  $10^{14}$  [II-1].

In other respects, the known sources are very different. Some vary in intensity; of these, some show rapid, fairly regular pulsations (the X-ray pulsars); whereas, others have an intensity variation which is rather like a nova light curve. Some sources cover an extended area (supernova remnants, for example); whereas, others seem to be associated with star-like objects. Some are apparently members of our own galaxy; a few have been identified with extragalactic objects. Some X-ray sources also emit in the radio wavelengths; others do not.

The distance of a discrete X-ray source can be determined only if the source can be identified with an optical object whose distance is known. Relatively few secure identifications exist, largely because of the low spatial resolution of most X-ray detectors. Generally, the extrasolar discrete sources are assumed to be located within our galaxy. The Sco X-1 source is estimated to be 100 to 400 pc distant.

A few X-ray sources are thought to be extragalactic. One source in Virgo is thought to coincide with the very peculiar galaxy M87. Other sources have been identified with Seyfert galaxies and with the quasi-stellar source 3C273. If these identifications are correct, these sources must emit large amounts of X-ray energy.

The luminosities of galactic X-ray sources are also impressive. Sco X-1, the strongest source visible from the earth, will serve as an example. If its distance is assumed to be no greater than 100 pc, its X-ray luminosity in the 1 to 10Å range is a few times  $10^{35}$  erg/sec, or about 100 times the bolometric luminosity of the sun [II-2]. The X-ray emission from this object is about 1000 times greater than its visible radiation. Clearly, for this source, X-ray emission is a major mode of energy output. Sco X-1 cannot be understood if its X-ray properties are not understood. Furthermore, it can be expected to affect the radiation field in the space surrounding it.

Two highly variable X-ray sources ("flare") have been discovered, providing further evidence of large-scale energy transfer in this wavelength range. Their behavior may be consistent with the explosive ejection of stellar material [II-3]. The flare pattern consists of a sudden sharp increase in brightness, followed by a drop of several orders of magnitude over a period of about two months. Other galactic sources also show evidence of variability and of distinctive spectral distributions, so they too are promising objects for study. This category also includes the recently discovered X-ray pulsars.

The mechanism by which the X-ray emission is produced is still unknown. Several different mechanisms may be responsible for the different types of sources. At least four possibilities have been suggested. To distinguish among them (or, perhaps, to prove that none is valid in a given case), it is necessary to obtain spectra of the sources over as much as possible of the X-ray region. This can be done only by satellite observations.

The nature of the diffuse X-ray background radiation also requires study. It is thought [II-3] to be of extragalactic origin, but its source has not yet been discovered. More observations should be made of its spectrum and possible departures from isotropy.

X-ray emissions thus reveal the existence of vast amounts of energy not previously detected. The luminosities and the large-scale variations in emission of some of these objects are evidence of transfer of very large amounts of energy. The X-ray sources are already recognized as significant elements of the known universe. Moreover, there is no reason to doubt that many more X-ray sources will be discovered.

In addition to searching for new sources, additional observations should be made of the known sources. Observations with higher spatial resolution will

give more precise positions and source sizes, and thus will allow identification of their optical counterparts. Variable sources should be observed over long time spans with high temporal resolution to obtain X-ray "light curves" describing the form of variability, and detailed spectra of both the discrete sources and the background are also needed.

## B. Experiments

1. List of Baseline Experiments. The baseline experiments listed in Table II-1 were initially chosen for the HEAO-C Phase A study. Subsequently, we were asked to study the feasibility of alternate experiments on HEAO-C; these are listed in Appendix A. The energy ranges in which the different experiments are responsive are listed in Table II-2.

2. Diagrams of Interrelations of Experiment Components. The experimental packages used with the present HEAO-C spacecraft study are shown in Figure II-1 in block diagram form. The interrelation of the various experiment components can be seen in this figure. In Figure II-2 the locations of the experiment components on the spacecraft are shown. In some cases, where the components are not well defined, only the envelope is depicted.

Three X-ray mirrors provide images in the focal regions which are analyzed by both image-sensitive and energy-sensitive detectors. A variety of experiments can be performed simultaneously on an X-ray source over a large energy range. Other experiments are used for monitoring purposes and for spectroscopy measurements at higher energies that are inaccessible to the X-ray mirrors.

It will be noticed that there are numbers down the right side of Figure II-1 under the heading "Variations." This is an attempt to point up the possible variations and combinations of experiments and experiment equipment that are available. Not all of the combinations numbered will necessarily be used, especially under normal conditions with no failures. However, the combinations are available and some degree of redundancy is provided through these possibilities.

The mathematics of the situation is partially revealed by the multiplicative factors being shown on the left side of the equal signs at the right side of Figure II-1. The sum of variations is shown at the bottom of the column.

TABLE II-1. BASELINE EXPERIMENTS AND ABBREVIATIONS

Experiment Hardware	Hardware Abbreviation	Type of Measurement
High Resolution Telescope Curved Crystal Spectrometer HR Imaging Detector  Objective (Transmission) Grating  Filter Wheel	HR CCS  HRID  OG  FWHR	X-ray Crystal spectrometry  Imaging, high resolution position determination Objective grating spectrometry (OG and HRID used) Broadband filter spectrometry (FWHR and HRID)
Large Area Telescope Solid State Detector LA Image Detector  Filter Wheel	LA SSD LAID  FWLA	X-ray Nondispersive spectrometry Imaging, faint source position determination Nondispersive spectrometry (FWLA and LAID)
Low Energy Telescope Position Sensitive Detector Low Background Detector  Filter Wheel	LE PSD  LBD  FWLE	X-ray Imaging, position determination Imaging, position determination Nondispersive spectrometry (FWLE and LBD)
Miscellaneous Experiments Monitor Proportional Counter Flat Crystal Spectrometer (Iron Line) Coarse Flare Detector  Fine Flare Detector  Aspect Detector	MPC  FCS  CFD  FFD  AD	Background counter  Crystal spectrometry  Flare detection, coarse resolution (4 deg) Flare detection, fine resolution (30 min) Aspect determination

TABLE II-2. EXPERIMENT ENERGY RANGES

Instrument	Energy Range (keV)	Minimum Detectable Flux in $10^3$ sec <sup>2</sup> (erg/cm <sup>2</sup> -sec) <sup>a</sup>	Minimum Detectable Surface Brightness in $10^3$ sec	Angular Resolution	Energy Resolution ( $\lambda/\Delta\lambda$ )	Time Resolution (msec) <sup>b</sup>
CCS	0.2 - 3	$10^{-12}$			50 - 6000	
HR Image Intensifier	0.2 - 4	$\approx 4 \times 10^{-13}$	$\approx 10_2^{-14}$ erg/cm <sup>2</sup> (arc-sec) <sup>2</sup>	<5 min		1
OG Spectrometer	0.2 - 2	$3 \times 10^{-12}$			200	
Broadband Filter Spectroscope	0.2 - 4	$4 \times 10^{-14}$			10	0.5
Solid-State Spectrometer	0.5 - 4	$2 \times 10^{-14}$			2 - 4	0.1
Position Sensitive Proportional Counter	0.2 - 4		$10^{-14}$ erg/cm <sup>2</sup> - sec (arc-min) <sup>2</sup>	30 min		
LE Telescope	0.124 - 0.62			few arc sec max		
FCS (Iron Line)	6.4 - 7.2	$10^{-11}$			$10^3, 10^4$	
Flare Alarm	1 - 10	$\approx 10^{-9}$		0.5 deg		

a. Indicates detector sensitivity for a 1000 second observation.

b. Indicates the minimum time in which an experiment can detect a change in the received flux.

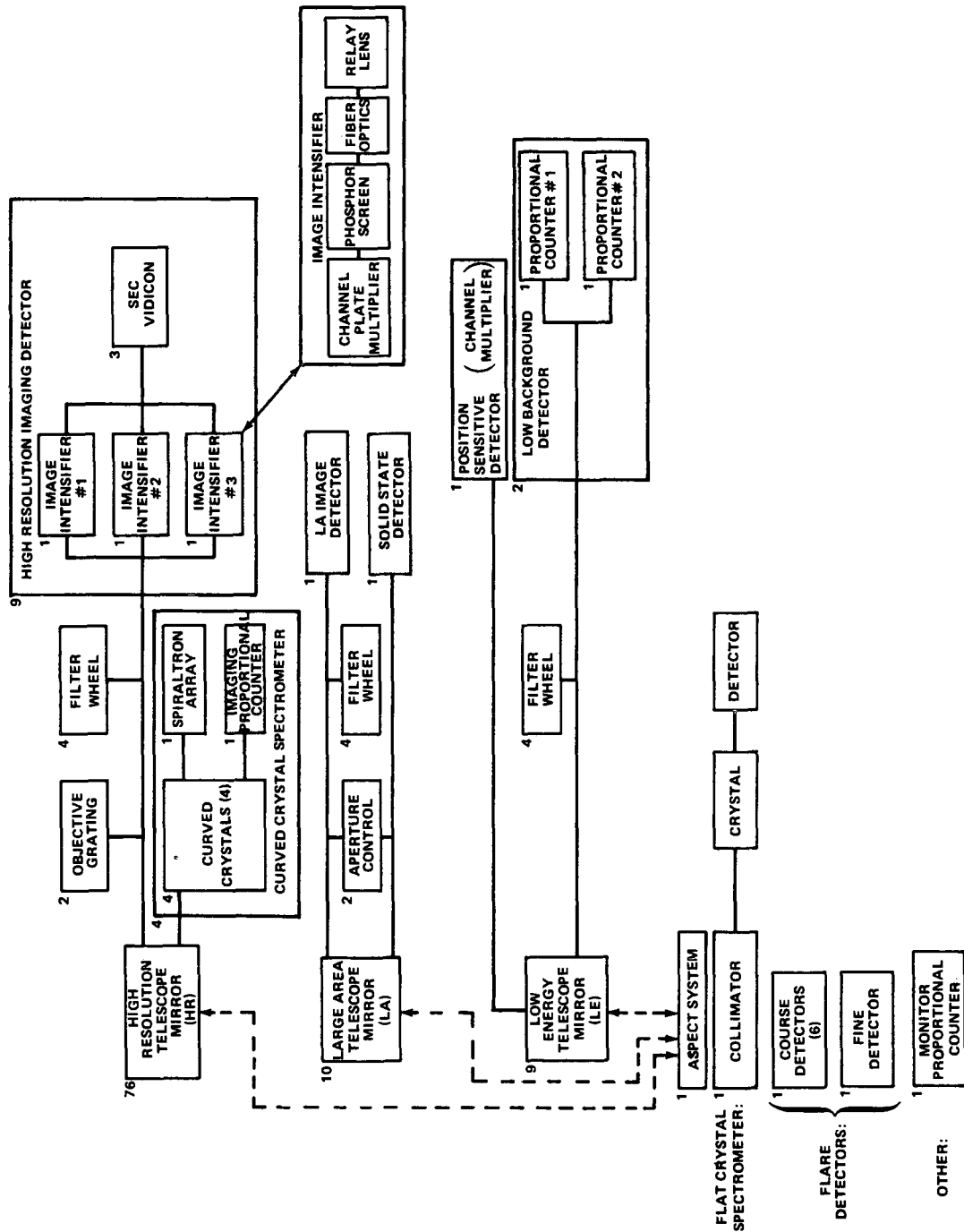


Figure II-1. Interrelations of experiment components for HEAO-C.

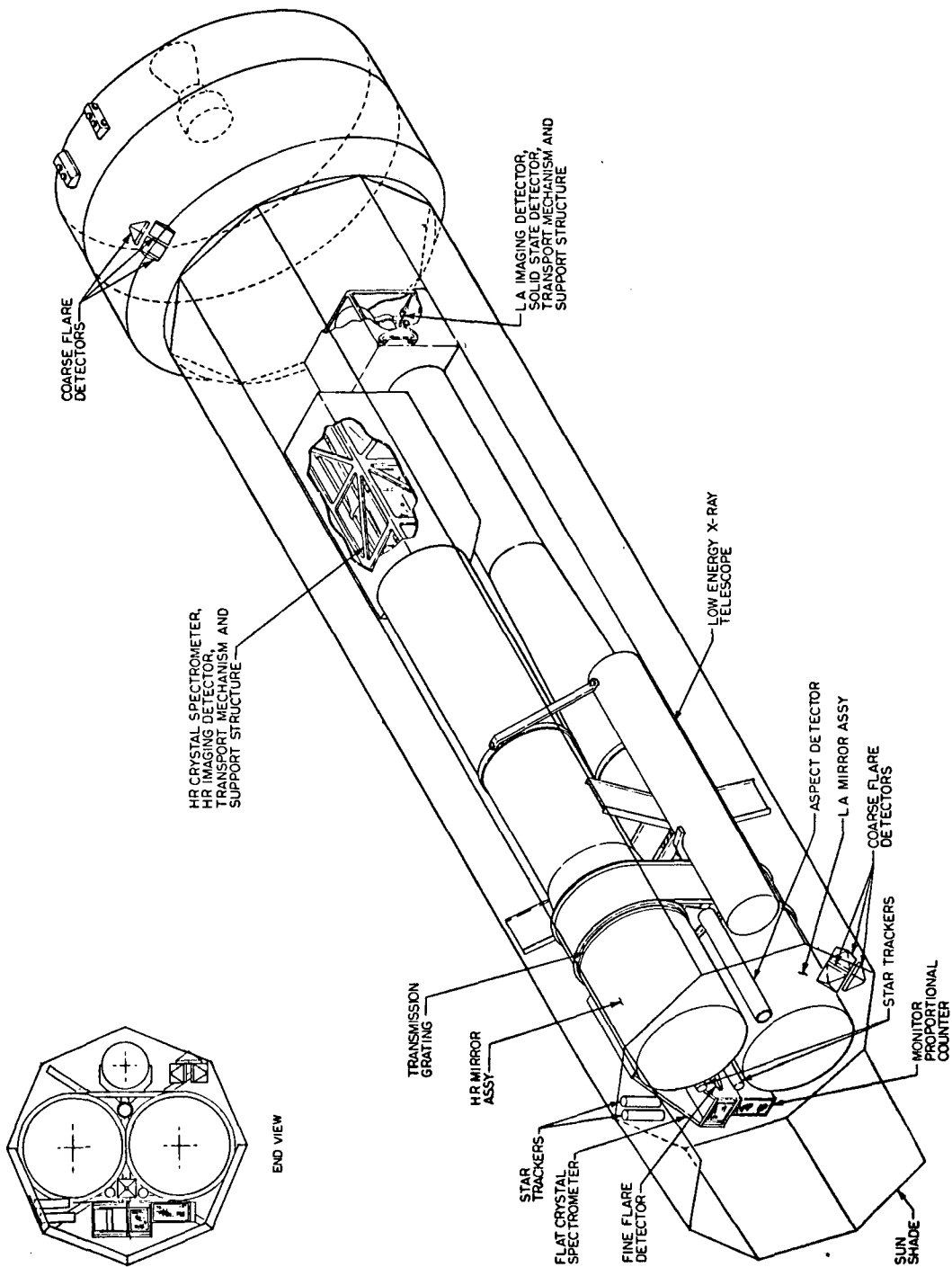


Figure II-2. HEAO-C baseline experiment layout.

The number of possibilities made available by any piece of equipment is depicted by the number that appears at the upper left of the box representing that component. For example, the secondary electron conduction (SEC) vidicon has three fields of view, or scan modes, available; therefore, the number three appears at the upper left side of that box. Each filter wheel is represented as having four sections (one an open window, the other three occupied by filters); therefore, the number four appears beside that box. (There may be as many as eight sections in the filter wheel.) The objective grating and the aperture control are considered to be either in or out; therefore, there are two possibilities for each.

3. Experiment Parameters. In the course of our study, we have tabulated a substantial amount of data; in Table II-3 is a listing of the power, weight, size and field of view (FOV) of the various baseline experiments. In Table II-4 are listed the requirements the telescope packages place on the spacecraft. Similar tables appear in Appendix A where they are expanded to include the auxiliary experiments.

#### 4. Description of Experiments and Scientific Objectives

a. Nature of Sources and Observations. The discussion of the value of X-ray observations suggests that many of the discrete X-ray sources have little in common except their X-ray emission. Because of this great diversity in source properties, it is important to have as much detailed information as possible about each source. At present, there do not seem to be any "typical" X-ray sources.

The goal of X-ray astronomy, like that of optical astronomy, is the determination of the physical properties of the sources (e.g., size, mass, and temperature), as well as the mechanisms by which their radiation is produced and emitted to space. All these things must be determined from a few observable quantities: spectra, luminosities, and positions. The various spectrometers, filters, and gratings on the HEAO-C X-ray experiments permit measurement at different resolutions and dispersions of the intensity of emitted radiation at different wavelengths, i. e., of the spectra. Provision is also made for determining the integrated intensity over a wide wavelength range — the apparent luminosity. The aspect determination system can be used to determine the celestial coordinates of the sources with sufficient precision for probable identification of their optical counterparts. When these identifications have been made, the distances of the sources can usually be estimated, and when the distances are known, the absolute X-ray luminosities can be found. From

Page intentionally left blank

the distance and the measured source size, the physical scale of an X-ray source can be determined. The luminosity and spectral data provide information on the temperature and energy generation processes.

Several X-ray sources have suddenly become visible where nothing had been detected previously and have, then, gradually faded again into obscurity. These "flares" are particularly interesting, and a complete record of the progress of a flare over the two months or so of its life would be of great value. The flare detectors on HEAO-C are intended to detect the onsets of such outbursts anywhere in the sky so that they can be studied with the higher resolution instruments.

From a scientific viewpoint, then, it is desirable to obtain as much spectral, photometric, and position information as possible for each source. Many X-ray sources are variable. For these, the same data should be obtained as a function of time, with the greatest possible time resolution. Obviously, complete observations cannot be made for every source. One of the problems in setting up an observing program is that of obtaining as much information as possible in the time available.

There are now about 60 fairly well established X-ray sources [II-4, II-5 and II-6]. Intensity values have not yet been published for some of the most recently discovered sources, so the numerical values given here were taken from Reference II-4 which includes 53 of the sources. During the next few years, thousands of fainter sources will probably be discovered, especially through the HEAO-A and -B missions. A crude prediction of the expected eventual intensity distribution of X-ray objects is given in Table II-5. An arbitrary X-ray magnitude scale was devised to classify the sources according to their photon fluxes measured in the 2 to 10 keV energy range. The number of sources brighter than or equal to a given magnitude was assumed to be inversely proportional to the X-ray flux corresponding to that magnitude. (This assumption is plausible for galactic sources because they tend to occur near the galactic plane, forming a two-dimensional distribution. That is why the intensity distribution of known sources, listed in the fourth column of Table II-5, is consistent with the projected distribution.) Of course, the actual distribution of faint X-ray sources may prove to be different from this prediction.

The total number of sources predicted to be known by 1977 is 4000, most of the objects being too faint to be detectable with present equipment. The fainter objects will require longer integration times for each observation; high dispersion spectroscopy will probably not be practical for these sources.

TABLE II-5. X-RAY SOURCE INTENSITY DISTRIBUTION

X-Ray Magnitude	$F^a$ (photons/cm <sup>2</sup> -sec)	No. = $10 F^{-1.0}$ (Cumulative)	Known at Present	Estimated Known by 1977
I	10	1	1	1
II	3	3	2	2
III	1	10	10	10
IV	0.3	30	34	34
V	0.1	100	53	100
VI	0.03	300	—	300
VII	0.01	1 000	—	1000
VIII	0.003	3 000	—	3000
IX	0.001	10 000	—	4000

a. 2 to 10 keV

Attempts will be made to obtain low resolution observations of each object and to examine some of the most interesting objects in more detail. Filter and objective grating observations, position data, and luminosity observations are typical low resolution investigations. The high resolution work will include observations with the high resolution spectrometer (CCS) and observations over extended time periods, either to increase the integration times for very faint sources or to study changes with time in a variable source.

Although the actual observing programs will be arranged by the experimenters, sequences of procedures are given in Chapter III of this report and detailed timelines are also presented.

b. Description of Mirrors

(1) High Resolution Telescope. The HR telescope consists of a set of five confocal, parabolic-hyperbolic, grazing-incidence mirrors (Fig. II-3). All mirrors have a physical length of 44 inches and a focal

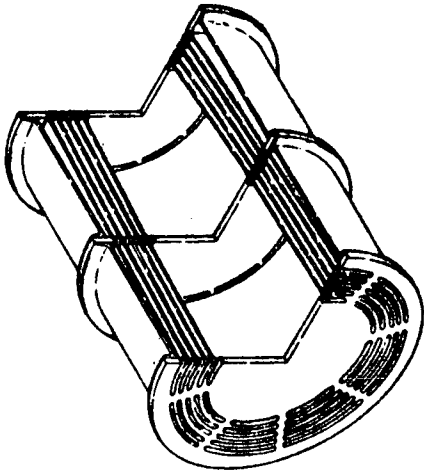
length of 240 inches. The outermost mirror diameter is 36 inches. The mirrors will probably be fabricated of a low expansion glass such as Cer-Vit with a thickness of 0.5 inch. The resolution of the HR mirror will be in the arc second range, the exact value depending on the wavelength under observation and the off-axis distance of the sources.

(2) Large Area Telescope. The need for a telescope mirror with a large collecting area at the sacrifice of high image resolution has resulted in the design of a large area mirror (LA) shown in Figure II-3. The focusing scheme is of the Baez type; X-rays are reflected at small angles off two nearly flat paraboloidal mirror segments which are approximately perpendicular to each other. The entire mirror system consists of 16 sets of identical Baez modules with a front and rear section. Each section is composed of a set of 25 nearly parallel plates. The individual plates are deformed to the proper parabolic figure by placing optical flats in a rigid holding fixture. The LA mirror assembly has a length of 49.5 inches, a diameter of 36 inches, and a focal length of 312 inches.

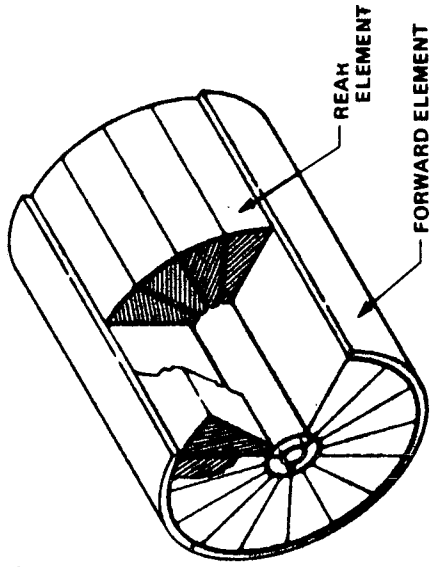
(3) Low Energy Telescope. Both the HR and LA mirrors are designed to operate in the energy region of 0.2 to 4 keV, requiring long focal lengths compatible with small grazing angles. To observe longer wavelength X-rays (lower energies), a low energy, Wolter-type mirror (LE) is proposed for the HEAO-C missions. This mirror consists of a single parabolic-hyperbolic surface of Kanigen-coated beryllium. The maximum grazing angle of the first element is 2 degrees and the focal length is 72 inches. The diameter of the mirror is 20 inches.

### c. High Resolution Telescope Experiments

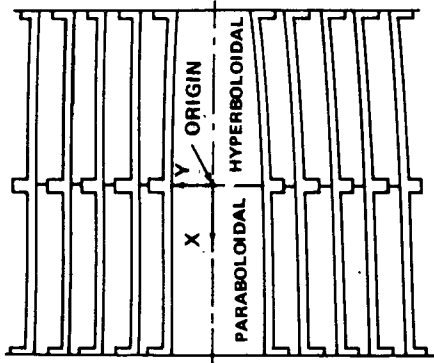
(1) High Resolution Crystal Spectrometer. The high resolution crystal spectrometer, shown in Figure II-4, is used in the focal plane of the high resolution X-ray mirror. It is a curved crystal Bragg spectrometer which will probably use either Johann or spherical optics. Its wavelength resolution ( $\lambda/\Delta\lambda$ ) will be as high as 6000 in certain energy regions. In operation, the diverging hollow cone X-ray beam formed by the X-ray mirror strikes one of four Bragg reflection crystals located at the center of the spectrometer. The diffracted X-ray beam is analyzed in a plane between the crystal and the conventional focal point on the Rowland circle. One of two instruments is used to determine the position and intensity of the diffracted beam: a close-spaced imaging proportional counter at higher energies and an array of spiraltron electron multipliers at lower energies. The mechanical design of the spectrometer allows a large range of diffraction angles.



CUT-AWAY VIEW OF FULL TELESCOPE

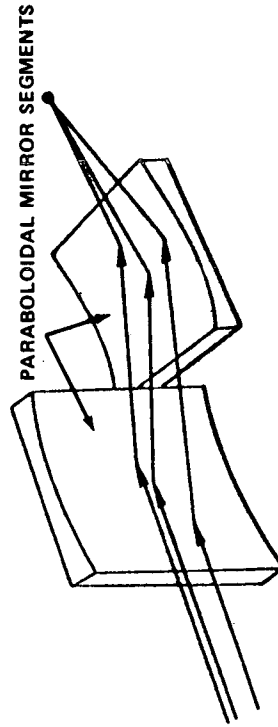


CUT-AWAY VIEW OF FULL TELESCOPE



SIDE VIEW OF ARRANGEMENT OF 5 CONCENTRIC WOLTER-TYPE MIRRORS

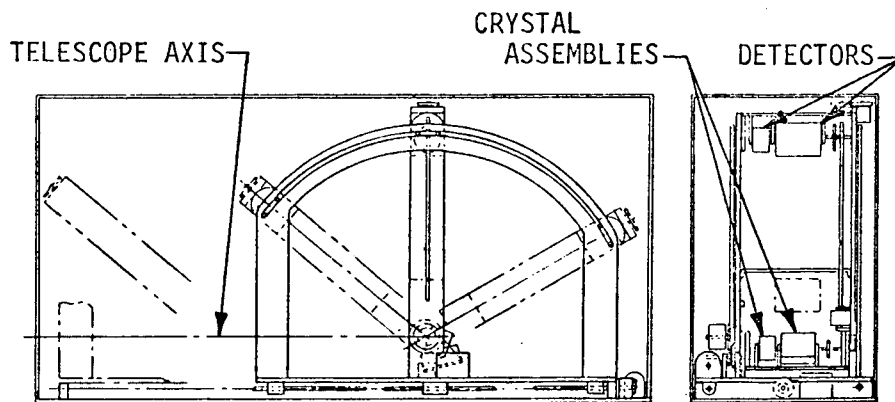
HR TELESCOPE CONCEPT



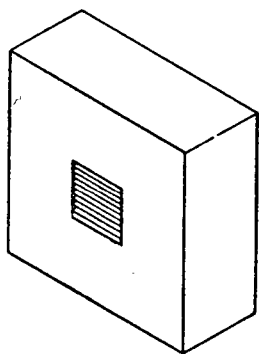
BAEZ MIRROR CONCEPT

LA TELESCOPE CONCEPT

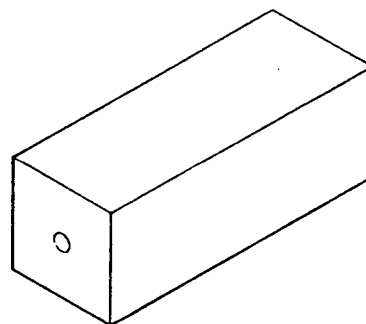
Figure II-3. High resolution and large area X-ray telescope mirror concepts.



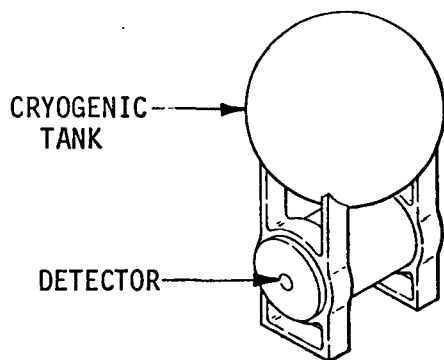
HR CRYSTAL SPECTROMETER



LA IMAGE DETECTOR



HR IMAGE DETECTOR



LA SOLID STATE DETECTOR

Figure II-4. X-ray telescope focal plane experiments.

(2) High Resolution Telescope Image Detector. The HR image detector, shown in Figure II-4, is designed to have an image resolution compatible with that of the HR mirror, about 1 arc second. The image detector consists of an image intensifier, a phosphor screen, and an SEC vidicon tube. In operation, the HR X-ray image produces photoelectrons at the photocathode of the image intensifier. These electrons are accelerated and multiplied through the length of the channel tubes and produce an optical image on a phosphor screen. By fiber optics and a relay lens, this image is transferred to and analyzed by a sensitive SEC vidicon tube.

For redundancy and higher efficiency at different energies, there are three interchangeable sets of image intensifier and optical transfer systems. Each of the three sets has a different photocathode material. The electronic readout system of the vidicon has three scanning modes with different field sizes and time resolutions.

(3) Objective Grating Spectrometer. A transmission grating is used with the HR mirror and high resolution imaging experiment to form a slitless objective grating spectrometer. In operation, the grating is placed in the path of the X-rays directly behind the HR mirror. The X-ray image in the focal plane is then dispersed into a line spectrum on either side of the real (undispersed) image. The image detector is able to analyze the line spectrum to give moderate resolution spectral information. This experiment is extremely efficient, since all accessible wavelengths and all sources within the field of view can be analyzed simultaneously. The grating material is composed of a thin parylene substrate onto which are deposited thin absorbing strips of gold. Two gratings are proposed with line densities of 500 and 1000 lines per millimeter, to obtain two different dispersions.

(4) Filter Wheel. A filter wheel is proposed for use with each of the three X-ray mirrors. Each filter wheel is used with the appropriate image detector, as shown in Figure II-1, to give crude spectral information in different wavelength regions. There can be four to eight windows in the wheel (depending on what is decided later). The filter wheel is placed close to the focal plane of the telescope. One of the windows of the filter wheel is left blank so that it is possible to observe without a filter. To bring a filter into the X-ray beam, the wheel is simply rotated.

#### d. Large Area Telescope Experiments

(1) Large Area Image Detector. The image detector, shown in Figure II-4, associated with the large area telescope uses a position-sensitive

proportional counter to locate the X-ray pattern to within 1 millimeter near the telescope axis. The counter has an array of resistive anode wires capable of locating the position of the photoelectrons produced in the counter gas by the incoming X-rays. The position resolution is compatible with the image resolution; i. e., the position resolution decreases as the distance from the telescope axis increases. Other features of the detector include a 1 micron thick parylene window for maximum X-ray transmission and anticoincidence anodes to lower the background counting rate.

(2) Solid State Detector. At energies greater than 0.5 keV, the solid state spectrometer (Fig. II-4) will have the highest resolution of any of the focal plane instruments. The active detecting component of the spectrometer is a lithium-drifted silicon crystal. A dead layer of approximately 0.1 micron of silicon acts as the X-ray entrance window for the detector. To achieve a low background for the silicon detector, the central crystal is surrounded on three sides by a lithium-drifted germanium crystal used as an anti-coincidence shield. Both sets of crystals are kept at cryogenic temperatures by means of a conductive cold finger leading into a cryogenic reservoir. In operation, the entire assembly is moved into the focal position of the large area X-ray mirror.

(3) Filter Wheel. As mentioned before, a filter wheel is proposed for use behind the LA telescope. The large area image detector is to be used as the detector for these spectrographic measurements. The purpose of the filter wheel is to determine the spectral shape and structural features on extended sources.

#### e. Low Energy Telescope

(1) Position Sensitive Image Detector. This detector consists of a position sensitive proportional counter to analyze the low energy telescope image. The field of view of the detector is 1 by 1 degree and has an angular resolution of 2 arc minutes. The detector has an array of 30 resistive wire anodes with a spacing of 1 millimeter. To give maximum transmission, the counter window is made of parylene which provides wavelength band passes from 20 to 30 Å and from 40 to 70 Å.

(2) Low Background Detector. The LE low background detector consists of a 2 arc second aperture which is mechanically scanned in front of one of two low background counters. The counters are of the proportional type and

have thin plastic windows. The positioning of the counter behind the scanning aperture is not critical since the aperture itself defines the X-ray beam.

(3) Filter Wheel. As mentioned before, a filter wheel is proposed for use behind the low energy telescope. It will be similar to the previously mentioned filter wheels, although it may be a more intimate part of the experiment.

#### f. Experiments Without Telescopes

(1) Flat Crystal Spectrometer. It is highly desirable to search for the k lines of the iron ions by performing high resolution spectroscopy of X rays at energies above the cutoff energy of the X-ray mirrors, 4 keV. For this purpose, a flat crystal spectrometer is included in the experimental package to be located near the X-ray mirrors. The FCS is shown in Figure II-5. The aluminum honeycomb collimator has a 0.5 degree FWHM field of view to be aligned within 3 minutes of the mirror axes. After passing through the collimator, X rays are diffracted from a flat crystal at the proper analyzing angle, which depends on the crystal used. The diffracted X rays then enter a sensitive proportional counter detector. The module will employ either a lithium fluoride (LiF) crystal or quartz crystal, depending on which characteristics of the X rays are deemed the most important when the final selection is made.

(2) Monitor Proportional Counter. A proportional counter (Fig. II-6) with a narrow field of view along the telescope axes is included in the experimental package near the telescope mirrors. Its function is to monitor any time variations of X-ray sources under observation by the focal plane instruments. The counter has a 0.5 degree FWHM collimator in front and an effective collecting area of about 600 cm<sup>2</sup>. To achieve sensitivity for both soft and hard X rays, the counter is divided into two sections. The front section has a thin organic window and a low gas pressure and the rear section has a beryllium window and a higher gas pressure. The rear counter also includes an anticoincidence section to reduce the background counting rate.

(3) Flare Detector. In the past three years, two unusually intense X-ray sources have suddenly appeared in the sky and have subsequently disappeared. The exact nature of these objects is unknown, mainly because there have been no optical or radio counterparts to these objects. It is suspected that they are due to large stellar flares within our galaxy. The HEAO-C mission will include flare detectors to survey the full sky at all times to detect the appearance of X-ray flare objects and to roughly determine their location so that more detailed observations may be performed by the focal plane experiments.

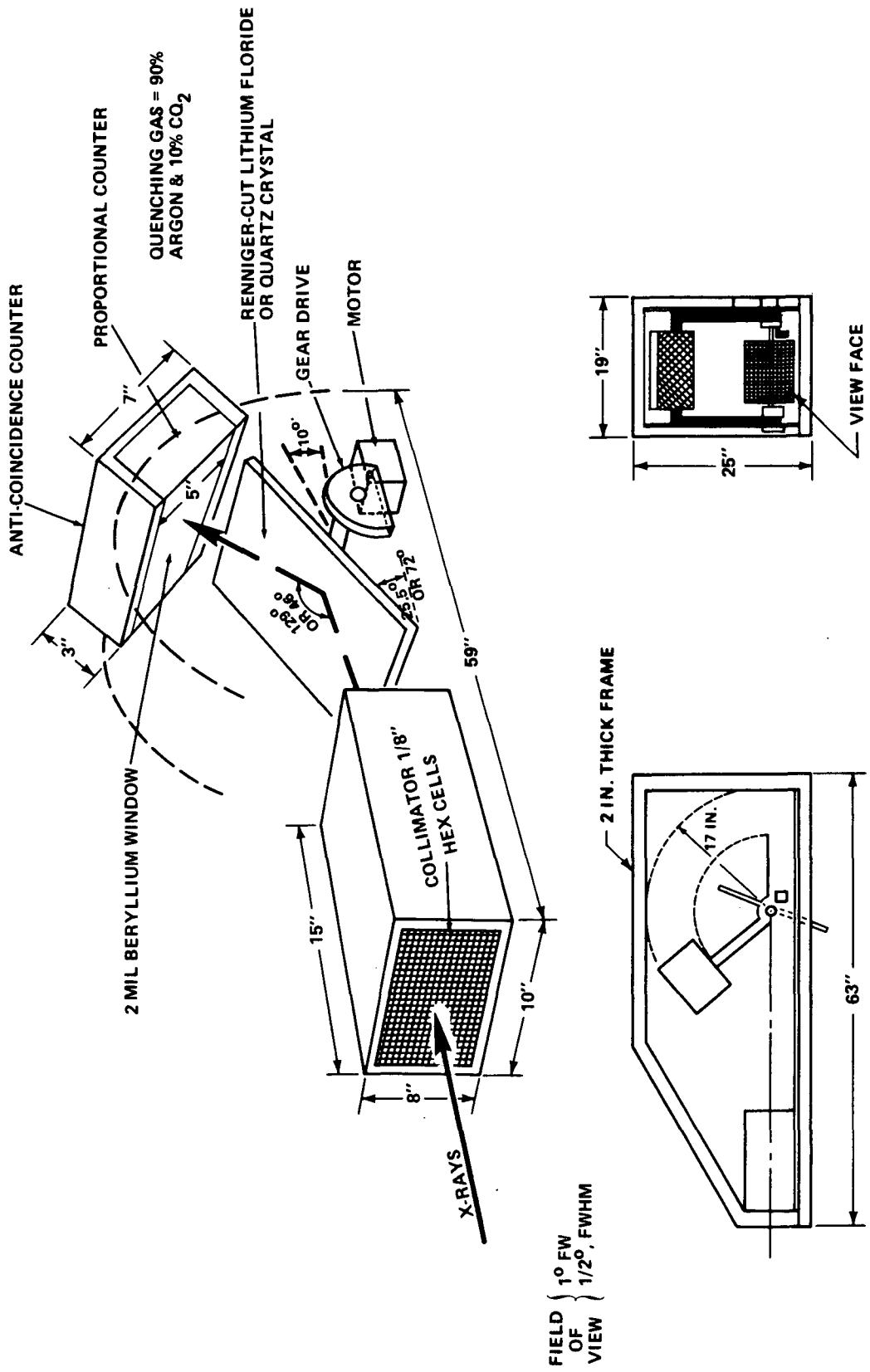


Figure II-5. Flat crystal (iron line) spectrometer — 500 cm<sup>2</sup>.

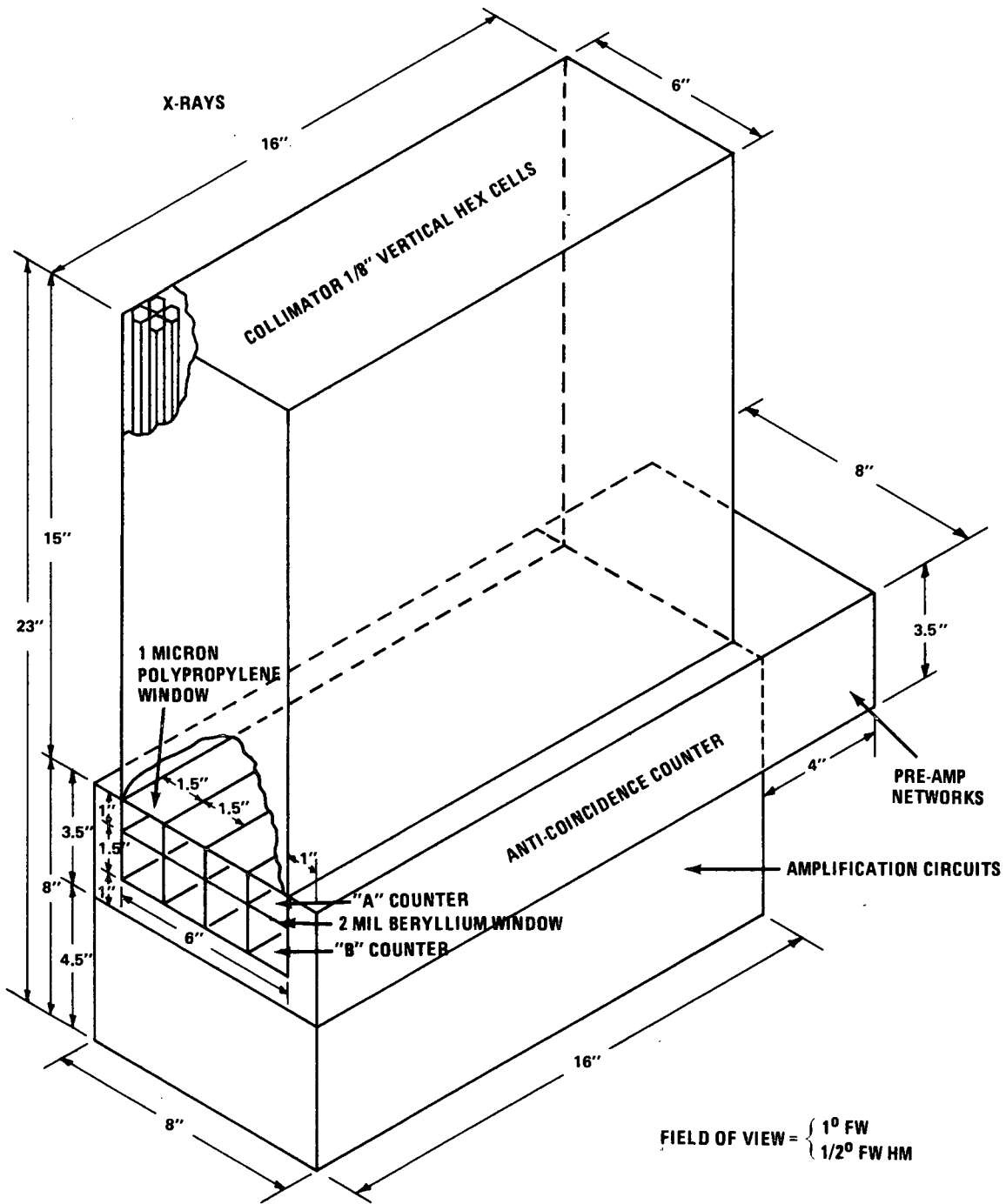


Figure II-6. Monitor proportional counter —  $620 \text{ cm}^2$ .

A coarse flare detector is shown in Figure II-7 and has a sensitivity approximately equal to 1 percent of Sco X-1 for a 1 orbit observation with a 4 degree resolution. The use of six coarse flare detectors would permit coverage of the entire celestial sphere and would be distributed on the spacecraft as shown in Figure II-2. A fine-pointing flare detector parallel to the mirror axes is used to obtain a more accurate location of the flare object; it has a resolution of approximately 30 minutes. In design, the fine flare detector is very similar to the coarse flare detector. The dimensions of the fine flare detector are different; the base is 10 by 10 inches, with an overall length of 4 feet, as compared to the coarse flare detector's 8 by 8 by 5.5 inches. All flare detectors utilize imaging proportional counters of the type previously<sup>2</sup> described. The entrance aperture of each detector is a "pinhole" with 1 cm<sup>2</sup> area.

It is informative to consider the sequence of events required to discover and study a flare. Having the coarse flare detectors recording data at all times will be desirable and striven for in the development of the HEAO-C spacecraft. After the data are recorded, they will be transmitted to the ground when the spacecraft is over a receiving station, as described in Chapter IX in more detail. Then the data will be analyzed to determine if there has been a flare. Of course, several sources in the sky are intense enough to be detected by the coarse flare detectors, so a computer program will have to screen out the known source positions.

After the position of a flare is determined using the  $\pm 4$  degree resolution capability of the coarse flare detectors, a command will have to be transmitted to the spacecraft to move it to point the fine flare detector's 8 degree field of view to the position. The fine flare detector will, then, take data and, again, the data will be transmitted to the ground when the spacecraft is over a tracking station. These data will then be analyzed to determine the position of the flare to the  $\pm 30$  minute resolution capability of the fine flare detector. This position is then telemetered to the spacecraft to point the main telescopes to the source to get the high resolution data from the source. Two of the telescopes have fields of view of 60 minutes. It will be noticed that the resolutions and fields of view must overlap sufficiently to allow us to eventually obtain the high resolution data from the flare.

#### g. Aspect and Computer Systems

(1) Aspect Determination System. Determinations of source positions and interpretation of observations require precise knowledge of the point in the sky at which the telescope is pointing. This information will be provided by the aspect determination system proposed by American Science and Engineering.

SENSITIVITY = 1% OF SCO X:1 (IN 1000 SECONDS)  
FIELD OF VIEW = 90° BY 90°  
RESOLUTION = 4°

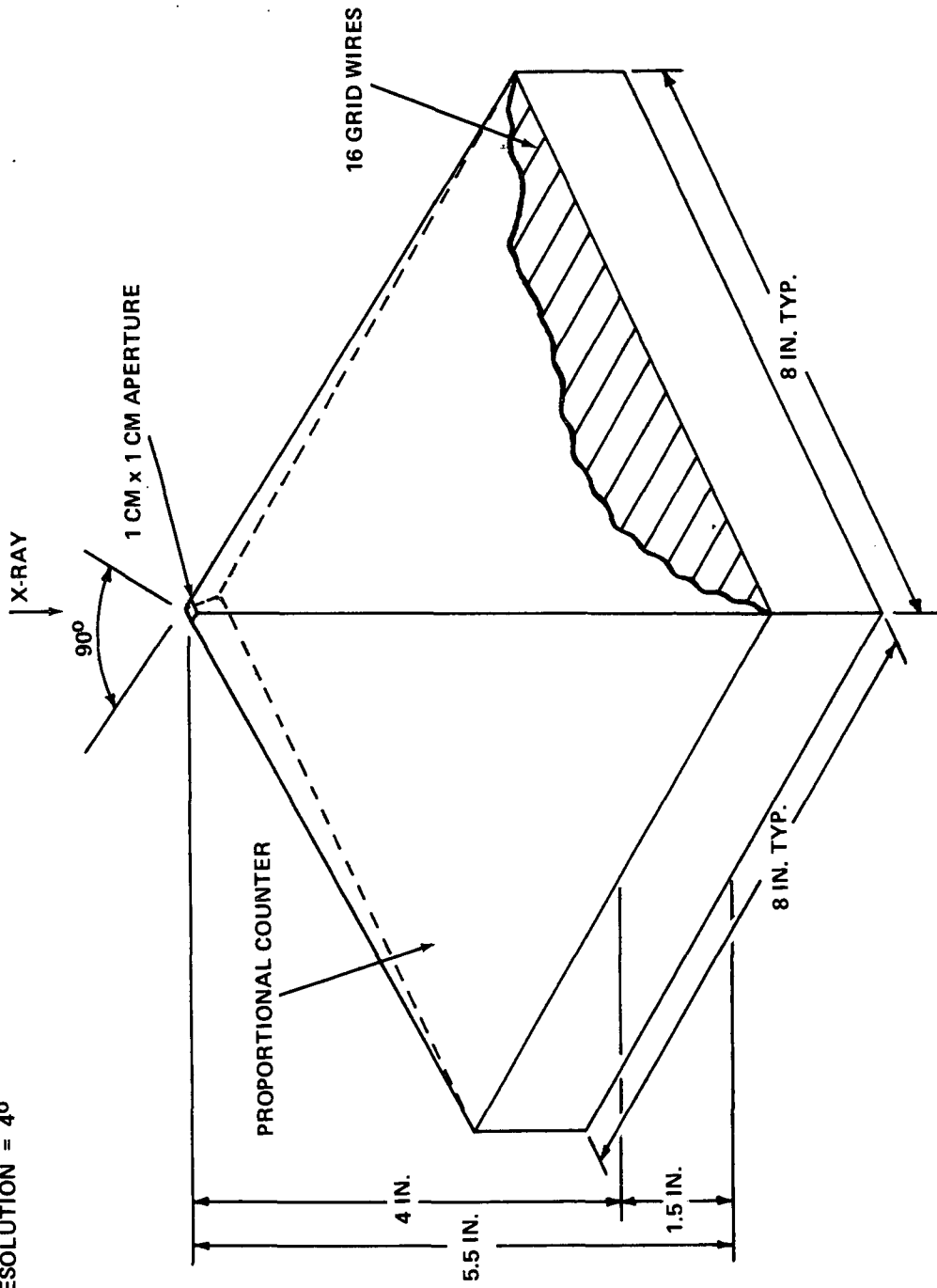


Figure II-7. Coarse flare detector.

Because the HR telescope imaging experiment requires the highest pointing accuracy, the aspect system axis is related to the HR telescope axis. The system will operate independently of the spacecraft aspect and attitude control system. It must provide aspect information which is reducible by ground processing to a precision of 1 arc second.

The imaging portion of the system will consist of an optical imaging system and an SEC vidicon camera. Locations will be referred to the centroids of the star images, since these can be located more precisely than the image sizes. Under the assumptions used, a resolution element on the face of the SEC tube corresponds to an angular resolution of approximately 10 arc seconds. Perhaps it should be kept in mind that the vertical resolution does not necessarily equal the horizontal resolution in such a system.

A fiducial light system is used to relate the line of sight of the X-ray telescope to a specific point in the sky. These lights are small sources placed in the focal plane of the X-ray telescope. Rays from the fiducial lights then pass through the X-ray imaging system (this is possible because the X-ray telescope uses grazing-incidence optics) and are reflected by means of a corner cube reflector into the aspect system. The fiducial light images then appear superimposed on the image of the star field on the vidicon face. Three or more fiducial lights will give an unambiguous position of the X-ray telescope field in the star field. The aspect system is illustrated in Figure 3.5.1-1 of Reference II-7.

In practice, the fiducial lights should be attached to the focal plane instruments themselves, so that they will correctly represent the detector positions. The design of the aspect system is insensitive to small alignment changes of the corner cube reflector, and the axes of the aspect system and X-ray telescope need not be exactly parallel. The same aspect system can be used to locate the centers of field of the LA and LE telescopes if fiducial lights and light paths are added to those telescope designs.

(2) Data Handling in Computer Subsystem. This section is included only to call attention to it and point out that it is discussed at length in Chapter IX.

## C. General Experiment Information

1. South Atlantic Anomaly Effects. Natural sources of radiation including trapped particulate radiation, cosmic rays, and earth albedo secondary cosmic radiation will produce background counting rates in the various detectors, which will ultimately determine their sensitivity. Because of the nature of the background radiation and the possibility of introducing additional secondary radiation, it is impractical and probably not advantageous to provide radiation shielding capabilities aboard the HEAO-C spacecraft beyond those internal to the detectors themselves.

Because of the sensitivity of the detectors, unshielded radioactive materials should be avoided on the spacecraft. Structural materials should be carefully screened for trace radioactive impurities of thorium and radium. Potential sources of radioactive materials in structures and subsystems have been identified for the HEAO-A mission [II-8]. The guidelines presented in Reference II-8 should be applied to the HEAO-C mission.

Trapped radiation in the region of the South Atlantic Anomaly will produce an intolerable background radiation level which will prevent useful observations from being performed. These high radiation levels may damage the detectors if they are allowed to operate during spacecraft traverses of this region. A typical form of damage is fatigue of the photomultiplier tube or electron imaging tube and depletion of the quenching gas in proportional counters. This damage may be prevented simply by removing the high voltage from these devices at a predetermined saturation limit. This limit could be sensed by the detectors themselves or by additional small detectors such as Geiger tubes placed at various positions in the spacecraft. The electronic circuits used to sense the saturation limit and turn off the high voltage are relatively simple and reliable and have been successfully used on other radiation-detecting satellites<sup>1</sup>.

Figures II-8 and II-9 show the flux contours in particles/cm<sup>2</sup>-sec for trapped protons with energies greater than 5 MeV and for electrons with energies greater than 0.5 MeV at an altitude of 500 km (270 n. mi.) [II-9]. The crosshatched areas in these figures represent the region of the HEAO-C orbit (inclination 28.5 deg). It can be seen that about one-half of the South Atlantic Anomaly will be traversed by the spacecraft. A typical particle flux that would

---

1. Holt, S.S., Private communication.

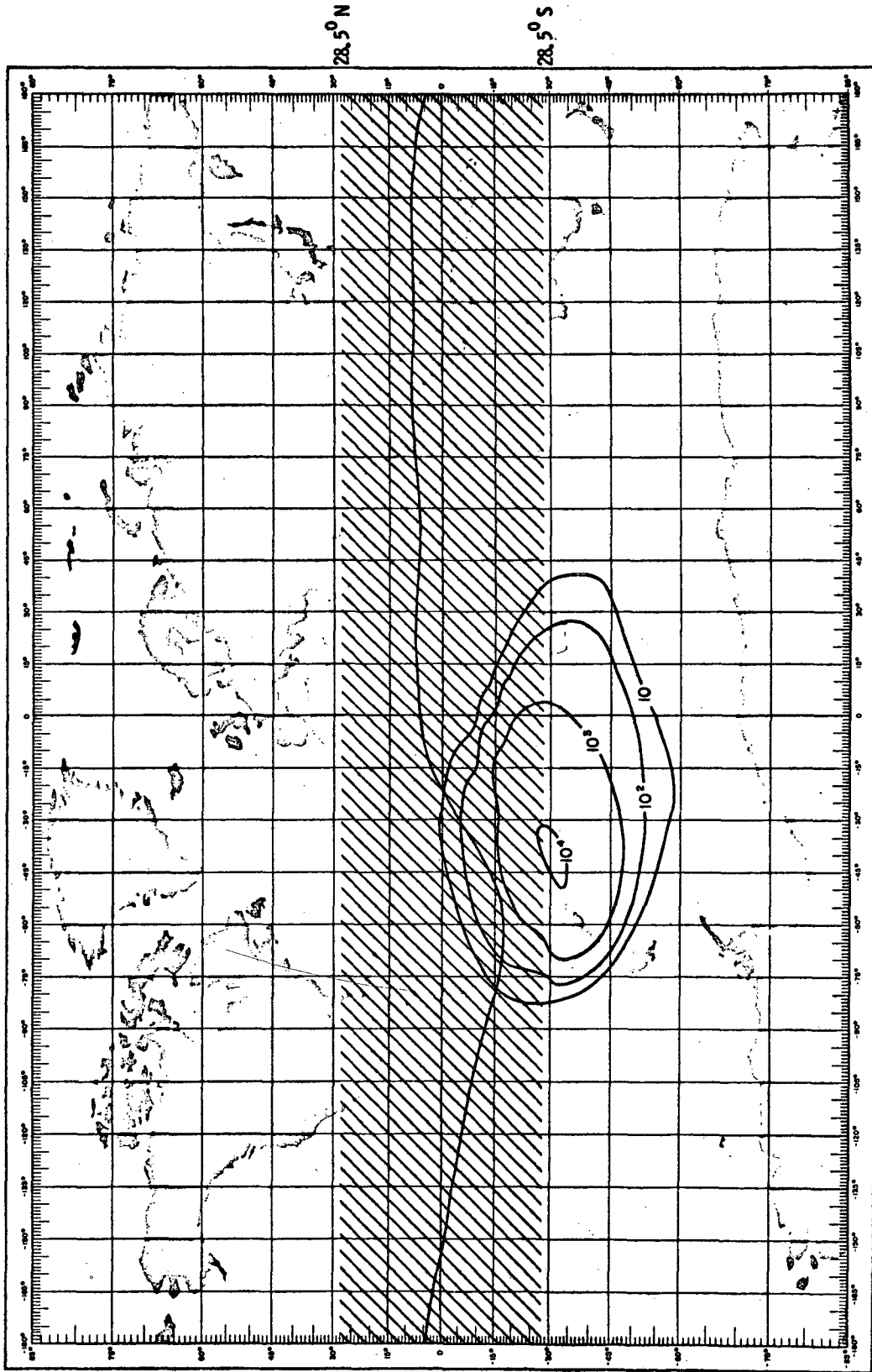


Figure II-8. Proton flux contours for E greater than 5 MeV at an altitude of 270 nautical miles.

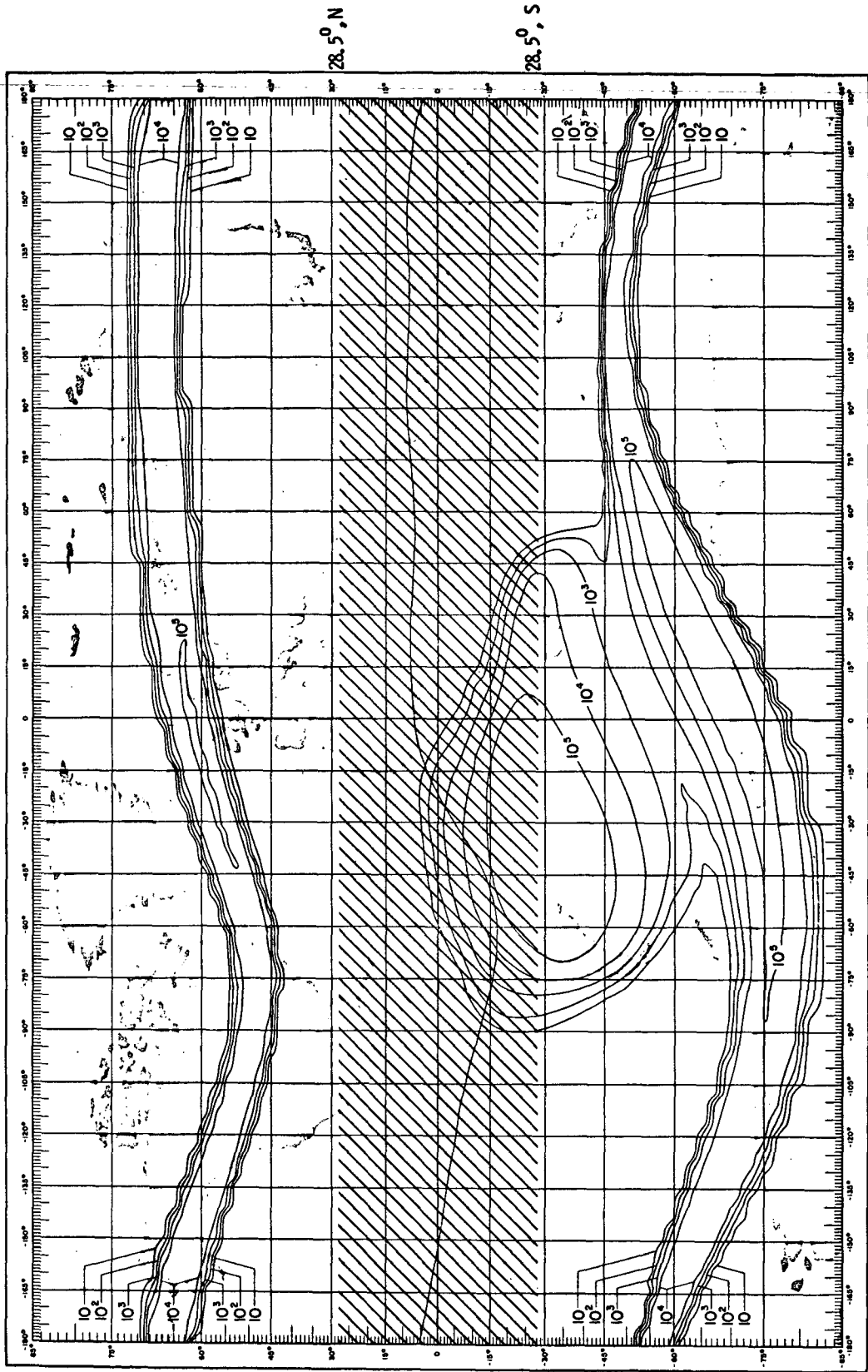


Figure II-9. Electron flux contours for  $E$  greater than 0.5 MeV at an altitude of 270 nautical miles.

produce a saturation limit in many of the detectors is  $10^3$  particles/cm<sup>2</sup>-sec. The average time the spacecraft will spend within this region is estimated to be 10 percent. However, not all of this 10 percent will be lost viewing time as some of it will coincide with target occultations, maneuvers, etc.

A representative time history of the background proton radiation over a 45 hour period is shown in Figure II-10<sup>2</sup>. Although the orbital altitude and inclination are slightly different from those of the assumed HEAO-C orbit, the general features of the time history remain the same. Earth rotation and orbital precession produce 3 to 5 successive passages through the South Atlantic Anomaly region, followed by approximately 15 hours without passing through the Anomaly. The rise and fall times of the radiation are very brief, on the order of 5 minutes. Similar time histories are obtained for the electron fluxes.

In conclusion, it seems that all X-ray experiments will need to be shut off as soon as the anomaly is entered. The quenching gas is depleted more rapidly if a large number of counts is obtained. The Orbital Astronomy Observatory (OAO) shuts off when it enters the anomaly and it is operating in the visible wavelengths. A number of principal investigators<sup>3</sup> were polled and it was found that most of them expect to shut off the high voltage circuits of their experiments in the South Atlantic Anomaly.

2. Gas Purges and Quenching Gas Quantities Required. At various times during the HEAO-C mission, the proportional counters must be purged of their gases and refilled to the proper pressure. These gases include argon and xenon and small amounts of quenching gases such as carbon dioxide and methane. The frequency of these operations will be determined by proportional counter lifetime and leakage rate information obtained from the HEAO-A experiments.

The total weight of the gas resupply system is estimated to be in excess of 11 pounds [II-7] for the HEAO-C spacecraft and is included in the experiment weights. The gas quantities required for HEAO-C are shown in

---

2. Watts, J.W., Jr.: Charge Particle Dose Rate in Low Altitude, 30 Degree Inclination Orbit. R-RP-INN-67-5, Marshall Space Flight Center.

3. Dr. Leon van Speybrock (April 30, 1971), Drs. Elihu Boldt and Steve Holdt (April 30, 1971), Dr. James Underwood (April 30, 1971), and Mr. James Milligan (April 6, 1971).

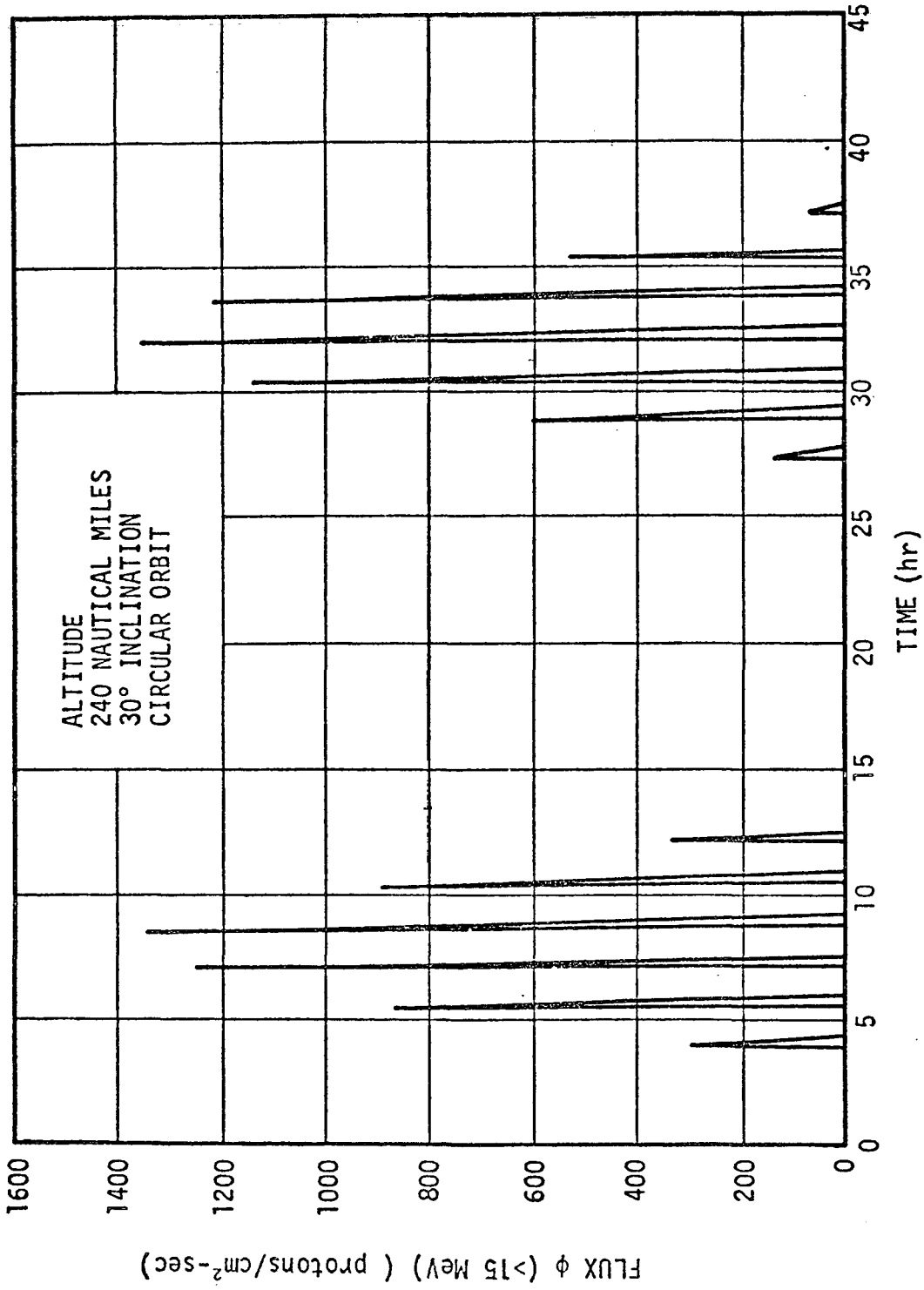


Figure II-10. Proton flux in the South Atlantic Anomaly.

Table II-6. The gas quantities required are much less than in HEAO-A and -B because the detector faces are so much smaller and, therefore, leak less gas. It is assumed that the counter gases will be vented to outer space in a manner which will not introduce serious disturbance torques to the spacecraft, i. e., slowly and through a nonpropulsive vent.

TABLE II-6. PURGING AND QUENCHING GAS QUANTITIES REQUIRED

Experiment	Counter Gas	Amount Of Resupply Gas Needed
Large Area Image Detector	Propane	1 lb
Monitor Proportional Counter		
Counter A	Propane	10
Counter B	90% argon, 10% CO <sub>2</sub>	0
Coarse Flare Detector	90% argon, 10% CO <sub>2</sub>	0
Fine Flare Detector		0
Low Energy Telescope		1 liter

3. Calibration of Experiments. The experiments will have to be calibrated for the subsequent data to be effectively interpreted. There are two possibilities for calibration: (1) external calibration and (2) internal calibration. External calibration will simply consist of choosing a known stable stellar source and performing the standard observations and data recording on it. Since the magnitude and other parameters of the source are already known, a zero point, or baseline, has been established for the later observations.

The second alternative of internal calibration will also probably be pursued. This will simply amount to choosing a known radioactive source of a certain flux and including it in the spacecraft behind an appropriate shield. At appropriate times, the source would be swung out into the field of view of the experiment and measurements will be taken to determine the efficiency of the detector at that moment, again establishing a zero point or baseline for subsequent observing.

It might also be possible to place the internal sources where they are visible to the experiments in their resting positions outside of the focal plane positions. This would allow the detectors to be checked while they are not in position to take data and would result in a more efficient operation.

After the initial spacecraft and experiment checkout period, the calibrations will probably be executed periodically. It is possible that the initial calibration will be in real time, but the later calibrations will probably be in a recorded mode. In the present timeline, simultaneous external and internal calibrations have been scheduled on a monthly basis. This is scheduled in the timelining in Chapter III.

However, it has been suggested that the internal calibrations will be performed more frequently since they are less trouble and that they might be performed as often as once per orbit, with an external calibration performed as often as once per week. This area will have to be investigated further but of course will never be known until the actual orbital conditions are experienced and operation of the detectors and experiments demonstrates how quickly they change and, therefore, need to be checked and calibrated.

An additional point that may be mentioned is the possibility of moving the experiments about in the focal plane after an external calibration suggests what movement is desirable. However, the calibration data would have to be analyzed on the ground and, then, commands would have to be sent to initiate the move and, possibly, another calibration would have to be done to see if the proper correction was made. The second calibration data would again have to be analyzed on the ground and, in view of the amount of time this procedure would take, it would seem desirable to avoid it in most cases.

The calibration procedure will presumably consist of observing the calibration source for a given time,  $T_c$ , and then checking the detector output against the desired values. It is not yet clear whether all experiments can be calibrated simultaneously or whether other experiments can operate while one is being calibrated. There are, then, three possible calibration sequences; they are listed in Table II-7 for the three major telescopes only.

TABLE II-7. CALIBRATION SEQUENCES

	Time	HR Telescope	LA Telescope	LE Telescope
Simultaneous Calibration	$0 \rightarrow T_c$	Calibrate each detector as prescribed by calibration routine		
Calibration Combined with Observation	$0 \rightarrow T_c$	Calibrate as prescribed	Free for desired project	
	$T_c \rightarrow 2T_c$	Free for desired project	Calibrate as prescribed	Free for desired project
	$2T_c \rightarrow 3T_c$	Free for desired project		Calibrate as prescribed
Sequential Calibration	$0 \rightarrow T_c$	Calibrate as prescribed	Off	Off
	$T_c \rightarrow 2T_c$	Off	Calibrate as prescribed	Off
	$2T_c \rightarrow 3T_c$	Off	Off	Calibrate as prescribed

4. Launch Environment Tolerated by Experiments. This area needs more study because it is a difficult one in which to obtain good information. There is concern about subjecting the experiments to high launch loads. Since experiment design is fairly coarse at this point and a detailed dynamic analysis of the total flight vehicle has not been performed, the loads at the experiments have not been determined. To ensure adequate protection, shock-mounting of the optical bench was provided.

When asked about this problem, all of the principal investigators believed they would be able to build experiments to withstand the launch environment. In expressing his outlook on the problem, Dr. James Underwood (April 30, 1971) said he could accept the ATM launch constraints. Dr. Leon van Speybrock (February 1971) said he expected the experiments to withstand a 6 g acceleration and pointed out that the Baez telescope was the experiment most

susceptible to vibration. The experiment environment is discussed further in section 4 of Reference II-10.

5. Spacecraft Degraded Mode Operation. An effort was made to evaluate the reliability of the spacecraft and experiments to determine the redundancy and failure mode provisions required in the spacecraft subsystems. The experiments are only in the preliminary stages of development and, therefore, it is difficult to assess their situation as far as reliability and failure modes. As part of this assessment, we attempted to assign a relative value to the experiments so that the greatest amount of subsystem redundancy could be placed in areas of greatest experiment value. Tables II-8 and II-9 show this assessment in terms of the expected operating times of the experiments.

Table II-10 shows our crude estimate of the percentage of science lost if a particular experiment is lost. Our subsystems are traded off on the basis of these estimates and the one graphed in Figure II-11. Figure II-11 crudely depicts the idea that since the HEAO-C spacecraft covers the sky every six months, each successive pass yields less important data. This is assuming that no flares occur and that the principal investigators would concentrate on collecting the most important data first. It is realized that many points could be made in this area and it would be appreciated if the reader would provide a more tenable graph.

#### D. Relationship of HEAO-A and -B to HEAO-C

In contrast to the experiments on the HEAO-A and -B satellites which study hard and soft X rays and gamma rays, the experiments proposed for HEAO-C concentrate on the soft to medium hard X-ray wavelength range, 1 to 100 Å or, roughly, 0.10 to 10 keV. Other comparative facts about the three payloads are shown in Table II-11. In the pointing area, the Announcement of Flight Opportunities for HEAO-A and -B offered a  $\pm 1$  degree spin axis control but, since then, it has been decided to use CMGs for all of the HEAO missions, and the ones to be used are capable of giving the A and B spacecrafts  $\pm 3$  arc minutes control accuracy. (This is the reason for the  $\pm 3$  arc minutes shown in Table II-11.)

The X-ray experiments on HEAO-A and -B are intended to be used in a scanning mode mainly for detecting new sources and determining their locations with moderate precision. The HEAO-C, on the other hand, is designed for a

TABLE II-8. HEAO-C OPERATIONAL EXPERIMENT TIME

	Telescope Experiments (%)	Coarse Flare Detectors (%)	Fine Flare Detectors (%)	Flat Crystal Spectrometer (%)	Monitor Proportional Counter (%)
Experiment in Operation	70	90	1	15	75
South Atlantic Anomaly	5	5			5
Target Occultation	7	-			7
Calibrations	5	5			5
Transporting Experiments	5	-			-
Spacecraft Motions	8	-			8
Strong Source or Flare not in Field of View	-	-			-
Total	100	100	100	100	100

Included in This Number → (from Fine Flare Detectors to Flat Crystal Spectrometer)  
 Included in This Number → (from Fine Flare Detectors to Monitor Proportional Counter)

TABLE II-9. HEAO-C TELESCOPE EXPERIMENT OPERATIONAL TIME

	High Resolution Telescope (%)	Large Area Telescope (%)	Low Energy Telescope (%)	Total Sources Observed <sup>a</sup> (%)
Image Observations	35 (HRID)	25 (LAID)	66 (PSD and LBD)	2000
Nondispersive Spectrometry	30 (FWHR)	50 (SSD) 25 (FWLA)	33 (FWLE)	1000
Spectrometry Observations with Objective (Transmission) Grating	25 (OG)	—	—	500
HR Curved Crystal Spectrometer	10 (CCS)	—	—	40 brightest sources
Total	100	100	100	

a. Percent of sources studied does not equal percent of time spent.

TABLE II-10. SCIENTIFIC WORTH LOST DUE TO MALFUNCTION

Loss of	Reduction of Science (%)	Reduction of Data Rate (%)
HR Telescope	60	50
Imaging	50	40
Spectrometer	10	10
LA Telescope	25	
Position	10	
Spectrometer	15	
LE Telescope	15	
Position	10	
Spectrometer	5	
Effect of 50% Loss of Experiment Power		
Case 1: Half Data Rate, Twice as Long, 90% of Science Accomplished		50
Case 2: Full Data Rate, Half Time, 60% of Science		0

TABLE II-11. COMPARISON OF HEAO-A AND -B TO HEAO-C

	A and B	C
Experiment Weight	12 500 lb	6875 lb
Pointing Required	±1 deg (±3 arc min)	±1 arc min
Smallest Field of View	1 deg × 1 deg	2.1 × 2.1 arc min
Objectives	Locating Sources	Studying Sources
Mode	Scanning	Pointing
Sources Known at Launch	100	3000 to 4000

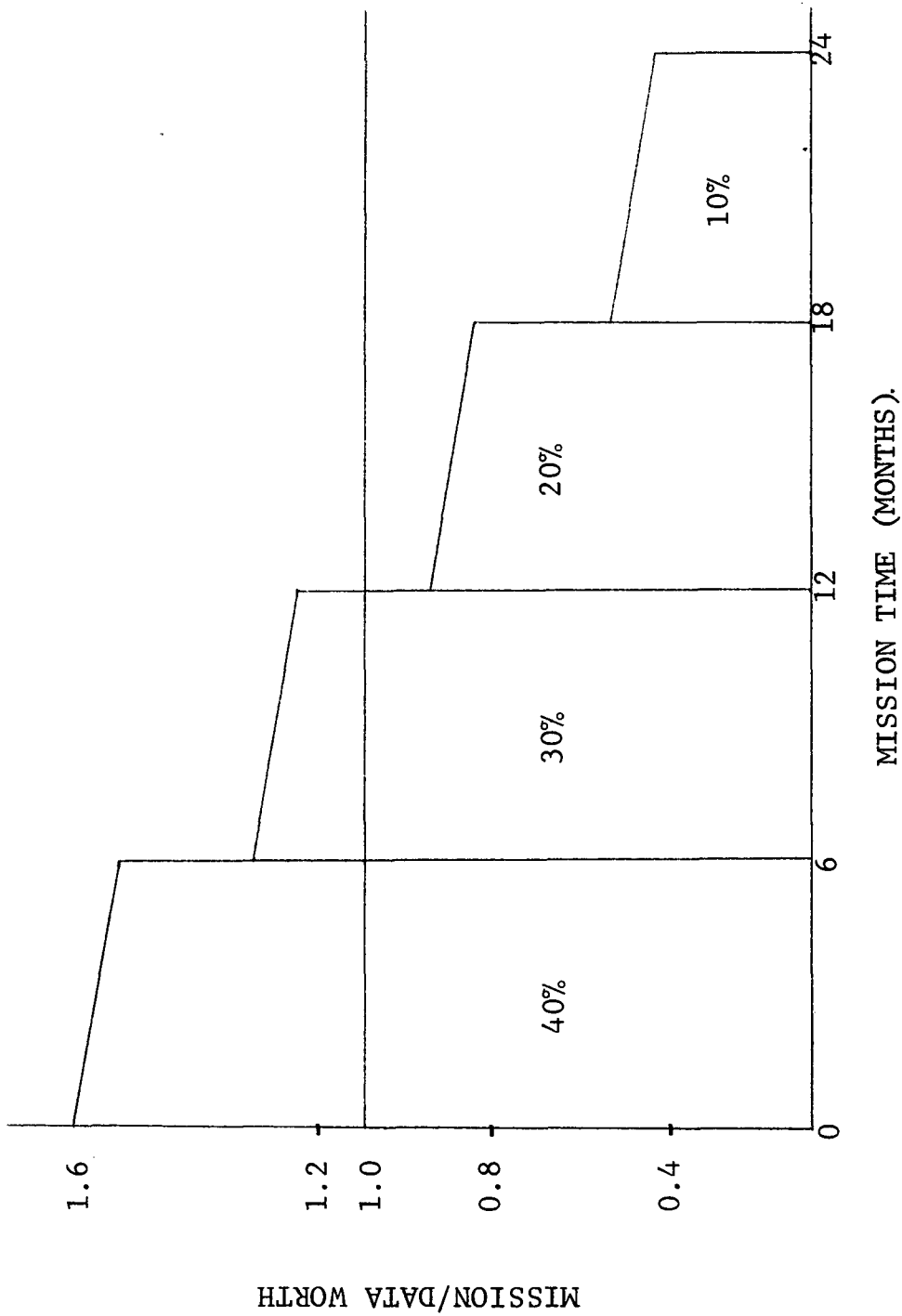


Figure II-11. Mission data worth versus time.

pointing mode to make detailed observations of the X-ray sources found by the two earlier satellites. The sources known at launch are estimates, the number in the A and B column estimated by Stephen Larson and the number in the C column estimated by Dr. Riccardo Giacconi.

## E. Recommendation for Phase B Study

More study effort should be placed on long-lead-time items such as the telescope mirrors. A more detailed analysis should be made of the data to be generated by the experiments, the required modes and sequences of operation of experiments, and the resulting requirements for the experiment computer.

## REFERENCES

- II- 1. Morrison, P.: Annual Reviews of Astronomy and Astrophysics, vol. 5, 1967, p. 325.
- II- 2. Rossi, B. B.: IAU Symposium No. 31, 1967, p. 439.
- II- 3. Pounds, K. A.: Nature, vol. 229, 1971, p. 303.
- II- 4. Dolan, J. F.: Astronomical Journal, vol. 75, 1970, p. 223.
- II- 5. Giacconi, R., et al.: Bulletin American Astronomical Society, vol. 3, 1971, p. 236.
- II- 6. Anon.: Sky and Telescope, vol. 41, 1971, p. 341.
- II- 7. Giacconi, R., et al.: Large Orbiting X-Ray Telescope for the HEAO. 2410-I, American Science and Engineering, Cambridge, Massachusetts, May 27, 1970.
- II- 8. Matteson, J.L.; Pelling, A.M.; and Peterson, L.E.: Radioactivity Specifications for HEAO-A and B. Document No. 2785-71-02, University of California, San Diego, 1971.
- II- 9. Stassinopoulos, E.G.: World Maps of Constant B, L, and Flux Contours. NASA SP-3054, Goddard Space Flight Center, 1970, pp. 23 and 77.
- II-10. HEAO Experiment Developer's Handbook. HSE 3015-1MSFC, February 23, 1971.

## TABLE OF CONTENTS

	Page
A. Orbit Selection and Lifetime Analysis . . . . .	III- 1
B. Titan IID/OAS Performance . . . . .	III-12
1. Assumptions . . . . .	III-12
2. Trajectory Profile . . . . .	III-13
3. Dispersion Analysis . . . . .	III-13
C. Occultation and Source Viewing . . . . .	III-17
1. Earth Occultation of Sun . . . . .	III-17
2. Target Source Viewing Accessibility . . . . .	III-26
a. Background Comments . . . . .	III-26
b. Target Source Viewing Opportunity . . . . .	III-27
3. HEAO Viewing and Target Acquisition Time Capability . .	III-40
D. Manned Space Flight Network Tracking and Data Acquisition Network Analysis . . . . .	III-46
E. Mission Timelines . . . . .	III-64
1. Purpose . . . . .	III- 64
2. Prelaunch Activities . . . . .	III-65
3. Launch-to-Orbit and Orbit Correction . . . . .	III-65
4. On-Orbit Experiment Operations . . . . .	III-69
5. Source Viewing Logic . . . . .	III-70
6. Gross Timeline . . . . .	III-70
7. Normal Viewing Day . . . . .	III-75
8. Scan of a Large Source . . . . .	III-77
9. Long Dwell Time on a Single Source . . . . .	III-77
10. Flare Observation Between $\pm 15$ Degree and $\pm 30$ Degree Band . . . . .	III-77
11. Flare Observation 180 Degrees from Sun . . . . .	III-80
12. Calibration of Experiments . . . . .	III-80
13. Loss and Reacquisition of Reference . . . . .	III-80
References . . . . .	III-86
Bibliography . . . . .	III-86

# LIST OF ILLUSTRATIONS

Figure	Title	Page
III-1.	Geometry for minimum average drag . . . . .	III- 3
III-2.	Geometry for maximum average drag . . . . .	III- 4
III-3.	HEAO-C configuration with OAS . . . . .	III- 5
III-4.	Drag coefficient for HEAO-C/OAS . . . . .	III- 6
III-5.	Variation in orbit lifetime with vehicle mass for HEAO-C . . . . .	III- 7
III-6.	Variation in orbit lifetime with vehicle mass for HEAO-C/OAS . . . . .	III- 8
III-7.	Variation in altitude with time for a 140 by 250 nautical mile altitude initial orbit . . . . .	III- 9
III-8.	Variation in altitude with time for a 100 by 300 nautical mile altitude initial orbit . . . . .	III-10
III-9.	Variation in percent experiment shutdown with altitude for circular orbits . . . . .	III-11
III-10.	Nominal Titan IID/OAS HEAO-C flight profile . . . . .	III-14
III-11.	Off-nominal Titan IID/OAS HEAO-C flight profile . . . . .	III-15
III-12.	Titan IID payload versus perigee altitude . . . . .	III-19
III-13.	Geometry of occultation parameters . . . . .	III-21
III-14.	Earth occultation of sun from earth orbit versus time . . . . .	III-22
III-15.	Earth occultation of sun from earth orbit versus altitude . . . . .	III-23
III-16.	Earth occultation of sun from earth orbit versus ascending node . . . . .	III-24

## LIST OF ILLUSTRATIONS (Continued)

Figure	Title	Page
III-17.	Earth occultation of sun from earth orbit versus orbit inclination . . . . .	III-25
III-18.	Definition of $\pm 15$ degree and $\pm 30$ degree access bands . . . . .	III-27
III-19.	Viewing planes in the equatorial coordinate system . . . . .	III-29
III-20.	Viewing area, equatorial coordinate system, 21 June . . . . .	III-30
III-21.	Viewing planes in the ecliptic coordinate system . . . . .	III-32
III-22.	Area of celestial sphere accessible to HEAO viewing . . . . .	III-33
III-23.	Cummulative percentage of area exposed to $\pm 15$ degree and $\pm 30$ degree viewing bands. . .	III-35
III-24.	Number of days required for viewing band to reach a source . . . . .	III-37
III-25.	Time of year to view a given point, ecliptic system . . . . .	III-38
III-26.	Maximum number of days a source is accessible for 180 days in orbit. . . . .	III-39
III-27.	Maximum source viewing time . . . . .	III-41
III-28.	Number of days required to reach a source . . . . .	III-42
III-29.	Number of sources able to be viewed by HEAO, 0 degree cone angle . . . . .	III-43
III-30.	Number of sources able to be viewed by HEAO, 15 degree cone angle . . . . .	III-44

## LIST OF ILLUSTRATIONS (Concluded)

Figure	Title	Page
III-31.	Areas within view on 21 June . . . . .	III-45
III-32.	Ground traces for Network Configuration A. . . . .	III-53
III-33.	Ground traces for Network Configuration B. . . . .	III-54
III-34.	Ground traces for Network Configuration C. . . . .	III-55
III-35.	Ground contact statistics for Network Configuration A . . . . .	III-58
III-36.	Ground contact statistics for Network Configuration B . . . . .	III-60
III-37.	Ground contact statistics for Network Configuration C . . . . .	III-61
III-38.	Prelaunch activities . . . . .	III-66
III-39.	Countdown of key events . . . . .	III-67
III-40.	Block logic of celestial sphere . . . . .	III-71
III-41.	Gross timeline. . . . .	III-72
III-42.	Normal viewing day . . . . .	III-75
III-43.	Scan of a large source. . . . .	III-78
III-44.	Long dwell time on a single source . . . . .	III-79
III-45.	Flare observation within 30 degree cone. . . . .	III-81
III-46.	Flare observation (antisolar viewing) . . . . .	III-82
III-47.	Calibration of experiments. . . . .	III-83
III-48.	Loss and reacquisition of reference. . . . .	III-84

## LIST OF TABLES

Table	Title	Page
III-1.	OAS Weight Summary for Stripped-Down Stage Weight . . . . .	III-12
III-2.	Summary of Open-Loop Accuracy . . . . .	III-16
III-3.	OAS Nominal and Off-Nominal Performance to 270 Nautical Mile, 28.5 Degree Circular Orbit . . . . .	III-18
III-4.	Earth Occultation of Sun from Earth Orbit for an Orbital Altitude of 270 Nautical Miles and an Orbital Period of 94.6 Min . . . . .	III-26
III-5.	MSFN Station Locations . . . . .	III-47
III-6.	Contact Summary of Tracking Stations with HEAO-C for Configuration A . . . . .	III-50
III-7.	Contact Summary of Tracking Stations with HEAO-C for Configuration B . . . . .	III-51
III-8.	Contact Summary of Tracking Stations with HEAO-C for Configuration C . . . . .	III-52
III-9.	MSFN Coverage Summary . . . . .	III-63
III-10.	Boost-to-Orbit Sequence of Events . . . . .	III-68

## CHAPTER III. MISSION ANALYSIS

This chapter presents an analysis of mission requirements of the HEAO-C, third in a sequence of High Energy Astronomy Observatory missions.

The approach to the study was, first, to select the preferred orbit. The orbit selection was based primarily on the requirement for a two year circular orbit lifetime consistent with the payload capabilities of the Titan IID/OAS<sup>1</sup> launch system. After orbit selection, consideration was given to the performance capability of the launch vehicle to the desired 270 nautical mile orbit. Both the nominal orbital insertion conditions and the off-nominal (considering guidance dispersions) orbital injection conditions were taken into account. Next, investigations were undertaken of the range of occultation parameters to determine the maximum and minimum occultation time per orbit and to establish the target source viewing and accessibility and the HEAO-C viewing and target acquisition capability.

To insure the compatibility of the HEAO-C with the ground network, three prime tracking network configurations in the Manned Space Flight Network were selected for comparison analysis, based on evaluation of the ground contact statistics and data processing capabilities. To integrate the various mission analysis activities and spacecraft systems into a totally integrated mission, timelines were prepared which identify the mission and operation activities that are representative of those that would be performed during the two year HEAO-C mission.

### A. Orbit Selection and Lifetime Analysis

The various lifetime and orbit selection parameters considered in the HEAO-C orbit selection analysis included spacecraft mass, spacecraft orientation, orbital altitude, launch date, and experiment interference induced by Van Allen radiation. The effects on orbital lifetime of spacecraft mass and orientation are reflected in the computation of the spacecraft ballistic coefficients. Launch date was a parameter because of the variation of atmospheric density with time induced by variations in solar activity. Experiment interference by trapped radiation was investigated because the use of the Titan IID launch vehicle gave the capability of spacecraft insertion into high initial altitude orbits.

---

1. OAS — Orbit Adjust Stage.

An "average" spacecraft orientation approach was utilized for computing drag, wherein the spacecraft was assumed to be deployed through various random orientations throughout its two year lifetime. In Figures III-1 and III-2 the pointing mode sun-star-orbital plane geometries are shown for minimum and maximum average drag, respectively. In this mode the spacecraft orientation remains fixed inertially with the longitudinal axis of the spacecraft aimed at the particular star of interest. Minimum average drag in this mode would occur when the star lies in the orbital plane and maximum average drag would occur when the earth-star line is perpendicular to the orbital plane. Average drag as used here implies an average over one orbital revolution.

The HEAO-C configuration with the OAS attached is shown in Figure III-3. The angle-of-attack employed in the orbital drag calculations is shown defined in the X-Z plane. In Figure III-4 the orbital drag coefficient for the HEAO-C configuration with and without the OAS attached is presented versus angle-of-attack. For the OAS attached case, the drag coefficient is shown for angles-of-attack from 0 to 360 degrees because of body asymmetry. As demonstrated by this figure, leaving the OAS attached increases the spacecraft maximum drag coefficient from 12.1 to 15.5.

The lifetime data for the HEAO-C configuration were computed assuming spacecraft deployment through various orientations. Therefore, maximum and minimum drag coefficients were used to define the upper and lower limits on orbital lifetime. The variation in orbital lifetime with vehicle mass for the HEAO-C configuration with and without the OAS attached is shown in Figures III-5 and III-6, respectively. The data shown are for a launch date of March 21, 1977, and initial circular orbital altitudes of 250 and 270 nautical miles. The maximum and minimum drag values for a given initial injection altitude define a band in which lifetimes for all spacecraft pointing orientations would be confined. Similar lifetime data for other launch dates, injection altitudes, and parameters can be found in Appendix B. From inspection of these figures it can be seen that for a 14 353 pound spacecraft with the OAS removed, a 265 nautical mile initial orbital altitude should be adequate to guarantee a two year lifetime even for a worst-drag orientation and a  $+2\sigma$  solar density. Leaving the OAS attached (15 585 pounds) requires approximately an additional 10 nautical miles or 275 nautical mile initial orbital altitude for a guaranteed two year lifetime for worst case conditions.

Prior to circular orbit injection, the OAS and spacecraft ascend after launch vehicle separation via elliptical orbit. A 140 by 250 nautical mile ascent ellipse was considered nominal (see Section 2). The lifetime of the spacecraft

- FIXED-POINTING MODE OF OPERATION
- VIEWED STAR IS IN THE ORBITAL PLANE AND THE SUN IS IN A PLANE NORMAL TO THE EARTH-STAR LINE

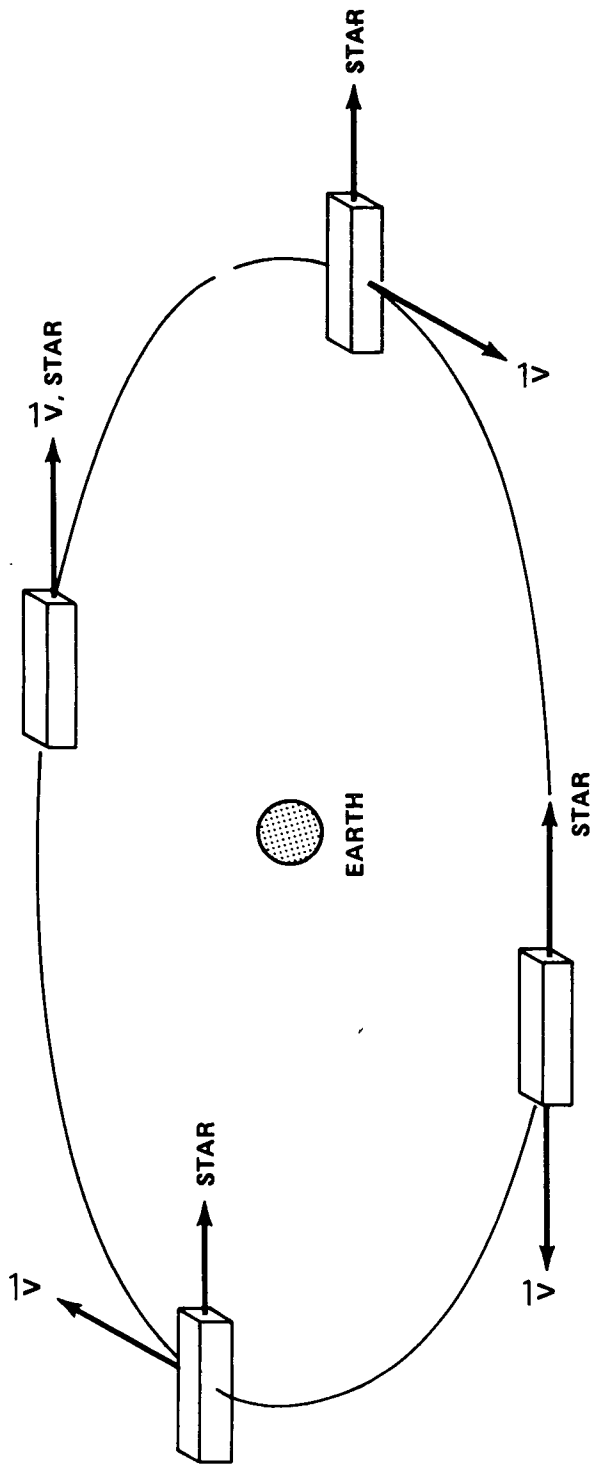


Figure III-1. Geometry for minimum average drag.

- FIXED-POINTING MODE OF OPERATION

- SUN IS IN THE ORBITAL PLANE AND EARTH-STAR LINE IS NORMAL TO THE ORBITAL PLANE

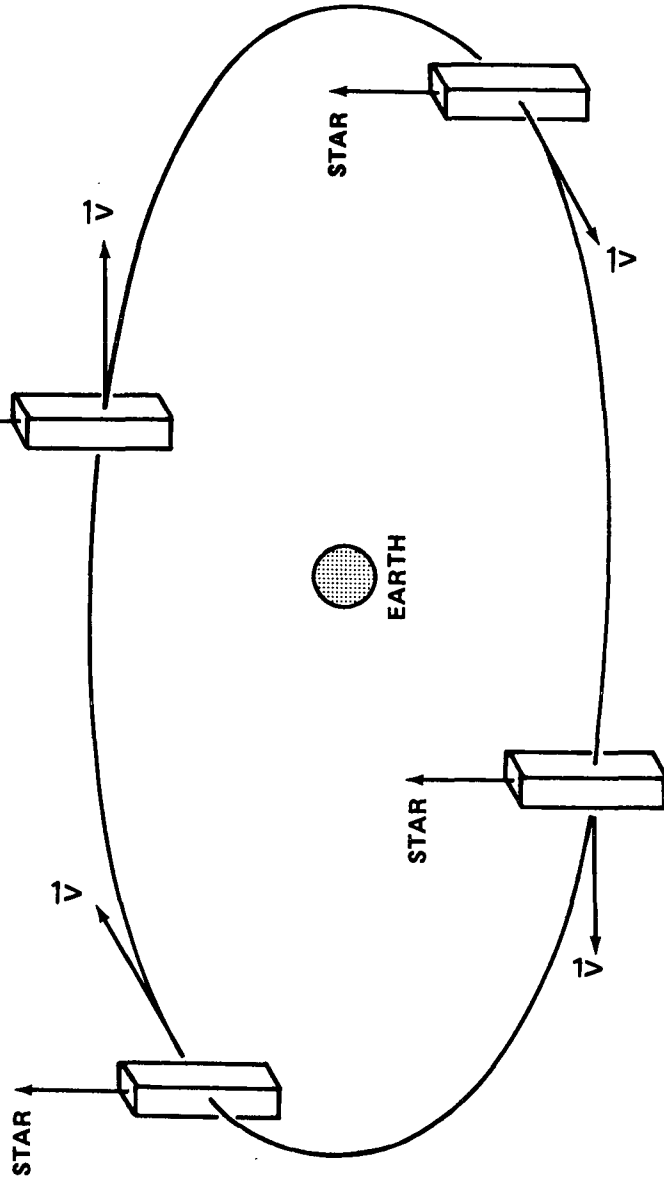


Figure III-2. Geometry for maximum average drag.

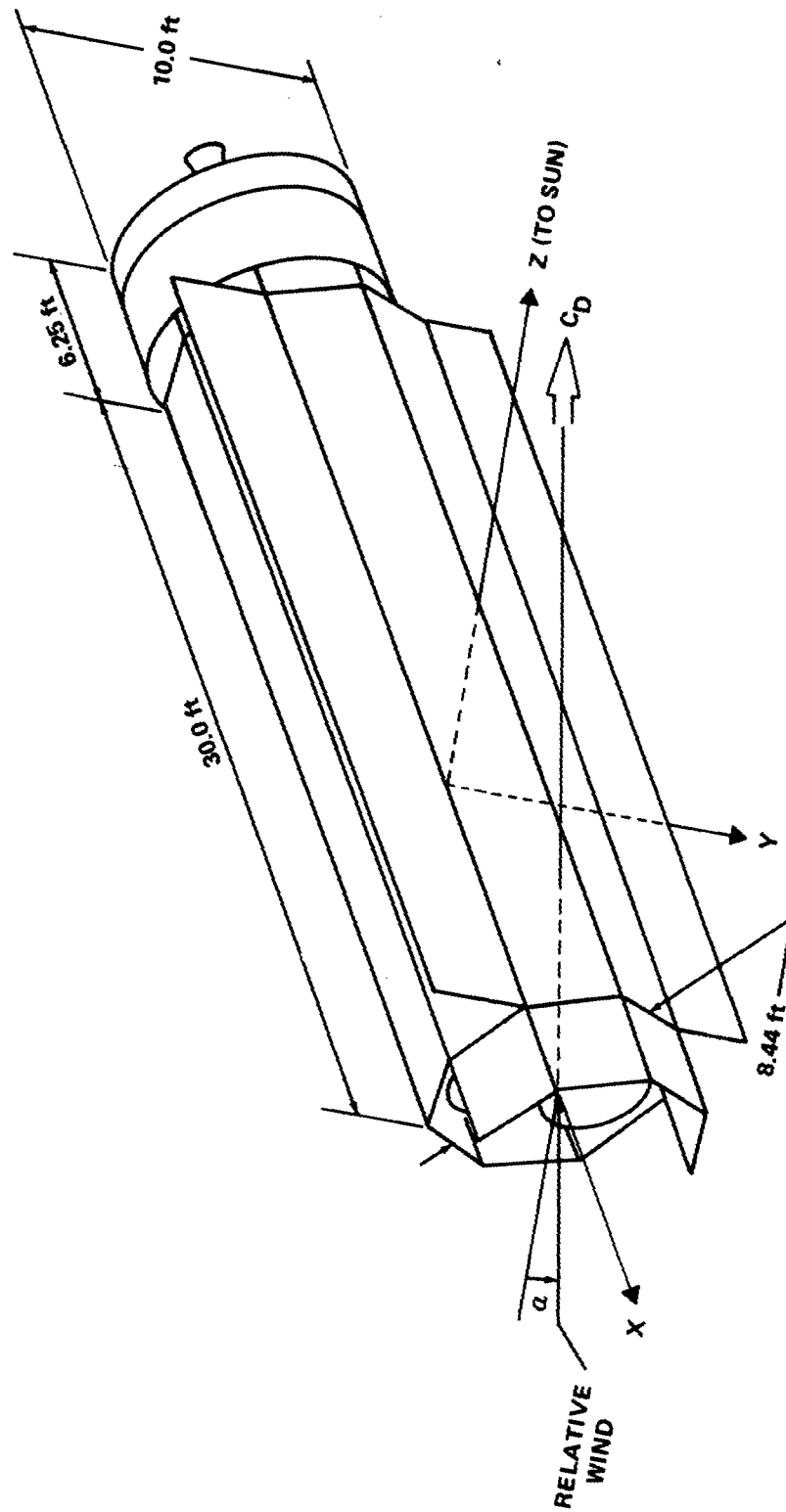


Figure III-3. HEAO-C configuration with OAS.

- ALTITUDE: 250 n. mi.
- REFERENCE AREA: 55.9467 ft<sup>2</sup>
- DIFFUSE REFLECTION;  
FREE MOLECULAR FLOW

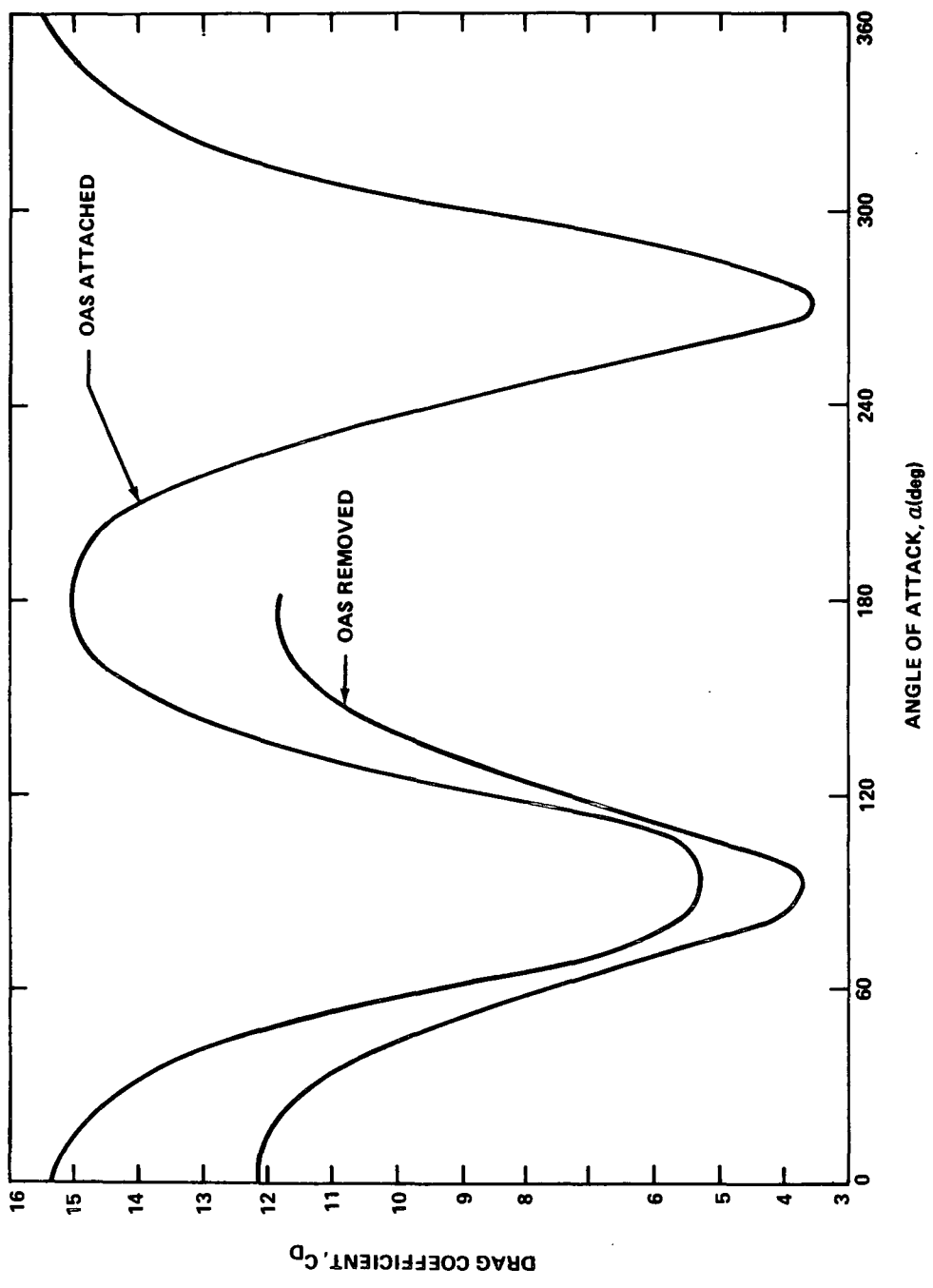


Figure III-4. Drag Coefficient for HEAO-C/OAS (fixed pointing mode).

- LAUNCH DATE: 3/21/77
- CIRCULAR ORBIT/28.5 deg INCLINATION
- ATMOSPHERE MODEL: MSFC MODIFIED 1967
- JACCHIA + 2 $\sigma$  DENSITY
- CODE: ——— MAX DRAG
- ——— MIN DRAG

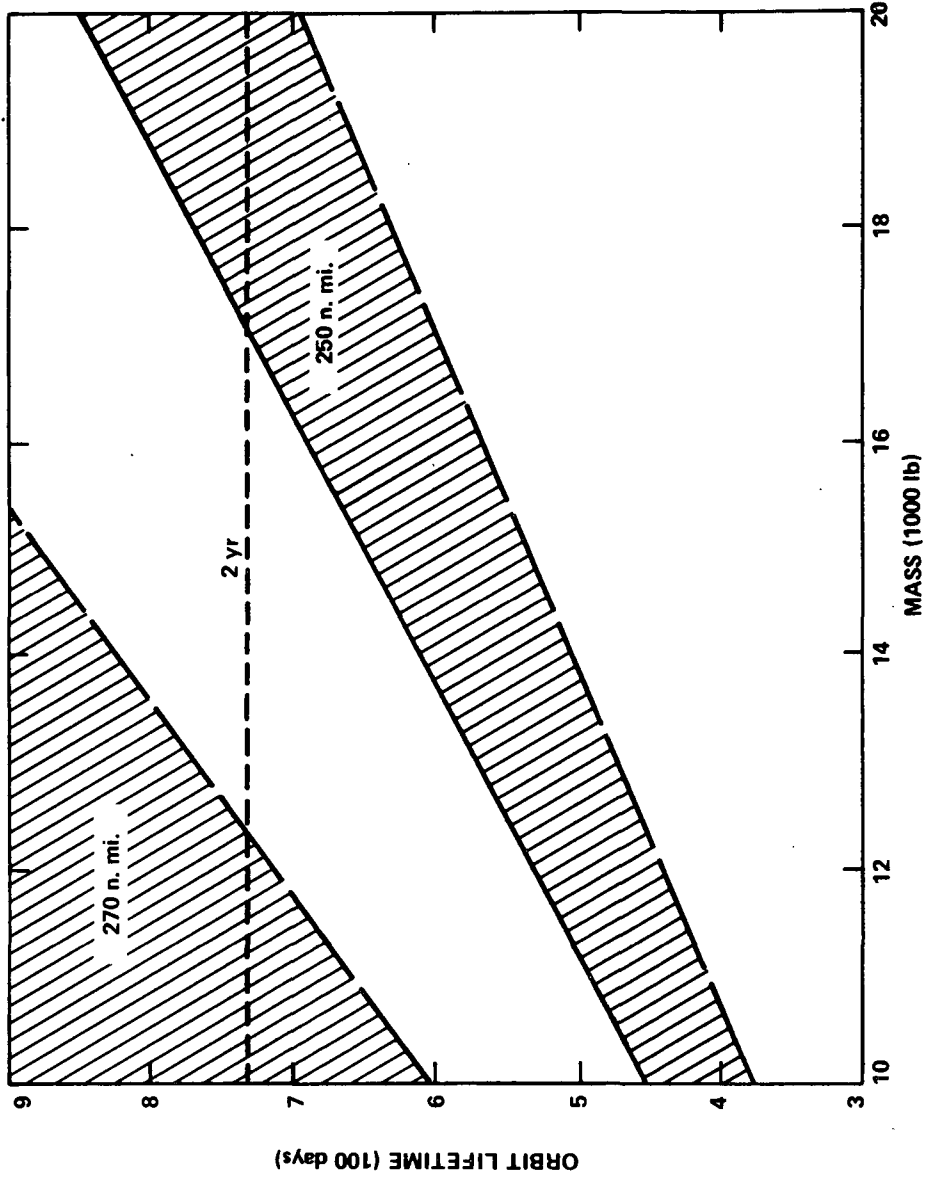


Figure III-5. Variation in orbit lifetime with vehicle mass for HEAO-C.

- LAUNCH DATE: 3/21/77
- ATMOSPHERE MODEL: MSFC MODIFIED 1967
- CIRCULAR ORBIT/28.5 deg INCLINATION
- JACCHIA + 2 $\sigma$  DENSITY
- CODE: ——— MAX DRAG
- MIN DRAG

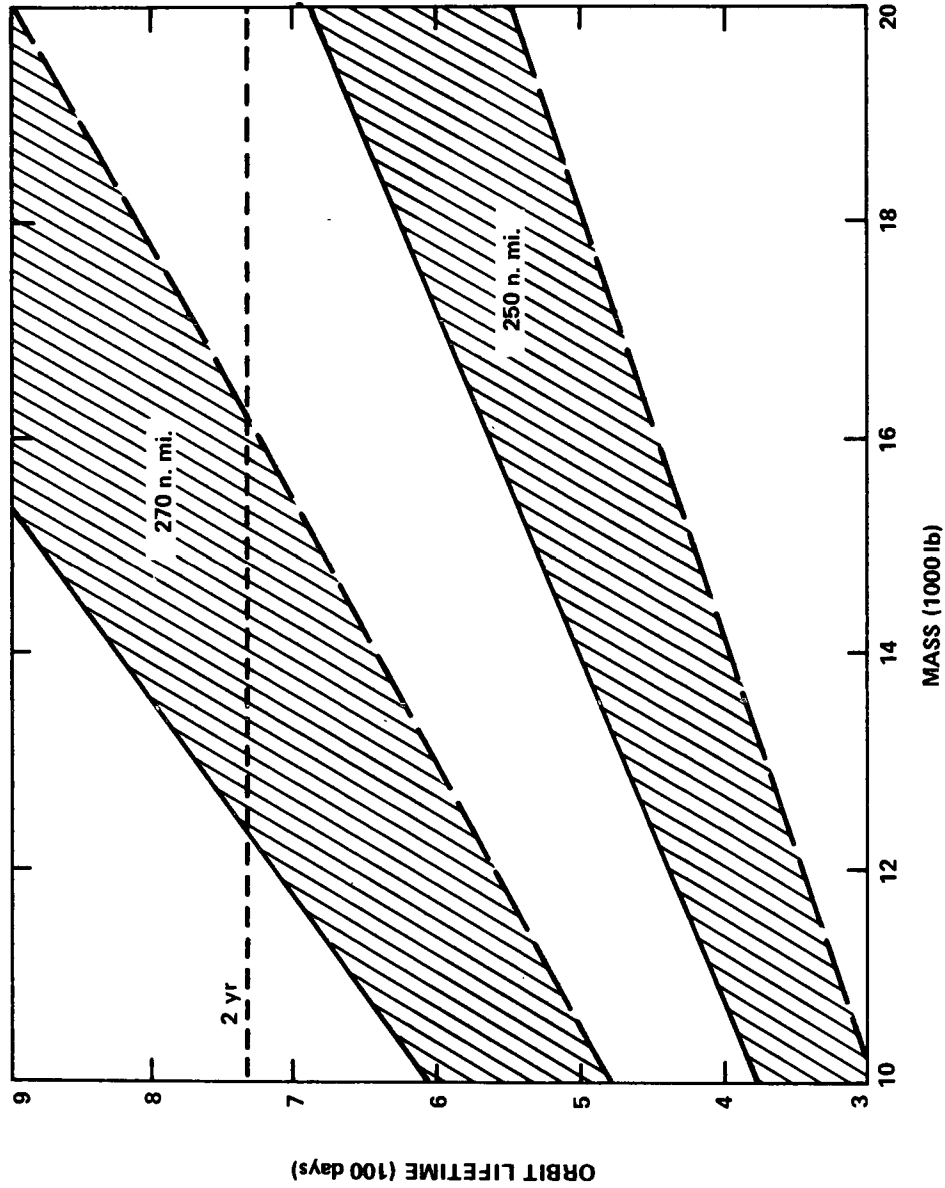


Figure III-6. Variation in orbit lifetime with vehicle mass for HEAO-C/OAS.

in this orbit must be sufficient to allow for the required phasing requisite to the burning of the OAS prior to injection into the target orbit. Orbit decay traces for the HEAO-C/OAS in maximum and minimum drag orientations for this nominal ascent orbit for the March 21, 1977, launch date are presented in Figure III-7. If the OAS could not propel the spacecraft out of this orbit, its lifetime would be approximately 58 to 74 days.

The maximum off-nominal ascent orbit predicted for a Titan IIID due to injection dispersion caused by guidance system error was a 103.6 by 316.6 nautical mile ellipse. A decay trace for the HEAO-C/OAS trapped in approximately a 100 by 300 nautical mile orbit is shown in Figure III-8. The lifetime in this orbit ranges between 22 and 26 days, allowing adequate time for orbit determination and adjustment.

- LAUNCH DATE: 3/21/77
- ORBITAL INCLINATION: 28.5 deg
- ATMOSPHERE MODEL: MSFC MODIFIED
- CODE: ——— APOGEE
- 1967 JACCHIA + 2 $\sigma$  DENSITY
- - - - - PERIGEE

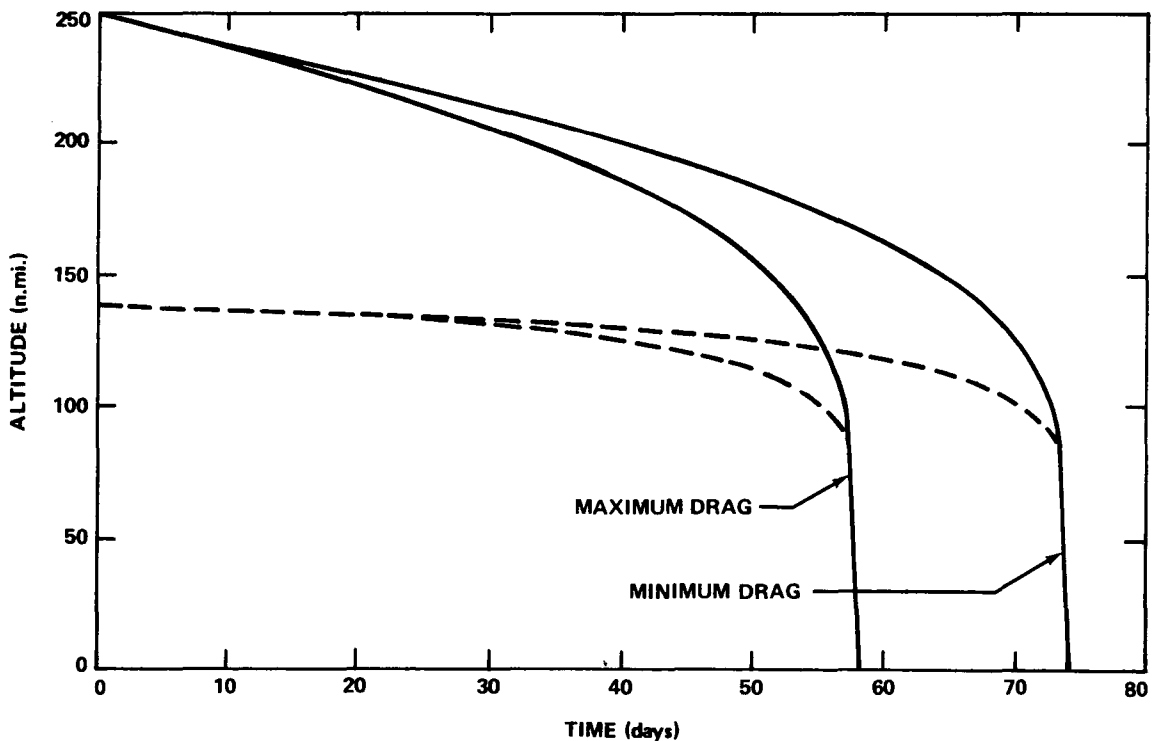


Figure III-7. Variation in altitude with time for a 140 by 250 nautical mile altitude initial orbit.

- LAUNCH DATE: 3/21/77
- ATMOSPHERE MODEL: MSFC MODIFIED 1967 JACCHIA  
+ 2 $\sigma$  DENSITY
- ORBITAL INCLINATION: 28.5 deg

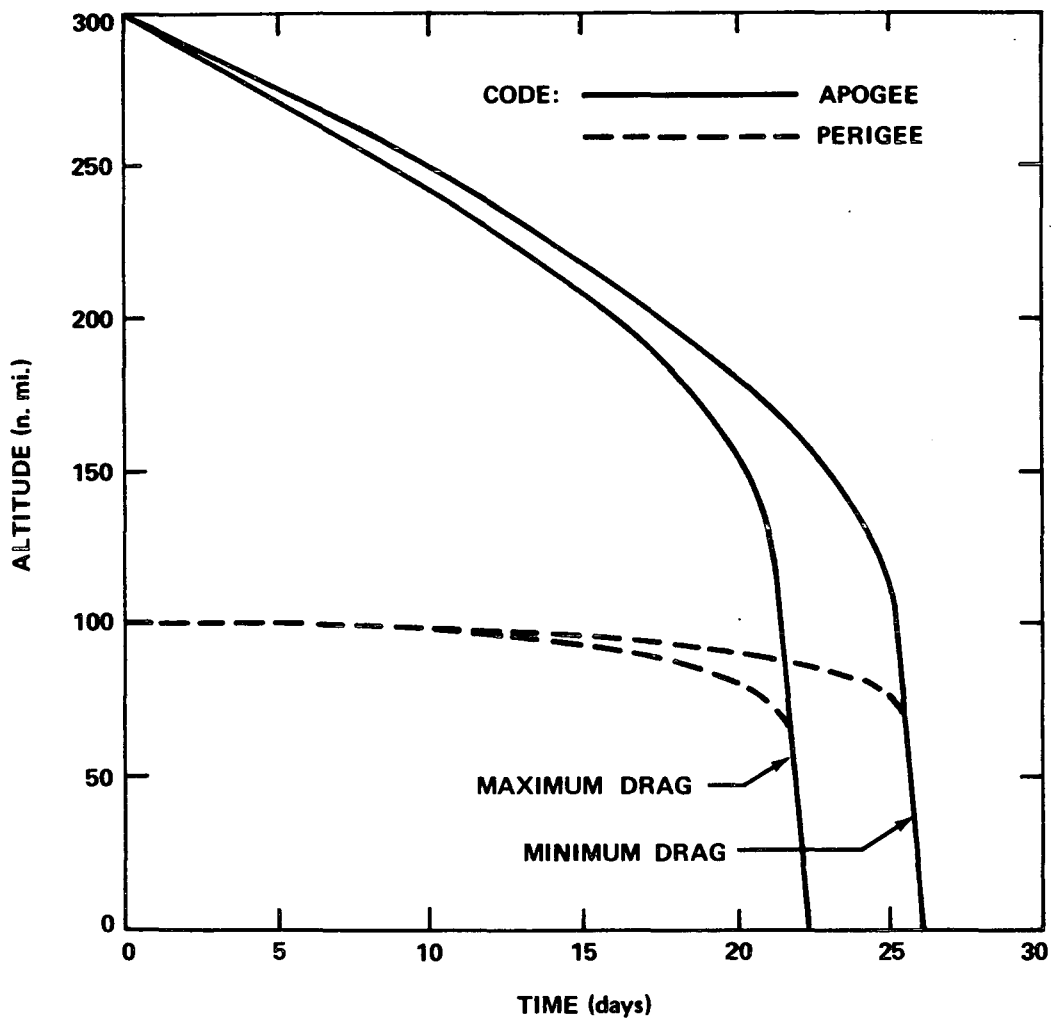


Figure III-8. Variation in altitude with time for a 100 by 300 nautical mile altitude initial orbit.

The Titan IIID launch vehicle and OAS combination being considered for HEAO-C offers adequate payload capability for placement of spacecraft currently under study in high altitude orbits which guarantee two year lifetimes. The disadvantage of the high altitude orbits is the percentage of experiment interference time or the collection of erroneous data when the radiation flux exceeds certain limits. Figure III-9 shows the variation in percent experiment shutdown time with altitude for circular orbits. Variations for 35 degree and 50 degree inclination orbits are given, in addition to the 28.5 degree inclination values for comparison. The radiation flux limit for experiment interference was taken as 1000 particles/cm<sup>2</sup>-sec and particle energy greater than 0.5 MeV (protons). As shown, for an inclination of 28.5 degrees, the percent experiment interference time varies from 5 percent at 200 nautical miles to 11 percent at 300 nautical miles. The percent shutdown time for a given altitude increases non-linearly with inclination due to the radiation concentrated at low altitudes at the South Atlantic Anomaly.

- FLUX GREATER THAN 1000 PARTICLES/cm<sup>2</sup> - sec
- PARTICLE ENERGY GREATER THAN 0.5 MeV

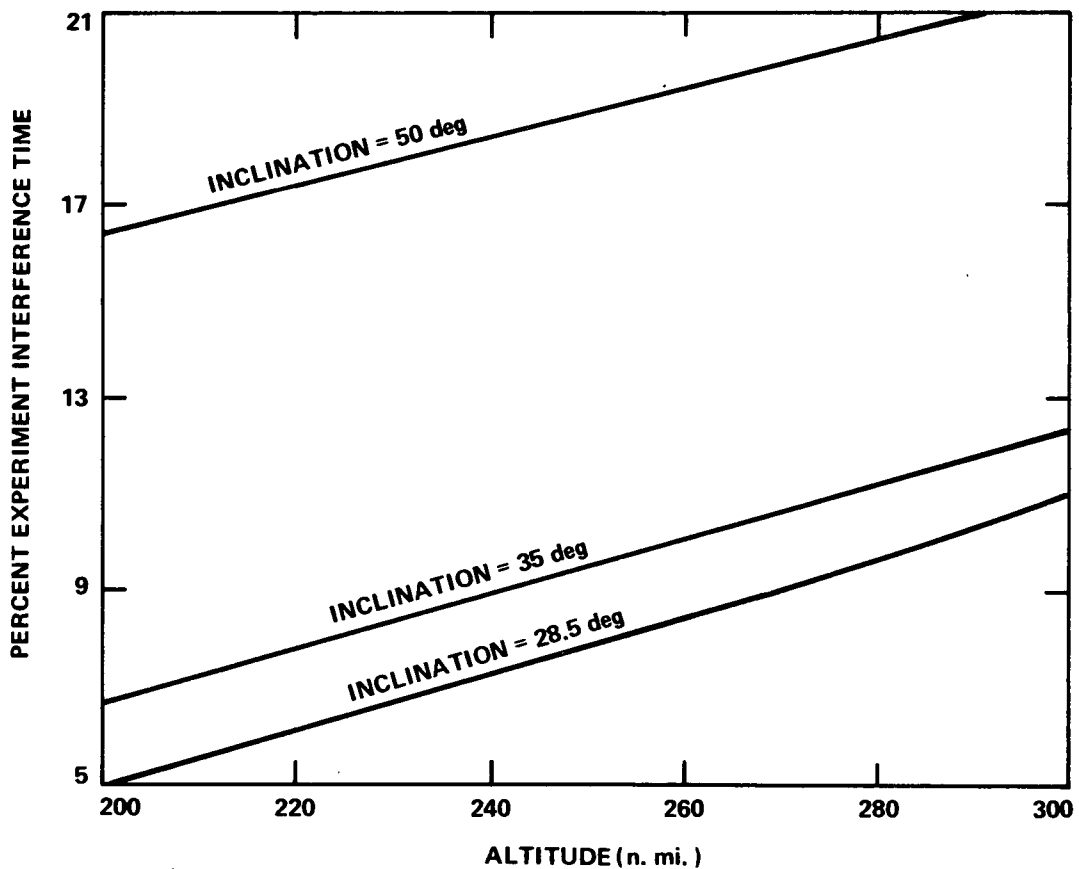


Figure III-9. Variation in percent experiment shutdown with altitude for circular orbits.

## B. Titan IIID/OAS Performance

After selection of the required orbital altitude, it was necessary to determine the performance of the launch vehicle to the 270 nautical mile orbit and to establish the maximum allowable weight of the HEAO spacecraft.

This section contains parametric performance and trajectory data which have been generated for the HEAO-C mission using the Titan IIID with the Lockheed OAS to achieve the final orbit.

The Titan IIID launch vehicle inserts the OAS and the HEAO-C spacecraft into an elliptical orbit. The OAS provides the velocity increments necessary for orbit correction of the Titan IIID injected dispersions and to insert the spacecraft into the 270 nautical mile circular orbit. The impact of the Titan IIID injecting into an off-nominal orbit has been considered. This information and its impact are discussed in part 3 of this section.

1. Assumptions. It was assumed that the Titan IIID/OAS launch vehicle for HEAO-C missions would be launched from the Eastern Test Range (ETR) with an azimuth of 90 degrees (measured from north to south over east).

The vehicle used in this study was the standard Titan IIID used by the Air Force and built by the Martin Company. It was assumed to be flown with an open-loop guidance from lift-off until burnout where injection of the OAS and spacecraft into a parking orbit occurs.

Table III-1 gives the weights for the stripped-down OAS stage used in this study (see Appendix B).<sup>2</sup> The Titan IIID/OAS aerodynamic, propulsion, and weight data for this study were obtained from References III-1 through III-5.

TABLE III-1. OAS WEIGHT SUMMARY FOR STRIPPED-DOWN STAGE WEIGHT (lb)

OAS (stripped)	1223
OAS Propellant & Pressurant	<u>1240</u>
OAS Gross Weight	2463
Spacecraft Adapter	212
Booster Adapter	221

The 2573 pound<sup>2</sup> Lockheed payload shroud design characteristics are such that it must be jettisoned when the vehicle has a lateral acceleration between 1.1 and 1.2 g. The vehicle reaches a lateral acceleration of 1.1 and 1.2 g at about 280 and 290 seconds, respectively. For this study the shroud was jettisoned at 283.68 seconds which was within the designed jettison g limits.

---

2. Subsequent data (May 1971) lists stripped-down OAS weight as 1499.2 lbs and the P-123 shroud as 2910.8 lbs.

2. Trajectory Profile. The three-stage Titan III D flies solid rocket motors (SRMs), Core I, and Core II direct ascent to the desired parking orbit. The OAS (Stage IV) is then used to correct the orbit injection errors and to circularize the payload into a 270 nautical mile orbit.

Titan III D/OAS HEAO-C nominal and off-nominal flight profiles are shown in Figures III-10, and III-11. A 140 by 250 nautical mile orbit was selected as the nominal parking orbit for the OAS and the spacecraft. This orbit was selected since preliminary data indicated that the Titan III D orbital injection dispersions and payload capabilities about this orbit would be acceptable for each of the HEAO missions. The possibility of occurrence of off-nominal orbits exists because the Titan III D flies with an open-loop guidance. For the nominal trajectory, the Titan III D was flown open-loop with no dispersions being considered. The orbit impact caused by open-loop  $3\sigma$  dispersions is discussed later.

For both nominal (140 by 250 nautical mile) and off-nominal (103.6 by 316.6 nautical mile) orbits, two burns were required by the OAS to adjust the spacecraft into the final 270 nautical mile orbit, if there is no requirement for the OAS to burn over a tracking station. The first burn was made at the 250 nautical mile apogee to raise the perigee to 270 nautical miles. The second burn was made at the new apogee to circularize into a 270 nautical mile orbit. Since there is a requirement to perform the OAS burns over a tracking station, three OAS burns are required instead of two. This is necessary because the spacecraft is not over a station long enough to complete the 13.7 minute burn requirement for the initial orbit correction. This will have no impact on the payload to the final orbit. For details on trajectory timeline of events, see discussion of mission timelines.

3. Dispersion Analysis. For the HEAO mission, the Titan III D is to be flown to parking orbit with an open-loop guidance; such an open-loop guidance system might possibly cause the Titan III D to inject the OAS and the HEAO spacecraft into an orbit other than the nominal 140 by 250 nautical mile parking orbit.

To determine the impact this would have on the performance of the Titan III D/OAS vehicle, a dispersion analysis was made for the Titan III D by the Martin Company [6]. Table III-2 summarizes the dispersions about a 140 by 250 nautical mile orbit for the Titan III D flown with an open-loop guidance and for  $3\sigma$  deviations.

Table III-2 shows a mean altitude of 133.2 nautical miles and a 29.6 nautical mile perigee altitude for a 1 percent command rate with a velocimeter in Stage II. This configuration is consistent with the launch vehicle selected for the HEAO-A mission which requires individual selection of guidance components, since the off-the-shelf vehicle has only a 2 percent guidance accuracy. The lower limit for perigee injection with  $3\sigma$  deviations is 103.6 nautical miles (133.2 - 29.6 nautical miles).

1. LIFT-OFF
2. SRM BURN-OUT AND SEPARATION
3. CORE STAGE I BURN-OUT AND SEPARATION
4. INJECT INTO NOMINAL 140 BY 250 n. mi. ORBIT
5. SEPARATE CORE STAGE II
6. BURN OAS 13.7 min TO INJECT INTO A 250 BY 270 n. mi. TRANSFER ORBIT
7. CIRCULARIZE AT 270 n. mi. APOGEE BY BURNING OAS FOR 2.05 min

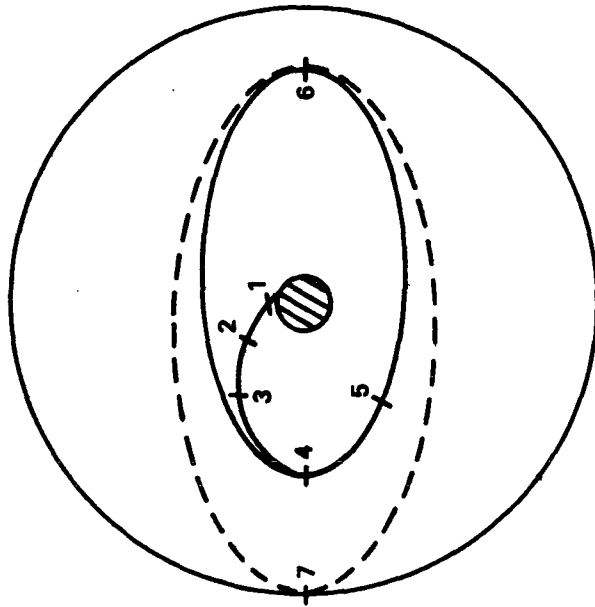


Figure III-10. Nominal Titan IID/OAS HEAO-C flight profile.

1. LIFT-OFF
2. SRM BURN-OUT AND SEPARATION
3. CORE STAGE I BURN-OUT AND SEPARATION
4. INJECT INTO OFF-NOMINAL 103 BY 317 n. mi. ORBIT
5. SEPARATE CORE STAGE II FROM OAS
6. BURN OAS 17.17 min TO INJECT INTO A 317 BY 270 n. mi. TRANSFER ORBIT
7. CIRCULARIZE AT 270 n. mi. PERIGEE WITH OAS DECELERATING BURN FOR 4.53 min

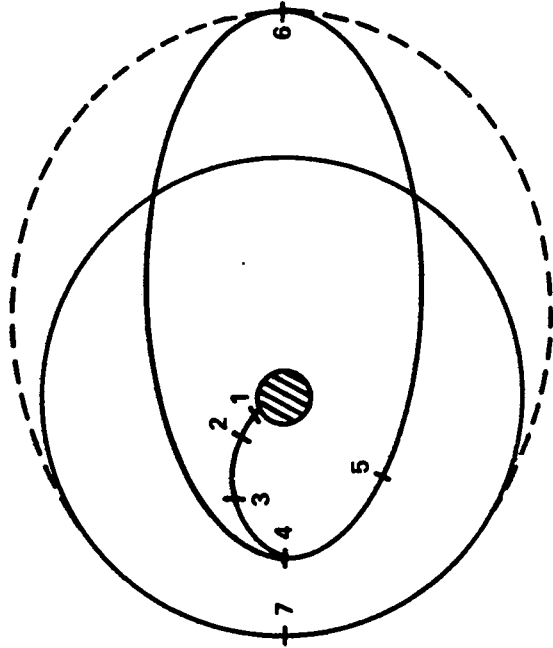


Figure III-11. Off-nominal Titan IID/OAS HEAO-C flight profile.

TABLE III-2. SUMMARY OF OPEN-LOOP ACCURACY<sup>a</sup>

Configuration	Oblate Spheroid					
	Perigee			Apogee		
	(Deviation > 100)			(Deviation < 100)		
	Mean (n.mi.)	3 $\sigma$ (n. mi.)	Prob. (%)	Mean (n.mi.)	3 $\sigma$ (n. mi.)	Prob. (%)
Stage II Velocimeter						
2% Command Rate	128.9	$\pm 43.1$	94.8	259.9	$\pm 90.2$	88.0
1% Command Rate	133.2	$\pm 29.6$	99.4	256.9	$\pm 59.7$	97.0

a. Reference III-6.

For the apogee altitude shown in Table III-2 the mean altitude is 256.9 nautical miles and a  $\pm 59.7$  nautical mile altitude with  $3\sigma$  deviations. Since the orbit deviation of 29.6 nautical miles was subtracted from the perigee mean of 133.2 nautical miles, the 59.7 nautical mile orbit deviation must be added to the apogee mean altitude giving an apogee altitude equal to 316.6 nautical miles. Therefore, the maximum deviation (worst case) would give an orbit of 103.6 by 316.6 nautical miles. The best case would be an orbit 162.8 by 270 nautical miles. In this case only one OAS burn would be required to achieve 270 nautical mile circular orbit, thereby, using less propellant which would give a maximum payload for the OAS. Table III-2 shows that the Titan IIID would inject the payload into a parking orbit with perigee altitudes greater than 100 nautical miles and apogee altitudes less than 300 nautical miles, 99.4 and 97.0 percent of the time.

The Titan IIID can inject a maximum payload above the Core II stage of 25 558 pounds into a 140 by 250 nautical mile orbit at an orbital inclination of 28.5 degrees (Fig. III-12). The 25 558 pound payload is the maximum (OAS, OAS propellant, and spacecraft) weight that can be loaded on the Titan IIID for the HEAO missions. This value is used to calculate the propellant required for the OAS to determine the maximum performance capability of the OAS from parking orbit to the final 270 nautical mile circular orbit.

Since the worst off-nominal orbit is 103.6 by 316.6 nautical miles, it is necessary to load sufficient propellant in the OAS for maneuvering the maximum weight from the worst orbit. As a result of transferring 25 558 pounds from the off-nominal orbit, the maximum weight allowable for the HEAO-C spacecraft will be 22 750 pounds. Table III-3 shows a comparison of the maximum weight that could be used for the HEAO-C if the off-nominal orbit injection of the open-loop Titan IIID did not have to be considered.

## C. Occultation and Source Viewing

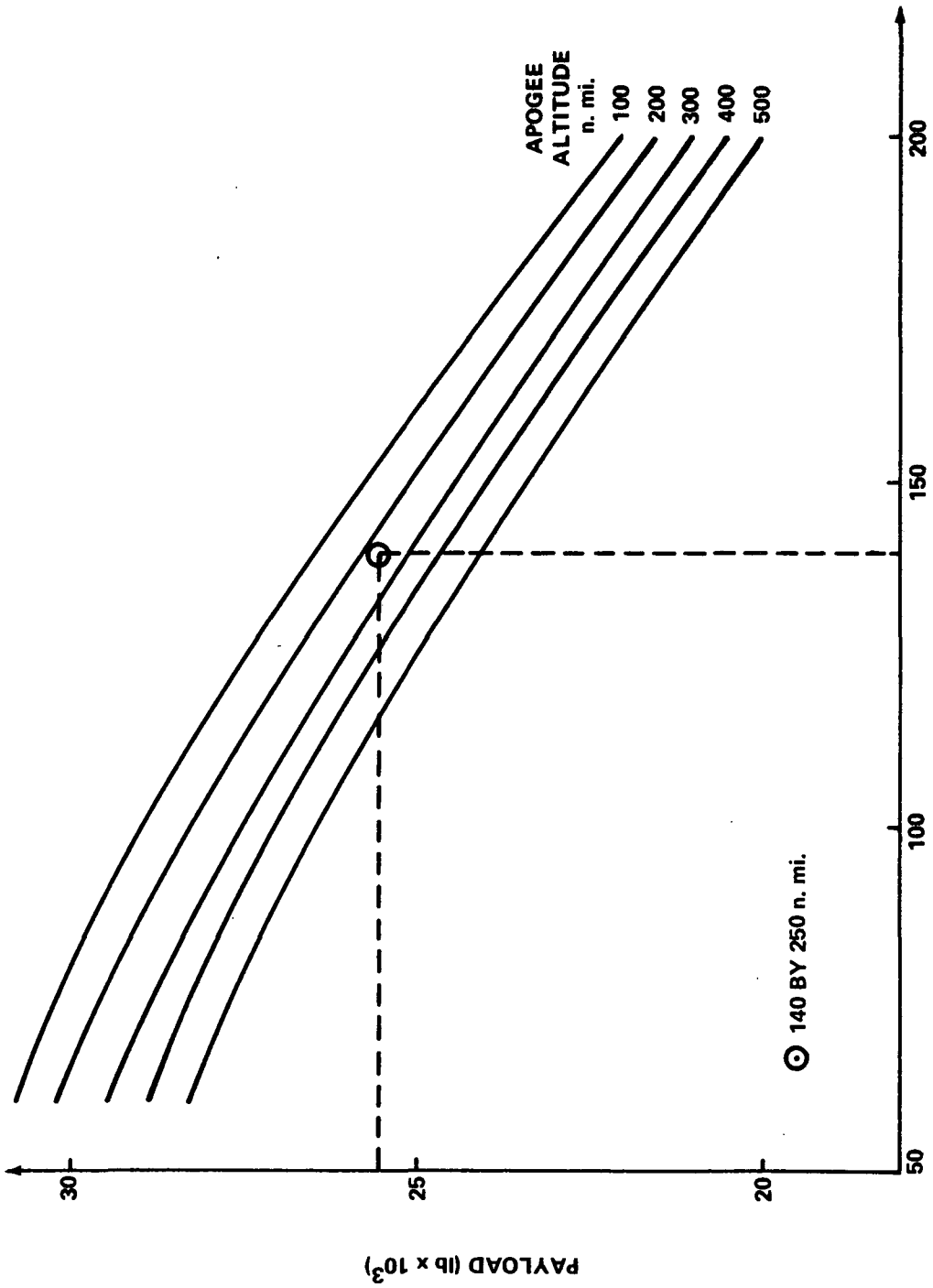
1. Earth Occultation of Sun. In the design requirement of thermal control, solar panel, and attitude reference system, earth occultation of the sun is of primary concern. An investigation over the complete range of occultation parameters was made to determine the maximum and minimum occultation time per orbit. Longitude of the orbital node was varied from 0 to 270 degrees, orbital inclination was varied from equatorial to polar orbit, variation in launch date was considered covering a one year period, and orbital altitude ranged from 150 to 400 nautical miles.

TABLE III-3. OAS NOMINAL AND OFF-NOMINAL PERFORMANCE TO 270 NAUTICAL MILE, 28.5 DEGREE CIRCULAR ORBIT

Stage	Item	Propulsion	Weight (lbs)	
			Nominal	Off-Nominal
IV	Vacuum Thrust (OAS)	215		
	Vacuum Specific Impulse	230	25 558	25 558
	Weight at Ignition			
	Propellant Capacity	2910	897 <sup>a</sup>	1 240 <sup>b</sup>
	Propellant Consumed		24 661	24 318
	Vehicle Weight at Stage Cutoff			
	Weight to be Subtracted			
	OAS (Stripped-Down)		1 223	1 223
	Flight Performance Reserves		90	124
	Spacecraft Adapter		<u>221</u>	<u>221</u>
Total Weight to be Subtracted		1 534	1 568	
Net Payload (HEAO Spacecraft)		23 127	22 750	

a. OAS first burn was 13.7 min (780 lb w<sub>p</sub> for 250 by 270 n.mi. orbit) and second burn was 2.05 min. (117 lb w<sub>p</sub> for 270 n.mi. orbit).

b. OAS first burn was 17.17 min (981 lb w<sub>p</sub> for 317 by 270 n.mi. orbit) and second burn was 4.53 min deceleration (259 lb w<sub>p</sub> for 270 by 270 n.mi. orbit).



PERIGEE ALTITUDE (n. mi.)

Figure III-12. Titan IIC payload versus perigee altitude.

Figure III-13 depicts the occultation parameters:

- $\Omega$  Longitude of orbital ascending node. Initially determined by launch time of day, and after launch, changes  $-6.72$  degrees per day for a 270 nautical mile,  $28.5$  degree orbit.
- $\alpha$  Right ascension of the sun. Determined by time of year.
- $i$  Orbital inclination relative to earth equator plane.
- $\beta$  Orbital sun angle, angular distance of the sun from the orbit plane. Function of  $i$ ,  $\alpha$  and  $\Omega$ .
- $X$  Reference axis, vector in direction of vernal equinox.
- $\bar{N}$  Vector in direction of orbital ascending node.

The occultation time is strongly dependent upon the magnitude of the sun angle  $\beta$ . Minimum occultation occurs when  $\beta$  is a maximum.

The effect of the time of year on earth occultation of the sun is shown in Figure III-14. The HEAO-C orbit of a 270 nautical mile altitude and  $28.5$  degree inclination was considered. The minimum sensitivity of occultation time occurs during the autumnal (September 21) and vernal (March 21) equinoxes. The sun is in equatorial plane on these dates and the maximum orbital sun angle,  $\beta$ , would be equal to the orbital inclination. The maximum occultation time occurs when  $\beta$  is equal to zero; nodal longitudes ( $\Omega$ ) of  $0$  and  $180$  degrees on September 21 and March 21 effects this condition. The resulting maximum occultation is 35.8 minutes per orbit. Maximum sensitivity of occultation time occurs during the winter (December 21) and summer (June 21) solstices. On these dates, the maximum sun angle,  $\beta$ , would be 52 degrees, which is the sum of the sun's latitude ( $23.5$ ) and orbital inclination ( $28.5$ ). The maximum sun angle occurs with a nodal orientation of  $180$  degrees, resulting in a minimum occultation time of 27.4 minutes per orbit. Occultation time for nodal alignment of  $\Omega = 0$  is nearly constant over the one year period since the  $\beta$  angle varies only from  $0$  to  $5$  degrees.

The launch date of June 21, when the sun is at its northern-most latitude, resulted in the maximum variation in occultation time. This date was selected to determine the sensitivity of the other occultation parameters.

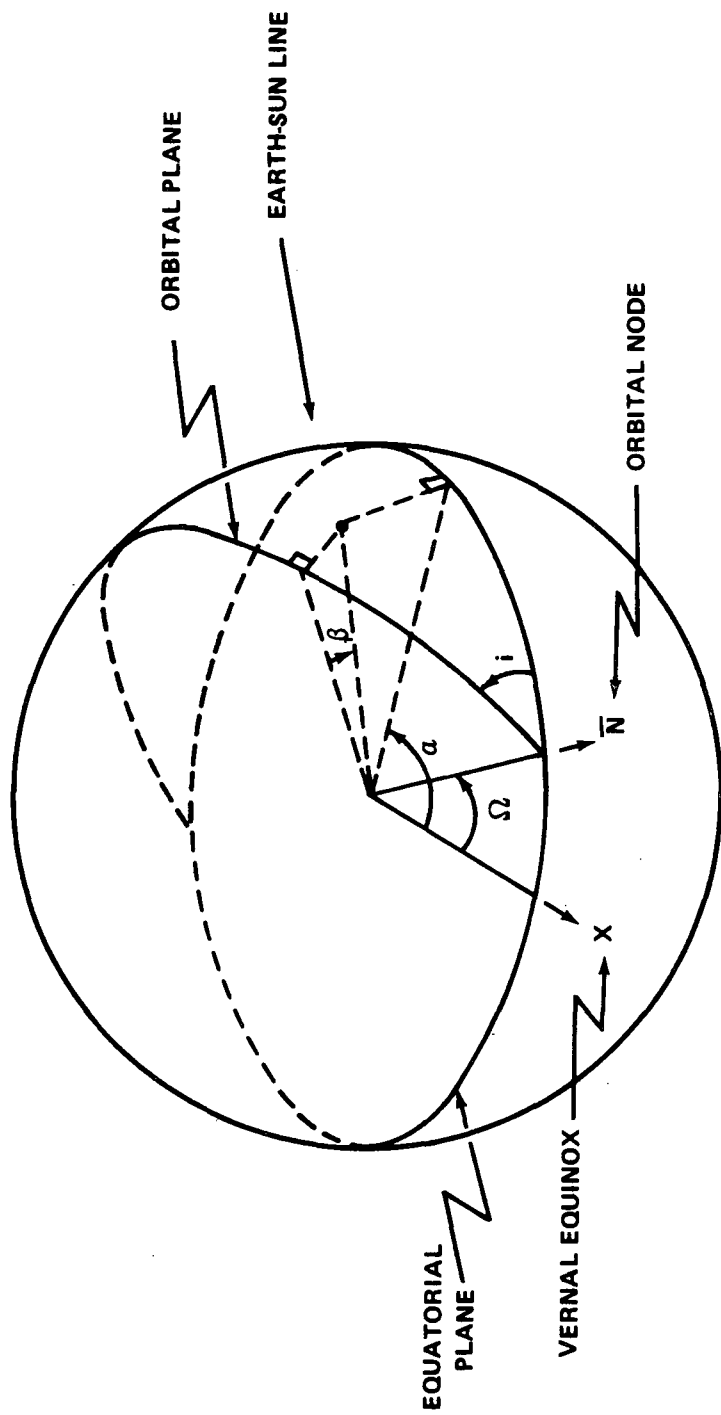


Figure III-13. Geometry of occultation parameters.

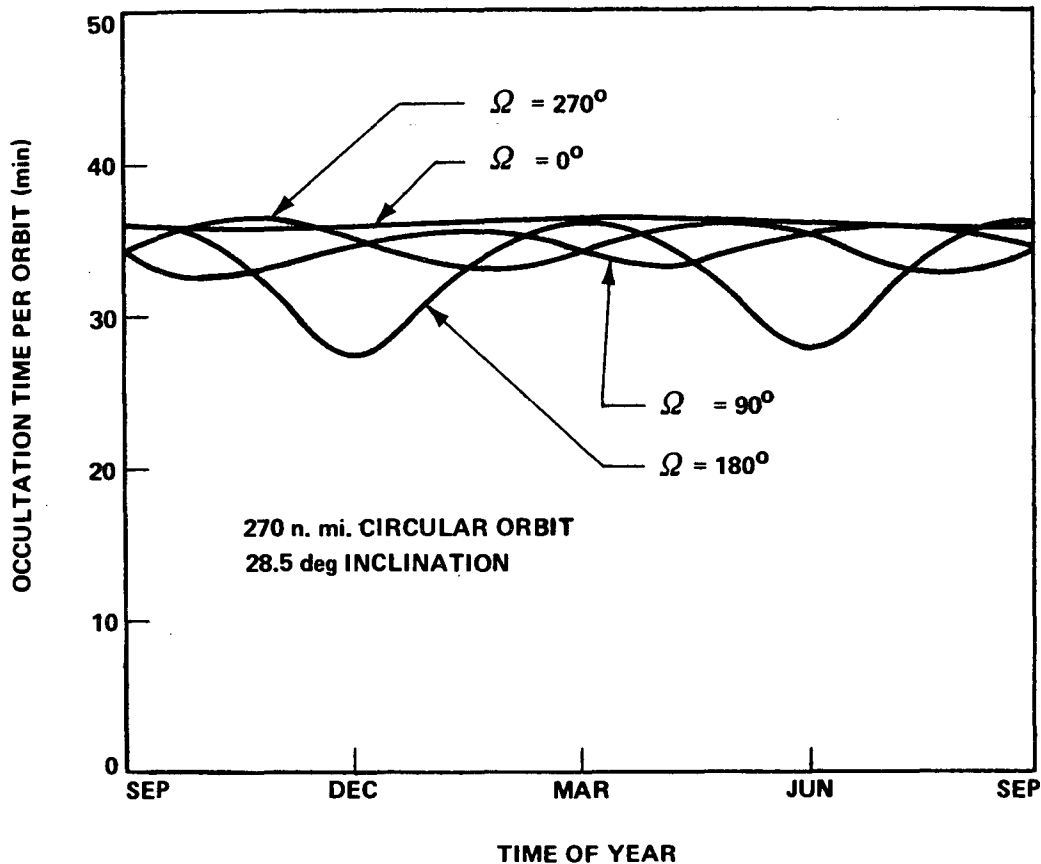


Figure III-14. Earth occultation of sun from earth orbit versus time.

Occultation time versus orbital altitude for a 28.5 degree inclination is shown in Figure III-15. Four different orbital node orientations,  $\Omega$ , of 0, 90, 180, and 270 degrees were considered. The least variation in occultation time versus altitude occurs when the sun angle,  $\beta$ , is zero; this is nearly the case when  $\Omega = 0$  for the June 21 launch date where  $\beta = 5$  degrees; a decrease of 0.8 minutes per orbit for an increase of 100 nautical miles in altitude would be a lower limit on the sensitivity of orbital altitude. Maximum variation in occultation time versus orbital altitude occurs when  $\beta$  is a maximum value; this condition happens for  $\Omega = 180$  degrees where  $\beta = 52$  degrees ( $28.5 + 23.5$ ). A decrease of 2.88 minutes per orbit for an increase of 100 nautical miles in altitude would be an upper limit on the sensitivity of orbital altitude with the inclination of 28.5 degrees.

The effect of orbital node orientation for a launch date of June 21 is shown in Figure III-16. The initial orientation is determined by the launch time of

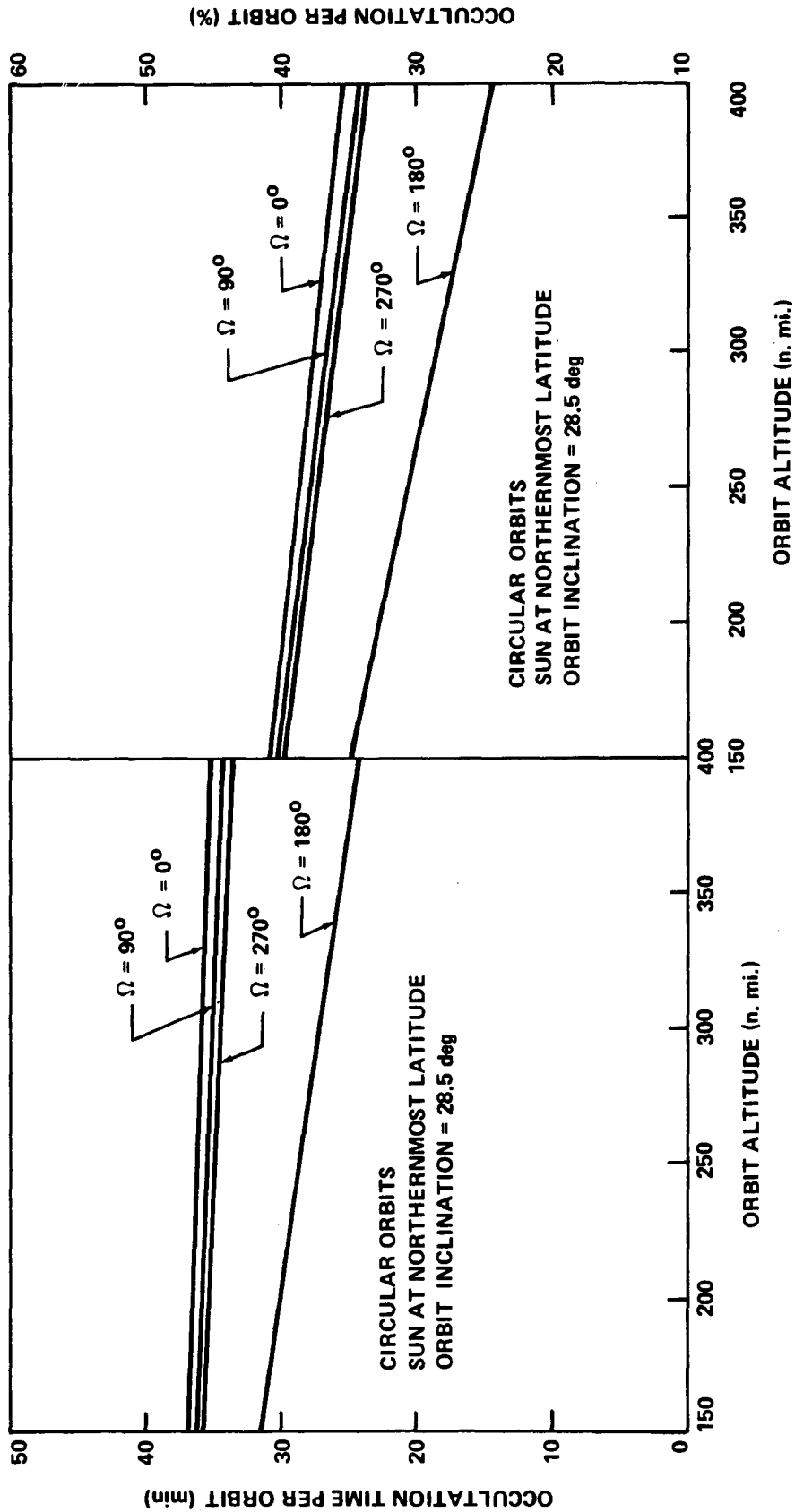


Figure III-15. Earth occultation of sun from earth orbit versus altitude.

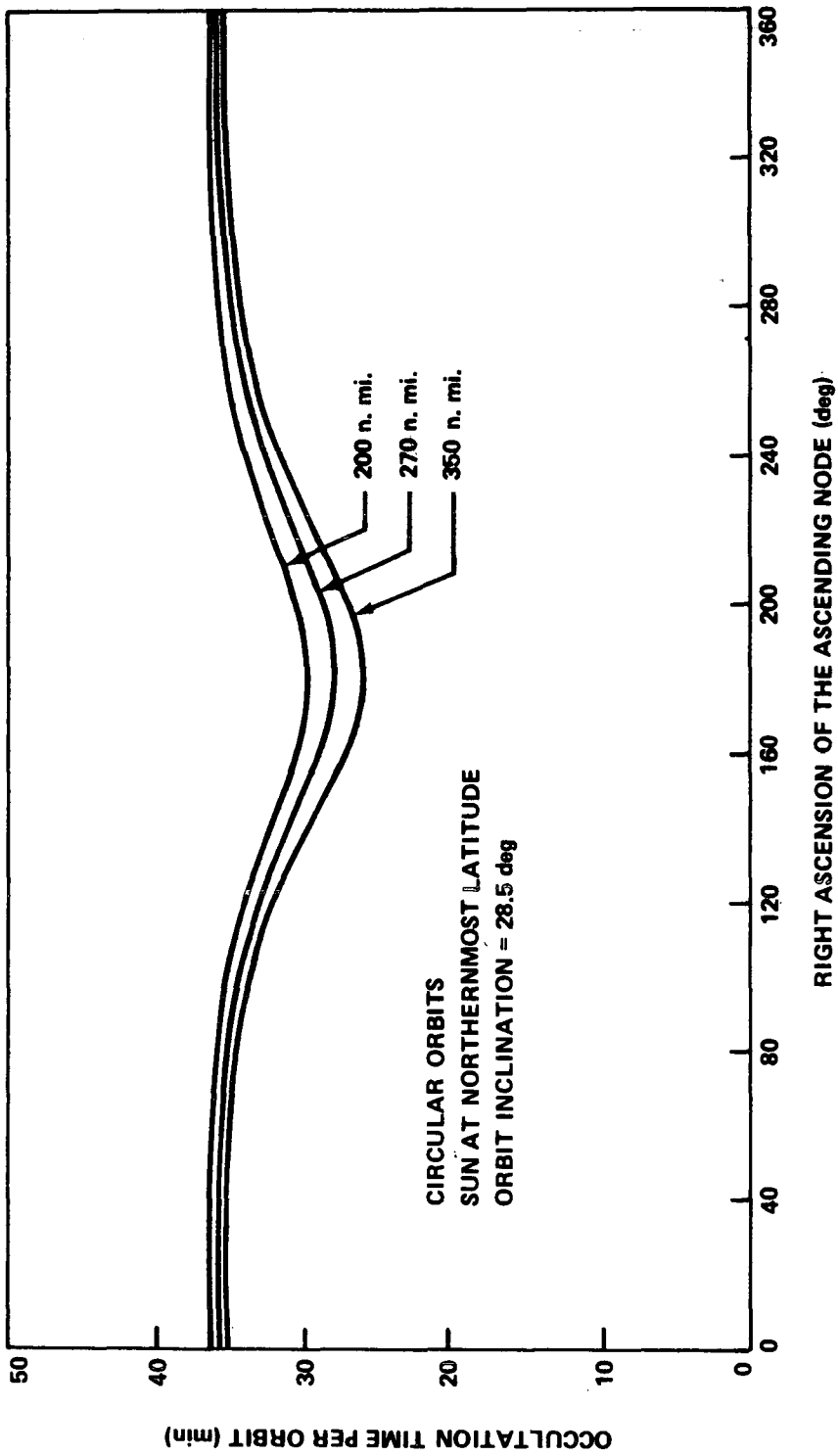


Figure III-16. Earth occultation of sun from earth orbit versus ascending node.

day and can be selected for values from 0 to 360 degrees over a 24 hour period of time. An ascending node of 0 degrees would dictate a launch time of 12 noon Eastern Standard Time. A 12 midnight launch would result in an ascending node of 180 degrees where the minimum occultation time of 27.4 minutes per orbit occurs for the 270 nautical mile orbit.

The most sensitive parameter, orbital inclination, is shown in Figure III-17. Inclination was allowed to vary from 0 to 90 degrees. A nodal orientation of 180 degrees resulted in the largest variation in occultation time

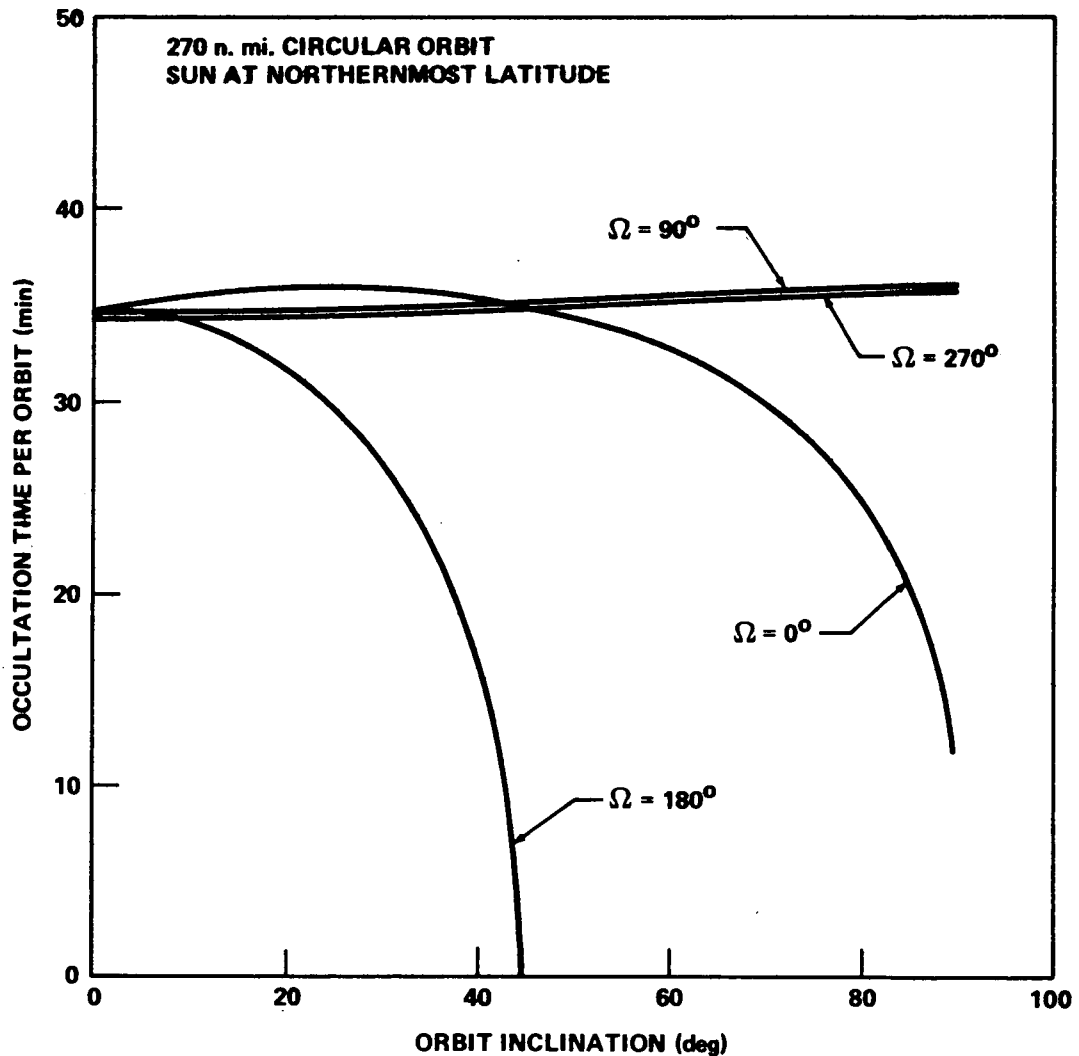


Figure III-17. Earth occultation of sun from earth orbit versus orbit inclination.

because the resultant sun angle,  $\beta$ , equaled 23.5 plus the orbital inclination. For this nodal orientation of 180 degrees, a 45 degree inclination would yield 100 percent sun illumination for a continuous period of time. Orientation of 90 and 270 degrees does not allow the sun angle to build up as the orbital inclination increases; this results in a nearly constant occultation time versus inclination.

Maximum and minimum occulted time associated with orbital inclinations of 0, 28.5, 55, and 90 degrees is given in Table III-4 for an altitude of 270 nautical miles. Maximum occultation occurs when the sun angle is zero and this condition will occur for any inclination; therefore, a constant time of 35.8 minutes for all inclinations is shown. Zero occultation time would occur with the 55 and 90 degree inclinations; as depicted in Figure III-17, an inclination greater than 45 degrees would result in zero occultation over a continuous period of time during a year's span.

TABLE III-4. EARTH OCCULTATION OF SUN FROM EARTH ORBIT FOR AN ORBITAL ALTITUDE OF 270 NAUTICAL MILES AND AN ORBITAL PERIOD OF 94.6 MIN

	Orbit Inclination (degrees)			
	0	28.5	55	90
Maximum Time Occulted Orbit (min)	35.8	35.8	35.8	35.8
Minimum Time Occulted Orbit (min)	34.5	27.4	0.0	0.0

## 2. Target Source Viewing Accessibility.

a. Background Comments. For analysis relative to the HEAO, there are two primary sets of inertial coordinate systems, the equatorial system and the ecliptic system. The intersection of the equatorial and ecliptic planes as the apparent motion of the sun crosses the equator from south to north is the positive X-axis for both systems. The position of a source is identified in the equatorial system by two angles: right ascension,  $\alpha$ , and declination  $\delta$ . The angle  $\alpha$  is measured counterclockwise from the X-axis to the projection of the source into the equatorial plane;  $\delta$  is the angular distance from the source to the equatorial plane. The two angles in the ecliptic system are the celestial longitude,  $\lambda$ , and celestial latitude  $\phi$ . The longitude and latitude are measured in a similar manner as the right ascension and declination with the ecliptic plane being the reference plane.

This section presents the results of analysis displayed in the two different coordinate systems for determining the opportunity to view a source, first, for a given date to determine the accessible viewing area and locate target sources within this range and, second, for a given source to determine the length of time it will present viewing opportunity for the pointing spacecraft. Also presented is the amount of time a source will be occultated by the earth for a 270 nautical mile altitude and 28.5 degree inclination orbit.

b. Target Source Viewing Opportunity

(1) Determination of Areas Within View on a Given Date. The coordinate of a target source is usually given in the equatorial coordinate system: right ascension,  $\alpha$ , and declination,  $\delta$ . However, the presentation of information relative to the viewing opportunity of the source is more conveniently displayed in the ecliptic coordinate system.

The spacecraft pointing direction is determined from the direction of the earth-sun line. With a 15 degree half cone angle about the sun direction, the spacecraft can view objects within a 30 degree band around the celestial sphere; the viewing band will be perpendicular to the ecliptic plane (Fig. III-18).

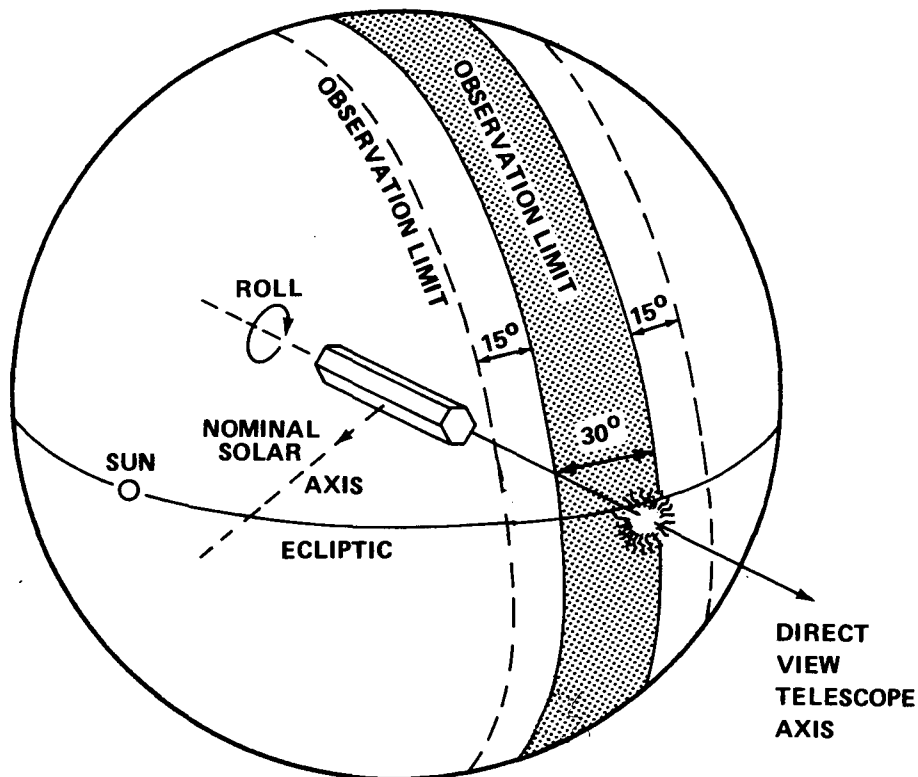


Figure III-18. Definition of  $\pm 15$  degree and  $\pm 30$  degree access bands.

(2) Equatorial System. Any point on the celestial sphere has coordinates equivalent to latitude and longitude. Latitude varies from -90 degrees to +90 degrees and longitude from 0 degrees to 360 degrees. For the present, the celestial sphere will be represented by plotting the right ascension as the abscissa and declination as the coordinate. Considerable distortion will result, but all points can be shown. Various planes that are on the celestial sphere will resemble either straight lines or sine functions.

Figure III-19 presents the celestial sphere using the equatorial coordinates, right ascension, and declination. (Right ascension is expressed in units of time rather than degrees, a common practice in astronomy; to get degrees, simply multiply hours by 15.) The galactic plane appears as a sine curve. Viewing bands for various orientations of the rotation axis are indicated by connected lettered points. The sun is in its March 21 position. The viewing plane that results when the spacecraft rotation axis is pointed directly at the sun is indicated as the "nominal" plane. The nominal  $\pm 15$  degree viewing band is obtained by fixing the solar axis 15 degrees ahead and behind the sun, and 15 degrees above and below the ecliptic plane, i. e., for each off-nominal case the following coordinates are set:

Case 1:	$\Delta \lambda = +15$	$\Delta \phi = 0$
Case 2:	$\Delta \lambda = -15$	$\Delta \phi = 0$
Case 3:	$\Delta \lambda = 0$	$\Delta \phi = +15$
Case 4:	$\Delta \lambda = 0$	$\Delta \phi = -15$

If the rotation axis is allowed to assume any orientation within the 15 degree cone angle of the sun, then the viewing planes can cover any point outside of the shaded area.

Note that the nominal viewing plane for this data is a straight line perpendicular to the equator. The nominal viewing plane will not usually be perpendicular to the equator; however, on March 21 (vernal equinox) the sun is at the intersection of the equatorial and ecliptic planes so that the viewing plane is perpendicular to both. Normally, the nominal viewing plane is perpendicular only to the ecliptic.

Figure III-20 shows how the area within view would normally appear in the equatorial system. This figure is for the date June 21, which is a time when the nominal viewing plane is not perpendicular to the equator. Note that the area within view in this figure is the shaded area, rather than the open area as in the other figures.

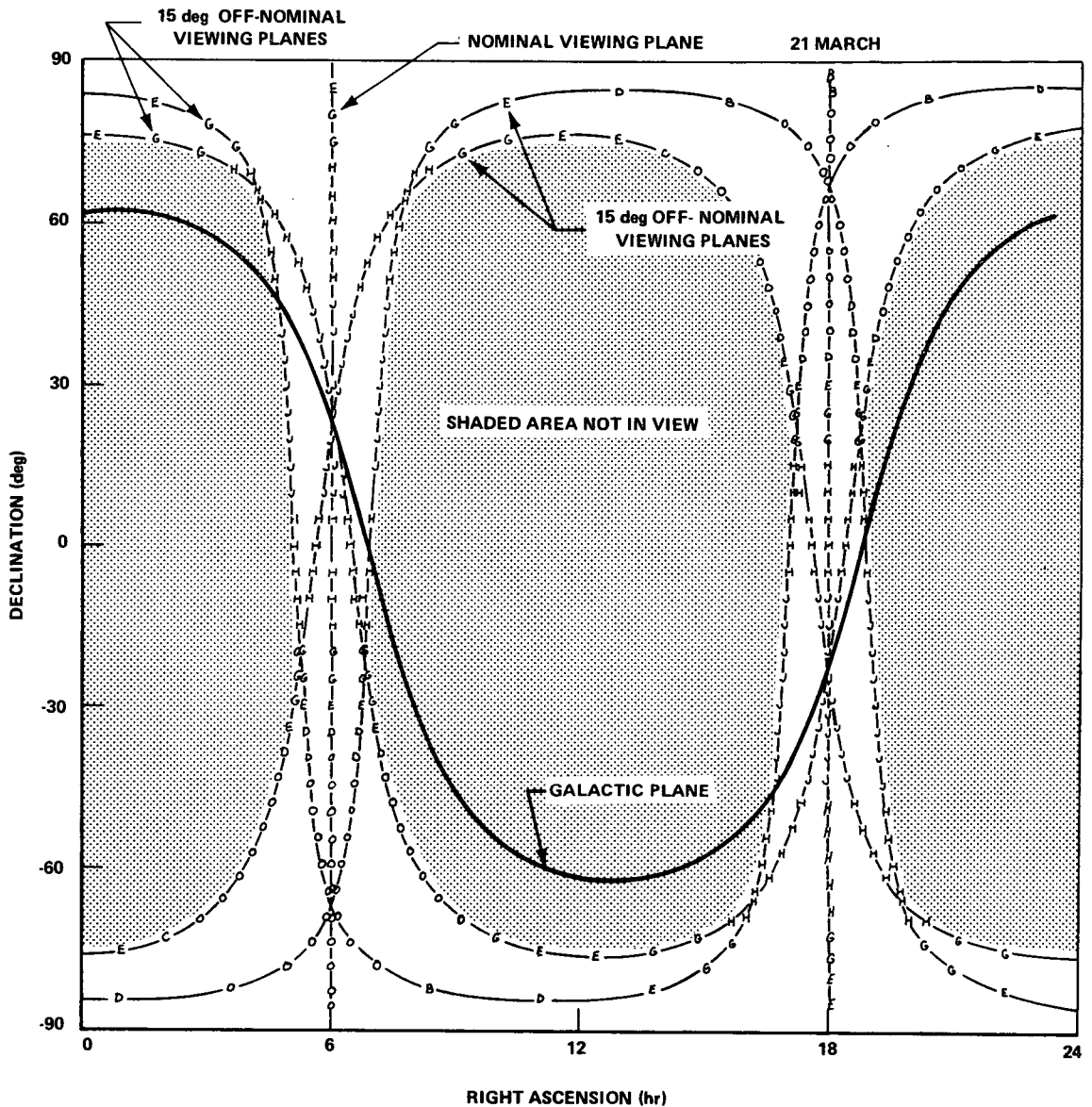


Figure III-19. Viewing planes in the equatorial coordinate system.

Note in Figure III-19 the extremely limited amount of area that would be within view if the spacecraft were not allowed any deviation from the sun line (cone angle of 0 degree). Only those points which fell directly on the nominal viewing plane could be monitored; no other points could be viewed on that date. The galactic plane is shown because it is expected that most of the sources of interest will lie close to it.

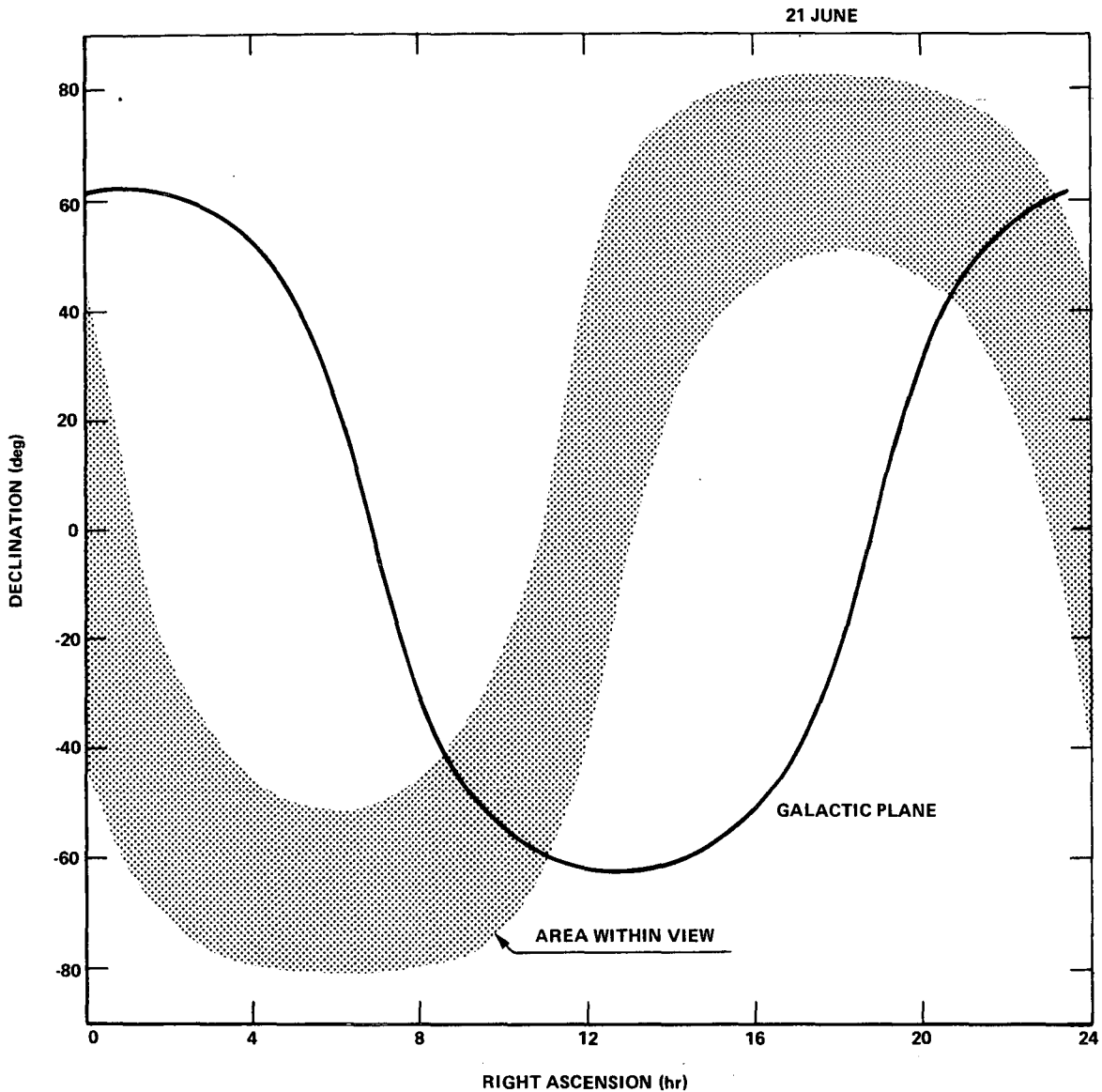


Figure III-20. Viewing area, equatorial coordinate system, 21 June.

Finally, the amount of time that each of the points would be occulted by the earth for a spacecraft in a 270 nautical mile circular orbit with inclination of 28.5 degrees and ascending node of 0 degrees is indicated by the letter used to plot the point. The following is a legend for these codes:

<u>Range of <math>t_0</math></u> <u>(min)</u>	<u>Symbol</u>
0	0
0 to 5	A
5 to 10	B
10 to 15	C
15 to 20	D
20 to 25	E
25 to 30	G
30 to 35	H
35 to 40	J
> 40	K

These times are good only for the specific orbit parameters mentioned. The estimation of minimum and maximum occultation time for an orbit with a given altitude and inclination will be discussed in another section. It is also assumed that if the point is within line of sight, there is no occultation; however, this may not be a valid assumption, as discussed later.

(3) Ecliptic System. The celestial sphere is shown in Figure III-21 in the longitude ( $\lambda$ ), and latitude ( $\phi$ ) coordinate system. The viewing area accessible for March 21 is given for the 15 degree off-solar vector pointing limit. Longitudes of 90 and 270 degrees is the viewing plane obtained when the spacecraft solar axis is pointed directly at the sun. Viewing planes are shown again for four different off-solar vector pointing cases when the spin axis is 15 degrees ahead and 15 degrees behind the sun in longitude and 15 degrees above and 15 degrees below the sun in latitude. The region outside the shaded area is within the viewing disk; this results from the 15 degrees limit for off-solar vector pointing.

Most of the known high energy sources are located near the galactic plane. The projection of this plane is shown in Figure III-21. For the March 21 date, a large percent of these sources are located near 270 degrees longitude, within viewing range of the spacecraft.

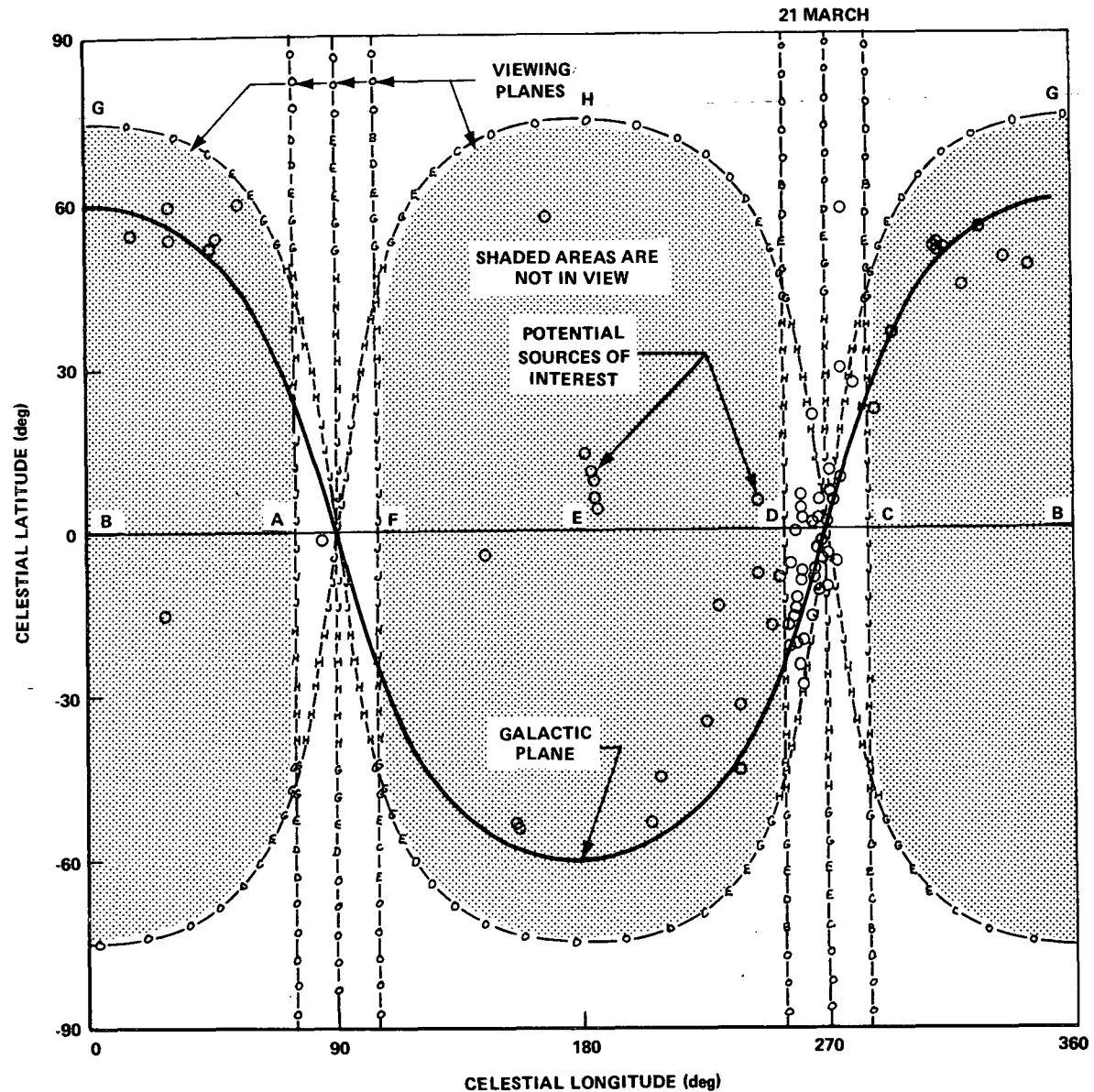


Figure III-21. Viewing planes in the ecliptic coordinate system.

The amount of time of earth occultation of the source for various latitudes and longitudes is denoted by the letters located in the different viewing bands. These occultation times are associated with a 270 nautical mile altitude, 28.5 degrees inclination, and orientation of the orbit ascending node of 0 degrees. The letter code for occultation time is the same as that given in (2).

Objects with latitude greater than 75 degrees can be seen any day during the year and still maintain an off-solar vector orientation equal to or less than 15 degrees. Figure III-22 gives the viewing area available for a given celestial longitude.

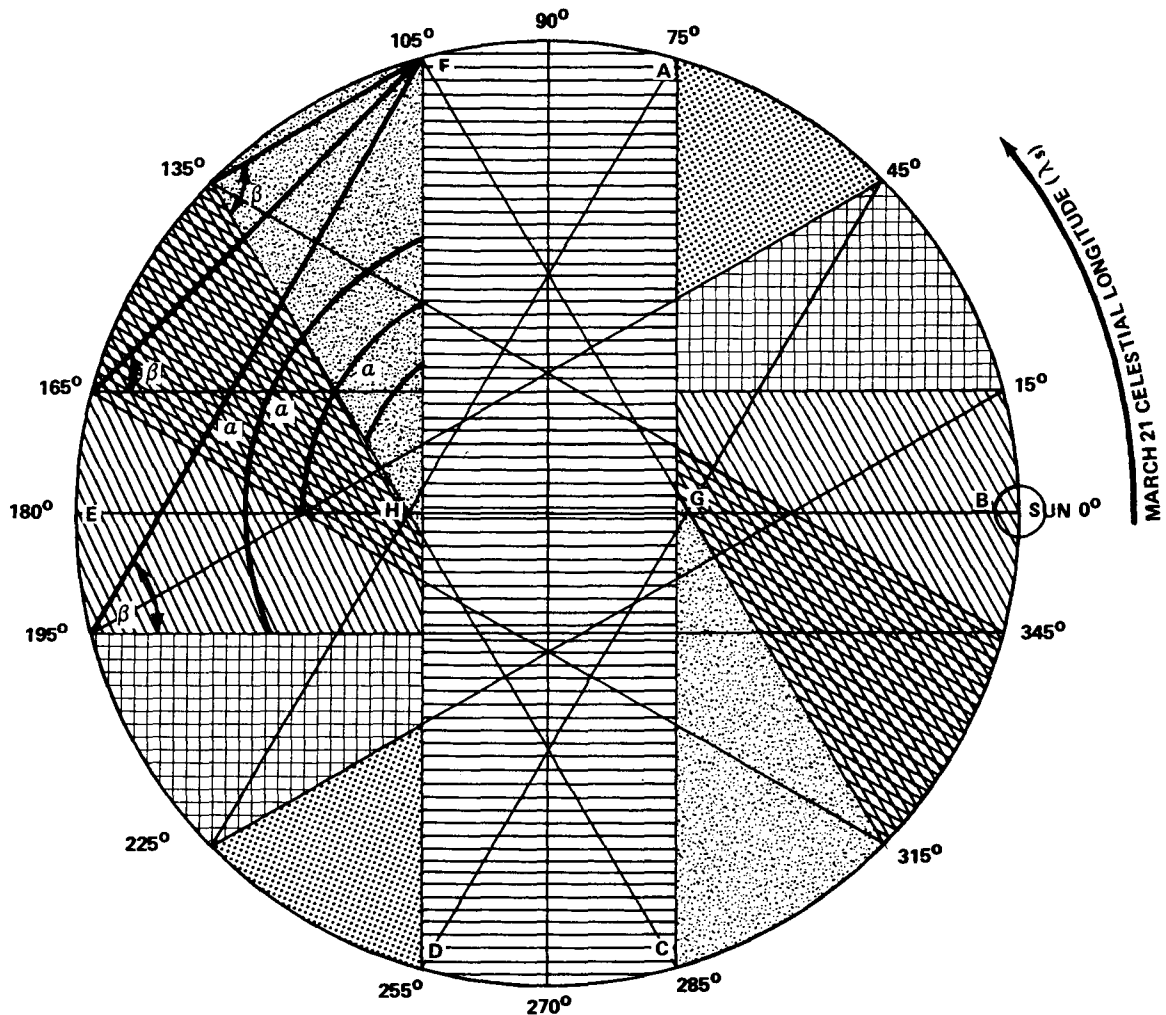


Figure III-22. Area of celestial sphere accessible to HEAO viewing.

(4) Area Exposed to Observatory's Viewing Bands. As stated previously, the nominal  $\pm 15$  degree viewing band is obtained by fixing the solar axis 15 degrees ahead and behind the sun and 15 degrees above and below the ecliptic plane. The area enclosed by this band, projected onto the celestial sphere for the March 21, is denoted by area A C D F in Figure III-22. This

figure shows a view of the celestial sphere as an observer would view it standing at the north ecliptic pole. As stated previously, it is very difficult to present a spherical surface in two dimensions and as a result, Figure III-22 has a certain amount of distortion in it. This distortion is most prevalent where straight lines drawn in two dimensions should, in fact, be curved lines in three dimensions. In light of this fact, close observation shows that the area represented by ABG, CBG, AFGH, DCGH, FHE, and DHE in Figures III-21 and III-22 are the same areas in both figures.

In spite of the distortion prevalent in Figure III-22, the problem of finding the cumulative area which the Observatory will have had access to on a given day is facilitated by the fact that the surface area of a unit sphere is proportional to the area of its Great Circle.

The area of the celestial sphere accessible for viewing by the Observatory during the day of viewing is indicated by area FACD of Figure III-22 (assuming a  $\pm 15$  degree viewing band about the normal). Figure III-23 shows the cumulative percentage of area of the celestial sphere exposed to a  $\pm 15$  degree viewing band and a  $\pm 30$  degree viewing band as a function of the number of days the spacecraft has been in orbit performing viewing activities.

The  $\pm 15$  degree viewing band curve shows that during the first day in orbit, the Observatory will have 32 percent of the celestial sphere accessible to it for viewing. Further, this curve shows that during the 30.4, 60.9, 91.3, 121.7, and 152.1 days in orbit the Observatory will have had, respectively, 47, 63, 77, 91, and 100 percent of the area accessible for viewing. The  $\pm 30$  degree curve indicates how the cumulative percentage of exposed area increases as a function of viewing band width.

Implied in this curve is the fact that doubling the width of the access band does not reduce to half the time required to cover the entire celestial sphere. As indicated, only 30 days are gained by doubling the viewing band-width.

(5) Number of Days Required for Spacecraft Access Bands to Reach a Source. The time required for the  $\pm 15$  degree access bands of the HEAO to reach a target primarily depends upon the location of the sun in the ecliptic plane. For a general case, consider the sun located in the ecliptic plane as indicated in Figure III-22. The ecliptic plane is shown in this figure as its projection on the celestial equator. Based upon this celestial longitude of the sun, the length of time required for the viewing bands of the spacecraft to reach a target as a function of the celestial longitude (celestial latitude  $\phi = 0$

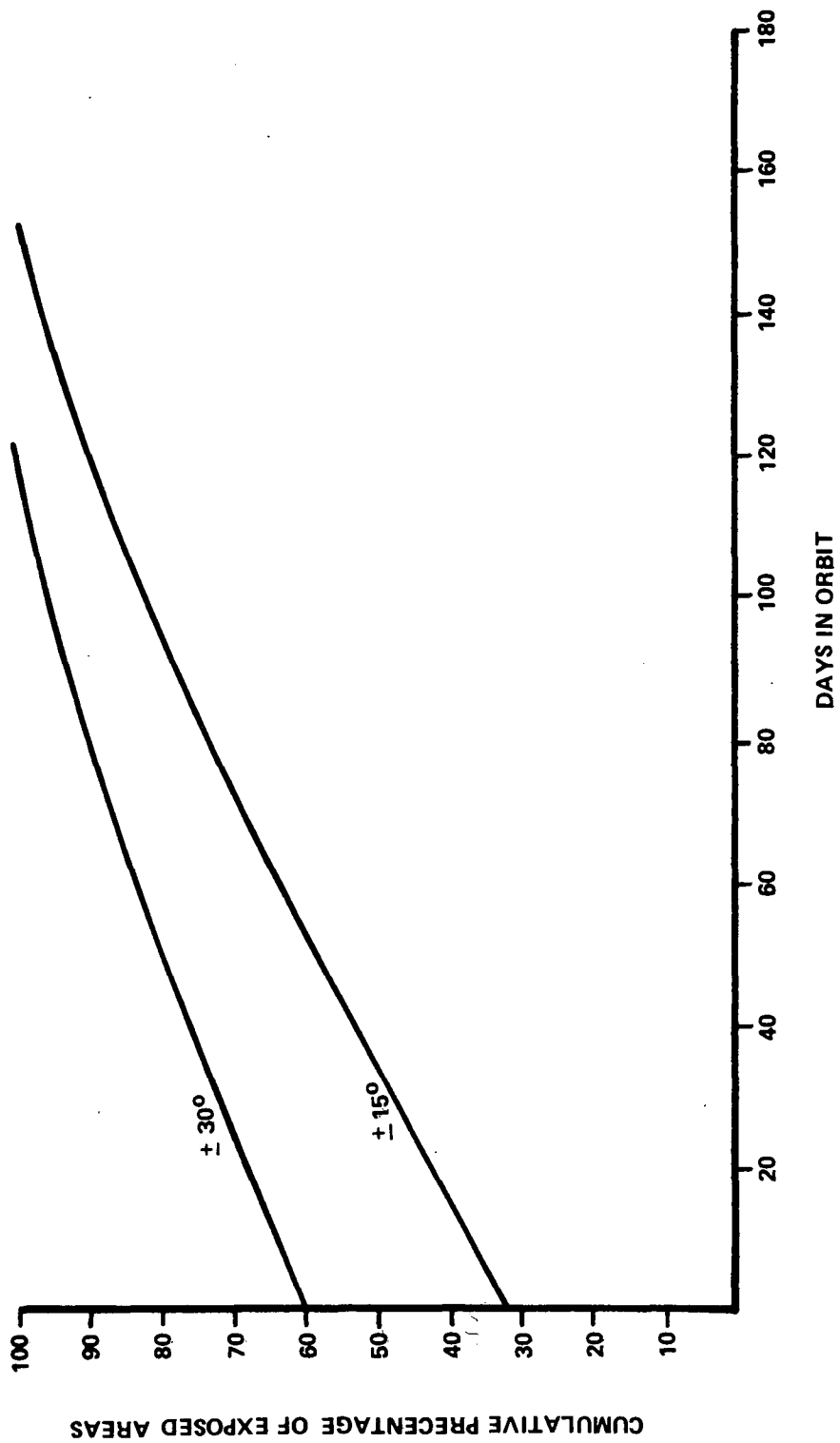


Figure III-23. Cumulative percentage of area exposed to ±15 degree and ±30 degree viewing bands.

degrees) of the source is shown in Figure III-24. Specifically, this curve shows that sources whose celestial longitudes are between 75 degrees and 105 degrees, coupled with those whose celestial longitudes are between 255 degrees and 285 degrees are available for observation during the first day in orbit.

In contrast to this, the curve in Figure III-24 shows, also, that the viewing of those sources whose celestial longitudes are 74.9 degrees and 254.9 degrees will require approximately 152 days in orbit based upon the March 21 situation shown in Figure III-23.

(6) Date to View a Given Point. A zero degree cone angle of the spacecraft's spin axis will allow two opportunities per year to view a particular target source with a short duration, in one day, of viewing time associated with both opportunities. The fifteen degree cone angle will allow a range of opportunity centered about the date derived from the zero cone angle.

Figure III-25 gives dates on which a source with a given longitude can be viewed assuming a zero angle of the spacecraft's spin axis. The viewing date is not dependent upon the source's latitude; for a given longitude all latitudes are available in the viewing plane. But the solution for the viewing dates in the equatorial system is dependent on the source's declination, and it is not as easy to work with data from the equatorial system as it is with the data presented in the ecliptic system.

(7) Maximum Number of Days a Source Will Remain Within the Spacecraft Viewing Bands. An important parameter that must be considered when defining a mission whose objectives are similar to those of the HEAO is the length of time a source will be accessible for observation and study. From a scientific point of view, this is one of the most important parameters of the entire mission. Figure III-26 presents this parameter (actual days target is accessible) per 180 days in orbit as a function of the target's absolute value of latitude ( $\phi$ ). Latitudes near zero require the rotation plane to be nearly 90 degrees inclined to the ecliptic. As a result of this, the  $\pm 15$  degree curve shows that sources located at 0 degrees celestial latitude can be viewed for only 30.4 days per 180 days in orbit and those located between  $\pm 75$  degrees and 90 degrees celestial latitude ( $\phi$ ) can be viewed during the entire mission. It is significant that those sources which are located between  $\pm 75$  degrees and 90 degrees are said to be within the circle of total access (COTA). The COTA is a function of the width of the viewing band and represents the area on the celestial sphere of a circle whose radius is one-half of the width of the viewing band utilized.

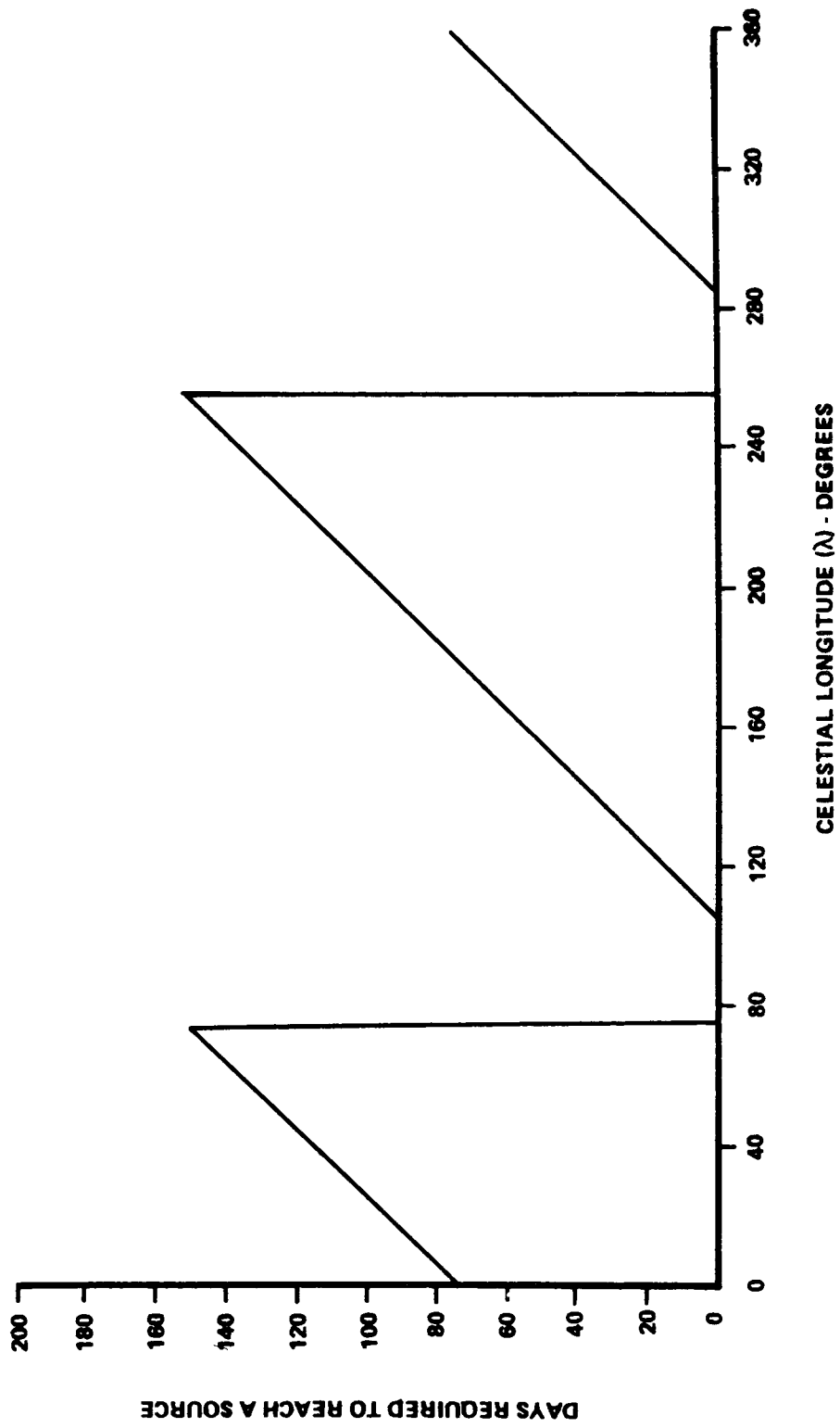


Figure III-24. Number of days required for viewing band to reach a source.

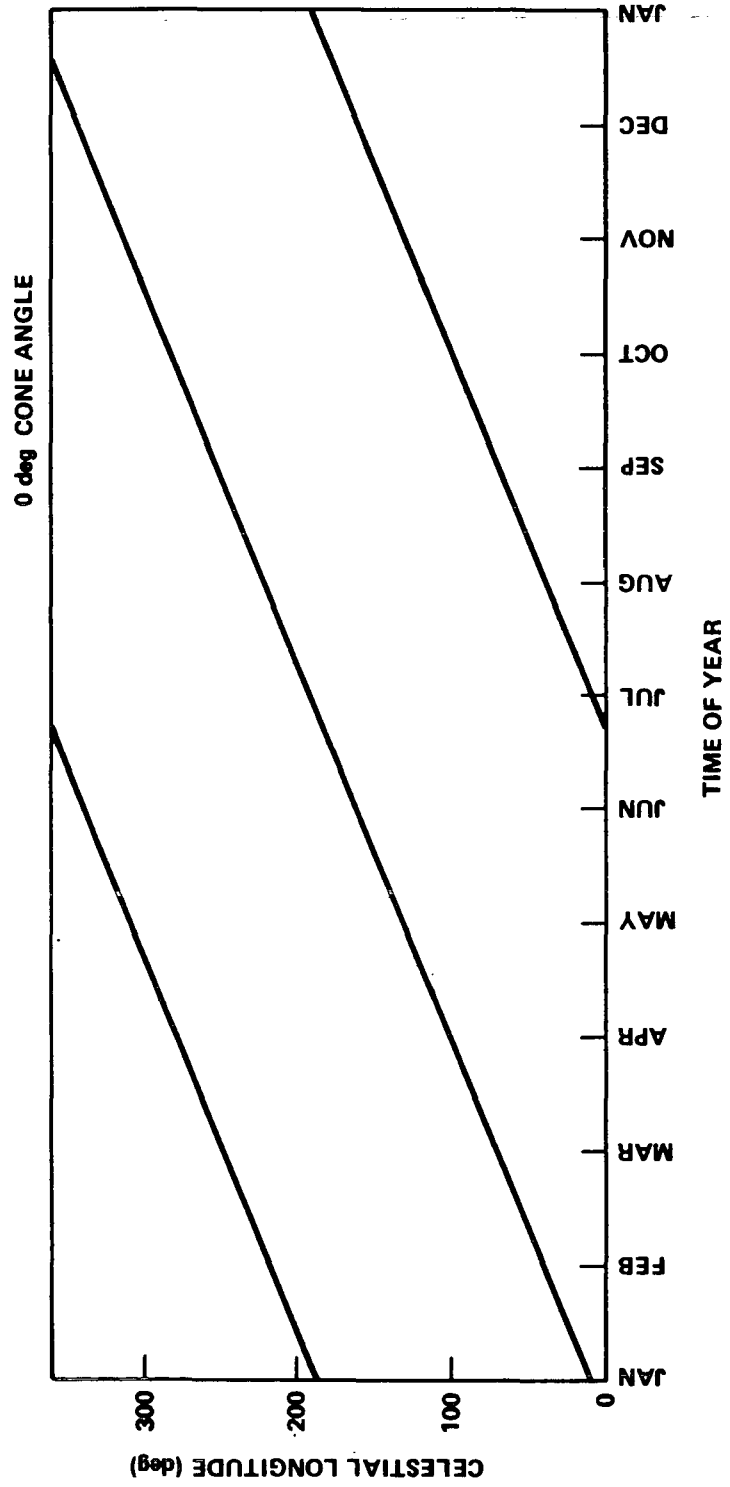


Figure III-25. Time of the year to view a given point, ecliptic system.

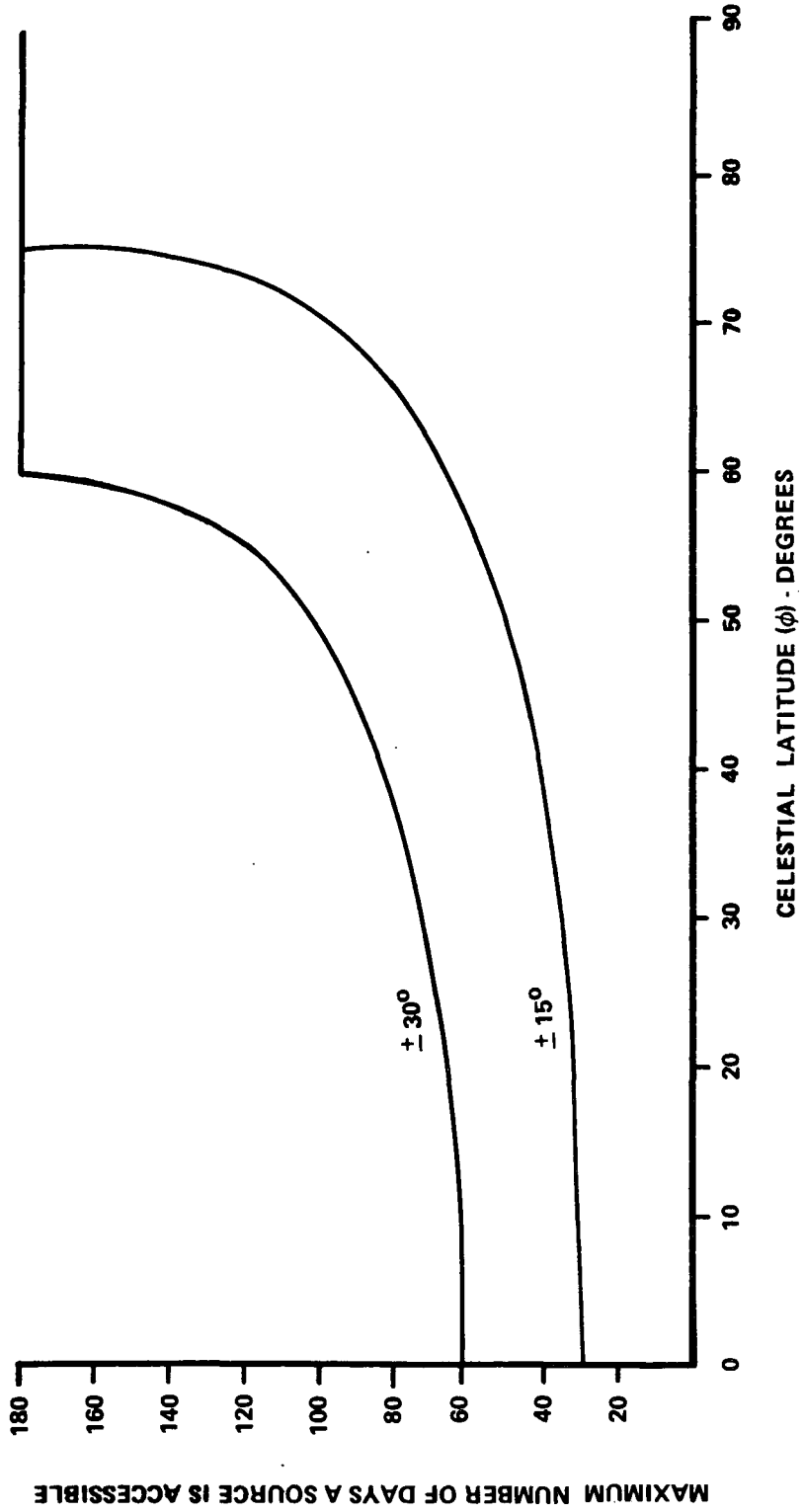


Figure III-26. Maximum number of days a source is accessible per 180 days in orbit.

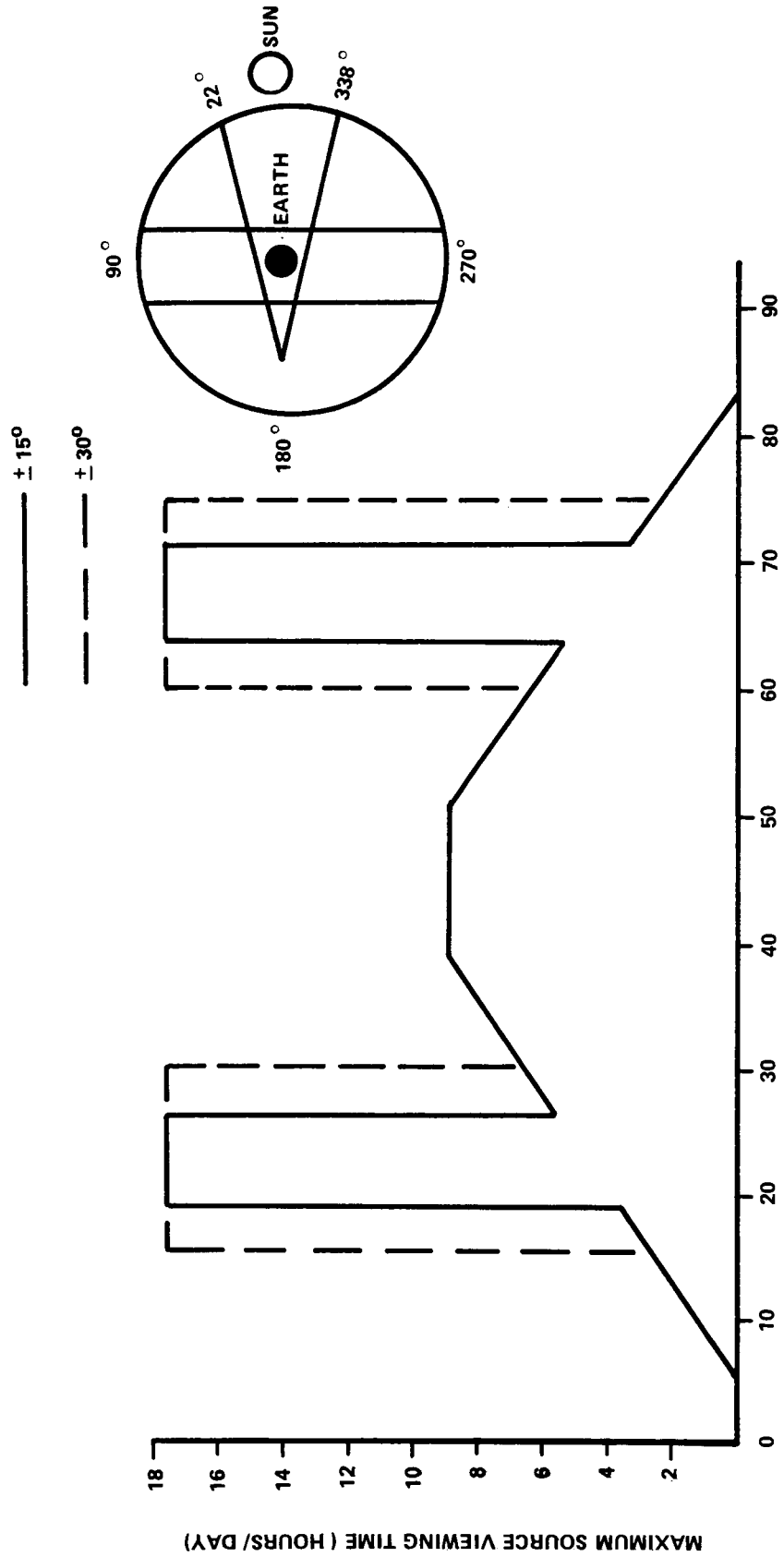
The  $\pm 30$  degrees is presented to show how the number of days a source will remain within the spacecraft's access band increases as the access bandwidth increases.

3. HEAO Viewing and Target Acquisition Time Capability. As the HEAO spacecraft orbits the earth, in a period of time of approximately 94 minutes, its solar panels will be occulted by the earth at a maximum of approximately 37 minutes of this time. During these 37 minutes the spacecraft can ignore the constraint that its solar axis must be maintained within a 15 degree half-cone in a direction perpendicular to the sun and, consequently, point to any sources on the celestial sphere which are not blocked by the earth. The capability for  $\pm 15$  degree and  $\pm 30$  degree access bandwidths based upon an altitude of 270 n.mi. is shown in Figure III-27. This capability is presented in terms of source viewing time (hours/day) as a function of the target's location for one day, as shown in the insert in Figure III-27. The  $\pm 15$  degree curve shows that sources located between 75 degrees and 105 degrees, in addition to these located between 255 degrees and 285 degrees, can be viewed considerably longer than sources at other locations. This is because the spacecraft can view these sources during the off-nominal mode as well as during the nominal mode. The combination of the nominal viewing time and the off-nominal viewing time gives rise to the capability of viewing these sources for considerable length of time per day.

Figure III-28 shows that during the time of one day in orbit for the location of the sun, as shown in the insert, the spacecraft can reach sources located between 22 degrees and 338 degrees. This implies that after 43 days in orbit, the spacecraft will have had access to the entire celestial sphere.

To determine the accessibility of these possible target sources positioned near the galactic plane, a list of 91 sources and their coordinates for these sources were taken from Reference III-7. The impact of 0 degree and 15 degree viewing angles of the spacecraft was considered in determining the accessibility of the targets.

A zero degree cone angle for the HEAO spacecraft spin-axis was considered in determining the viewing opportunity of the 91 sources. The time when these sources could be viewed is shown in Figure III-29. During most of the year, only one source is available on a given day; however, in the month of March many of the sources are within the viewing plane when as many as six sources can be seen during a day. This fact is also brought out in Figure III-21 where a large number of sources are seen to be near a longitude of 270 degrees. There are many days when there are no sources within viewing range. The viewing profile given in Figure III-29 will repeat every six months.



CELESTIAL LONGITUDE (λ) - DEGREES

Figure III-27. Maximum source viewing time.

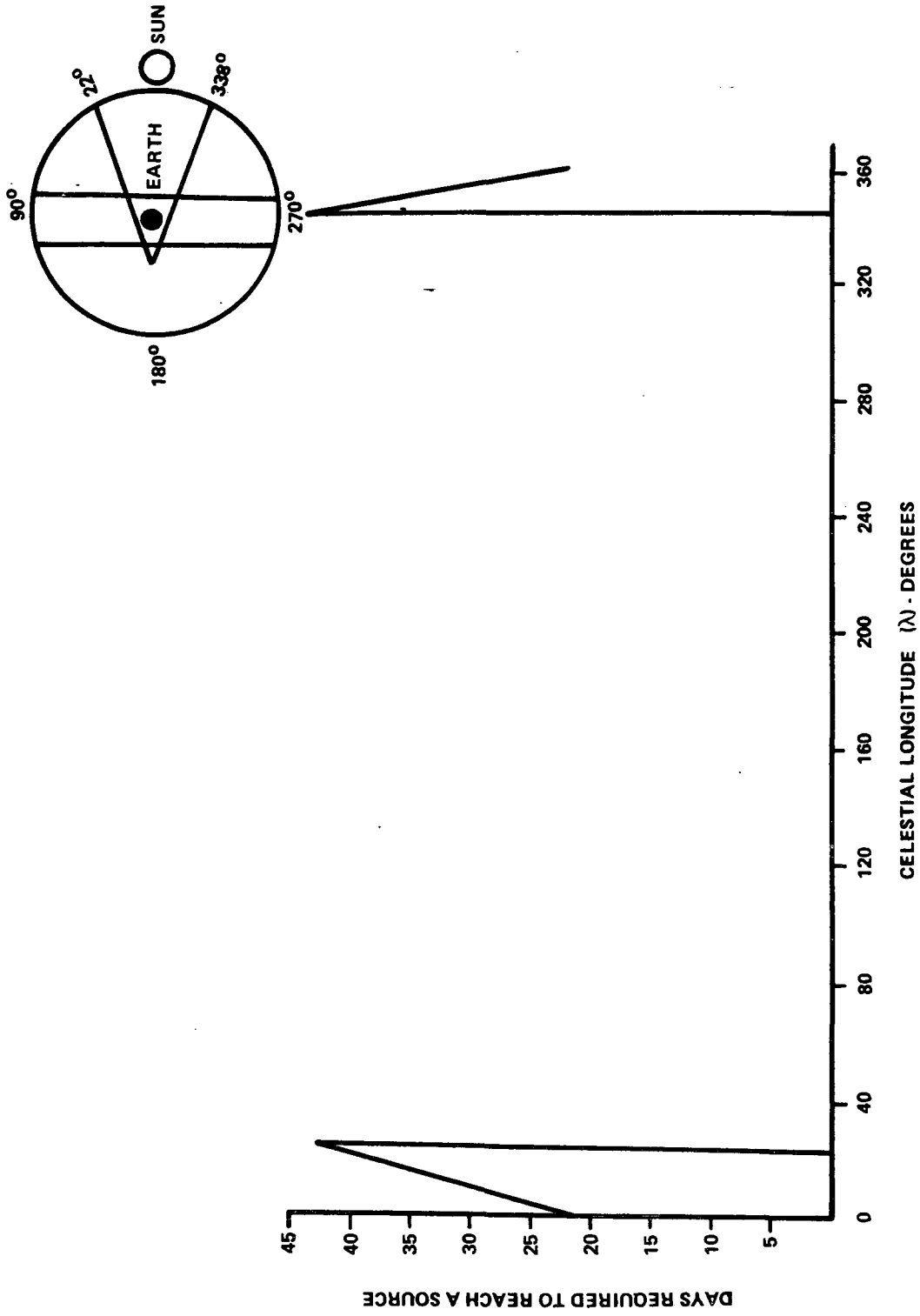


Figure III-28. Number of days required to reach a source.

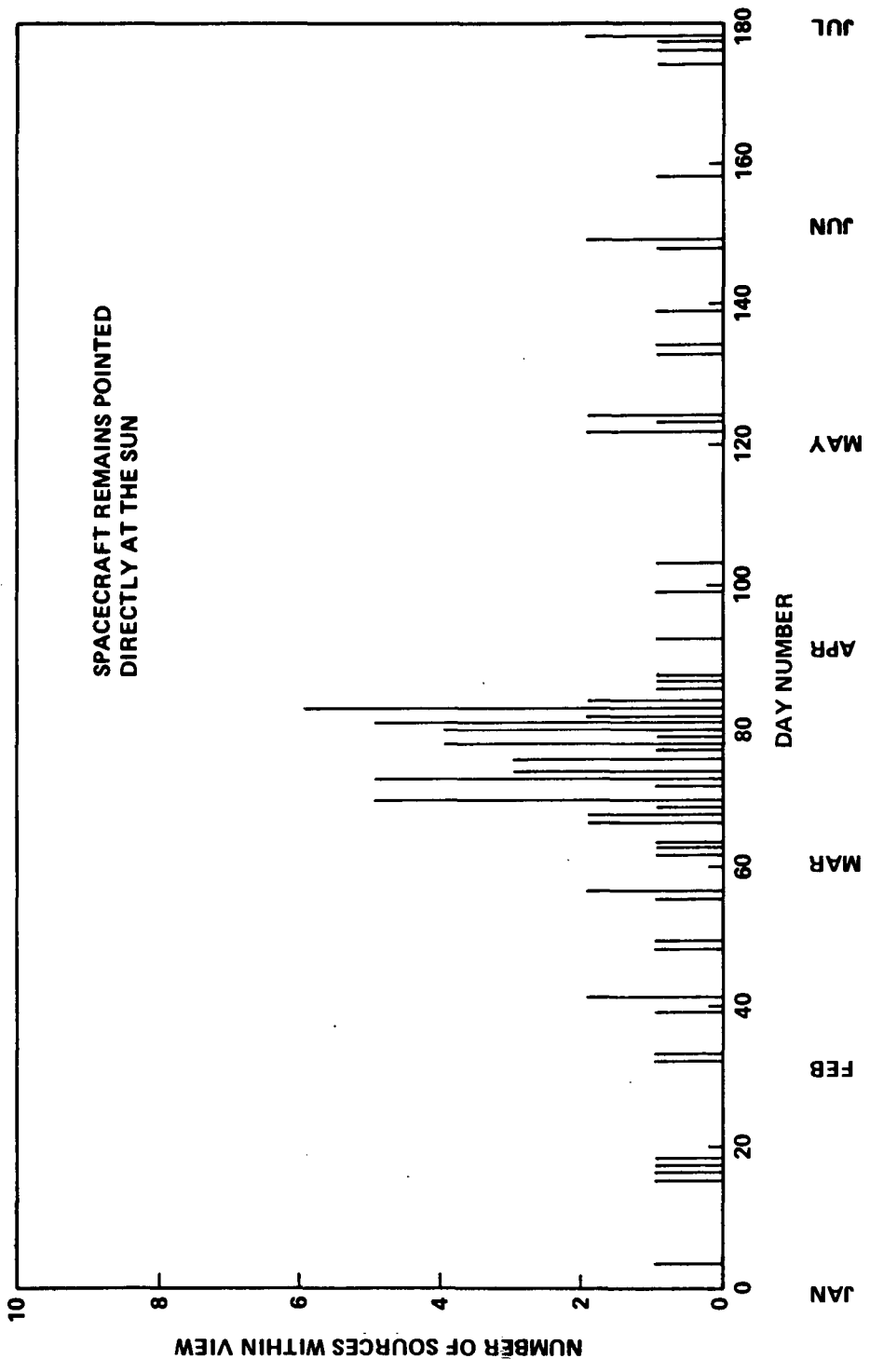


Figure III-29. Number of sources able to be viewed by HEAO, 0 degree cone angle.

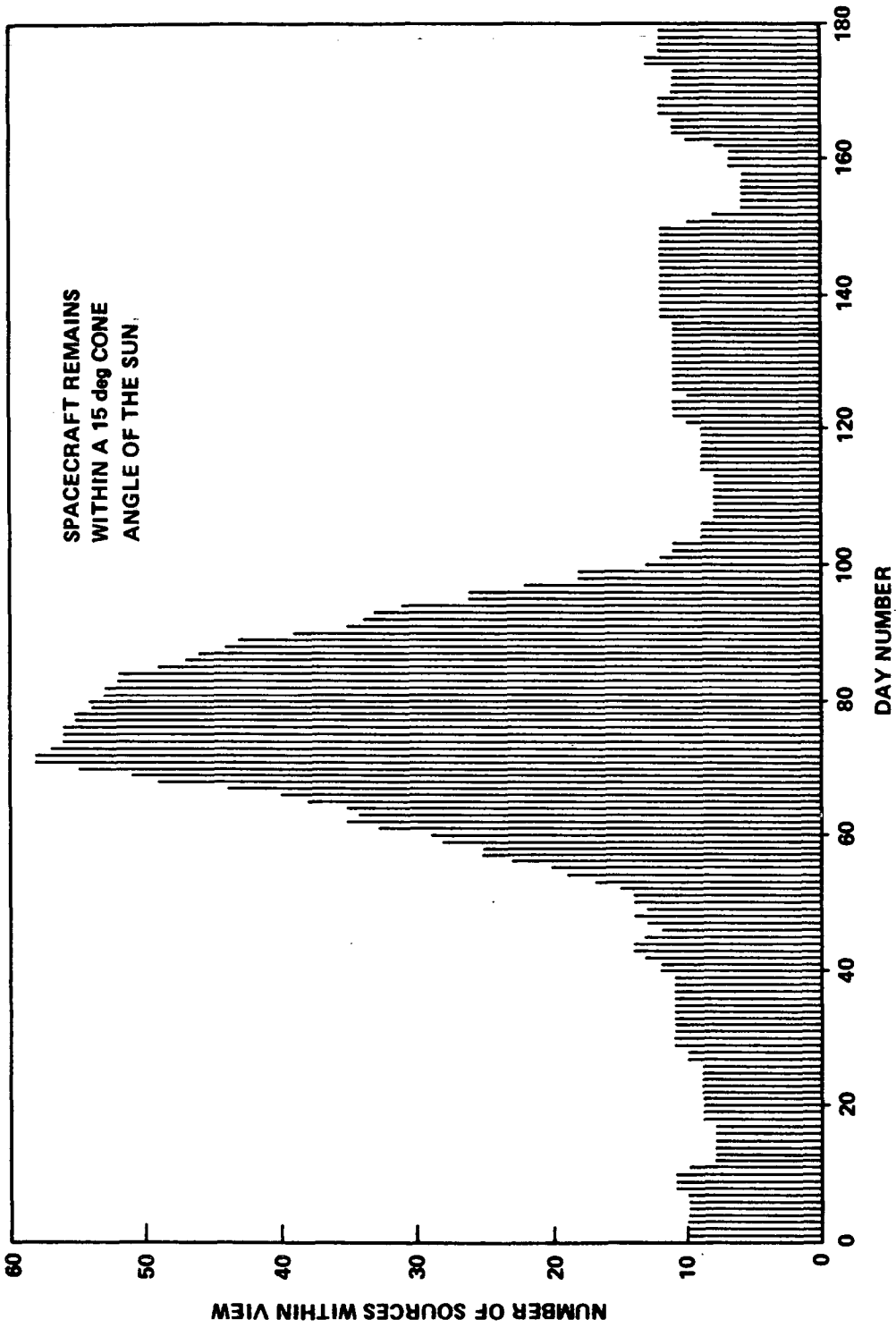


Figure III-30. Number of sources able to be viewed by HEAO, 15 degree cone angle.

Viewing accessibility for the 91 sources listed in Reference III-7 were determined for an off-solar angle of 15 degrees. This information is given in Figure III-30. During most of the year there are approximately 10 sources available per day within the 15 degree pointing limit. However, during the month of March and up to mid-April and again during the month of September and up to mid-October there are a large number of sources available for data gathering. A peak of 58 sources are within viewing range on March 21; these source positions are illustrated in Figure III-21. The viewing disk of June 21 is given in Figure III-31; here it is shown that only about 10 sources are available for potential monitoring.

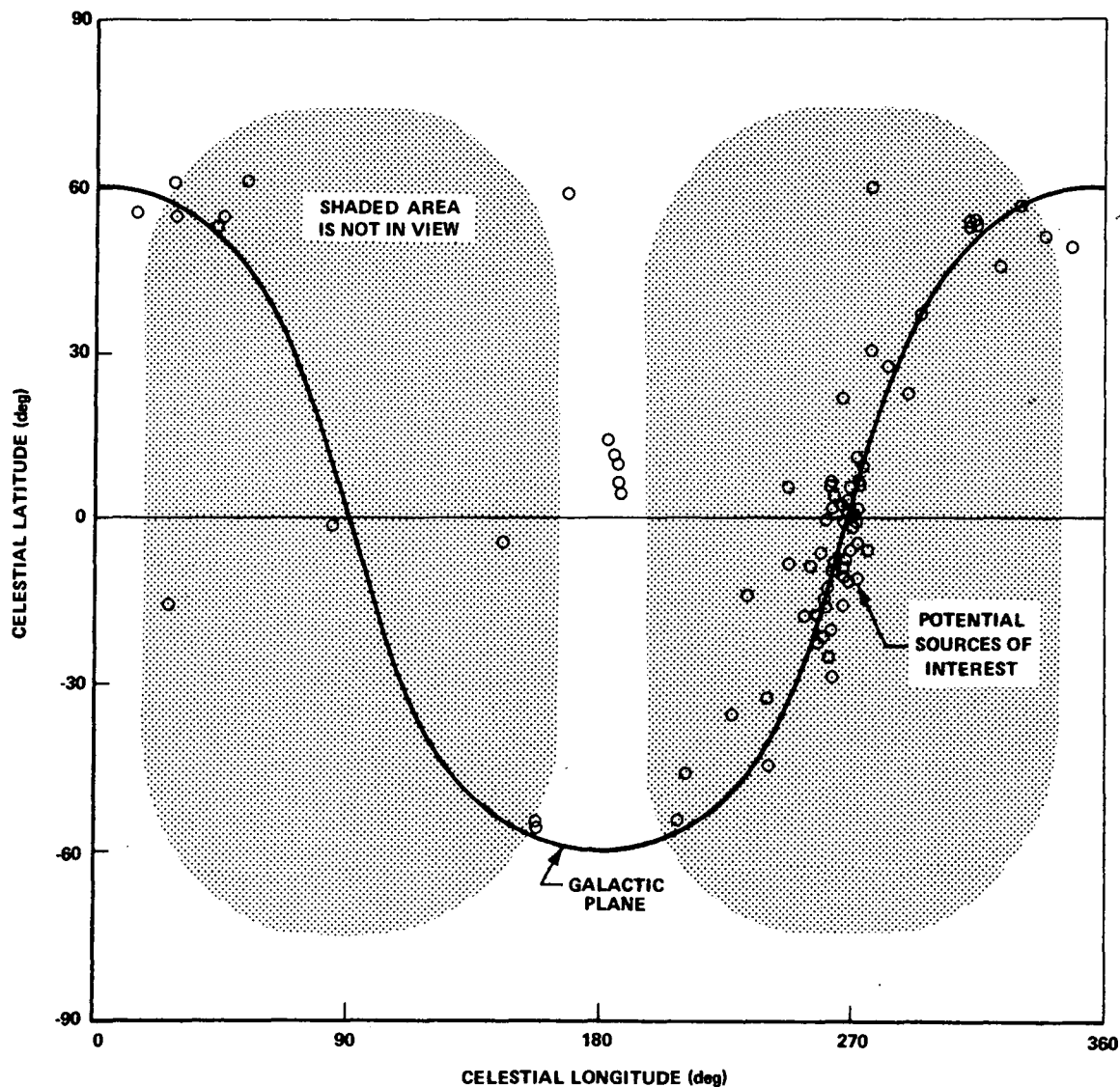


Figure III-31. Areas within view on 21 June.

Depending on the list of sources, it has been shown that there can be a wide variation in their accessibility for data gathering. To minimize the amount of maneuvering required by the HEAO spacecraft, effort will have to be expended in sequencing the target pointing schedule.

### D. Manned Space Flight Network Tracking and Data Acquisition Network Analysis

To determine the most efficient means of providing maximum network support for HEAO-C, ground network statistics were analyzed for the Manned Space Flight Network (MSFN). Accordingly, three prime network configurations in the MSFN unified S-band system were selected for comparison analysis, based on evaluation of the ground contact statistics and data processing capabilities together with increasingly more precise mission objectives. The selected configurations are designed to receive the stored wide-band experimental data and narrow-band real time data from the HEAO spacecraft. The following remote sites were considered and identified, with station code in parenthesis, for each configuration:

#### Network Configuration A

Ascension Island (ACN)	Hawaii (HAW)
Carnarvon (CRO)	Texas (TEX)
Canary Islands (CYI)	Santiago (SAN)
Guam (GWM)	

#### Network Configuration B

Canary Islands (CYI)	Hawaii (HAW)
Guam (GWM)	Texas (TEX)

#### Network Configuration C

Ascension Island (ACN)	Guam (GWM)
Canary Islands (CYI)	Hawaii (HAW)

Geodetic coordinates for MSFN station locations and antenna size data are shown in Table III-5.

TABLE III-5. MSFN STATION LOCATIONS

Network	Station	Code Name	Antenna Size (m)	Geodetic Coordinates			Height Above Ellipsoid (m)
				Latitude	Longitude		
MSFN	Ascension Island	ACN	9.144	07°57'17.26"S	345°40'22.58"E		522.0
	Carnarvon, Australia	CRO	9.144	24°54'23.68"S	113°43'33.78"E		15.0
	Grand Canary Island	CYI	9.144	27°45'52.33"N	344°21'59.05"E		173.0
	Guam, Marianas Islands	GWM	9.144	13°18'38.07"N	144°44'11.74"E		143.0
	Kauai, Hawaii	HAW	9.144	22°07'34.71"N	200°20'06.21"E		1135.0
	Corpus Christi, Texas	TEX	9.144	27°39'13.50"N	262°37'16.99"E		-20.0
	Santiago, Chile <sup>a</sup>	SAN	9.144	33°08'58.106"S	289°19'51.283"E		695.0

a. Coordinates and land masking data for STADAN SAN station were used.

The first configuration includes all the MSFN tracking stations which are equipped with the hardware that could best meet the HEAO support requirements. The remaining two were examined to determine whether they would provide the minimum requirements for compatibility and the necessary efficiency. Those complements of the remote sites were proposed by the Phase B study contractors as adequate for the HEAO Missions A and B.

The three MSFN network configurations selected for coverage analysis were to meet the following demands:

1. Provide a minimum of one contact or more per orbital revolution with a minimum time between contacts.
2. Minimize the number of remote tracking sites at a considerable savings of both budgeted and proposed funds.
3. Eliminate any split tape recorder dumps, if possible, in the event of station downtime or spacecraft failure.
4. Minimize constraints that may be imposed upon the tape recorders for data storage purposes.
5. Ensure a complete transfer of all experiment and housekeeping data recorded.

Network Configurations A and B encompassed an additional requirement that at least one tracking station (namely, Texas) in the continental United States be used for tracking and data acquisition in such a manner that rapid analysis of the recorded data would be permitted.

Although the Texas station could provide approximately 90 percent coverage of the United States for tracking and data receiving at a 270 nautical mile altitude, it may be deleted from the future network system. In this case, the Goldstone station, using the MSFN TEX equipment, would yield similar results, since these two stations are near each other from a tracking standpoint. The Space Tracking and Data Acquisition Network (STADAN) tracking station at Rosman, North Carolina, must also be considered, even though, at the 28.5 degree inclination, the contact time during some orbital revolutions is found to be less than the required minimum of 5 minutes. The Rosman site is attractive for augmenting the MSFN for S-band command and data acquisition support because of the 1 MHz tie line to the control facility in real time or delayed real time for fast data analysis.

The current mission plans dictate that the HEAO-C be launched into a nominal 270 nautical mile circular orbit inclined 28.5 degrees to the equator in late 1976 or 1977, which is a time of increasing solar activity resulting in a marked increase in the value of  $2 \sigma$  atmospheric densities.

Figures III-32, III-33, and III-34 illustrate schematically for Network Configurations A, B, and C, respectively, the mercator maps with ground orbital traces and visibility contours of each tracking station for the HEAO-C at given orbital parameters. The orbital revolution range on each map is 0 through 8. The coverage contours were computed, using the variable terrain and keyhole land masking data. The MSFN SAN station used the masking data of the STADAN station at Santiago since the former was not scheduled to become operational until 1972.

On the world maps, the mission coverage analysis started with the HEAO trajectory in a southerly direction at a latitude of 28.5 degrees and a longitude of 294.53 degrees. In the three figures, a longitude of 50 degrees east was designated as an orbital revolution counter, thus permitting easy counting of total contact times per orbital revolution without overlapping of contact time from one revolution to the next one. The orbital revolution time from the particular longitude to the same longitude was approximately 101 minutes.

The ground track for the HEAO-C repeated itself at approximately 13 days. However, only 70 orbital revolutions were evaluated because data from 70 revolutions were sufficient for the total coverage analysis.

For the first 70 orbital revolutions, contact summaries are tabulated in Tables III-6, III-7, and III-8 for three given network configurations. The contact made with the HEAO by each ground station during any particular orbital revolution is indicated by an X, using at least three principal external constraints, namely, a required minimum of 5 minutes, land masking, and elimination of one or more stations with smaller contact time during multicoverage occurrence. The contact time in excess of 5 minutes included 45 seconds for the acquisition-of-signal time and 45 seconds prior to the loss of signal and was used to minimize the number of contacts and split tape recorder dumps. The orbital revolution "0" is normally one-third of an orbit, due to a fixed location of the revolution counter.

To illustrate an example of what impact the sudden unavailability of a particular tracking station would generate on the contact statistics, the HEAO-C, in Table III-8 for Network Configuration C, was assumed to be unable to contact the CYI station throughout the 70 revolutions; this was assumed to be

TABLE III-6. CONTACT SUMMARY OF TRACKING STATIONS  
 WITH HEAO-C FOR CONFIGURATION A  
 (Altitude = 270 n.mi., Inclination = 28.5 degrees)

Orb. Rev. No.	Tracking Station							Orb. Rev. No.	Tracking Station						
	CYI	ACN	GRO	GWM	HAW	TEX	SAN		CYI	ACN	CRO	GWM	HAW	TEX	SAN
0	X							36		X		X			X
1		X	X		X	X		37	X			X			
2		X	X		X	X		38	X			X			
3		X	X	X	X	X		39	X						
4				X	X	X		40	X		X				
5				X	X			41	X		X			X	
6				X	X		X	42	X		X			X	
7		X		X	X		X	43		X	X		X	X	
8		X		X			X	44		X	X		X	X	
9	X			X				45		X	X	X	X	X	
10	X			X				46				X	X	X	
11	X							47				X	X		
12	X		X					48				X	X		X
13	X		X			X		49		X		X	X		X
14	X		X			X		50		X		X			X
15		X	X		X	X		51	X			X			
16		X	X		X	X		52	X			X			
17		X	X	X	X	X		53	X						
18				X	X	X		54	X		X				
19				X	X			55	X		X			X	
20		X		X	X		X	56	X		X			X	
21		X		X	X		X	57		X	X		X	X	
22		X		X			X	58		X	X	X	X	X	
23		X		X				59		X	X	X	X	X	
24	X			X				60				X	X	X	
25	X							61				X	X		
26	X		X					62		X		X	X		X
27	X		X			X		63		X		X			X
28	X		X			X		64		X		X			X
29		X	X		X	X		65	X			X			
30		X	X		X	X		66	X			X			
31		X	X	X	X	X		67	X						
32				X	X	X		68	X		X				
33				X	X			69	X		X			X	
34				X	X		X	70	X		X			X	
35		X		X	X		X								

TABLE III-7. CONTACT SUMMARY OF TRACKING STATIONS  
 WITH HEAO-C FOR CONFIGURATION B  
 (Altitude = 270 n. mi., Inclination = 28.5 degrees)

Orb. Rev. No.	Tracking Station				Orb. Rev. No.	Tracking Station			
	CYI	GWM	HAW	TEX		CYI	GWM	HAW	TEX
0	X				36		X		
1			X	X	37	X	X		
2			X	X	38	X	X		
3		X	X	X	39	X			
4		X	X	X	40	X			
5		X	X		41	X			X
6		X	X		42	X			X
7		X	X		43			X	X
8		X			44			X	X
9	X	X			45		X	X	X
10	X	X			46		X	X	X
11	X				47		X	X	
12	X				48		X	X	
13	X			X	49		X	X	
14	X			X	50		X		
15			X	X	51	X	X		
16			X	X	52	X	X		
17		X	X	X	53	X			
18		X	X	X	54	X			
19		X	X		55	X			X
20		X	X		56	X			X
21		X	X		57			X	X
22		X			58		X	X	X
23	X	X			59		X	X	X
24	X	X			60		X	X	X
25	X				61		X	X	
26	X				62		X	X	
27	X			X	63		X		
28	X			X	64		X		
29			X	X	65	X	X		
30			X	X	66	X	X		
31		X	X	X	67	X			
32		X	X	X	68	X			
33		X	X		69	X			X
34		X	X		70	X			X
35		X	X						

TABLE III-8. CONTACT SUMMARY OF TRACKING STATIONS  
 WITH HEAO-C FOR CONFIGURATION C  
 (Altitude = 270 n. mi., Inclination = 28.5 degrees)

Orb. Rev. No.	Tracking Station				Orb. Rev. No.	Tracking Station			
	CYI	ACN	GWM	HAW		CYI	ACN	GWM	
0	X				36		X	X	
1		X		X	37	X		X	
2		X		X	38	X		X	
3		X	X	X	39	X			
4			X	X	40	X			
5			X	X	41	X			
6			X	X	42	X			
7		X	X	X	43		X		X
8		X	X		44		X		X
9	X		X		45		X	X	X
10	X		X		46			X	X
11	X				47			X	X
12	X				48			X	X
13	X				49		X	X	X
14	X				50		X	X	
15		X		X	51	X		X	
16		X		X	52	X		X	
17		X	X	X	53	X			
18			X	X	54	X			
19			X	X	55	X			
20		X	X	X	56	X			
21		X	X	X	57		X		X
22		X	X		58		X	X	X
23		X	X		59		X	X	X
24	X		X		60			X	X
25	X				61			X	X
26	X				62		X	X	X
27	X				63		X	X	
28	X				64		X	X	
29		X		X	65	X		X	
30		X		X	66	X		X	
31		X	X	X	67	X			
32			X	X	68	X			
33			X	X	69	X			
34			X	X	70	X			
35		X	X	X					

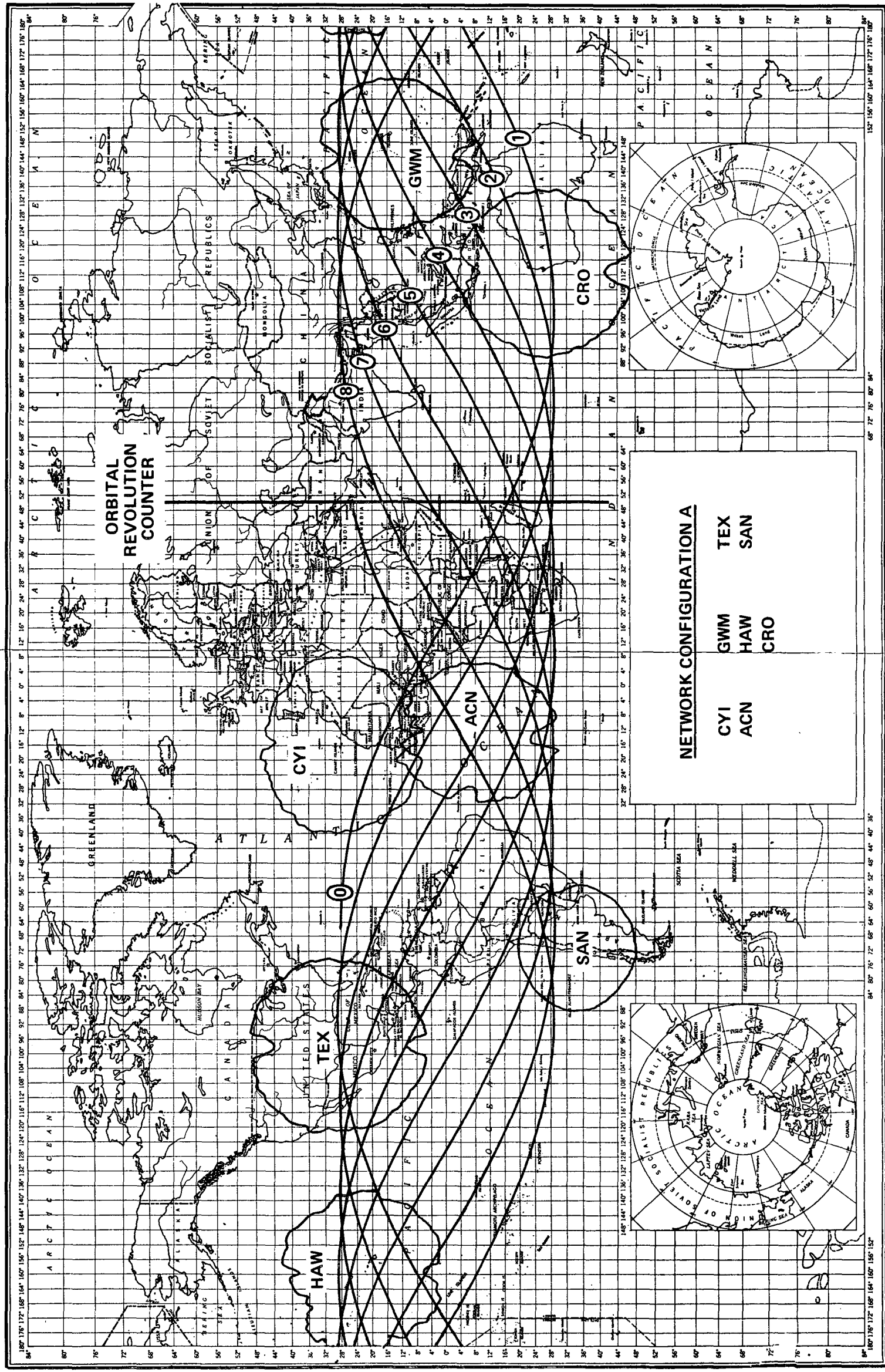


Figure III-32. Ground traces for Network Configuration A  
(H = 270 n.mi., i = 28.5 degrees).

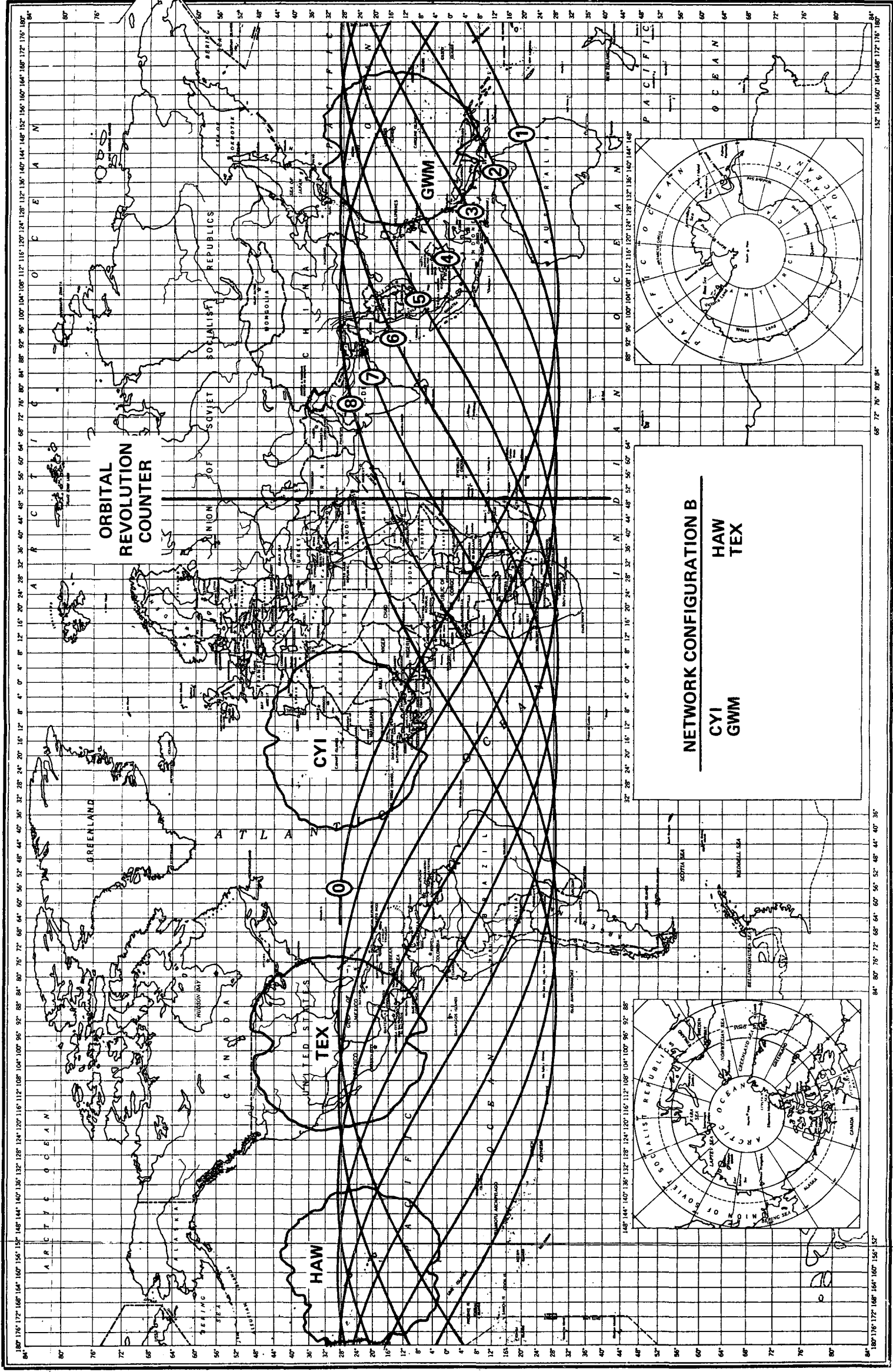


Figure III-33. Ground traces for Network Configuration B  
 (H = 270 n. mi., i = 28.5 degrees).

EOLDOUT FRAME

EOLDOUT FRAME

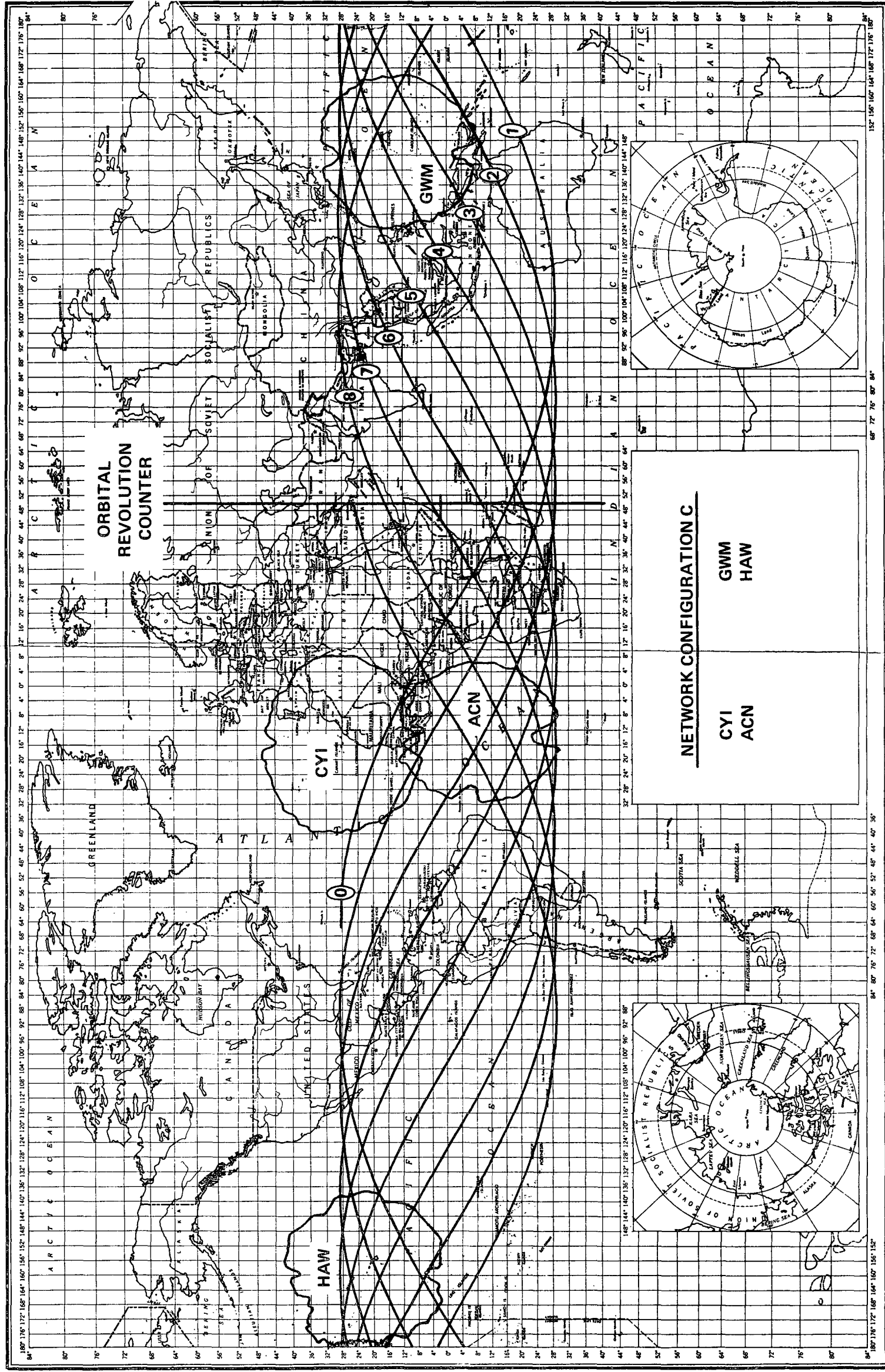


Figure III-34. Ground traces for Network Configuration C (H = 270 n. mi., i = 28.5 degrees).

attributable to station downtime or use of station by higher priority spacecraft. This failure resulted in a substantial number of revolutions (23) without a single station contact in the given revolution frame; whereas, only 11 revolutions failed to obtain station contact for Network Configuration B. In addition, Configuration C failed to achieve any contact during four successive passes and Configuration B for two successive passes.

Ground contact and gap statistics are compared in Figures III-35, III-36, and III-37 for three respective configurations. The solid blocks, depicting the contact interval, indicate ground contacts equal to or greater than 5 minutes, using actual land masking data. The time since initial insertion, identified in hours, is also shown. Based on the nominal HEAO-C trajectory, the TEX station of interest made four contacts with the spacecraft during the first 7 hours and was not contacted until almost 22 hours later. Consequently, the TEX station provided approximately 65 minutes of coverage time during a 24 hour period.

HEAO-C tracking and data storage requirements have been analyzed for the three network configurations. While orbiting the earth, the HEAO records the data continuously in real time at a maximum input bit rate of 27.5 kilobits per second. This handling capacity consists of 25 kilobits per second experiment data and 2.5 kilobits per second engineering status data. When in sight of a ground station, stored spacecraft telemetry data can be dumped at an output bit rate of 500 kilobits per second. Although 1 megabit per second is a maximum output rate limited by processing capability of the ground station equipment, the 500 kilobits per second rate has been used for receiving and bit-conditioning the tape recorder dump to remain within the equipment capability.

The analysis of data in storage was based on an assumption that the spacecraft contained four onboard tape recorders for simultaneous recording and reproducing. Based on both input and output bit rates, the minimum average contact time required to retrieve all stored data was determined to be 5.5 percent of the whole time of orbital revolution. So, at the orbital revolution period of approximately 101 minutes, the required minimum average contact time was calculated to be 5.6 minutes per revolution. The time in excess of 5.6 minutes included 90 seconds for acquisition of signal and loss of signal. Examination revealed the minimum average contact time per orbit of 11.80 minutes for Network Configuration A, 8.93 minutes for Network Configuration B, and 10.40 minutes for Network Configuration C.

For the 270 nautical mile/28.5 degree orbit, the spacecraft was capable of recording 167 megabits of data per orbital revolution, assuming the input

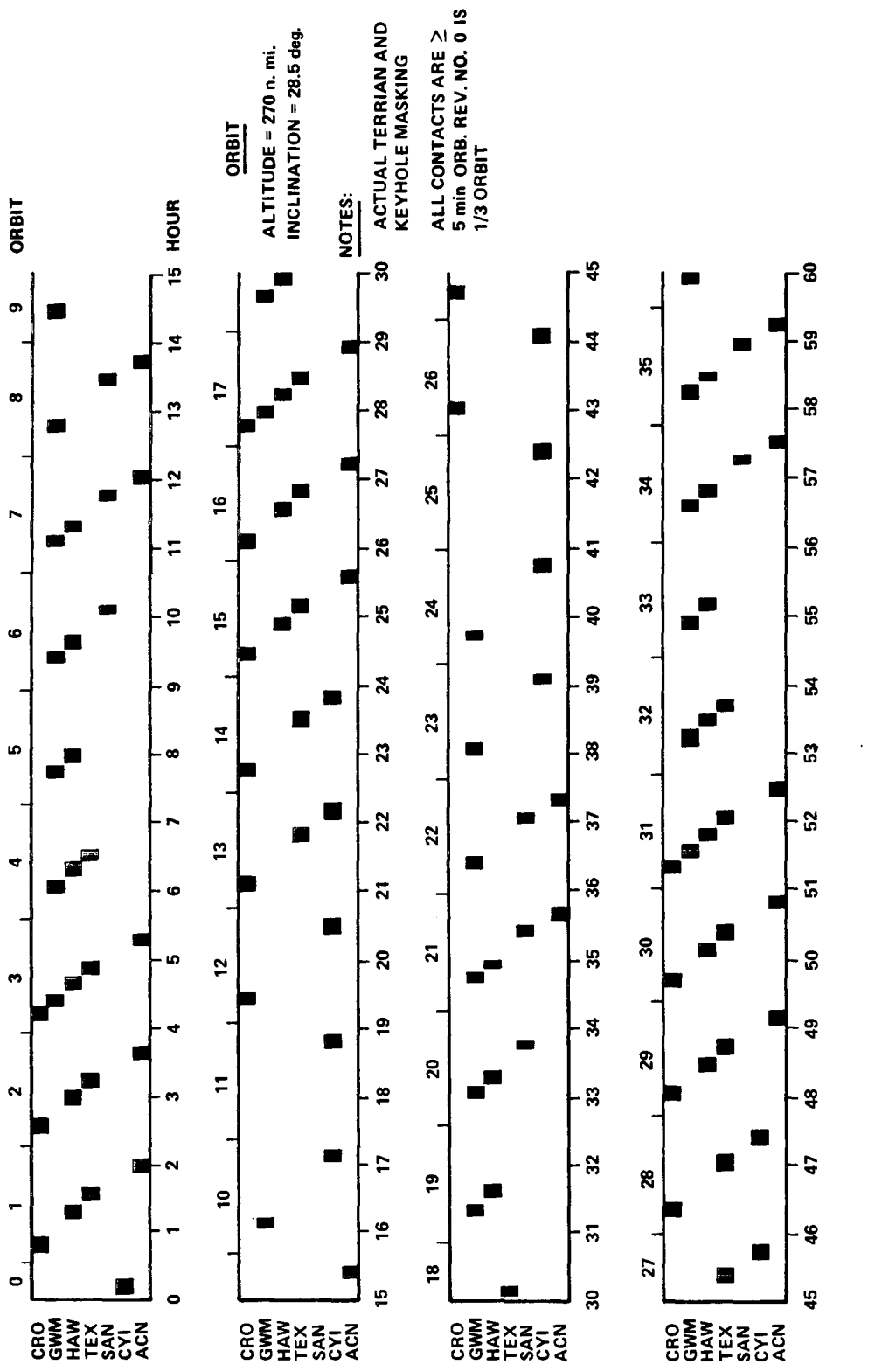


Figure III-35. Ground contact statistics for Network Configuration A.

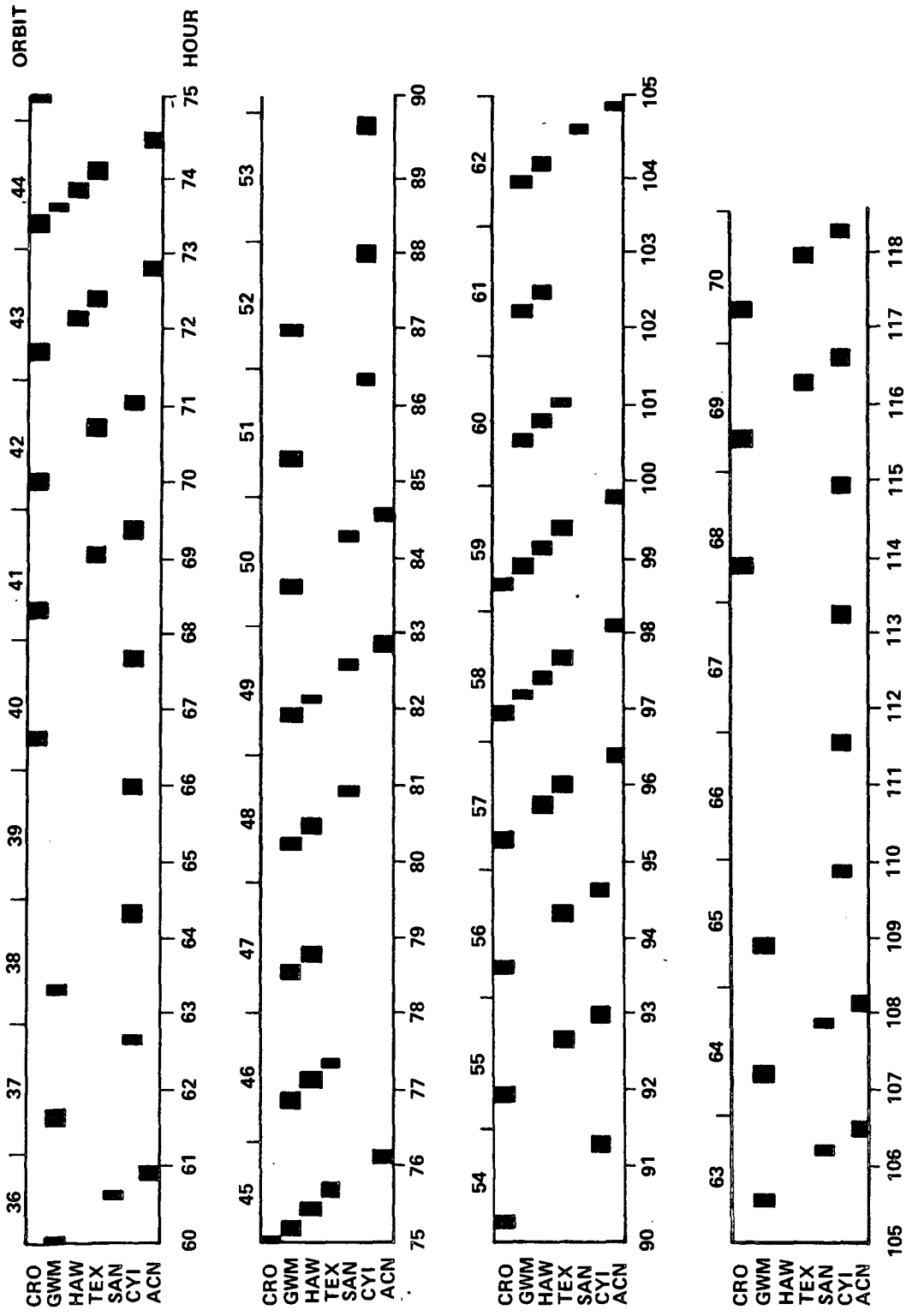


Figure III-35. (Concluded).

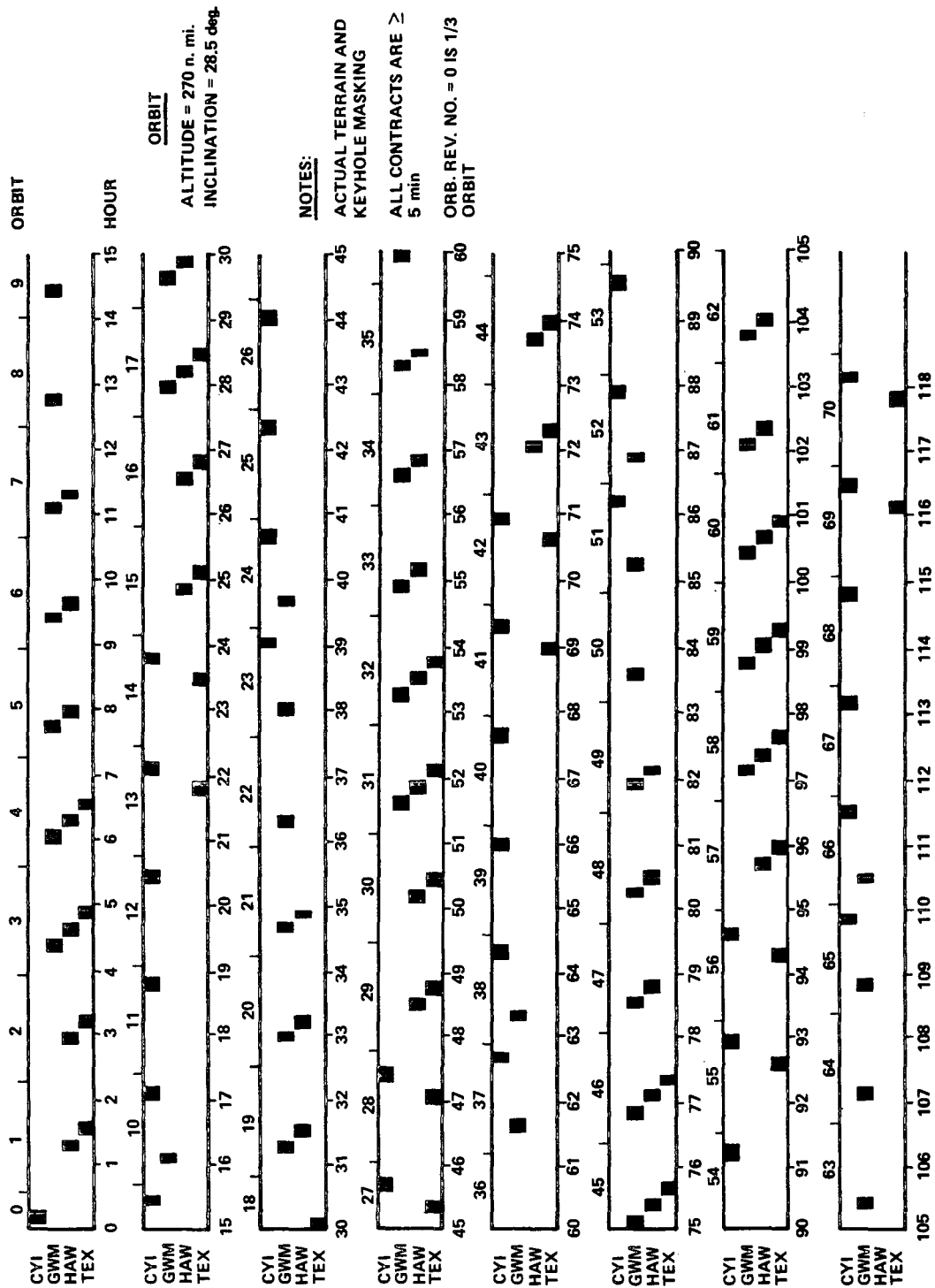


Figure III-36. Ground contact statistics for Network Configurations B.

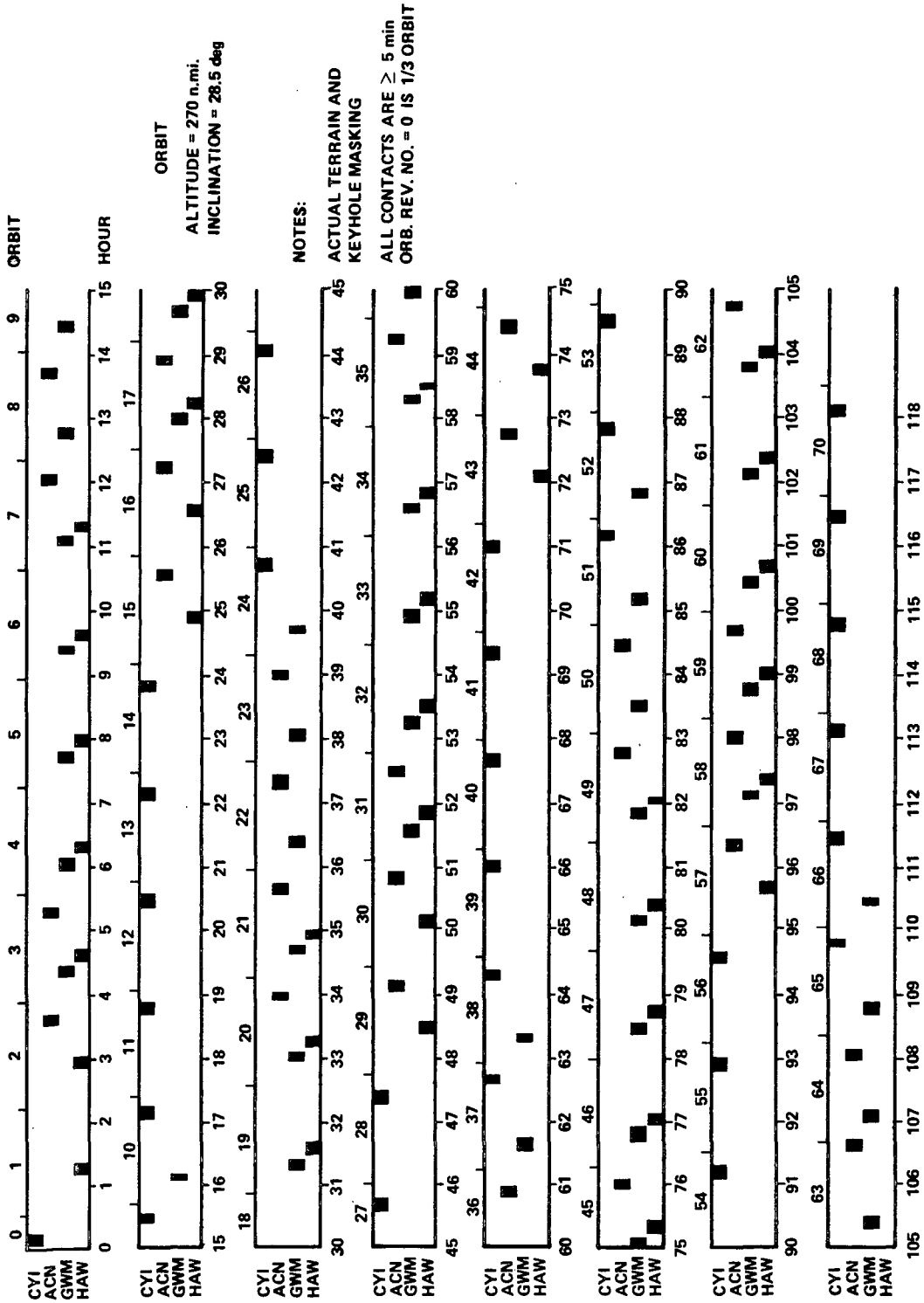


Figure III-37. Ground contact statistics for Network Configuration C.

rate of 27.5 kilobits per second. Hence, at the delayed real time data rate, the analysis showed that 334 seconds would be required for playback of one revolution of the HEAO data. However, the maximum value of 167 megabits was not exceeded, although the three network configurations reached a peak of approximately 165 megabits several times, whenever the longer gap occurred. The Network Configuration B had the longest gap duration of 90.62 minutes. The study did not show any split dump when the 165 megabits of stored data were dumped at the next station for the three configurations. Consequently, only two tape recorders were required throughout the 70 revolutions for all three configurations. However, if either four-site configuration loses one station for any reason, a third tape recorder probably would be required. The recording and dumping pattern continued to repeat throughout 70 revolutions.

Table III-9 illustrates a trade-off in tracking data versus the number of tracking stations of MSFN to determine the capabilities of mission coverage and data in storage. The results from the computer simulation indicated that two tape recorders were probably adequate to meet the data storage requirements. However, a third tape recorder or more may be necessary for the contingency situations.

Regardless of the number of tracking stations, an average of 90 minutes was found to be the maximum gap duration for any one of three configurations. The gap duration may increase when one particular station is shut down in either one of the four-site configurations. Network Configuration B contained six significant gaps more than Network Configuration A for 70 revolutions. Shutdown of the Canary Islands station would result in a loss of 322.4 minutes of data for the first 70.3 revolutions.

Total contact times in minutes are given for each following MSFN tracking station for the 70.3 revolutions:

CYI	-	322.4	HAW	-	345.7
ACN	-	266.6	TEX	-	320.8
CRO	-	320.2	SAN	-	102.4
GWM	-	381.5			

Total contact times included all coverage times over stations in excess of 5 minutes.

TABLE III-9. MSFN COVERAGE SUMMARY (Orbital Count = 70 Revolutions, Altitude = 270 n.mi., Inclination = 28.5 degrees)

Tracking Data	Network Configuration		
	A	B	C
Total Contact Time (70 revs) (min)	2059.53	1376.30	1316.22
Number of Contacts	208	136	133
Percent of Contact Time	28.98	19.37	18.52
Average Contact Time Per Revolution (min)	29.27	19.51	18.65
Minimum Time of Contacts Per Revolution (min)	11.80	8.93	10.40
Average Number of Contacts Per Day	42	27	27
Minimum Number of Contacts Per Revolution	1	1	1
Number of Revolutions Without Contact	0	0	0
Maximum Gap Duration (min)	88.50	90.62	88.82
Average Gap (min)	24.35	42.39	43.81
Percent of Coverage Gap Less than 1 Hour Long	92.79	63.24	75.19
Maximum Peak of Data in Storage (Megabits)	164.615	165.255	165.904
Number of Peaks of Data in Storage	5	16	20
Maximum Time for Data Acquired and Dumped (min)	111.58	112.00	109.68

The two 4-site configurations achieved 16 or more peaks of maximum data in storage during the 70 revolutions, as compared to 5 for the 7-site configuration. (The term "peak" should not constitute an influential factor in the design; the 167 megabits value is not considered a large capacity for tape recorder technology.)

It could be concluded that the four-station configurations are just as efficient as the seven-station configuration from the standpoint of maximum data in storage. Apparently the only factor to influence the design of the HEAO depends on the case of specific station outage.

## E. Mission Timelines

1. Purpose. The purpose of the timeline analysis was to identify the mission and operation activities which are representative of those that would be performed during the two year HEAO-C mission. The exploring of these activities, presented in the form of mission timelines, aided in identifying particular problem areas in mission operations, subsystems design, and systems integration.

The timelines are divided into the following three mission phases: (1) Prelaunch, (2) Launch-to-orbit and final orbit insertion, and (3) On-orbit experiment operations. The major activities which are necessary during the prelaunch phase of operations are discussed in Section 2. The activities which are encompassed during the launch-to-orbit and final orbit insertion phase are discussed in Section 3. This includes the events necessary for final preparation for source viewing.

A gross overview of the two year operations is discussed in Section 6. Also included are the detailed timelines for the events of particular interest and a discussion of the logic utilized for viewing the sources on the celestial sphere. These events and the frequency of their occurrence represent what has been assumed as characteristic of the activities which will be required by the HEAO spacecraft.

The timelines are based on the mission requirements and the subsystems capabilities. They represent a compilation of information from other study results into a typical integrated mission. Such restrictions as the launch vehicle capabilities and the tracking station network were considered in timelining

the launch phase of the mission. The orbit characteristics, the experiment requirements, and the HEAO spacecraft capabilities were considered in the development of the on-orbit experiment operations.

2. Prelaunch Activities. Figure III-38 shows the major activities that are necessary during the prelaunch phase of the mission. Approximately 50 days before launch, the HEAO (spacecraft mated with OAS) arrives at ETR. Thirty-six days before launch, the HEAO is installed on the booster and compatibility and systems tests are performed. The OAS and spacecraft is loaded with propellants and pressurants twenty-days before launch. The shroud is installed at T-10 days. Batteries are charged 3 1/2 days before launch.

Figure III-39 shows a typical countdown beginning 360 minutes before launch. At 10 minutes before launch the Observatory systems go off external power and begin to utilize internal battery power only, on which they will remain until the Observatory acquires the sun and deploys its solar panels. A period of approximately one orbit of coast within the 140 by 250 nautical mile orbit will be required before the Observatory will have been stabilized and rate dumped, acquired the sun, and deployed its solar panels. This results in a total elapsed time of about 1 and 1/2 hours on battery power.

3. Launch-to-Orbit and Orbit Correction. The activities and events required from lift-off through injection into the desired orbit, including final preparation for the viewing of sources, are presented in Table III-10.

Three basic assumptions underline the events of putting the HEAO spacecraft in the desired orbit. First, the spacecraft will perform its delta velocity ( $\Delta V$ ) burns while in contact with a tracking station. This is based on the desire to monitor the spacecraft during the burn time so that such characteristics as the orientation of the vehicle and the magnitude and duration of burn can be verified. The second assumption is that prior to injection into the transfer orbit the spacecraft will have passed over three tracking stations so that the orbital parameters can be determined. The third assumption is that final desired orbital altitude is 270 nautical miles. This altitude gives the desired two year lifetime at 28.5 degrees inclination.

As explained in Section B, the OAS/HEAO spacecraft is injected into a nominal 140 by 250 nautical mile parking orbit by the Titan IIDD. Approximately two days coasting (31 orbits) are required after injection into the parking orbit before the first opportunity for an apogee burn occurs over a

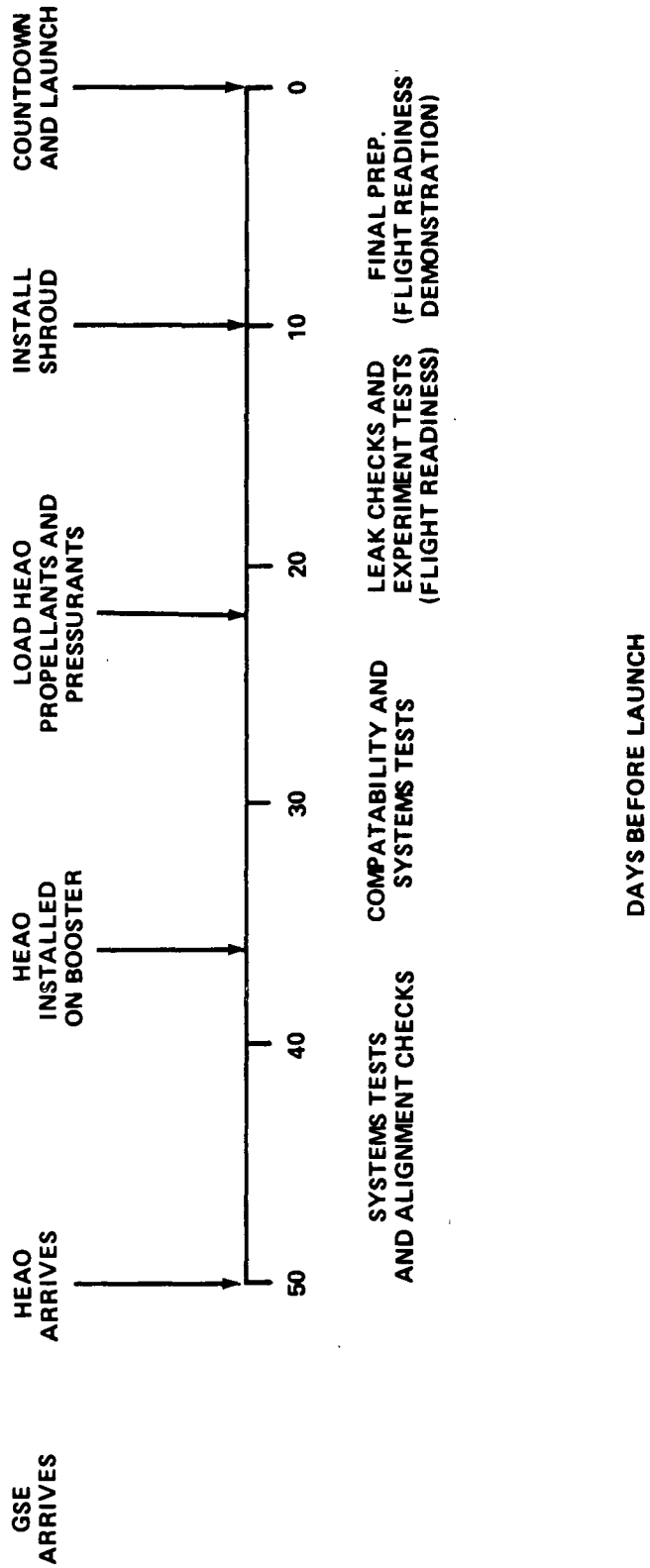


Figure III-38. Prelaunch activities.

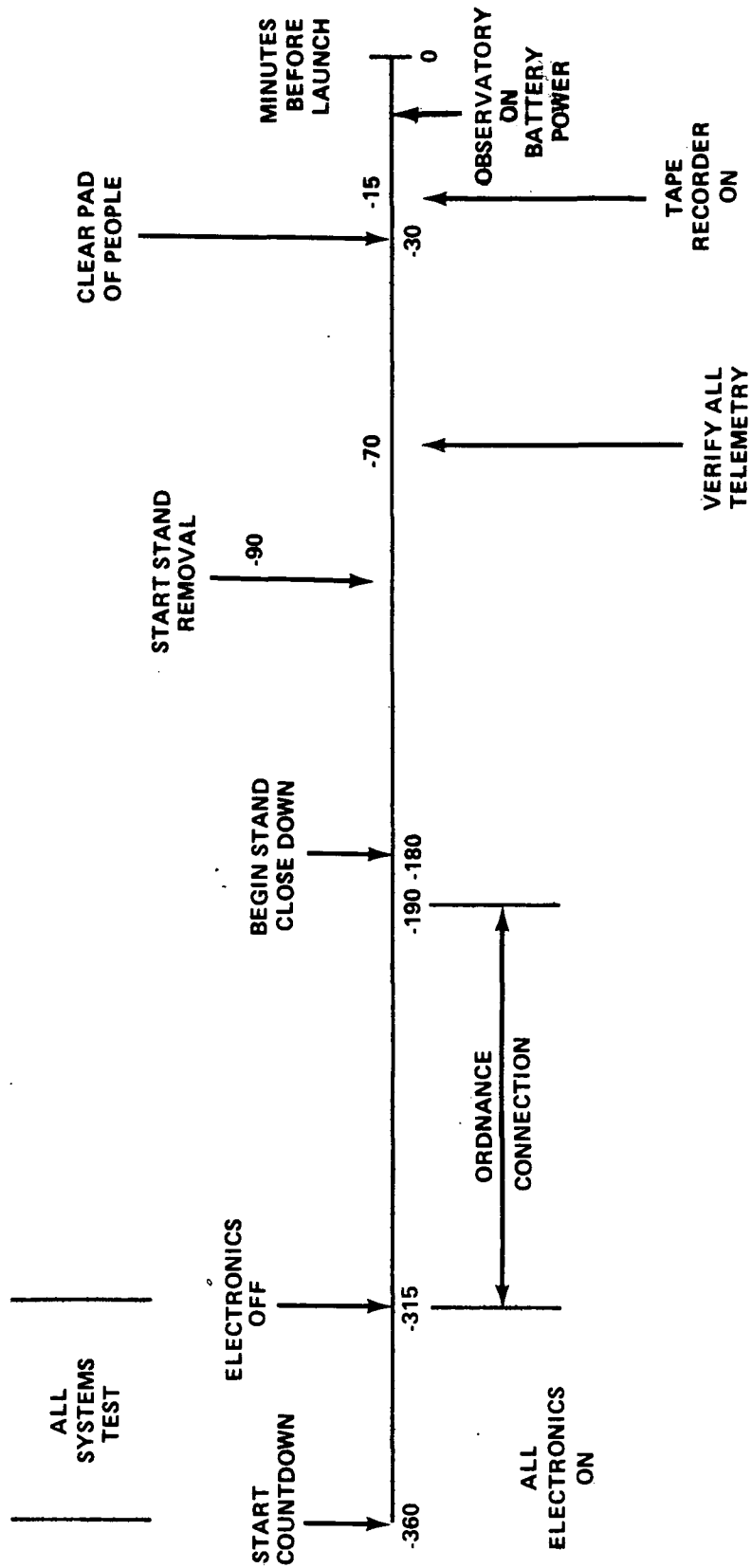


Figure III-39. Countdown of key events.

TABLE III-10. BOOST-TO-ORBIT SEQUENCE OF EVENTS

Time of Initiation	Event Duration	Event No.	Event
Days:Hrs:Min:Sec	Days:Hrs:Min:Sec		
00:00:00:00		1	Ignite rocket motors.
00:00:01:48		2	Ignite Core Stage I.
00:00:02:02		3	Jettison solid rocket motors.
00:00:04:16		4	Separate Core Stage I/Ignite Core Stage II.
00:00:04:41	00:00:00:03	5	Jettison payload shroud.
00:00:04:44	00:00:02:49	6	Inject into a 140 by 250 nautical mile orbit and separate Core Stage II.
00:00:07:33	02:01:42:25	7	Coast in 140 by 250 nautical mile orbit/ Stabilize and rate damp spacecraft/Acquire Sun and deploy solar panel/Activate star trackers and obtain tracking star/Establish attitude reference alignment/Determine orbital parameters.
02:01:49:58	00:00:07:01	8	Inject into a 250 by 210 nautical mile orbit (over Carnarvon tracking station).
02:01:56:59	01:10:18:24	9	Coast in 250 by 210 nautical mile orbit for approximately 23 orbits.
03:12:13:23	00:00:06:24	10	Inject into a 250 by 270 nautical mile orbit (over Ascension Island tracking station).
03:12:19:47	00:10:29:57	11	Coast in 250 by 270 nautical mile orbit for approximately seven revolutions.
03:22:49:44	00:00:02:01	12	Circularize 250 by 270 nautical-mile orbit into 270 nautical mile orbit (over Ascension tracking station).
03:22:51:45	00:01:34:00	13	Coast in 270 nautical mile orbit for approximately one revolution/Typically begin earth occultation for this orbit. Earth occultation will reoccur and terminate in intervals of 94 minutes and 37 minutes, respectively, from this time. The 94 minutes is the period of a 270 nautical mile orbit.
04:00:25:45	00:04:00:00	14	Turn on CMGs.
04:04:25:45	00:01:34:00	15	Establish attitude reference alignment.
04:05:59:45	07:00:00:00	16	Acquire x-ray source for subsystems and experiment checkout and calibration/Checkout and calibrate experiments.

prime tracking station. The baseline tracking station network was previously discussed in Section D. The OAS then performs the first of three burns which will be required to place the Observatory into a 270 nautical mile circular orbit. This burn, which is performed over Carnarvon tracking station, has a duration of approximately 7 minutes and 1 second and places the Observatory into a 210 by 250 nautical mile orbit. A 23 orbit coast period is then required before the next opportunity occurs for the second apogee burn over a tracking station. This burn, performed over Ascension Island tracking station, places the Observatory in a 250 by 270 nautical mile orbit and has a duration of approximately 6 minutes and 24 seconds. The third burn, which circularizes the Observatory into a 270 nautical mile orbit, is also performed over Ascension Island tracking station (approximately seven revolutions after the second burn) and has a duration of approximately 2 minutes. Since a burn of 13.7 minutes is required to raise the initial perigee to 270 nautical miles, the desire to burn over a tracking station combined with the fact that the contact time over a single station is less than 8 minutes dictates that this required burn be broken into two separate burns. After the desired 270 nautical mile orbit has been achieved and circularization dispersions corrected, the CMGs are turned on. This activity requires approximately 4 hours and is followed by attitude reference alignment. Immediately prior to viewing the first source as a part of the actual experiment program, the experiments are checked and calibrated. Although seven days have been allocated for checkout of the experiments, additional time could be utilized if necessary. The maneuvers required for calibration of the instruments are discussed in Section 12.

4. On-Orbit Experiment Operations. In preparing the on-orbit experiment timelines, all of the events, activities, and conditions indicated on the timelines were constructed according to their relative duration and occurrence. For instance, the period of time that a source is occulted is shown, in scale, relative to the time that the source could be seen.

The various times of the year are considered in the timelines to aid in assessing the impact of the relative daylight and dark periods of the year upon source viewing opportunities, the thermal control system, and power system. The occurrence of an event and the timelines are varied so that the sun is located at the vernal equinox, autumnal equinox, and summer and winter solstices. Known sources on the celestial sphere are considered to add an element of realism to the timelines. These known sources can be viewed during the period of the year indicated on the timelines containing the respective known sources.

Any combination of experiments is possible as long as the guideline that only one experiment can occupy the focal plane of any single telescope at any single time is not violated. The combinations of experiments on the timelines are only examples of what might occur.

It is emphasized that these timelines only typify those activities and their duration which will characterize the actual HEAO-C mission. The actual mission, of course, will be dictated mainly by the sources under study and the requirements of the principal investigators.

5. Source Viewing Logic. Figure III-40 illustrates the method used in the viewing of sources on the celestial sphere within the  $\pm 15$  degree access band. It is assumed that these sources will be known in advance and that their locations will be preprogrammed onboard the Observatory each day for each day's viewing. From some predetermined starting point, the spacecraft rotates about its nominal sun axis (Z-axis) to the first source.

During a normal viewing day, five sources will be preprogrammed for viewing. Five typical sources of sufficient interest for viewing are also presented in Figure III-40. They are SGRX-1, SCOX-6, SCOX-5, SCOX-3, and SCOX-2, and will be available for viewing when  $\lambda$  (celestial latitude) is around 90 degrees. Nominally the spacecraft will view these five sources in a manner that minimizes spacecraft maneuvers in moving from source to source (for example, beginning with SGRX-1 and proceeding to SCOX-6, SCOX-2, SCOX-5, and SCOX-3).

After a day's viewing is completed the spacecraft then rotates a few degrees around the Z-axis to the next set of sources. The objective of this type of logic is to eliminate large rotations about the Z-axis as a normal viewing program and minimize maneuver.

6. Gross Timeline. Figure III-41 presents a two year timeline of the major activities which have been baselined as representative of those that will be carried out during the actual HEAO-C mission. These baseline viewing activities, extra mission activities, and their frequency of occurrence during a two year mission were derived with the primary objective of exercising the HEAO-C onboard systems. The timelines served the purpose of acting as a center around which these systems were evaluated and assessed.

The following are the activities considered during the nominal two year mission including the time allotted to each of the events:

a. Normal Viewing Day

- (1) Viewing time — 67 percent (469 days)
- (2) Viewing method — 5 sources/day
- (3) Angular movement — Within  $\pm 15$ -degree band, total movement dictated by density of sources of interest

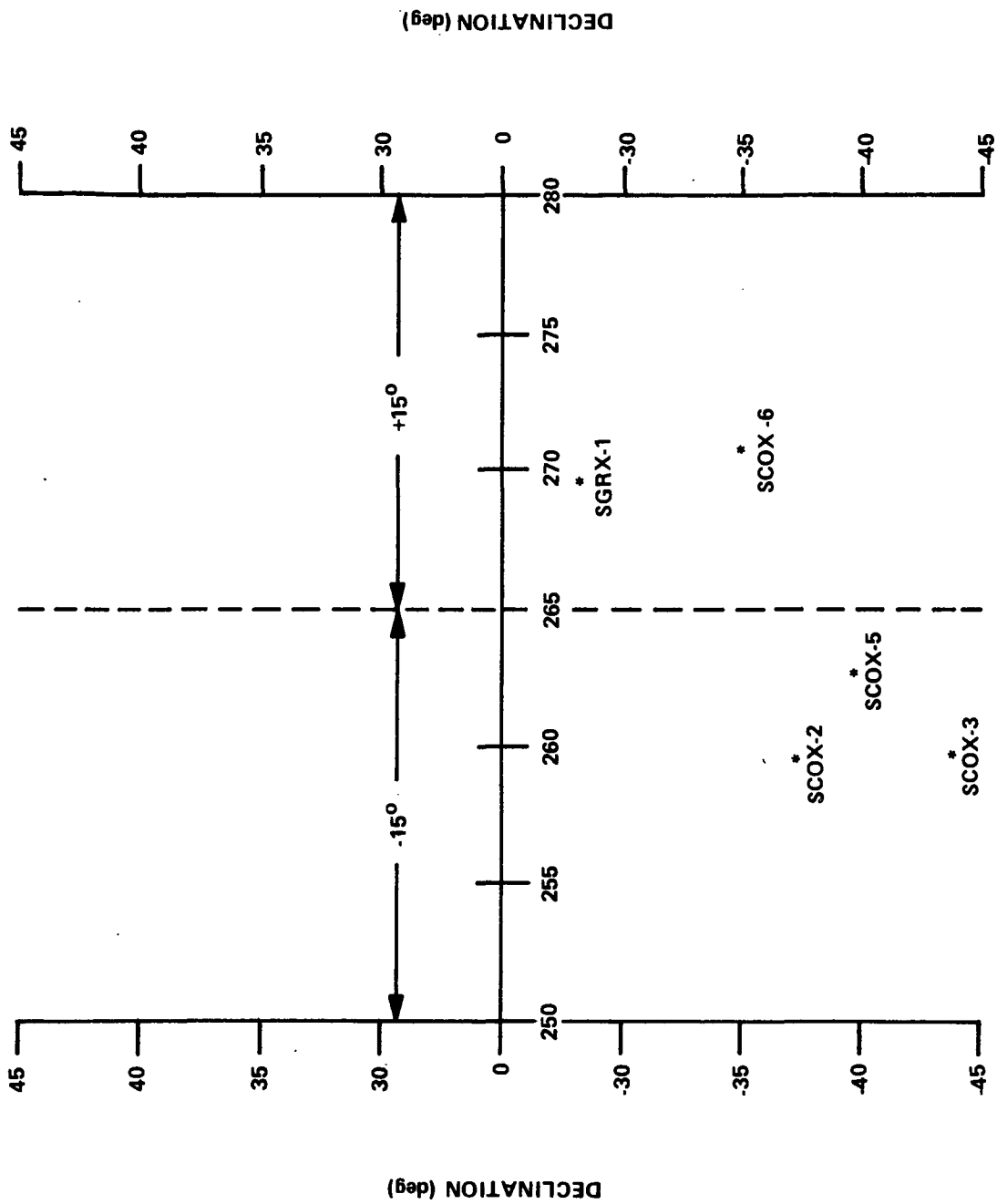


Figure III-40. Block logic of celestial sphere.

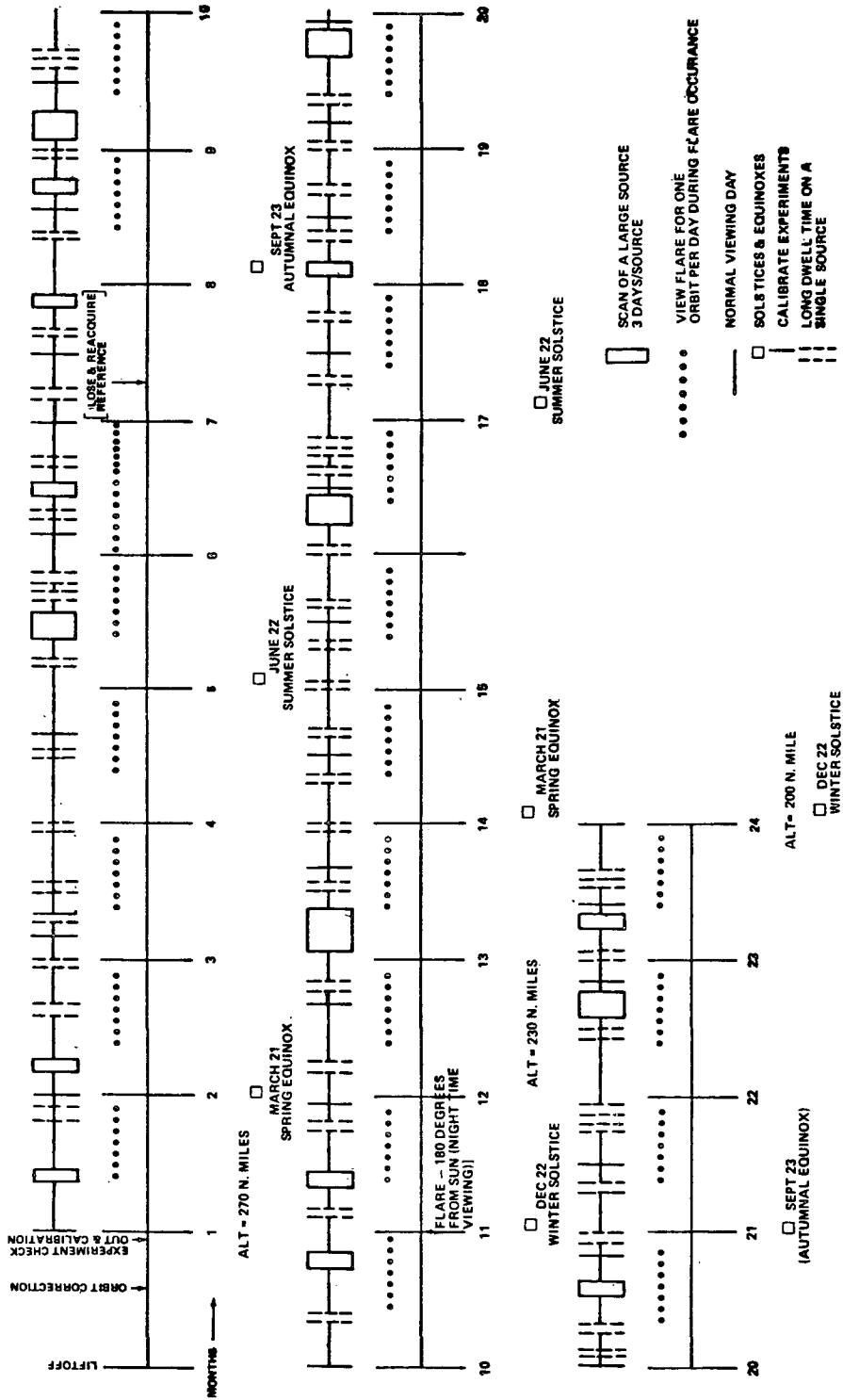


Figure III-41. Gross timeline.

- b. Scan of a Large Source
  - (1) Viewing time — 10 percent (70 days)
  - (2) Viewing method — 1 point/day 3 days/source
  - (3) Angular movement — 2 arc min/day
  
- c. Long Dwell Time On a Single Source
  - (1) Viewing time — 15 percent (105 days)
  - (2) Viewing method — 2 days/source
  - (3) Angular movement — 0 degrees/day
  
- d. Flare Observation Between  $\pm 15$  Degree and  $\pm 30$  Degree Band
  - (1) Viewing time — 4 percent (28 days)
  - (2) Viewing method — View for one orbit per day
  - (3) Angular movement — As required
  
- e. Flare Observation (Antisolar Viewing)
  - (1) Absolute viewing — 1 percent (7 days)
  - (2) Viewing method — View flare during dark period of orbit
  - (3) Angular movement — As required
  
- f. Calibration of Experiments (Monthly)
  - (1) Absolute viewing — 3 percent (21 days)
  - (2) Viewing method — 1 day
  - (3) Angular movement — 0 degrees after source is locked onto by instruments
  
- g. Loss of Reference
  - (1) Absolute viewing — As required
  - (2) Viewing method — Spacecraft will reacquire sun in an "emergency sun acquisition mode" and then rotate about solar axis until source is located
  - (3) Angular movement — As required

All activities represented on the gross timeline are structured relative to their duration and occurrence. The normal viewing day which has been projected to comprise 67 percent of the mission time is represented by a horizontal bar in Figure III-41.

The scan of a large source was estimated to consume 10 percent of the mission duration. It was assumed that two or three large sources could occur close to each other, therefore, requiring several days of continuous viewing of these large sources. It was also assumed that some sources would be of sufficient interest to require a longer viewing time than normal; viewing time of two days per single source was allotted for this activity and 15 percent of the total mission duration was devoted to this event. Five percent of the mission was consumed by the viewing of flares. Observation of these could occur between the  $\pm 30$  degree excursion band or during the darkside of the orbit. Each of these activities will be discussed in detail in the following sections.

The above baseline viewing activities were dictated by the objective of viewing a minimum of about 2500 sources plus flares during the two year mission lifetime. This number of sources is based upon the expectation, desirability, and professional projections of the potential principal investigators and other involved scientific personnel. By viewing about 5 sources per day for 469 days, scanning about 23 sources at 3 days each, and viewing about 50 for an extended period of time at 2 days each, the Observatory should have access to approximately 2500 sources excluding flares at mission termination. Obviously the actual activities and the frequency with which they shall be performed will be dictated by what sources are known and their characteristics when the actual mission is flown. However, based upon principal investigator expectations and desires, coupled with the projections of other involved scientific personnel, it is believed that these timelines are suitable for exercising the HEAO-C Observatory systems.

The timelines served this purpose in many ways. For example, the normal viewing day activity calls for the capability to store the commands for the viewing of five sources per day for each day. In light of this, a communications and data handling system was required which would accommodate this capability. The scan of a large source and long dwell time on a single source had impacts for the attitude sensing and control system in that this system would have to possess the capability of meeting pointing accuracies of 2 arc minutes. The thermal control system was influenced significantly by the flare observation in the  $\pm 30$  degree band. This activity led to the sizing of the sunshade to shield the entire viewing end of the spacecraft when it is tilted to the sun at an angle of 30 degrees. Further, flare observation (antisolar viewing) influenced the sizing of the CMG system; the capability to maneuver at rates which would provide adequate darkside viewing times was required for this activity to be successful.

7. Normal Viewing Day. A normal viewing day of the HEAO-C mission is characterized by pointing at five different x-ray sources per day. Figure III-42 presents a timeline depicting a normal viewing day and considers the viewing of the known sources previously discussed: SGRX-1, SCOX-6, SCOX-5, SCOX-3, and SCOX-2. Included in this timeline, also, are source occultation times, tracking station acquisition times, target occultation times, and recommended times to transport experiments into the focal planes of the telescopes.

As an example, a typical viewing of the source SGRX-1, as depicted in Figure III-42, is explained. First, the spacecraft maneuvers to source SGRX-1 whose right ascension and declination angles are, respectively,

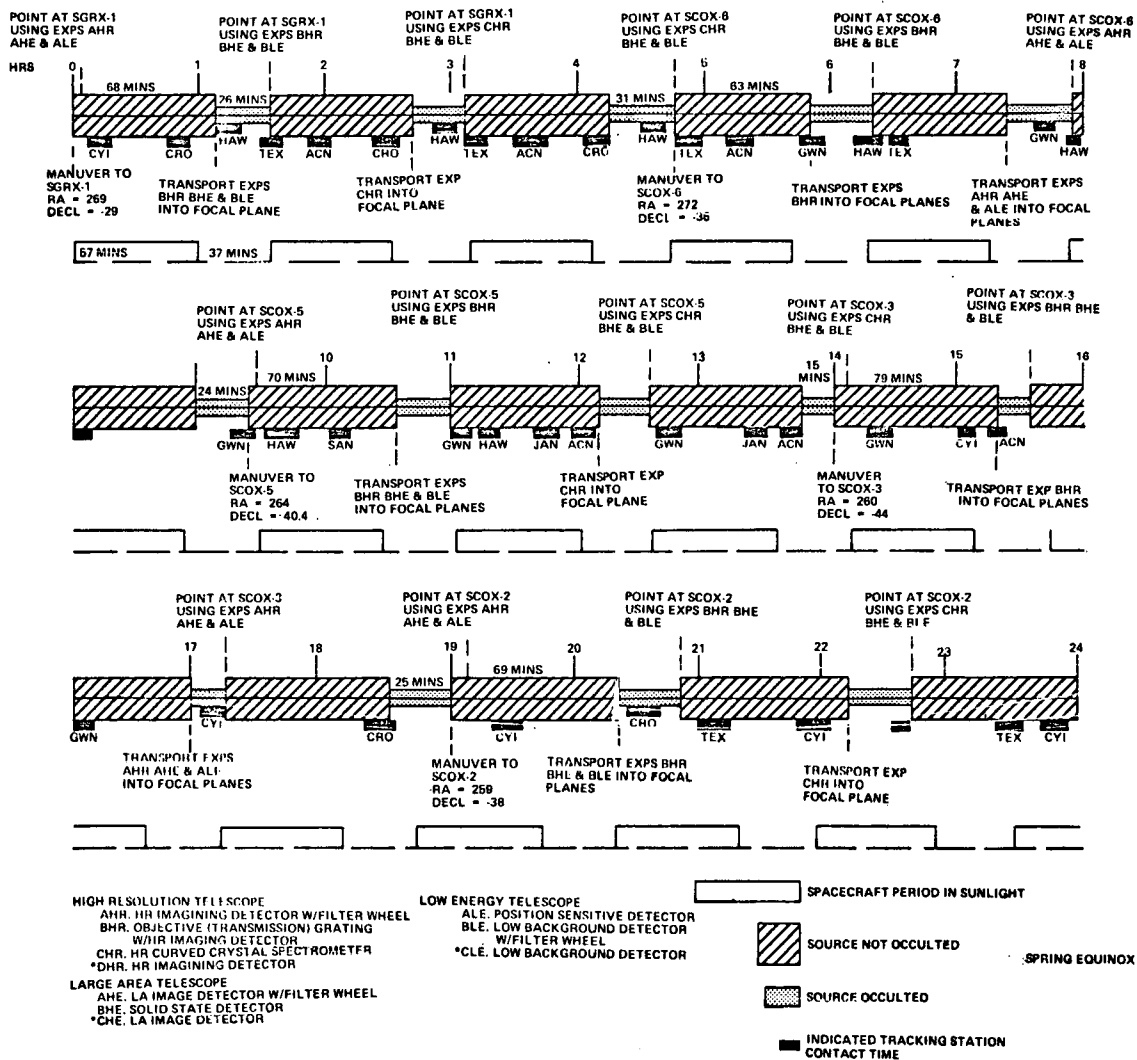


Figure III-42. Normal viewing day.

+269 degrees and -29 degrees. It is assumed that the high resolution imaging detector with filter wheel (indicated by AHR at bottom of Figure III-42), the large area image detector with filter wheel (AHE) and the position sensitive detector (ALE) are in the focal planes of the high resolution (HR) telescope, large area (LA) telescope and low energy (LE) telescope, respectively. After maneuvering to SGRX-1, the spacecraft views this source for approximately 68 minutes, that is, the time the source is not occulted by the earth. During the time the Observatory is viewing this source, the Observatory will pass over two tracking stations: Canary Island and Carnarvon.

After the spacecraft has viewed SGRX-1 for approximately 68 minutes, SGRX-1 becomes occulted by the earth for approximately 26 minutes, during which time a new combination of experiments are transported into the focal planes of the telescopes. At the beginning of this source occultation period, the objective (transmission) grating with high resolution imaging detector, the solid state detector and the low background detector with filter (indicated by BHR, BHE, and BLE, respectively) are transported into the focal planes of the HR telescope, the LA telescope and LE telescope, respectively. During this time, also, the Observatory passes over the Hawaii and Texas tracking stations. When SGRX-1 comes back into view it is viewed using this new combination of experiments until it is again occulted by the earth. During the time SGRX-1 is being viewed, the Observatory passes over the Texas, Ascension Island, and Carnarvon tracking stations.

During the time SGRX-1 is occulted for the second time by the earth, the high resolution, curved, crystal spectrometer (indicated by CHR) is transported into the focal plane of the HR telescope. Also during this time, the spacecraft passes over the Hawaii tracking station again. After SGRX-1 comes into the field of view of the telescopes, it is viewed using the high resolution, curved, crystal spectrometer in addition to the two experiments remaining in the focal planes of the LA telescope and LE telescope from the previous combination of experiments. During the viewing of SGRX-1 with this new combination of experiments, the Observatory passes over the Texas, Ascension Island, and Carnarvon tracking stations.

These activities complete the viewing of source SGRX-1 and the spacecraft maneuvers to view source SCOX-6 when it comes into the field of view of the telescopes after being occulted for 31 minutes. Approximately 3 orbits are required to view SGRX-1.

8. Scan of a Large Source. Twenty-three sources have been assumed whose individual dimensions would exceed the smallest field of view of all detectors onboard the Observatory. These sources, as a result, could not be covered with one pointing of the telescope but would typically require on the average of three different pointings dictated by the detector onboard the Observatory with the smallest field of view.

Figure III-43 presents a timeline which demonstrates the proposed method for covering these large sources. For purposes of this timeline a source whose dimensions are roughly 2.1 arc minutes by 6.3 arc minutes has been assumed. The smallest field of view onboard the observatory is associated with the high resolution imaging detector. This field of view is 2.1 by 2.1 arc minutes, and is the smallest of three used in the high resolution imaging experiment. Thus a source typically this size would be split into three spots, requiring one day for viewing each spot as indicated in Figure III-43, utilizing the experiments onboard the Observatory.

9. Long Dwell Time on a Single Source. Fifty-three sources have been assumed to exist which will provide interest sufficient enough to warrant a long dwell time. Long dwell time means an extended source viewing time during which data can be collected for each experiment onboard the spacecraft.

A typical known source sufficient to provoke such interest is SCOX-2, the viewing timeline of which is presented in Figure III-44. This timeline specifically shows source occultation and nonoccultation time for a typical long dwell time period of two days. Also, it shows the indicated periods of dwell time and experiment transporting times (experiments transported in and out of the telescope focal planes).

10. Flare Observation Between  $\pm 15$  Degree and  $\pm 30$  Degree Band. Current guidelines call for the spacecraft to have the capability to operate typically at a maximum off-sun excursion of  $\pm 30$  degrees for one orbit per day to view those flares which occur outside the normal  $\pm 15$  degree daytime band but inside the  $\pm 30$  degree viewing band. This capability is limited to one orbit per day in order to maintain battery recharge requirements within acceptable limits (see Chapter VIII for an expanded discussion of this point).

The presence and general location of a flare will be determined within an 8 degree region by the onboard coarse flare detectors. Following this detection and during the period of time the Observatory is inside the contact region of a tracking station with command up-link capability, a command will be sent to the Observatory to interrupt its normal viewing program, locate the flare within a 0.5 degree region, and view the flare for one orbit during that particular day.



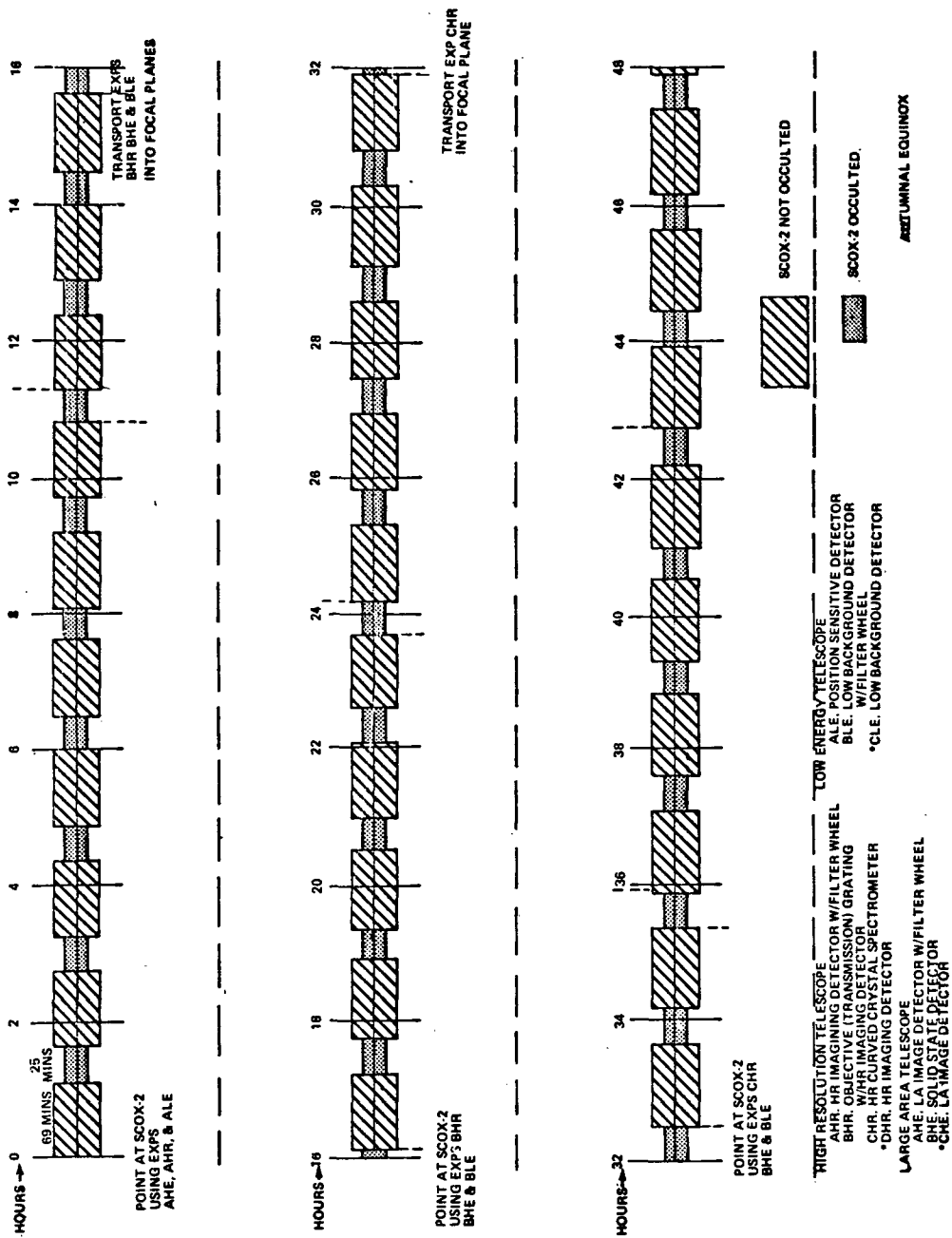


Figure III-44. Long dwell time on a single source.

Figure III-45 presents a timeline typical of this activity. Specifically, it shows first the Observatory operating within the  $\pm 15$  degree viewing band performing the "long dwell time on a single source" activity. Approximately half-way between the first and second orbit, a flare is detected by the onboard coarse flare detectors and is located within an 8 degree by 8 degree region. This gross location is transmitted to the ground as the Observatory passes over the Hawaii tracking station. Approximately 7 hours later, the Observatory passes over a tracking station where a command is sent to the Observatory to interrupt its preprogrammed viewing and to maneuver so that it can view the flare at the beginning of the 13th orbit. At the beginning of this orbit, the Observatory maneuvers to view the flare for a period of one orbit. Upon completing this orbit, the Observatory maneuvers back and continues its preprogrammed "long dwell time on a single source" activity.

11. Flare Observation 180 Degrees From Sun. Figure III-46 presents a timeline showing the observation of a flare whose location is 180 degrees from the sun. For this type of situation, the flare shall be viewed by the spacecraft only when it (spacecraft) is on the dark side of the earth. To view sources located in this antisolar direction, maximum angle excursions of 90 degrees each will be required for maneuvering the spacecraft to and from the source. With the current CMG attitude maneuvering system, approximately 6 minutes will be required for maneuvering the 90 degrees, including settling out time, leaving a maximum effective viewing time of 24 minutes when the sun is at the summer and winter solstices and a minimum effective viewing time of 14 minutes when the sun is at the vernal and autumnal equinoxes.

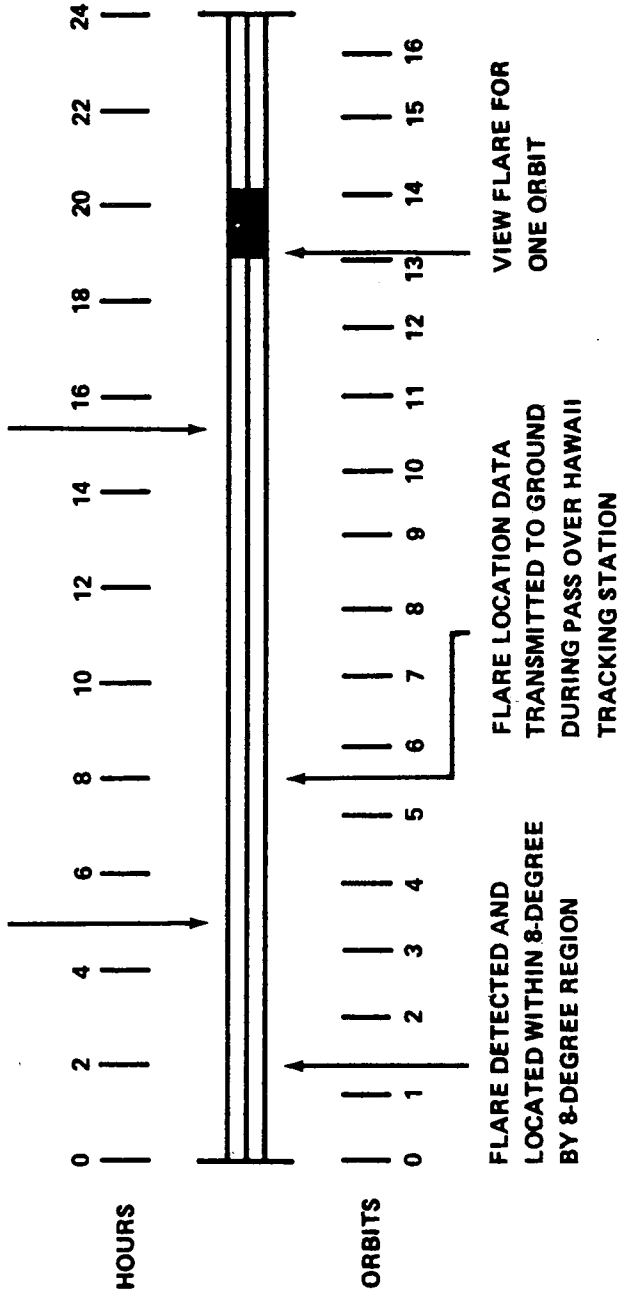
12. Calibration of Experiments. Calibration of experiments is essentially a correction of the data received from the experiments. Basically, this method is to point a group of the experiments onboard the spacecraft at a known source, the data characteristics of which are already known. After receiving data from the group of experiments onboard the spacecraft, the data are compared and corrected to the expected known data.

Figure III-47 shows typical groups of experiments which are pointed simultaneously at a source and whose data are transmitted back to earth at the indicated time and location. SCOX-3 used as the source to calibrate the experiments and was selected primarily because of its low earth occultation time and known data characteristics.

13. Loss and Reacquisition of Reference. During the desired mission length of two years, the HEAO spacecraft might possibly lose the reference star from the field of view of one of its star trackers. The method of reacquiring this reference is indicated in Figure III-48.

FLARE LOCATED WITHIN 0.5-DEGREE  
BY 0.5-DEGREE REGION BY FINE  
FLARE DETECTOR

OVER ASCENSION TRACKING STATION  
COMMAND OBSERVATORY TO VIEW  
FLARE DURING ORBIT NO. 13



LONG DWELL TIME ON A  
SINGLE SOURCE

VIEW FLARE FOR ONE ORBIT

Figure III-45. Flare observation within 30 degree cone.

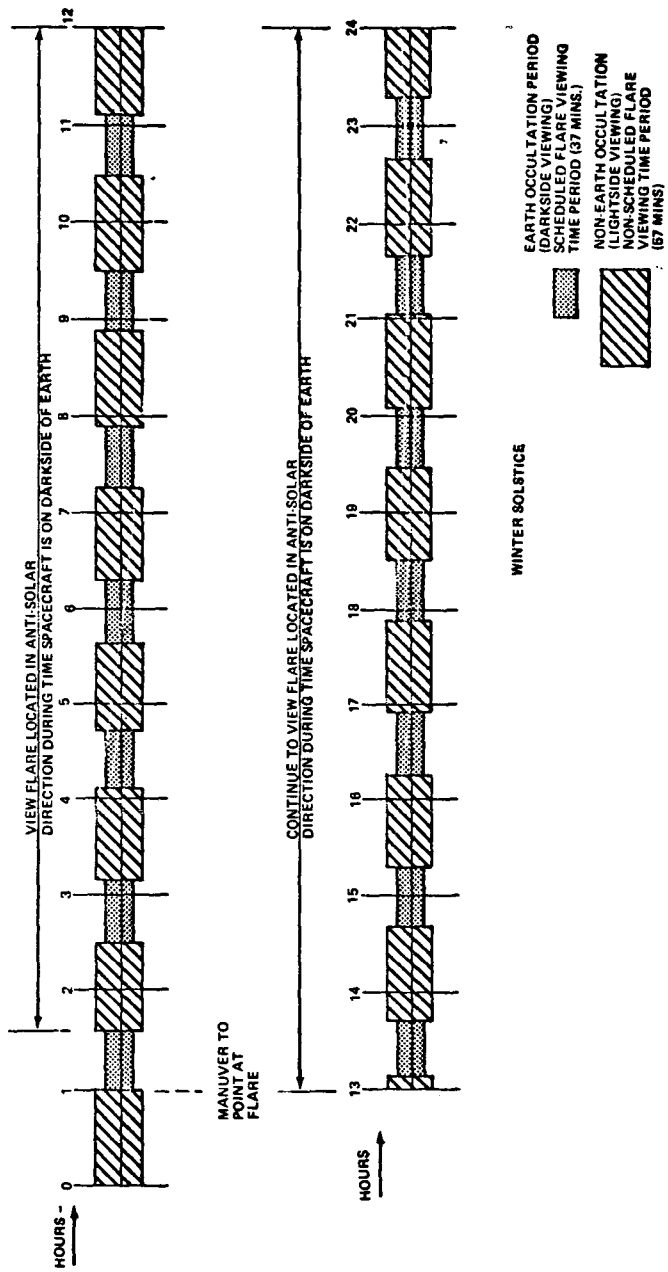


Figure III-46. Flare observation (antisolar viewing).



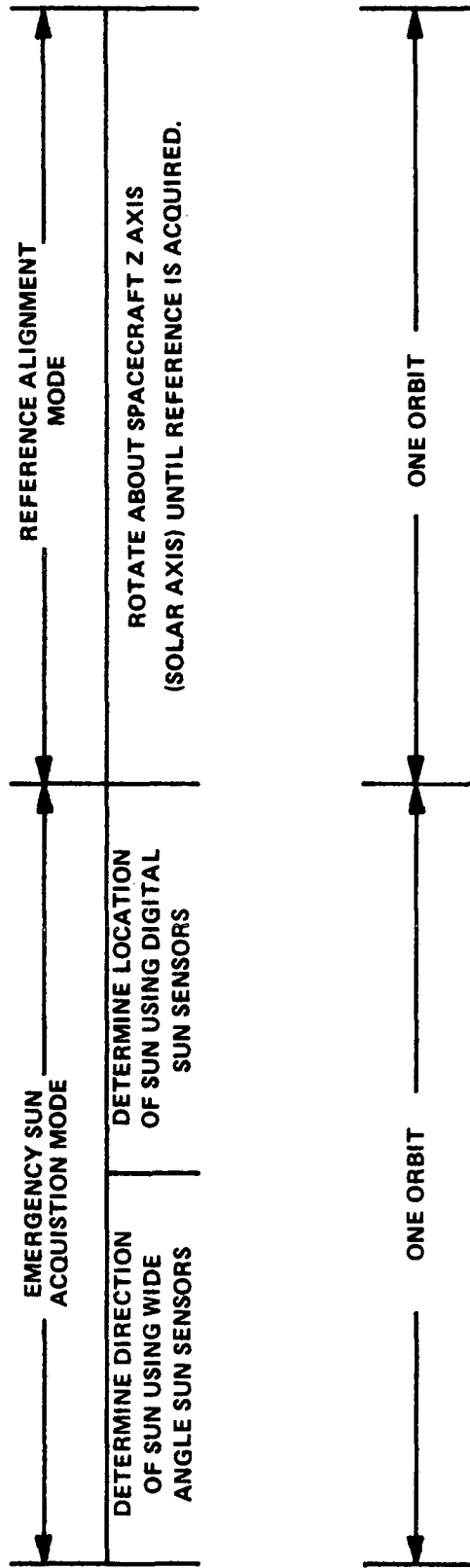


Figure III-48. Loss and reacquisition of reference.

This method consists of basically two modes. The first mode is the "sun acquisition mode" where the direction and location of the sun will be determined using the wide angle sun sensors and digital sun sensors, respectively. The second mode is the "reference alignment mode," where the spacecraft rotates about its solar axis (Z-axis) until a star reference is acquired.

The completion of each of these modes should require approximately one orbit maximum time.

## REFERENCES

- III-1. Martin Company: Titan III Data Book for Performance Calculations (U). AF04 (695)-997, Report SSD-CR-66-103, August 1967 (Confidential).
- III-2. Harmon, R.L.: Titan III Vehicle Descriptions. Brown Engineering Summary Report, SMSD-PVEL-191, August 1968.
- III-3. Martin-Marietta Corporation: Titan III Family Review. (Unnumbered document) January 1968.
- III-4. Fischer, N.H.: Titan IIC, Titan IID, and Titan IID/Centaur Performance (to 200-Nautical-Mile Orbits). Battelle Memorial Institute Memorandum, BMI-ICM-69-92, July 17, 1969.
- III-5. Price, W.B.: Lockheed Satellite Control Section Data. MSFC Memorandum PD-DO-PM-71-1, January 11, 1971.
- III-6. Martin-Marietta Corporation: Titan IID/OAS-HEAO Accuracy Analysis of 140- by 250-Nautical-Mile Orbit. Martin Company Report S71-4154S -2 L. V. 104-71, February 17, 1971.
- III-7. Hoover, Richard B.: X-Ray Astronomy (A Survey of Recent Developments). McGraw Hill Encyclopedia of Science and Technology, 1971 Yearbook.

## BIBLIOGRAPHY

- Grumman Aerospace Corporation: High Energy Astronomy Observatory Performance Review Report. MSFC Contract No. NAS8-26272, September 16, 1970.
- TRW Systems Group: HEAO, High Energy Astronomy Observatory. MSFC Contract No. NAS8-26273, January 19, 1971.

## TABLE OF CONTENTS

	Page
A. Overall Configuration . . . . .	IV- 1
B. Baseline Observatory Systems . . . . .	IV-12
1. Systems Description . . . . .	IV-12
a. Experiments . . . . .	IV-17
b. Attitude Sensing and Control System . . . . .	IV-17
c. Electrical System . . . . .	IV-17
d. Communication and Data Handling System . . . . .	IV-18
e. Structure . . . . .	IV-19
f. Thermal Control System . . . . .	IV-19
g. OAS . . . . .	IV-20
2. Systems Integration . . . . .	IV-20
a. Electrical Power Summary . . . . .	IV-20
b. Mass Characteristics . . . . .	IV-20
c. Interface Considerations . . . . .	IV-25
d. Two Year Lifetime Considerations . . . . .	IV-30
e. Reliability . . . . .	IV-31
f. Commonality . . . . .	IV-36
g. Design Characteristics Summary . . . . .	IV-36
h. Design Margin and Growth . . . . .	IV-36
i. Suggestions for Phase B Study . . . . .	IV-43
C. Experiment Transport Mechanisms . . . . .	IV-44
1. Requirements . . . . .	IV-44
2. General Description . . . . .	IV-47
3. Specific Transport Mechanisms . . . . .	IV-48

## TABLE OF CONTENTS (Concluded)

	Page
D. Pointing Error Analysis . . . . .	IV-50
1. Introduction. . . . .	IV-50
2. Requirements . . . . .	IV-52
3. Error Sources . . . . .	IV-55
4. Misalignments Within Telescopes . . . . .	IV-59
E. Observatory Operating Modes. . . . .	IV-61
1. Normal Operating Mode. . . . .	IV-66
2. Emergency Operating Mode . . . . .	IV-69
3. Degraded Operating Mode . . . . .	IV-70
References . . . . .	IV-71

# LIST OF ILLUSTRATIONS

Figure	Title	Page
IV-1.	Baseline HEAO-C Observatory . . . . .	IV- 3
IV-2.	HEAO-C configuration . . . . .	IV- 5
IV-3.	HEAO-C sunshade . . . . .	IV- 7
IV-4.	Internal support structural arrangement. . . . .	IV- 9
IV-5.	Details of internal support structures. . . . .	IV-10
IV-6.	Thermal bending effects . . . . .	IV-11
IV-7.	Possible HEAO-C assembly scheme. . . . .	IV-13
IV-8.	Baseline Observatory systems . . . . .	IV-15
IV-9.	Baseline experiment mounting scheme . . . . .	IV-16
IV-10.	Reference axes for location of discrete masses . . . . .	IV-24
IV-11.	Commands and power across major interfaces. . . . .	IV-27
IV-12.	Discrete measurements across major interfaces . . . . .	IV-28
IV-13.	Analog measurements across major interfaces . . . . .	IV-29
IV-14.	Mission/data worth model . . . . .	IV-35
IV-15.	Observatory equipment $\Delta$ cost versus reliability . . . . .	IV-43
IV-16.	LA telescope transport mechanism . . . . .	IV-45
IV-17.	LA telescope transport mechanism isometric . . . . .	IV-49
IV-18.	HR telescope transport mechanism . . . . .	IV-51
IV-19.	Coalignment of three telescope axes and the pointing axis with pointing axis equidistant from telescope axes . . . . .	IV-53

## LIST OF ILLUSTRATIONS (Concluded)

Figure	Title	Page
IV-20.	Telescopes coaligned to 1 arc minute with HR telescope axis the pointing axis . . . . .	IV-54
IV-21.	Example of tilt angle . . . . .	IV-55
IV-22.	Example of deflection angle . . . . .	IV-55
IV-23.	Example of elongation of detector distance from focal point . . . . .	IV-56
IV-24.	Telescope LOS coincident with mirror axis and source located on telescope LOS — conditions for maximum telescope resolution . . . . .	IV-60
IV-25.	Telescope LOS coincident with mirror axis, source located off LOS, but within field of view of mirror and detector . . . . .	IV-62
IV-26.	Mirror axis shifted, source on telescope LOS but not on mirror axis . . . . .	IV-63
IV-27.	Detector has shifted, but the mirror axis has not . . . . .	IV-64
IV-28.	General case: Both mirror axis and detector axis have shifted, source neither on mirror axis nor telescope LOS . . . . .	IV-65

# LIST OF TABLES

Table	Title	Page
IV-1.	Master Equipment List . . . . .	IV- 4
IV-2.	HEAO-C On-Orbit Electrical Load Summary. . . . .	IV-21
IV-3.	HEAO-C Baseline Observatory Weight Summary . . . . .	IV-22
IV-4.	Baseline Mass Characteristics Summary . . . . .	IV-24
IV-5.	HEAO-C Reliability Numerics Summary. . . . .	IV-32
IV-6.	Cumulative Mission/Data Worth . . . . .	IV-34
IV-7.	Degraded Mode Assessment. . . . .	IV-37
IV-8.	Potential HEAO-C Design Drivers For HEAO-A and -B .	IV-39
IV-9.	Significant HEAO-C Design Characteristics . . . . .	IV-41
IV-10.	HEAO-C Systems Margin Summary. . . . .	IV-42
IV-11.	Telescopes and Experiment Alignment Error Budget . . .	IV-57
IV-12.	Observatory Operating Modes. . . . .	IV-67

## CHAPTER IV. OBSERVATORY BASELINE DESIGN

### A. Overall Configuration

A layout of the baseline Observatory configuration is shown in Figure IV-1. The layout is keyed to the Master Equipment List (Table IV-1) for identification of the components.

The Observatory has a 105 inch maximum outside diameter and is 360 inches long (excluding the sunshade, OAS, and adapter). The cross section of the outer structure is octagonal, and one corner of the octagon is pointed toward the sun during normal operation.

Foldout solar array panels along two sides of the octagon provide the majority of the power, with body-mounted panels on the two sides nearest the sunline providing the remainder of the power and providing room for growth (Fig. IV-2). The foldout panels can be identical to those on HEAO-A and -B spacecraft, although the hinge attach points on the spacecraft are different. The use of foldout panels rather than body-mounted panels allows the array to operate at a lower, more efficient temperature, with only a minimal increase in orbital drag.

The OAS and its adapter remain attached to the rest of the spacecraft throughout the mission. (This decision was made late in the study, so as to be commensurate with a similar decision which was made late in the HEAO-A and -B Phase B study.) The RCS tanks, thrusters, lines, valves, etc., and three coarse flare detectors are located in the OAS.

A sunshade is provided to give thermal protection to experiments when the spacecraft pointing axis is tilted toward the sun (as much as 30 degrees) and/or when the spacecraft is rolled about the pointing axis (as much as 15 degrees). The sunshade and its worst-case shadow line are shown in Figure IV-3.

Alignment and pointing accuracy are the most critical design requirements and, as such, provide strong influence on the structure and thermal control concepts. The baseline design contains a dual structure arrangement. The outer structure supports the inner structure (on which all experiments are mounted), the subsystems, sunshade, etc. To preclude high temperatures inside the Observatory and to prevent large temperature gradients across the outer structure, 0.5 inch of multilayer aluminized mylar insulation is provided

around the outside of the outer structure, with alzak skin mounted on standoff insulators external to the insulation and spaced from it about 0.2 inch. Multi-layer insulation is also judiciously applied to parts of the experiments to further control their environments. An aluminized polypropylene membrane covers the entire pointing end of the Observatory except for the view faces of the experiments and star trackers. The outer structure and thermal control concepts are similar to those employed by Grumman Aerospace Corporation (GAC) in Reference IV-1. Most of the subsystems are located on the antisolar side of the spacecraft to facilitate their thermal control by utilizing the un-insulated thermally stable exterior surface.

The telescope tubes and the attached forward beam assembly which supports the miscellaneous experiments and the alignment-critical attitude sensors (star trackers, rate gyros, and digital sun sensors) comprise an optical bench. The optical bench is attached to the main Observatory structure by means of two forward ball joints and two aft linkages (Fig. IV-4). The two large telescope tubes are attached at the upper ends to the circular rings around each mirror frame. The rings are bolted to the deep oval frame around the two tubes. A cross beam at the middle of the oval frame is used to transmit the total load through a ball joint to another beam which then distributes the load to rubber pads. The ball joint is designed to isolate any thermal bending of the outer shell from the tubes. These two tubes are rigidly joined at the aft end. The large area (LA) telescope tube is attached to the outer structure by two delta-frames, using self-aligning bearings, to take out lateral and torsional launch loads and to stabilize the aft end of the telescopes during slew maneuvers in orbit. The delta-frames have self-aligning bearings on each end so that thermal deformation of the outer Observatory structure, even at an unusual off-sun angle, does not induce a stress into the optical bench.

The forward end of the low energy (LE) telescope is attached through its own ball joint to the same beam which supports the two large telescopes. The aft end of the LE telescope tube is linked to the large telescopes by an A-frame and strut, using self-aligning bearings and pins, to maintain alignment between the telescopes.

Shock mount pads are provided between the ball joint sockets and the crowfoot beam assembly to give protection from vibration to the optical bench during the Titan flight. Three of these rubber pads are provided and are mounted atop the crowfoot beam assembly which distributes optical bench loads to the outer structure. The shock mount pads and internal support structure arrangement are shown in Figure IV-5. The pads will carry both longitudinal and lateral launch loads.

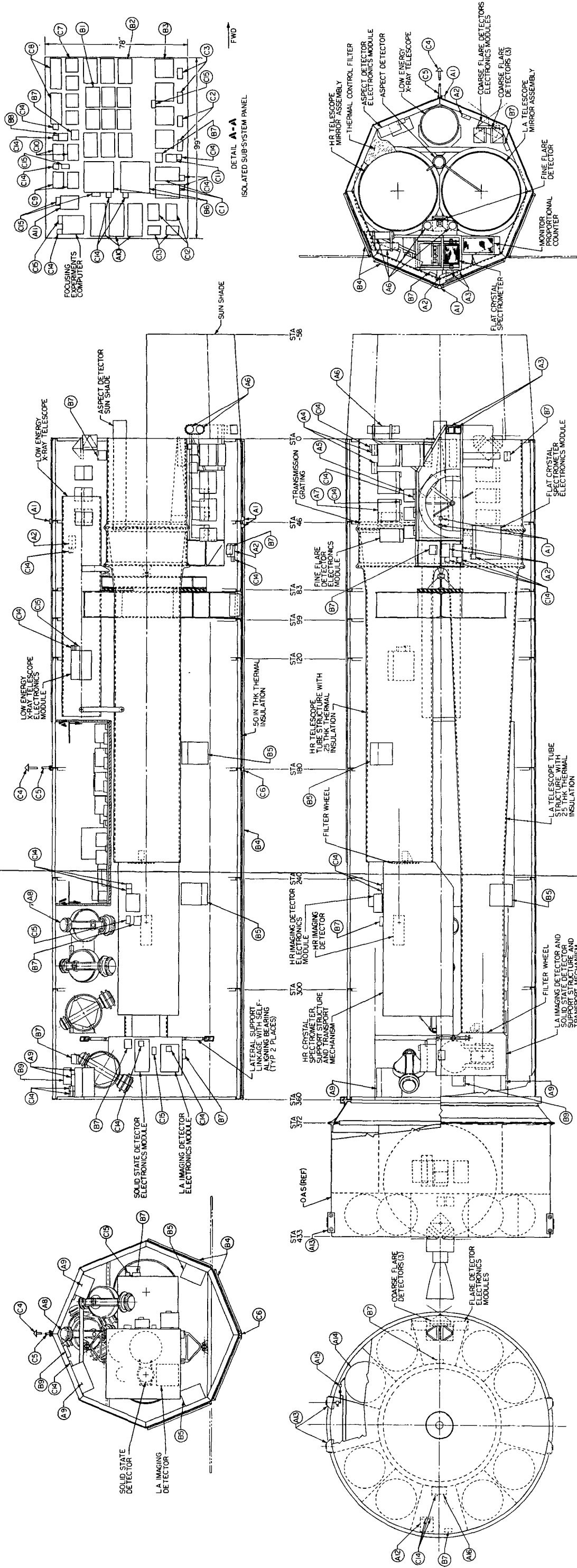


Figure IV-1. Baseline HEAO-C Observatory.

TABLE IV-1. MASTER EQUIPMENT LIST

Identification Number	System/Component	No. Used	No. Required	Unit Power (W)	Operating Time	Power Required (W)	Size (in.) L x W x H	Total Volume (in. <sup>3</sup> )	Unit Weight (lb)	Total Weight (lb)	Operating Temperature Limits (°F)	Remarks
A1	WASS <sup>a</sup>	3	2	0.0	Continuous	0.0	2 x 1.9 x 2	23	1.0	3	-120 to 130	b
A2	WASS Electronics	3	1	0.4	Continuous	0.4	5 x 7 x 2	210	1.0	3	-4 to 122	b
A3	DSS <sup>c</sup>	2	1	0.0	Continuous	0.0	3.8 x 3.8 x 1.5	434	0.75	1.5	-4 to 130	b
A4	DSS Electronics	2	1	1.7	Continuous	1.7	7.8 x 5 x 2.5	98	2.5	5	-4 to 130	b
A5	Gyro Package (2/pkg)	3	3	15.0	Continuous	45.0	7 x 8 x 6	1 008	11.0	33	32 to 130	d
A6	FHS <sup>e</sup>	4	2	0.0	Continuous	0.0	15 L x 4 Dia.	756	9.0	36	-4 to 130	f
A7	Star Tracker Electronics	4	2	8.0	Continuous	16.0	5 x 11 x 12	2 640	14.0	56	TBD	f
A8	CMG <sup>f</sup>	4	4	9 operating 32 spinup	Continuous	36.0	32 x 19 x 9	21 888	135.0	540	-22 to 140	b
A9	CMG Electronics	4	4	18.0	Continuous	72.0	12 x 16 x 7	5 376	27.0	108	-4 to 130	b
A10	Digital Processor	3	1	65.0	Continuous	65.0	18.5 x 5 x 8	740	20.0	60	0 to 130	b
A11	Transfer Assembly	1	1	5.0	Continuous	5.0	5 x 7 x 10	350	10.0	10	0 to 130	b
A12	RCS <sup>h</sup> Electronics	1	1	11.0	Continuous	11.0	9 x 14 x 7	1 784	16.0	16.0	-4 to 120	b
A13	Thruster Module	4	4	4.5	2 Percent	20.6	6 x 7 x 11	1 848	9.0	36	TBD	b
A14	RCS Tank	8	8	6.12	TBD	5.2	22 Dia.	45 000	17.2	138	TBD	b
A15	Other RCS Items	N/A	N/A		N/A	16.1	N/A	N/A	33	TBD	TBD	b
A16	OAS <sup>i</sup> Electronics	1	1	9.0	Orbital Adjust	9.0	7 x 8 x 4	224	TBD	TBD	TBD	b
B1	Batteries	6	6	N/A <sup>k</sup>	Continuous	N/A	13.1 x 6.67 x 7.4	3 890	56.0	336	40 to 60	1
B2	Chargers	6	6	N/A	Continuous	N/A	11 x 8 x 6	3 168	14.0	84	-40 to 140	f
B3	Regulators	4	2	N/A	Continuous	N/A	11 x 8 x 5	1 760	8.0	32	-40 to 140	f
B4	Solar Array	1	1	N/A	Continuous	N/A	240 ft <sup>2</sup>	1.1 lb/ft <sup>2</sup>	264		-40 to 212	b
B5	Solar Power Distribution	2	2	N/A	Continuous	N/A	13 x 11.5 x 6.75	2 018	18.0	36	-40 to 140	b
B6	Power Control Unit	2	2	N/A	Continuous	N/A	14 x 8 x 8	1 792	16.0	32	-40 to 140	f
B7	EIA <sup>m</sup>	10	10	1.0	Continuous	10	5 x 4 x 3	600	2.5	25	-40 to 140	b
B8	Thermal Control Unit	1	1	TBD	Continuous	TBD	TBD	TBD	TBD		TBD	b
B9	Cable Interface Unit	1	1	N/A	Continuous	N/A	9 x 6 x 2	108	8.0	8	N/A	
Communication and Data Handling												
C1	Dual Transponder Receivers	2	2	3.5	Continuous	14.0	13 x 8 x 6	1 248	23.3	47	32 to 130	d
C2	Transmitter	4	2	21.0	5 Percent	2.0						
C3	PSK <sup>n</sup> Demodulator	2	2	0.4	Continuous	4.0	1.3 x 2.8 x 6	44	2.0	4	32 to 130	d
C4	Frequency MUX	2	2	2.0	Continuous	0.8	7.25 x 5.0 x 1.6	116	2.0	4	32 to 130	d
C5	Antenna, Conical	1	1		Continuous		Base 12, 12 L		3.0	3	TBD	d
C6	Boom	1	1		Continuous	10.0	1.5 Dia., 72 L		1.0	1	TBD	d
C7	Antenna, Flat Spiral	1	1		Continuous				1.0	1	TBD	d
C8	Tape Recorders	4	1 Rec. 1 P/B	10 Rec. 20 P/B	Continuous	10.0	9 x 7.25 x 5.75	1 501	15.0	60	14 to 120	b/d
C9	Tape Recorder Control Unit	1	1	1.0	Continuous	1.0	6 x 7.3 x 1.6	700	3.0	3	32 to 130	b
C10	PCM <sup>o</sup> Encoder	2	2	3.2	Continuous	6.4	6 x 9 x 2.8	302	4.0	8	32 to 130	b
C11	Format Generator	2	2	2.1	Continuous	4.2	6 x 9 x 2.8	302	4.0	8	32 to 130	1
C12	Clock	1	1	14.0	Continuous	14.0	6 x 3 x 3	54	3.0	3	32 to 130	1
C13	CMD <sup>p</sup> Processor	2	2	7.8	Continuous	15.6	6 x 9 x 2.8	302	2.0	4	32 to 130	1
C14	CMD Memory	2	2	3.5	Continuous (Unit 2; 5 Percent)	3.7	6.2 x 7 x 4.1	356	6.0	12	-22 to 140	1
C15	RAU or RDU	40	1	1.2	Continuous	1.2	2.8 x 2.8 x 1	312	0.3	12	-22 to 140	b

- a. Wide angle sun sensor
- b. Component selected for HEAO-A/B by GAC in Phase B study
- c. Digital sun sensor
- d. Component selected for HEAO-A/B by TRW in Phase B study
- e. Fixed head star tracker
- f. Component exists from other programs but not proposed for HEAO-A/B
- g. Control moment gyro
- h. Reaction control system
- i. To be determined
- j. Orbit adjust stage
- k. Electrical power system components not considered to consume load power
- l. New design required for HEAO-C
- m. Electrical integration assembly
- n. Phase shift keyed
- o. Pulse code modulator
- p. Command

FOLDOUT FRAME

FOLDOUT FRAME

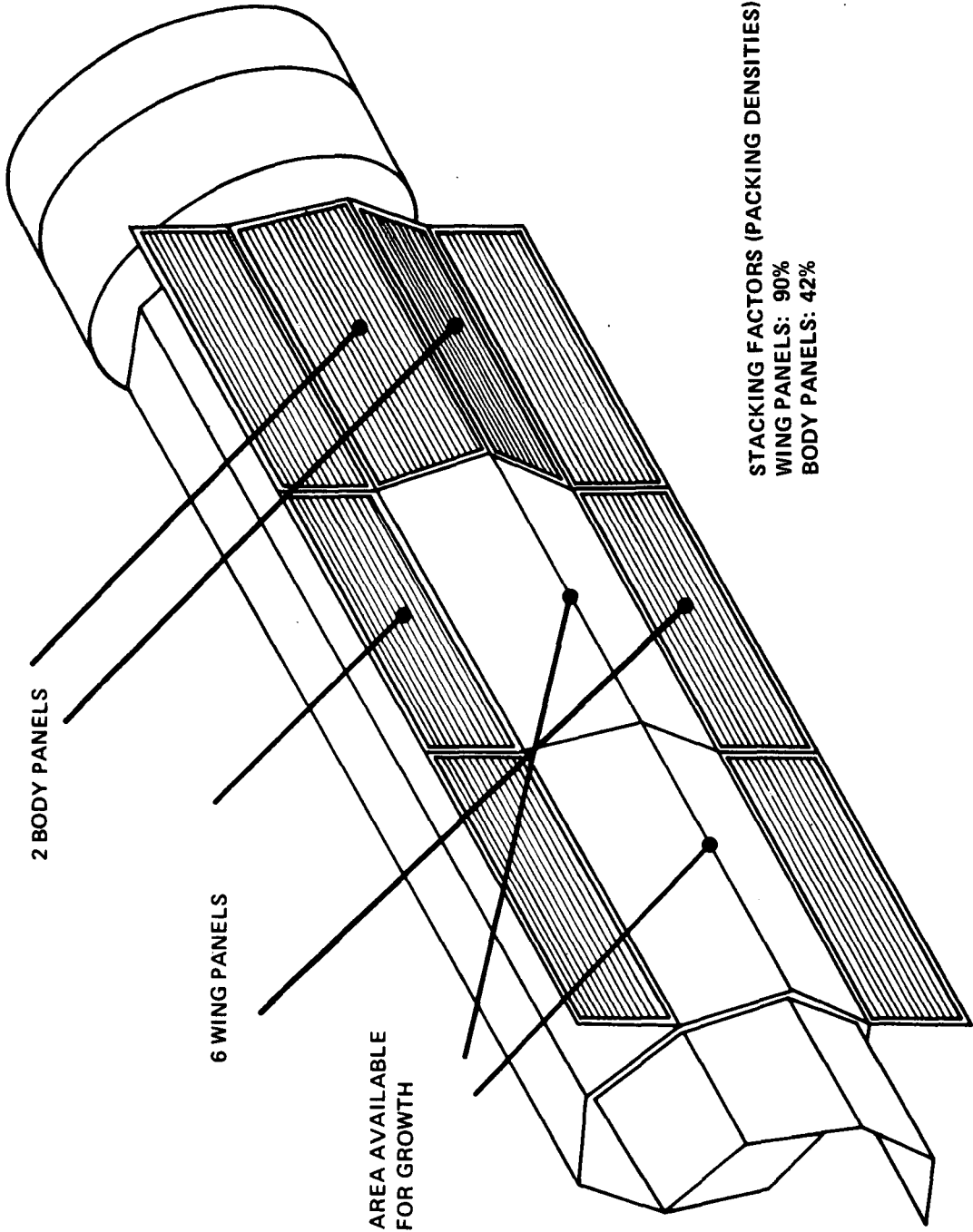


Figure IV -2. HEAO-C configuration.

The large telescope tubes are fabricated of graphite-epoxy, primarily because of the excellent thermal properties of that material. The deep oval ring which ties the large telescopes together is made of titanium for low thermal conductivity. All other structure is made of aluminum.

Figure IV-6 shows an exaggerated view of the action of the internal support arrangement under thermal bending of the external structure. Rotations of the A-frame-and-strut and delta-frame as indicated in this figure, due to thermal deformation of the outer structure, do not affect the alignment and parallelism of instruments mounted on the optical bench; the bench would tilt with respect to the main spacecraft structure, but this would not affect pointing since the optical bench rather than the outer structure is the reference for pointing. View (a) shows the normal spacecraft orientation (arrays normal to sun) and view (b) shows the spacecraft rolled 90 degrees about the longitudinal (X) axis from the orientation in (a). As indicated, no torquing or bending of the tubes will occur, and they remain parallel.

Several alternate mounting concepts were considered for the experiments, and these are described in Appendix C. The concept using the ball joints, shock mounts, and linkages (B/S/L concept), however, offers the following advantages:

- No bending forces are applied to the optical bench.
- Deformation of the outer structure does not affect the Observatory operation.
- No linkages have to be dropped in orbit (can eliminate some hardware and the associated failure probability).
- Considerable tolerance for thermal control system failure or degradation is provided by this mounting arrangement.
- Good thermal isolation of the bench from the crowfoot beam is provided by the ball joints and shock mounts.
- A high degree of insensitivity of telescope tilt angle to joint shifts is provided, due to the large mounting base.

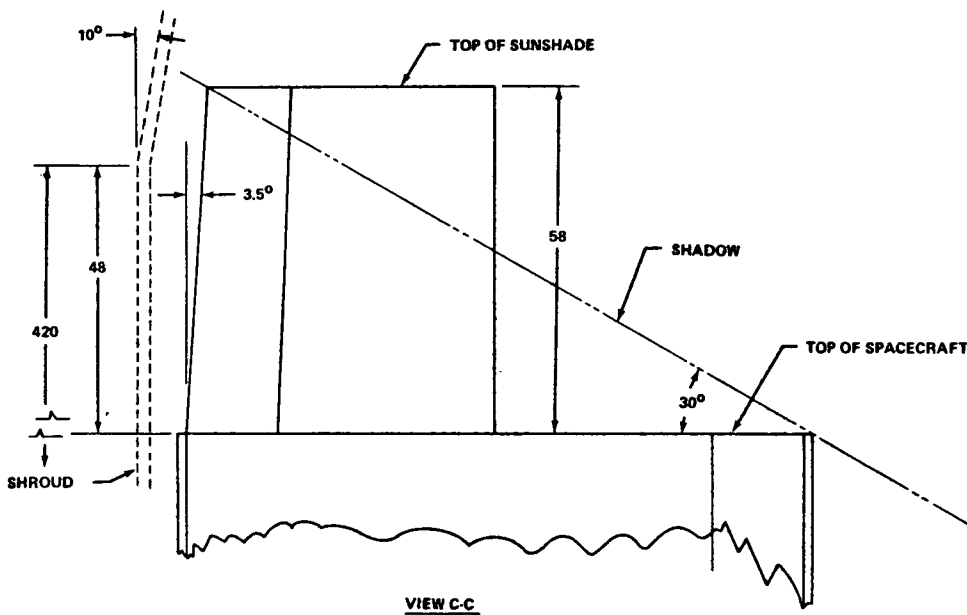
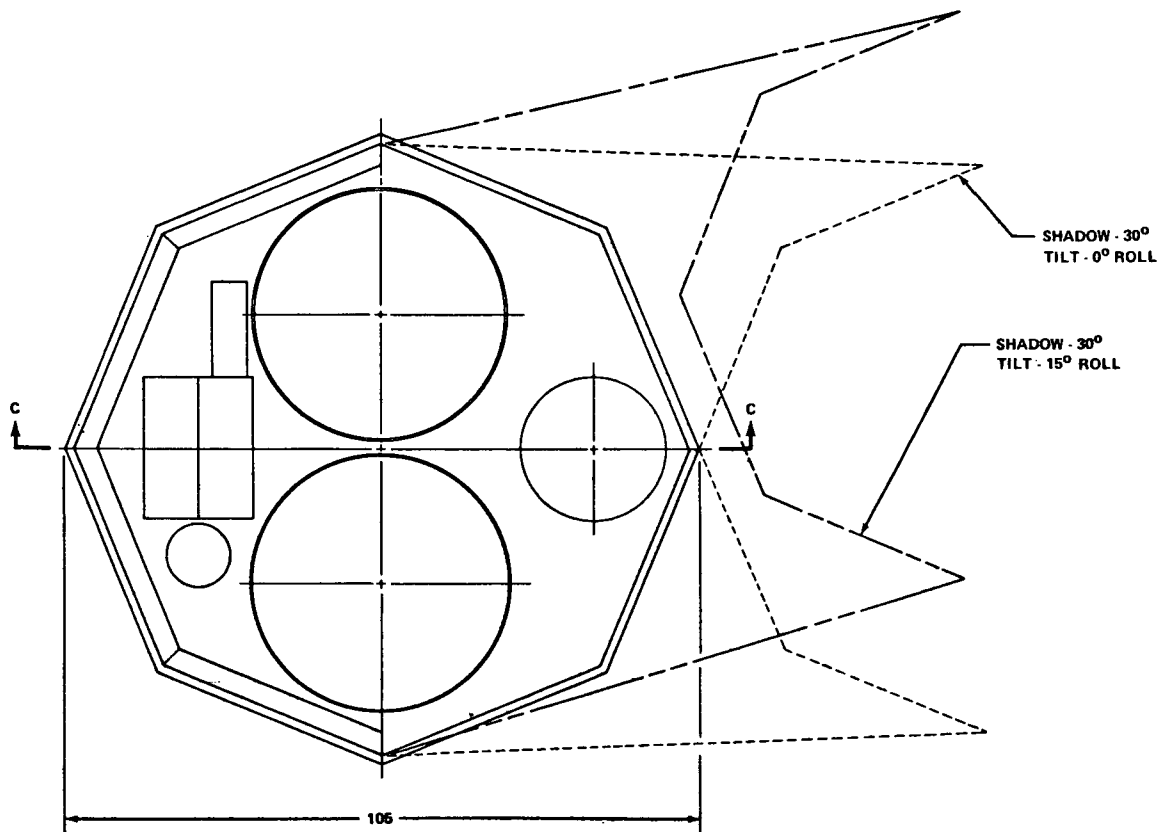


Figure IV-3. HEAO-C sunshade.

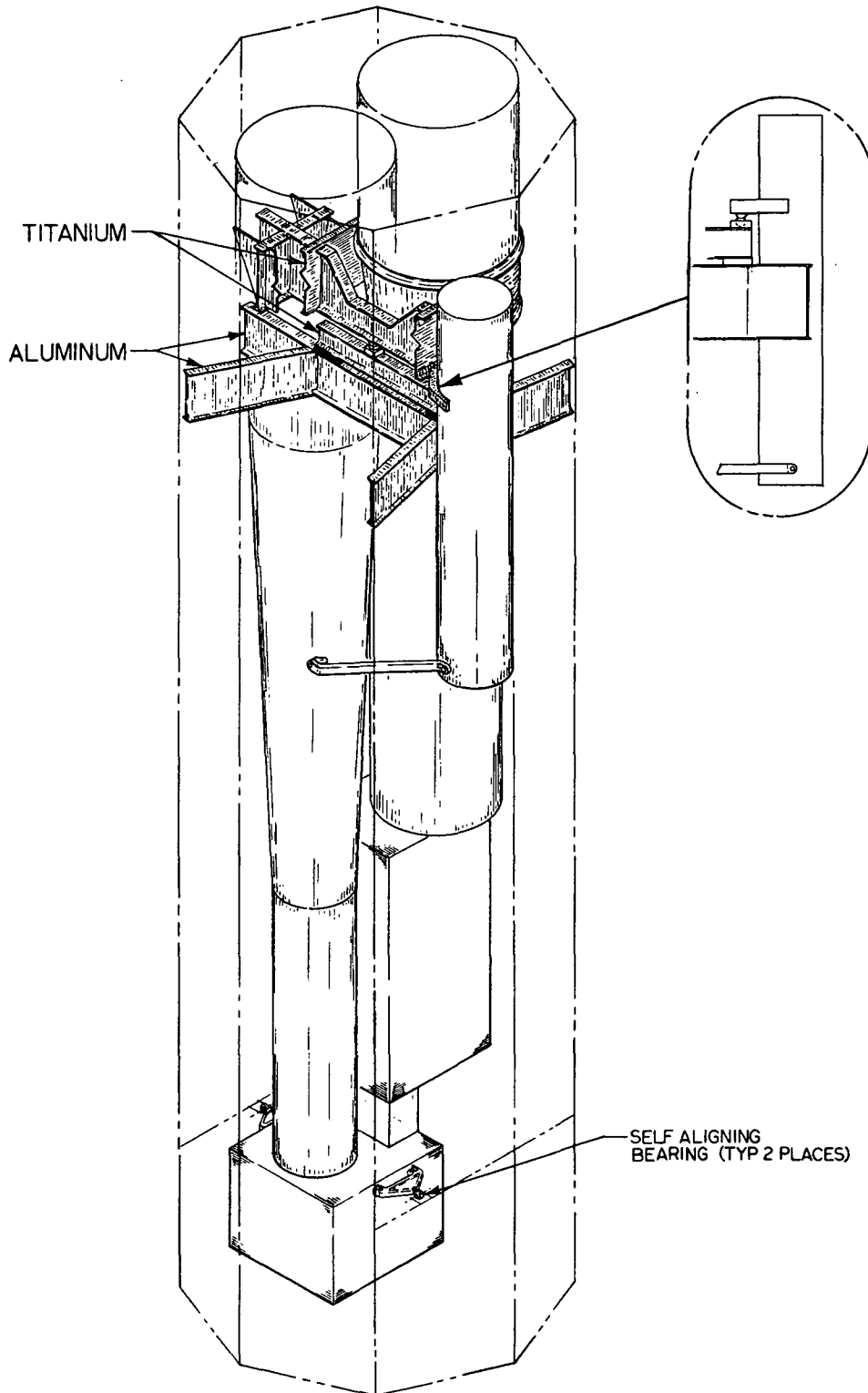


Figure IV-4. Internal support structural arrangement.

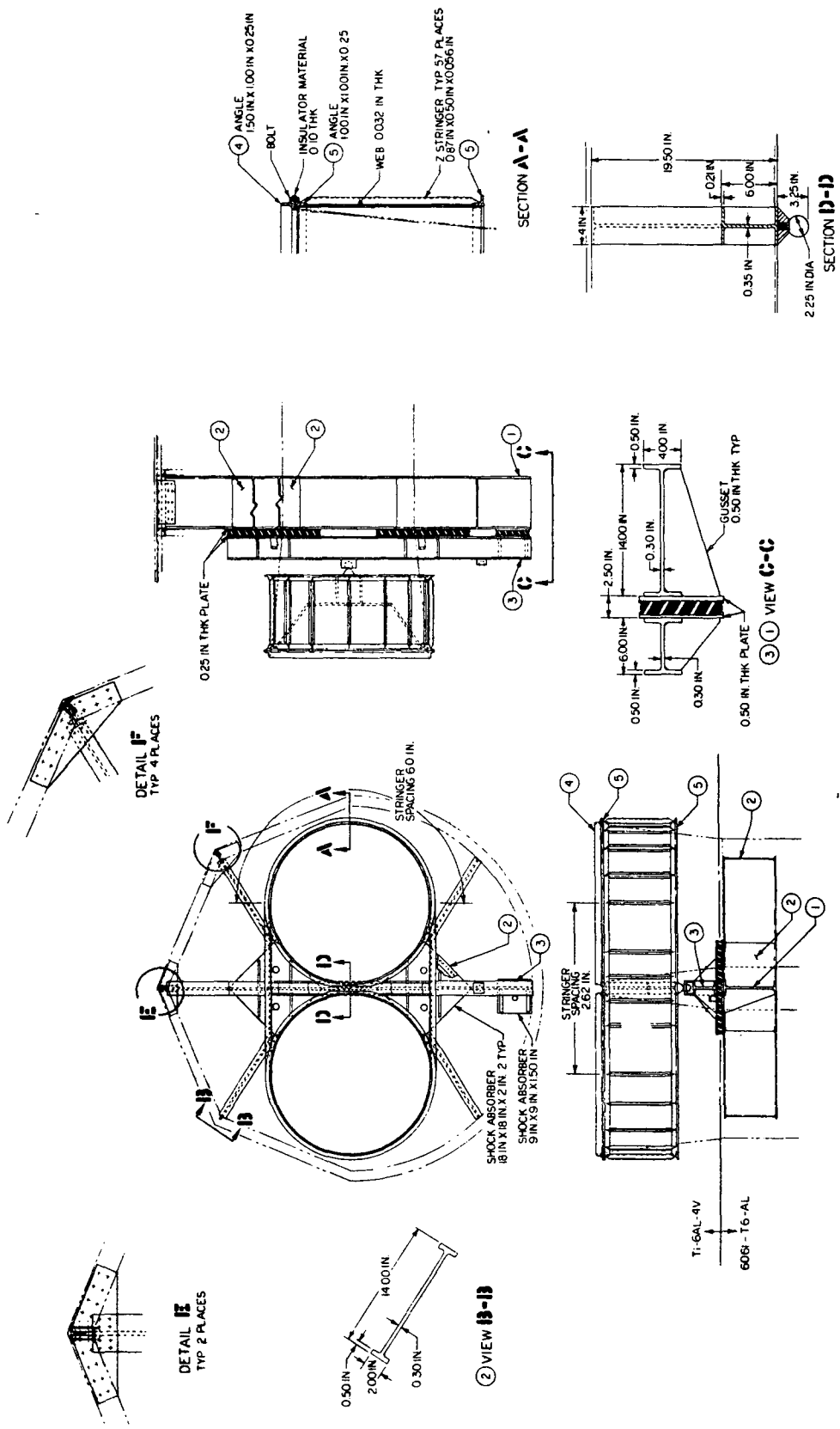
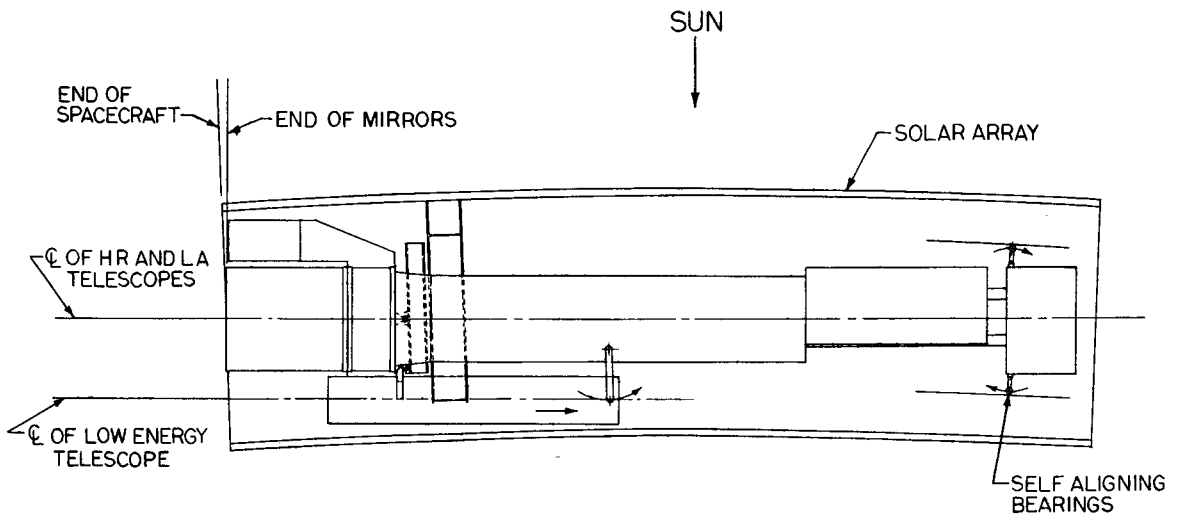
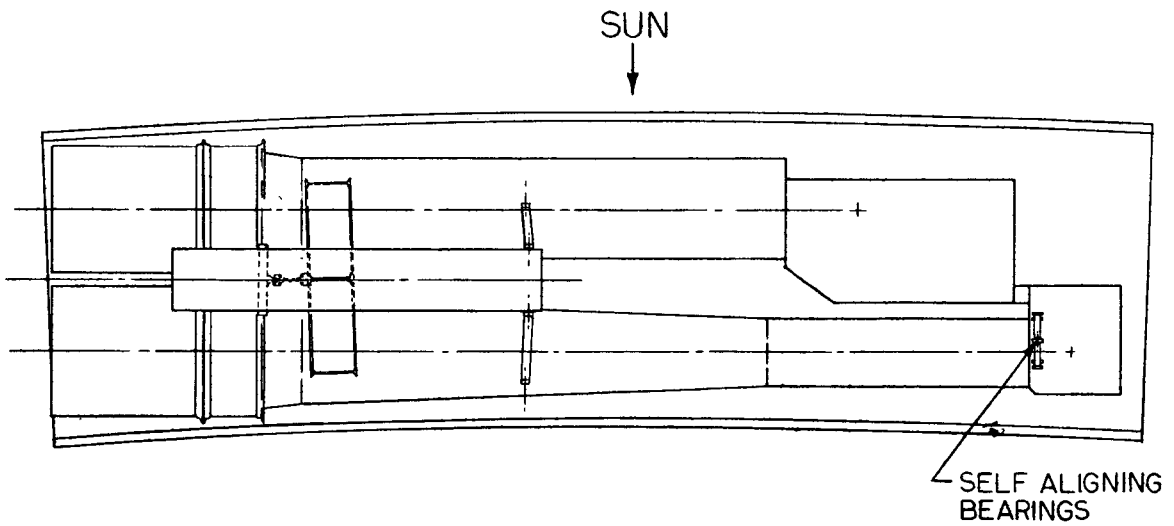


Figure IV-5. Details of internal support structures.



(a) In X-Z plane.



(b) In X-Y plane.

Figure IV-6. Thermal bending effects.

The use of separate tubes for each telescope also provides several advantages over other concepts which were considered (see Appendix C). Among these are (1) the simplification of structural and thermal interfaces among telescopes, and simplification of integration and development by allowing each telescope to be designed, built, and tested more easily and realistically as an entity before having to be integrated into the Observatory; (2) greater programmatic flexibility to accommodate schedule changes, development problems, etc.; (3) the insensitivity of each telescope to changes in design in other telescopes or Observatory systems; (4) greater availability of space in the Observatory for packaging subsystems; and (5) greater structural efficiency.

For ease of manufacturing and assembly, the spacecraft outer structure might be assembled into two longitudinal halves, with telescopes mounted prior to joining the halves (Fig. IV-7). Disassembly could be accomplished in the same fashion should removal of telescopes be required. Normal access to the interior for installation, testing, etc., could be accomplished by using removable panels on the antisolar side (no insulation on some of these) and by entering through the ends of the Observatory using access equipment.

## B. Baseline Observatory Systems

1. Systems Description. Figure IV-8 is a block diagram showing the baseline Observatory systems and subsystems, and Figure IV-9 is a schematic diagram depicting the experiment mounting scheme.

The Observatory<sup>1</sup> systems and subsystems are defined as follows:

- a. Experiments
- b. Attitude Sensing and Control System (ASCS)
  - (1) Attitude Sensor Subsystem
  - (2) Attitude Control Subsystem
  - (3) Reaction Control Subsystem

---

1. The Observatory consists of the spacecraft plus experiments.

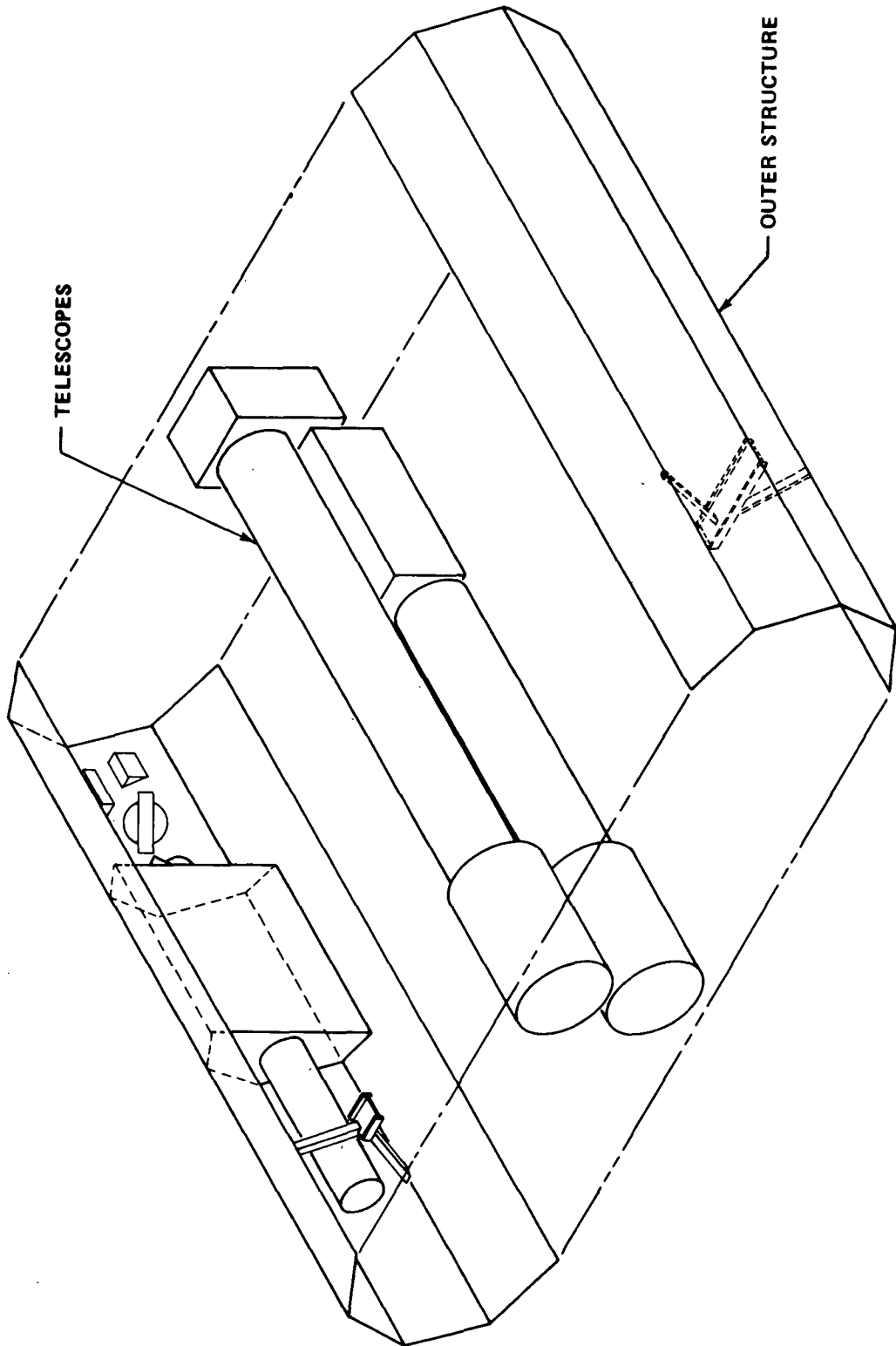


Figure IV-7. Possible HEAO-C assembly scheme.

- c. Electrical System
  - (1) Electrical Power Subsystem
  - (2) Electrical Distribution and Control Subsystem
- d. Communication and Data Handling System (CDHS)
  - (1) Communication Subsystem
  - (2) Data Handling Subsystem
- e. Structure
  - (1) Outer Structure
  - (2) Crowfoot Beam Assembly
  - (3) Optical Bench
  - (4) Miscellaneous Mounting Hardware
- f. Thermal Control System
  - (1) Insulation
  - (2) Coatings
  - (3) Alzak skin
  - (4) Heaters
  - (5) Filters (Membrane)
- g. OAS<sup>2</sup>
  - (1) Main Propulsion Equipment
  - (2) RCS Equipment
  - (3) Separation Equipment

---

2. The OAS is considered an element of the spacecraft, although not a system per se.

FOLDOUT FRAME 1

FOLDOUT FRAME 2

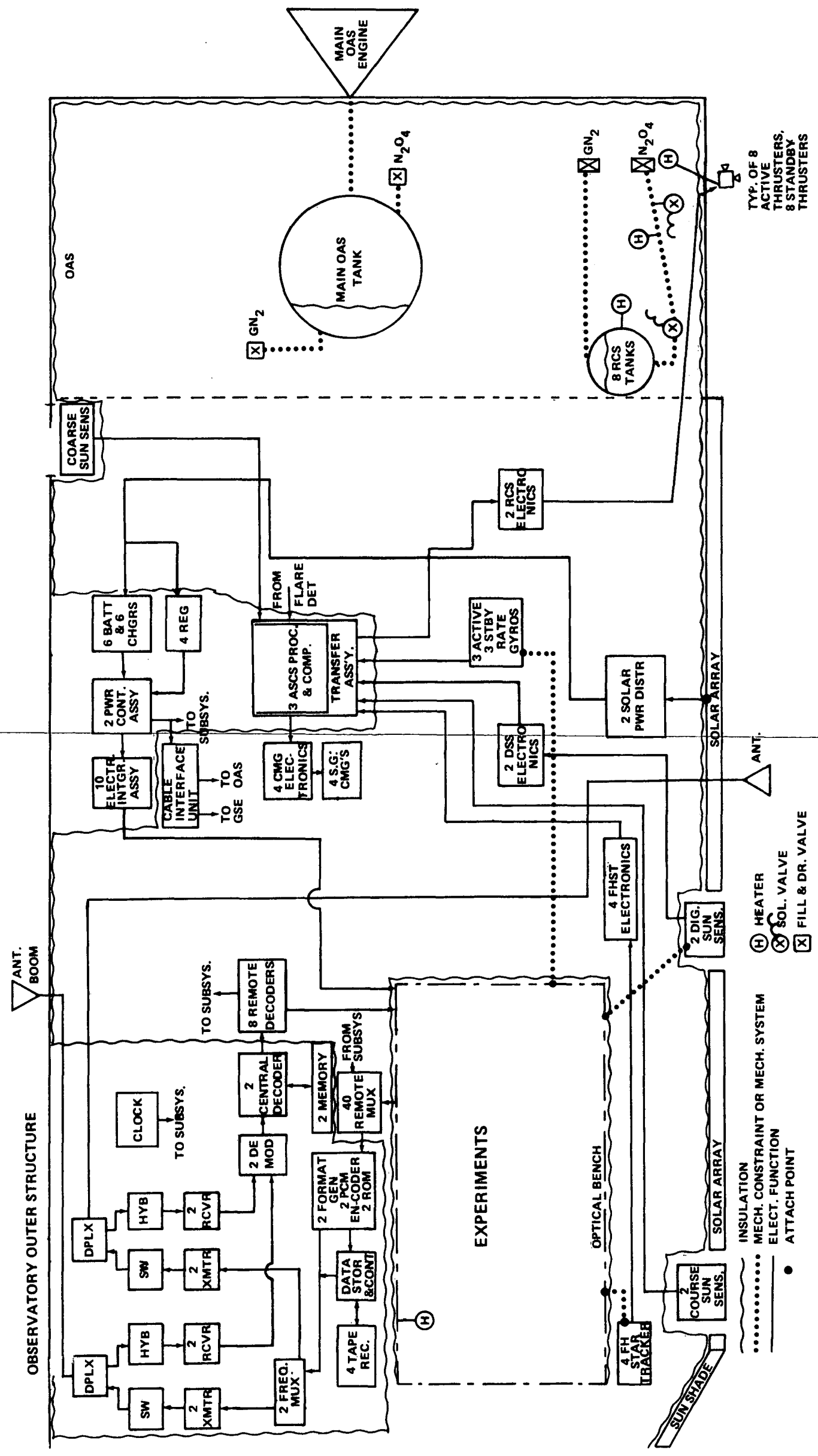


Figure IV-8. Baseline Observatory systems.

FOLDOUT FRAME 2

FOLDOUT FRAME 1

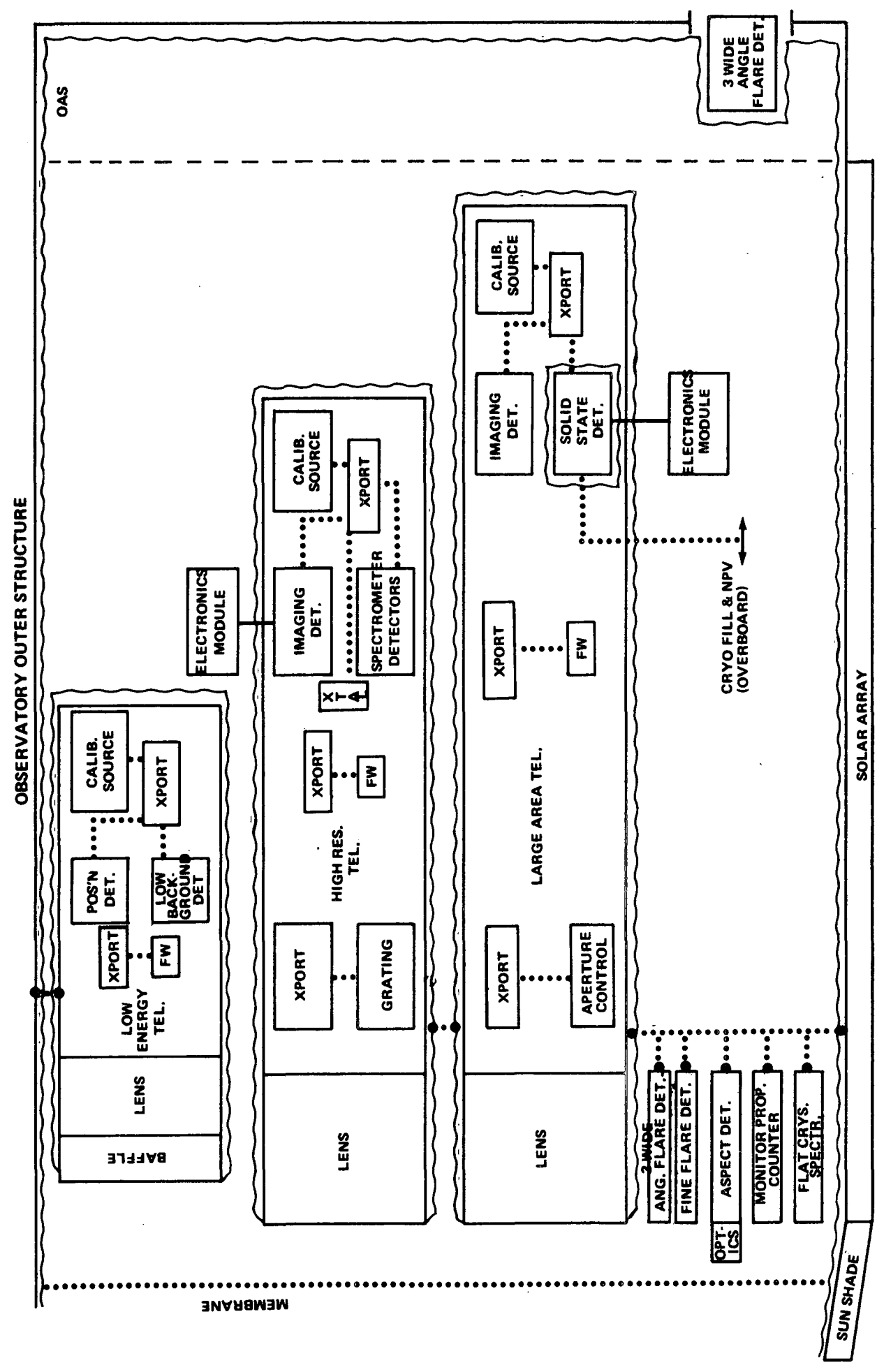


Figure IV-9. Baseline experiment mounting scheme.

The following paragraphs briefly describe these HEAO-C systems.

a. Experiments. The experiments are described in Chapter II.

b. Attitude Sensing and Control System. The baseline ASCS consists of 3 coarse sun sensors, 2 digital sun sensors, 6 reference gyros, 4 fixed-head star trackers, 4 single-gimbal CMGs, 3 processor/computers, 1 transfer assembly, 16 RCS thrusters, and 8 tanks with associated lines and valves. The CMGs were selected to furnish the required pointing accuracy and stability. The RCS was chosen for CMG unloading, since it is required for attitude control during OAS burns and since HEAO-A and -B plans similar RCS utilization. The coarse sun sensors are used for sun acquisition, and the DSS is used for two axis fine sunline orientation. The star trackers provide three axis information; their fields of view, sensitivity, and physical arrangement were selected for a high probability of always seeing usable guide stars with any Observatory orientation, and for ability to perform the mission with minimal degradation in performance with as many as three trackers failed. The transfer assembly serves as an interface between the sensors, actuators, and processor/computer.

Most of the items are similar to those specified in References IV-1 and IV-2, but the star trackers are different from those in either reference, due to the HEAO-C pointing requirements.

c. Electrical System. The solar array consists of 6 deployable panels (90 percent cell packing density) and 2 fixed panels (42 percent packing density). The array deployment devices are torsion rod/viscous damper assemblies released by redundant pyrotechnics. Half of the array modules are connected to one solar array distributor and half to another. The two distributors are mounted near the solar array to save cabling weight. Each distributor can be switched to either of two charger-battery groups consisting of three chargers and three batteries. The batteries are 22 cells rated at 20 ampere-hours per cell. The output of each group can be switched to either of two electrical control assemblies (ECA). Four regulators are used; two are capable of supplying full power. Each ECA feeds input power and receives regulated power from two regulators. Each ECA output can supply all or part of the subsystem load and part of the experiment load through five EIAs.

d. Communication and Data Handling System. This system gathers, formats, and records the experiment and housekeeping data, and transmits them to a ground station on command; it also receives, stores, and distributes ground commands to experiments and subsystems. The hardware consists of the following items:

- Multiple (40) remote multiplexers and one central unit.
- PCM encoders.
- Format generators.
- A dual tape recorder control unit and four tape recorders.
- Two internally redundant transponders with RF switches, diplexers, and hybrids.
- Two antennas, one of which is boom-mounted.
- Two PSK demodulators.
- Two central and eight remote command decoders.
- Two command memory units.
- A redundant clock.

The command memory was not identified as a required item for HEAO-A and -B.

The system can gather and store data in any of four fixed-selectable formats. Data are stored on one recorder until it is filled (approximately  $1.65 \times 10^8$  bits per recorder, or 1.06 orbits), then it is transmitted to the ground on command. The system normally transmits recorded data over a 500 kbs downlink and simultaneously transmits real-time data (27.5 kbs) on a subcarrier, using frequency diversity techniques. The system receives commands on a frequency of 2100 Mhz. Real-time commands are acted upon by the remote decoders as they are received. Delayed commands are ignored

by the remote decoder and are stored in the command memory. A command is called up from storage at the proper time and appears as a real-time command to the remote decoders. There is a 24 hour command storage capability which can be bypassed in case of malfunction.

e. Structure. There are four major portions of the structure: (1) the outer structure, consisting of ring frames, eight longerons, stringers, skin, and sunshade; (2) a forward crowfoot beam assembly on which the optical bench is supported; (3) the optical bench, which consists of a dual beam assembly, two ball-and-socket joints, telescope tubes, and aft tube linkages; and (4) miscellaneous mounting hardware. The outer structure serves to isolate the optical bench from direct solar radiation and supports the subsystems (including solar arrays), the sunshade, and the optical bench.

Some of the outer structure members (stringers, ring frames, and longerons) from HEAO-A and -B might be useable on HEAO-C, but this commonality may not be great because of the differences in experiments and their attach points and load paths. One key difference in outer structure design is that HEAO-C must utilize structural skin for shear strength; whereas, HEAO-A and -B obtain shear strength through transverse shear webs and bulkheads.

The crowfoot beam assembly takes all the longitudinal launch loads of the optical bench and distributes this load to several points around the circumference of the outer structure. The optical bench serves as a reference structure for precision alignment of the experiments and the most accurate sensors (rate gyros, star trackers, and digital sun sensors). The mounting scheme can be seen in Figures IV-1 and IV-4. The ball-and-socket joints allow relative movement between the optical bench and the outer structure, so that thermal or other distortion of the outer structure does not induce stress into the optical bench. The aft linkages on the tubes are required for transverse and torsional launch loads and also limit the movement of the telescope aft ends during on-orbit maneuvers (the link from the LE telescope to the others serves also to maintain experiment coalignment). The alzak skin used for thermal control also serves as a micrometeoroid bumper. Miscellaneous mounting hardware is provided for the experiments and systems.

f. Thermal Control System. Thermal control is maintained by coatings on the spacecraft inner and outer surfaces; by multilayer aluminized mylar insulation; by use of alzak skin, mirror heaters, sunshade, and a thermal control filter; by judicious choice of structural materials and choice of equipment location. Insulation is provided on the outside of the outer structure to minimize "hot-dogging." The LA and HR tubes are constructed of graphite-epoxy to minimize thermal distortion, and some insulation is also

provided on the outside of the tubes. Most of the systems are located on the cold side of the spacecraft for easy control of the thermal coupling to the back surface. Some hardware is compartmentalized and louvers may be utilized in the battery compartments.

g. OAS. A stripped OAS, similar to that used in the HEAO-A and -B studies, was assumed for the purpose of this study. It consists of the main engine, main propulsion tank and pressurant supply; RCS thruster assemblies; RCS tanks, lines, valves, etc., and separation hardware. The OAS remains attached in orbit and is considered part of the spacecraft. A more detailed description of the OAS is provided in Appendix B.

## 2. Systems Integration

a. Electrical Power Summary. A summary of the power requirements for the Observatory is shown in Table IV-2 for normal on-orbit viewing operations. A more detailed breakdown of each subsystem's requirements for each mission phase can be found in Chapter VIII. It is significant to note that the power requirements are greater than those defined for HEAO-A and -B in the Phase B studies (approximately 640 watts for those missions if CMGs are used, including 20 percent contingency, compared to 722 watts for HEAO-C). Excluding contingencies, the experiment power requirements on HEAO-C are approximately 10 watts less, but spacecraft subsystems power requirements are approximately 80 watts greater.

b. Mass Characteristics. Mass data were developed for several configurations during the study. The alternate configurations and their mass characteristics are discussed in Appendix C. The baseline configuration mass characteristics are provided below.

Table IV-3 gives a detailed weight breakdown of the Observatory. The total weight of the HEAO-C spacecraft (including RCS propellant, but excluding OAS weight and the Titan adapter) without contingency is 14 353 pounds, which is approximately 4650 pounds less than HEAO-A. The primary changes in HEAO-C system weights from HEAO-A weights are listed below (all weights are approximate):

- 5325 pound decrease in experiment weight (HEAO-A  
≈ 12 500 lb)
- 675 pound increase in subsystems weight (HEAO-A  
≈ 6500 lb)

TABLE IV-2. HEAO-C ON-ORBIT ELECTRICAL LOAD SUMMARY

Load	Average Power (W)	Peak Power (W)
Experiments	234.0	294
Communications and Data Handling	79.3	141.6
Attitude Sensing and Control	252.1	353.1 <sup>a</sup>
Experiment Thermal Control <sup>b</sup>	10.0	40.0
RCS	41.9	295
Electrical System	<u>16.0</u>	<u>25.0</u>
Baseline Total	633.3	1148.7
Contingency (~ 14%)	<u>89.0</u>	<u>89.0</u>
Total Design Load	722.3	1237.7

a. Assumes simultaneous spinup of all CMGs.

b. All other thermal control power is listed under the applicable systems.

The principal increase in subsystems weight is attributed to the structure, approximately 500 pounds. The weight of the two large telescope tubes (460 pounds) has been included here rather than in experiment weight. The remainder of the differences are distributed among the subsystems. The lighter weight of the HEAO-C Observatory helps in the launch vehicle performance area but hurts in the orbital lifetime area (ballistic coefficient is worse). A 20 percent contingency is suggested for the HEAO-C control weight during the next phase of the study, or an Observatory orbital weight of 18 700 pounds at start of mission.

TABLE IV-3. HEAO-C BASELINE OBSERVATORY WEIGHT SUMMARY

Experiments			7175
HR Telescope (less tube)		2636	
Mirrors	2025		
Detectors and Misc.	611		
LA Telescope (less tube)		2820	
Mirrors	2400		
Detectors and Misc.	420		
LE Telescope		840	
Mirrors	400		
Detectors and Misc.	140		
Structure (tube)	300		
Miscellaneous Experiments		879	
Aspect Detector	121		
Flare Detectors	297		
Monitor Proportional Counter	142		
Flat Crystal Spectrometer	162		
Cabling	157		
Subsystems			6966
Structure		3375	
Outer Shell (including sunshade)	1417		
Bench (tubes and mounts)	1497		
Crowfoot Beam Assembly	261		
Mounting Brackets	200		
Attitude Sensing and Control		1927	
Attitude Sensing	138		
Attitude Control	734		
RCS (dry)	207		
Propellant and Pressurant	848		
Thermal Control		505	
Insulation	120		
Coatings	70		
Alzak Skin	300		
Heaters	15		

TABLE IV-3. (Concluded)

Communication and Data Handling		178	
Communication	60		
Data Handling	118		
Electrical Power		856	
Arrays	332		
Storage	396		
Regulation and Control	32		
Distribution	96		
Cables		125	
Miscellaneous			
OAS (stripped)			1 223
OAS Propellant			1 240
Spacecraft Adapter			212
Titan Adapter (212 Drop Weight)			221
Observatory Lift-off Weight			17 037
Observatory Weight After Titan Separation			16 825
Observatory Weight After Final Orbit Circularization			15 585 <sup>a</sup>

- a. More recent data lists stripped OAS as 1499.2 pounds and shroud non-separation weight as 97.6 pounds. The Observatory weight after orbit circularization is 15 959 pounds.

Fourteen discrete masses were utilized to help simplify the mass characteristics determination. The inertia contribution of each mass about its own centroid was accounted for. Estimates for the inertia of each mass were calculated on the basis of a homogeneous solid. The total mass characteristics for the baseline configuration are given in Table IV-4. The reference axes used for these calculations are depicted in Figure IV-10. Also shown in the table are characteristics for the cases where 25 percent contingency weight and 50 percent contingency weight are distributed homogeneously within the Observatory. It should be noted that the inertias about the Y and Z axes are much larger than those about the roll axis (X). This distribution results from the heavy mirror with its supporting structure located at the

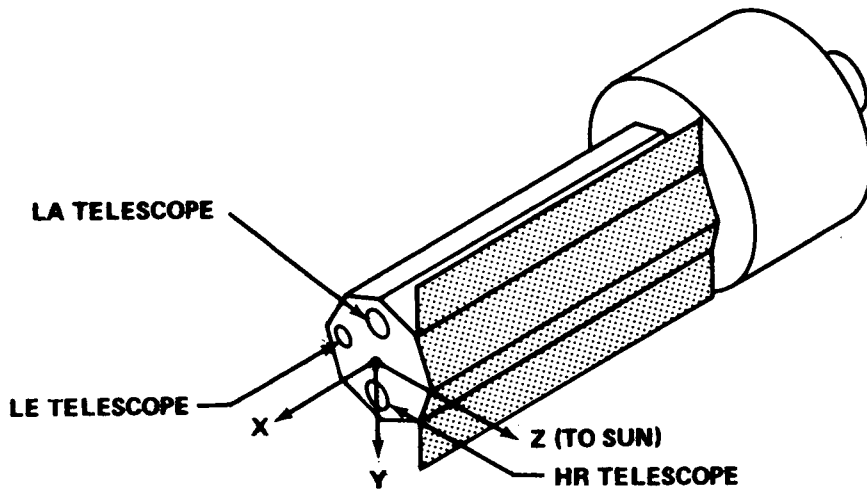
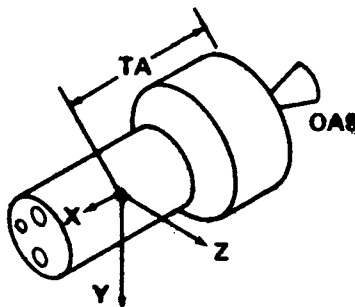


Figure IV-10. Reference axes for location of discrete masses.

TABLE IV-4. BASELINE MASS CHARACTERISTICS SUMMARY

Configuration	Weight (lb)	Torque Arm, TA (in.)	Centroidal Inertia (slugs-ft <sup>2</sup> × 10 <sup>3</sup> )		
			I <sub>x</sub>	I <sub>y</sub>	I <sub>z</sub>
Baseline plus OAS	15 585	250	2.88	69.51	70.05
Baseline plus 25%	19 481	249	3.46	77.48	78.01
Baseline plus 50%	23 378	235	3.75	97.14	98.00



forward end and the OAS attached at the aft end. The contingency of 50 percent is close to the maximum capability of the launch vehicle, 24 318 pounds. The reference axes shown in this table are used in discussion of the Observatory in the various sections of this report.

c. Interface Considerations. The key Observatory requirements and considerations which affect physical and/or functional systems interface design are listed below:

- Pointing Accuracy — Requires that the attitude sensor locations/orientations be unaffected by environmental perturbations; hence, they should be located on the optical bench.
- Experiment Coalignment — Requires accurate initial alignment and minimum effects from environmental perturbations; hence, all experiments should be mounted on the optical bench.
- Thermal Control — Requires that system hardware mounting locations and arrangements be optimum for achieving thermal balance; the antisolar side is preferred for system hardware.
- Electromagnetic Control (EMC) Considerations — Require that hardware which contains high voltage switching circuits or other electromagnetic interference (EMI) generating circuits be shielded and/or located remotely from EMI susceptible hardware, such as cathode ray tubes (CRTs), photomultiplier tubes, tape recorders, star trackers, etc.
- Modular Interference Hardware — A great deal of commonality/modularity can be utilized in the design of interface equipment such as the remote multiplexers. A standard size unit can be used for each experiment and subsystem, and its capability can be increased by using identical add-on units where required. The same approach can be used for remote decoders and power distribution hardware (EIAs, etc.). The principal investigator (PI) must supply required buffer storage as a part of his experiment.

- Mass Moment of Inertia/Center of Gravity (MMI/CG) Considerations — The location of equipment affects the MMI and CG, but in general these considerations are secondary to others, such as thermal control.
- Maximum Utilization of Existing Designs — The primary effect of this consideration, from an interface standpoint, was to aid in determining the locations and amount of equipment mounted inside the OAS.
- Launch Vehicle Interface — There are 300 words available on the Titan IID telemetry system (see Appendix B) for transmitting critical payload parameters during launch. A small amount of power and a few commands will have to be transmitted across this interface for stage separation functions; there must be at least 16 structural attach points at this interface.
- GSE Interface — Observatory equipment which will probably be active at launch is the communications and data handling system (except for transmitters), attitude sensing and control system (except for CMGs, sun sensors, and star trackers), heaters, and the portions of the power system required to sustain the other activated systems. There is no umbilical arm at the payload level on the launch pads (Pad No. 40 or 41 at Patrick Air Force Base). Consequently, there are no present plans for any Observatory umbilical connections. Most connections to ground support equipment (GSE) for launch or checkout will be through use of drag-on test cables. The gantry at the launch pad must be rolled back about 2 hours prior to launch, and some of the systems mentioned above will be activated at that time. The GSE power can be supplied through the Titan interface until "power transfer," and controls can be supplied during this 2 hour period and the succeeding 2 hour launch window period via RF link, by using an RF window or a parasitic antenna on the shroud.

The Observatory systems block diagram (Fig. IV-8) gives some indication of the types of interfaces which exist on HEAO-C. The chapters on each system provide more details on the complexity of these interfaces. The functions which must occur between major elements of the Observatory and launch vehicle are defined in Figures IV-11, IV-12, and IV-13.

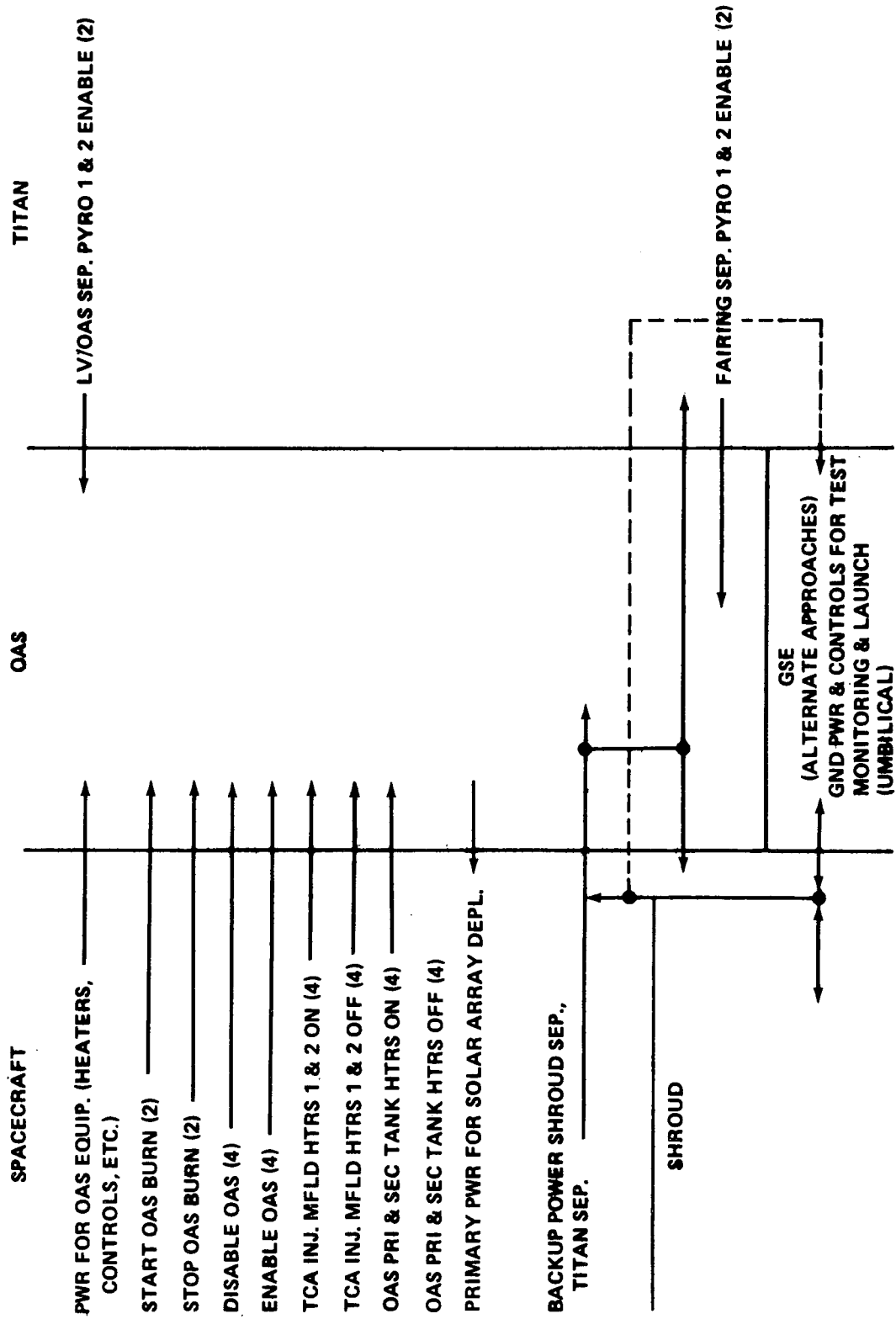


Figure IV-11. Commands and power across major interfaces.

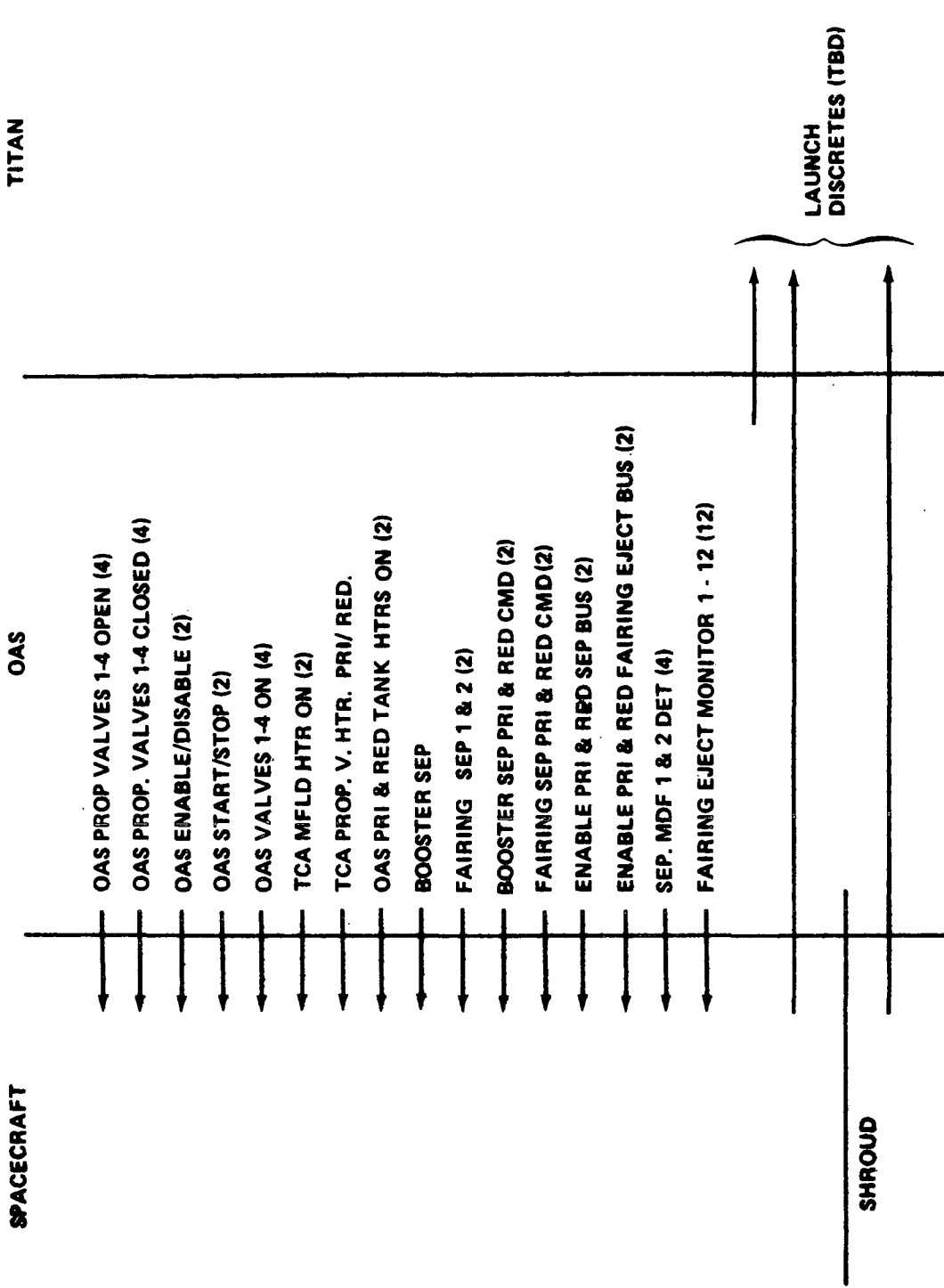


Figure IV-12. Discrete measurements across major interfaces.

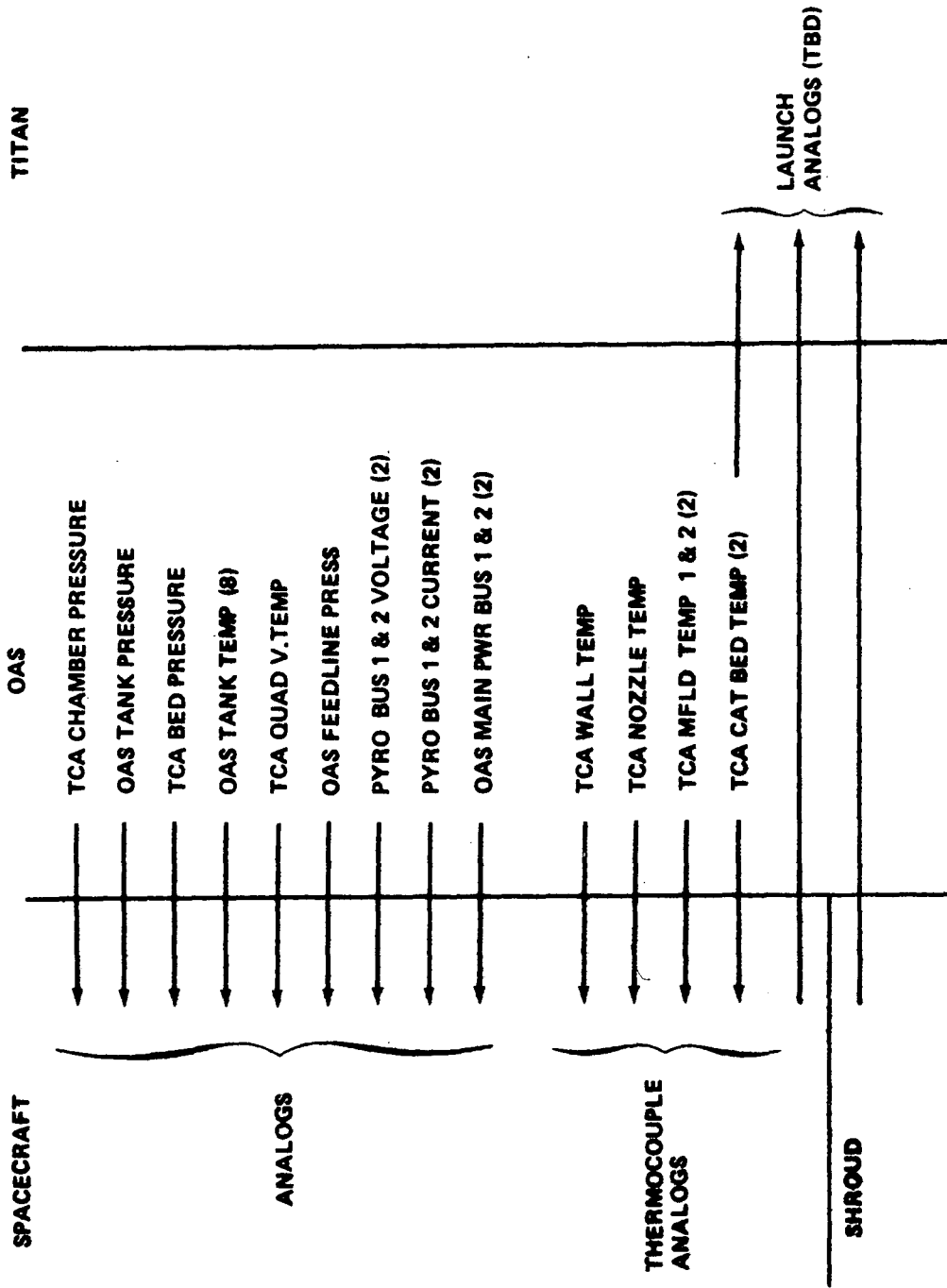


Figure IV-13. Analog measurements across major interfaces.

d. Two Year Lifetime Considerations. The HEAO-C requirement of a two year operational lifetime is a more stringent requirement than that specified for HEAO-A and -B missions (one year required lifetime with a two year lifetime goal). In the phase B studies, expendables and energy sources were sized for a two year lifetime, and the other subsystems designed to a one year reliability goal. Even the subsystems which were sized for a two year lifetime do not possess the high two year reliability required for the HEAO-C mission. Hence, design changes and increases in development testing will be necessary, both for the increase in lifetime and the increase in required reliability, for the HEAO-C design to make maximum use of existing HEAO hardware. Since commonality of HEAO-C hardware with HEAO-A and -B hardware is a strong design driver, the general approach to achieving the two year lifetime and associated high second year reliability in the HEAO-C study was to improve the effectiveness of the same components by better systems utilization and integration techniques and to add components in standby redundancy where required. Such an approach stresses commonality of components but not necessarily of systems, so costs will increase due to this difference.

The approach just described may not be achievable in all cases (depending on the final design of HEAO-A and -B); hence, in some cases, the longer lifetime and higher reliability for the second year may necessitate the following (assuming the intent is still to maintain maximum commonality across missions):

- Redesign/modification of HEAO-A and -B off-the-shelf hardware (if its design life was not for two years).
- Additional testing complexity caused by the additional redundancy previously mentioned.
- Additional development, qualification, and/or requalification testing (if HEAO-A and -B hardware was designed and qualified to the less stringent requirements), particularly for the life-critical and cycle-critical items such as solar arrays, batteries, tape recorders, gyros, CMGs, star trackers, RCS components, etc.

The foregoing considerations all tend to lead to a general conclusion, which is a recommendation of the study. That is, the lifetime and reliability requirements of HEAO-A, -B, and -C should all be the same if maximum cost-effectiveness in the area of commonality across missions is to be achieved.

There are several other factors which must be taken into consideration in thinking of the two year, high reliability mission; these are listed below:

- Experiments must be designed with a two year lifetime and a high second year reliability. Indications are that the PIs may prefer a lower reliability requirement for the second year, due to complexity, cost, etc.
- Priority for utilization of the tracking network traditionally decreases as time in orbit increases. If there is a great demand for the network from many spacecraft, there will be a greater probability of losing HEAO data later in the mission due to this factor. Hence, there may be less return on the investment in the second year of lifetime and high second year reliability.
- Using a mission/data worth model which decreases with time in orbit (see Reliability paragraph which follows), the value of the data and the mission is less for the second year; hence, from this standpoint also, the return on the investment in the second year lifetime and high, second year reliability will be less.

e. Reliability. The design approach in the study was to plan for a reliability of 0.95 for one year, determine what the corresponding reliability would be for two years, then assess the cost impact of raising the reliability to 0.90 at the end of two years. It was desired to perform a classical reliability analysis on the Observatory subsystems so that the results could be compared with those from the HEAO-A and -B studies. In performing this analysis, the same component failure rates from those studies were utilized wherever a similar component existed in the HEAO-C design unless there was some indication that the failure rates should be changed. The results of this analysis are summarized in Table IV-5. The complete analysis is provided in Appendix G.

The results of the classical numerical reliability analysis were used as a guide rather than a rigid requirement in designing the HEAO-C systems; since such an analysis depends on the definition of success, and success is a relative rather than an absolute quantity, engineering judgement must be utilized with the reliability numerical analysis to obtain a reliable but practical design. Using this philosophy, a concept of Mission Worth and degraded mode operation was defined giving a high probability of having an acceptable degree of success in high-failure conditions of operation. The single parameter which gives the best

TABLE IV-5. HEAO-C RELIABILITY NUMERICS SUMMARY

Subsystem	Reliability	
	1 yr	2 yr
Attitude Sensing and Control	0.94520	0.81024
Electrical Power (EPS)	0.99199	0.94403
Communications (COMM)	0.99963	0.99792
Data Handling (DHS)	0.98890	0.95895
Reaction Control	0.99739	0.92948
Baseline	0.92446	0.68035
Alternate 1 <sup>a</sup>	0.96188	0.76363
Alternate 2	0.96717	0.83899

a. See Volume III, Appendix G for discussion of alternates.

indication of mission success (from the spacecraft systems standpoint) is "percent of valid data returned." Here, it must be assumed that the data are valid if all systems are performing per specifications. The data collected early in the mission will be more valuable than data collected later in the mission, for several reasons:

- (1) The most interesting targets will be selected for viewing early in the mission.
- (2) Experiments and/or systems may degrade later in the mission.
- (3) Traditionally, priority on the tracking network decreases with time.

It is recommended that a more extensive analysis of degraded modes of operation be undertaken in the next phase of the study. In particular, it would be desirable to have high(er) reliability and extra confidence in the functions and hardware which have the greatest contribution to the value of the scientific objectives. An attempt should be made to identify those spacecraft

operating parameters and hardware components which would have the greatest adverse effect on the experiments in the event of their degradation or failure. Having identified these functions, a maximum amount of backup should be provided for them in the spacecraft design. Each Principal Investigator should be requested to provide judgment of the relative value of his experiments by providing information such as that listed below, based on the current concept of his experiment.

1. Rank each of the experiments (combination of end items of hardware and the applicable modes) according to relative importance with respect to each other.

2. With each of the above experiments, determine the most critical spacecraft parameters (listed below) in terms of adverse effect on experiment if they degrade:

- a. Long-term drift (stability)
- b. Short-term drift (jitter rate)
- c. Pointing accuracy
- d. Clock accuracy and resolution
- e. Clock stability
- f. Aspect quality (includes experiment aspect system)
- g. Misalignment

Even if coalignment degrades considerably, it is assumed that all experiments could still be pointed sequentially to a source. Therefore, the greatest effects that should be considered here are the loss of simultaneous data from a source on all experiments and the loss of viewing efficiency.

3. Provide a graph showing how the most critical experiment parameters vary as a function of the most critical spacecraft parameter(s) defined in item 2 above. On the same graph, show the data rate and data handling impact as a function of the variation in spacecraft parameter(s).

A quantity denoted as mission/data worth was defined as a measure of the instantaneous value of the data being generated at any time. A model showing the mission/data worth for the entire mission is shown in Figure IV-14, and a table showing cumulative mission/data worth for each month of the mission is provided as Table IV-6. Such a model seemed to be practical and realistic to most PIs and engineers with whom it was discussed during the study. The mission/data worth does not decrease as rapidly as models generated earlier [IV-1] for Missions A and B (cube root and square root models); this seems to be logical since HEAO-A and -B repeat their scans of the celestial sphere each 6 months (although they point at progressively more and more sources), whereas HEAO-C will point at different sources (albeit sources of decreasing interest).

TABLE IV-6. CUMULATIVE MISSION/ DATA WORTH

Time (Months)	Cumulative Worth (%)	Time (Months)	Cumulative Worth (%)
1	6.67	13	73.35
2	13.34	14	76.68
3	20.01	15	80.01
4	26.68	16	83.34
5	33.35	17	86.67
6	40.02	18	90.00
7	45.02	19	91.67
8	50.02	20	93.34
9	55.02	21	95.01
10	60.02	22	96.68
11	65.02	23	98.35
12	70.02	24	100.02

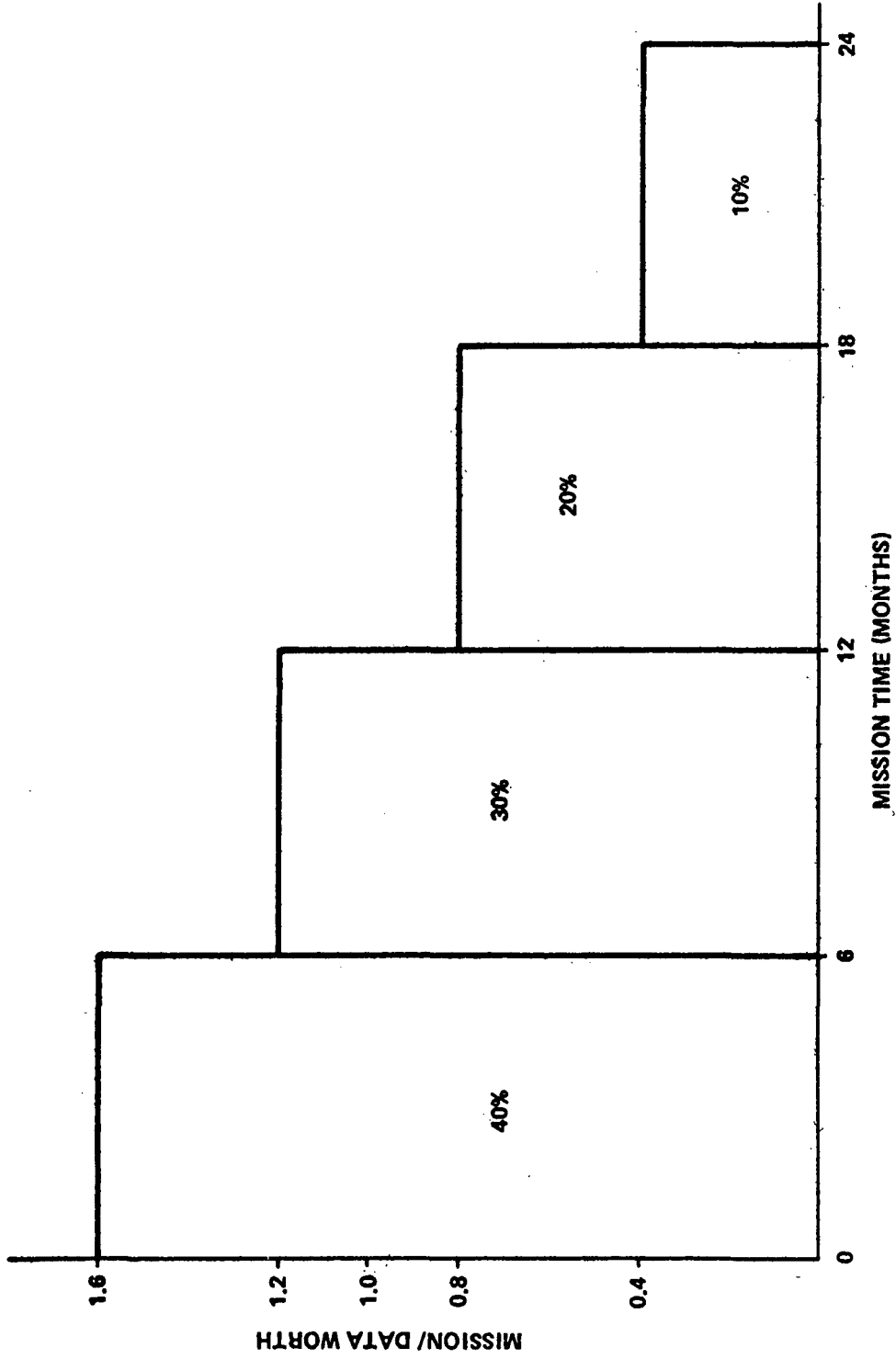


Figure IV-14. Mission/data worth model.

Consequently, using the foregoing philosophy, the quantity which should be utilized to measure mission success is the total returned data worth (the total data returned multiplied by the value of data). The common denominator for determining the contribution of each system to the mission success is the number of months of successful operation of that system.

An indication of the capability of the spacecraft to operate with a high quantity of failures is provided in Table IV-7. The level of success shown in the table is based on the capability of the spacecraft after the cited failure mode has occurred. The true mission success level is dependent on the time at which the failure occurs. For example, degraded mode two of the ASCS leaves enough capability to continue performing some experiments. If this failure mode occurs at mission beginning, the most data available is approximately 20 percent of spacecraft capability. If this failure mode occurs at the one year point, the mission would be 70 percent (first year contribution) plus the worth after the failure mode.

Figure IV-15 shows the cost penalty of increasing reliability above the level of the present baseline spacecraft. The cost represents only the cost of the hardware. More details are provided in Appendix G.

f. **Commonality.** Commonality of HEAO-C hardware with HEAO-A and -B hardware (as defined by the Phase B studies) was a strong driver in the HEAO-C design. The degree of commonality in components can be seen in Table IV-1 for the functional systems hardware. In addition, the thermal control concept, insulation, alzak skin, and coatings can be essentially the same. Many elements of the outer structure can be the same, such as the full length longerons and the ring frames. The adapter and stripped OAS can be the same. The areas in which HEAO-C requirements seem to be the driver for commonality across all missions are listed in Table IV-8. Obviously, achieving commonality may be more costly than remaining uncommon in some areas, and cost-effectiveness studies must be performed to determine the optimum approach in each specific instance.

g. **Design Characteristics Summary.** A summary of the significant HEAO-C design characteristics is provided in Table IV-9.

h. **Design Margin and Growth.** An estimate of the margin which presently exists in the HEAO-C design and the growth which could be accommodated with minimum design impact are provided in Table IV-10. From this table, it can be seen that there is considerable margin and room for growth in almost every parameter. In fact, once these systems have been

TABLE IV-7. DEGRADED MODE ASSESSMENT

System	System 2 Yr Probability of X % or Better Success (Degraded)	Post-Failure Level of Success (X%)	Conditions Existing
Data Handling			
Degraded Mode 1	0.873	90	Loss of 3 tape recorders. Assume level of success due to required change in data dump scheme.
Degraded Mode 2	0.946	60 <sup>a</sup>	Loss of onboard command storage capability. Quantity of targets investigated limited to realtime commands.
Electrical Power			
Degraded Mode 1	0.971	40	Loss of four of the six batteries. Limits life of remaining batteries to 3000 total cycles (slightly over 6 months).
Degraded Mode 2	0.979	85	Loss of three of the four regulators. Limits the power available to 400 watts due to regulator rating. This is 55 percent of the power required for full operation.

a. Assumes all available MSFN station usable.

TABLE IV-7. (Concluded)

System	System 2 Yr Probability of X % or Better Success (Degraded)	Post-Failure Level of Success (X%)	Conditions Existing
Attitude Sensing and Control  Degraded Mode 1  Degraded Mode 2	0.803  0.935	>95  ~20	Loss of coarse sun sensing ability  Loss of two CMGs. RCS used to control one axis. Experiment limited to flare detec- tor, monitor proportional counter and solid- state detector due to pointing accuracy limitation.
Reaction Control  Degraded Mode 1	0.998	85	Loss of two propellant tanks. Limits life of mission.

Category	Design Req. or Drivers	Design Characteristics	HEAO-C	HEAO-A, -B <sup>a</sup>
1, 2	2 yr lifetime	Hardware design, qualification testing	To be designed and qualified for 2 yr lifetime	To be designed and qualified for 1 yr lifetime except for expandables and energy sources
1	Large no. of sources	Command storage	24 hr command storage	None
2	Tape recorder	1. Design philosophy	1. Tape recorder highest reliability mode and drives design and operation mode	1. Tape recorder design partially driven by spacecraft design and operation
2	Size and reliability of data interfaces	Quantity of remote multiplexers	40	4 - 10
2	Power system efficiency, reliability	Battery cell/assembly sizes and arrangement	22 cells per assembly, 6 assemblies, 20 Ah per assembly	30 cells per assembly, 3 assemblies, 28 Ah per assembly
1	Lifetime, reliability	OAS electrical power and networks modifications	Additional tank and valve control and heating circuits, additional pyro battery, 2 EIAs, and junction boxes	Not defined in detail
1	Pointing accuracy	CMG steering law	Pseudo inverse	3-gimbal inverse
1	Pointing accuracy	Feedback gains	High	Low
1	Pointing accuracy	Star tracker error	0.5 arc min	4 arc min
1, 2	Momentum management	CMG desaturation	RCS, once per orbit	RCS, anytime
1	Life/reliability	No. of CMGs	4 or 5	4
1	Life/reliability	RCS fuel	High	Low
1	Antisolar maneuver	CMG size	High torque	Low torque
1	Maneuver/splump	Actuator use	CMGs/CMGs	CMGs/RCS
2	CMGs	Mounting configuration	Z-axis symmetry	X-axis symmetry
1	Large no. of sources	Digital computer onboard for altitude calculations	Onboard computation	Ground control feasible
1	RCS Reliability and Lifetime	Isolation valves, type and quantity	Isolation provided for each tank and each 2 thrusters; solenoid-type valves provide return capability	Each tank not completely isolatable; squib-type valves limit return capability
1	RCS reliability and Lifetime	RCS plumbing arrangement	Propellant line cross-strapping provided	Alternate propellant lines limited
1, 2	RCS reliability, Lifetime, and cost	Thruster module design	4 thrusters per module <sup>b</sup> (identical to LMSC SCS)	3 thrusters per module and added series redundant thruster valve; modifications increase cost
1, 2	RCS reliability, Lifetime, and cost	Thruster module location	2 modules together, 180 deg mounting location separation	2 modules 90 deg apart
1	Shuttle retrieval	Docking mechanisms	Docking mechanisms required; may require jettison of all or a part of the OAS	Not addressed
1	Shuttle retrieval	Solar array design	Must be collapsible or removable	Not addressed
1	Shuttle retrieval	Antenna boom design	Must be collapsible or removable	Not addressed

a. The data in this column represent either the Phase C/D Statement of Work requirement or the most applicable Phase B study concept, whichever was deemed to be most appropriate for the consideration at hand.  
 b. Lockheed Missiles and Space Company Satellite Control Section.

TABLE IV-8. POTENTIAL HEAO-C DESIGN DRIVERS FOR HEAO-A AND -B

Definitions:

Category 1: Difference is due to design requirements - HEAO-A and -B can utilize HEAO-C approach, but not vice versa.

Category 2: Difference is caused by design improvement - HEAO-C can utilize HEAO-A and -B approach but considerable impact will result in some cases - vice versa would be preferable.

FOLDOUT FRAME 2

FOLDOUT FRAME 1

TABLE IV-9. SIGNIFICANT HEAO-C DESIGN CHARACTERISTICS

Design Required or Driver	Design Feature	Performance Capability
Pointing Accuracy: $\pm 1$ arc min	CMGs	$\pm 1/2$ arc min
Pointing Stability: Good	CMGs	$\approx 2$ to 5 arc sec per 1/2 orbit
Jitter Rate: 1 arc sec/sec	CMGs	$< 1$ arc sec/sec
No. of Maneuvers: $> 3600$	CMGs	$> 3600$
Experiment Coalignment: $\pm 1$ arc min	Tight thermal control, minimum structural shifts and deformations, optical bench with ball and linkage mounting	$< \pm 1$ arc min coalignment, max $\Delta T$ of $\pm 1^\circ$ F across tube, max $\Delta T$ of $\pm 5^\circ$ F along tube, max $\Delta T$ of $\pm 2.5^\circ$ F across outer structure
Exp. Vibration Limits: $<$ Titan Levels	Shock-mounting of experiments	Undetermined
Exp. and Optical Surface Sensitivity: Critical	Remote thruster location, elimination of consideration of some propellants	Undetermined
No. of Detectors per Telescope: Multiple	Exp. transport mech.	Adjustment in $\pm Z$ and $\pm X$ directions to $> 0.001$ in. accuracy
Telescope Sensitivity Degrada- tion: Minimum	Exp. transport mech.	Same
Exp. Calibration with Onboard Source (Partly)	Exp. transport mech.	Same
Power: 723 W Plus Growth Capability	Foldout arrays	857 W EOL 15 deg off-sun
Off-sun Pointing: 15 deg Continuously at End of Life	Foldout arrays	$\approx 40$ deg off-sun continuously at end of life
Data Recording Rate: 27.5 kbs	Onboard data com- pression/processing (experimenter-supplied computer) to decrease from data rate of $> 50$ kbs	27.5 kbs
Sequential Pointing Without Frequent Ground Contact	Command Storage	24 hr command storage
No. of Commands: 767	10 bit command data word	1124 commands
Launch Date: 1976-77	270 n. mi. orbit	$> 2$ yr
Lifetime: 2 yr	Redundancy and high failure condition operation	$> 2$ yr
Reliability: 0.95 for 1 yr (up to 0.9 for 2 yr)	Redundancy and high failure condition operation	0.924 for 1 yr (0.680 for 2 yr)

TABLE IV-10. HEAO-C SYSTEMS MARGIN SUMMARY

Baseline Capability	Margin in Present Capability				Growth	
	No Degradation	Cause	Effect	Margin	Approach	Growth Capability
Electrical Power 963 W	241 W	15 deg off-solar vector plus space exposure  30 deg off-solar vector plus space exposure	Loss of illumination plus degradation of 8% over 2 years  Loss of illumination plus degradation of 8% over 2 years	135 W  70 W	Increase packing factor of body-mounted cells from 15 to 62%	223 W margin at 15 deg off-solar vector after 2 years
Battery Lifetime, 35 Months (14.3% DOD)	8 Months	Premature failure of battery(s)	Increases DOD resulting in reduced life-time	Variable depending upon time of failure	Use of additional batteries	Undetermined - limited by weight, volume, wiring, complexity, and cost
Power, 963 W	241 W	Loss of Experiments Flare Detector FCS Monitor Proportional Counter Aspect Detector  LE Telescope LA Imaging HR Spectrometer LA SS Detector HR Imaging	Inability to detect flares Loss of data Loss of data Loss of spatial resolution Loss of data Loss of data Loss of data Loss of data Loss of data	<u>W</u> 261 298 307 321  345 353 353 361		
Communications and Data Handling, Data Record Rate 27.5 Kbs	7.2 kbs	Loss of Experiments Flare Detector FCS Monitor Proportional Counter Aspect Detector LE Telescope LA Imaging HR Spectrometer LA SS Detector HR Imaging	Inability to detect flares Loss of data Loss of data Loss of spatial resolution Loss of data Loss of data Loss of data Loss of data	<u>kbs</u> 7.2 7.3 7.9 8.2 9.0 9.0 9.0 17.4		
Ground Contact Time; 29.3 min/orbit average with 7 MSFN <sup>a</sup> stations	19.9 min/orbit (9.4 min/orbit required)	Loss of ground stations	Reduced contact time	Function of which station is lost	Add more stations to network	Undetermined

a. Manned Space Flight Network

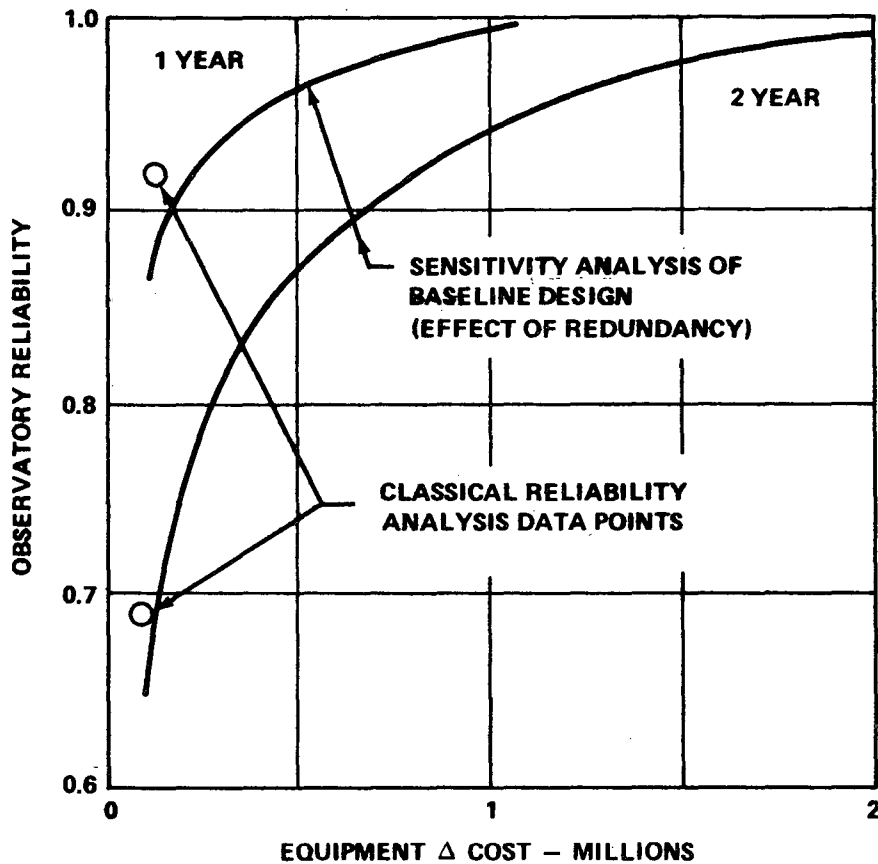


Figure IV-15. Observatory equipment  $\Delta$  cost versus reliability.

developed, they could be utilized for many similar payloads applications, such as are now being investigated in the Research and Applications Module studies and other studies in progress within NASA.

i. Suggestions for Phase B Study. The following items are suggested for considerations in the Phase B Study:

- Trade studies to determine viewing sensitivity of experiments versus their data rate requirements versus Observatory control system accuracy and stability.
- Further studies of contamination of optical, thermal, power, and experiment surfaces during launch and orbit.
- Further studies of magnetic control system.

- Tape recorder studies.
- More detailed structural dynamic analyses, including total space vehicle (launch vehicle plus Observatory).
- Refinement of transport mechanism design to handle more experiments.

## C. Experiment Transport Mechanisms

1. Requirements. Transport mechanisms for the HEAO-C spacecraft are required to position experiments at the focal plane of the telescopes. The concepts of transport mechanisms with fixed stops and with variable stops were considered but were discarded in favor of a concept with no stops (except the two end ones). Utilization of any transport mechanism introduces the possibility of failure of the mechanism but also provides a capability of in-orbit adjustment which can be very valuable where precision alignment and pointing are required. The fixed stops (and even the variable stops) at the focal points penalize this concept by limiting the adjustment capability inordinately, hence, the decision to drop those concepts. Some cost savings in the precision manufacturing and ground alignment of the hardware inside the telescope tubes can be effected because of the presence of the transport mechanisms. During typical operation, the mechanisms will be shifted to one or the other end stops, occasionally, for recalibration of the position encoding device. Peaking of the signal can be accomplished by sweeping a detector slowly across the optical axis at the center of the focal plane while viewing a fairly strong source. Data can be evaluated to determine the exact location of the strongest reading. There appears to be no reason why this could not also be accomplished in real time while over a tracking station, if the capability to monitor real-time counts from the detectors is provided.

As shown in Figure IV-16, the mechanisms are attached directly to the telescope tubes and are contained in thermally insulated housings. Generally, the requirements for the mechanisms are as follows:

- A rigid base must be provided for the experiments.
- The mechanisms must be capable of finite positioning of the experiments.
- They must be designed for a two year life with high reliability.

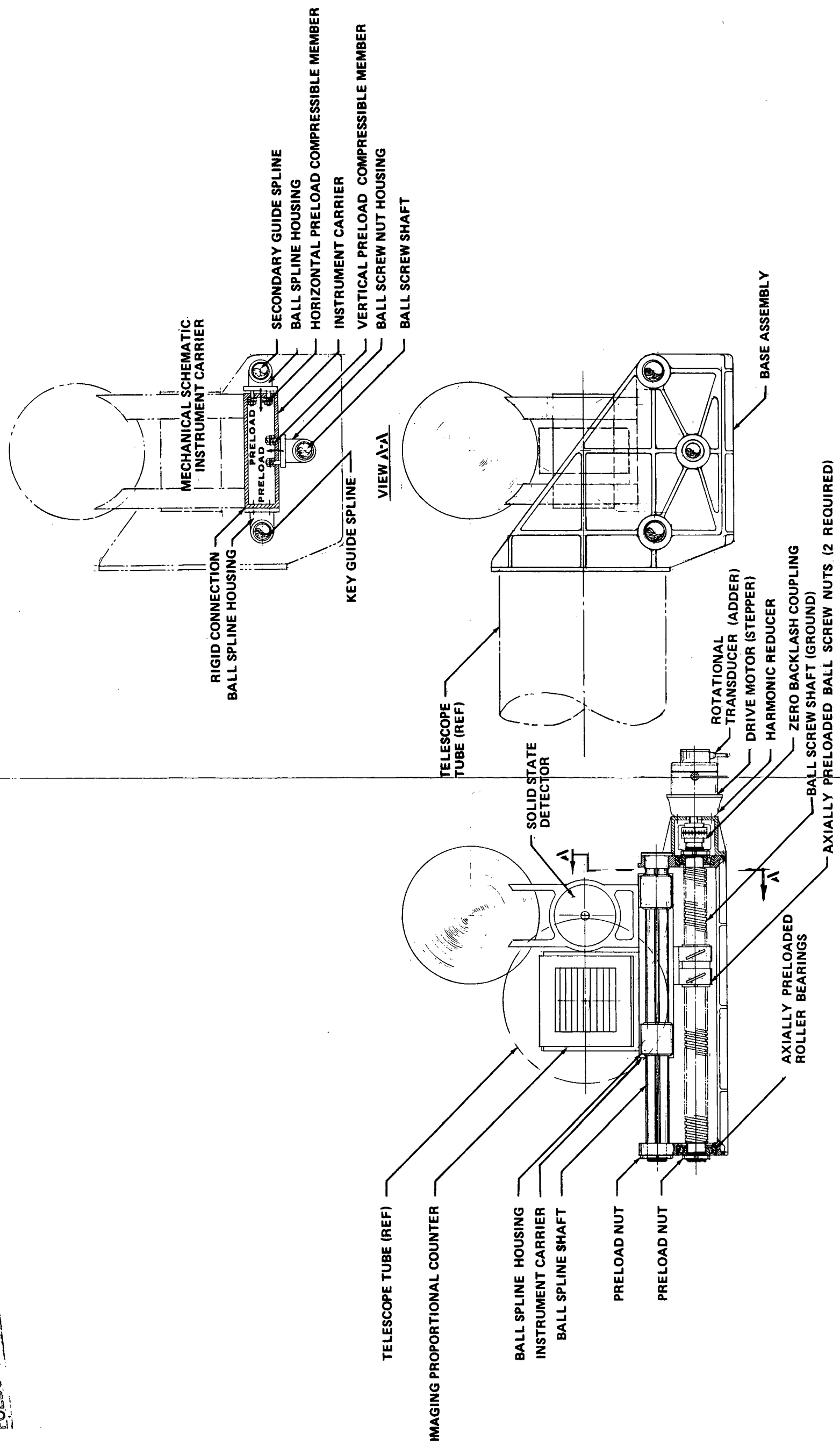


Figure IV-16. LA telescope transport mechanism.

- They must have good position repeatability.
- The mechanisms should have a means of recalibration of the transport (carrier) position.
- The rigidity and accuracy must not degrade as a result of wear of the mechanism.
- The mechanism must be compatible with space (vacuum) environment.

Specifically, the requirements for the mechanisms are as follows:

- LA Telescope
  - The mechanism must position the solid-state detector or the imaging proportional counter at the focal plane of the telescope within a tolerance of  $\pm 0.020$  inch in three axes.
  - The temperature of the mechanism should not vary by more than  $\pm 20^\circ$  F from the calibration temperature.
- HR Telescope
  - The mechanism must position the X-ray spectrometer or the image detector at the focal plane of the telescope within a tolerance of  $\pm 0.005$  inch transversely and  $0.002$  inch axially.
  - The temperature of the mechanism should not vary by more than  $\pm 10^\circ$  F from the calibration temperature.
- LE Telescope
  - No specific investigation was made during the study, but it is anticipated that a modified version of the ones for the other telescopes can be used.

2. General Description. One method by which these requirements can be met is the use of a preloaded assembly driven by a ball-screw drive. This is a common application on certain tape-controlled machine tools and earth-based telescope antennas where rigidity and zero play/zero backlash are

required. Basically, the mechanisms consist of a movable instrument carrier on which the experiments are mounted. The carrier moves on two ball splines and is driven by a recirculating ball-screw drive. In this design, only rolling friction occurs (no sliding surfaces), which makes the assembly particularly suited to dry film lubrication and resistant to cold welding, galling; and other problems associated with sliding surfaces exposed to high vacuums.

Backlash and play within the system are eliminated by preloading the splines and ball screw. The spline shafts and ball-screw shaft are first pretensioned using preload nuts. This eliminates any play between the housing and the shafts and within the roller bearings. As shown in Figure IV-16, View A-A, the spline-ball housings and the ball-screw-nut housing are readily preloaded by the use of compressible members to eliminate vertical and lateral play. Finally, the ball-screw nuts are preloaded axially with respect to each other to eliminate longitudinal play. As a result, as long as the wear induced in the system is within the preload range, no play or backlash will occur.

A secondary advantage of this concept is the low drive forces which result. The overall mechanical efficiencies of the ball screw and ball spline are exceptionally high, ranging from 90 to 98 percent. This range results from the amount of preload, the surface finish, the fit of the ball screws and ball splines, and the roller bearings used on the ball-screw shaft.

The ball-screw shaft is driven by a stepper-type motor, such as a Slo-Syn, through a high reduction, zero backlash gear reducer and coupling. A gear reducer which is suited to this application is a Harmonic Drive, which intrinsically has little or no backlash and is capable of high reductions in a small, lightweight unit.

3. Specific Transport Mechanisms. Figure IV-17 shows a concept for the transport mechanism for the LA telescope. This mechanism is required to transport the solid-state detector and the imaging proportional counter.

The position of the experiments in the focal plane of the LA telescope is much less critical than that of the HR telescope because of the coarser spatial resolution of the instruments. The finest wire spacing of the imaging proportional counter is 1 millimeter, corresponding to an angular resolution of less than 0.5 arc minute. The depth of the active volume of the counter is about 1 centimeter. Thus, a positioning accuracy of  $\pm 0.5$  millimeter ( $\pm 0.020$  inch) is compatible with the inherent spatial resolution of the imaging detector along all three axes. Since the aperture of the solid-state detector is 1 centimeter, the above positional accuracy is also adequate for this experiment.

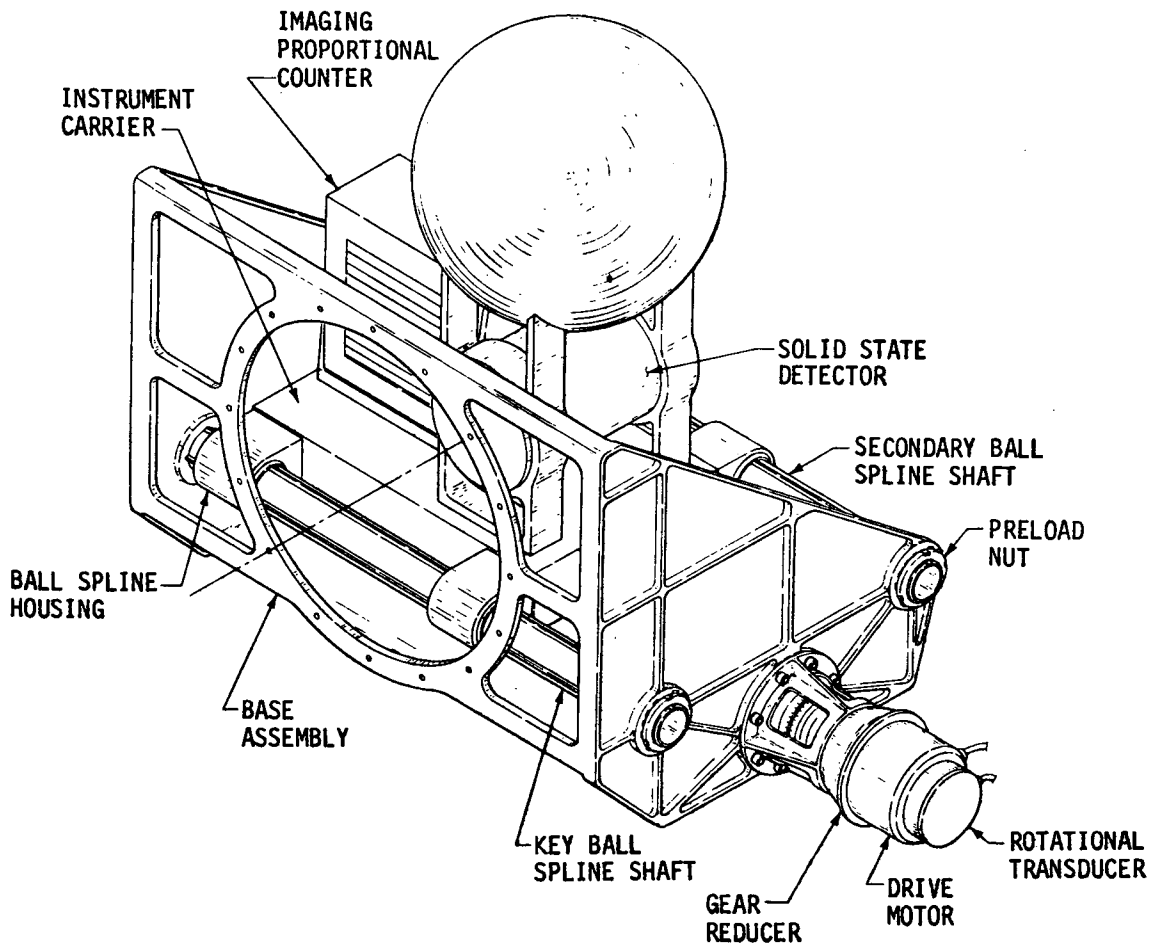


Figure IV-17. LA telescope transport mechanism isometric.

It is anticipated that the longitudinal and vertical positions of these instruments can be readily held through the static rigidity of the system and the lateral movement can easily position the experiments within  $\pm 0.002$  inch if necessary. (For instance, most numerically-controlled milling machines employing this principle hold position tolerances within  $\pm 0.001$  inch using standard components.)

The latter tolerance does not include temperature effects; however, it is anticipated that the mechanism will be housed in an insulated enclosure in which the temperature differential can vary from  $10^{\circ}$  F to  $20^{\circ}$  F without causing the position to vary by more than the  $+0.020$  inch requirement.

The concept approach, to attach both experiments to a common base, offers a weight savings over separate driving units along with simplified control logic, i. e., one experiment cannot interfere or get out of position with respect to the other. Thus, only the position of the instrument carrier must be controlled.

Figure IV-17 shows only one drive motor and gear reducer. If duality of the drive is required, this can easily be accomplished by using a detented magnetic clutch where the coupling is now located and duplicating this drive on the other end of the ball-screw shaft. The secondary drive would be disengaged from the screw by the detented-open clutch and would be utilized only in the event of failure of the primary drive system.

A weight estimate of the transfer system for the LA telescope, excluding the insulated enclosure, the control logic, and the experiments themselves, is approximately 90 pounds. This estimate is conservative, and detail design would possibly show a weight reduction in this area.

Figure IV-18 shows a concept of a transport mechanism for the HR telescope. This mechanism is required to position the X-ray spectrometer and the image detector. Although the position tolerance for the X-ray spectrometer is on the order of 0.020 inch, the image detector requires precision positioning on the order of  $\pm 0.005$  inch transversely and  $\pm 0.002$  inch axially. These are the most demanding tolerances among the experiment motion requirements.

It is anticipated that the transverse position can be held through the static rigidity of the system; however, the axial tolerance of  $\pm 0.002$  inch applies to a 240 inch distance from the telescope lens to its focal point. Because of the temperature variance, structural loading, and differential loads resulting in calibration at 1 g to operation at 0 g, this tolerance will be exceptionally hard to hold structurally.

## D. Pointing Error Analysis

1. Introduction. The experiment payload of the HEAO-C spacecraft is expected to include three X-ray grazing incidence telescopes and several corollary viewing experiments that do not utilize the telescope optics. Maximum data return can be achieved if all of the experiment viewing axes are nearly enough parallel so that all telescopes and the corollary experiments may view the same X-ray source simultaneously. To achieve simultaneous viewing, the

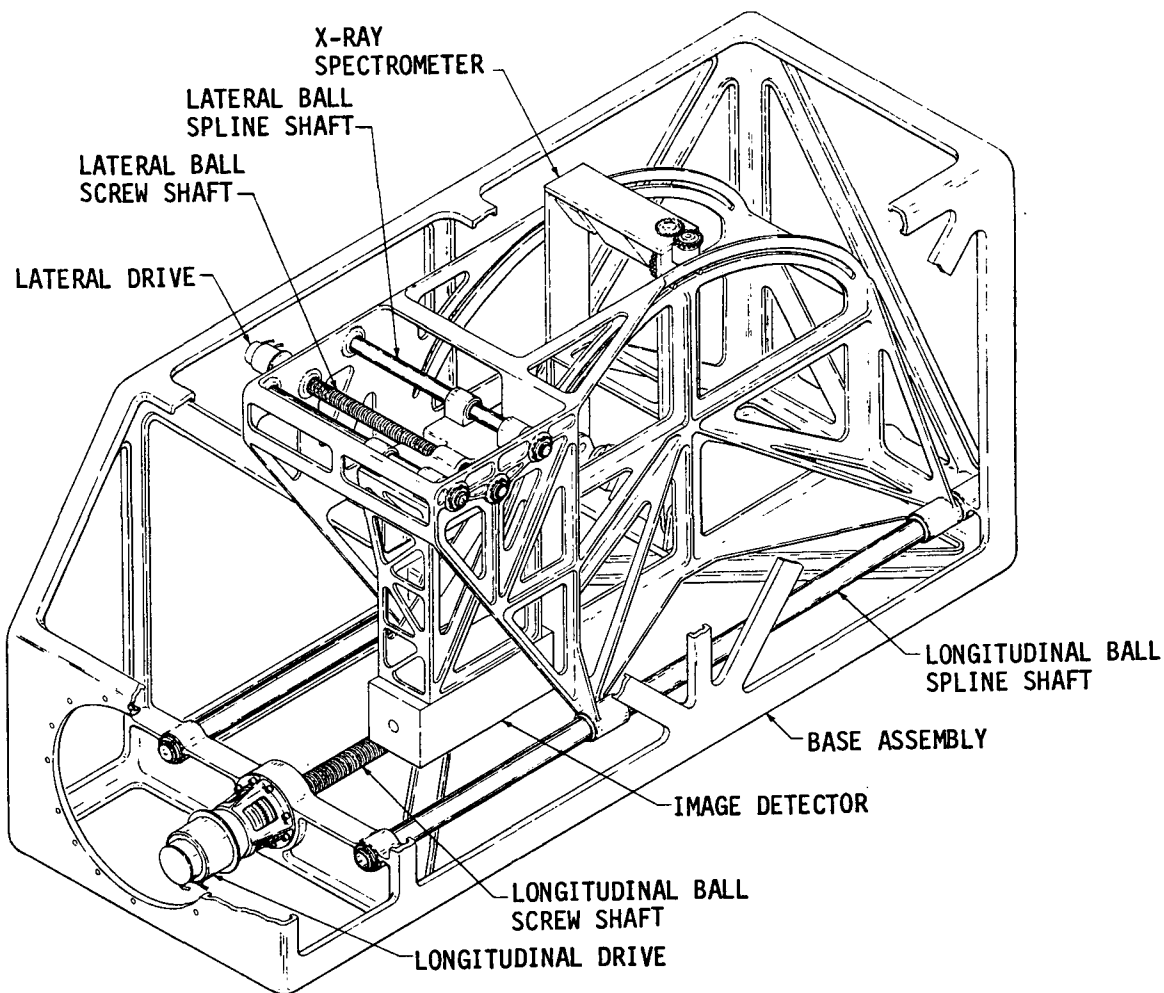


Figure IV-18. HR telescope transport mechanism.

optical axes of three telescopes and the corollary experiments must be aligned to a common pointing axis (coaligned). The proper positioning of this pointing axis by the spacecraft attitude control system will then permit simultaneous viewing of the X-ray source.

Coalignment of the experiments was considered to be one of the strongest design drivers during the study and, consequently, the Observatory design has some margin in this area. However, the effect of misalignments greater than those allowed would not be a catastrophic failure but, rather, a degradation in performance in the area of either decreased sensitivity of individual experiments, decreased ability to make simultaneous temporal measurements of a source using several experiments, or increased time required to

make measurements. In general, a choice could be made as to which of the foregoing types of degraded performance would be most acceptable by selecting the pointing axis to be at the centroid of the experiment optical axes, selecting it to be coaxial with one of the experiments, or shifting the detector(s) with the focal plane transport mechanisms. Further discussion of these choices is provided in later paragraphs.

2. Requirements. The coalignment requirement is that all optical axes be aligned within 1.0 arc minute of each other. The 2-axis pointing requirement of the pointing (reference) axis is  $\pm 1.0$  arc minute. These conditions are illustrated for three telescope axes in Figure IV-19 where the angle between each pair of telescope axes is 1 arc minute; the pointing axis in this illustration is the centroid of the triangle formed by joining the telescope axes. If there is a shift of telescope axes during launch, or in orbit, it might be desirable to move the location of the pointing axis. This could be accomplished in orbit by software changes in the onboard attitude control processor.

For the axes locations shown in Figure IV-19, the probability that a source that is within 1 arc minute of the pointing axis is also within 1 arc minute of each of the three telescope axes is the ratio of the area common to all three telescopes to the area within 1 arc minute of the pointing axis. This probability is approximately 0.23. The probability that a source that is within 1 arc minute of the pointing axis is also within 1 arc minute of at least two telescope axes is approximately 0.39. The probability that a similarly located source is within 1 arc minute of at least one telescope axis is 1.0. This indicates that, if the pointing axis is held within 1 arc minute of the source (the mission pointing requirement), one telescope will always be within 1 arc minute of the source, two telescopes will be within 1 arc minute of the source about 30 percent of the time, and all three telescopes will be within 1 arc minute of the source about 23 percent of the time. Since the fields of view of all experiments are greater than 1 arc minute, the source will always be visible to all three instruments. The maximum off-axis angle for the configuration shown in Figure IV-19 is about 1.6 arc minutes. If the pointing accuracy of the spacecraft is better than 1 arc minute, the probabilities that two or all three telescope axes will be within 1 arc minute of the source will be increased.

If one of the telescope viewing axes is designated the pointing axis, the probability that the source will be nearer that axis will be increased. This may be desirable when the smallest field of view of the HR telescope imaging experiment (7 arc minutes) is used. This effect is illustrated in Figure IV-20, where the source will always be within 1.0 arc minute of the HR axis, but may be up to 2.0 arc minutes away from the LA or LE telescope axes. Similarly,

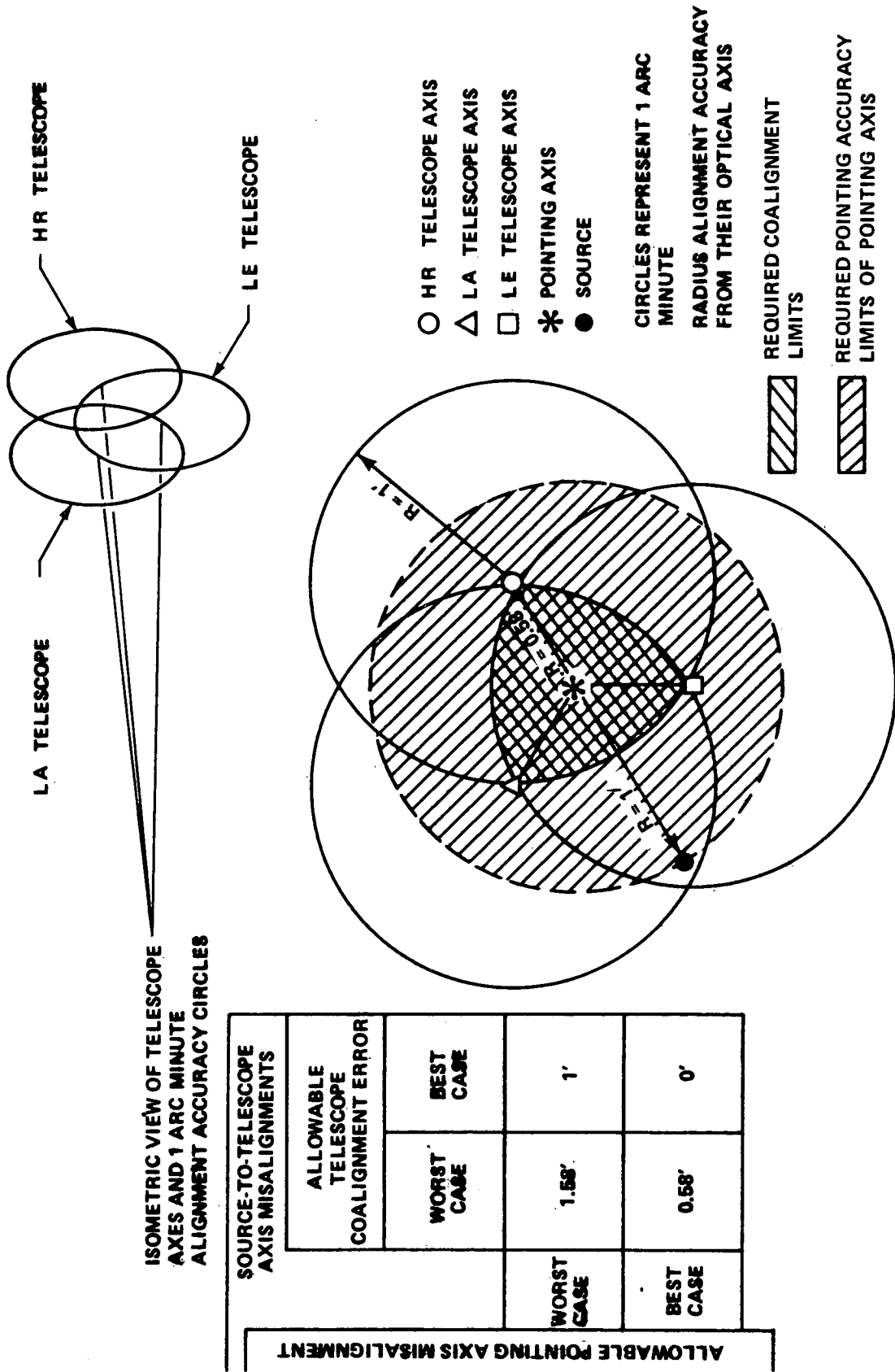


Figure IV-19. Coalignment of three telescope axes and the pointing axis with pointing axis equidistant from telescope axes.

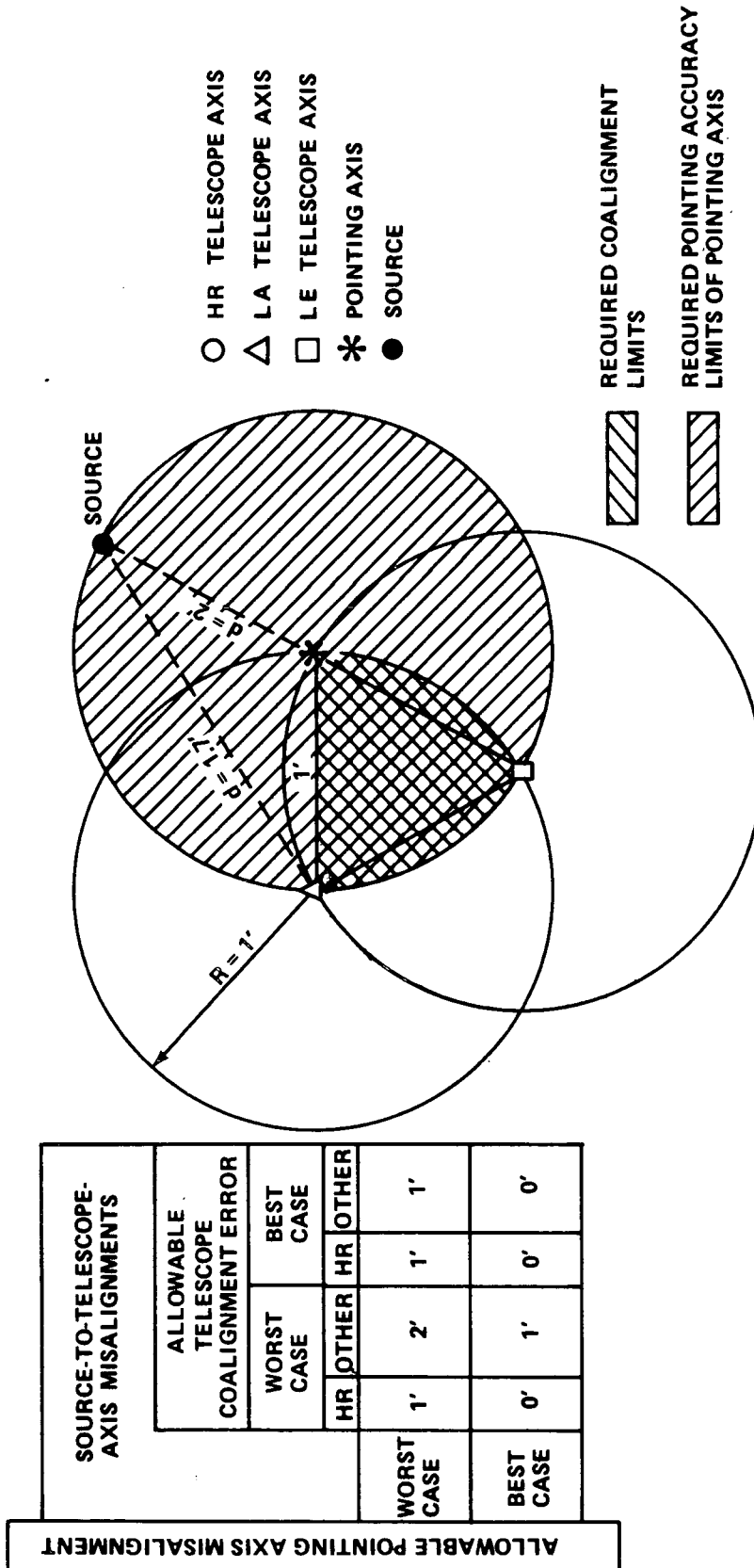


Figure IV-20. Telescopes coaligned to 1 arc minute with HR telescope axis the pointing axis.

it may be desirable to designate the LA telescope axis the pointing axis when the solid state detector experiment is in operation. It should be possible to move the location of the pointing axis at almost any time during the mission and as often as desired, by software biasing.

### 3. Error Sources

a. The basic contributors to pointing error are alignment errors, structural shifts, and systems operational errors. The effects of all individual experiment misalignments can ultimately be expressed in terms of one or more of the following terms:

(1) Tilt angle ( $\alpha$ ) of the experiment undeflected (0, 0) axis with respect to the undeflected reference axis (Fig. IV-21).

(2) Deflection angle ( $\theta$ ) of the detector with respect to the lens (Fig. IV-22).

(3) Elongation or shortening ( $x$ ) of the detector distance from the focal point (Fig. IV-23).

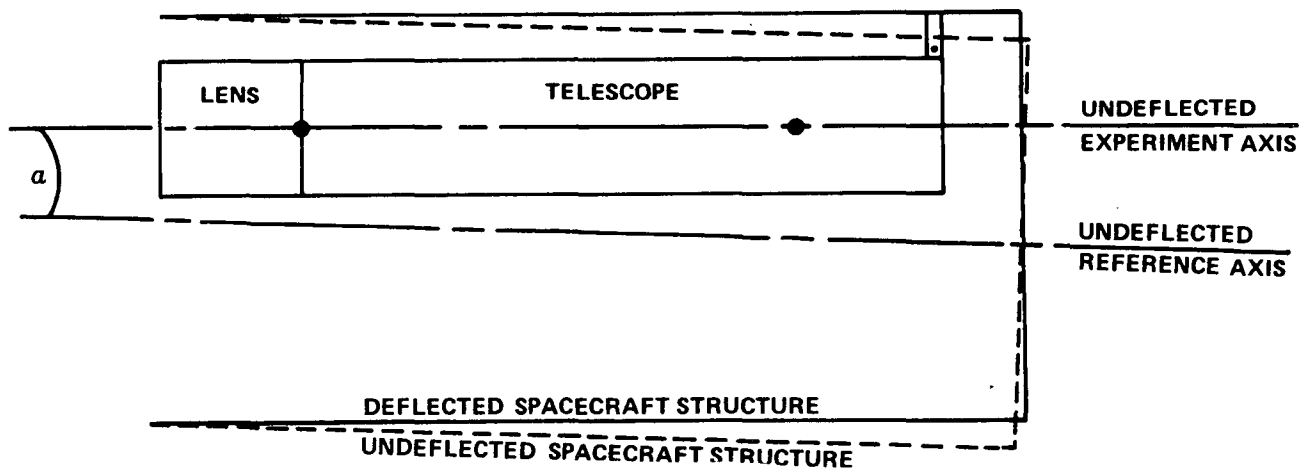


Figure IV-21. Example of tilt angle.

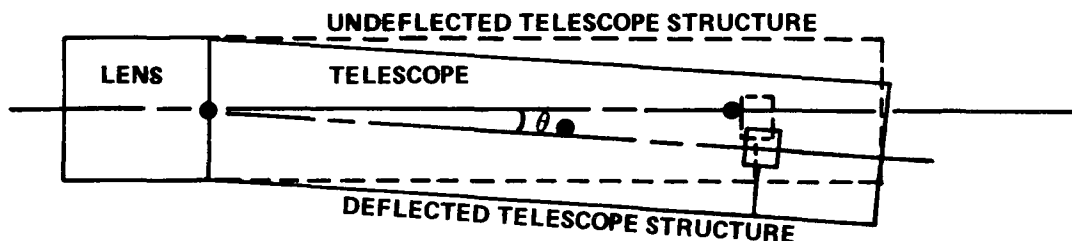


Figure IV-22. Example of deflection angle.

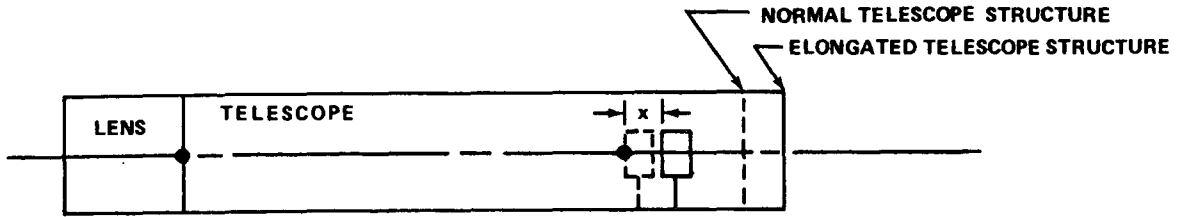


FIGURE 23 EXAMPLE OF ELONGATION OF DETECTOR DISTANCE FROM FOCAL POINT

Figure IV-23. Example of elongation of detector distance from focal point.

b. The individual experiment tilt angles ( $\alpha$ ) combine to produce experiment coalignment errors. These are discussed in more detail in a later paragraph. The deflection angles ( $\theta$ ) also cause coalignment errors and both the tilt angles and deflection angles can cause degradation in resolution. The elongations or shortenings ( $x$ ) of focal distance cause degradation in focusing (blurring). Some of the contributors to these errors are listed below (see also Table IV-11).

- (1) Manufacturing, assembly, and alignment transverse and longitudinal errors.
- (2) Transverse and longitudinal structural shifts due to transportation, handling, launch, one-g unloading, etc.
- (3) Thermally induced transverse deflections due to  $\Delta T$  across outer structure and across experiments.
- (4) Uncompensated thermal expansion or contraction of focal distance due to  $\Delta T$  along tube, along and across mirrors, and along transport mechanism.
- (5) Transport mechanism operational tolerances.
- (6) Systems operational errors (thresholds, noise, drift, etc.).
- (7) Ground processing tolerances.
- (8) Tolerances in knowledge of guide star and target locations.

TABLE IV-11. TELESCOPES AND EXPERIMENT ALIGNMENT ERROR BUDGET

Error Types	Error Source				Single Telescope/Experiment Alignment Error (arc sec)				Three Telescopes Minimum Errors (arc sec)	All Telescopes and Experiments Minimum Errors (arc sec)	
	Mfg. Assembly and Alignment	Structural Shifts	Thermal Distortion	Detector Reposition	RSS - No Compensation	RSS With Compensation		ASCS Operational Error			Minimum Error
						Transport Mech.	Sensor Bias				
Telescope Internal											
High Resolution Large Area	10	10	0	1	14	10	0		0	0 (Ref)	0 (Ref)
Low Energy	10	10	0	1	14	10	0		0	10	10
	10	10	0	2	14	10	0		0	10	10
Telescope External											
High Resolution Large Area	10	10	0		14	10	0		0	0 (Ref)	0 (Ref)
Low Energy	10	10	0		14	10	0		0	10	10
	10	10	0		14	10	0		0	10	10
Other Experiments											
Monitor Proportional Counter											
Internal	10	10	0		14				0		14
External	10	10	0		14				0		14
Flat Crystal Spectrometer											
Internal	10	10	0		14				0		14
External	10	10	0		14				0		14
Attitude Sensing	10	10	0		0			31 to 46	31 to 46	31 to 46	31 to 46
Attitude Control	10	10	0		0			5	5	5	5
Single Telescope or Experiment RSS Error											
									31.4 to 46.3		
Three Telescopes RSS Error										37.2 to 50.4	
All Telescopes and Experiments RSS Error											46.6 to 57.7

c. The errors previously listed contribute as follows:

(1)  $\alpha = \sum$  errors external to experiment of the types just listed in (1), (2), and (3).

(2)  $\theta = \sum$  transverse errors internal to experiment of the types just listed in (1), (2), (3), and (5).

(3)  $x = \sum$  longitudinal errors internal to experiment of the types (1), (2), (4), and (5) just listed.

(4) Items (7) and (8) were not assessed during the study.

Table IV-12 shows a typical pointing error budget for transverse errors. The largest components of the budget are those for manufacturing and assembly tolerances, structural shifts, and systems operational errors. More detailed analyses were made of structural shifts since they are such large contributors to the error budget and since they contribute heavily to coalignment errors. Part of the analyses appear in paragraphs below, and part is in Appendix C. The critical systems operational errors are those associated with the attitude sensing equipment. The pointing accuracy performance of the Observatory is heavily dependent on an accurate, noise-free error signal; hence, methods of improving the error signal were examined in the study. A more detailed discussion of the error signal is provided in Chapter VII and Appendix E. It is very significant that the thermal distortion components of the error budget are so small, since this is always an area of great concern in Observatory design. It was desired to design the Observatory to be as insensitive as possible to thermal gradients, variations, and thermal control system degradation or failure. Consequently, the  $\Delta T$  across both the outer structure and experiments is very low, variations are small, and the transport mechanisms can compensate for any deflections which do occur.

In the budget shown in Table IV-11, the magnitude of initial misalignments is estimated to be 10 arc seconds based upon very early ATM alignment experience. The magnitude of the launch shift is estimated to be of the same order as the initial misalignment, or 10 arc seconds.

The table also indicates the estimated error-correction capability for single-experiment operation and multiple-experiment operation. For single-experiment operation, all tilt angle errors can be corrected by changing the pointing axis by software bias, and some telescope deflection angle errors can be corrected by using the transport mechanism to shift the detector transversely. The latter approach can correct all errors which are in the same

direction as the mechanism traverse, if they are not larger than the traverse capability. Shifting the detector transversely can cause a decrease in resolution of the telescope, as explained in succeeding paragraphs. For multiple-experiment operation, the tilt angle error can be corrected completely for one experiment, or partially for all of them, by changing the pointing axis; the deflection angle errors for telescopes can be partially corrected as described above.

After orbit attainment, the direction of all viewing axes relative to the reference axis can be determined by pointing the axes at known strong signal sources (easily identifiable guide stars or strong X-ray sources). This orbit alignment procedure is expected to include ground processing of aspect sensor data and will provide accurate measurements of the actual instrument orientations relative to the reference axis.

4. Misalignments Within Telescopes. Misalignments within a telescope may be divided into three classifications: between mirrors of a nested set, between surfaces of a mirror pair, and between a mirror set and the detector. The HR telescope mirrors are a nested set of five dual surface mirrors. Misalignment between mirrors of a nested set and/or between surfaces of a mirror pair produce fuzziness of the image, since rays striking different mirrors are focused at different points. This effect is different from the others considered in this analysis in that these misalignment errors do not decrease the accuracy with which the telescope axis can be aligned with a source or the accuracy with which the source image can be positioned within the experiment detector.

The line of sight (LOS) of the HR telescope is the extension of the straight line from the detector center to the center of the circle formed by the intersection of the two surfaces of a mirror pair. The LOS of the other telescopes are similarly defined. If this LOS coincides with the mirror (geometrical) axis, the detector is perfectly aligned with respect to the mirrors. The highest mirror resolution is obtained when a source that is on the mirror axis is viewed. As the source location moves away from the mirror axis, resolution is lost. Data from Reference IV-3 indicate that the resolution of the HR mirrors is greater than 1 arc second for all source locations within about 4 arc minutes of the mirror axis. The resolution of some experiment detectors, however, is also a function of the image distance from the detector face center. This is true for the solid state detector in the LA telescope. Figure IV-24 illustrates the case of the detector being perfectly aligned with the mirror axis and the source lying on the telescope line of sight. Under these conditions, maximum telescope resolution is obtained.

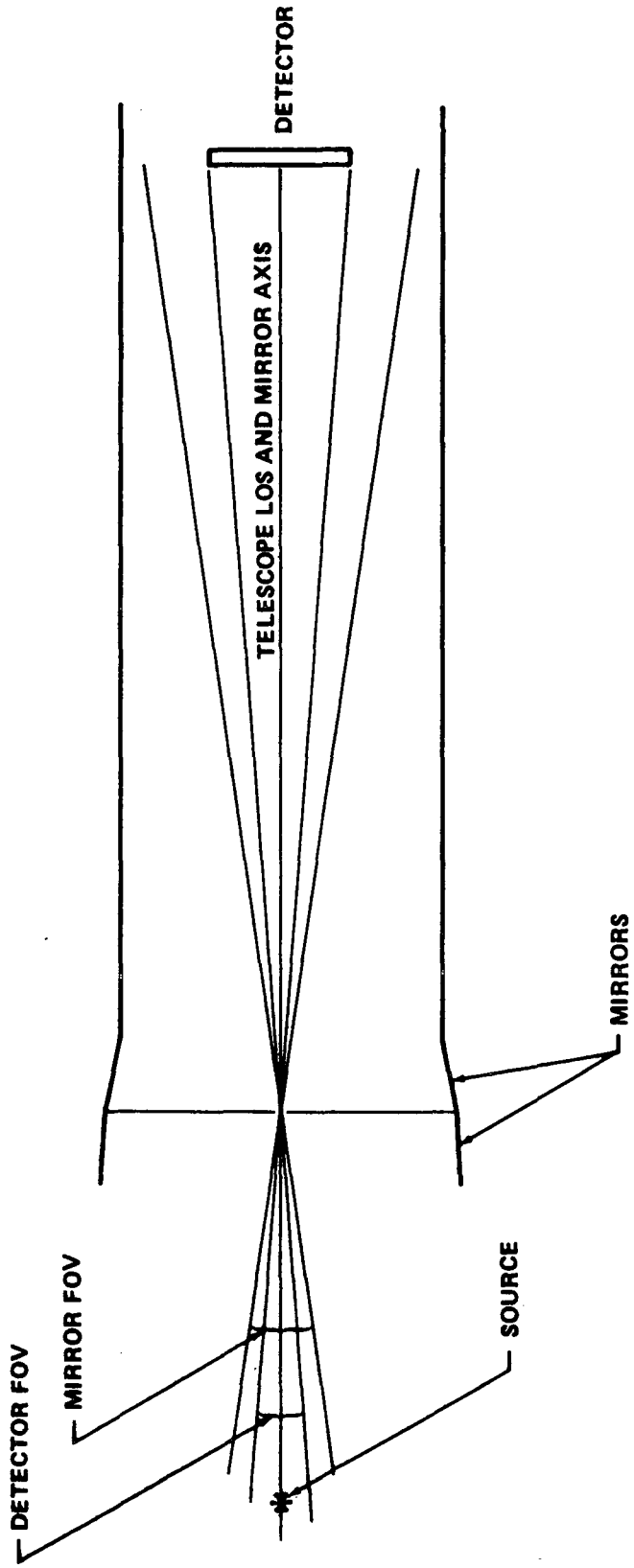


Figure IV-24. Telescope LOS coincident with mirror axis and source located on telescope LOS — conditions for maximum telescope resolution.

The case where the source is not located on the telescope line of sight, but within the field of view (FOV) of both the mirrors and detector is shown in Figure IV-25. There is some loss of mirror resolution and also a loss of detector resolution for those experiments for which detector resolution is a function of image position.

The case where the mirror axis has shifted through the angle  $\phi$  but the detector has not shifted and the source lies on the telescope LOS is shown in Figure IV-26. There is a loss of mirror resolution because the source is not on the mirror axis; there is no loss of detector resolution because the image is at the detector center. If the source lies on the shifted mirror axis rather than on the LOS and the shifted mirror axis still intersects the detector face, there is no loss of mirror resolution. Also, if the detector resolution is not a function of image position on the detector, there is no loss of detector resolution. Therefore, it is possible under these special circumstances that there is no loss of image resolution even though the mirror axis is not coincident with the telescope line of sight.

Figure IV-27 illustrates the case where the detector position has shifted by the distance  $\delta$  but the mirror axis has not shifted. Again, the source lies on the telescope LOS, and again there is a loss of mirror resolution but no loss of detector resolution. From Figures IV-26 and IV-27, it can be seen that movement of the detector moves the telescope LOS but that movement of the mirrors does not. Movement of the telescope LOS tends to increase the misalignment between telescopes. The general case in which shifts of both mirror axis and detector have occurred and the source does not lie on the telescope LOS is illustrated in Figure IV-28. For the source to be detected, it must lie within the fields of view of both the mirrors and the detector. It is indicated in Figure IV-28 that the detector shift and the mirror axis shift are in opposite directions; therefore, they are additive. This will not necessarily be true, however, for one movement may tend to counteract the other. For this reason RSS errors rather than simple sums are calculated in Table IV-11.

## E. Observatory Operating Modes <sup>3</sup>

A list of the normal and abnormal operating mode functions and the criteria for entering and leaving each is provided as Table IV-12. It is assumed that mission-critical hardware will have sensing circuitry which activates standby redundant units automatically; such sensing and activation will probably

---

3. These modes do not correspond directly with those defined for the ASCS. The ASCS has five distinct operational modes: (1) sun acquisition, (2) reference alignment, (3) orbit adjust, (4) celestial pointing, and (5) special pointing (see Chapter VII).

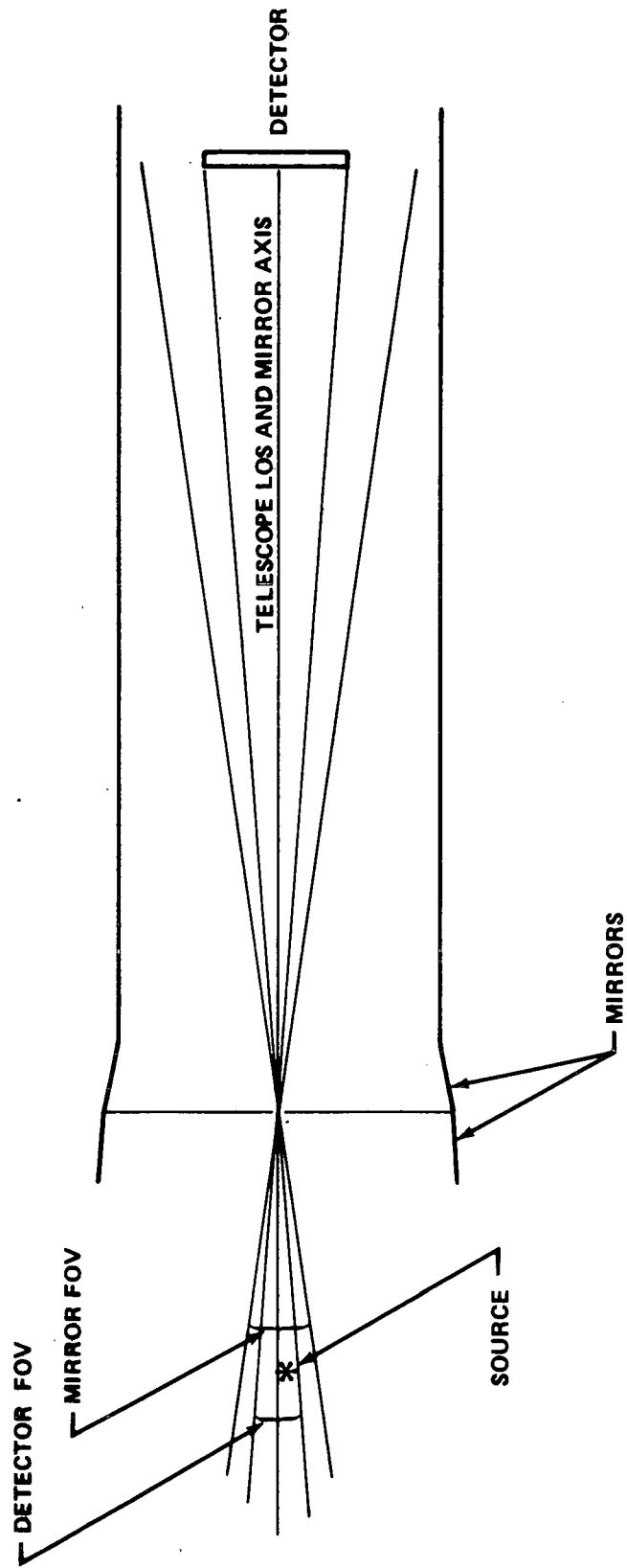


Figure IV-25. Telescope LOS coincident with mirror axis, source located off LOS, but within field of view of mirror and detector.

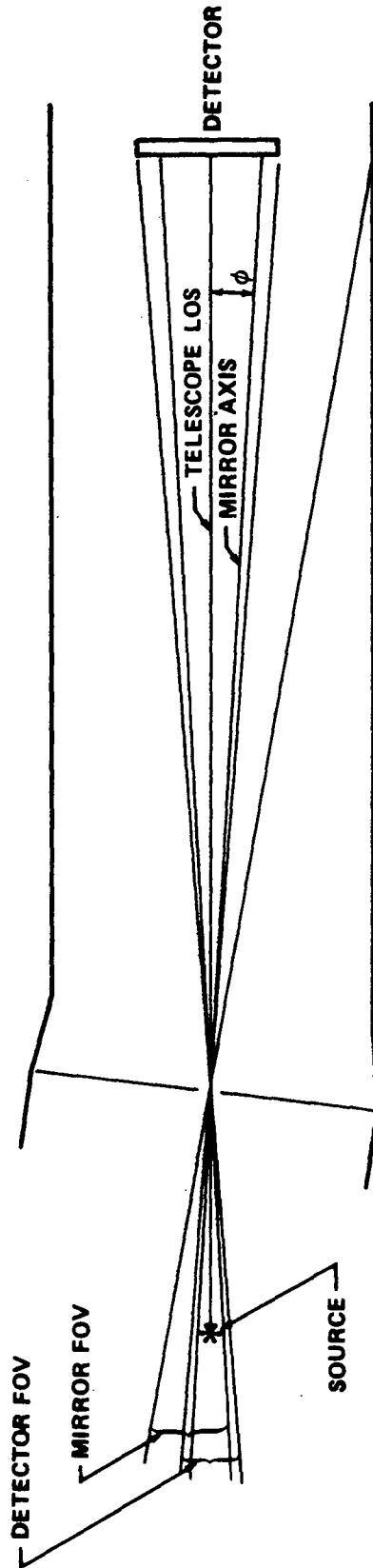


Figure IV-26. Mirror axis shifted, source on telescope LOS but not on mirror axis.

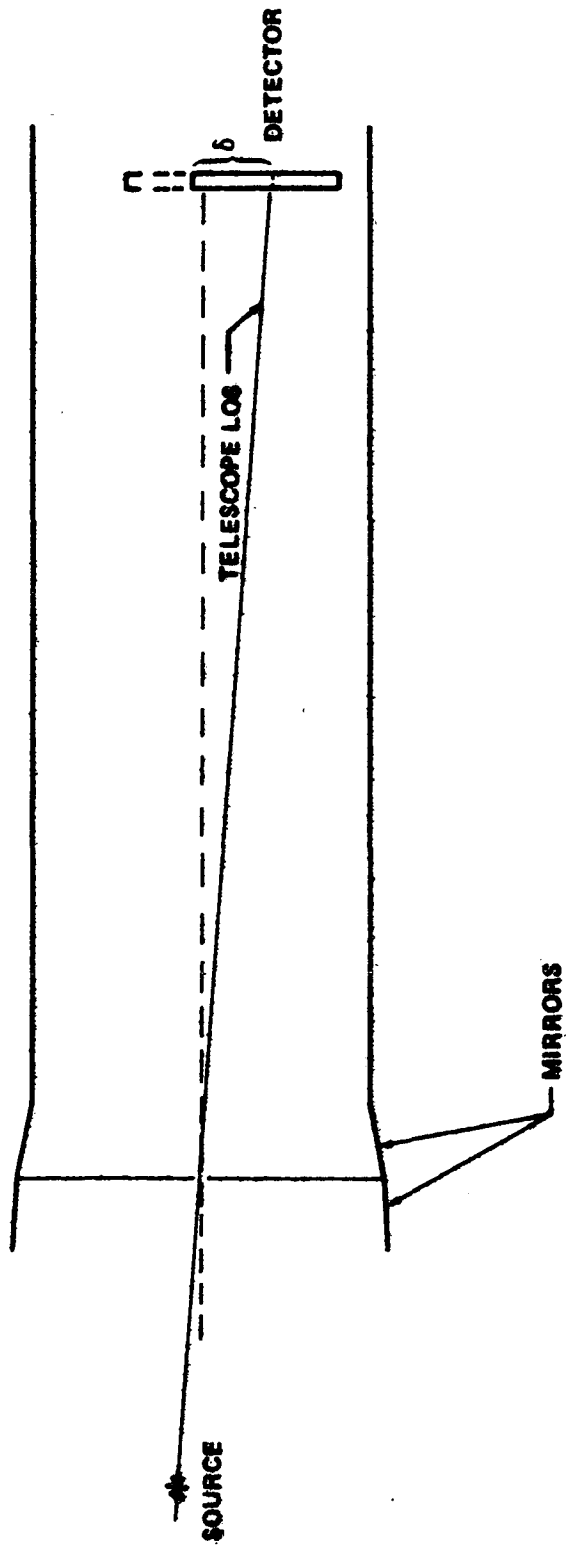


Figure IV-27. Detector has shifted, but the mirror axis has not.

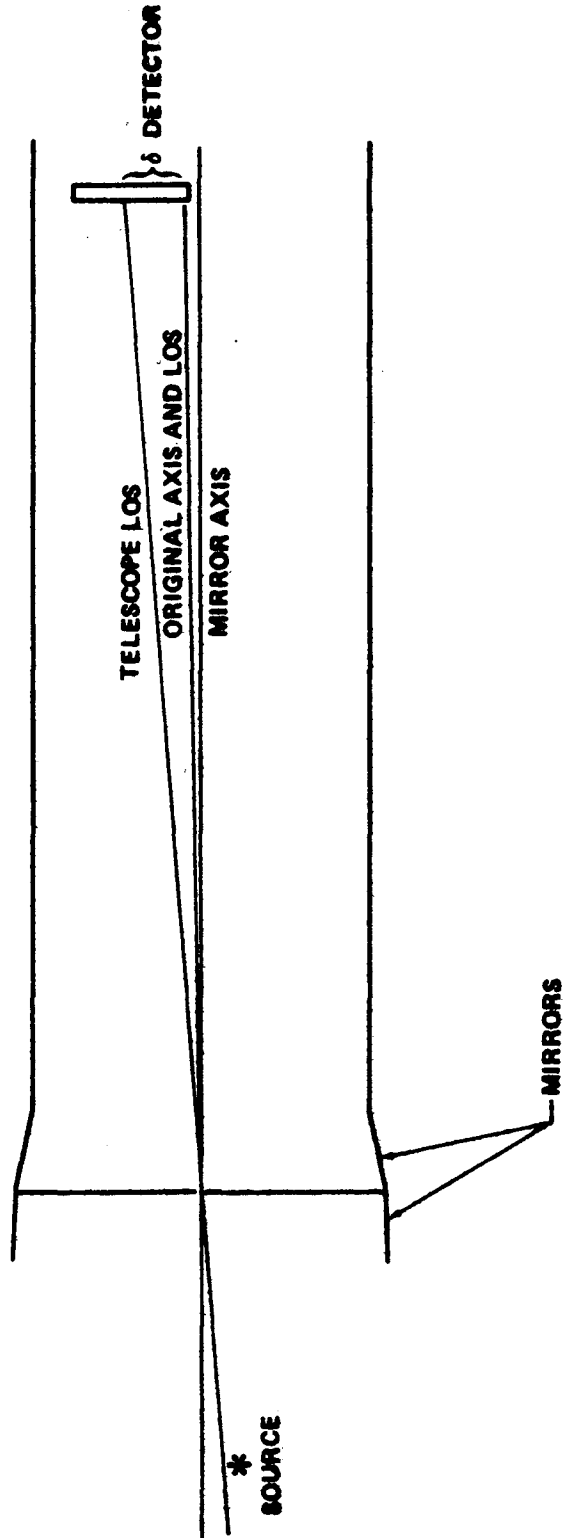


Figure IV-28. General case: Both mirror axis and detector axis have shifted, source neither on mirror axis nor telescope LOS.

be provided locally in the subsystem and will not require a decision from an onboard computer or the ground. The automatic operation indicated in Table IV-12 generally implies a more complicated function than the sensing and switching of a redundant device and/or generally requires more time to perform the function than would be allowable in mission-critical hardware. Consequently, such functions may require onboard computer tie-in.

1. Normal Operating Mode. Pointing of the experiment telescopes at a source permits the experiment detectors to gather data on that source. The detectors will be switched in and out of the telescope focal planes, and other experiment components, such as filter wheels and transmission gratings, will be sequenced according to a predetermined pattern to provide complete experiment coverage. Experiment and spacecraft data are recorded on a tape recorder. When the tape on one recorder is completely filled, the data output is switched to a different recorder. At the next opportunity to transmit to a ground station, playback of the filled recorder is begun. Playback is suspended when ground contact is lost and is resumed when the next station is acquired.

Spacecraft attitude control is maintained by the control moment gyros (CMGs) responding to attitude sensor error signals. Periodic dumping of the momentum accumulated in the CMGs is required. This is accomplished by firing the RCS thrusters to produce a momentum vector opposite to that of the stored momentum vector. The CMGs respond to this disturbance, resulting in a decrease of stored momentum. The dumping operation is expected to occur on the order of every one or two orbits and be triggered by an onboard logic process. Source viewing will be interrupted for a minute or two as a consequence of the dumping operation.

The spacecraft will pass through the South Atlantic Anomaly region of high radiation during many of its orbits. The experiments will become saturated in this region and will be turned off to conserve proportional counter quenching gas. This procedure should be automated onboard the spacecraft and could be triggered for each experiment separately or simultaneously for all by detecting when the radiation count rate exceeds a predetermined level.

After completing the sequence of experiment observations on one source, the spacecraft will be slewed to view a different source. It is anticipated that this procedure can be automated onboard the spacecraft using a stored series of commands. It may be desirable in the early days of the mission to verify source acquisition through a ground loop before beginning observations. However, an onboard operation will save much time and is, therefore, very desirable.

The portion of the celestial sphere that is within 15 degrees from the plane normal to the earth-sunline will always be accessible to the viewing instruments. In addition, the area that is within 30 degrees from the plane normal to

TABLE IV-12. OBSERVATORY OPERATING MODES

Criteria For Leaving	Criteria For Entering	Description	Functions
<ul style="list-style-type: none"> <li>• Systems operational and valid command present</li> <li>• Valid new command</li> <li>• Pointing at source where Z-axis &lt; 15 deg for &gt; 24 hr<sup>a</sup></li> <li>• Valid new command</li> <li>• Battery discharge <math>\approx 50\%</math><sup>a</sup></li> <li>• Occultation ended<sup>a</sup></li> <li>• Valid new command</li> <li>• New azimuth reached<sup>a</sup></li> <li>• Accumulated momentum in CMGs <math>\leq</math> min desired level<sup>a</sup></li> <li>• Dumped during this orbit<sup>a</sup></li> <li>• Valid power up command</li> <li>• Valid calibration command present</li> <li>• Calibration command absent<sup>a</sup></li> </ul>	<ul style="list-style-type: none"> <li>• Initial orbit operation is in effect</li> <li>• When no pointing command</li> <li>• Valid pointing command in region where Z-axis <math>\leq 30</math> deg off-sun</li> <li>• Valid pointing command in region where Z-axis &gt; 30 deg off-sun</li> <li>• Trackers shutdown due to occultation of guide star by earth or shutter</li> <li>• Valid pointing command</li> <li>• Accumulated momentum in CMGs <math>\geq</math> max desired level and CMGs have not been dumped during this orbit<sup>a</sup></li> <li>• Valid calibration command present</li> <li>• Valid calibration command present</li> </ul>	<p>Point Z-axis at sun and hold</p> <p>Point at source which requires Z-axis off-sun <math>\leq 30</math> deg</p> <p>Point at source which requires Z-axis off-sun &gt; 30 deg</p> <p>Hold on target using reference gyro assemblies</p> <p>Hold Observatory to desired azimuth</p> <p>Hold with RCS while CMGs are unloaded</p> <p>Turn on all spacecraft systems, in sequence, check them then turn on all experiments in sequence and check them</p> <p>Sequentially apply calibrated source voltages, loads, etc., to subsystems</p> <p>Slew spacecraft to preselected strong X-ray target and hold for predetermined time</p>	<p><u>I. Normal Mode</u></p> <p>Sun Acquisition</p> <p>Normal Pointing</p> <p>Abnormal Pointing</p> <p>Occultation Hold</p> <p>Slew Maneuver</p> <p>Momentum Dump</p> <p>Power Up</p> <p>Calibrate Systems</p> <p>Calibrate Experiment (external)</p>
<ul style="list-style-type: none"> <li>• Completion of selection and setup of experiment hardware<sup>a</sup></li> <li>• Changeover completed<sup>a</sup></li> <li>• Dump completed<sup>a</sup></li> <li>• Station contact lost<sup>a</sup></li> <li>• When out of South Atlantic Anomaly<sup>a</sup></li> <li>• When not viewing earth<sup>a</sup></li> <li>• When tracker views sun<sup>a</sup></li> <li>• When tracker views earth<sup>a</sup></li> <li>• When tracker views moon<sup>a</sup></li> <li>• Valid command for other data mode</li> <li>TBD</li> <li>TBD</li> <li>TBD</li> </ul>	<ul style="list-style-type: none"> <li>• Valid selection command present</li> <li>• Tape filled<sup>a</sup></li> <li>• Recorder malfunction<sup>a</sup></li> <li>• Valid dump command present</li> <li>• When in South Atlantic Anomaly<sup>a</sup></li> <li>• When experiment views earth (or sun, if tumbling)<sup>a</sup></li> <li>• When tracker views sun<sup>a</sup></li> <li>• When tracker views earth<sup>a</sup></li> <li>• When tracker views moon<sup>a</sup></li> <li>• Normal open</li> </ul>	<p>While viewing strong target, translate detector slowly off-zero in <math>\pm Z</math> directions a total amount equal to the detector FOV while monitoring instantaneous signal strength; move detector to location of strongest signal; repeat in <math>\pm X</math> direction (total movement 0.008 in.)</p> <p>Select, transport, and turn on, if necessary, the appropriate detector, filter, aperture, and/or crystal to perform the desired measurement</p> <p>Turn on and switch in an off-line recorder, turn-off and switch out the on-line recorder.</p> <p>Switch the full recorder with the oldest data into a transmitter and command it to play back</p> <p>Turn off high voltage in experiment (and open output circuit)</p> <p>Close shutter over tracker; use other tracker, rate gyro, or sun sensor data</p> <p>Normal data mode</p>	<p>Calibrate Experiment (internal)</p> <p>Focus</p> <p>Experiment Select</p> <p>Change Recorder</p> <p>Dump Recorder</p> <p>Experiment Saturation Shutdown</p> <p>Tracker Saturation Shutdown</p> <p>Data Mode 1</p> <p>Data Mode 2</p> <p>Data Mode 3</p> <p>Data Mode 4</p>
<ul style="list-style-type: none"> <li>• Systems operational and valid command present</li> <li>• Power failure<sup>a</sup></li> <li>• Decision to "rest" spacecraft</li> <li>• Control Systems failures<sup>a</sup></li> <li>• Power System failures<sup>a</sup></li> <li>• Decision to "rest" spacecraft</li> <li>• Temperature extremes<sup>a</sup></li> <li>• Low battery charge<sup>a</sup></li> <li>• RCS leakage<sup>a</sup></li> <li>• Thruster hung open<sup>a</sup></li> <li>• RCS electronics malfunction<sup>a</sup></li> <li>• Decision to "rest" spacecraft</li> <li>• Viewing completed</li> <li>• Valid new pointing command</li> <li>• Gyro drift excessive</li> <li>• Digital sun sensor occulted</li> <li>• Probably none (assumes redundant memories already utilized)</li> </ul>	<ul style="list-style-type: none"> <li>• Control Systems failures<sup>a</sup></li> <li>• Power System failures<sup>a</sup></li> <li>• Decision to "rest" spacecraft</li> <li>• Power failure<sup>a</sup></li> <li>• Decision to "rest" spacecraft</li> <li>• Temperature extremes<sup>a</sup></li> <li>• Low battery charge<sup>a</sup></li> <li>• RCS leakage<sup>a</sup></li> <li>• Thruster hung open<sup>a</sup></li> <li>• RCS electronics malfunction<sup>a</sup></li> <li>• Decision to "rest" spacecraft</li> <li>• No reference star exists within desired operating region</li> <li>• All star trackers failed</li> <li>• Command memory failure</li> </ul>	<p>Point Z-axis at sun and hold</p> <p>Turn off nonessential equipment</p> <p>Close all solenoid valves at tank outputs</p> <p>Hold on target using reference gyro assemblies and/or digital sun sensor</p> <p>Bypass command storage; use real time capability only</p>	<p><u>II. Emergency Mode</u></p> <p>Sun Acquisition</p> <p>Power Down</p> <p>Propellant Lockup</p> <p><u>III. Degraded Mode</u></p> <p>Off-star Pointing</p> <p>Command Memory Lockout</p>

FOLDOUT FRAME 3

FOLDOUT FRAME 2

FOLDOUT FRAME 1

the earth-sunline will be accessible for up to one orbit per day. Slewing to sources in this area is expected to be executed like any other pointing operation, i. e., by stored command. However, it may be desirable to provide some additional checks, such as verification of proper battery depth of discharge, before initiating this maneuver.

Spacecraft attitude sensing will normally be accomplished using two star trackers, one on the spacecraft X-axis (telescope viewing axis) and one on the spacecraft Y-axis. There may be source locations where two guide stars cannot be found in one or in either of the tracker fields of view. In this event, it will be possible to utilize the nearest guide stars to zero the reference gyros and then to slew to the desired source and hold on the source using only reference gyro rate data. This method of pointing will not provide the precision of guide star pointing, and pointing accuracy will degrade with time due to gyro drift. However, viewing could be interrupted periodically to return to the guide stars for rezeroing of the reference gyros.

Experiment detectors will be calibrated periodically using onboard radioactive sources that will be switched in and out of position. The frequency of this procedure has not been established, but once a week might be typical. In addition, periodic alignment and calibration checks are expected to be made using visible celestial X-ray sources. The frequency of this operation is expected to be much less than calibration using the onboard sources.

2. Emergency Operation Mode. The spacecraft emergency operating mode is entered when there is some mishap that might endanger further operations. Entrance into this mode is a response to attempt to minimize the effects of the mishap. An example of such a mishap is an excessive electrical power drain caused by a short circuit. The electrical system detects and minimizes the effects of such events by the utilization of such devices as resettable circuit breakers.

When an excessive power drain is detected onboard the spacecraft, it is anticipated that the spacecraft will enter into the emergency operating mode. If the solar panels are not receiving maximum solar illumination, the spacecraft attitude should be changed to achieve this. Experiments and non-essential functions should be suspended and available power conserved until the cause of the trouble can be determined, isolated, and redundant units switched in if possible. It is anticipated that the spacecraft attitude change and the turning off of nonessential functions would be commanded by onboard logic. Fault determination, isolation, and restitution of services could then be done through the ground control loop.

In a similar fashion, the spacecraft could enter the emergency mode in the event of a low state of battery charge. Normal operation would be suspended until the batteries were completely recharged.

Sticking of a thruster engine in the firing position could have very serious consequences on the spacecraft. During the time required for ground station recognition of the malfunction and transmission of a correction command, the operation of the spacecraft could be impaired. For this reason there should be an onboard logic process to detect this failure and hardware should be available to provide emergency thruster shutdown. Then, fault determination, isolation, and rectification procedures could be worked out on the ground, while the spacecraft was in no imminent danger.

Temperature control of the telescope mirrors is critical to their operation. Excessive heating could occur if the spacecraft attitude permitted direct-incident sunlight on or very near the mirror surfaces. Such an attitude could occur, for example, while a flare observation was being made. Provision should be made for onboard detection of and response to this condition. The response would be the standard spacecraft reorientation to full solar panel illumination. The added electrical power would not be needed in this instance, but this orientation would insure no direct-incident sunlight on the mirrors.

3. Degraded Operating Mode. A degraded mode of spacecraft operation results when a component failure occurs. This results in a loss of some spacecraft function, which may or may not be restored. If there is a redundant unit, spacecraft operation is returned to normal after the redundant unit comes on the line. There may be instances in which full operation cannot be restored, for example, failure of all tape recorders. In this case the only data recovered will be that transmitted in real time and received at a tracking station. The mission can be continued with partial data recovery. Additional ground stations may be utilized to increase spacecraft telemetry coverage with a resultant increase in data recovery.

Loss of command memory would require execution of all commands in real time. This would cause much waste of time, but the mission could be continued with lowered efficiency and less data recovery. Again, additional ground stations might be utilized for commanding the spacecraft.

The loss of an experiment component, such as the filter wheel, would eliminate the taking of certain data, but would not cause loss of the entire experiment. Similarly, loss of an entire experiment would not prevent operation of the remaining ones. In these cases the sequencing of experiments would be modified to make maximum use of the remaining operational units.

## REFERENCES

- IV-1. Grumman Aerospace Corporation: High Energy Astronomy Observatory Phase B Final Study Report. NASA Contract No. NAS8-26272, April 1971.
- IV-2. TRW Systems Group: High Energy Astronomy Observatory Phase B Final Study Report. NASA Contract No. NAS8-26273, April 1971.
- IV-3. American Science and Engineering, Columbia University, Goddard Space Flight Center, and Massachusetts Institute of Technology: Large Orbiting X-Ray Telescope (LOXT) Technical Proposal for the High Energy Astronomy Observatory. May 27, 1970.

TABLE OF CONTENTS

	Page
A. Introduction . . . . .	V- 1
B. Structural Requirements . . . . .	V- 1
C. Method of Analysis . . . . .	V- 3
D. Results of Analysis . . . . .	V-10
1. Load Distributions . . . . .	V-10
2. Shear and Bending Stiffness Diagrams . . . . .	V-10
3. Component Weight Summary . . . . .	V-10
4. Estimate of Static Deflections . . . . .	V-15
E. Spacecraft/OAS Adapter . . . . .	V-16
F. Free Vibration of Spacecraft Structure . . . . .	V-18
G. Dynamic Analysis of Shock Mounts . . . . .	V-20
H. Thermal Bending Analysis . . . . .	V-29
1. Geometry . . . . .	V-29
2. Theory . . . . .	V-29
3. Temperature Distribution . . . . .	V-31
4. Boundary Conditions . . . . .	V-33
5. Solutions . . . . .	V-34
6. Results of Analysis . . . . .	V-36
I. Evaluation of Methods for Relieving Thermal Bending of Telescope Tubes Mounted Without Ball Joint . . . . .	V-36
1. Relative Bending Stiffnesses . . . . .	V-39
2. Maximum Allowable Differential Temperature . . . . .	V-40
3. Estimate of the Natural Frequency of the Telescope Tube Mounted Without Ball Joint . . . . .	V-40
4. Effect of Shock Mount Deformation . . . . .	V-41

## TABLE OF CONTENTS (Concluded)

	Page
J. Solar Cell Substrate Analysis . . . . .	V-42
K. Meteoroid Protection Analysis . . . . .	V-45
L. Conclusions and Recommendations . . . . .	V-49
References . . . . .	V-50

## LIST OF ILLUSTRATIONS

Figure	Title	Page
V-1.	Details of outer structural design . . . . .	V - 4
V-2.	HEAO-C structural coordinate system . . . . .	V - 9
V-3.	Axial load as a function of spacecraft station . . . . .	V-11
V-4.	Shear as a function of spacecraft station . . . . .	V-12
V-5.	Bending moment as a function of spacecraft station . . . . .	V-13
V-6.	Shear stiffness as a function of spacecraft station — all axes . . . . .	V-14
V-7.	Bending stiffness as a function of spacecraft station — all axes . . . . .	V-14
V-8.	Details of adapter design . . . . .	V-17
V-9.	First three bending mode shapes including shear deformation . . . . .	V-19
V-10.	Schematic representation of telescope assembly and spacecraft structure connections . . . . .	V-21
V-11.	Frequency dependence of (a) the dynamic shear modulus and (b) the damping factor possessed by unfilled neoprene rubber at 25° C . . . . .	V-23
V-12.	Frequency dependence of (a) the dynamic shear modulus and (b) the damping factor possessed by unfilled natural rubber . . . . .	V-24
V-13.	Transmissibility as a function of frequency . . . . .	V-28
V-14.	Geometry of shell . . . . .	V-30
V-15.	Predicted temperature distribution on the spacecraft skin as a function of equivalent wall thickness . . . . .	V-32

## LIST OF ILLUSTRATIONS (Concluded)

Figure	Title	Page
V-16.	Spacecraft thermal bending . . . . .	V-37
V-17.	Schematic of panel support points . . . . .	V-44
V-18.	Modal deformation, natural frequency — 38 Hz . . . . .	V-46
V-19.	Modal deformation, natural frequency — 40 Hz . . . . .	V-46
V-20.	Modal deformation, natural frequency — 45 Hz . . . . .	V-46
V-21.	Component meteoroid protection thickness requirements . . . . .	V-48

## LIST OF TABLES

Table	Title	Page
V-1.	General Requirements for the Structural Configuration . . . . .	V - 2
V-2.	Initial Estimate of HEAO-C Component Weights and CG Locations Used for Structural Analysis . . . . .	V - 6
V-3.	Component Weight Breakdown . . . . .	V-15
V-4.	Spacecraft/OAS Adapter Weight Breakdown . . . . .	V-18
V-5.	Natural Frequencies and Free End Dynamic Displacements . . . . .	V-20
V-6.	Response Characteristics for Various Damping Factors and Frequency Ratios . . . . .	V-25
V-7.	HEAO-C Solar Panel Vibration Environment . . . . .	V-43
V-8.	Panel Support Point Reactions . . . . .	V-45

# CHAPTER V. STRUCTURAL ANALYSIS

## A. Introduction

The structural data, comments, and conclusions given in this chapter are applicable to the baseline design as defined in the various chapters of this report in which major subsystems are discussed and defined. In many instances, this work was done before the subsystems that affect the structure were defined; therefore, data used in the structural analysis are not based on the final data that appear in the other chapters.

For the Phase A definition, it is important to establish a logical and workable baseline definition of the structure; but it is also important to define the capability limits of the structure and the effects that changes to the basic requirements have on it. With this in mind, it can be seen that in most cases finite input data and requirements are not of the utmost importance, but rather, the trends that they set in the structure are the important factors. Furthermore, it makes little sense to compute quantities such as design margins, because they, if meaningful, require finite definition of the structure.

As in most preliminary analyses, the results can be considered linear within limits. For instance, the structural weight may be changed by a percentage comparable to the percentage weight change of the supported components without changes to the basic geometry of the structural components.

It is believed that the data in this chapter will provide an adequate structural definition of the baseline design, as well as an understanding of the effects that various design requirements have on the structure.

## B. Structural Requirements

The spacecraft structure must mechanically support the scientific experiments, must fulfill the requirements listed in Table V-1, and must withstand the vibration, acoustic, and shock environments that are discussed in Appendix B.

The Titan User's Guide requests, as a design goal, that lateral natural frequencies from 1 to 6 Hz for a payload and adapter which weigh under 1000 pounds be avoided so that payload dynamic loads and launch vehicle control problems can be minimized; however, the Martin Marietta Corporation verbally

TABLE V-1. GENERAL REQUIREMENTS FOR THE STRUCTURAL CONFIGURATION

- Provide a lifetime of two years
- Be capable of being launched with a Titan IID/OAS kick stage launch vehicle
- Be capable of withstanding the launch loading environment of 6.0 g longitudinal and 1.5 g lateral acceleration, simultaneously, and an ultimate load factor of 1.5
- Maintain a maximum spacecraft dynamic envelope of less than 108.7 in. in diameter
- Maintain parallelism among the telescopes and associated equipment within 1.0 arc min
- Provide isolation of the experiments from the launch-induced vibration
- Provide sufficient structure to limit spacecraft deflections to the following:

<u>High Resolution (HR) Telescope</u>	<u>Large Area (LA) Telescope</u>
<u>Deflection Caused by Thermal Gradients</u>	
±0.002 in. Longitudinal	±0.02 in. Longitudinal
±0.02 in. Lateral	±0.02 in. Lateral
<u>Total Deflection Caused by Loads and Thermal Gradients</u>	
±0.004 in. Longitudinal	±0.04 in. Longitudinal
±0.04 in. Lateral	±0.04 in. Lateral

states that other payloads, in the same weight class as HEAO-C, which have natural frequencies as low as 2 Hz have been designed for Titan IID launches. Martin also states that the present Titan IID program is designed for payloads having a natural frequency range of 1 to 4 Hz; therefore, 4 Hz has been established as the minimum acceptable lateral natural frequency for the design.

The spacecraft structure must remain within the dynamic envelope of the modified LMSCP-123 shroud. Reliable data on the shroud were not available during much of the study, so the dynamic envelope was established at 108.7 inches in diameter. Additional information on the dynamic envelope is included in Appendix B.

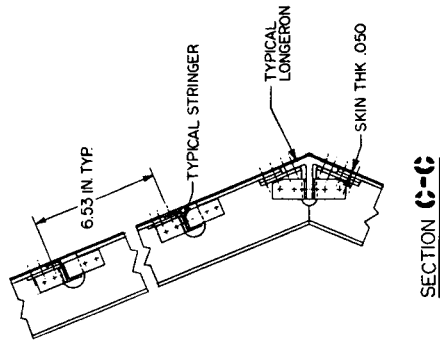
Prelaunch loads and environment are not considered in the study because it is assumed that handling and transportation techniques will be established to prevent the prelaunch loads from exceeding the launch loads.

### C. Method of Analysis

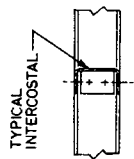
The octagonal spacecraft shown in Figure V-1 was simulated as a space truss for simplicity in the analysis and all of the structural elements were assumed to be load-carrying members according to their respective stiffness. The digital computer program "Structural Engineering Systems Solves (STRESS)" was used in computing component loads.

An initial estimate of the total system weight and its distribution over the assumed structural geometry is required to generate load input to the analysis. Table V-2 shows the detailed breakdown of the spacecraft system initial weight estimate and the location of each major component. The station reference system, shown in Figure V-2, was used to specify center of gravity (CG) locations of the components.

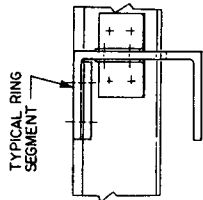
The initially estimated structural weight given in Table V-2 was assumed to be uniformly distributed over the total spacecraft length (360 in.). The spacecraft systems weight given in Table V-2 was assumed to be uniformly distributed between Station 100.0 and Station 369.0. These distributed weights, together with the concentrated weights shown in Table V-2, were used as inputs to the STRESS program. Results of this program were used in conjunction with another computer program, "Stiffened Panels" (STPAN), to determine the panel sizes, skin thickness, and member cross sections shown in Figure V-1.



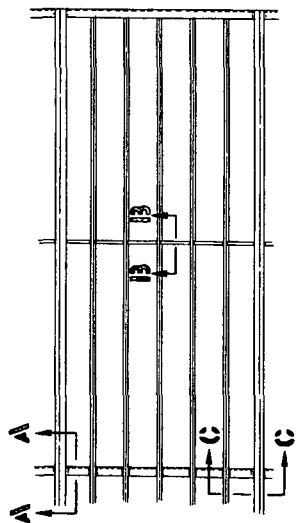
SECTION C-C



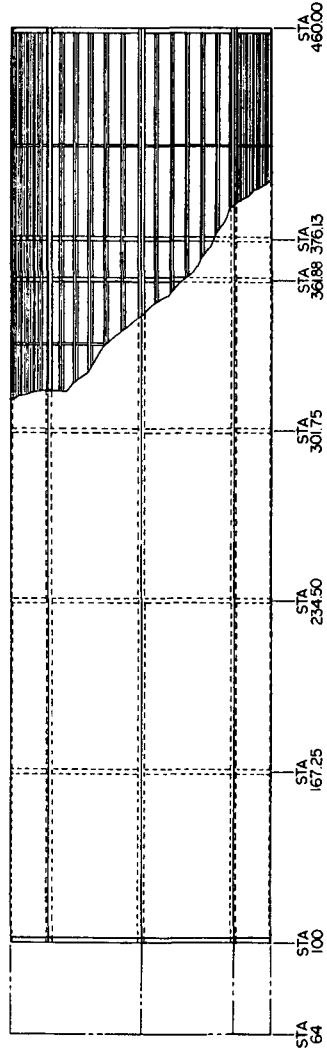
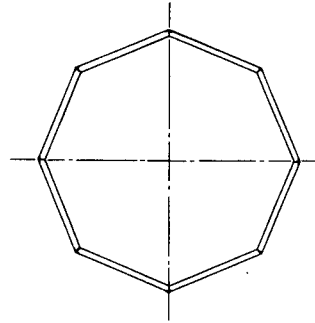
SECTION B-B



SECTION A-A



TYPICAL SKIN PANEL



* LONGERON SIZE (IN)	RING SEGMENTS	* INTERCOSTALS SIZE (IN)	STRINGERS SIZE (IN)
T-2.50 X 1.70 X .25	E-2.50 X 1.75 X .156	E-.87 X .50 X .05	L-3.75 X .36 X .05

Figure V-1. Details of structural design.

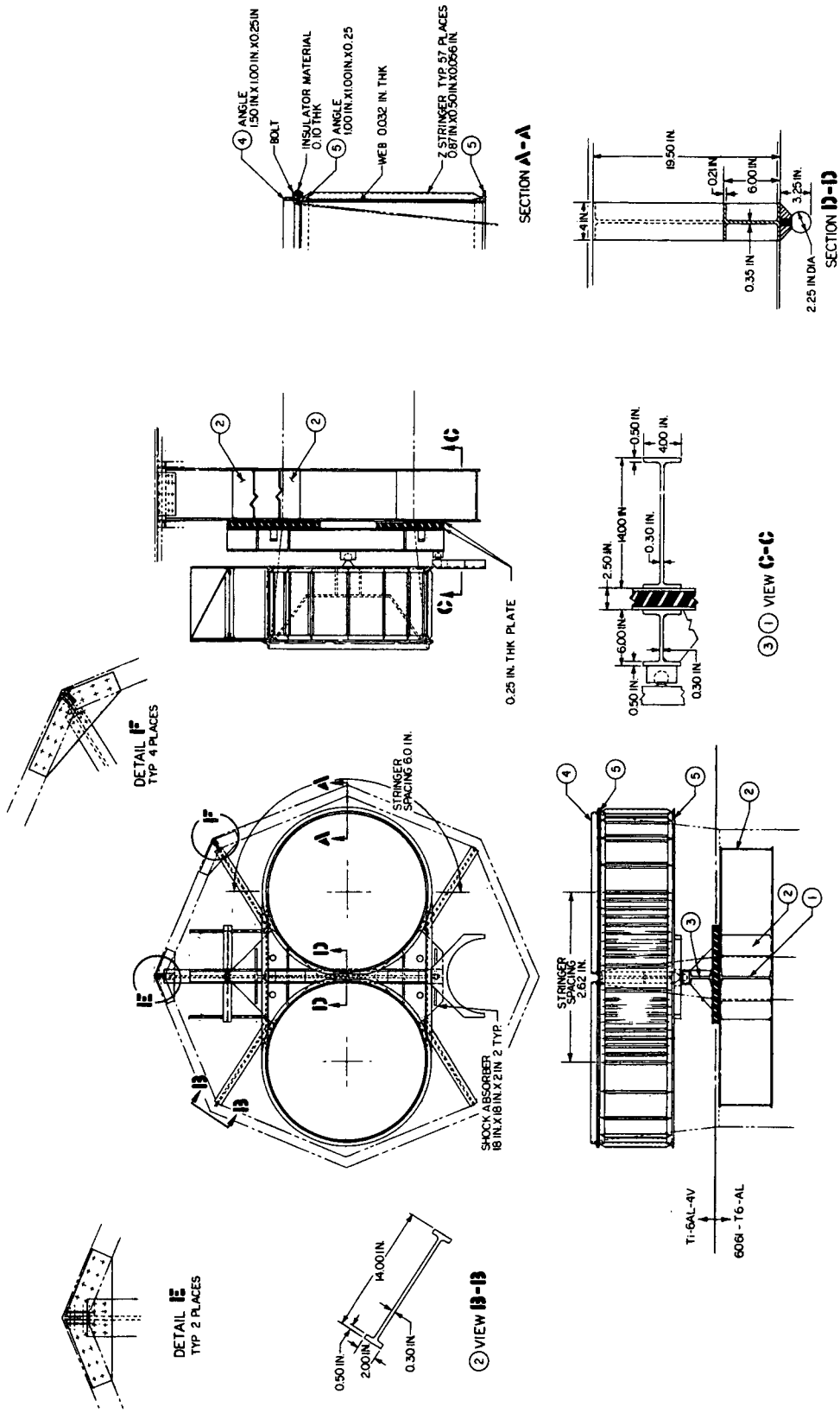


Figure V-1. (Concluded)

TABLE V-2. INITIAL ESTIMATE OF HEAO-C COMPONENT WEIGHTS AND CG LOCATIONS  
USED FOR STRUCTURAL ANALYSIS

Item	Description	Weight (lb)	CG Locations (Refer to Figure V-2)			Comment
			u	v	w	
1	Spacecraft Structure	2170	280.0	0.0	0.0	Uniformly distributed
2	HR Telescope Experiments	2733				Total weight of all components
	HR Image Detector	20	195.75	23.0	- 1.5	
	HR Transport Mechanism	45	195.75	23.0	- 1.5	
	HR Crystal Spectrometer	397	182.50	12.5	- 1.5	
	Filter Wheel	40	222.50	19.25	0.0	
	HR Mirror Assembly	2025	436.0	23.0	0.0	
	Estimated Experiment Mounting Structure	200	296.0	23.0	0.0	
Transmission Grating	60	412.0	23.0	0.0		
3	Telescope Tube and Insulation	146	295.0	23.0	0.0	Total weight of all components
	LA Telescope Experiments	3138				

TABLE V-2. (Continued)

Item	Description	Weight (lb)	CG Locations (Refer to Figure V-2)				Comment
			u	v	w		
	Imaging Detector	100	123.25	-24.0	0.0		
	Transport Mechanism	100	116.25	-24.0	0.0		
	Solid State Detector	90	123.25	-14.0	12.0		
	LA Mirror Assembly	2400	441.25	-24.0	0.0		
	Estimated Experiment Mounting Structure	200	285.0	-24.0	0.0		
	Telescope Tube and Insulation	248	280.0	-24.0	0.0		
4	Spacecraft Systems	3660	234.50	0.0	0.0	Uniformly distributed between Station 100.0 and Station 369.0	
5	LE X-Ray Telescope	1200	347.0	2.0	-36.0		
6	Items Attached to Telescope (Support but not Parts of Major Experiments)						
	Aspect Detector	100	442.50	0.0	16.0		

TABLE V-2. (Concluded)

Item	Description	Weight (lb)	CG Locations (Refer to Figure V-2)			Comment
			u	v	w	
	Fine Flare Detector	27	428.0	-30.0	28.0	
	Star Tracker (4)	160	451.0	0.0	0.0	
	Large Oval Ring Assembly	152.0	400.5	0.0	0.0	
	Shock Absorbers	10	394.0	0.0	0.0	
	Load Distribution Beam	17	398.0	0.0	0.0	
	Internal Truss	294	369.0	0.0	0.0	

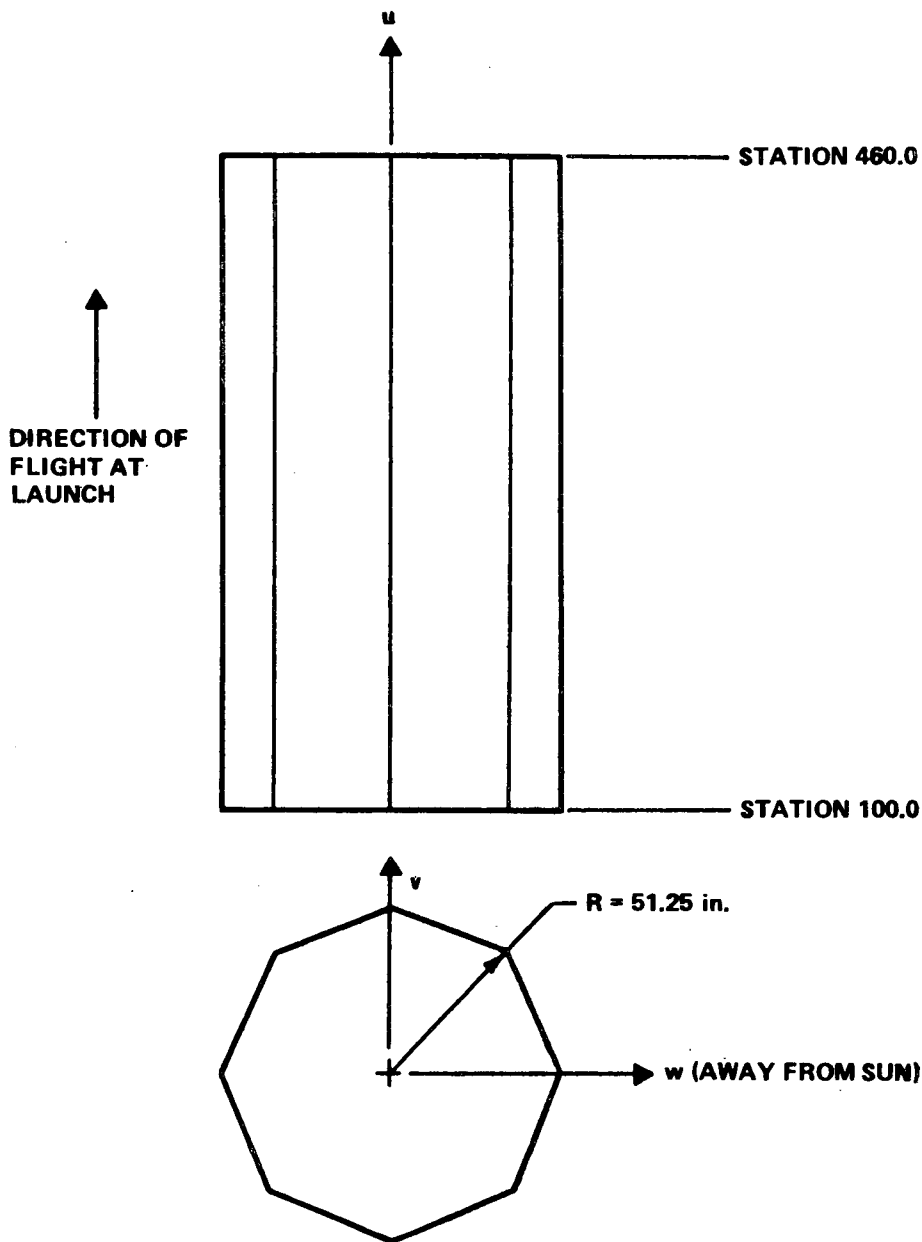


Figure V-2. HEAO-C structural coordinate system.

The results obtained from the STPAN program were based on the criterion that the skin should not be allowed to buckle under the limit load conditions, i. e. , 1.5 g lateral and 6.0 g longitudinal accelerations. Some of the results were modified to bring dimensions into more realistic ranges.

The internal frame arrangement shown on the second page of Figure V-1 was simulated as a space frame using the STRESS program. The axial and lateral loads from the tubular telescope structures were distributed over the area of the two vibration pads. The results of the STRESS runs were used to size the individual frame members.

Spacecraft axial load, bending moment, and shear distributions were computed using the weight data and CG locations shown in Table V-2.

## D. Results of Analysis

1. Load Distributions. Figures V-3, V-4, and V-5 give the axial load, shear, and bending moment distributions obtained using the initially estimated weight distribution shown in Table V-2. The limit loads are computed based on the 1.5 g lateral and 6.0 g longitudinal accelerations. At the spacecraft/adaptor interface, the following loads were obtained:

$$\text{Bending Moment} = 4.75 \times 10^6 \text{ in. -lb}$$

$$\text{Shear} = 21.09 \times 10^3 \text{ lb}$$

$$\text{Axial Load} = 86.07 \times 10^3 \text{ lb}$$

These values were used for the design of the adaptor.

2. Shear and Bending Stiffness Diagrams. The shear and bending stiffness distributions of the spacecraft are shown in Figures V-6 and V-7. These values of the stiffness were obtained using the following properties of 6061-T6 aluminum alloy:

$$\text{Modulus of Elasticity (E)} = 10.0 \times 10^6 \text{ lb/in.}^2$$

$$\text{Modulus of Rigidity (G)} = 3.75 \times 10^6 \text{ lb/in.}^2$$

The shear correction factor (k) is 0.5 for skin-stringer construction as given in Reference V-1. The data given are adequate to determine the dynamic characteristics of the spacecraft during launch.

3. Component Weight Summary. Table V-3 gives the computed weights of the various structural components. These structural weights are the results of various analyses performed during the course of this study.

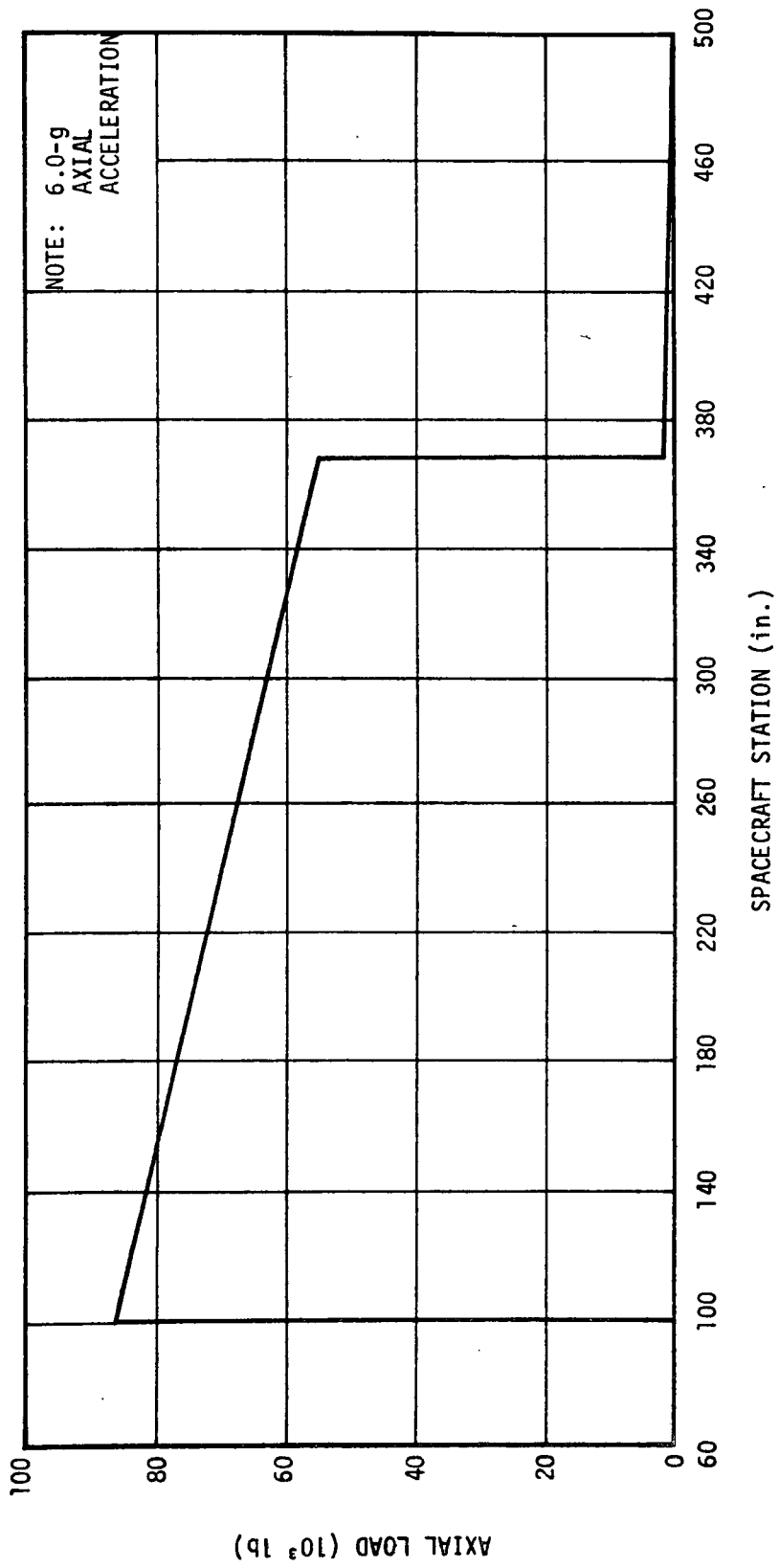


Figure V-3. Axial load as a function of spacecraft station.

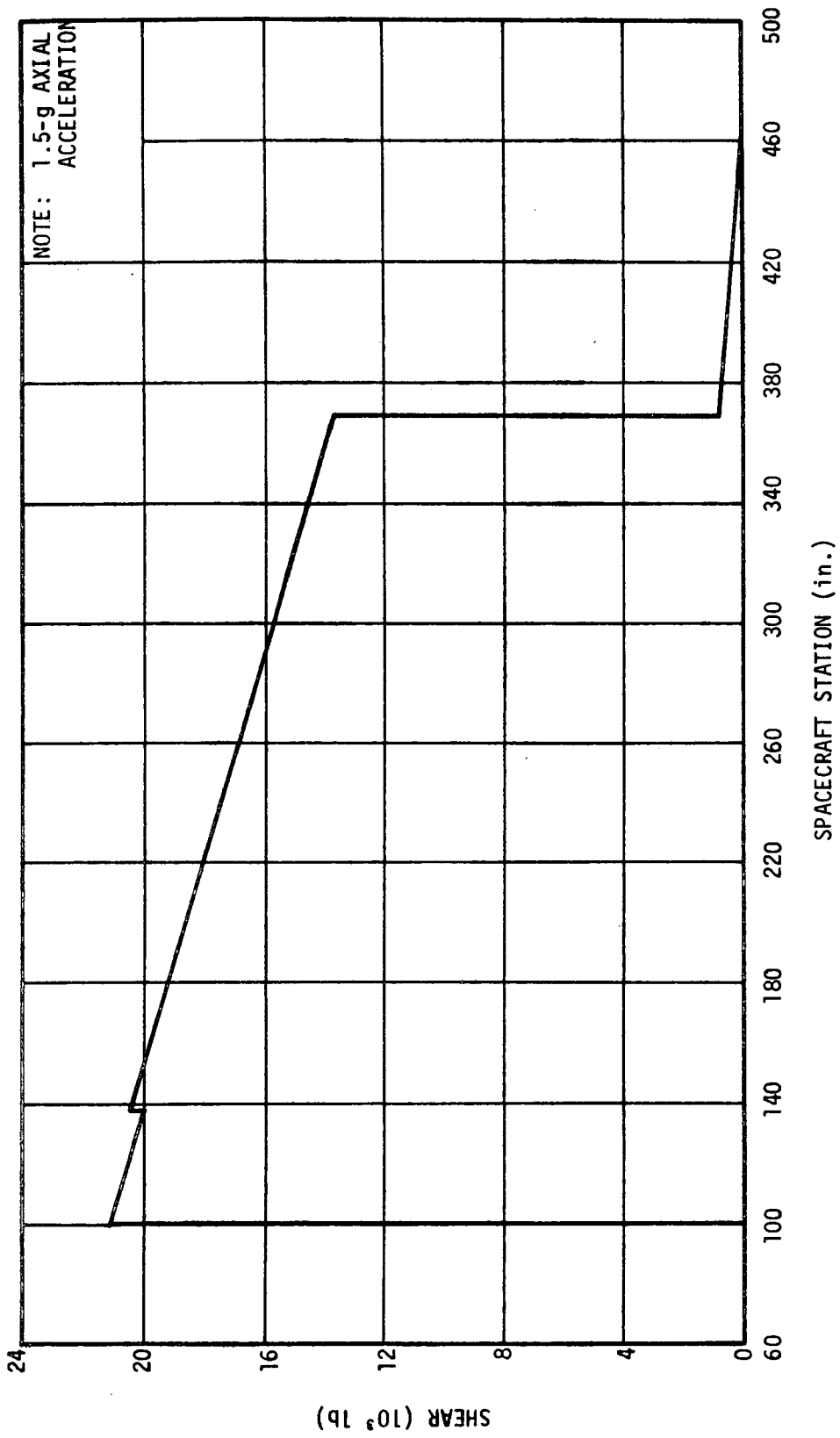


Figure V-4. Shear as a function of spacecraft station.

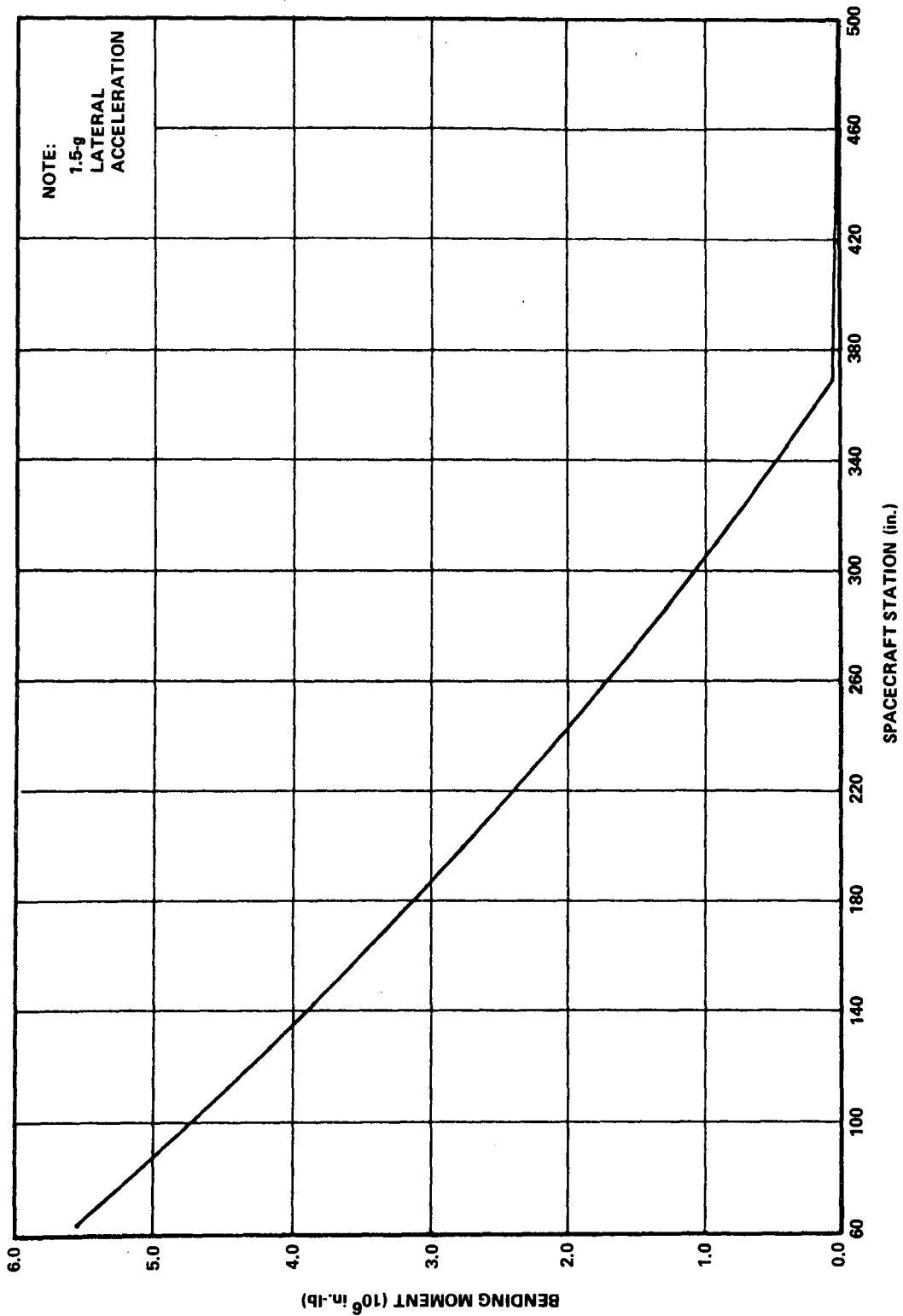


Figure V-5. Bending moment as a function of spacecraft station.

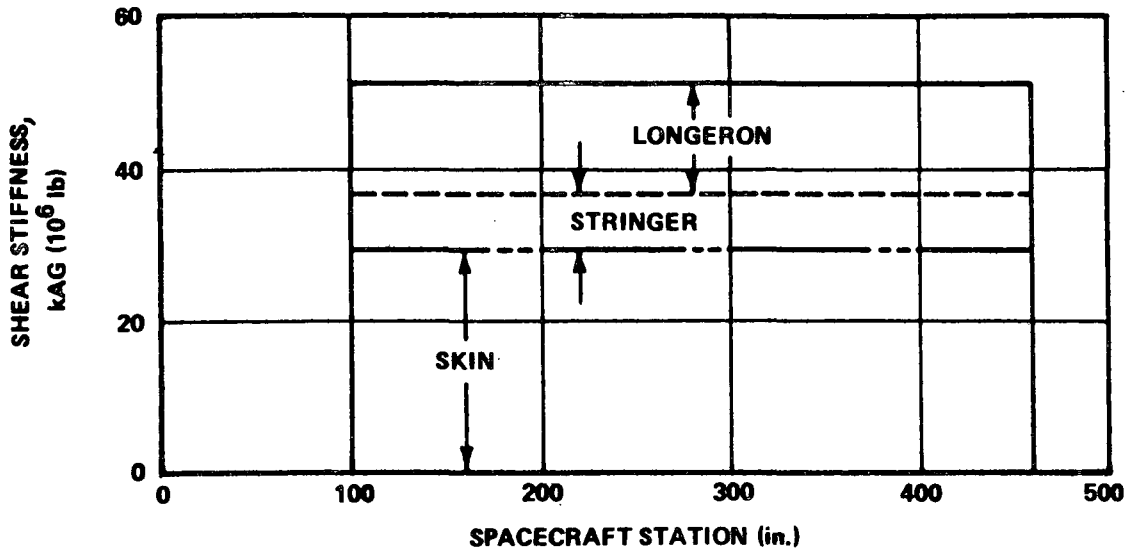


Figure V-6. Shear stiffness as a function of spacecraft station — all axes.

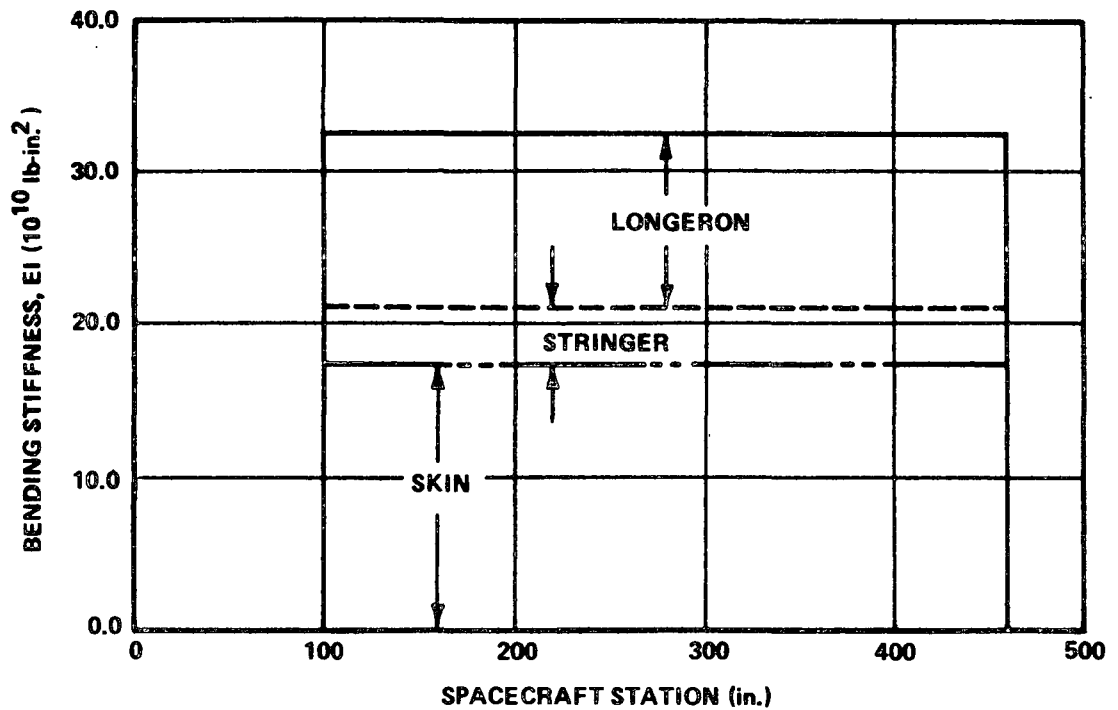


Figure V-7. Bending stiffness as a function of spacecraft station — all axes.

TABLE V-3. COMPONENT WEIGHT BREAKDOWN

Item	Weight (lb)
Structure	3328
Outer Shell	1370
Frames (7)	197
Stringers	143
Longerons (8)	292
Skin	560
Intercostals (5)	15
Clips (estimated)	20
Adapter Angle (8)	15
Aft End Closure	128
Internal Support	1758
Telescope Support Frame	309
Shock Mount	179
Load Distribution Beam	80
Ball and Socket (2)	35
Oval Ring Frame	252
HR Telescope Tube	167
LA Telescope Tube	293
Bars and Delta Frames, Bearings, Mounts, and Associated Structure (estimated)	443
Mounting Brackets	200

4. Estimate of Static Deflections. Spacecraft bending stiffness and shear stiffness diagrams, Figures V-6 and V-7, were constructed using the member sizes and skin thicknesses determined. Conjugate beam theory was then used to obtain the quasi-static bending deflection of the spacecraft under the limit load conditions. Because the length-to-depth ratio of the spacecraft is relatively small and large shear deformation is anticipated, it was assumed that the bending deflection obtained would represent 67 percent of the total deflection, with deflection due to shear deformation being the remaining 33 percent.

The bending deflection determined at the top end of the spacecraft is 0.489 inch under the maximum load conditions. With the shear deformation included, the total quasi-static deflection is 0.734 inch.

The quasi-static deflection of the titanium oval frame was computed to be 0.048 inch in the longitudinal direction between the unsupported ends to the center of the frame.

## E. Spacecraft/OAS Adapter

The truncated conical shell used in the design for the adapter shown in Figure V-8 was sized by equations (1) and (3), as follow:

$$\frac{P}{P_{cr}} + \frac{M}{M_{cr}} \leq 1 \quad , \quad (1)$$

where  $P$  is the applied compressive load, lb;  $M$  is the applied bending moment, in.-lb;  $P_{cr}$  is the critical compressive load for cone not subjected to bending moment, lb; and  $M_{cr}$  is the critical bending moment for cone not subjected to compressive load, in.-lb;

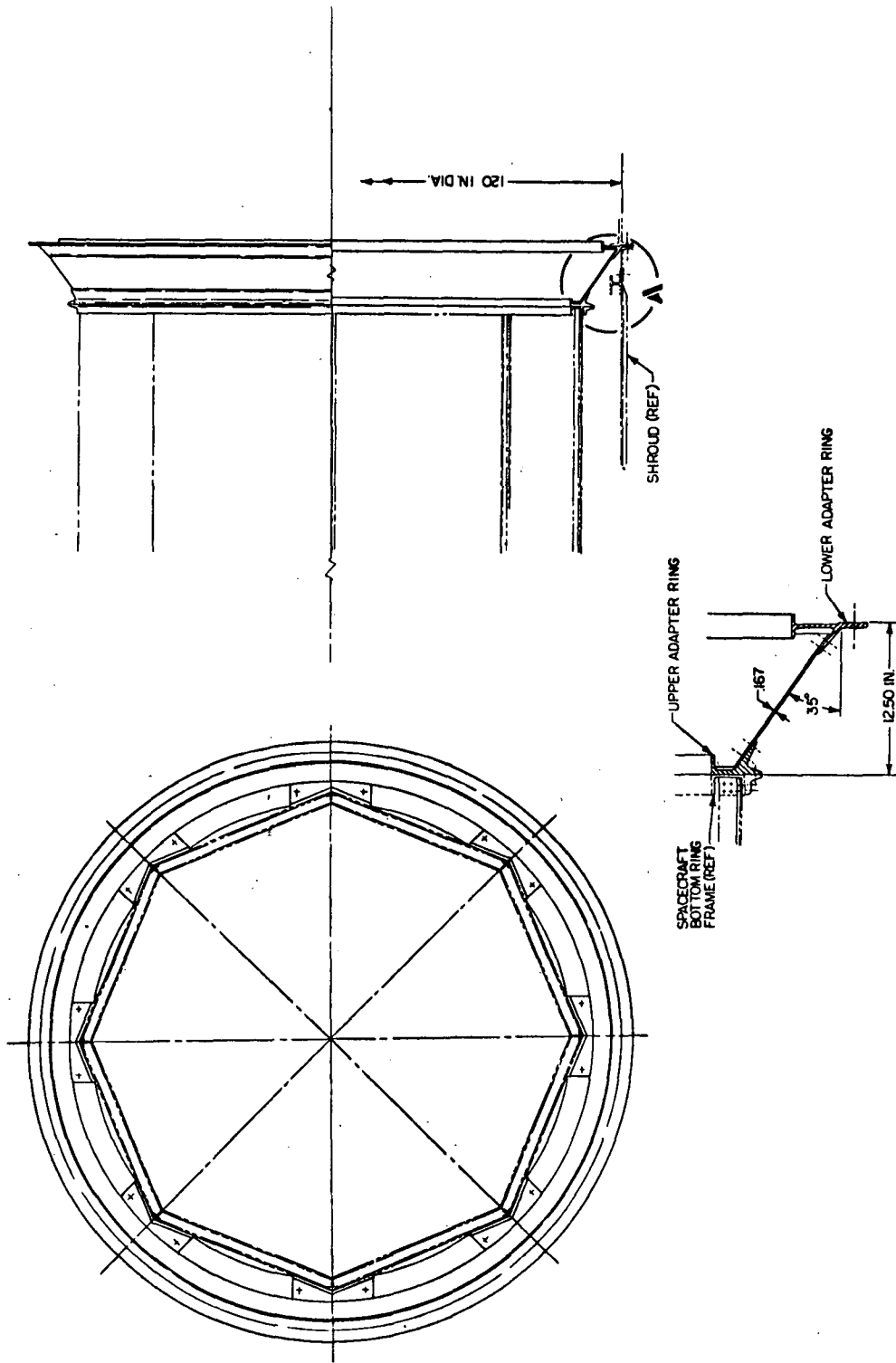
$$P_{cr} = \gamma_1 \frac{2\pi Et^2 \cos^2 \alpha}{[3(1 - \mu^2)]^{1/2}} \quad ; \quad (2)$$

and

$$M_{cr} = \gamma_2 \frac{\pi Et^2 r_1^2 \cos^2 \alpha}{[3(1 - \mu^2)]^{1/2}} \quad , \quad (3)$$

where  $\gamma_1$ ,  $\gamma_2$  are the correction factors based on experiments to account for the initial imperfection of shells;  $E$  is the modulus of elasticity of material, lb/in.<sup>2</sup>;  $r_1$  is the radius of the small end of the cone frustum, in.;  $t$  is shell thickness, in.;  $\alpha$  is the semivertex angle; and  $\mu$  is Poisson's ratio of material.

Reference V-2 recommends a value of 0.33 for  $\gamma_1$  and 0.40 for  $\gamma_2$  in spacecraft designs.



DETAIL A

Figure V-8. Details of adapter design.

The applied axial load and bending moment, which are used in the interaction equation [equation (1)], are given in Section C of this chapter. A weight breakdown for the spacecraft/OAS adapter is given in Table V-4.

TABLE V-4. SPACECRAFT/OAS ADAPTER  
WEIGHT BREAKDOWN

Item	Weight (lb)
Top Ring	50
Bottom Ring	58
Skin, Splices, and Fasteners	<u>104</u>
Total Weight of Adapter	212

## F. Free Vibration of Spacecraft Structure

The natural frequencies and their associated mode shapes of the spacecraft structure were computed with the aid of a computer program which employs the fourth-order Runge-Kutta method to numerically integrate the governing differential equation of the free vibration of a beam and includes the effect of the shear deformation. The rotational inertia was neglected in the analysis. Because of the relatively small aspect ratio, i. e. , the length divided by the depth of the beam, the shear deformation will have a greater impact on the frequencies and mode shapes of the beam than the rotational inertia.

The shear and bending stiffness, and the mass distributions, as shown in Figures V-6 and V-7 and Table V-2, respectively, were used as inputs to the computation. The spacecraft was assumed to be a cantilevered beam 360.0 inches long and fixed at Station 100.0.

The output of the computation consists of the three lowest natural frequencies and their associated mode shapes. The mode shapes are shown in Figure V-9, and the natural frequencies are given in Table V-5. For a periodic excitation with a 1.5 g peak acceleration amplitude and an assumed transmissibility of 1.50, the free end displacement responses for the three

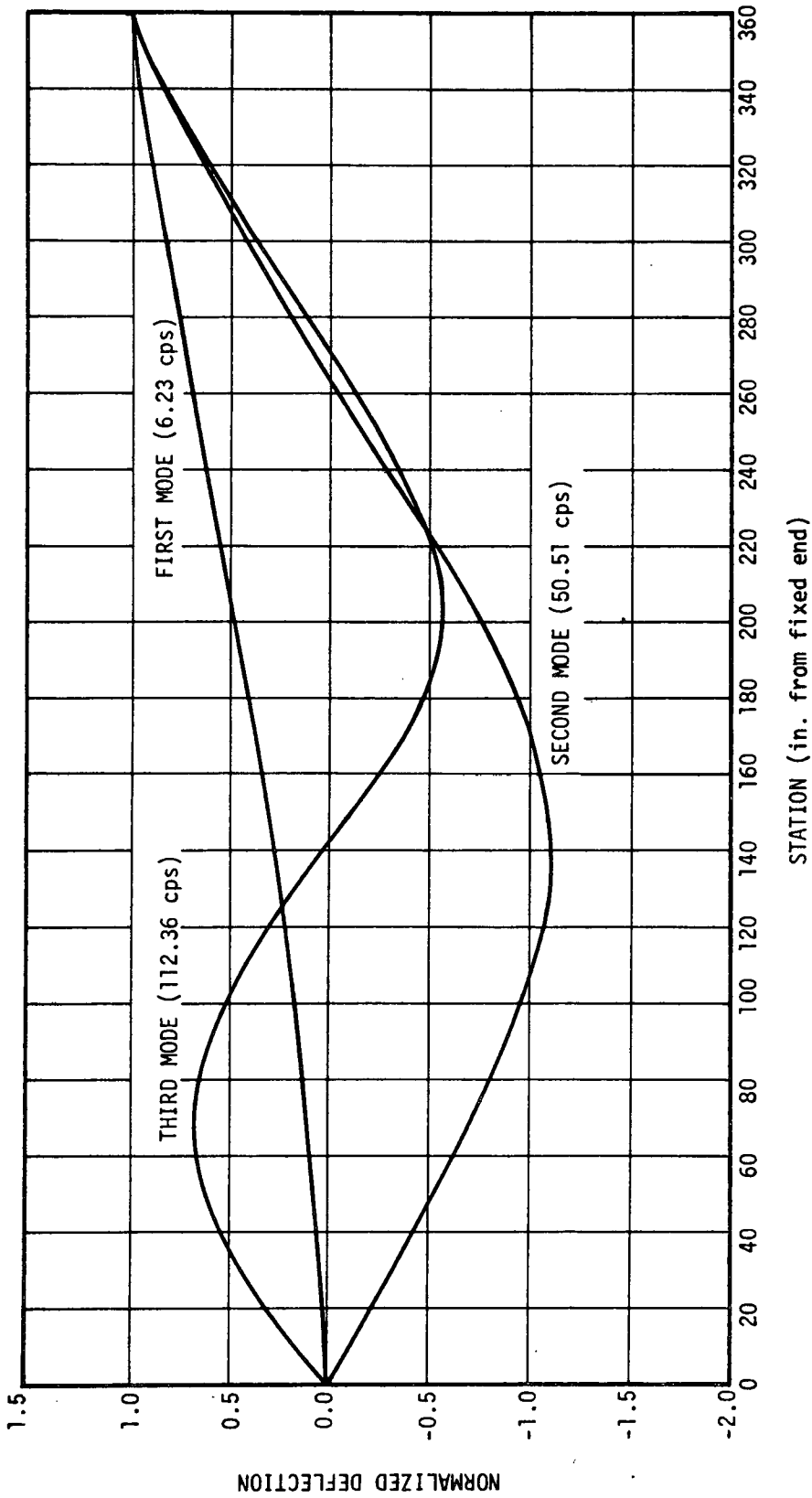


Figure V-9. First three bending mode shapes including shear deformation (normalized with respect to the deflection at Station 360).

TABLE V-5. NATURAL FREQUENCIES AND FREE END DYNAMIC DISPLACEMENTS

Mode	Frequency $f_n$ (cps)	Displacement $\Delta_{out}$ (in.)
1	6.230	$568.320 \times 10^{-3}$
2	50.506	$8.654 \times 10^{-3}$
3	112.355	$1.747 \times 10^{-3}$
		Total 0.58

lowest modes are shown in Table V-5. The relationship used to obtain the response  $\Delta_{out}$  in inches is

$$\Delta_{out} = \frac{G_{in} Q \phi}{0.102 f_n^2} \quad (4)$$

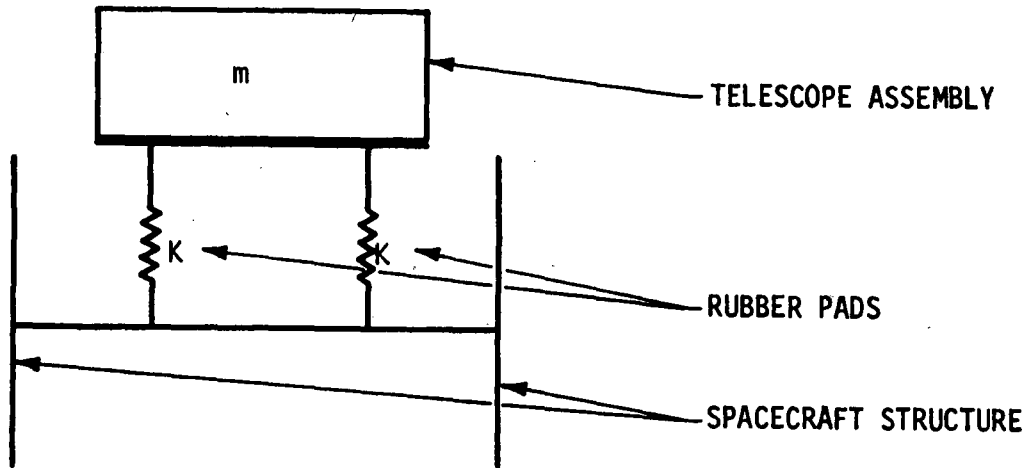
where  $G_{in}$  is the input acceleration amplitude, g; Q is transmissibility;  $\phi$  is mode shape at point of interest; and  $f_n$  is the nth mode natural frequency, cps.

The assumed dynamic envelope of the proposed modified LMSC-P123 payload shroud is 108.7 inches, which includes a 0.45 inch manufacturing tolerance. The baseline spacecraft, with 1.5 inches of insulation, is 105.0 inches in diameter.

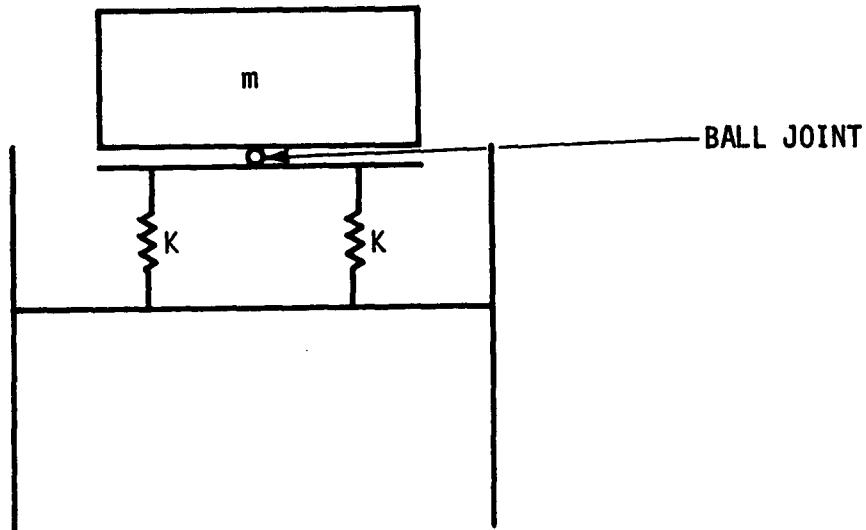
Assuming a 0.35 inch spacecraft manufacturing tolerance, the maximum allowable spacecraft tip deflection would be 1.5 inches, which is much greater than the estimated spacecraft deflection of 0.58 inch.

## G. Dynamic Analysis of Shock Mounts

Schematic representations of two concepts that could support the telescope assemblies are shown in Figure V-10. Concept (a) of the figure does not have a ball joint, while concept (b), the baseline design, employs the



(a) Alternate design with rubber pads but no ball joint.



(b) Baseline design with rubber pads and ball joint.

Figure V-10. Schematic representation of telescope assembly and spacecraft structure connections.

joint. Both configurations have two rubber pads represented by springs that are 42 inches apart and that have a complex modulus of elasticity.

The telescope assembly without the ball joint has three degrees of freedom corresponding to three modes of vibration of the assembled telescope mass, two rotational modes about axes in the plane normal to the spacecraft

longitudinal axis, and one translational mode along the longitudinal axis. Only the longitudinal mode of vibration exists for the configuration with the ball joint since the rotational motions of the mass do not deflect the springs. The longitudinal mode is the one considered in this analysis and the results are applicable to both support schemes.

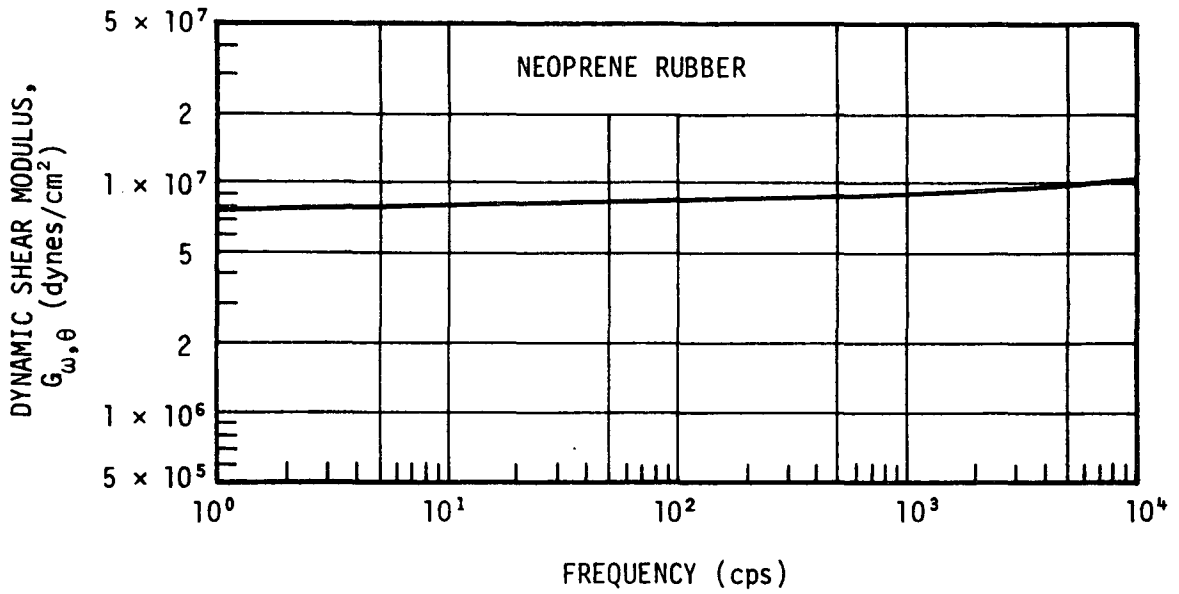
The rubber shock mounts proposed in this study have an approximate spring rate of 256 lb/in.<sup>2</sup>/in. Data obtained for two types of rubber (neoprene and natural rubber) show that the damping factor ranges from 0.1 to 0.3, depending on the frequency and temperature. These data are shown in Figures V-11 and V-12. The damping factor is defined as the ratio of the imaginary part to the real part of the complex modulus of elasticity. The shear modulus is one-third of the Young's modulus of elasticity because the Poisson's ratio for rubber type materials is 0.5.

The frequency dependency of the modulus of elasticity is considered to be small, as shown in Figures V-11 and V-12, and, therefore, is neglected. The transmissibility (T) and the phase angle ( $\theta$ ) for the system are found as follows:

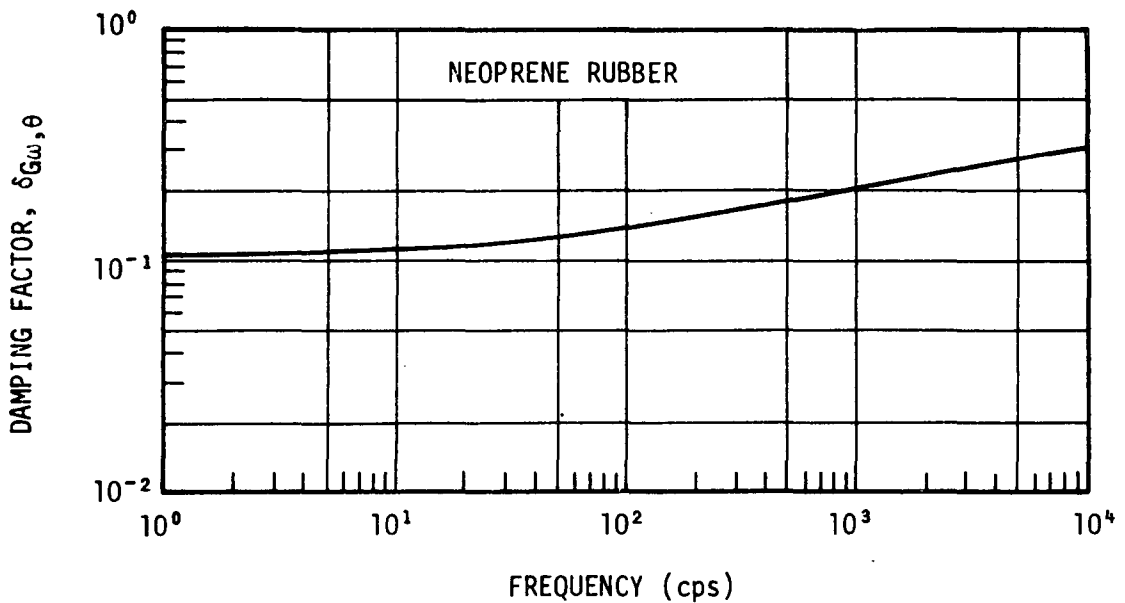
$$T = \frac{\left(1 + \delta_{G\omega, \theta}^2\right)^{1/2}}{\left[\left(1 - \frac{\omega^2}{\omega_n^2}\right)^2 + \delta_{G\omega, \theta}^2\right]^{1/2}} \quad (5)$$

$$\theta = \tan^{-1} \left[ \frac{-\delta_{G\omega, \theta} \omega^2 / \omega_n^2}{\left(1 - \frac{\omega^2}{\omega_n^2}\right)^2 + \delta_{G\omega, \theta}^2} \right] \quad (6)$$

where  $\delta_{G\omega, \theta}$  is the damping factor;  $\omega$  is the excitation frequency; and  $\omega_n$  is the natural frequency. Results of computation for four values of  $\delta_{G\omega, \theta}$  ( $= 0.0, 0.1, 0.2, 0.3$ ) and a range of frequency ratios from 0.1 to 800 are presented in Table V-6. As an illustration, a portion of the data are shown in Figure V-13, which shows that high frequency excitations can be damped out effectively with rubber mounts.

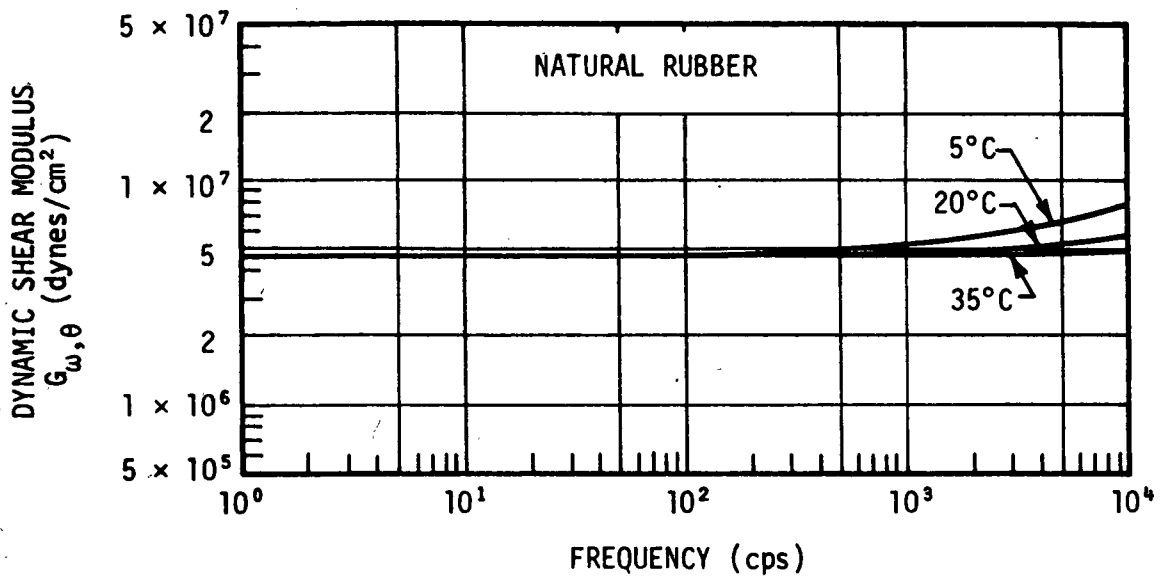


(a)

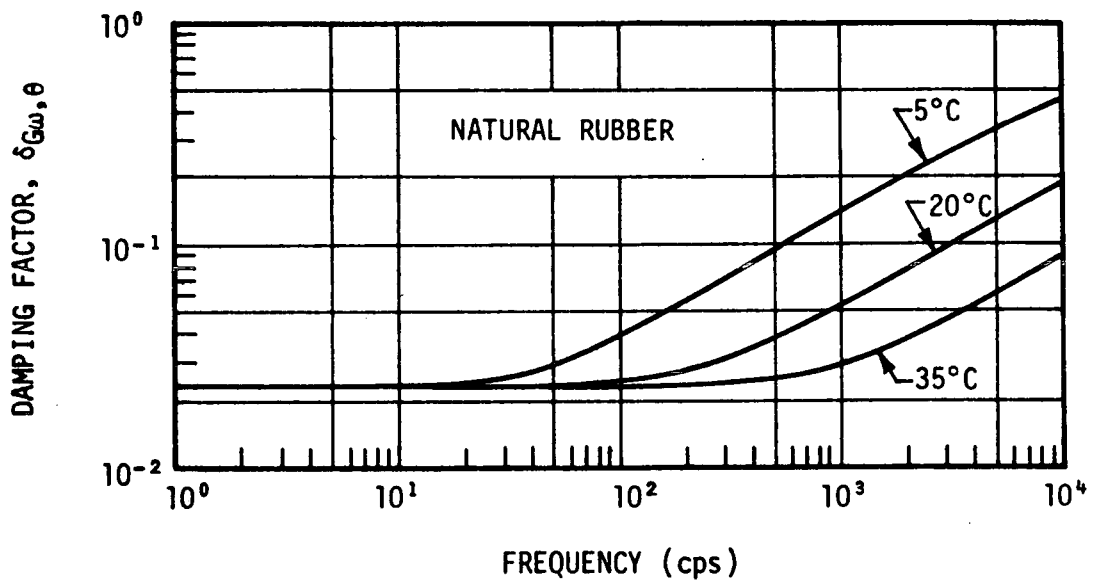


(b)

Figure V-11. Frequency dependence of (a) the dynamic shear modulus and (b) the damping factor possessed by unfilled neoprene rubber at 25°C (Ref. V-3, Figure 1.5).



(a)



(b)

Figure V-12. Frequency dependence of (a) the dynamic shear modulus and (b) the damping factor possessed by unfilled natural rubber (Ref. V-3, Figure 1.6).

TABLE V-6. RESPONSE CHARACTERISTICS FOR VARIOUS DAMPING FACTORS AND FREQUENCY RATIOS

$\delta_{G\omega, \theta}^a$	$\omega/\omega_n^b$	Transmissibility	Tangent of Phase Angle
0.0	0.1	0.1010101E 01	0.0000000E 00
0.0	0.2	0.1041666E 01	0.0000000E 00
0.0	0.3	0.1098901E 01	0.0000000E 00
0.0	0.4	0.1190476E 01	0.0000000E 00
0.0	0.6	0.1562500E 01	0.0000000E 00
0.0	0.8	0.2777777E 01	0.0000000E 00
0.0	1.0	0.1000000E 01	0.0000000E 00
0.0	2.0	0.3333333E 00	0.0000000E 00
0.0	3.0	0.1250000E 00	0.0000000E 00
0.0	4.0	0.6666666E-01	0.0000000E 00
0.0	6.0	0.2857143E-01	0.0000000E 00
0.0	8.0	0.1587301E-01	0.0000000E 00
0.0	10.0	0.1010101E-01	0.0000000E 00
0.0	20.0	0.2506265E-02	0.0000000E 00
0.0	30.0	0.1112347E-02	0.0000000E 00
0.0	40.0	0.6253909E-03	0.0000000E 00
0.0	60.0	0.2778549E-03	0.0000000E 00
0.0	80.0	0.1562744E-03	0.0000000E 00
0.0	100.0	0.1000100E-03	0.0000000E 00
0.0	200.0	0.2500062E-04	0.0000000E 00
0.0	300.0	0.1111123E-04	0.0000000E 00
0.0	400.0	0.6250039E-05	0.0000000E 00
0.0	600.0	0.2777785E-05	0.0000000E 00
0.0	800.0	0.1562502E-05	0.0000000E 00
0.1	0.1	0.1009999E 01	-0.1009999E-02
0.1	0.2	0.1041228E 01	-0.4293689E-02
0.1	0.3	0.1097773E 01	-0.1073857E-01
0.1	0.4	0.1188025E 01	-0.2235886E-01
0.1	0.6	0.1551468E 01	-0.8579595E-01
0.1	0.8	0.2689787E 01	-0.4584525E 00
0.1	1.0	0.1004987E 02	-0.1000000E 02
0.1	2.0	0.3348099E 00	-0.4439512E-01
0.1	3.0	0.1256136E 00	-0.1406030E-01
0.1	4.0	0.6699769E-01	-0.7110795E-02
0.1	6.0	0.2871381E-01	-0.2938752E-02
0.1	8.0	0.1595216E-01	-0.1612492E-02
0.1	10.0	0.1015138E-01	-0.1020302E-02
0.1	20.0	0.2518766E-02	-0.2512547E-03
0.1	30.0	0.1117894E-02	-0.1113584E-03
0.1	40.0	0.6285101E-03	-0.6257819E-04
0.1	60.0	0.2792408E-03	-0.2779321E-04
0.1	80.0	0.1570538E-03	-0.1562988E-04
0.1	100.0	0.1005088E-03	-0.1000200E-04
0.1	200.0	0.2512531E-04	-0.2500125E-05

TABLE V-6. (Continued)

$\delta_{G\omega, \theta}^a$	$\omega/\omega_n^b$	Transmissibility	Tangent of Phase Angle
0.1	300.0	0.1116665E-04	-0.1111135E-05
0.1	400.0	0.6281212E-05	-0.6250079E-06
0.1	600.0	0.2791639E-05	-0.2777793E-06
0.1	800.0	0.1570295E-05	-0.1562505E-06
0.2	0.1	0.1009706E 01	-0.1960592E-02
0.2	0.2	0.1039967E 01	-0.8319469E-02
0.2	0.3	0.1094540E 01	-0.2073493E-01
0.2	0.4	0.1181037E 01	-0.4291846E-01
0.2	0.6	0.1520910E 01	-0.1601422E 00
0.2	0.8	0.2476302E 01	-0.7547167E 00
0.2	1.0	0.5099020E 01	-0.5000000E 01
0.2	2.0	0.3391817E 00	-0.8849558E-01
0.2	3.0	0.1274356E 00	-0.2810743E-01
0.2	4.0	0.6798088E-01	-0.1421969E-01
0.2	6.0	0.2913678E-01	-0.5877359E-02
0.2	8.0	0.1618728E-01	-0.3224961E-02
0.2	10.0	0.1030102E-01	-0.2040599E-02
0.2	20.0	0.2555899E-02	-0.5025092E-03
0.2	30.0	0.1134376E-02	-0.2227168E-03
0.2	40.0	0.6377761E-03	-0.1251563E-03
0.2	60.0	0.2833576E-03	-0.5558643E-04
0.2	80.0	0.1593692E-03	-0.3125976E-04
0.2	100.0	0.1019905E-03	-0.2000400E-04
0.2	200.0	0.2549573E-04	-0.5000250E-05
0.2	300.0	0.1133127E-04	-0.2222271E-05
0.2	400.0	0.6373815E-05	-0.1250015E-05
0.2	600.0	0.2832796E-05	-0.5555587E-06
0.2	800.0	0.1593446E-05	-0.3125010E-06
0.3	0.1	0.1009255E 01	-0.2803476E-02
0.3	0.2	0.1038027E 01	-0.1186239E-01
0.3	0.3	0.1089603E 01	-0.2940855E-01
0.3	0.4	0.1170485E 01	-0.6033183E-01
0.3	0.6	0.1477073E 01	-0.2161728E 00
0.3	0.8	0.2227907E 01	-0.8743168E 00
0.3	1.0	0.3480103E 01	-0.3333334E 01
0.3	2.0	0.3462831E 00	-0.1320132E 00
0.3	3.0	0.1304121E 00	-0.4212825E-01
0.3	4.0	0.6958812E-01	-0.2132480E-01
0.3	6.0	0.2982835E-01	-0.8815679E-02
0.3	8.0	0.1657172E-01	-0.4837380E-02
0.3	10.0	0.1054571E-01	-0.3060883E-02
0.3	20.0	0.2616617E-02	-0.7537637E-03
0.3	30.0	0.1161324E-02	-0.3340753E-03

TABLE V-6. (Concluded)

$\delta_{G\omega, \theta}$ <sup>a</sup>	$\omega/\omega_n$ <sup>b</sup>	Transmissibility	Tangent of Phase Angle
0.3	40.0	0.6529272E-03	-0.1877345E-03
0.3	60.0	0.2900891E-03	-0.8337965E-04
0.3	80.0	0.1631552E-03	-0.4688964E-04
0.3	100.0	0.1044135E-03	-0.3000599E-04
0.3	200.0	0.2610142E-04	-0.7500374E-05
0.3	300.0	0.1160047E-04	-0.3333407E-05
0.3	400.0	0.6525232E-05	-0.1875023E-05
0.3	600.0	0.2900093E-05	-0.8333379E-06
0.3	800.0	0.1631300E-05	-0.4687514E-06

a. Damping factor.

b. Ratio of excitation frequency to natural frequency.

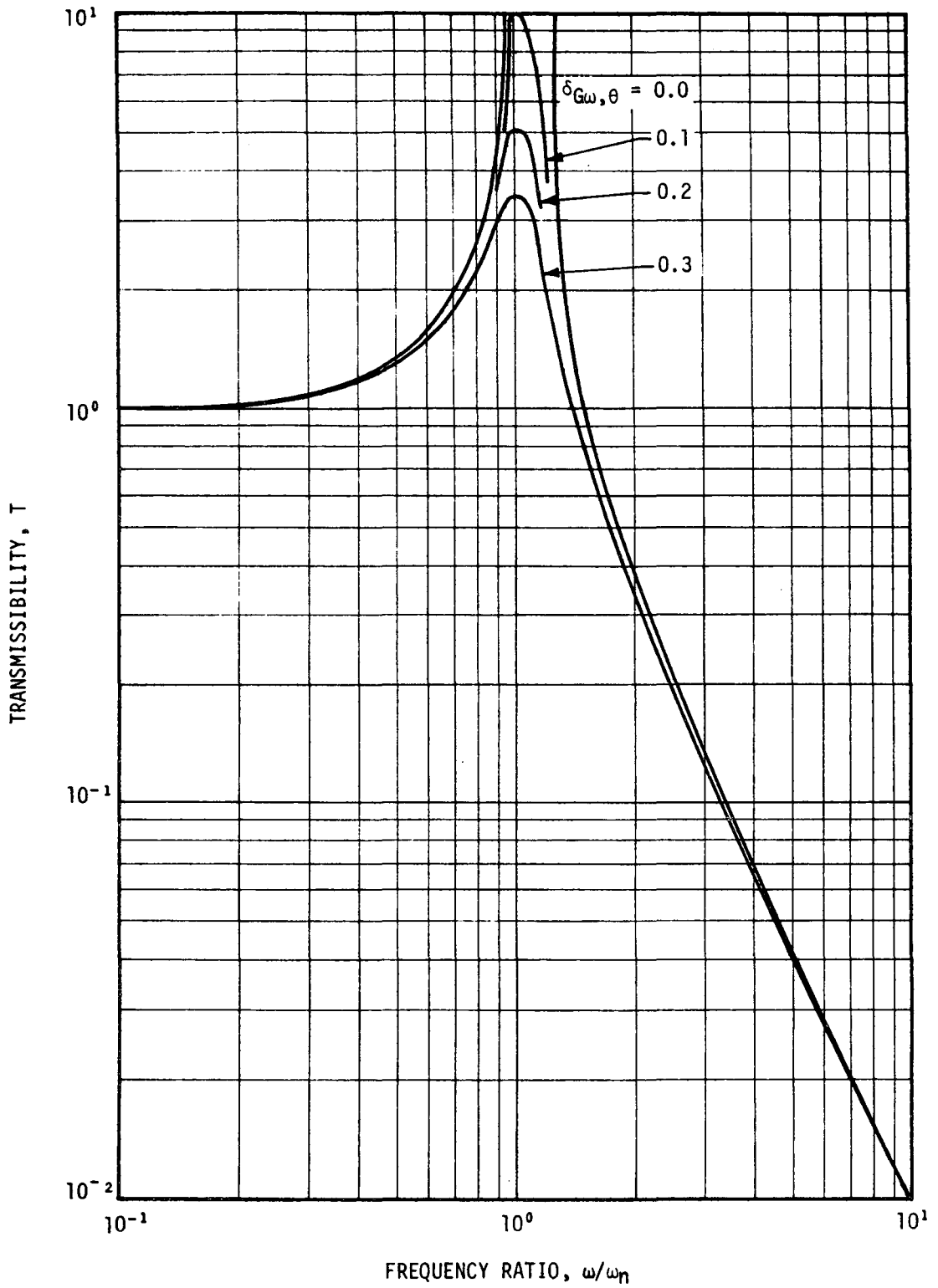


Figure V-13. Transmissibility as a function of frequency.

Considering a design with two 18.0 by 18.0 inch pads, the total spring stiffness is 165 888 lb/in. Therefore, the natural frequency is

$$\omega_n = \left[ \frac{165\,888}{(8000 \ 32.2 \times 12)} \right]^{1/2} = 87.393 \text{ radians/sec}$$

or 13.91 cps. At resonance,  $\omega = \omega_n = 13.91$  cps, and  $\delta_{G\omega, \theta} = 0.12$

[Fig. V-11(b)]. The transmissibility is about 8.6 (Fig. V-13), which means that the response acceleration is about 51.6 g for a 6 g longitudinal excitation.

## H. Thermal Bending Analysis

1. Geometry. The thermal bending of the HEAO-C spacecraft, due to the temperature variation in the circumferential direction, was predicted initially by simple beam theory. A more accurate thermal deflection calculation was believed mandatory because of the stringent requirements in the pointing accuracy of the telescopes; furthermore, complete definition of the thermal distortion would be necessary if the telescopes were hard mounted to the support frame.

The aspect ratio (the length divided by the average transverse dimension of the spacecraft) is relatively small; therefore, the cylindrical spacecraft structure cannot logically be represented as a beam. The octagonal shell is treated as a circular cylindrical shell for simplicity in the analysis which is consistent with the way the temperature distribution was generated.

The geometrical notations of the shell are shown in Figure V-14, with  $s = 0$  being the location of the ball joint,  $s = L_1$  the bottom end, and  $s = L_2$  the pin connections of the telescope detector boxes to the spacecraft shell structure. Dimensions of the spacecraft are 360 inches long and 102.0 inches in diameter.

2. Theory. Let  $u$ ,  $v$ , and  $w$  be the deflection component in  $s$ ,  $\theta$ , and  $z$  directions, respectively. The direction of  $z$  is toward the spacecraft longitudinal axis and perpendicular to the surface, as shown in Figure V-14. The standard equations governing the deflections of the circular cylindrical shell are given by Timoshenko [V-4] or Wang [V-3]. Since  $t/r$  (the thickness over radius of the shell) is small, terms associated with  $t^2/r^2$  are neglected. The governing differential equations given in either Reference V-3 or V-4 can be written as follows:

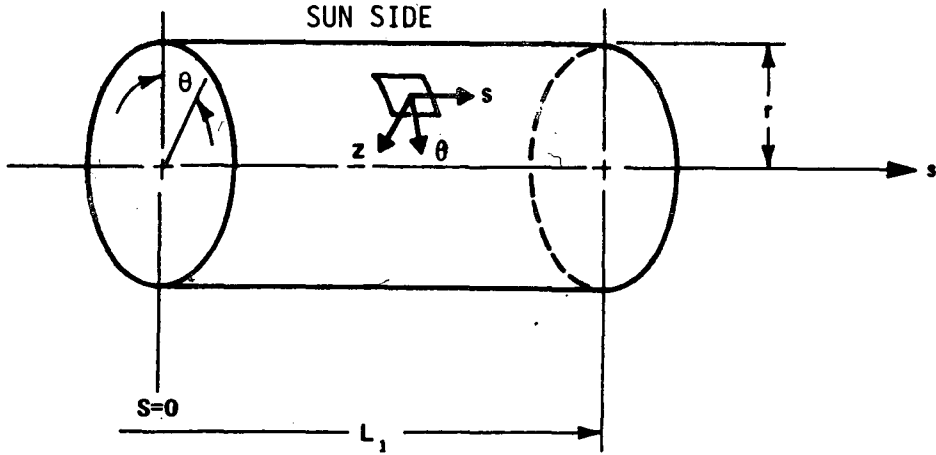


Figure V-14. Geometry of shell.

$$\frac{\partial^2 u}{\partial \xi^2} + \frac{1 - \nu}{2} \frac{\partial^2 u}{\partial \theta^2} + \frac{1 + \nu}{2} \frac{\partial^2 v}{\partial \xi \partial \theta} - \frac{\nu \partial w}{\partial \xi} - r \alpha (1 + \nu) \frac{\partial T_m}{\partial \xi} = 0 \quad ; \quad (7)$$

$$\frac{1 + \nu}{2} \frac{\partial^2 u}{\partial \xi \partial \theta} + \frac{1 - \nu}{2} \frac{\partial^2 v}{\partial \xi^2} + \frac{\partial^2 v}{\partial \theta^2} - \frac{\partial w}{\partial \theta} - r \alpha (1 + \nu) \frac{\partial T_m}{\partial \theta} = 0 \quad , \quad (8)$$

$$\nu \frac{\partial u}{\partial \xi} + \frac{\partial v}{\partial \theta} - w - r \alpha (1 + \nu) T_m = 0 \quad , \quad (9)$$

where  $\xi$  is the normalized variable defined as  $s/r$ ;  $\nu$  is Poisson's ratio of the material;  $\alpha$  is the thermal expansion coefficient of the material;  $T_m$  is the mean skin temperature rise from the room temperature at which the shell is undeformed; and  $r$  is the radius of the shell. From equation (9), the normal deflection  $w$  can be represented in terms of  $u$  and  $v$ :

$$w = \nu \frac{\partial u}{\partial \xi} + \frac{\partial v}{\partial \theta} - r \alpha (1 + \nu) T_m \quad . \quad (10)$$

Substitution of  $w$  into equations (7) and (8) yields

$$\frac{\partial^2 u}{\partial \xi^2} + \frac{1}{2(1+\nu)} \frac{\partial^2 u}{\partial \theta^2} + \frac{1}{2(1+\nu)} \frac{\partial^2 v}{\partial \xi \partial \theta} - r\alpha \frac{\partial T_m}{\partial \xi} = 0 \quad , \quad (11)$$

$$\frac{\partial^2 u}{\partial \xi \partial \theta} + \frac{\partial^2 v}{\partial \xi^2} = 0 \quad . \quad (12)$$

Partial differentiation with respect to  $\xi$  in equation (11) and with respect to  $\theta$  in equation (12) and subtraction gives

$$\frac{\partial^3 u}{\partial \xi^3} - r\alpha \frac{\partial^2 T_m}{\partial \xi^2} = 0 \quad . \quad (13)$$

Since the mean temperature rise  $T_m$  is uniform in the  $s$ -direction, the second term in equation (13) is zero. Therefore, the solution of equation (13) can be written as follows:

$$u = C_1 \xi^2 + C_2 \xi + C_3 \quad , \quad (14)$$

where  $C_1$ ,  $C_2$ , and  $C_3$  can be functions of  $\theta$  only. From equations (12) and (10), the deflection components  $v$  and  $w$  can be written in terms of  $C_1$ ,  $C_2$ , and  $C_3$ , their first and second derivatives, and an additional function of  $\theta$ ,  $C_4$ :

$$v = - \left( \frac{1}{3} \frac{dC_1}{d\theta} \xi^3 + \frac{1}{2} \frac{dC_2}{d\theta} \xi^2 + \frac{dC_3}{d\theta} + C_4 \right) \quad , \quad (15)$$

$$w = \nu(2C_1 \xi + C_2) - \left( \frac{1}{3} \frac{d^2 C_1}{d\theta^2} \xi + \frac{1}{2} \frac{d^2 C_2}{d\theta^2} \xi^2 + \frac{d^2 C_3}{d\theta^2} \xi + \frac{dC_4}{d\theta} \right) - r\alpha(1+\nu)T_m \quad . \quad (16)$$

3. Temperature Distribution. The in-orbital skin temperature distribution over three assumed equivalent thicknesses was computed for an early spacecraft configuration that had internal insulation. These values are shown in Figure V-15. The general distribution is the important factor since the magnitude of the temperature can and will be adjusted to any particular value. The skin temperature ( $\tilde{T}_m$ ) can be conveniently represented in the following form:

$$\tilde{T}_m = 60 + 140 \cos \theta \quad (\text{in } ^\circ \text{F}) \quad . \quad (17)$$

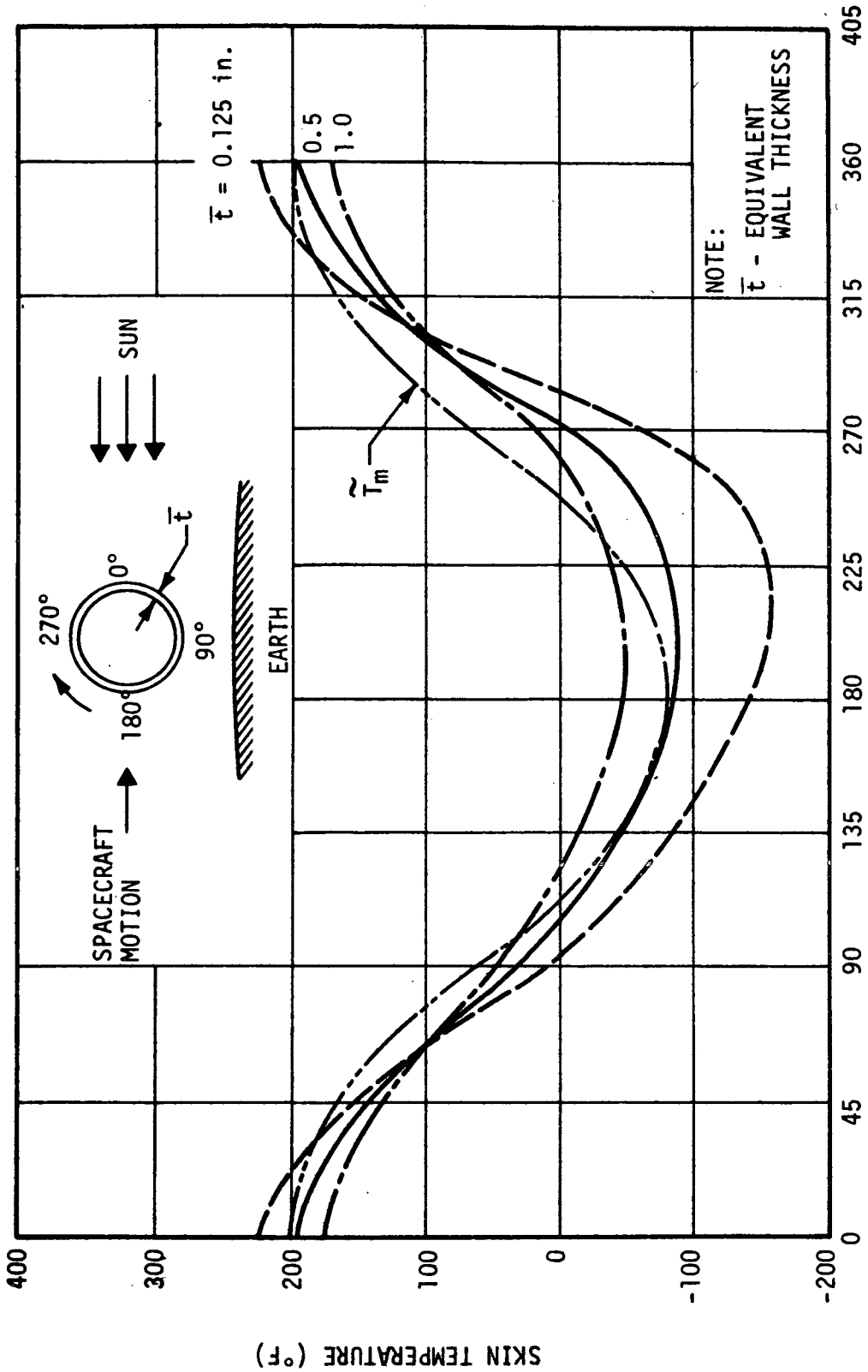


Figure V-15. Predicted temperature distribution on the spacecraft skin as a function of angular position on spacecraft,  $\theta$  (deg) of equivalent wall thickness (aluminum).

The mean skin temperature rise is then

$$T_m = \tilde{T}_m - T_{\text{room}} \quad , \quad (18)$$

or

$$T_m = T_0 + T_1 \cos \theta \quad , \quad (19)$$

where  $T_0 = -8^\circ\text{F}$ ,  $T_1 = 140^\circ\text{F}$ , with the room temperature being  $68^\circ\text{F}$ . Equation (19) represents a temperature rise of  $132^\circ\text{F}$  on the sun side and a temperature drop of  $148^\circ\text{F}$  on the side opposite the sun, or a total difference of  $280^\circ\text{F}$ .

4. Boundary Conditions. The longitudinal displacements on the sun side and the side opposite the sun should be equal and opposite in direction at the stations where the ball joint and the lateral linkages are located. These two conditions can be written in the following mathematical forms:

$$u(\xi = 0, \theta = 0) = -u(\xi = 0, \theta = \pi) \quad , \quad (20)$$

$$u(\xi = L_2/r, \theta = 0) = -u(\xi = L_2/r, \theta = \pi) \quad . \quad (21)$$

The stiff internal frames to which the ball joint is mounted will prevent relative movement between the ball joint and the spacecraft shell. Therefore, the normal displacement of the shell,  $w$ , should be zero, i. e. ,

$$w(\xi = 0, \theta) = 0 \quad .$$

The linkages connecting the aft end of the LA telescope and the spacecraft structure are pivoted to prevent bending in the telescope tubes. A ring frame in the shell at this location will prevent circumferential deflection of the shell. Therefore, the  $v$  deflection component should be zero, i. e. ,

$$v(\xi = L_2/r, \theta) = 0 \quad . \quad (23)$$

At the free end of the spacecraft structure,  $\xi = L_1/r$ , the total bending moment and transverse shear should vanish; i. e. ,

$$\int_0^{2\pi} N_s(r \cos \theta) (r d\theta) = 0 \quad (24)$$

$$Q_s(\xi = L_1/r, \theta) = 0 \quad , \quad (25)$$

where  $N_s$  is the in-plane force in the direction of the s-axis and  $Q_s$  is the transverse shear on the plane normal to the s-axis.  $N_s$  and  $Q_s$  can be represented in terms of the deflection components  $u$ ,  $v$ , and  $w$  as follows [V-3 or V-4]:

$$N_s = \frac{Et}{1 - \nu^2} \left[ \frac{1}{r} \frac{\partial u}{\partial \xi} + \frac{\nu}{r} \left( \frac{\partial v}{\partial \theta} - w \right) - \alpha(1 + \nu) T_m \right] \quad , \quad (26)$$

$$Q_s = \frac{Et^3}{12(1 - \nu^2)} \left[ \frac{1}{r^3} \frac{\partial^3 w}{\partial \xi^3} + \frac{1}{r^3} \frac{\partial^3 w}{\partial \xi \partial \theta^2} + \frac{1}{r^3} \left( \frac{1 + \nu}{2} \right) \frac{\partial^2 v}{\partial \xi \partial \theta} \right] \quad . \quad (27)$$

Substitution of equations (26) and (27) into equations (24) and (25) and substitution of equations (14), (15), and (16) into equations (20) through (25) yields a set of six coupled, ordinary differential equations of  $C_1$ ,  $C_2$ ,  $C_3$ , and  $C_4$ , with  $\theta$  as the single variable.

5. Solutions. Solutions of  $C_1$ ,  $C_2$ ,  $C_3$ , and  $C_4$  of the following forms satisfy the differential equations:

$$C_1 = \sum_{n=0}^{\infty} \bar{C}_{1n} \cos n\theta \quad , \quad (28)$$

$$C_2 = \sum_{n=0}^{\infty} \bar{C}_{2n} \cos n\theta \quad , \quad (29)$$

$$C_3 = \sum_{n=0}^{\infty} \bar{C}_{3n} \cos n\theta \quad , \quad (30)$$

$$C_4 = \sum_{n=0}^{\infty} \bar{C}_{4n} \sin n\theta \quad . \quad (31)$$

Substitution of equations (28) through (31) into the six ordinary differential equations corresponding to equations (20) through (25) yields the following set of seven algebraic equations:

$$\bar{C}_{31} + \bar{C}_{30} = -(-\bar{C}_{31} + \bar{C}_{30}) \quad , \quad (32)$$

$$\nu \bar{C}_{20} - r \alpha (1 + \nu) T_0 = 0 \quad , \quad (33)$$

$$\nu \bar{C}_{21} - \bar{C}_{41} - r \alpha (1 + \nu) T_1 = 0 \quad , \quad (34)$$

$$\left( \frac{L_2}{r} \right) \bar{C}_{10} + \bar{C}_{20} = 0 \quad , \quad (35)$$

$$\frac{2L_1}{r} \bar{C}_{11} + \bar{C}_{21} - \alpha r T_1 = 0 \quad , \quad (36)$$

$$\left[ \left( \frac{L_1}{r} \right)^2 - 4 \right] \bar{C}_{11} + \left( \frac{L_1}{r} \right) \bar{C}_{21} + \bar{C}_{31} = 0 \quad , \quad (37)$$

$$\frac{1}{3} \left( \frac{L_2}{r} \right)^3 \bar{C}_{11} + \frac{1}{2} \left( \frac{L_2}{r} \right)^2 \bar{C}_{21} + \left( \frac{L_2}{r} \right) \bar{C}_{31} - \bar{C}_{41} = 0 \quad . \quad (38)$$

These seven equations involve only those coefficients, in equations (28) through (31), for  $n = 0$  and  $1$ . The coefficients for  $n > 1$  are zero, since the temperature terms of the differential equations involve only terms of  $n = 0$  and  $1$ .

Equations (32) through (38) are used to solve for the unknown coefficients as follows:

$$\bar{C}_{30} = 0 \quad , \quad (39)$$

$$\bar{C}_{20} = \frac{r(1 + \nu)}{\nu} \alpha T_0 \quad , \quad (40)$$

$$\bar{C}_{10} = - \frac{r^2(1 + \nu)}{\nu L_2} \alpha T_0 \quad , \quad (41)$$

$$\bar{C}_{11} = \frac{r}{2L_1} (\alpha r T_1 - \bar{C}_{21}) \quad , \quad (42)$$

$$\bar{C}_{41} = \nu \bar{C}_{21} - r(1 + \nu) \alpha T_1 \quad , \quad (43)$$

$$\bar{C}_{31} = -\frac{1}{2L_1} [(L_1^2 - 4r^2) \alpha r T_1 + (L_1^2 + 4r^2) \bar{C}_{21}] \quad , \quad (44)$$

$$\bar{C}_{21} = \left[ \frac{L_2^3 - 3L_2(L_1^2 - 4r^2) + 6r^2 L_1(1 + \nu)}{L_2^3 - 3L_1 L_2^2 + 6r^2 \nu L_1 + 3L_2(L_1^2 + 4r^2)} \right] r \alpha T \quad . \quad (45)$$

Once these coefficients are computed,  $C_1$ ,  $C_2$ ,  $C_3$ , and  $C_4$  are known and, thus, the deflections,  $u$ ,  $v$ , and  $w$  at every point of the shell can be computed. A computer program was written to compute these deflections.

6. Results of Analysis. The deflections  $u$ ,  $v$ , and  $w$  are computed for various longitudinal stations at  $\theta = 0, 45, 90, 135$ , and  $180$  degrees. The material considered is 6061 aluminum alloy with the thermal expansion coefficient of  $14.1 \times 10^{-6}$  in./in. °F. The longitudinal extension ( $u$ ) and the lateral deflection ( $w$ ) for the elemental surface that faces the sun and that is directly away from the sun ( $\theta = 0$  and  $\theta = 180$  degrees, respectively) are plotted in Figure V-16. The telescope support frame rotation about the ball joint is found to be  $1.295 \times 10^{-3}$  radians (4.452 arc minutes). There is also a rotation in the opposite direction caused by the movement of the telescope linkage which causes the tubes to be pulled away from sun side by an average of 0.108 inch. This corresponds to a rotation of 1.467 arc minutes about the ball joint. Since the two rotations are in opposite directions, their effects are additive; therefore, the total angle change between the telescope pointing axis and the spacecraft longitudinal axis is 5.919 arc minutes.

The maximum radial deflection is found to be 0.24 inch at the forward free end. Between the ball joint and the lower linkages, the largest radial deflection is 0.126 inch.

This analysis was completed before the spacecraft's baseline thermal design was established. The baseline thermal design has insulation on the outside which greatly reduces the temperature differentials across the spacecraft. The deflections computed in this analysis can be ratioed with respect to the later-calculated temperature differentials to obtain more meaningful values.

The impact of the much lower temperature differentials will be discussed in Section L.

## I. Evaluation of Methods for Relieving Thermal Bending of Telescope Tubes Mounted Without Ball Joint

The baseline structural design of the HEAO-C spacecraft includes two ball and socket joints supporting the three X-ray telescopes. The ball joints are attached to a shock mount, which in turn is supported by the telescope support frame near the viewing end of the spacecraft. The other attachment between the telescopes and the spacecraft structure is the frame linkage located near the opposite end of the spacecraft. This arrangement will allow the spacecraft structure to deflect without bending the telescope tubes.

FOLDOUT FRAME 2

FOLDOUT FRAME 1

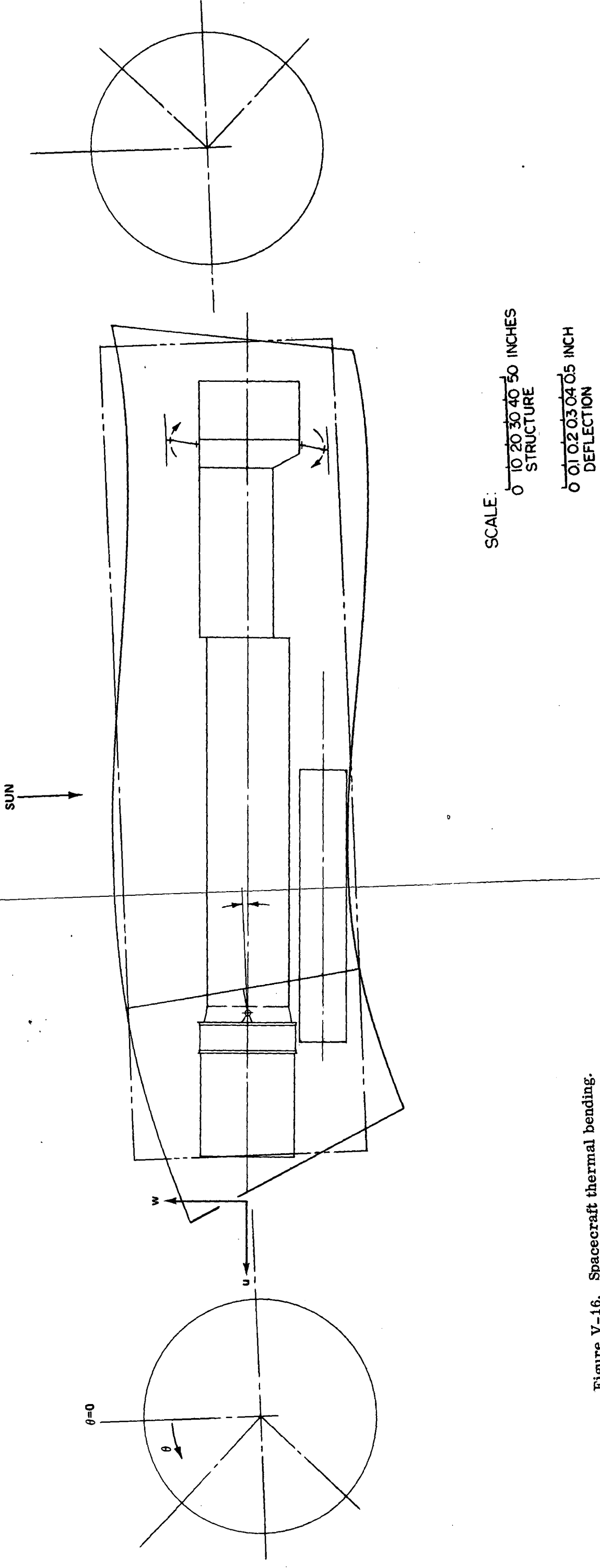


Figure V-16. Spacecraft thermal bending.

The major feature of all alternatives to the baseline mounting concept is the elimination of the ball joints between the oval frame and the telescope support frame. Since this is such an elementary consideration, it shall be considered as a basic analysis and will be discussed in this portion of the report.

Without ball and socket joints, thermal bending of the spacecraft would induce bending in the telescope tubes through the frame linkage connections between the spacecraft structure and the detector support structure. The bending of the telescope tubes would produce a relative lateral deflection between the mirrors and the detectors.

1. Relative Bending Stiffnesses. The bending stiffness of the spacecraft structure is  $325 \times 10^9$  lb-in.<sup>2</sup>, as shown in Figure V-7. The structural concept of the telescope tubes is a monocoque cylinder made of graphite/epoxy composite, and the bending stiffness of the tubes (EI) is approximated by

$$EI = E \cdot \pi R^3 t \quad , \quad (46)$$

where E is the modulus of elasticity, lb/in.<sup>2</sup>; R is the radius of the tube cylinder, in.; and t is the thickness of the tube cylinder, in.

The radius of the cylinder was assumed to be 21.0 inches, and for a 0.032 inch thick graphite/epoxy cylinder,  $EI = 16.758 \times 10^9$  lb-in.<sup>2</sup>. A direct comparison of bending stiffnesses of the graphite/epoxy cylinder to the spacecraft structure stiffness reveals that the spacecraft bending stiffness is about 20 times that of the telescope tubes; therefore, thermal bending of the spacecraft structure would not be reduced by the combined effects of the telescope tubes.

In the baseline configuration with the ball joints, the total angle change at the joint between the telescope support frame and the telescope axis induced by the thermal bending of the spacecraft is computed to be 5.919 arc minutes, or  $1.722 \times 10^{-3}$  radian, as given in a previous section. If the telescope tubes are mounted rigidly to the frame, without the ball joint, as they are in the alternate designs, they will deform this total angle since they are not stiff enough to react the spacecraft structure deformation.

Considering a telescope tube length of 250 inches, the relative lateral deflection is 0.431 inch, which is based on a temperature differential of 280° F. This deflection is an order of magnitude larger the maximum allowable deflection of 0.02 inch. At this point, a preliminary conclusion can be drawn that a hard mount concept is not feasible without an effective thermal control system to lower the temperature differential to a value much lower than 280° F.

2. Maximum Allowable Differential Temperature. Computation of the structural temperature distribution for the thermal control approach of insulating the outside of the spacecraft is tedious and the results were not available for inclusion in this report. However, by estimating the maximum allowable differential temperature across the spacecraft and judging the feasibility of designing a system to control the temperature difference, a conclusion can be drawn on the concept feasibility.

The relative lateral deflection of the telescope tube of 0.431 inch was computed for a spacecraft differential temperature of 280°F and this deflection does not represent an angular rotation of the shock mount (i. e., the analysis considers the shock mount rigid). The approximate thermally induced deflection per degree Fahrenheit therefore is  $1.529 \times 10^{-3}$  inch. The maximum allowable deflection is 0.02 inch; therefore, the maximum allowable differential temperature is 13.5°F.

3. Estimate of the Natural Frequency of the Telescope Tube Mounted Without Ball Joint. The frame links at the lower end of the telescope tubes are designed to maintain lateral stability during the launch phase; but, if the telescopes were mounted without the ball joint, the links can be disconnected by mechanical or explosive means after the spacecraft is injected into orbit. Then, the thermal bending of the spacecraft structure would not introduce bending in the telescope tubes.

When the links are disconnected, the telescope tube behaves like a cantilever beam with a large mass at the free end. The mass is approximately 600 lb for the high resolution telescope. The equivalent spring constant, K, is

$$K = (3 EI)/(L^3) \quad , \quad (47)$$

where EI is the bending stiffness of a tube and is computed to be  $16.758 \times 10^9$  lb-in.<sup>2</sup> for graphite/epoxy construction, and L, the length of the tube, is about 250 inches. The fundamental natural frequency of the cantilever is then estimated to be

$$f_n = \frac{1}{2\pi} \left( \frac{3 EI}{m L^3} \right)^{1/2} \quad , \quad (48)$$

or

$$f_n = \frac{1}{2\pi} \left( \frac{3 \times 15.129 \times 10^9}{\frac{600}{32.2 \times 12} \times 250} \right)^{1/2} = 6.88 \text{ cps} \quad . \quad (48a)$$

The control frequency for spacecraft slewing or pointing is much less than this value; therefore, there should be no resonance.

4. Effect of Shock Mount Deformation. When the spacecraft is not insulated from the outside environment, the telescope bending would produce a relative deflection of 0.431 inch, if the tubes are hard-mounted at the top, with linkage at the bottom. The transverse force exerted on two tubes is approximately

$$F = 0.431 \times \frac{3EI}{L^3} \times 2 \quad , \quad (49)$$

or

$$F = 2500 \text{ pounds.} \quad (49a)$$

The stiffness of the rubber proposed for use in the shock mounts is about 256 lb/in.<sup>2</sup>/in. For an 18 inch square pad, the equivalent spring constant is 83 000 lb/in. The rubber pads are located about 42 inches apart. The equivalent rotational spring constant is then  $K_{\text{pads}} = 73.206 \times 10^6 \text{ in. -lb/radian.}$

The equivalent rotational spring constant of two tubes is  $2 \times (3EI/L)$ , or,  $K_{\text{tubes}} = 363.0 \times 10^6 \text{ in. -lb/radian.}$  The rotations taken by the rubber mounts and the tubes are distributed according to their angular flexibilities, which are defined as the reciprocals of their angular stiffnesses. Therefore, the angle change (bending) of the tubes for a temperature difference of 280° F is

$$\theta_{\text{tube}} = \theta_{\text{total}} \times \frac{\frac{1}{K_{\text{tubes}}}}{\frac{1}{K_{\text{tubes}}} + \frac{1}{K_{\text{pads}}}} \quad ; \quad (50)$$

or

$$\theta_{\text{tube}} = \theta_{\text{total}} \times \frac{K_{\text{pads}}}{K_{\text{pads}} + K_{\text{tubes}}} \quad , \quad (50a)$$

where  $\theta_{\text{tube}}$  is the angle change of the tubes;  $\theta_{\text{total}}$  is the total spacecraft angle change due to thermal bending, which is  $1.722 \times 10^{-3}$  radian;  $K_{\text{tubes}}$  is the angular spring constant of tubes; and  $K_{\text{pads}}$  is the equivalent angular spring constant of pads;

or

$$\begin{aligned}\theta_{\text{tube}} &= 1.722 \times 10^{-3} \times \frac{73.206 \times 10^6}{73.206 \times 10^6 + 363.0 \times 10^6} \\ &= 0.289 \times 10^{-3} \text{ radian} \quad .\end{aligned}\tag{50b}$$

The lateral tube deflection  $\Delta_{\text{tube}}$  is then

$$\Delta_{\text{tube}} = \theta_{\text{tube}} \times L_{\text{tube}} \quad ,\tag{51}$$

where  $L_{\text{tube}}$  is the tube length, i. e. , 250 inches, or

$$\Delta_{\text{tube}} = 0.289 \times 10^{-3} \times 250 = 72.25 \times 10^{-3} \text{ inch} \quad ,\tag{52}$$

which is still several times the maximum allowable deflection, 0.02 inch. If the thermal insulation around the spacecraft can reduce the maximum differential temperature to within 77° F, the lateral tube deflection can be reduced to 0.02 inch., the maximum tolerance. Tube deflection could also be reduced by increasing the tube thicknesses.

## J. Solar Cell Substrate Analysis

A structural analysis of the HEAO-C solar panel substrate was made to insure that the panel has adequate stiffness.

The solar cell panels are subjected to the random and sinusoidal excitation during launch, as shown in Table V-7, as well as the primary launch loads shown in Table V-1. It is important to know the response of the panel to these loads since large panel deflections can damage the solar cells.

The structure analyzed was a 38.2 inch wide, 120 inch long rectangular honeycomb panel, 0.700 inch thick, with 0.010 inch thick 7075-T6 aluminum alloy facing sheets, and 2.3 lb/ft<sup>3</sup> 5052 aluminum alloy core with 0.25 inch cell size.

Four hinges are equally spaced along the length of the panel, as shown schematically in Figure V-17. The forward hinge takes load in all directions while the remaining hinges take normal and transverse load only. Five snubbers are equally spaced along the other longitudinal edge. The snubbers are designed to take loads in a direction normal to the panel, only; they also incorporate the array release mechanism.

TABLE V-7. HEAO-C SOLAR PANEL VIBRATION ENVIRONMENT

Randon Vibration (all axes)	
20 to 150 Hz	+3 dB/oct increase
105 to 300 Hz	0.15 g <sup>2</sup> /Hz
300 to 1000 Hz	-3 dB/oct decrease
1000 Hz	0.045 g <sup>2</sup> /Hz
1000 to 2000 Hz	-9 dB/oct decrease
10.3 g overall	
Sinusoidal Vibration (all axes)	
1.0 to 3.2 Hz	3.0 in. DA
3.2 to 10 Hz	1.5 g
10 to 18 Hz	0.3 in. DA
18 to 50 Hz	3.0 g

A load of  $67.0 \times 10^{-4}$  psi of panel surface was applied to the panel. This load represents the total weight of the solar cells, cover slides, micaplies, adhesives, and paints that make up the solar cell module assemblies.

With this load input and an acceleration of 6.0 g longitudinal and 1.5 g lateral, the static analysis yields the limit load reactions at the various hinge and snubber points, as shown in Table V-8.

The deflection associated with this loading condition is maximum at a point that is 6.4 inches off the longitudinal centerline of the panel toward the hinges and is midway between the end and adjacent hinge. The displacement of this point is 0.013 inch and the stress in the facing sheets is about 1000 psi.

The natural frequencies and mode shapes were calculated for the panel to determine the effectiveness of the support/hinge point locations and to better predict the frequencies where significant displacement can occur when the panel is excited with external forces.

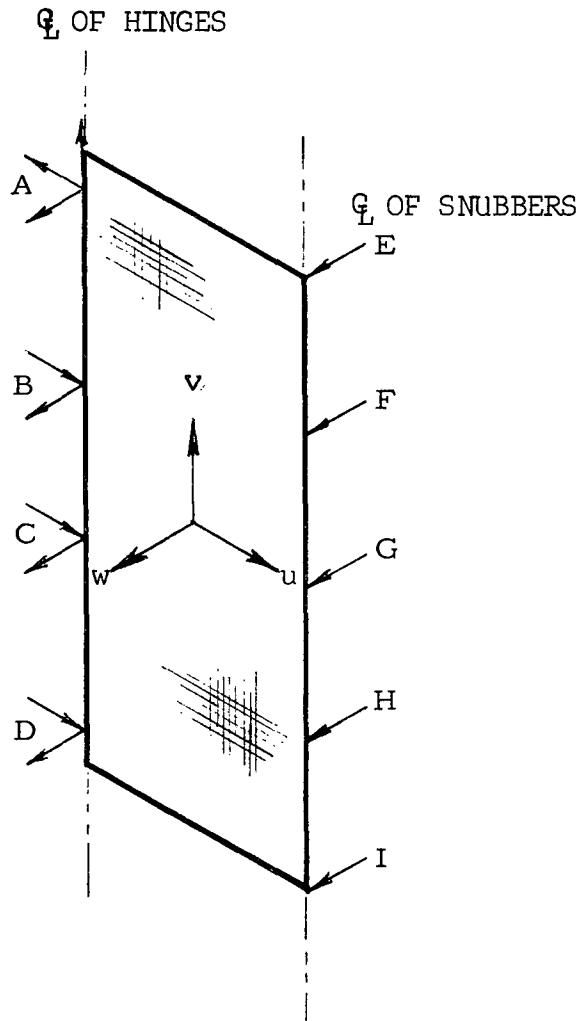


Figure V-17. Schematic of panel support points.

The first three natural frequencies of the panel are as follows:

Mode 1            38 Hz

Mode 2            40 Hz

Mode 3            45 Hz

Scale plots of the normal mode shapes corresponding to the natural frequencies are shown in Figures V-18, V-19, and V-20. These displacements are normalized to the maximum displacement of the system.

TABLE V-8. PANEL SUPPORT POINT REACTIONS

Support Point	Component Direction (u, v, w)	Load (lb)
A	-u	84.60
	+v	226.07
	+w	7.10
B	+u	56.76
	+w	2.05
C	+u	24.62
	+w	7.05
D	+u	3.22
	+w	7.10
E	+w	3.00
F	+w	7.83
G	+w	6.59
H	+w	7.83
I	+w	3.00

### K. Meteoroid Protection Analysis

The HEAO-C spacecraft will be exposed to near-earth meteoroid environment during its orbital lifetime and must be protected from damage so that mission reliability will be maintained at a high level. The spacecraft meteoroid protection requirement was determined by a method that relates the ballistic limit of the protection material to the exposed spacecraft surface area, exposure time, and desired probability of no penetration. A dual-wall meteoroid shield consisting of a relatively thin outer skin and a heavier

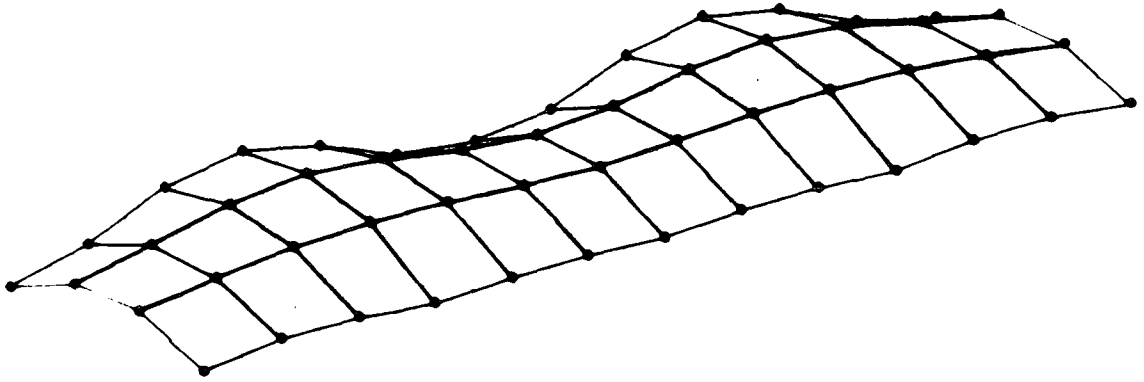


Figure V-18. Modal deformation, natural frequency — 38 Hz.

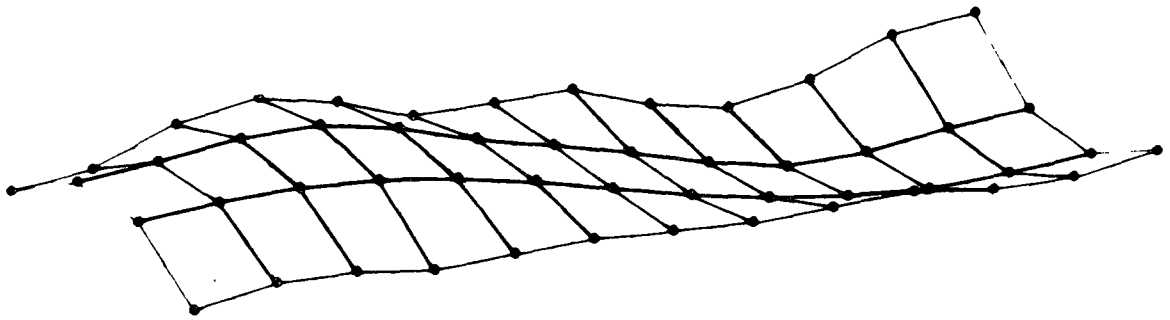


Figure V-19. Modal deformation, natural frequency — 40 Hz.

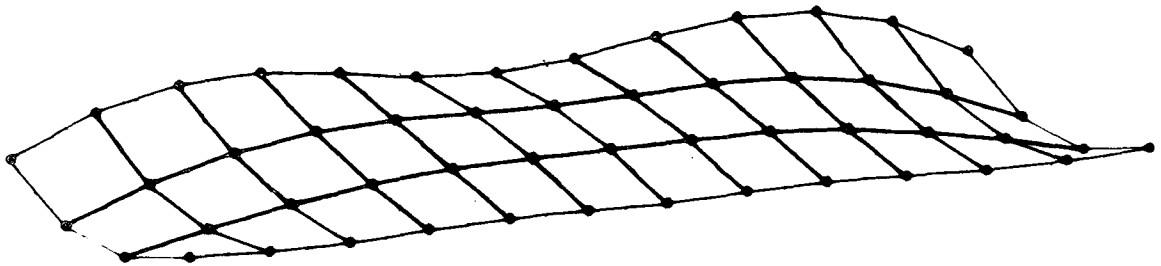


Figure V-20. Modal deformation, natural frequency — 45 Hz.

backup sheet is the most weight-effective type of system and is employed in the analysis. The function of the outer skin is to break the incoming meteoroid into small particles and the second or backup sheet provides the resistance to penetration by the debris.

The structural skin of the spacecraft, which is 0.050 inch thick, serves as the outer meteoroid protection sheet and the backup sheet will be provided by the covers for particular instruments and components, experiment structure, or separate shield when required.

Figure V-21 gives the backup sheet thickness requirements for 0.98 and 0.99 probability of no penetration as a function of the distance from the spacecraft skin. This requirement is based on a lifetime of two years in a 270 n. mi. orbit. The external thermal insulation on the spacecraft was not considered in the analysis, but would certainly provide additional protection. The cutoff of the curves represents the height of the internal stiffeners on the spacecraft skin and is, therefore, the closest the backup sheet can be placed to the outer skin.

The thickness requirement should be considered conservative since it is based on the total spacecraft surface area and not on the area of a particular component to be protected. It is believed, however, that most of the internal structure (covers, etc.) will be about 0.050 inch thick, or will be further from the spacecraft skin than 3 inches; therefore, the components will have an adequate probability of no penetration for the mission.

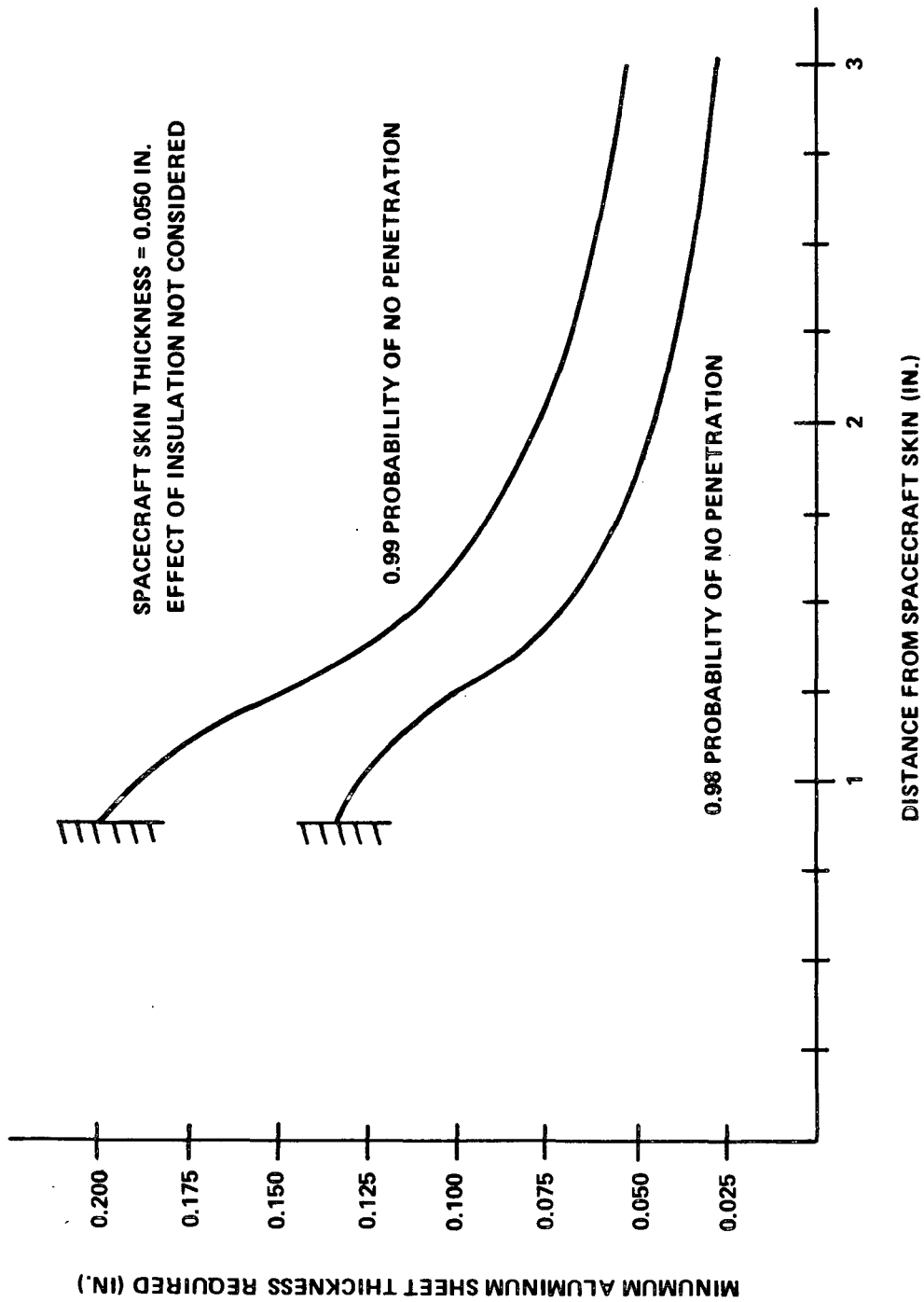


Figure V-21. Component meteoroid protection thickness requirements.

## L. Conclusions and Recommendations

The structural configuration discussed herein satisfies all the structural requirements and is an efficient, lightweight design. From the analysis, it can be concluded that a ball joint configuration is necessary if the expected temperature across the spacecraft were in the order of 280° F; however, it is also shown that the ball joint could be eliminated if the temperature differential could be held to 77° F and, if the shock mount is considered rigid in rotation, the allowable temperature differential would be 13.5° F.

As stated in Section H, the 280° F temperature differential is based on a spacecraft with internal insulation. The maximum calculated temperature differential for the baseline design, which has the insulation on the outside, is 2.5° F and a detailed discussion of this differential is given in Chapter VI.

It can be concluded, therefore, that the ball joint could be eliminated without detrimentally affecting the performance of the spacecraft.

For the HEAO-C Phase B study activities the following general tasks are recommended:

1. Reconfigure the baseline spacecraft without a ball joint and expand the thermal/structural analysis of the configuration.
2. Expand the dynamic analysis to determine the more detailed requirements of the shock mounts and other affected structure.
3. Optimize the structure for the more detailed requirements and perform stress and strain analysis for the detail parts and subassemblies.
4. Determine the detail physical characteristics of the materials proposed to be used.

## REFERENCES

- V-1. Roark, R. J. : Formulas for Stress and Strain. McGraw-Hill Book Company, Inc. , New York, 1954.
- V-2. Snowden, J. C. : Vibration of Damped Mechanical Systems. John Wiley & Sons, 1969.
- V-3. Wang, C. T. : Applied Elasticity, McGraw-Hill Book Company, 1953.
- V-4. Timoshenko, S. and Woinowky-Krieger, S. : Theory of Plates and Shells. McGraw-Hill Book Company, 1969 (Second Edition).

PRECEDING PAGE BLANK NOT FILMED  
TABLE OF CONTENTS

	Page
A. Introduction . . . . .	VI- 1
B. Requirements . . . . .	VI- 1
C. Thermal Control Approach . . . . .	VI- 2
D. Discussion of Requirements . . . . .	VI- 8
1. Telescope Tubes and Observatory Structure . . . . .	VI- 8
2. Subsystems and Solar Arrays . . . . .	VI-10
3. Mirror Assembly Temperature Requirements . . . . .	VI-10
E. Assumptions . . . . .	VI-21
F. Analytical Methods and Results . . . . .	VI-26
1. Solar Array Temperature . . . . .	VI-28
2. Subsystems Temperature . . . . .	VI-32
3. Experiment Temperatures. . . . .	VI-36
a. High Resolution Telescope . . . . .	VI-36
b. Low Energy Telescope . . . . .	VI-38
c. Auxiliary Experiments and Detectors . . . . .	VI-40
4. Thermal Control System Weights . . . . .	VI-40
G. Summary and Recommendations . . . . .	VI-40
References . . . . .	VI-42

## LIST OF ILLUSTRATIONS

Figure	Title	Page
VI - 1.	HEAO-C thermal control system components .....	VI - 3
VI - 2.	Thermal control filter properties .....	VI - 5
VI - 3.	Thermally isolated subsystems compartment and CMG location .....	VI - 7
VI - 4.	HR telescope mirror optical design .....	VI-14
VI - 5.	Simplification of HR mirror optics to two equivalent frusta .....	VI-15
VI - 6.	Simplification of HR mirror optics to a single equivalent frustum .....	VI-16
VI - 7.	Displacement of HR telescope focal point due to radial expansion of the single equivalent frustum .....	VI-18
VI - 8.	Variation of HR telescope focal point displacement with mirror temperature change .....	VI-20
VI - 9.	Structural model assumed in the derivation of solar panel thermal properties .....	VI-24
VI-10.	Observatory and orbit orientations considered in the thermal analysis .....	VI-27
VI-11.	Solar array orbital temperature history for the hot orbit and Observatory perpendicular to earth-sun line .....	VI-29
VI-12.	Solar array orbital temperature history for the cold orbit and Observatory perpendicular to earth-sun line ....	VI-30
VI-13.	Maximum body mounted solar array temperature as a function of solar cell packing density .....	VI-31

## LIST OF ILLUSTRATIONS (CONCLUDED)

Figure	Title	Page
VI-14.	Solar array orbital temperature history for the hot orbit and Observatory inclined 30 degrees toward the sun.....	VI-33
VI-15.	Subsystems compartment average orbital temperature versus external surface emmissivity .....	VI-35
VI-16.	HR telescope temperature with no heater power applied.....	VI-37
VI-17.	LE telescope temperature with no heater power applied.....	VI-39

## LIST OF TABLES

Table	Title	Page
VI-1 .	Subsystems Compartment Components Average Power Dissipations and Temperature Limits .....	VI-11
VI-2 .	Average Power Dissipations and Temperature Limits For Components Not Contained By Subsystems Compartment .....	VI-12
VI-3.	Thermal Control System Component Weights .....	VI-40

## CHAPTER VI. THERMAL CONTROL SYSTEM

### A. Introduction

The HEAO-C thermal control system must provide a limited, predictable and stable thermal environment for the spacecraft structure, experiments and subsystems. While in orbit the HEAO-C will receive energy from three sources: the sun, earth, and its own internal energy dissipators. The function of the thermal control system is to exploit and manage this energy to the satisfaction of the imposed requirements.

Except for thermostatically controlled redundant heaters on the X-ray telescope mirror assemblies, the HEAO-C thermal control system is essentially passive. Judicious use is made of thermal control coatings, multilayer super-insulation, and thermally attractive materials. There is a considerable amount of flexibility and potential for growth.

### B. Requirements

The requirements imposed on the thermal control system by the X-ray experiments are as follows:

- Limit the thermally induced displacement of the detectors at the high resolution (HR) telescope focal plane to  $\pm 0.002$  inch axially and  $\pm 0.02$  inch transversely;<sup>1</sup>
- Limit the thermally induced displacement of the detectors at the large area (LA) telescope focal plane to  $\pm 0.02$  inch axially and transversely;<sup>2</sup>

---

1. The maximum allowable axial and transverse deflections are  $\pm 0.004$  inch and  $\pm 0.04$  inch, respectively, for the HR telescope and  $\pm 0.04$  inch for the LA telescope. It was assumed that half of these deflections could be allowed for thermal deformation.

2. *ibid.*

- Maintain the HR and LA telescope mirror assembly temperatures to within  $\pm 5^{\circ}\text{F}$  transversely and  $\pm 2.5^{\circ}\text{F}$  axially from the nominal design operating temperature;<sup>3</sup>
- Maintain the low energy (LE) telescope temperature to within the  $50^{\circ}\text{F}$  to  $68^{\circ}\text{F}$  temperature band;<sup>4</sup>
- Design the thermal control system for optimum contribution to the maintenance of the telescope co-alignment requirement of  $\pm 1.0$  arc minute.

In addition, the solar arrays must be maintained at a temperature below  $212^{\circ}\text{F}$ .

### C. Thermal Control Approach

The Observatory's thermal control system consists of multilayer superinsulation on the telescope tubes and mirror assemblies and surrounding most of the external structure, thermostatically controlled heaters on the mirror assemblies, a thermal control filter over the aperture end, graphite/epoxy as the telescope tube material, a thermally independent subsystems compartment, Alzak external skin, thermal control coatings, and a sun shade. Analyses of alternate configurations and trade studies which support the baseline configuration are contained in Appendix D.

Figure VI-1 is an isometric drawing of the Observatory which shows the baseline thermal control system features. The Observatory structure is insulated externally by 0.5 inch of multilayer superinsulation. This effectively eliminates all transient orbital effects and yields a thermally stable structure and experiment complement. The telescope mirror assemblies and tubes are also insulated to provide additional stability. A sun shade is employed to protect the telescopes and other experiments and sensors from the intense solar radiation when the viewing end of the Observatory is inclined toward the sun. The sun shade is of laminar construction with 0.25 inch of fibrous

---

3. These limitations are prescribed by the Principal Investigators (PIs) [VI-1].

4. *ibid.*

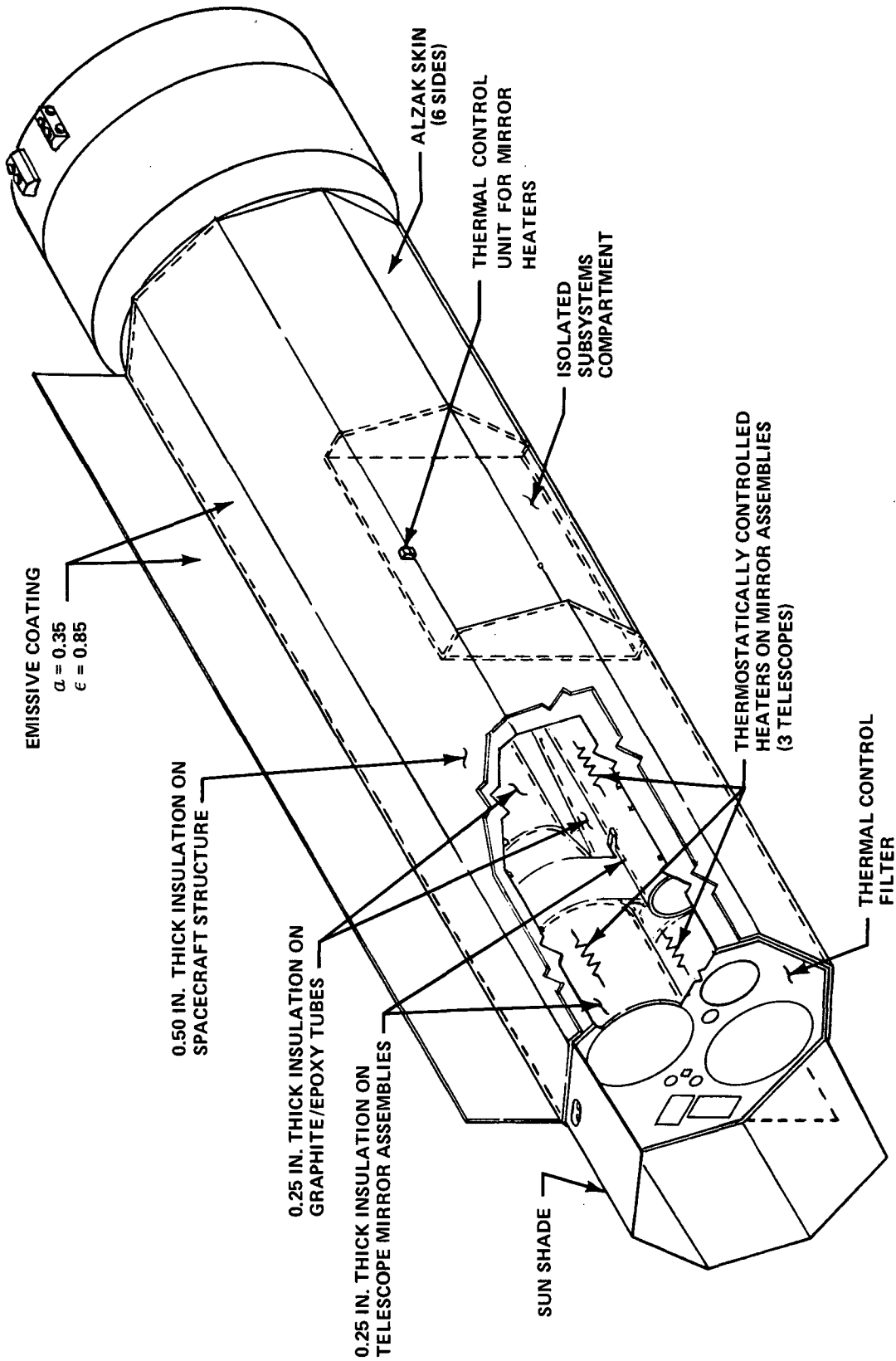


Figure VI-1. HEAO-C thermal control system components.

insulation sandwiched between two aluminum sheets with proper surface properties and is designed for a 30 degree tilt of the Observatory toward the sun with a coincidental  $\pm 15$  degree roll maneuver. The laminar composite material graphite/epoxy has been chosen for the two large telescope tubes. The thermal expansion properties of graphite/epoxy make it extremely attractive for this application. It has been shown that this material is technically and economically feasible for use in the telescope tubes and, in fact, presents the least complex overall Observatory design, compared with the other candidate materials (see Appendix D, Section 1). For example, it is nonmagnetic and, therefore, does not present the control problems associated with Invar, the iron-nickel alloy, and its extremely low thermal expansion coefficient overcomes the complex alignment problems associated with the use of aluminum. Composite material technology is progressing rapidly but some development may be necessary. Additional cost incurred is considered negligible since the use of another material would complicate the thermal control and other subsystems. Graphite/epoxy is currently being used in both spacecraft and aircraft construction and is being considered for use as the substrate for the X-ray mirrors.

Figure VI-2 illustrates the features of the thermal control filter. The thermal analyses have shown that an absorptivity of 0.35 and an emissivity of 0.27 on the alterable portion of the filter covering the HR telescope aperture (center circle) provides for the proper amount of energy dissipation from that telescope. The portion of the filter which transmits X-rays was assumed to possess the properties specified by the PIs [VI-1]. The remainder of the thermal control filter possesses a high emissivity, low absorptivity surface so that the LE telescope and auxiliary experiments and sensors are maintained at the proper temperature.

To further assure acceptable mirror assembly temperature level and gradient, thermostatically controlled heaters are applied to the three telescopes. The heaters are expected to require a relatively negligible amount of average power. Although this Phase A analysis does not encompass such detail, it is highly advisable to adjust the thermal control filter properties in such a way that during relatively hot orientations, the steady state average mirror assembly temperature is approximately equal to the nominal operating temperature, with the heater system designed to regulate mirror assembly temperature during operation in colder orientation. This will assure that the mirrors do not exceed their maximum allowable temperature.

The internal HR mirror assembly support was initially conceived as including the use of support plates at the front, middle, and rear of the mirrors

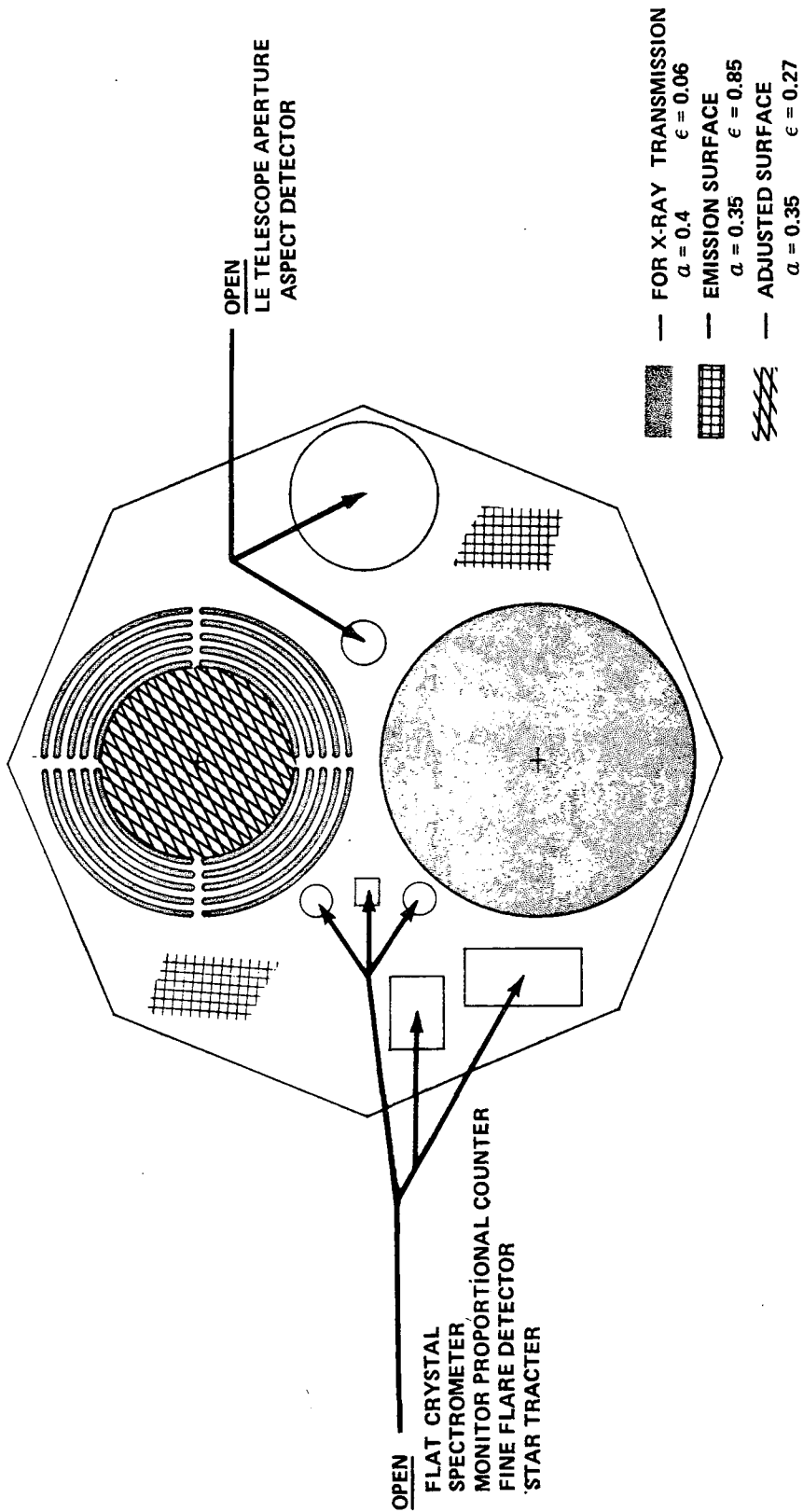


Figure VI-2. Thermal control filter properties.

(see Chapter II, Figure II-3). Since this concept greatly restricts the amount of energy to be dissipated from the aperture end of the Observatory and would tend to create larger temperature gradients, the support plates were replaced by struts. It was assumed that the strut arrangement caused a 65 percent blockage of the central portion of the HR mirror assembly.

Most of the Observatory external surface is covered with a thin (0.020 inch) aluminum sheet (e. g. , Alzak). This surface adds to the micrometeoroid protection scheme, protects the fragile external insulation during transportation and handling, and can be coated to satisfy particular thermal control requirements (e. g. , solar arrays and subsystems).

Thermal control of the subsystems electronics is aided by the availability of volume and thermally stable external surface of the antisolar side of the Observatory. A thermally isolated subsystems compartment is employed to house most of the electrical power system (EPS) and the communication and data handling (C&DH) system components which are mounted to the inboard side of the compartment (Fig. VI-3). The temperature of these components is adjusted by altering the emissivity of the external surface of the compartment. This approach provides for easy maintainability and low cost flexibility. It is thermally attractive since a relatively large number of items, possessing similar thermal control requirements, are controlled as a unit and the potentially complex interaction between subsystems electronics and experiments is avoided. The thermal stability of the antisolar side of the Observatory is also utilized in the thermal control of the control moment gyros (CMG) and related electronics and in the dissipation of excess energy from the X-ray detectors. The CMGs and CMG electronics are mounted directly to the spacecraft structure and are maintained within the allowable temperature band while allowing energy to be transferred from the experiment detectors to the external surface of the Observatory. The thermophysical properties of the external surface adjacent to the above-mentioned components can be easily altered to provide reliable temperature control for both the components and the detectors. With the Alzak skin as the outer surface of the subsystems compartment, the emissivity is 0.75 and can be reduced to the proper value by applying low emissivity tape.

Solar array passive thermal control is accomplished by specifying the nominal Observatory orientation as "corner to the sun," by selecting the solar cell packing density on the body mounted arrays to the satisfaction of both the

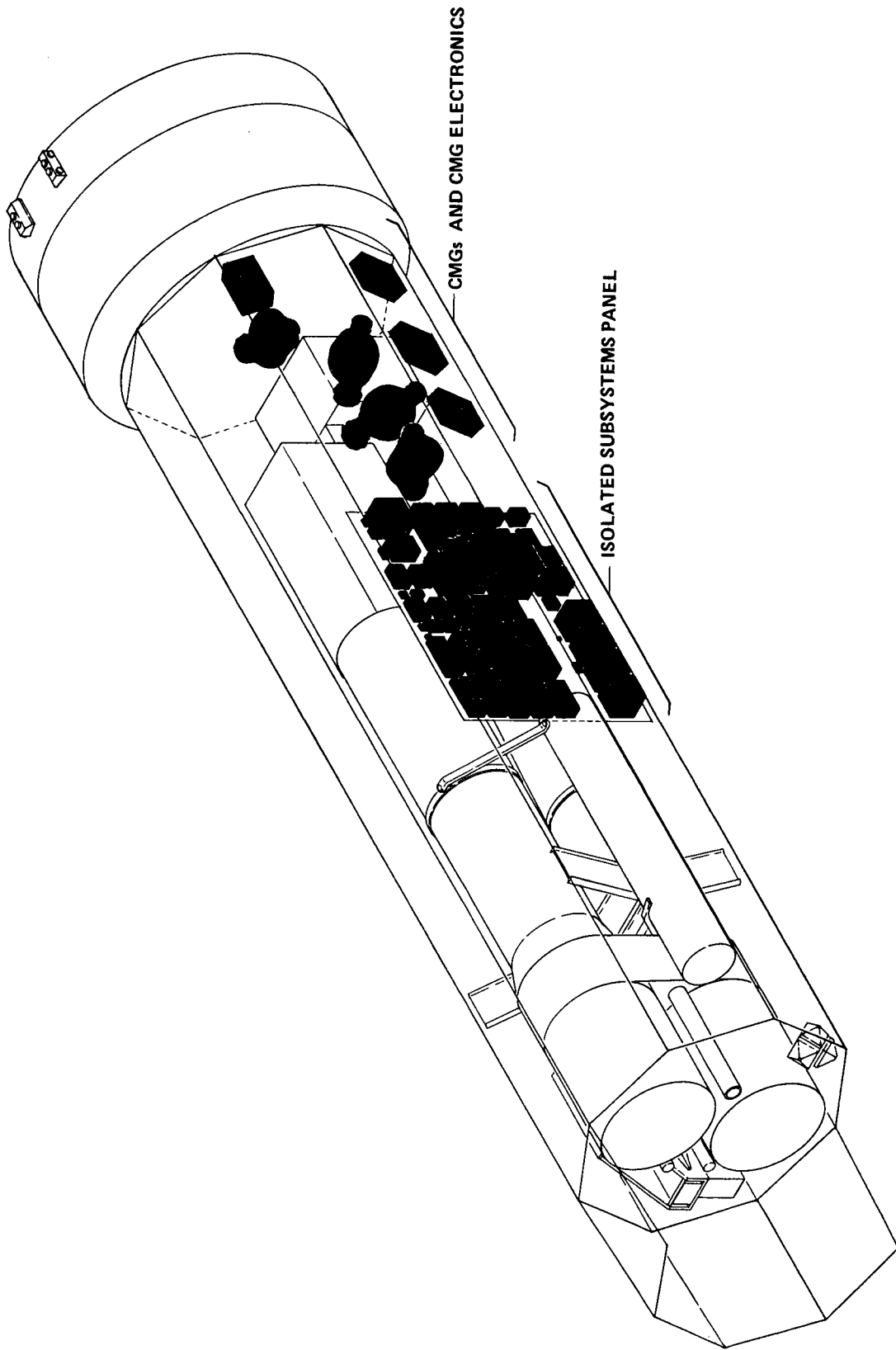


Figure VI-3. Thermally isolated subsystems compartment and CMG location.

thermal and power constraints and by properly coating the back sides of the foldout arrays and the adjacent spacecraft panels to allow for sufficient radiation from the foldout arrays. Trade studies associated with solar array thermal control are contained in Appendix D, Sections 3 and 4.

Although the Orbit Adjust Stage (OAS) is to remain attached to the Observatory throughout the mission, it was assumed for this Phase A Study that it would be thermally independent. That is, it was assumed that multilayer insulation separated the Observatory from the OAS. Reaction control system propellant tanks and thrusters, contained within the OAS, require thermal control. However, since the OAS is, relatively speaking, an off-the-shelf item, no analyses were conducted during the Phase A Study.

The thermal analysis did not include the prelaunch, launch and parking orbit phases of the mission. Results from the Phase B Studies of Missions A and B indicate little or no impact on the thermal control system.

## D. Discussion of Requirements

1. Telescope Tubes and Observatory Structure. The temperature limitations of the telescope tubes and Observatory structure are dictated by the above deflection limits (Section VI-B). For example, HR telescope mirror/detector alignment may be disturbed by mirror assembly thermal deformation and by expansion, contraction, and/or bending of the telescope tubes due to temperature gradients. With the mirror assembly allowable temperature limits specified, limits on the telescope tubes and Observatory structure temperature must be determined.

The most severe alignment requirement is the axial displacement limitation on the HR telescope detectors. Consequently, the maximum allowable deviation of the telescope tube temperature from the temperature at which alignment takes place is calculated from the relation.

$$\Delta T_m = \frac{\Delta L_f}{\alpha L_f} ,$$

where  $\Delta T_m$  is the mean change in tube temperature from alignment temperature;  $L_f$  is the focal length;  $\Delta L_f$  is the maximum allowable change in focal length; and  $\alpha$  is the coefficient of linear thermal expansion. For the HR telescope, the

following values are used:

$$L_f = 240 \text{ in. ,}$$

$$\Delta L_f = 0.002 \text{ in. ,}$$

$$\alpha = 0.06 \times 10^{-6} \frac{\text{in.}}{\text{in. } ^\circ\text{F}}$$

(typical coefficient of linear thermal expansion of graphite/epoxy).

This relation yields a maximum allowable deviation of the tube temperature from the alignment temperature of 138.9°F.

The maximum allowable transverse temperature difference of the telescope tubes was not determined because of the analysis complexity of the telescope tube/Observatory structure support scheme. However, since (1) there is a relatively broad limitation on transverse displacement, (2) the tubes are fabricated from the graphite/epoxy composite, and (3) a transverse temperature difference of less than 5°F can be expected (due to the insulation of the Observatory structure), it is assured that thermal bending of the telescope tubes is not significant. As a justification for this assumption, consider the bending of a solid bar due to transverse temperature gradient, calculated from the relation

$$\delta = \frac{\alpha L^2 \Delta T}{2D} ,$$

where  $\delta$  is the maximum deflection due to bending; L is the focal length;  $\Delta T$  is the transverse temperature difference; D is the diameter; and  $\alpha$  is the coefficient of linear thermal expansion.

Assuming that this relation can be used to estimate the HR telescope focal plane transverse deflection due to bending of the tube, the proper values are

$$L = 240 \text{ in.}$$

$$\Delta T = 5^\circ\text{F} ,$$

$$D = 40 \text{ in. , and}$$

$$\alpha = 0.06 \times 10^{-6} \frac{\text{in.}}{\text{in. } ^\circ\text{F}} ,$$

and, thereby,

$$\delta = 0.0002 \text{ in.}$$

For this simplified approach, then, the transverse deflection at the focal plane is 0.0002 inch when the temperature difference across the telescope tube is 5°F. This result justifies the assumption that thermal bending of the telescope tubes is not significant.

Since the Observatory structure is insulated externally and the telescope tubes are mounted by the ball joint/shock mount/link concept, a high degree of mechanical independence exists between the telescopes and the Observatory structure. Should the ball joint be removed, a transverse temperature difference of approximately 77°F can be tolerated on the structure (see Chapter V, Section 1). With the ball joint/shock mount/link concept, structural deformation has virtually no effect on telescope alignment.

2. Subsystems and Solar Arrays. The maximum allowable solar array temperature assumed for this Phase A Study is 212°F. This temperature limit is based on the use of Skylab Workshop type solar cell modules. The analyses of alternative solar array configurations (Appendix D, Section 3) assume Apollo Telescope Mount (ATM) type modules.

The temperature limitations of the subsystems components [EPS, attitude sensing and control system (AS&C) and C&DH system] and their average orbital power dissipations are listed in Table VI-1 for the components contained by the subsystems compartment and in Table VI-2 for the other components.

3. Mirror Assembly Temperature Requirements. An important function to be performed by the thermal control system is the maintenance of HR telescope alignment. Perhaps the most critical item in providing this alignment is the thermal control of the HR mirror assembly. Although not considered in detail in this Phase A Study, it may be possible to fabricate the HR telescope tube in such a way that its thermal expansion will compensate for mirror assembly thermal expansion with the net result being a zero (or negligibly small) movement of the focal point relative to the detectors. The use of graphite/epoxy as the tube material makes this possible although detailed knowledge of the movement of the focal point with mirror assembly temperature change is required. The thermal analyses documented herein are based on the assumption that the temperature and deflection limits specified by the PIs (Section VI-B) are representative and sufficiently

TABLE VI-1. SUBSYSTEMS COMPARTMENT COMPONENTS  
AVERAGE POWER DISSIPATIONS AND TEMPERATURE LIMITS

	Average Dissipation (W)	Temperature Limits (° F)
Batteries (6)	126.0	40 to 60
Regulators (4)	64.	-40 to 140
Chargers (8)	45.	-40 to 140
Power Control Assembly (2)	60.	-40 to 140
Experiment Integration Assembly	12.	-40 to 140
Computer and Processor (3)	65.	32 to 140
Transfer Assembly	0	32 to 140
Dual Transponder (2)	17.	32 to 130
Phase Shift Keyed (PSK) Demodulator (2)	0.8	32 to 130
Frequency Multiplexer (MUX)	2.	32 to 130
Tape Recorders (4)	30.	14 to 120
Tape Recorder Control (2)	1.	32 to 130
Pulsed Code Modulator (PCM) Encoder (2)	3.2	32 to 130
Format Generator (2)	2.0	32 to 130
Clock	14.	32 to 130
Command (CMD) Processor (2)	7.6	32 to 130
CMD Memory (2)	3.5	-22 to 140
Experiment Computer	10.0	32 to 140

TABLE VI-2. AVERAGE POWER DISSIPATIONS AND TEMPERATURE LIMITS FOR COMPONENTS NOT CONTAINED BY SUBSYSTEMS COMPARTMENT

	Average Dissipation (W)	Temperature Limits (° F)
HR Image Intensifier	13.5	14 to 86
HR Crystal Spectrometer	21.0	14 to 86
LA Position Sensitive Detector	14.5	14 to 86
Solid State Detector	2.0	14 to 86
LE Telescope Detector	24	50 to 68
Monitor Proportional Counter	9.0	14 to 86
Flat Crystal Spectrometer	17.0	14 to 86
Flare Detectors	40.0	14 to 86
Sun Sensor	1	-4 to 130
Aspect Detector <sup>a</sup>	14.0	
Wide Angle Sun Sensor (WASS)	0.	-120 to 130
WASS Electronics	0.4	-4 to 122
Digital Sun Sensor	0.	-4 to 130
Fixed Head Star Trackers (FHST)	0.	-4 to 130
FHST Electronics <sup>a</sup>	8.	
Gyro Package	45	32 to 130
CMGs	36	-22 to 140
CMG Electronics	72	-4 to 130
Reaction Control System (RCS) Electronics	11.	-4 to 120
Solar Power Distribution	42	-40 to 140
Remote MUX	1.0	-22 to 140
Remote Decoder	1.4	-22 to 140

a. Temperature limits to be determined.

conservative. Since, however, future technical or economic developments may make it advisable to exploit an ability for passive focal plane adjustment by "matching" mirror and tube expansion properties, the following analysis is presented where an attempt is made to determine the axial movement of the focal point of the HR telescope due to mirror assembly temperature change.

The HR telescope mirror is a paraboloidal-hyperboloidal type device as shown in Figure VI-4. The mirror assembly consists of five concentric cylindrical mirrors each with different paraboloidal and hyperboloidal surfaces. The equations of the surfaces are determined by geometry, focal length, and mirror diameter at the intersection of the two surfaces. This analysis exploits the fact that the grazing angles at both surfaces must be the same and that at such low angles X-rays reflect like visible light (angle of incidence equals angle of reflection).

The basic approach to the problem is illustrated in Figure VI-5. Since, for the grazing incidence optics under consideration, the angles of incidence on the two sections must be equal and since the incidence angle equals the reflection angle, a particular ray can be chosen such that the paraboloidal and hyperboloidal surfaces can be replaced by frusta with half-cone angles equal to the grazing angle and twice the grazing angle, for the "front" and "rear" frusta, respectively. The two frusta can now be replaced by one equivalent frustum with cone angle  $2\theta$ . It can be shown geometrically that the ray to be traced must be the one which is incident on a point in the middle of the paraboloid, as illustrated in Figure VI-5.

Once the paraboloidal and hyperboloidal surfaces are replaced (for a particular ray) by an equivalent frustum, the axial shift of the focal point due to thermal expansion of the mirror may be determined. At this point an assumption is made: The radial expansion of the mirror influences focal point shift significantly more than axial expansion. This assumption is justified by the existence of extremely small grazing angles. Therefore, only radial expansion is considered.

With reference to Figure VI-6, the radius of the single equivalent frustum, at the point of incidence of the particular ray, which represents both the paraboloidal and hyperboloidal surfaces, is estimated from the relation

$$R' = R + 11 \sin \theta \quad ,$$

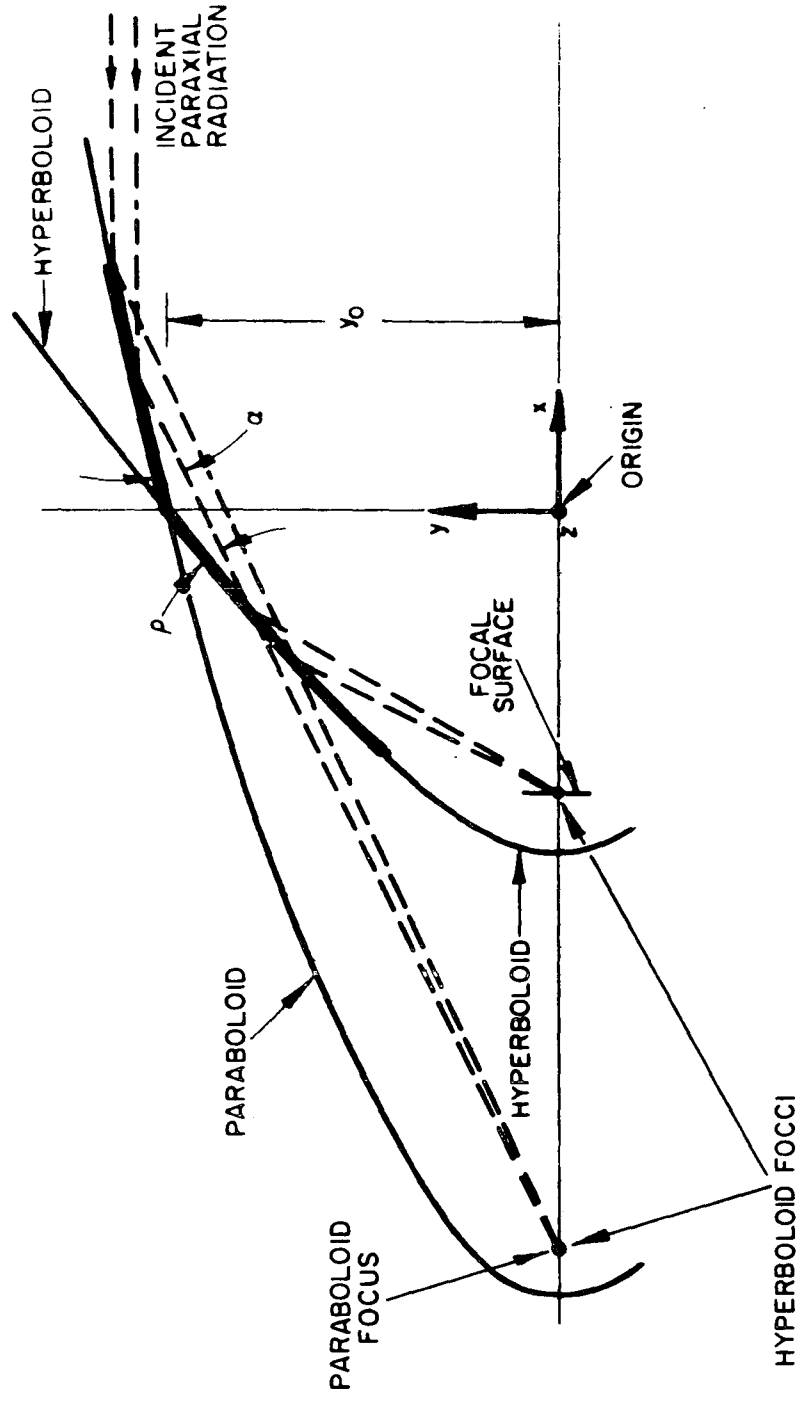


Figure VI-4. HR telescope mirror optical design.

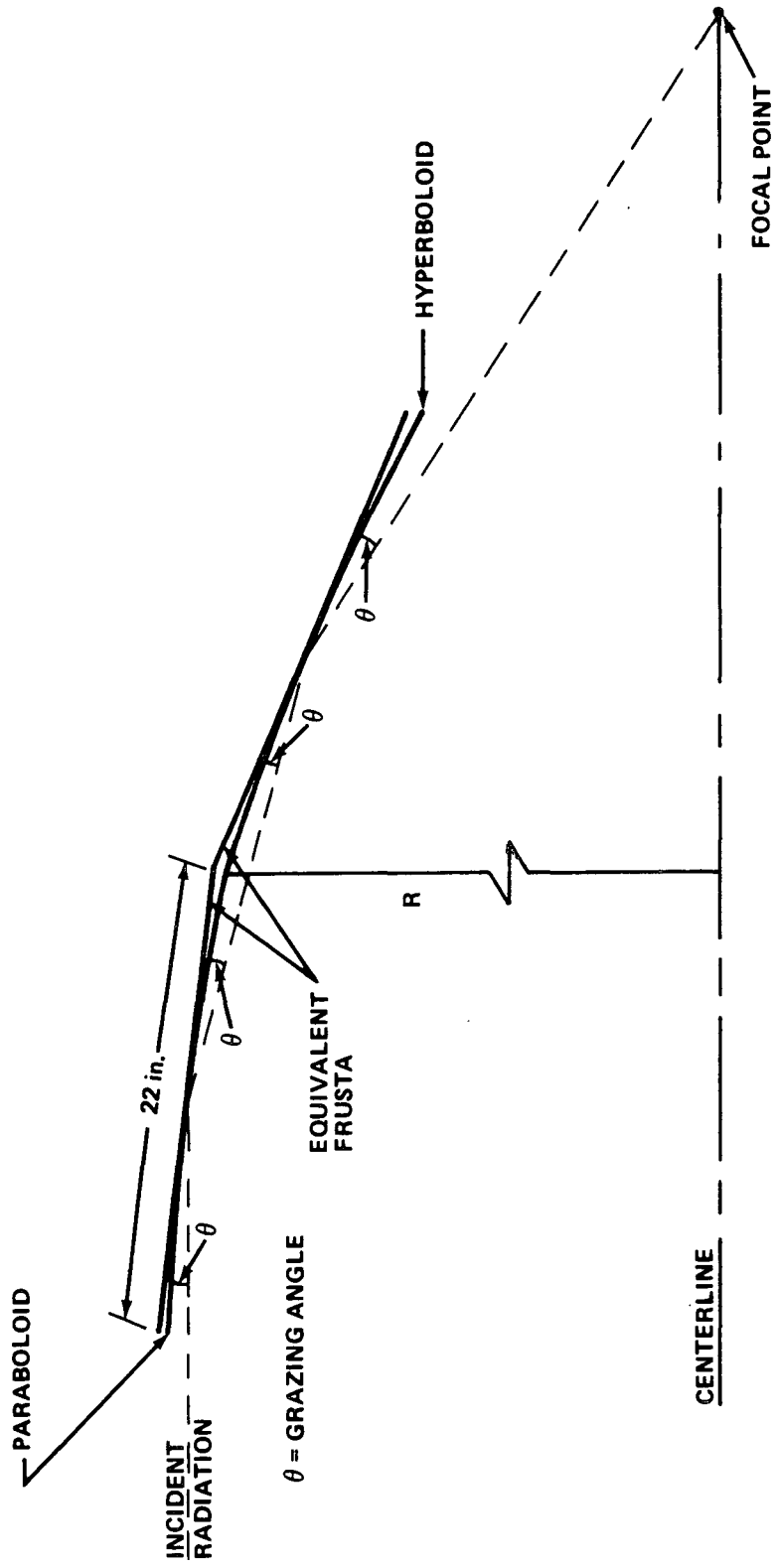


Figure VI-5. Simplification of HR mirror optics to two equivalent frusta.

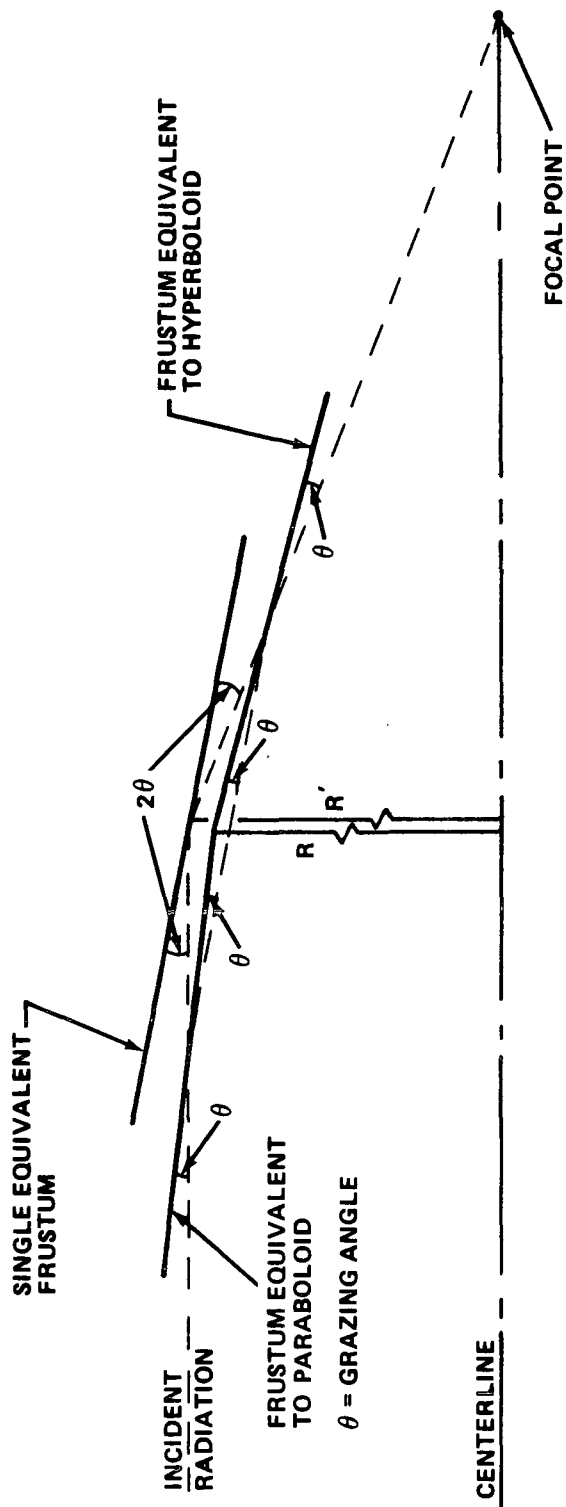


Figure VI-6. Simplification of HR mirror optics to a single equivalent frustum.

where  $R'$  is the radius of the single equivalent frustum (in.);  $R$  is the radius of paraboloidal-hyperboloidal mirror at the intersection of the two surfaces (in.);  $\theta$  is the grazing angle; and 11 inches is one-half the length of the paraboloidal surface.

To illustrate, consider the smallest of the five concentric mirrors, where

$$R = 27.41 \text{ in. and}$$

$$\theta = 0.01428 \text{ radian} = 49.1 \text{ arc min.}$$

The radius of the equivalent frustum mirror ( $R'$ ) is found to be 13.862 inches.

This calculation is slightly inaccurate since the value  $R$  should be the radius at the intersection of the two frusta which represent the paraboloidal and hyperboloidal surfaces individually. Since the change in radius with temperature is of primary interest, the calculation as shown is considered sufficiently accurate.

The axial shift of the focal point is now determined as a function of radial thermal expansion of the mirror (frustum), change in average mirror temperature, mirror material, and grazing angle. The change in mirror radius due to a change in average temperature can be shown to be

$$\Delta R' = \alpha R' \Delta T$$

where  $\Delta R'$  is the change in radius of the single equivalent frustum at the point of incidence of the particular ray;  $\alpha$  is the coefficient of linear thermal expansion of the mirror material;  $R'$  is the original radius as calculated above; and  $\Delta T$  is the change in average mirror temperature. As illustrated in Figure VI-7, the axial shift of the focal point can be calculated from the relation

$$\Delta f = \frac{\alpha R'}{\tan 2\theta}$$

or

$$\frac{\Delta f}{\Delta T} = \frac{\alpha R'}{\tan 2\theta},$$

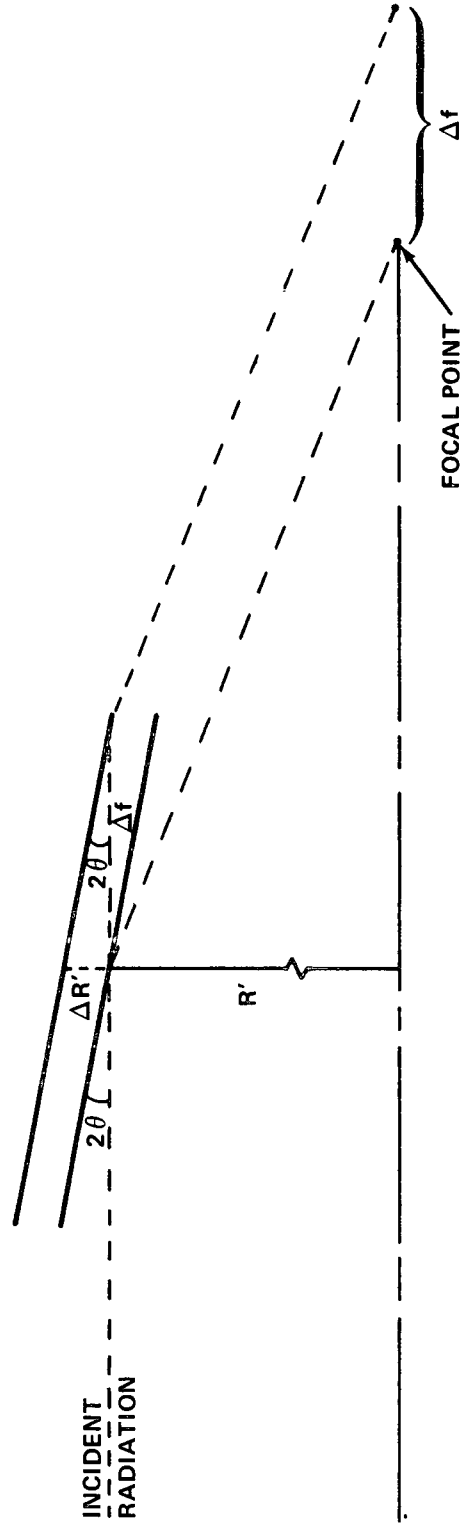


Figure VI-7. Displacement of HR telescope focal point due to radial expansion of the single equivalent frustum.

where  $\Delta f$  is the axial displacement of the focal point due to radial thermal expansion of the mirror. For the smallest of the five concentric mirrors the following values are given:

$$\alpha = 1.0 \times 10^{-7} \frac{\text{in.}}{\text{in. } ^\circ\text{F}} \text{ for Cer-Vit,}$$

$$R' = 13.862 \text{ in. (as shown above),}$$

$$\tan \theta \approx \theta = 0.01428 \text{ radian.}$$

Thereby

$$\frac{\Delta f}{\Delta T} = 0.486 \times 10^{-4} \frac{\text{in.}}{^\circ\text{F}}$$

It can be shown that this value for focal point axial displacement with mirror average temperature is virtually constant for all five mirrors

Figure VI-8 is a plot of focal point axial displacement versus increase in average mirror temperature. It can be seen that if the mirror assembly changes in temperature by the maximum allowable amount,  $5^\circ\text{F}$ , the focal point is displaced approximately  $2.4 \times 10^{-4}$  inch, well below the maximum allowable axial displacement of  $2.0 \times 10^{-3}$  inch. At that maximum allowable displacement it can be seen from the figure that a change in average mirror temperature of approximately  $41^\circ\text{F}$  is acceptable.

These data should not be interpreted to indicate that the temperature and deflection limits specified by the PIs are too stringent and, consequently, that the thermal control system described in the remainder of this chapter is too conservative. The simplifying approximations of the above analysis, the complexity of the HEAO-C X-ray optical systems, and the importance of the overall mission objectives support conservative design philosophy. That conservatism can be enhanced further by the fabrication of the telescope tubes in such a way that tube thermal expansion will compensate for focal point displacement due to mirror expansion.

Assuming the mirror assembly average temperature is  $5^\circ\text{F}$  above the nominal value, the required value of the thermal expansion coefficient of the graphite/epoxy tube can be calculated from

$$\alpha = \frac{\Delta f}{f \Delta T}$$

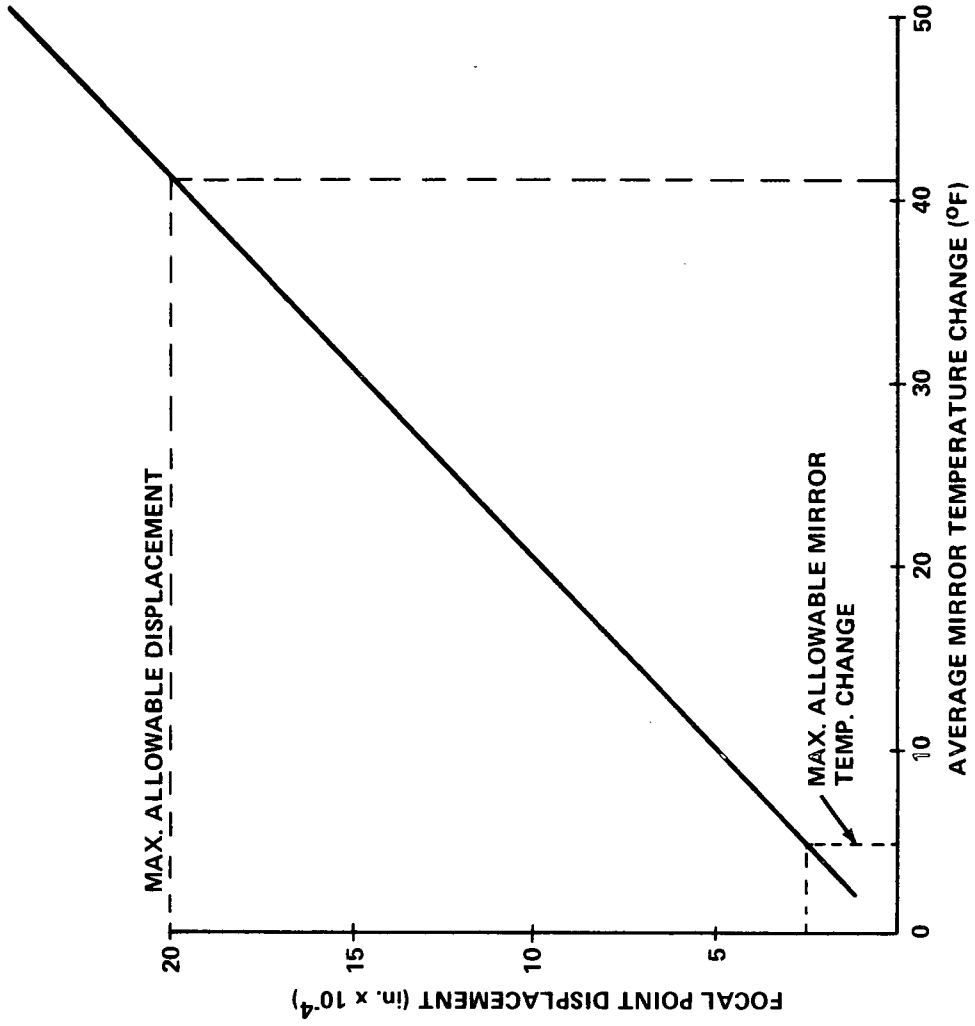


Figure VI-8. Variation of HR telescope focal point displacement with mirror temperature change.

where  $\Delta f = 2.4 \times 10^{-4}$ , focal point axial displacement corresponding to a  $\Delta T$  of  $5^\circ\text{F}$  (Figure VI-8), and  $f = 240$  in. , focal length of HR telescope.

Therefore, to maintain a net zero focal point axial displacement, the thermal expansion coefficient of the graphite/epoxy tube would be

$\alpha = 0.2 \times 10^{-6} \frac{\text{in.}}{\text{in. } ^\circ\text{F}}$ . This  $\alpha$  value can be closely approximated in the fabrication of the tube.

It should be pointed out, however, that unless the temperature and deflection requirements become much more stringent, it is not necessary to specify accurately this expansion coefficient value. Also, the detector transport mechanisms, as described in Chapter IV, provide any necessary active focal plane adjustment.

## E. Assumptions

The following is a compilation of assumptions made in the study:

### 1. Environmental and Orbital Parameters

#### a. Solar Constant (Maximum)

- $448 \frac{\text{Btu}}{\text{hr ft}^2}$

#### b. Albedo

- 0.4 Maximum
- 0.3 Nominal

#### c. Planetshine

- $83.0 \frac{\text{Btu}}{\text{hr ft}^2}$  Maximum
- $75.0 \frac{\text{Btu}}{\text{hr ft}^2}$  Nominal

#### d. Orbit altitude

- 270 n.mi. (circular)

e. Orbit Inclination

- 28.5 degrees

2. Material Properties

a. Aluminum Structure (6061-T6)

- Thermal Conductivity:  $96.8 \frac{\text{Btu}}{\text{hr ft } ^\circ\text{F}}$
- Specific Heat:  $0.23 \frac{\text{Btu}}{\text{lb } ^\circ\text{F}}$
- Density:  $170.0 \frac{\text{lb}}{\text{ft}^3}$

b. Aluminized Mylar TC Filter

- Absorptivity: 0.4
  - Emissivity: 0.06
  - Absorptivity: 0.35
  - Emissivity: 0.27
  - Absorptivity: 0.35
  - Emissivity: 0.85
- } For X-ray transmission
- } Central portion of HR telescope
- } Remainder of surface

c. Multilayer Super-Insulation

- Thermal Conduction:  $2.5 \times 10^{-5} \frac{\text{Btu}}{\text{hr ft } ^\circ\text{F}}$  (Normal to surface)
- Thermal Conduction:  $3.0 \times 10^{-2} \frac{\text{Btu}}{\text{hr ft } ^\circ\text{F}}$  (Parallel to surface)
- Specific Heat:  $0.3 \frac{\text{Btu}}{\text{lb } ^\circ\text{F}}$
- Density:  $2.5 \frac{\text{lb}}{\text{ft}^3}$

d. Cer Vit (HR and LA mirror material)

- Thermal Conductivity:  $1.0 \frac{\text{Btu}}{\text{hr ft } ^\circ\text{F}}$
- Specific Heat:  $0.22 \frac{\text{Btu}}{\text{lb } ^\circ\text{F}}$

e. Graphite/Epoxy

- Thermal Conduction:  $28.0 \frac{\text{Btu}}{\text{hr ft } ^\circ\text{F}}$
- Specific Heat:  $0.23 \frac{\text{Btu}}{\text{lb } ^\circ\text{F}}$
- Density:  $100.0 \frac{\text{lb}}{\text{ft}^3}$
- Thermal Expansion Coefficient:  $0.06 \times 10^{-6} \frac{\text{in.}}{\text{in. } ^\circ\text{F}}$

f. Solar Arrays<sup>5</sup>

- Body Mounted (solar cell packing density = 0.35)

$$\alpha = 0.5$$

$$\epsilon = 0.84$$

- Fold Out (solar cell packing density = 0.89)

$$\alpha = 0.78$$

$$\epsilon = 0.83$$

- Effective thermal conductivity, density, and specific heat were determined from Figure VI-9.

g. Beryllium (LE mirror material)

- Density:  $115.8 \frac{\text{lb}}{\text{ft}^3}$
- Thermal Conductivity:  $87.0 \frac{\text{Btu}}{\text{hr ft } ^\circ\text{F}}$

---

5. Solar cell  $\alpha$  and  $\epsilon$  values effectively vary with load. The values quoted are conservatively high.

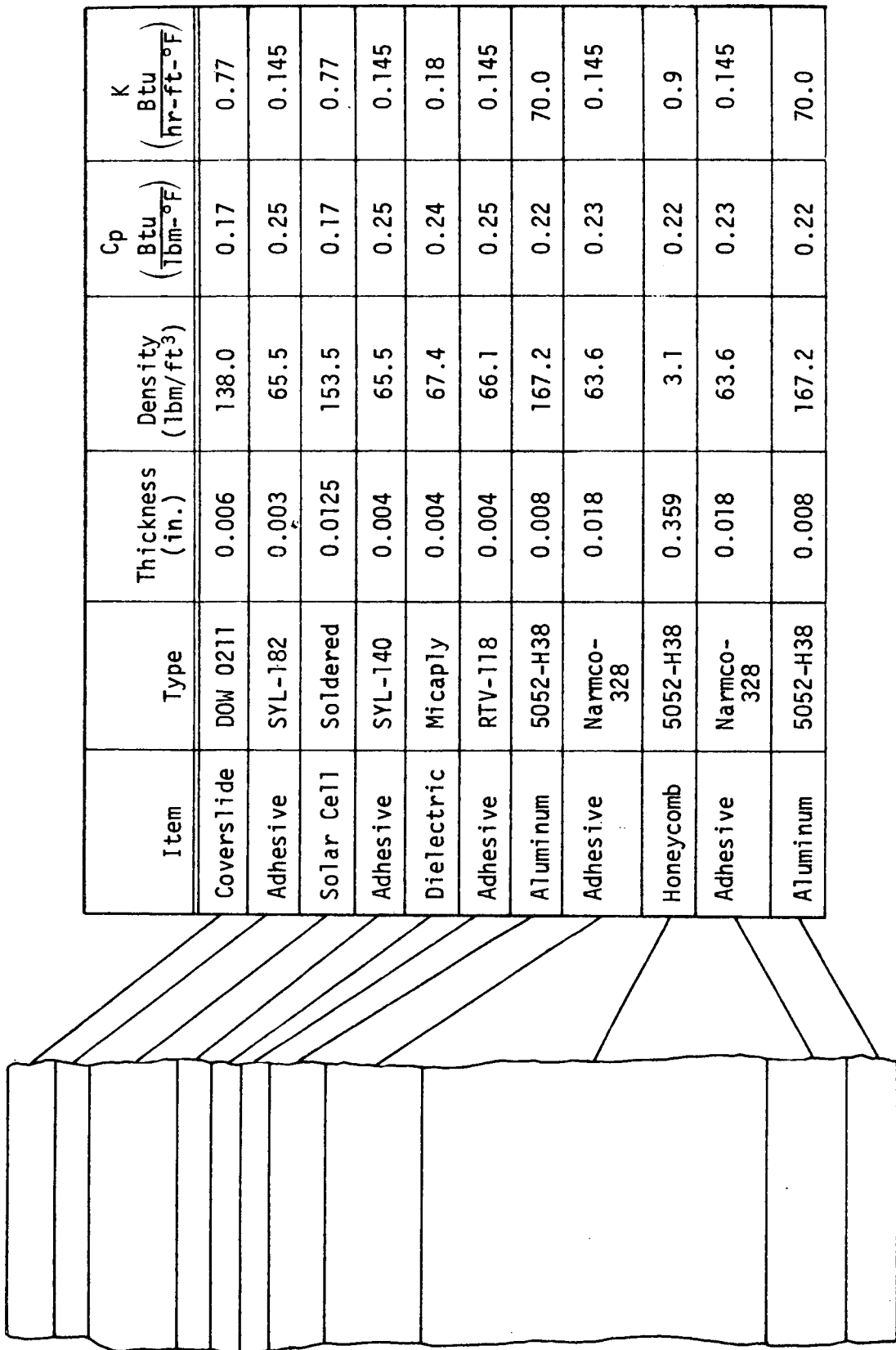


Figure VI-9. Structural model assumed in the derivation of solar panel thermal properties.

- Specific Heat:  $0.23 \frac{\text{Btu}}{\text{lb } ^\circ\text{F}}$

### 3. Surface Properties

#### a. Viewing Surfaces of Auxiliary Experiments

- $\alpha = 0.5$
  - $\epsilon = 0.5$
- } Nominal values assumed

#### b. Viewing Surface (outermost baffle) of LE Telescope

- $\alpha = 0.35$
- $\epsilon = 0.85$

#### c. Intratelescope Tube Surfaces

- $\alpha = 0.4$
- $\epsilon = 0.9$

#### d. All Other Internal Surfaces

- $\alpha = 0.35$
- $\epsilon = 0.85$

#### e. External Surface

- $\alpha = 0.15$
  - $\epsilon = 0.75$
- } Alzak
- $\alpha = 0.35$
  - $\epsilon = 0.4$
- } Multilayer insulation
- $\alpha = 0.35$
  - $\epsilon = 0.85$
- } Antisolar side of foldout solar arrays and adjacent spacecraft panels

4. Power dissipation levels (orbital average) and temperature limits for components/experiments not contained in subsystems compartment are given in Table VI-2.

Average orbital power dissipation and temperature limits of components located in subsystems compartment is shown in Table VI-1.

## F. Analytical Methods and Results

The analytical methods used in analyzing the thermal control system of HEAO-C are outlined as follows:

- The environmental heating rates for the Observatory and orbit orientations of interest are determined using the Lockheed 140 Node Heat Rate Program [VI-2].
- The Observatory internal gray body radiation interchange factors are determined using the Chrysler Shape Factor Program [VI-3].
- With the environmental heating rates, radiation interchange factors, and Observatory configuration as input, the transient temperature response of the Observatory is determined using the Chrysler Improved Numerical Differencing Analyzer (CINDA) computer program [VI-4].
- Iterate to reflect refinements in thermal control system or other Observatory updates.

Environmental heating effects on the external surface of the HEAO-C were predicted for the three Observatory/orbit orientations shown in Figure VI-10. With  $\beta = 52.0^\circ$  (Case 1), the Observatory experiences its maximum sunlight condition ("hot" orbit). The minimum sunlight but maximum instantaneous heating rate is experienced when the sun line is contained by the orbit plane (Case 2, "cold" orbit). To substantiate the feasibility of the sun shade approach to telescope thermal control, the Observatory environment was determined for the hot orbit with the Observatory inclined 30 degrees toward the sun.

The transient temperature response of the entire spacecraft to the predicted environmental heating rates was determined by means of the CINDA

---

6.  $\beta$  is the angle between the earth-sun line and the orbit plane measured in a plane perpendicular to the orbit plane.

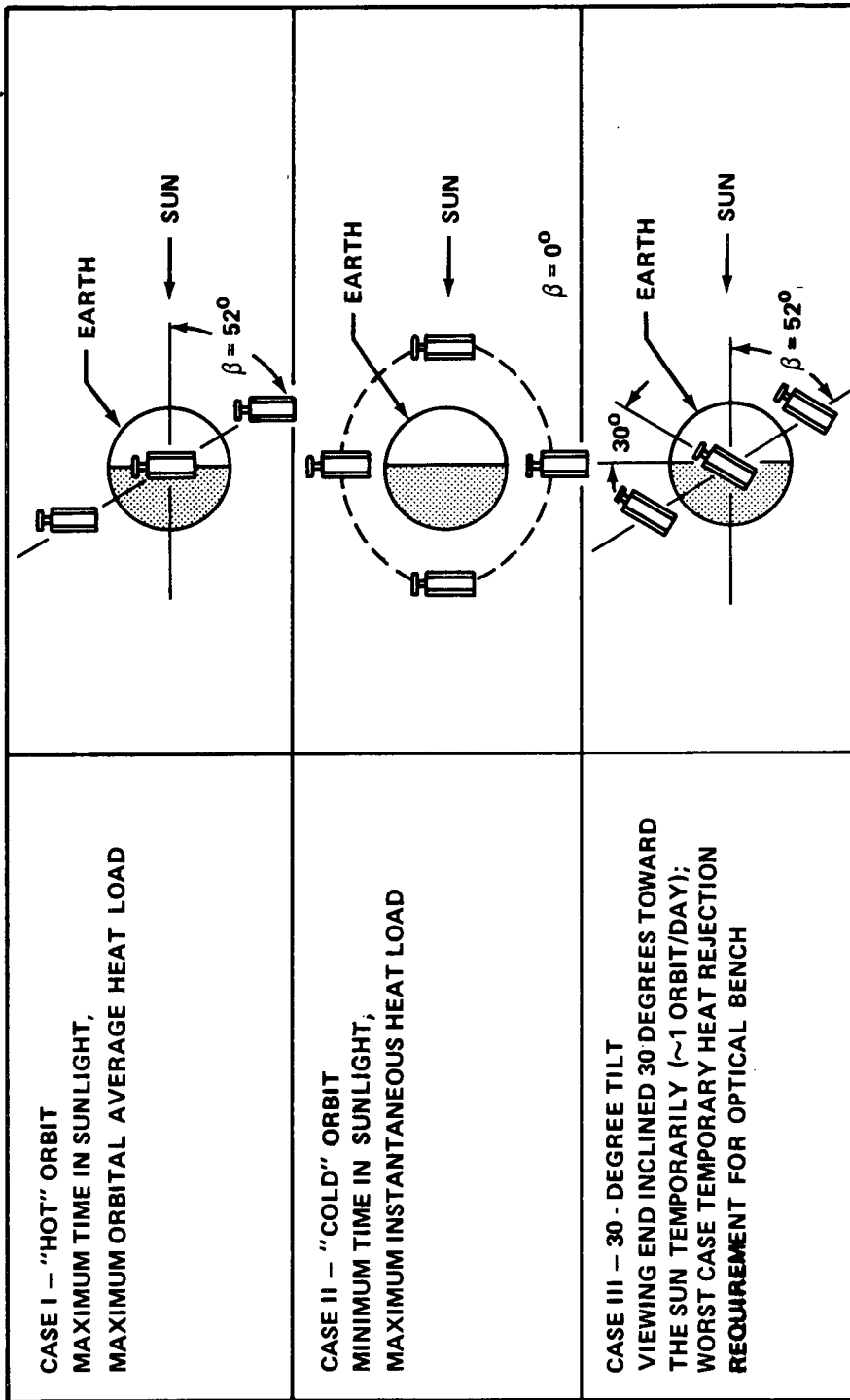


Figure VI-10. Observatory and orbit orientations considered in the thermal analysis.

digital computer program. In this technique, the physical system is first transformed into an equivalent thermal resistance/capacitance network which is input to the CINDA program. The program then employs finite difference techniques to solve for the transient temperature response of the nodal network, subject to the input boundary heating conditions.

The HEAO-C was divided into a total of 132 nodes. The thermally isolated subsystems compartment was analyzed separately as a one dimensional steady state radiosity network.

The 132 node thermal model was input to the CINDA program and the transient temperature response of each node was calculated for a simulated period of 31 hours (approximately 20 orbits) after orbit insertion. The initial temperature was assumed to be 70°F.

1. Solar Array Temperature. Solar array orbital temperature histories were determined for the initial baseline<sup>7</sup> array configuration for both the "hot" and "cold" orbit. In the hot orbit case the Observatory solar arrays are oriented normal to the incident solar radiation with the Observatory in a maximum sunlight orbit. Maximum environmental heating constants (solar constant, albedo, earth infrared) are assumed. The cold orbit is characterized by a minimum amount of sunlight time. The Observatory remained normal to the solar radiation and, since environmental heating is of primary concern in solar array thermal control, maximum constants were assumed. Figures VI-11 and VI-12 contain solar array orbital temperature histories for the hot and cold orbits, respectively. A noteworthy point to be made from Figure VI-11 is that even for the hottest possible<sup>8</sup> orbital conditions, the arrays are well below the assumed maximum allowable temperature of 212°F. (See Appendix D for further discussion of solar array temperature requirements). These data are based on the assumption that the solar cell packing density is 0.89 on the foldout panels and 0.35 on the body mounted panels. As illustrated in Figure VI-13, the solar cell packing density on the body mounted panels may be increased to a maximum of 0.63 with the maximum possible ("hot" orbit) temperature of those panels still being maintained below the upper limit of 212°F.

To verify feasibility of the sun shade design, Observatory external surface orbital temperature histories were determined for the hot orbit case

---

7. See Chapter VIII, Section C.

8. "Hottest possible" because it is extremely unlikely that maximum environmental constants will accompany hot orbit ( $\beta = 52$  degrees) orientations.

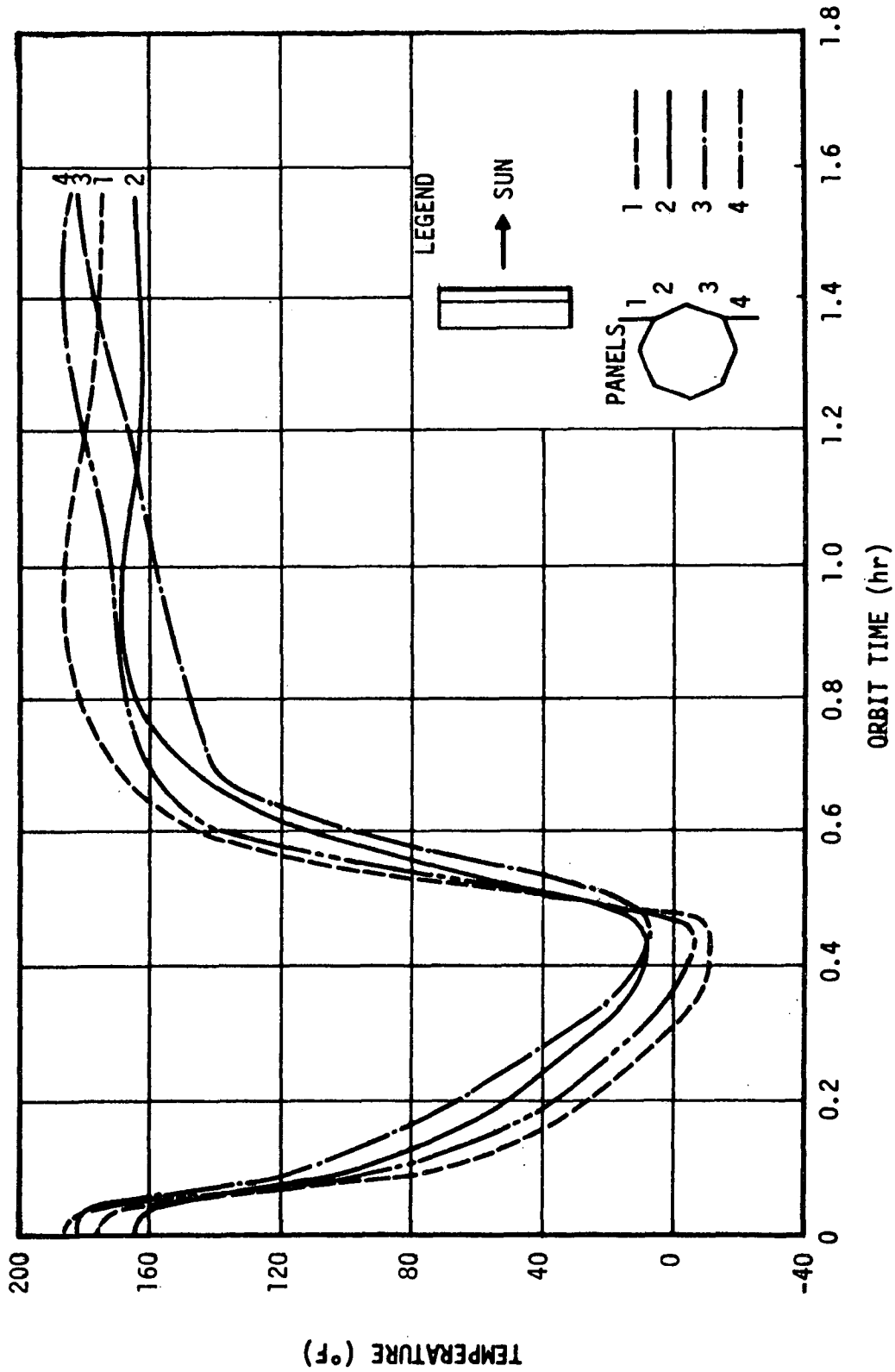


Figure VI-11. Solar array orbital temperature history for the hot orbit and Observatory perpendicular to earth-sun line.

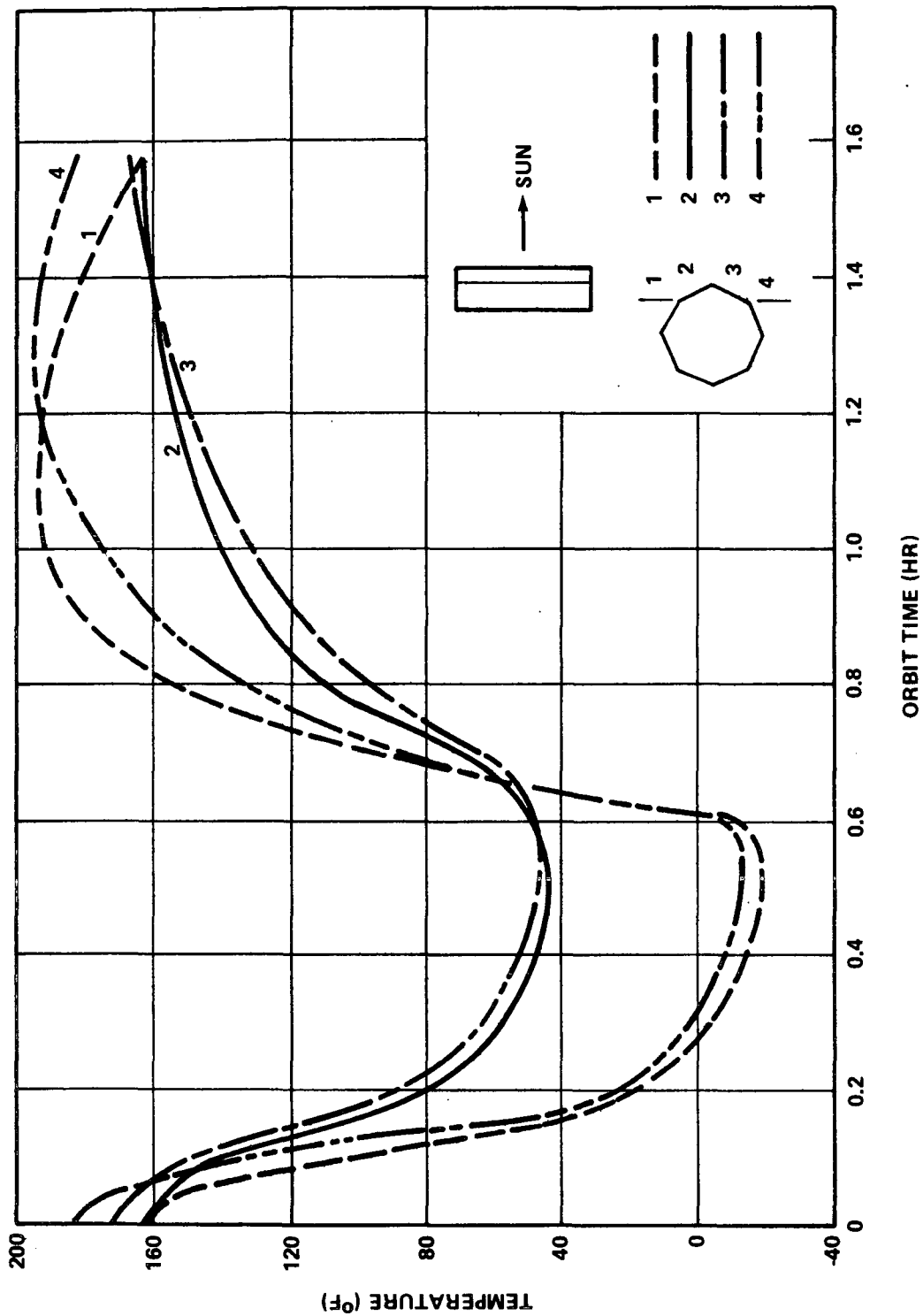


Figure VI-12. Solar array orbital temperature history for the cold orbit and Observatory perpendicular to earth-sun line.

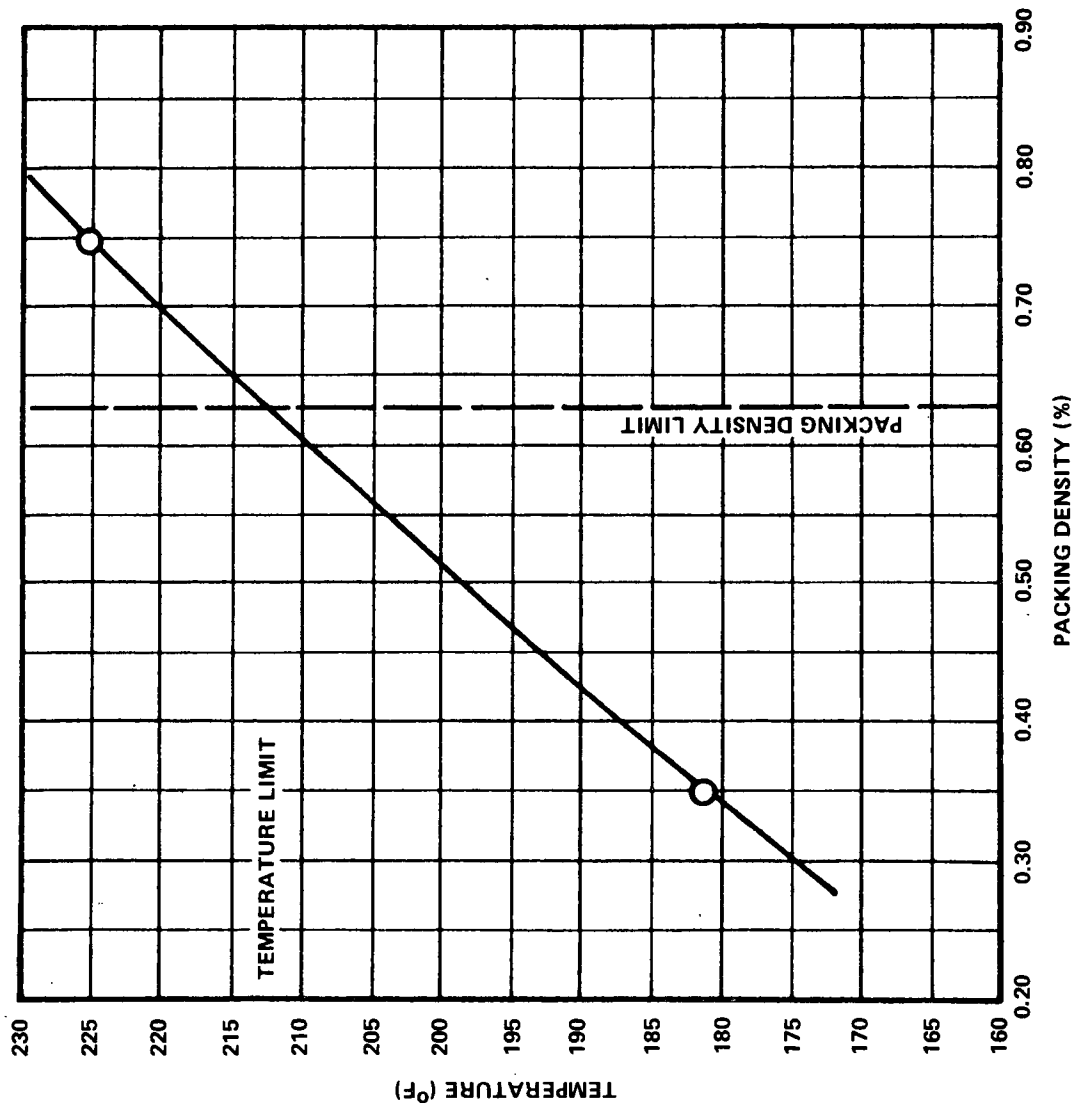


Figure VI-13. Maximum body mounted solar array temperature as a function of solar cell packing density.

with the Observatory inclined 30 degrees toward the sun. The solar array orbital temperatures for this case are shown in Figure VI-14.

Section 2 of Appendix D is devoted to a detailed discussion of sun shade feasibility. The data presented there are based on an earlier Observatory configuration and the sun shade design was assumed to be simply an aluminum sheet properly coated on both sides, as opposed to the laminar configuration described above (Section C).

2. Subsystems Temperature. All subsystem electronics except those few components which are location sensitive are thermally controlled by exploiting the available volume and the thermally stable external surface on the antisolar side of the Observatory. The EPS, the C&DH system and the AS&C system components listed in Table VI-1 are located in this region in addition to the CMGs and CMG electronics. Subsystem components which must be located elsewhere in the Observatory include the two solar power distributors (adjacent to the solar arrays for cable weight savings and power conversion efficiency), AS&C system sensors (located to satisfy alignment or viewing direction constraints, or both) and RCS hardware in OAS (for propellant and plumbing weight savings and commonality with missions A and B).

The primary means for thermal control of the components contained by the thermally independent subsystems compartment is the capability of the uninsulated external surface of this compartment to maintain the average orbital temperature inside the compartment within the allowable limits by emitting excess energy to space. If there is sufficient surface area, this can be accomplished by specifying the external surface emissivity.

Verification of the availability of sufficient surface area and determination of the desired emissivity for that surface are accomplished by representing the subsystems compartment by a one dimensional radiosity network. For a given surface area, external and internal surface properties, and internal energy dissipation, the average orbital temperature within the subsystems compartment is calculated from the following simultaneous equations:

$$T_{3\text{eff}} = \left( \frac{q_{\text{abs}}}{\sigma \epsilon_2 \frac{1}{A_2}} \right)^{1/4},$$

$$T_2 = T_{3\text{eff}} + \left[ \frac{q_{\text{gen}}}{\sigma} \left( \frac{1}{A_2} + \frac{1 - \epsilon_2}{\epsilon_2 \frac{1}{A_2}} \right) \right]^{1/4},$$

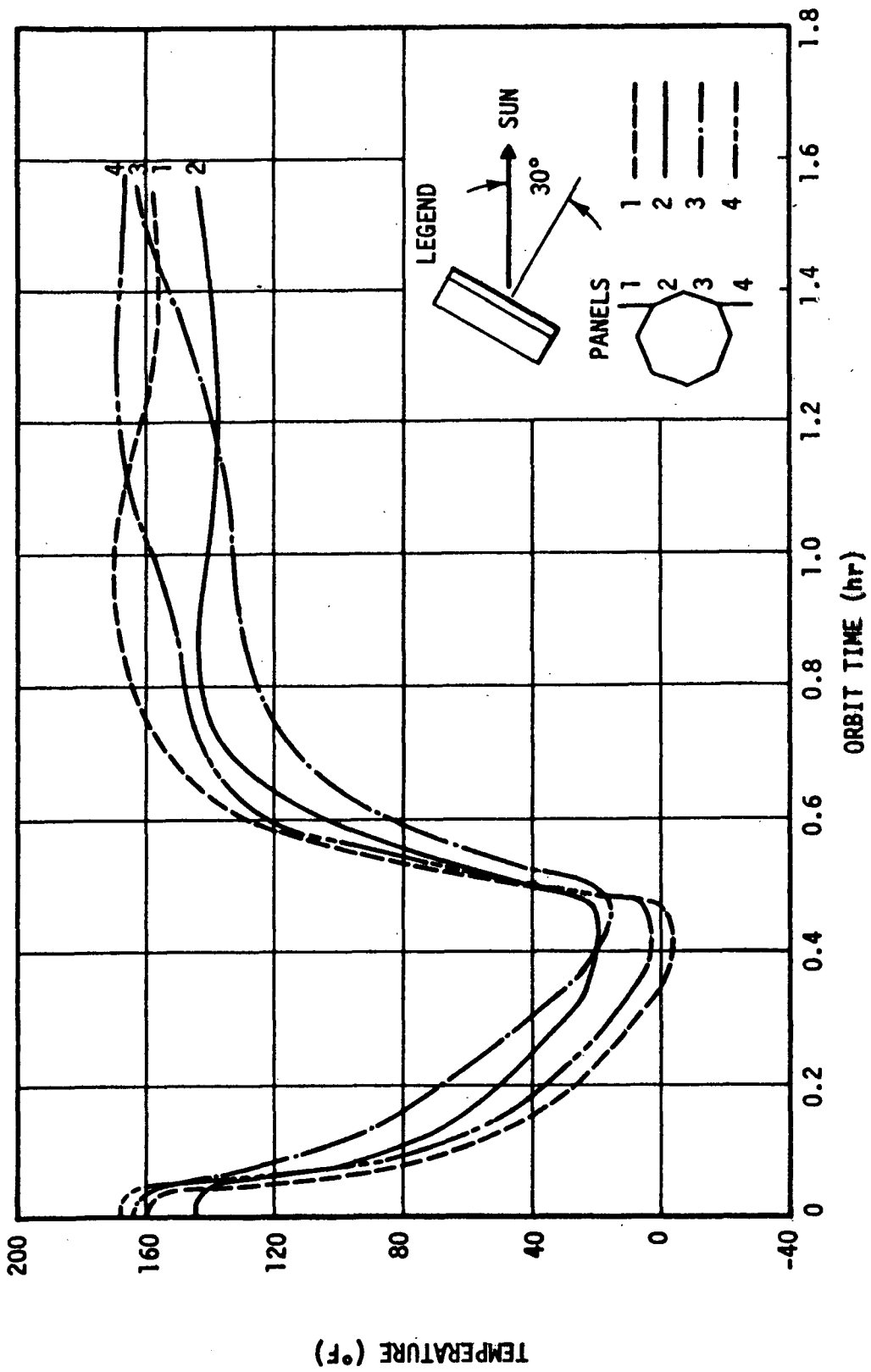


Figure VI-14. Solar array orbital temperature history for the hot orbit and Observatory inclined 30 degrees toward the sun.

and

$$T_1 = T_2 + \left[ \frac{q_{\text{gen}}}{\sigma} \left( \frac{1 - \epsilon_2}{\epsilon_2 A_2} + \frac{1}{A_1} + \frac{1 - \epsilon_1}{\epsilon_1 A_1} \right) \right]^{1/4},$$

where terms are defined as follows:

$\sigma$	Stefan-Boltzmann constant
$\epsilon_1, \epsilon_2$	subsystems compartment internal surface emissivity
$\epsilon_2^1$	external surface emissivity
$A_1$	total area for mounting electronics
$A_2$	external surface area
$q_{\text{gen}}$	energy dissipated by electronics
$q_{\text{abs}}$	energy absorbed by external surface
$T_{3\text{eff}}$	effective space sink temperature
$T_2$	external surface temperature
$T_1$	subsystems temperature

Subsystems temperature,  $T_1$ , is plotted versus external surface emissivity,  $\epsilon_2^1$ , in Figure VI-15 for internal emissivities of 0.92 (Cat-a-lac black paint), external and internal surface areas of 55 square feet and an internal energy dissipation of 408 watts.<sup>9</sup> From the figure it can be seen that with an external surface emissivity of 0.62 (assuming an absorptivity of 0.35) the average orbital subsystems temperature is 50°F. This emissivity value is easily

---

9. 408 watts is conservatively high since it assumes that all components are operating simultaneously.

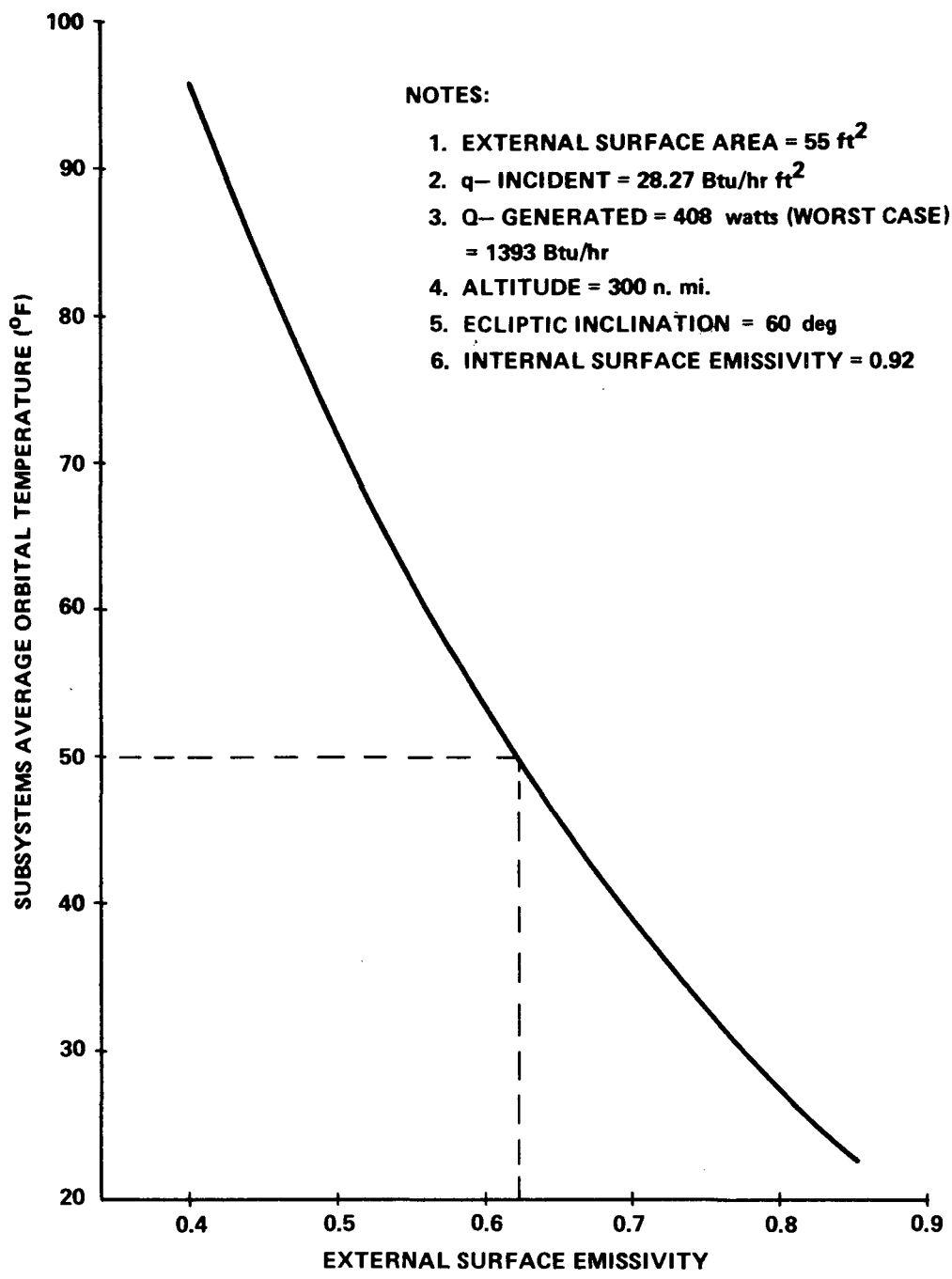


Figure VI-15. Subsystems compartment average orbital temperature versus external surface emissivity.

obtainable and should not degrade in space since no solar radiation is received. As noted in the figure, these data are based on an altitude of 300 n. mi. and an ecliptic inclination of 60 degrees. These parameters are slightly different from the values baselined in this study, 270 n. mi. and 52 degrees, but the effect is considered insignificant.

Time did not permit the calculation of temperatures for the individual components within the subsystems compartment. Components with relatively high dissipation rates, e.g., batteries, may require additional thermal control techniques (utilization of louvers) to maintain temperature stability.

Thermal control of the CMGs and CMG electronics is accomplished, similar to the subsystems compartment, by exploiting the available volume and thermally stable external surface. These components are mounted directly to the Observatory structure. The properties of the surface adjacent to these components are specified so that the CMGs and CMG electronics are maintained at the proper temperature and so that the excess energy can be dissipated from the experiment detectors. The average orbital temperature of the CMGs for the hot, cold, and 30 degree tilt cases are 73°F, 84°F, and 71°F, respectively. Temperature of the CMGs during the cold orbit is higher than during the hot orbit because the external radiating surface adjacent to the CMGs receives more energy from the environment.

The desirability of this approach to subsystems thermal control is supported by its simplicity, flexibility, and low cost. Feasibility has been proven during the thermal-vacuum test phase of previous development programs by demonstrating that surface properties can be easily adjusted by the application of, for example, aluminized Kapton or aluminum Teflon tape.

3. Experiment Temperatures. The Phase A Thermal Control Studies included transient analyses of the HR and LE telescopes. The LA telescope was not studied in detail because of its geometrical and power dissipation level similarities to the HR telescope and also because the thermal control requirements of the LA telescope are significantly less stringent than those of the HR telescope. It was, thereby, assumed that the analytically justified approach to thermal control applied to the HR telescope would be sufficient for the LA telescope.

a. High Resolution Telescope. High resolution telescope temperature as a function of distance along the telescope is shown in Figure VI-16. (There are virtually no orbital temperature variations because of the externally insulated Observatory structure and the large thermal mass of the mirror assembly.) It can be seen from Figure VI-16 that the difference in temperature from the front to rear of the mirror assembly is approximately 7°F. These mirror temperature gradients and the shift in average mirror temperature with change in orbit orientation justify the need for thermostatically controlled

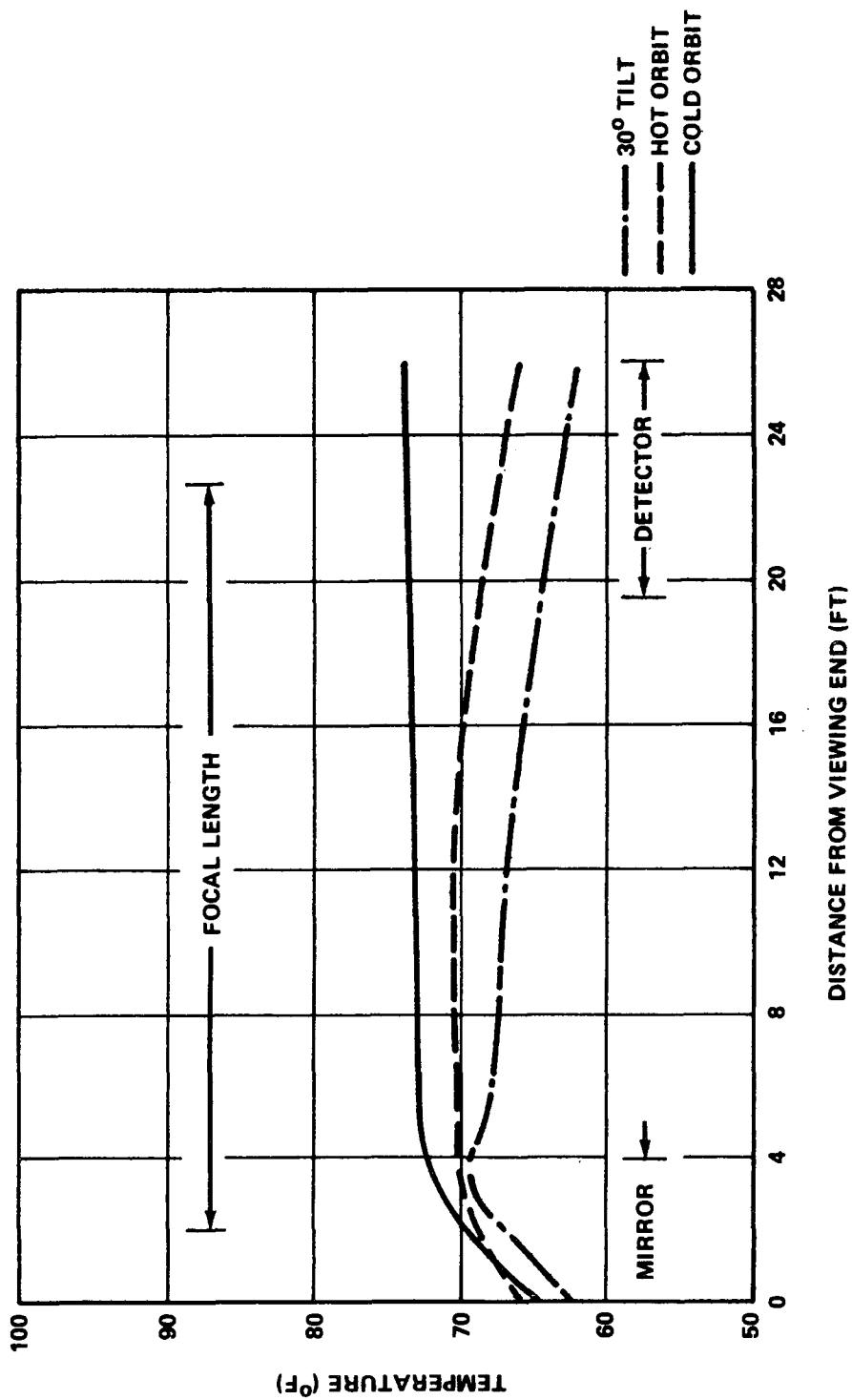


Figure VI-16. HR telescope temperature with no heater power applied.

heaters. The data shown below are based on a nominal operating temperature of 70°F which was chosen because of the expected mirror grinding and alignment environment. This analysis does not consider heater power effects on mirror temperature. It is interesting to note from Figure VI-16 that during cold orbit conditions the HR telescope is typically of higher temperature than during hot orbit conditions. The reason for this is that the Observatory surface adjacent to the CMGs, which dissipates excess energy from both the CMGs and experiment detectors, receives more orbital average energy (from earth) during the cold orbit.<sup>10</sup> Consequently, that radiating surface is typically warmer during cold orbits than during hot orbits, driving the experiment detectors, and eventually the entire telescope, to a higher temperature. Tilting the Observatory toward the sun reduces telescope temperatures primarily because of the decrease in thermal control filter temperature which results from decrease in the amount of solar radiation reflected from earth and the amount of infrared radiation due to the earth incident upon the filter.

The important conclusions which are drawn from the data illustrated in Figure VI-16 are that a purely passive thermal control approach nearly satisfies the requirements but that active, thermostatically controlled heaters are necessary for mirror assembly thermal control. The heater system should be designed so that during relatively hot orbit conditions (from an experiment viewpoint) the mirror assembly maintains a temperature distribution equal to the nominal value ( $70 \pm 2.5^\circ\text{F}$ ), with the heaters providing control during the cold conditions.

b. Low Energy Telescope. Figure VI-17 illustrates LE telescope temperature as a function of distance from the viewing end. These data are based on the assumption that the telescope is insulated externally except for a portion of the surface at the detector end. It is seen that the temperature of the detectors is approximately 8°F higher than the allowable. It is difficult at this time to judge the significance of this discrepancy (due to an understandable lack of telescope design detail); however, temperatures consistent with the current requirements (50°F to 68°F) are seen as being easily obtainable by altering the telescope and/or Observatory insulation scheme. It is noteworthy to mention that the LE telescope temperatures shown are virtually constant

---

10. Recall that "hot" and "cold" orbits are defined according to the amount of orbit time that the Observatory receives solar radiation. For hot and cold orbits the Observatory receives solar radiation approximately 73 percent and 62 percent of the orbit, respectively.

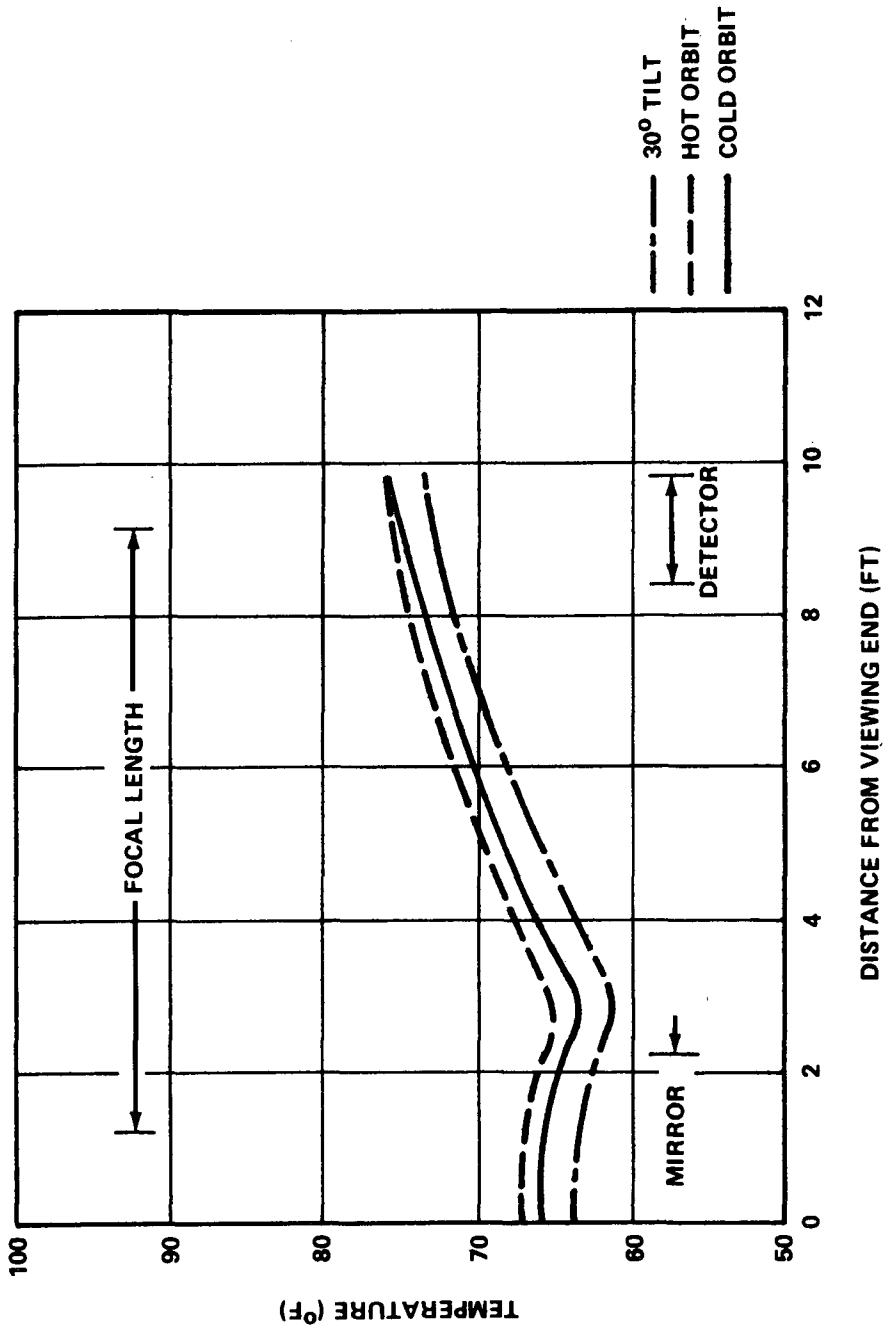


Figure VI-17. LE telescope temperature with no heater power applied.

with changes in Observatory or orbit orientation and that the ball joint support scheme does not degrade the thermal performance of the experiment.

c. Auxiliary Experiments and Detectors. The auxiliary experiments and detectors which are attached to the solar array side of the HR and LA mirror assemblies are maintained at 71°F during cold orbit orientations, 74°F during the hot orbit, and 65°F when the Observatory is inclined 30 degrees toward the sun. These values are well within the allowable limits.

4. Thermal Control System Weights. A listing of thermal control system components and their weights is given in Table VI-3.

TABLE VI-3. THERMAL CONTROL SYSTEM COMPONENT WEIGHTS

Item	Weight (lb)
External Multilayer Superinsulation	90
Heaters and Thermostats	15
Internal Insulation	30
Thermal Control Coatings (0.01 in. thick)	70
External Skin (Aluminum 0.02 in. thick)	<u>300</u>
Total	505

## G. Summary and Recommendations

The HEAO thermal control concept documented herein can satisfy all of the imposed requirements. Except for redundant thermostatically controlled heaters, the system is essentially passive. The ball joint telescope support scheme and the use of graphite/epoxy in the telescope tubes supports a thermally stable and highly conservative thermal control system. The use of graphite/epoxy presents the only potential development consideration but incurs no foreseeable technological difficulties. It is suggested in Appendix D that not only from a thermal control but also from a structural and economic viewpoint, the use of graphite/epoxy is feasible and, in fact, desirable.

As discussed in Chapter V and mentioned above in Section VI-D-1, a 77°F temperature difference can be tolerated across the observatory structure when the ball joint is replaced by a hard mount. (With the ball joint, a  $\Delta T$  of

approximately 140° F corresponds to the maximum allowable lateral deflection of ±0.02 inch.) Since this analysis was not completed until well into the Phase A study, it was judged inadvisable to change from the baseline ball joint concept.

To expand the analyses documented here, the following tasks are recommended for the HEAO-C Phase B Study activities:

1. Define in detail the mirror assembly thermostatically controlled heater system [that is, specify the type of heater desirable (e.g., strip, mesh, or spray-on), method of application to mirrors, associated thermostat and electronics, and power requirements];
2. Determine requirements and methods for thermal control during prelaunch, launch, and parking orbit; and, in addition, for the Space Shuttle retrieval, and on-orbit maintenance;
3. Determine in detail the LA and LE telescopes (when sufficient design detail is available) thermal control approach;
4. Optimize thermal control filter and subsystems compartment external surface properties.
5. Determine the temperatures of the individual components within the subsystems compartment and assess the need for additional control devices to compensate for the effect of locally high dissipation rates.
6. Assess in detail, from a thermal control viewpoint, the advisability of changing the telescope tube support scheme from the baseline ball joint to a hard mount concept.

## REFERENCES

- VI-1. American Science and Engineering: Large Orbiting X-Ray Telescope Proposal. Cambridge, Mass., May 1970.
- VI-2. Newby, T. S.: Lockheed (140 Node) Orbital Heat Rate Program. Contractor Report No. CR-59281, October 1966.
- VI-3. Ponder, C. A.: Chrysler Shape Factor Program. Chrysler Technical Report HSM-R588-70, March 1970.
- VI-4. Gaski, J. D.: Chrysler Improved Numerical Differencing Analyzer. Chrysler Technical Note TN-AP-67-287, April 1966.

## TABLE OF CONTENTS

	Page
A. Requirements . . . . .	VII-1
1. Guidelines and Constraints . . . . .	VII-1
2. Reference Attitudes . . . . .	VII-4
3. Mission Sequence . . . . .	VII-6
a. Operational Modes . . . . .	VII-6
b. Mission Description . . . . .	VII-11
4. Disturbing Torques . . . . .	VII-11
a. Gravity Gradient . . . . .	VII-11
b. Aerodynamic . . . . .	VII-17
c. OAS Engine Misalignments . . . . .	VII-17
B. Baseline System Description . . . . .	VII-17
1. System Configuration . . . . .	VII-17
2. Sensors . . . . .	VII-24
a. Sensor Characteristics . . . . .	VII-24
b. Reference Gyros . . . . .	VII-26
c. Wide Angle Sun Sensors . . . . .	VII-29
d. Star Trackers . . . . .	VII-32
e. Digital Sun Sensors . . . . .	VII-38
3. Actuators . . . . .	VII-43
a. CMG Configuration . . . . .	VII-43
b. Reaction Control System . . . . .	VII-48
4. Signal Processing . . . . .	VII-68
a. Digital Computer . . . . .	VII-68
b. Transfer Assembly . . . . .	VII-72
C. System Operation . . . . .	VII-78

## TABLE OF CONTENTS (Concluded)

	Page
1. Attitude Control Using RCS . . . . .	VII-78
a. Initial Stabilization After Booster Separation . . . . .	VII-78
b. Sun Acquisition/Reacquisition . . . . .	VII-78
c. Initial Orbit . . . . .	VII-78
d. Reference Update . . . . .	VII-80
e. Attitude Maneuvering . . . . .	VII-83
f. Intermediate Orbit . . . . .	VII-84
g. Final Orbit . . . . .	VII-86
h. CMG Spinup . . . . .	VII-86
2. Attitude Control Using CMGs . . . . .	VII-87
a. Experiment Pointing . . . . .	VII-87
b. Attitude Maneuvering . . . . .	VII-89
c. Experiment Calibration . . . . .	VII-90
D. System Errors . . . . .	VII-90
E. Baseline Performance Simulation . . . . .	VII-93
1. RCS . . . . .	VII-93
2. CMG System . . . . .	VII-98
a. Description . . . . .	VII-98
b. Parameters and Cases Simulated . . . . .	VII-100
c. Simulation Results . . . . .	VII-107
d. Response Capabilities . . . . .	VII-122
F. ASCS Reliability Summary . . . . .	VII-122
G. Conclusions and Recommendations . . . . .	VII-127
References . . . . .	VII-133

## LIST OF ILLUSTRATIONS

Figure	Title	Page
VII-1.	HEAO solar reference and Euler angles . . . . .	VII-2
VII-2.	HEAO-C ASCS mode flowchart . . . . .	VII-8
VII-3.	Orbit adjust procedure — HEAO-C . . . . .	VII-10
VII-4.	HEAO-C control modes timeline . . . . .	VII-12
VII-5.	Aerodynamic and gravity gradient torques . . . . .	VII-18
VII-6.	Thrust required for OAS burn phase . . . . .	VII-19
VII-7.	HEAO-C ASCS baseline configuration . . . . .	VII-21
VII-8.	Location of the ASCS components . . . . .	VII-23
VII-9.	Reference gyro assembly summary specification . . . . .	VII-27
VII-10.	Gyro channel functional block diagram . . . . .	VII-28
VII-11.	WASS outline drawing type 1818787 . . . . .	VII-29
VII-12.	Operation diagram . . . . .	VII-30
VII-13.	Output versus zenith angle . . . . .	VII-31
VII-14.	WASS outline drawing type 1771853 . . . . .	VII-32
VII-15.	Simplified WASS electronics schematic . . . . .	VII-33
VII-16.	HEAO-C star tracker configuration . . . . .	VII-34
VII-17.	Optical data corrector (ODC) Questar configuration . . . . .	VII-36
VII-18.	Optics and sensor . . . . .	VII-37

## LIST OF ILLUSTRATIONS (Continued)

Figure	Title	Page
VII-19.	Digital sun sensor schematic . . . . .	VII-39
VII-20.	Digital sun sensor outline . . . . .	VII-41
VII-21.	Digital sun sensor electronics . . . . .	VII-42
VII-22.	Four-CMG skewed configuration . . . . .	VII-44
VII-23.	CMG electronics block diagram for one channel . . . . .	VII-46
VII-24.	System schematic of the baseline HEAO-C RCS . . . . .	VII-50
VII-25.	Layout of baseline RCS major component locations . . . . .	VII-51
VII-26.	Reaction engine assembly/reaction engine module configuration . . . . .	VII-56
VII-27.	RCS electronics function diagram . . . . .	VII-69
VII-28.	DCU simplified flow diagram . . . . .	VII-73
VII-29.	Computer software . . . . .	VII-74
VII-30.	Transfer assembly . . . . .	VII-77
VII-31.	HEAO-C ASCS configurations . . . . .	VII-79
VII-32.	Celestial point and reference alignment mode-ASCS . . . . .	VII-82
VII-33.	Strap down processing concept . . . . .	VII-84
VII-34.	Maneuver profiles . . . . .	VII-85
VII-35.	The RCS control law used in the baseline studies . . . . .	VII-94
VII-36.	HEAO-C thruster characteristics . . . . .	VII-95

## LIST OF ILLUSTRATIONS (Continued)

Figure	Title	Page
VII-37.	Engine actuation for the worst case in the 270 nautical mile circular orbit . . . . .	VII-97
VII-38.	HEAO-C RCS, actuations per orbit versus impulse . . . . .	VII-99
VII-39.	Simulation block diagram . . . . .	VII-101
VII-40.	Gravity gradient torque versus orbital time ( $10^3$ sec) . . . . .	VII-105
VII-41.	Gravity gradient momenta versus orbital time . . . . .	VII-106
VII-42.	Pointing error and jitter versus orbital time . . . . .	VII-108
VII-43.	CMG gimbal angles versus orbital time ( $10^3$ sec) . . . . .	VII-109
VII-44.	Vehicle performance with CMG number 3 failed . . . . .	VII-111
VII-45.	CMG gimbal angles (CMG number 3 out) versus orbital time ( $10^3$ sec) . . . . .	VII-112
VII-46.	Gravity and CMG momenta, CMG number 3 failed . . . . .	VII-113
VII-47.	Earth's magnetic field versus orbital time ( $10^3$ sec) . . . . .	VII-115
VII-48.	Alternate system performance . . . . .	VII-117
VII-49.	CMG gimbal angles with magnetic momenta dump . . . . .	VII-118
VII-50.	Gravity and CMG momentum with continuous dump . . . . .	VII-119

## LIST OF ILLUSTRATIONS (Concluded)

Figure	Title	Page
VII-51.	Electromagnet dipole moments versus orbital time ( $10^3$ sec) . . . . .	VII-120
VII-52.	Magnetic torque to dump CMG momenta versus orbital time ( $10^3$ sec) . . . . .	VII-121
VII-53.	Vehicle response capabilities . . . . .	VII-123
VII-54.	ASCS reliability block diagram . . . . .	VII-124
VII-55.	RCS schematic . . . . .	VII-126

## LIST OF TABLES

Table	Title	Page
VII-1.	Reference Attitudes . . . . .	VII-6
VII-2.	Baseline HEAO-C Characteristics . . . . .	VII-15
VII-3.	HEAO-C Attitude Sensing and Control System Hardware Summary . . . . .	VII-22
VII-4.	ASCS Sensor Characteristics . . . . .	VII-25
VII-5.	MA-500 Single Gimbal CMG Characteristics . . . . .	VII-47
VII-6.	Reaction Control System Weight Summary . . . . .	VII-52
VII-7.	Propellant Tank Data and Performance . . . . .	VII-56
VII-8.	REA/REM Performance Capabilities . . . . .	VII-59
VII-9.	REA Design Summary . . . . .	VII-61
VII-10.	REA Performance Summary Nominal Operating Conditions . . . . .	VII-63
VII-11.	Physical Chemical, and Thermodynamic Properties of $N_2H_4$ . . . . .	VII-67
VII-12.	RCS Impulse and Actuation Budget . . . . .	VII-81
VII-13.	Attitude Determination Error Summary . . . . .	VII-92
VII-14.	ASCS Reliability Numerics Summary . . . . .	VII-125
VII-15.	RCS Reliability Numerics Summary . . . . .	VII-125

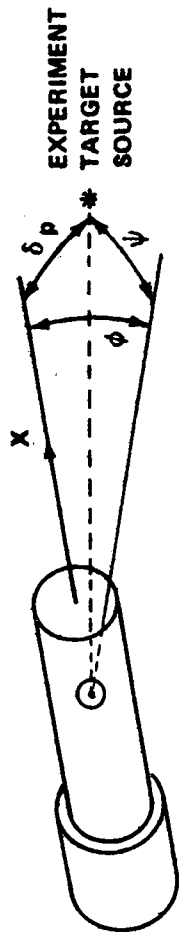
## CHAPTER VII. ATTITUDE SENSING AND CONTROL SYSTEM

### A. Requirements

1. Guidelines and Constraints. Although the basic mission requirements and operational constraints of the HEAO-C had a primary influence on the design of the attitude sensing and control system (ASCS), an established guideline for commonality with HEAO-A and -B was a strong driver for subsystem and component selection in all areas. In addition, the guideline, established late in the HEAO-A and -B study, that the Orbit Adjust Stage (OAS) remain attached throughout the mission has also been adopted as a HEAO-C guideline. The basic mission guidelines and Observatory operational constraints considered in the ASCS design consist of pointing and control accuracies of the experiments, Observatory configuration, power and thermal constraints, and operational mode requirements of the HEAO-C.

Since the field-of-view (FOV) of each experiment is oriented along the HEAO X-axis, experiment pointing accuracy has been established as  $\pm 1$  arc min about each of the Y- and Z-axes with a  $\pm 5$  arc min accuracy required about the X-axis (Fig. VII-1). Pointing jitter rate of the experiments must remain within  $\pm 1$  arc sec per sec for each of the Y- and Z-axes and  $\pm 1.5$  arc min per sec about the experiment FOV direction. However, because of the FOV of the ASCS fixed star trackers, an additional jitter constraint of  $\pm 5$  arc sec per sec about the reference line-of-sight to the target star had to be imposed to meet the more stringent of the experiment pointing jitter rate requirements. As generated by the ASCS, an attitude determination accuracy requirement of  $\pm 1$  arc min for each of three axes was assumed adequate to support the experiment data reduction and correlation task. An experimenter-supplied aspect sensor provides aspect data to an accuracy of better than 1 arc sec.

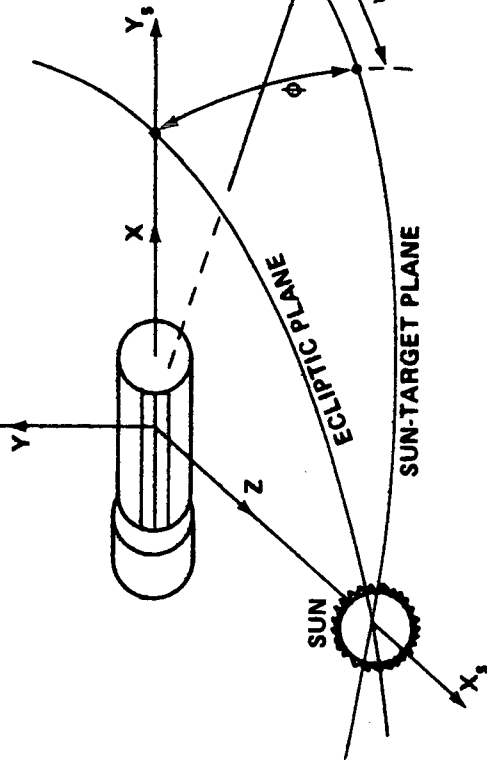
The configuration of the Observatory imposed several ASCS design constraints and considerations. The guideline that the OAS be located opposite the telescope viewing end and remain attached throughout the mission duration is an important ASCS design driver. This directly dictates a relatively high maximum moment-of-inertia value and the corresponding high gravity gradient torque levels and their effects must be included in the design of the ASCS. Also, this guideline was a key consideration in the decision to locate the HEAO-C reaction control system (RCS) in the OAS. Thus the reaction engine modules (REMs) are located as far away as possible from the telescope viewing end, thereby reducing any contamination effect that may occur. Since the Observatory solar panels must be kept sun-oriented to provide power to the onboard



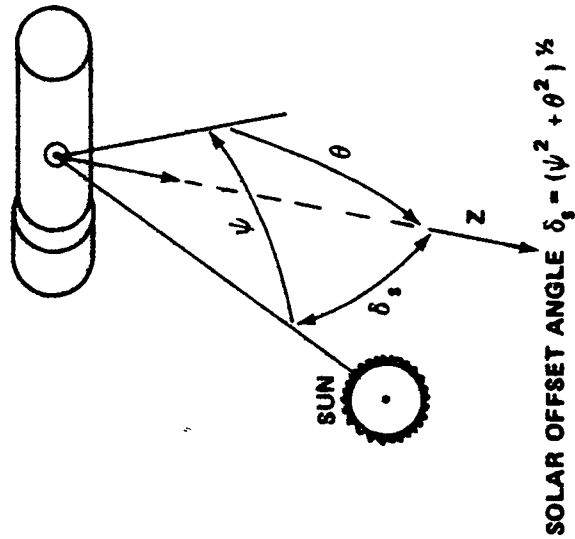
POINTING ERROR  $\delta_p = (\phi^2 + \psi^2)^{1/2}$

NORTH (PEP)

$Z_s$



SOLAR REFERENCE FRAME



SOLAR OFFSET ANGLE  $\delta_s = (\psi^2 + \theta^2)^{1/2}$

Figure VII-1. HEAO solar reference and Euler angles.

systems, there is a limit to the degree of continuous solar panel (Z-axis) off-set from the sunline (Fig. VII-1). This offset also must be consistent with the thermal requirements of the Observatory. The maximum requirement for Z-axis offset from the sun has been set at 15 degrees for continuous operation or 30 degrees for one orbit, although for sufficiently short periods of time, the HEAO-C is permitted to acquire any inertial attitude. The Observatory capability from a power standpoint is 40 degrees off-sun continuously, but the sun shade is designed for only 30 degrees toward the sun.

The following are additional guidelines and constraints used in the formulation of the ASCS for HEAO-C:

a. RCS Functions

- Remove HEAO rates after separation from the Titan IIRD launch vehicle.
- Provide control torques for maneuvering and attitude control prior to control moment gyro (CMG) activation.
- Attitude control the HEAO during OAS burn phases.
- Desaturate the CMGs after CMG activation.
- Provide backup maneuver and attitude control capability for critical ASCS failures.

b. CMG Functions

- Attitude control the HEAO during experiment operation phases.
- Maneuver the HEAO for experiment target acquisition.

c. Target Selection

- Establish by ground commands.

d. Target Hold

- Utilize reference gyro assembly (RGA) during experiment target occultation.
- Use fixed head star trackers (FHSTs) and RGA during unocculted experimentation.

- e. Observing Program
  - Consists of approximately one-half orbit continuous experiment viewing per target source with some observations of up to one week integrated viewing time.
- f. Attitude Maneuvers
  - Perform using RGA.
  - Precision slew or scan maneuvers not required.
- g. Attitude Determination
  - Generate by ground processing of the ASCS sensor outputs.
- h. Experiment Aspect System
  - Not used as a part of the ASCS.
- i. CMG Desaturation
  - Permit once per orbit for two minutes maximum.
- j. Reliability
  - No single point failures permitted.
  - 0.95 one year reliability goal.
  - Two year life potential.
  - Maximum use of existing hardware.
  - Experiment, launch phase, system integration (checkout, fault isolation, and redundancy switching) hardware reliability excluded.

2. Reference Attitudes. Based on the guidelines and constraints, several reference attitudes must be defined to which the HEAO body-fixed axes must be oriented during various operational modes. In Figure VII-1, the body principal axes and geometric axes are assumed to be identical and are denoted

by the right-hand triad (X, Y, Z). To facilitate Observatory to launch vehicle integration and structural studies, the HEAO axes have been selected to correspond to the launch vehicle coordinates. The X-axis is along the launch vehicle longitudinal (minimum inertia) axis at lift-off. Since the majority of the experiments are aligned with the X-axis, it is referred to as the experiment or pointing axis. The Z-axis (maximum inertia) is normal to the solar panels and the Y-axis completes the right-hand triad. The origins of the coordinate systems are assumed to be located at the HEAO center of mass.

Since the HEAO depends upon solar energy to supply its power needs, the Z-axis must point toward the sun during normal operations and not exceed an angle of approximately 30 degrees off the sunline for a maximum of one orbit to satisfy both power and thermal requirements. However, for short periods of time, the solar power and thermal constraints can be disregarded and the Observatory is permitted to acquire any inertial attitude. Table VII-1 lists six reference orientations for HEAO of which the third and sixth represent unusual operating modes in which solar power may not be received. During any normal operating mode, the Z-axis is always oriented sunward, hence solar ecliptic coordinates are selected as a basis for describing the HEAOs attitude. Each reference orientation, with the exception of the solar ecliptic, has been defined to satisfy an operational mode. During normal experiment operation, the vehicle maneuvers from one experiment pointing attitude to the next without going back to a sun acquisition reference.

The vehicle centered solar ecliptic coordinate system is defined relative to the sun and ecliptic plane by the right-hand triad ( $X_s$ ,  $Y_s$ ,  $Z_s$ ) as illustrated in Figure VII-1. The  $X_s$ -axis points to the sun in the ecliptic plane; the  $Z_s$ -axis is perpendicular to the ecliptic plane (PEP) directed in a northerly direction; and the Y-axis completes the triad in the ecliptic plane. The Observatory's attitude relative to the solar reference coordinates can be specified by three Euler angles, phi ( $\phi$ ) about the sunline, psi ( $\psi$ ) in the sun experiment target plane, and theta ( $\theta$ ) about the experiment axis. Relative to solar ecliptic coordinates, the Euler sequence is a 1, 3, 2 type. To facilitate performance, simulation, and analysis studies, the body axes are redefined in terms of solar axes such that the body and solar coordinates are identical in the solar reference attitude. As defined, experiment target source pointing error for small angles is given by the deviation of  $\psi$  and  $\phi$  from their commanded values and roll error about the target line of sight is given by deviation of  $\theta$ . The solar offset angle,  $\sim\sqrt{\psi^2 + \phi^2}$ , is denoted by delta ( $\delta$ ). Appendix E contains a more detailed description of the coordinate systems and axis definitions that are necessary to evaluate the HEAO performance with respect to the reference attitudes.

7 (9)

TABLE VII-1. REFERENCE ATTITUDES

Reference Attitudes	Orientation	Use
Sun Acquisition	The Z-axis points toward the sun and all body rates are nulled.	Initial sun acquisition or reacquisition
Reference Alignment	The Z-axis points toward the sun and fixed star trackers on the two transverse axes are pointed toward guide stars.	Establish celestial orientation
Orbit Adjust	All axes are inertially fixed to required OAS burn attitude.	Align vehicle for OAS burn
Solar Ecliptic	The Z-axis points to the sun, the Y-axis points north perpendicular to the ecliptic plane, and the X-axis completes a right-hand triad in the ecliptic plane.	Reference for description of vehicle attitude
Celestial Pointing	The X-axis points to an experiment source, the Y-axis points toward a guide star, and the Z-axis is within 15 degrees of the sunline.	Normal experiment operation
Special Pointing	The Observatory can assume any inertial attitude. Solar power may not be received.	Unusual experiment operation for short periods

3. Mission Sequence

a. Operational Modes. The principal control modes of operation can be described under the following five major headings:

- (1) Sun Acquisition
- (2) Reference Alignment

- (3) Orbit Adjust
- (4) Celestial Pointing
- (5) Special Pointing

Figure VII-2 is a flow chart showing the mode flow concept in changing from mode to mode. The normal flow in the initial phases of the mission, including orbit adjustment, is the following:

- Sun acquisition
- Reference alignment
- Orbit adjust
- Sun acquisition

After orbit adjustment, the normal flow is as follows:

- Sun acquisition
- Reference alignment
- Celestial pointing

Although used infrequently, the special pointing mode is normally entered from the celestial pointing mode. If the analytical reference is maintained through star reference updates during the special pointing mode, the celestial pointing mode can be reentered directly from the special pointing mode. However, if an accurate analytical reference frame is not maintained, the ASCS must recycle the Observatory through the sun acquisition and reference alignment modes to return to the celestial pointing mode.

The sun acquisition mode can be entered directly from any other mode. This can provide for emergency operation or can be the first step for a reference realignment if required. This mode is designed to rapidly place the spacecraft into a two-axis solar oriented attitude that provides full solar panel output and optimum conditions for subsystems activation, operation confirmation, and checkout as required.

Two main functions are provided by the sun acquisition mode. First, a stable two-axis attitude is provided from which a three-axis reference can be

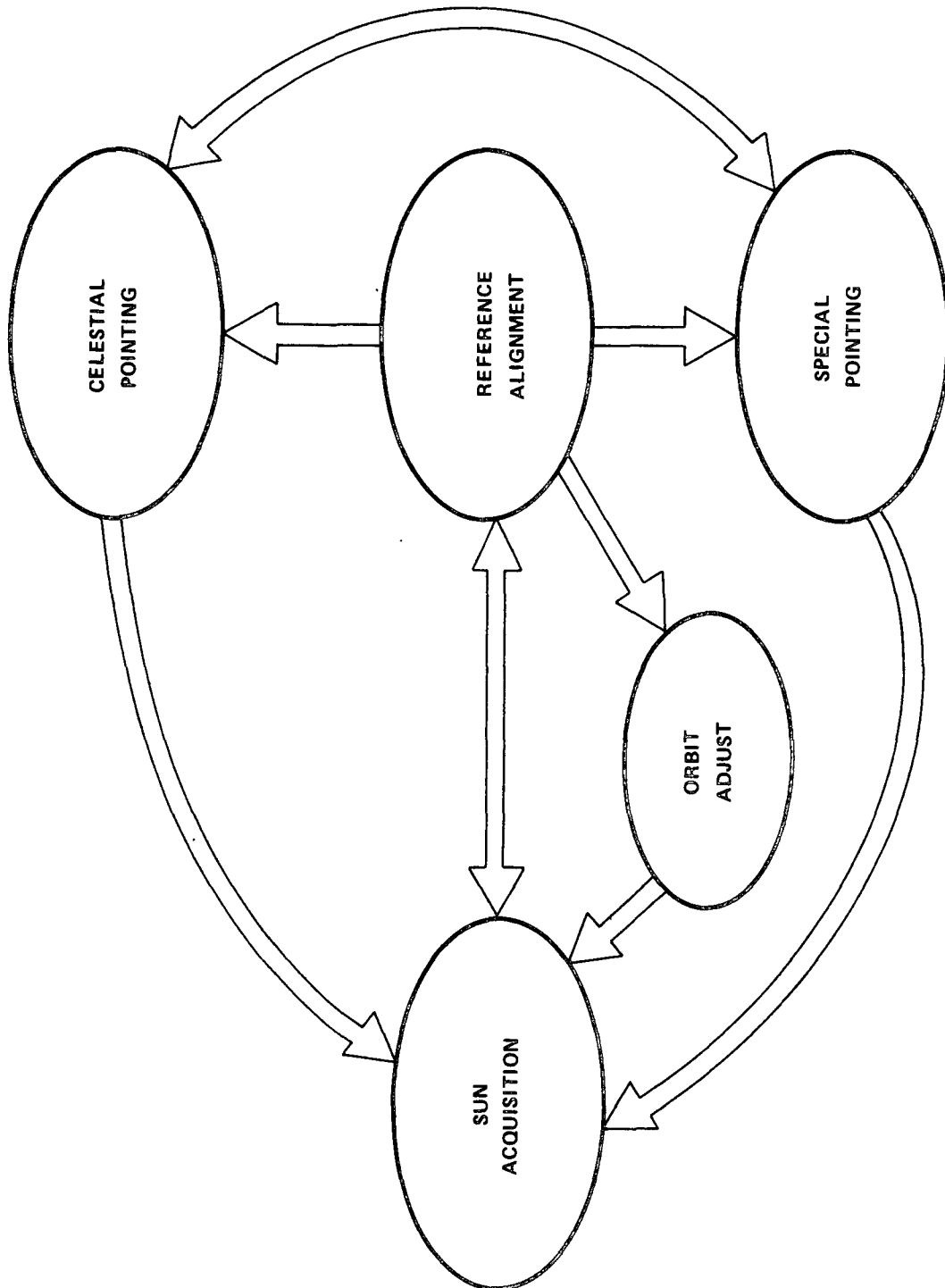


Figure VII-2. HEAO-C ASCS mode flowchart.

easily obtained by rotating the spacecraft about the solar vector to acquire known reference stars with the star trackers. Secondly, an emergency mode is provided so that if the attitude reference is lost or component failures occur, the spacecraft can be oriented to the solar vector and maintained in this attitude for troubleshooting analysis or reacquisition of a reference attitude. In this mode, the alignment of the Z-axis with the solar vector is maintained within 1 arc min, with near zero rate about the solar vector.

The reference alignment mode serves to establish an initial analytic inertial reference frame for the onboard computation of the slew maneuver required to position the spacecraft in the orbit adjust attitudes and to acquire the initial experiment orientation. During the experimentation phase of the mission, an inertial reference frame will be maintained in a continuously updated state in the computer software. Since celestial bodies are the primary reference sources for establishing an initial reference frame, gyro drift compensations can be computed and implemented as well as the computer software attitude solution parameters. Use of this mode and the associated onboard computation capability greatly reduces the criticality of ground station contacts during any required maneuvers. In the reference alignment mode, the spacecraft is in the two-axis solar vector orientation described for the sun acquisition mode but, in addition, the spacecraft has been rotated about the solar vector until reference stars have been acquired by the star trackers.

The orbit adjust mode provides the capability to inertially align and hold the spacecraft in the required attitude during each orbit adjust stage burn. This mode is entered initially from the reference alignment mode so that the reference frame has been established to compute the slew maneuvers to the orbit adjust attitude. Additional orbit adjust attitudes can be obtained by computing the required maneuvers with respect to the stored reference frame data. Figure VII-3 illustrates two spacecraft orientations for this mode.

The celestial pointing mode provides the capability to point the experiment axis to any point on the celestial sphere to a two-axis pointing accuracy of one minute of arc. Once the target has been acquired and experimentation has begun, the pointing direction is held with a rate stability of less than one arc sec per sec, and the angle about the experiment optical axis varies less than five minutes of arc. Target selections are made by the principal investigators and the target location, reference star identification, and other pertinent information is transmitted to the spacecraft where the maneuver is computed by the ASCS. Attitude determination to better than one arc min for each of three axes is provided to the mission control center from the onboard ASCS sensors for use in correlating spacecraft attitude with experiment data. Where more precise attitude determination is required, it will be provided by the experiment package.

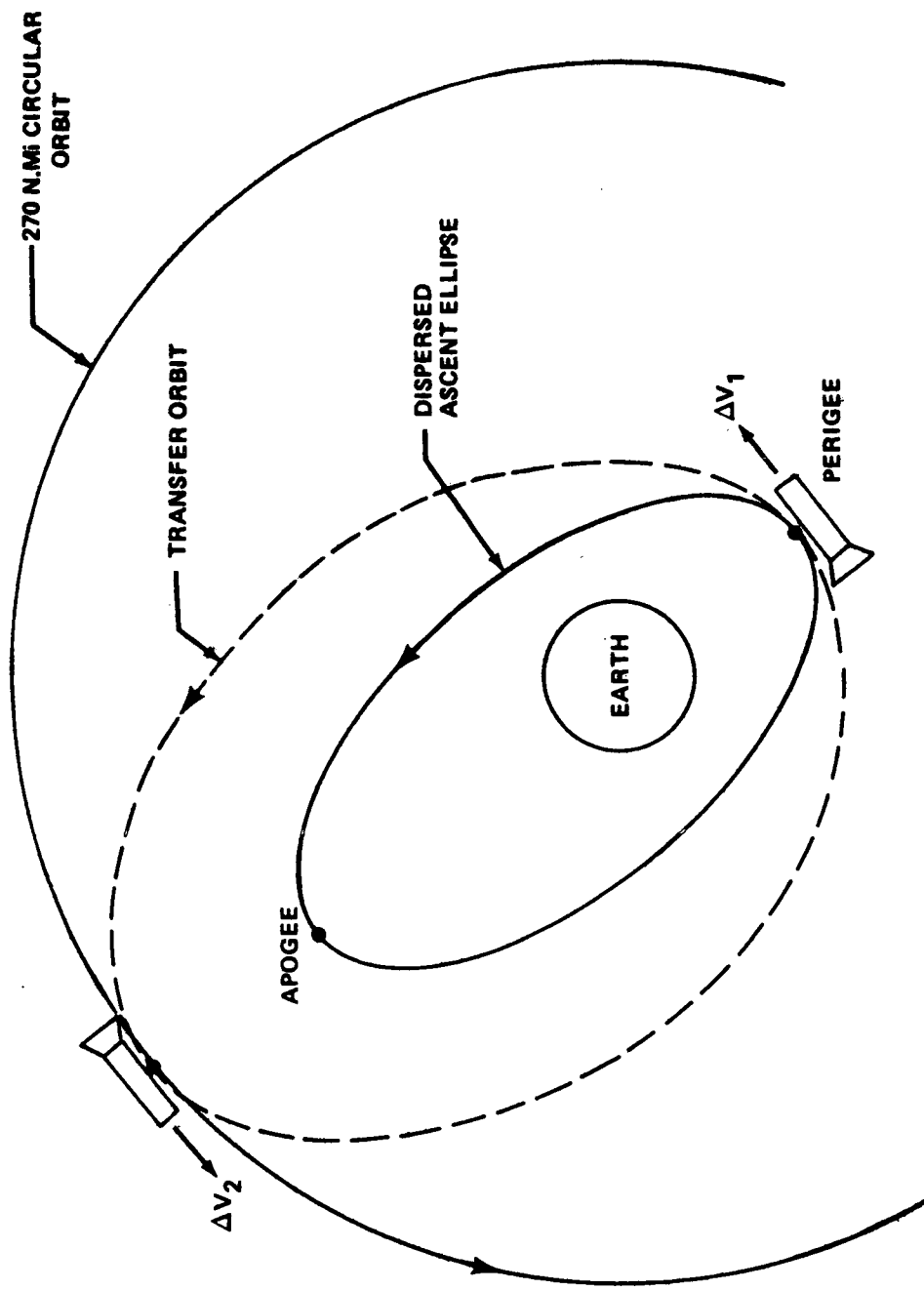


Figure VII-3. Orbit adjust procedure--HEAO-C.

The special pointing mode provides the capability to point the experiment at infrequently occurring sources such as solar flares. This mode differs from the celestial pointing mode in the magnitude and rates of the maneuver, the sensor configuration, target viewing time, accuracy of pointing, and permissible solar panel offsets from the solar vector. Special detectors sense the occurrence of the unusual energy sources and provide the information to the control center where the decision to view is made and the required spacecraft commands are generated. The ASCS provides the maneuver capability and maintains source acquisition. If available, however, additional fine angle detectors could provide the two-axis error signals necessary to maintain source acquisition if desired. Attitude determination is provided by a combination of the ASCS and experiment sensors.

b. Mission Description. Figure VII-4 shows a typical normal mission profile as visualized from the ASCS standpoint. The time periods indicated are not necessarily mission required but have been inserted as a guide to the approximate times required by the ASCS to perform its function. An overall mission timeline should use these as minimum values that can be increased, if desired, within the constraints of other subsystem and mission requirements. All ASCS modes depicted on this mission profile have been described previously.

The reference alignment mode must be entered prior to the orbit adjust mode. Orbital lifetime is the primary consideration, dictating orbit adjust as soon as possible although RCS propellant consumption during hold as well as the desire to maximize experiment time are additional considerations. From an ASCS standpoint, the sun acquisition mode is an excellent standby mode that is easily maintained. Only two OAS burns are shown but this is not an ASCS restriction. If additional burns are required, the timeline would pick up after the last burn at the point shown after the second burn and continue.

Ground commands are the final authority in specifying spacecraft operation. As required, the celestial pointing and the special pointing modes will be selected from the ground during the experimentation phase of the mission as experiment targets become available. This also will take place during the second year of the mission operation which has been identified as being generally of the same nature as the first year of operation. The actuators used for certain periods of the timeline are indicated. Other key milestones to be noted are solar panel deployment and CMG activation.

#### 4. Disturbing Torques

a. Gravity gradient. A cursory analysis of disturbing torques acting on the HEAO indicates that gravity gradient (g. g.) torque will dominate

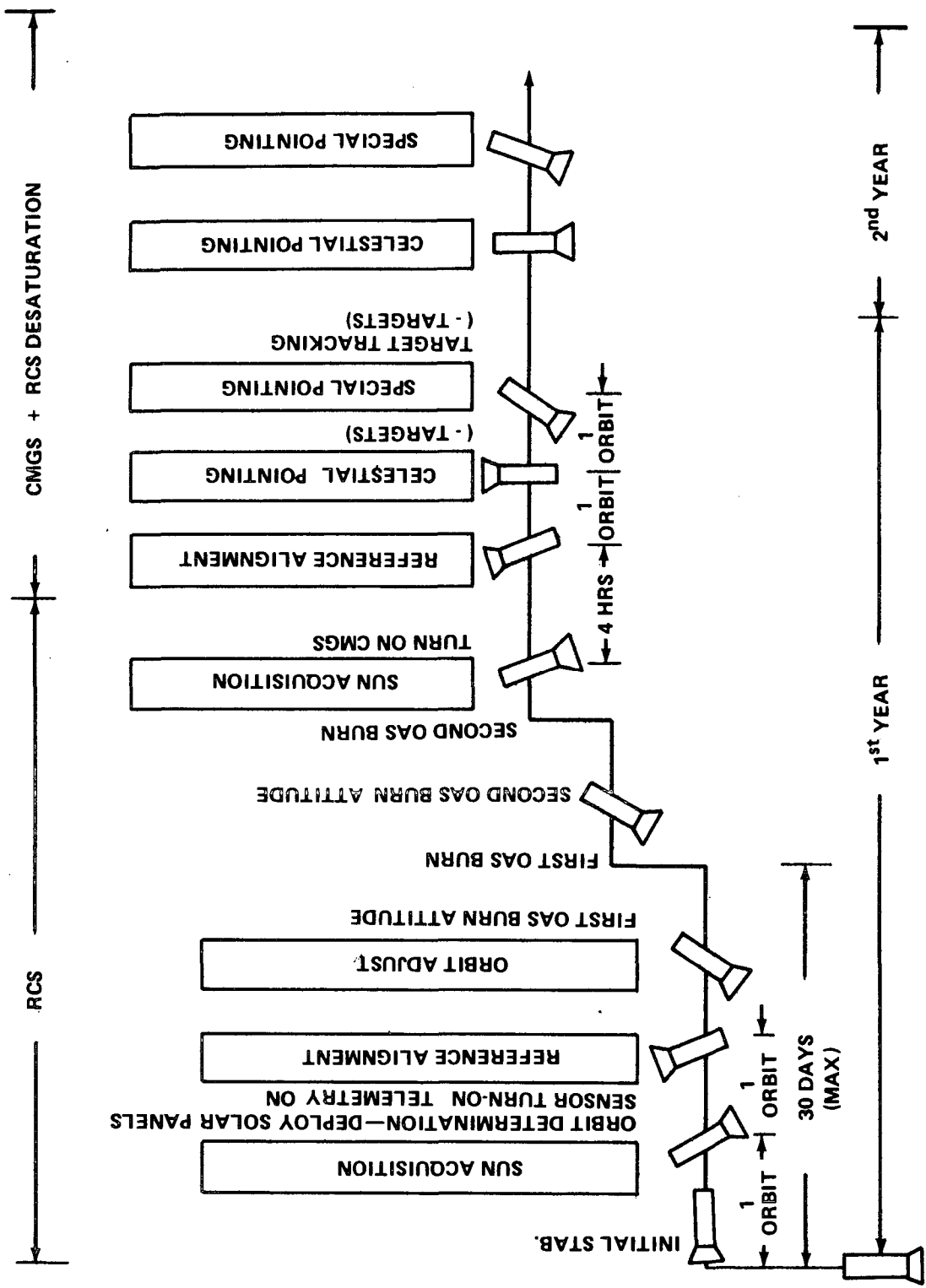


Figure VII-4. HEAO-C control modes timeline.

the actuator requirements for attitude hold in a 270 nautical mile circular orbit. In general, the g. g. torque vector components are cyclic. If a component is cyclic and biased from its null reference, the effect on the spacecraft is one-sided; that is, the momentum added to the system accumulates in one direction over a time period, in which case the momentum is defined as secular. The maximum g. g. torque determines a lower bound on the actuator torque needed for control and, assuming an orientation to maximize the secular g. g. effects, determines an upper bound on the required energy for attitude hold. For study purposes, the "energy" may be expressed equivalently as impulse, angular momentum, or RCS fuel weight. For the CMG system, the cyclic g. g. momentum establishes a lower bound on the CMG momentum capacity; whereas, the secular g. g. momentum establishes the RCS fuel required for momentum management (CMG dump).

The gravity gradient torque components acting along the principal body axes of the spacecraft are as follows [VII-1]:

$$T_{gx} = 2 C_x R_z R_y ,$$

$$T_{gy} = 2 C_y R_x R_z ,$$

and

$$T_{gz} = 2 C_z R_y R_x ,$$

where the Cs represent the maximum g. g. torque potential per vehicle axis and the Rs represent a unit vector along the local vertical projected into the body principal axis coordinate system. Using baseline HEAO-C parameters, the maximum torque potentials are as follows:

$$C_x = G (I_z - I_y) = 0.0098 \text{ ft-lb} ,$$

$$C_y = G (I_x - I_z) = 0.123 \text{ ft-lb} ,$$

and

$$C_z = G (I_y - I_x) = 0.122 \text{ ft-lb} \quad ,$$

where

$$G = 3M/2R_o^3 = 3 W_o^2/2$$

for which  $M$  is the gravity constant,  $I_x, y, z$  are principal Observatory inertias, and  $W_o$  is the earth orbital angular rate. As indicated, the gravity constant varies inversely as the cube of the distance,  $R_o$ , from the earth's center to the orbiting spacecraft. The torque potentials become larger as the altitude is lowered or the vehicle becomes less symmetric. The  $R$ s establish the shape of the g. g. torque profiles, depend upon the orientation of the HEAO relative to the local vertical, and are independent of the Observatory configuration or physical properties. The maximum torque potentials,  $C_s$ , are independent of the orientation and depend only on the altitude and HEAO inertial properties. The maximum value that the product  $2R_i R_j$  ( $i, j = x, y, z$ ) can attain is unity, and for an inertially oriented spacecraft, the shape is typically a sine function at twice the orbital period. Because of the aforesaid reasons, only the maximum torque potential per axis is calculated to form a basis for comparing various HEAO configurations or options.

Table VII-2 lists the vehicle parameters for three HEAO-C configurations and the expected gravity gradient effects. The configurations compared are the baseline HEAO-C, the baseline with a 25 percent distributed weight increase, and the baseline with a 50 percent weight increase. The baseline-plus-50-percent configuration is close to the maximum Titan IIID/OAS payload capability. The principal inertias are given in slug-ft<sup>2</sup>; the center of gravity, X-CG, is measured from the top of HEAO; the RCS lever arm,  $L_x$ , is measured from X-CG to the thrusters located on the OAS stage; and the vehicle weights are given in lbm. The lower half of Table VII-2 lists some calculated g. g. effects for each configuration. The maximum g. g. torque on any axis is denoted by  $T_g$  in ft-lb. Assuming that the torques are cyclic at twice the orbital period, the maximum quarter orbit momentum is given by  $H_{yq}$  in ft-lb-sec.

TABLE VII-2. BASELINE HEAO-C CHARACTERISTICS

	Configuration		
	Baseline (OAS + HEAO)	Base Plus 25%	Base Plus 50%
$I_x$ (slug-ft <sup>2</sup> )	2878	3455	3749
$I_y$ (slug-ft <sup>2</sup> )	69 513	77 478	97 139
$I_z$ (slug-ft <sup>2</sup> )	70 050	78 010	97 998
X-CG (ft)	14.5	14.6	16.5
$L_x$ (ft)	21.6	21.5	19.6
Weight (lb)	15 585	19 481	23 378
Altitude (n. mi.)	270	270	270
ISP <sup>a</sup> (sec)	140	140	140
$T_g$ (max) (ft-lb)	0.123	0.137	0.173
$H_{yq}$ (max) (ft-lb-sec)	111.4	123.7	156.3
$H_s$ (secular/orb) (ft-lb-sec)	445.6	494.8	625.2
ESM <sup>b</sup> /orb (ft-lb-sec)	209.2	232.3	293.4
Fuel ( $H_s$ ) (lb/2 yr)	1612	1797	2492
Fuel (ESM) (lb/2 yr)	756	844	1169

a. Specific impulse.

b. Estimated secular momentum.

If the g. g. momentum is cyclic, the baseline HEAO accumulates 111.4 ft-lb-sec after which the momentum decays to zero during the next quarter orbit. The quarter orbit momentum is indicative of the minimum CMG size needed per axis. If the momentum is secular, the maximum accumulated momentum per orbit,  $H_s$ , is 445.6 ft-lb-sec for the baseline configuration. With a 21.6 foot lever arm, the equivalent impulse is 20.6 lb-sec per orbit. At a 270 nautical mile altitude, there are about 15.2 orbits per day and assuming a fuel specific impulse of 140 sec, the fuel weight required to counteract the maximum secular momentum over a two year period is 1612 lbm, or equivalently, 225 760 lb-sec impulse.

However, it is unrealistic to base fuel weight for momentum management on worst case conditions. Since HEAO-C will have the capability of pointing to any experiment target on the celestial sphere within the solar power and thermal constraints, it would be just as unrealistic to base fuel weight on the best conditions. For these reasons, an estimated secular momentum (ESM) per orbit has been calculated by assuming that each axis accumulates its maximum secular momentum. The components are root sum squared and the result is divided by three to obtain an ESM of 209.2 ft-lb-sec per orbit for the baseline HEAO. In terms of fuel weight, 756 lbm (105 910 lb-sec impulse) is required over the two year mission to counteract the ESM for the baseline HEAO-C configuration. For the CMG momentum exchange system as selected for HEAO-C, only the secular momentum must be dumped.

However, if an all-RCS were used for HEAO-C, then both the cyclic and secular momentum must be compensated by mass expulsion. For the baseline configuration, the total accumulated momentum under worst case orientation is about 892 ft-lb-sec per orbit. With 15.2 orbits per day, a fuel specific impulse of 140 sec, and a lever arm of 21.6 ft, the fuel weight for a two year mission is 3228 lbm. This does not include fuel for maneuvering, initial stabilization, or control during OAS burn. Also, as the orbit decays, the g. g. and aerodynamic torques become larger and the fuel required for an all-RCS system could appreciably increase. Total fuel weight required indicates that an all-RCS is impractical for HEAO-C and that a momentum exchange system (CMGs) should be utilized for attitude control. An RCS system appears practical for dumping only the secular momentum and, since there is an RCS baselined for HEAO-A and -B, a similar system was baselined for HEAO-C to achieve as much commonality as possible with these designs. However, for long lifetime missions, it is also practical to consider utilizing environmental forces, such as magnetics, for momentum management of CMGs. A cold gas RCS for initial stabilization and OAS burn control, CMGs for maneuvering and attitude control, and electromagnets for momentum management form an attractive attitude control system alternative for HEAO-C. This alternate system is defined and described in Appendix E.

b. Aerodynamic. Some calculations were made to determine the maximum contribution aerodynamic torques would make to the overall torque profile affecting the HEAO-C. The aerodynamic coefficient equations used were taken from NASA TMX-53976 and were programmed for a digital computer. A search was then made for maximum torques over the orbital altitude range of 100 n. mi. to 270 n. mi. using both a nominal density profile for mid-1977 and a  $+2\sigma$  worst case profile for January 1978 [VII-2]. The maximum torque profiles obtained are shown in Figure VII-5. As can be seen, the aerodynamic torques play a significant role, compared to gravity gradient torques, below 150 n. mi. for the nominal case and below 175 n. mi. for the  $+2\sigma$  worst case. Above 150 n. mi., nominal aerodynamic effects rapidly disappear and by 200 n. mi., the effects are less than one-tenth of the gravity gradient torques. However, for the  $+2\sigma$  worst case density, the aerodynamic torque effects are approximately one-tenth those of gravity gradient even at the 270 n. mi. altitude.

Since the initial orbit presently planned for the HEAO-C is highly elliptical with a nominal perigee of 140 n. mi., the HEAO-C is not affected by aerodynamic torques to a large degree. Simulations run on the initial orbit with a nominal density profile show negligible effects on actuation rates and impulse requirements. Unless an orbit of lower perigee or less eccentricity, or both, is selected, it is felt that aerodynamic torques are relatively insignificant compared to gravity gradient torques.

c. OAS Engine Misalignments. During OAS burn, the RCS will be used to compensate all thrust vector misalignments of the main OAS engine. Assuming that the vehicle center of gravity is known very accurately, the main error will be OAS engine misalignment which may be as large as 0.5 degree. The minimum RCS thrust required to control this misalignment is easily calculated (Fig. VII-6.) By a simple trigonometric relation, the misalignment lever arm can be found and when multiplied by the OAS engine thrust gives a turning moment of 51.6 ft-lb. Since the RCS lever arm is known, a simple division gives 2.4 pounds of thrust minimum at the indicated RCS location. During the initial mission phases, the 5 pound thruster is more than adequate and even at the end of the mission when the thrust could be down to 2.5 pounds, any OAS firing can still be controlled.

## B. Baseline System Description

1. System Configuration. A basic guideline used in selecting the components for the HEAO-C ASCS was to preserve commonality as much as possible with the ASCS selected for Missions A and B. Based on the Phase B study

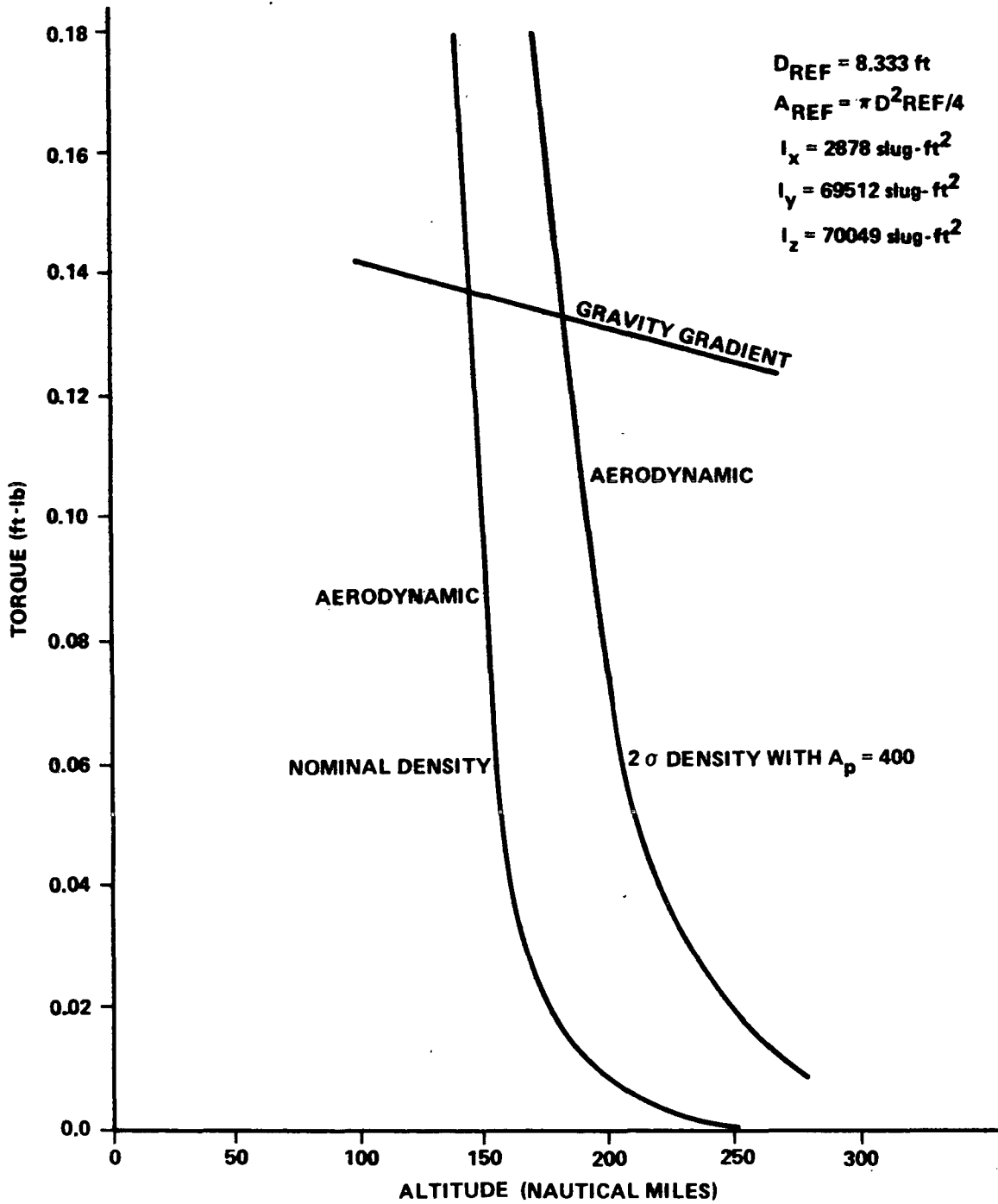
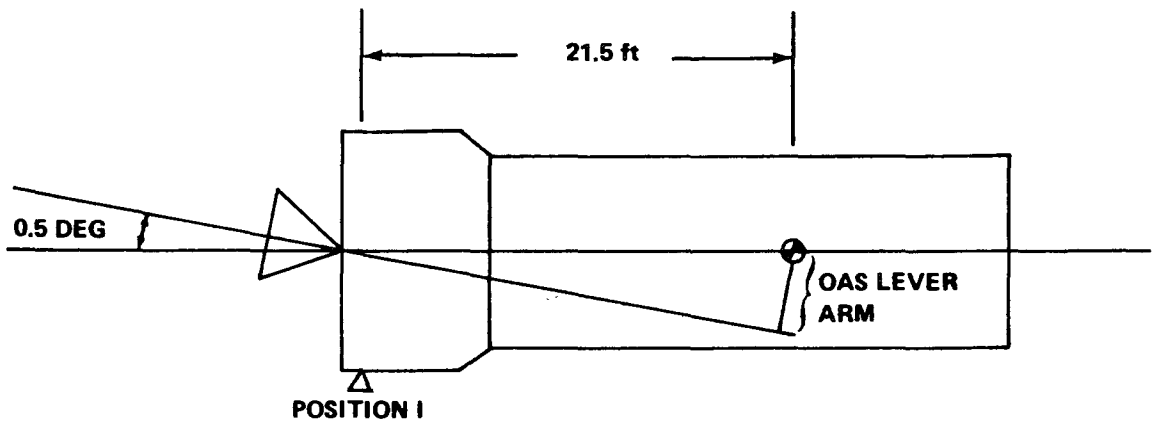


Figure VII-5. Aerodynamic and gravity gradient torques.



<b>OAS ENGINE THRUST</b>	<b>275 LB</b>
<b>OAS ENGINE MISALIGNMENT</b>	<b>0.5 DEG</b>
<b>OAS THRUST VECTOR LEVER ARM</b>	<b>2.25 IN.</b>
<b>OAS TURNING MOMENT</b>	<b>51.6 FT-LB</b>
<b>REQUIRED THRUST AT POSITION I TO COMPENSATE TURNING MOMENT</b>	<b>2.4 LB</b>
<b>NUMBER OF 5 LB THRUSTERS REQUIRED</b>	<b>1</b>

Figure VII-6. Thrust required for OAS burn phase.

results for HEAO-A and -B, hardware items were, as a rule, selected from one of the baseline Phase B systems for use on the HEAO-C if the more stringent requirements could be met using this hardware. Though hardware selections have been made on this basis, the final hardware selections for the A, B, and C vehicles eventually will be made from additional tradeoff studies that will take into consideration the requirements for all missions.

Two hardware items essential to the HEAO-C mission are the star trackers and CMGs. The CMGs selected by one Phase B contractor have been baselined for HEAO-C. Neither of the star sensing systems selected for HEAO-A and -B are satisfactory for HEAO-C. Therefore a new design star tracker was selected. In the case of the star trackers and CMGs, it may prove feasible to incorporate the HEAO-C designs into the HEAO-A and -B vehicles to preserve commonality and to reduce costs of the overall programs. This will be a critical tradeoff decision.

Figure VII-7 provides a functional block diagram of the baseline HEAO-C ASCS with a complete complement of sensors and actuators to perform all phases of the mission and Table VII-3 is the corresponding hardware summary. Section VII-C describes the utilization of various groupings of these individual components in the various operational phases and control system modes. Figure VII-8 presents the approximate locations and orientations of the baseline ASCS components.

Three wide angle sun sensors (WASSs) provide a  $4\pi$  steradian field of view for the solar acquisition mode so that the solar vector offset of the Z-axis can be sensed from any spacecraft attitude. Two of the sensors are aligned to the +Z-axis and are used in a redundant manner. Each WASS has a fine cell section that takes over when the solar vector is in its FOV and provides error signals to perform a final alignment to the solar vector.

The digital sun sensor (DSS) provides an accurate error sensing device having basically the same accuracy for its entire FOV. It can be used as a primary source for position updates and gyro calibration. Two sensors aligned to the +Z-axis are used to provide redundancy.

Four star trackers (one redundant per axis) provide the most important celestial reference source. The trackers acquire known star sources and provide the three-axis error signals required to accurately maintain the inertial hold condition. The outputs are used in the generation of gyro calibrations and position updates and also provide the attitude determination information for correlation with experiment data.

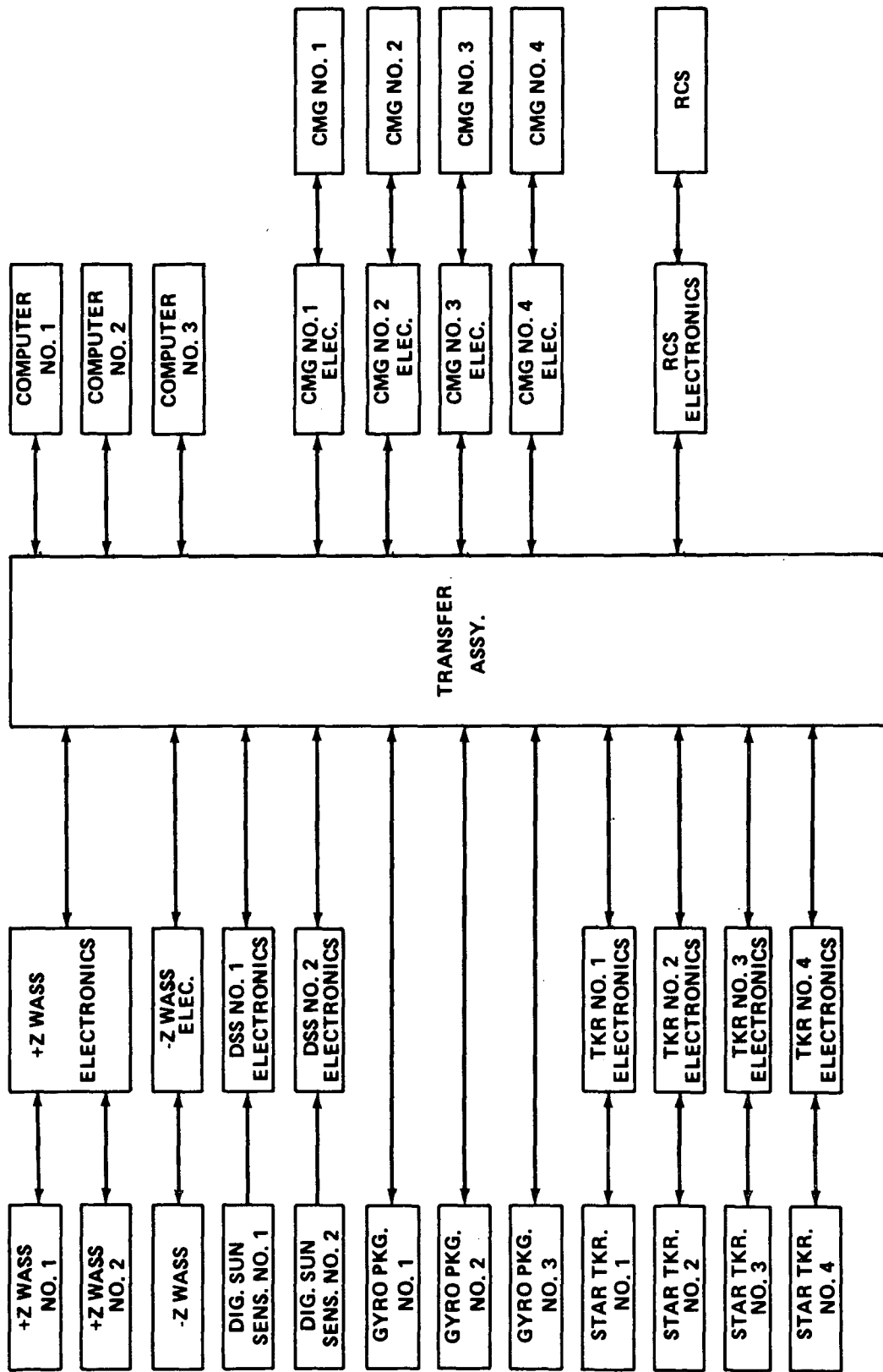


Figure VII-7. HEAO-C ASCS baseline configuration.

TABLE VII-3. HEAO-C ATTITUDE SENSING AND CONTROL  
SYSTEM HARDWARE SUMMARY

Item	Number of Units	Unit Weight (lb)	Unit Size (in.)	Avg Unit Power (W)	Type
Wide Angle Sun Sensors	3	1	2 × 1.9	0	Bendix 1818787
WASS Electronics	3	1	5 × 7 × 2	0.4	Bendix
Digital Sun Sensors (DSS)	2	0.75	3.8 × 3.8 × 1.5	0	Adcole
DSS Electronics	2	2.5	7.8 × 5 × 2.5	1.7	Adcole
Gyro Package	3 (2-Gyro)	11	7 × 8 × 6	15	TRW (Nortronics)
FHSTs	4	9	15 long × 4 dia	0	ITT
Star Tracker Electronics	4	14	5 × 11 × 12	8 (Estimate)	ITT
CMG (250 ft-lb-sec)	4	135	32 × 19 × 19	9 (32 spinup)	Bendix
CMG Electronics	4	27	12 × 16 × 7	18	Bendix
Processor and Computer	3	20	18.5 × 5 × 8	65	Bendix
Transfer Assembly	1	10	5 × 7 × 10	5	Bendix
RCS Electronics	1	16	9 × 14 × 7	11	Bendix
Total System Weight		871.5			
Average System Power				252.1	

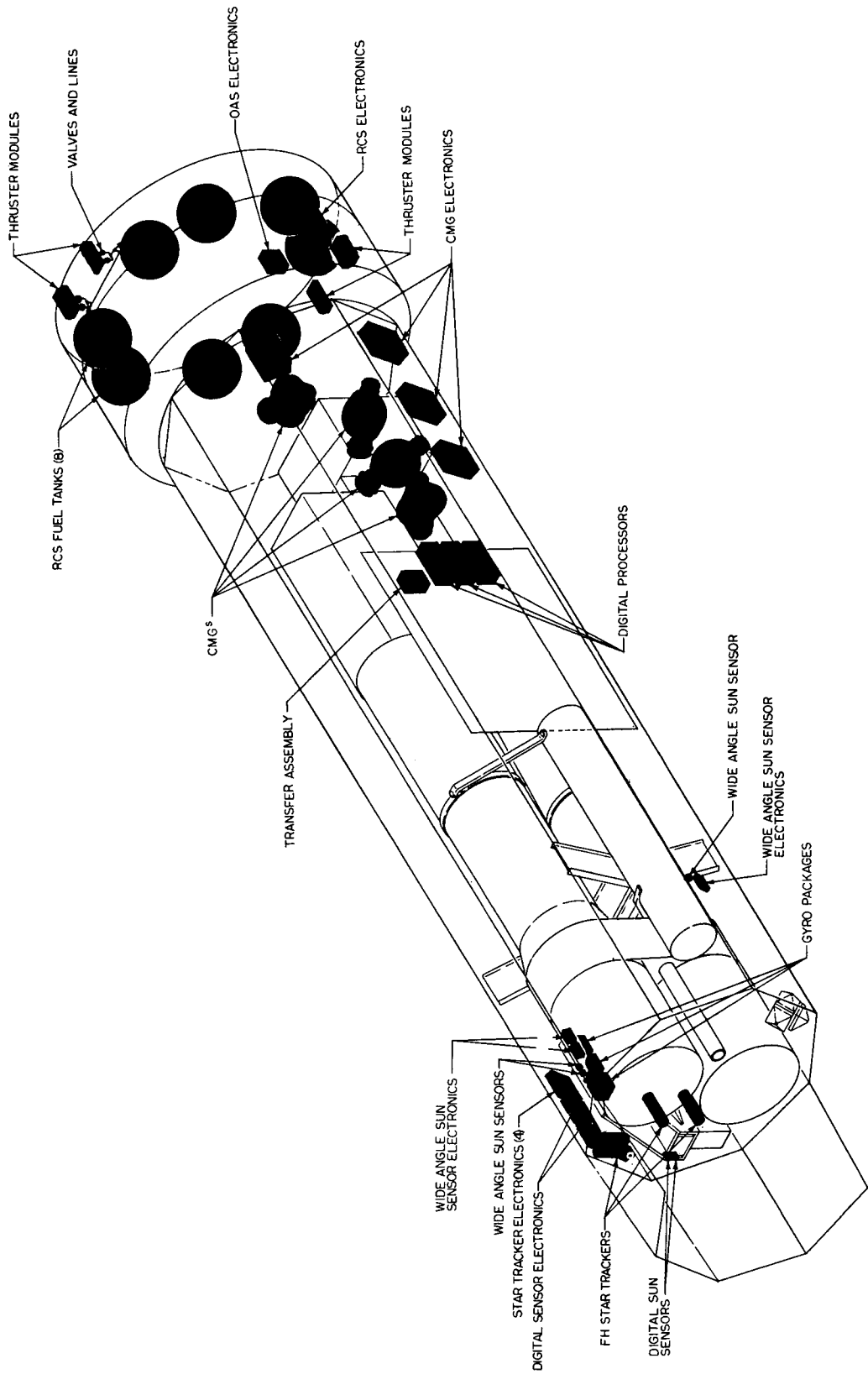


Figure VII-8. Location of the ACS components.

Three reference gyro packages, each containing two gyros with aligned input axes, are arranged orthogonally with respect to the Observatory axes. The outputs provide rate and position information for spacecraft control and attitude determination. During star tracker occultation periods, the gyros provide the information to completely control the spacecraft attitude. All slew maneuvers are performed under gyro control.

The RCS provides the actuation torques prior to CMG activation and provides torques for CMG momentum desaturation. A backup mode for spacecraft control is provided by the RCS in the event of CMG or digital computer failure during the course of the mission. Four single gimbal CMGs are mounted in a skewed configuration so that each CMG can provide a portion of the momentum requirements for each of the three Observatory control axes. The CMGs provide the momentum storage capability required to maintain the Observatory in an accurate inertial hold attitude and provide the vehicle torques required to maneuver the HEAO.

The digital computer unit (DCU) receives data inputs from the attitude and rate sensors and provides the following outputs:

- Outputs to the CMG and RCS electronics.
- Gyro compensation using sensor and/or ground update attitude information.

The transfer assembly serves as an interface assembly to bring on line the configurations of sensors and actuators as required, to route signals, to provide failure isolation, and to provide a certain amount of low level processing for fault detection, signal processing, switching logic, and command implementation.

## 2. Sensors

a. Sensor Characteristics. The baseline sensors and their characteristics are summarized in Table VII-4. The star tracker performance number is a worst case value that occurs when a star is being tracked on the extreme edge of the field of view. This is expected to occur for a very few experiment pointing directions. It has been assumed in error calculations that the random gyro drift is the only drift present and that it occurs in one direction. In practice, over long periods of time there is an averaging effect on this drift that tends to reduce errors somewhat during periods of total gyro control. The one arc minute error for the digital sun sensor is the expected maximum

TABLE VII-4. ASCS SENSOR CHARACTERISTICS

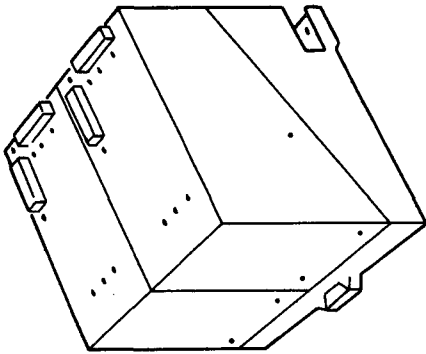
Sensor	No. of Units	No. of Active Units	FOV	Operating Temperature Range	Performance ( $3\sigma$ )
WASS	3	2	$2\pi$ steradians	-120°F to +130°F	$\pm 0.1$ deg at null
DSS	2	1	$64 \times 64$ deg	0°F to 130°F	1 arc min
Fixed Star Tracker (FST)	4	2	6 deg dia circular	-32°F to 160°F	$\pm 0.5$ arc min (max)
Reference Gyro Package	3 (2 gyros per RGA)	1 gyro per RGA		32°F to 135°F	Random Drift 0.015 deg/hr

that will occur for any sun position within the field of view. This requires certain calibrations by the supplier to minimize the effects of temperature and optical distortion. A detailed description of each sensor is contained in the following sections.

b. Reference Gyros. The baseline RGA selection consists of six hydrodynamic gas bearing spin axis gyros packaged in three reference gyro packages. Each package contains two gyros arranged with parallel input axes. The input axes of the three packages are aligned to three orthogonal control axes. A separate set of electronics supports each gyro in a package with only one gyro and associated electronics operative per package, thus providing complete standby redundancy in the event of failure in any axis. Figure VII-9 contains the characteristics of a reference gyro package.

Figure VII-10 illustrates a simplified block diagram of a single channel of the RGA. Six channels make up the total RGA. For reliability purposes, each channel is equipped with an independent power supply that regulates the incoming power and produces all of the dc and ac excitations required. The temperature of each gyro is maintained at its operating point by means of circuitry that senses the gyro temperatures and controls the power dissipated in the gyro heater. A precise indication of the gyro input angular rate is provided by the torquing current in the torque rebalance loop. This current maintains the gyro pickoff at null in the presence of input angular rates. The current is passed through a precision resistor and the resulting voltage is converted to frequency by means of a precision voltage to frequency converter (VFC). Increments of sensed vehicle angular motion are represented by the VFC output pulses and the pulses are accumulated in the control DCU for further processing. A spin-motor rotation detector provides a positive indication that the gyro wheels are running at synchronous speeds by its use in developing a telemetry signal. Other signals are monitored and conditioned for telemetry for use in ground detection of a failure.

The Northrop GI-K7G gas bearing gyro was selected instead of a ball bearing spin axis gyro to meet the mission lifetime requirements and to satisfy the low drift requirements. The GI-K7G gyro has a ceramic hydrodynamic gas spin bearing operating in a beryllium float. The float is constrained along the output axis by a frictionless, taut wire suspension system with backup pivots to prevent damage to the wire suspension system during excessive lateral loading. The backup pivots are not engaged during normal operation. The gyro unit is approximately 1.7 inches in diameter, 3.3 inches long, and weighs 10 ounces. The GI-K7G is a scaled-down and simplified version of the Northrop GI-T1B gyro presently being used in the Minuteman ICBM system as an inertial guidance alignment reference. A number of these gyros are being used for inertial navigation on the C5-A transport.



REFERENCE GYRO ASSEMBLY MODULE  
(ONE OF THREE)

**PHYSICAL CHARACTERISTICS  
(PER MODULE)**

- WEIGHT: 11 lb
- POWER: 15 WATTS (ONE GYRO OPERATING)\*
- SIZE: 7.0 x 8.0 x 6.0 in.
- RELIABILITY:  $\lambda = 5070 \times 10^{-9}$  FOR EACH GYRO CHANNEL
- LIFETIME: >10 000 GYRO START- STOPS

\* POWER CONSUMPTION INCLUDES  
5 WATTS FOR HEATER

**SPECIFICATIONS**

- FIXED BIAS: 5 DEG/HR
- RANDOM DRIFT: 0.004 DEG/HR ( $1\sigma$ )
- SCALE FACTOR UNCERTAINTY: 50 PPM ( $1\sigma$ )
- MAXIMUM ANGULAR RATE: 1.5 DEG/SEC
- OUTPUT QUANTIZATION: 0.2 ARC SEC/PULSE
- OPERATING TEMPERATURE: 50 TO 90 °F

**DESIGN CHARACTERISTICS**

- THREE SENSOR MODULES USED
- EACH MODULE CONTAINS TWO GYROS AND SUPPORT ELECTRONICS
- ONE GYRO IN EACH MODULE ON AT A TIME
- SECOND GYRO (AND ELECTRONICS) IS REDUNDANT TO FIRST
- OPERATES FROM  $28 \pm 5$  VDC

Figure VII-9. Reference gyro assembly summary specification.

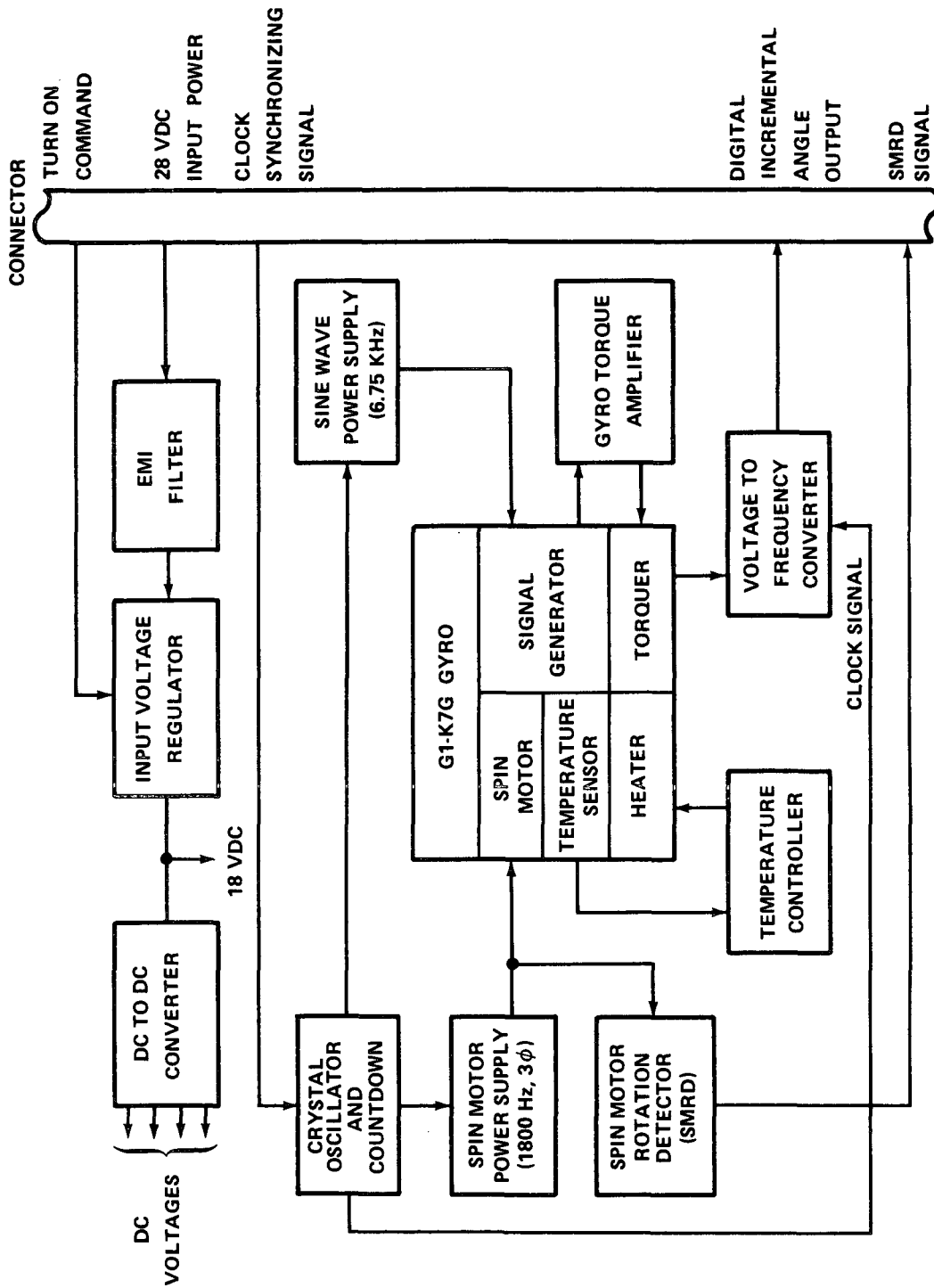


Figure VII-10. Gyro channel functional block diagram.

c. Wide Angle Sun Sensors. The baseline WASS is the Bendix 1818787 sun sensor (Fig. VII-11). Referring to the operation diagram (Fig. VII-12), four photovoltaic cells mounted on an aluminum casting behind a square aperture sense the sun rays in the central, 20 degree solid cone. Each pair of diametrically opposed cells is interconnected, one pair per channel. Eight additional photovoltaic cells are mounted on the periphery of the casting at right angles to the quad cell structure and sense the complete solid hemisphere beyond the central, 20 degree solid cone. Shadowing bosses shield these cells during the first 10 degrees of rotation. Diametrically opposed cells are interconnected, four per channel, in series with the two electrically isolated output channels. The cell structures are hermetically sealed by a glass dome.

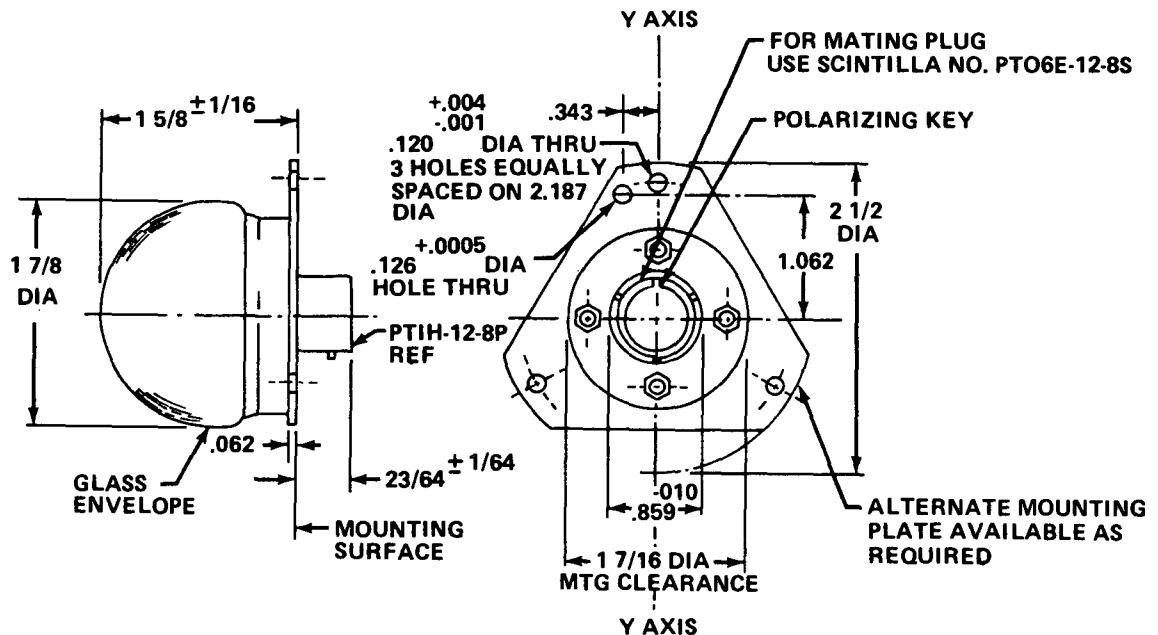


Figure VII-11. WASS outline drawing type 1818787.

Parallel sunlight entering perpendicular to the square aperture illuminates the quad cells equally, but does not fall upon the peripheral cells due to shadowing bosses. For this condition, no net current is passed. When parallel light enters at some angle other than normal, a proportional current is generated by the quad cells and the proportionality between the deviation angle and the corresponding electrical output is maintained linearly through the central cone of 20 degrees by the action of the aperture plate. As the sun sensor rotates beyond the central 20 degree cone, into its saturated region, the response of the quad cells falls and that of the peripheral cells increases,

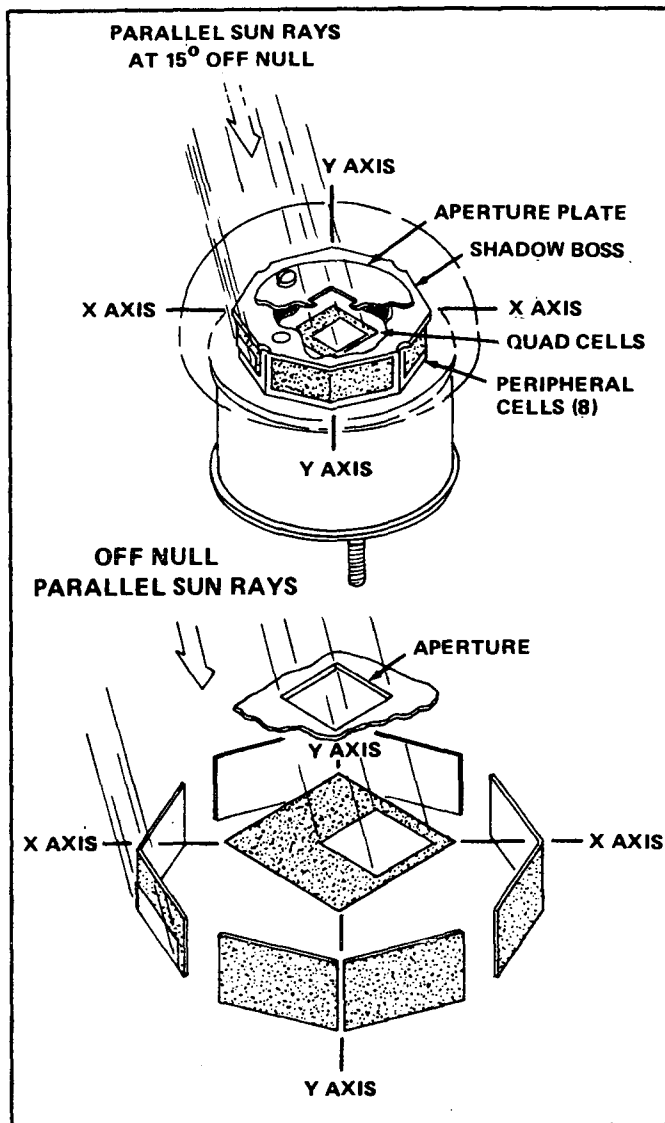


Figure VII-12. Operation diagram.

providing a smooth transition in the output signals as shown in Figure VII-13. Shown in Figure VII-14 is an alternate mounting configuration for the WASS designated type 1771858 having identical output versus input characteristics to the selected configuration. Figure VII-15 schematically depicts the two identical WASS electronic channels, each of which processes the electrical outputs of a sun sensor element array and provides two-axis information. The three primary functions of each electronic channel are the following:

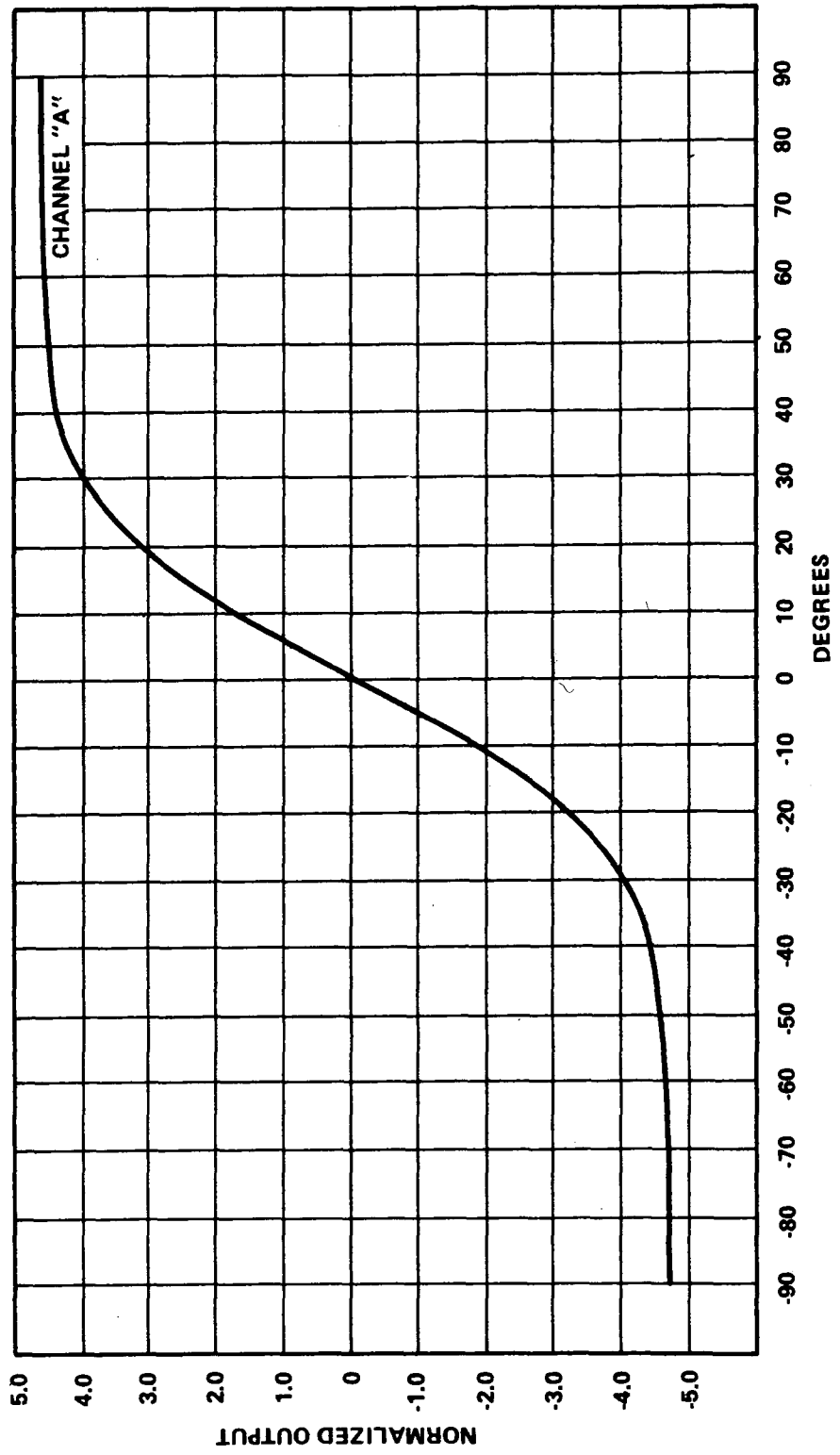


Figure VII-13. Output versus zenith angle.

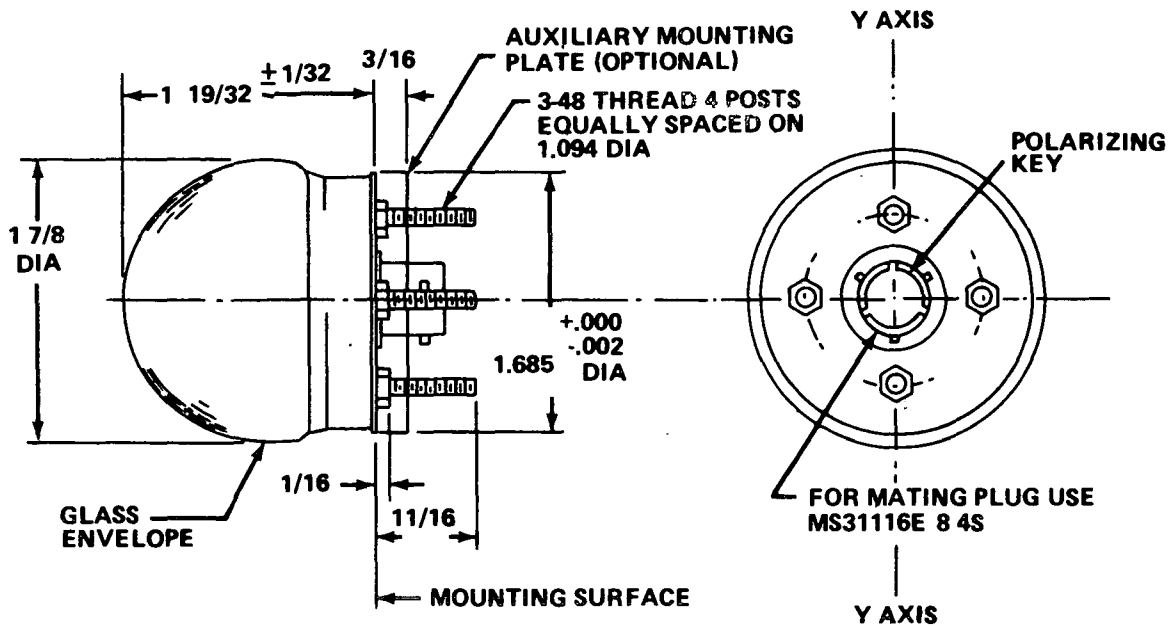


Figure VII-14. WASS outline drawing type 1771853.

- (1) Amplification of the WASS signals for the digital computer unit and for the emergency mode electronics in the transfer assembly.
- (2) Buffering the amplified signals for telemetry.
- (3) Generation of its own regulated bias power from spacecraft power.

d. Star Trackers. The baseline ASCS utilizes four FHSTs in the configuration illustrated by Figure VII-16. One tracker per axis is active with the remaining trackers in a standby mode. A detailed description of the considerations used in selecting fixed-head trackers in this configuration for the baseline ASCS is given in Appendix E.

For any pointing direction on the celestial sphere, the baseline configuration provides a star fix 91 percent of the time. A star fix is defined such that one reference star is present simultaneously in each of the X and Y axes trackers. The star-empty directions are primarily in the galactic pole regions and are well separated. Thus the probability appears to be small that an experiment target and a star-empty region will coincide. Each star tracker alone provides better than 95 percent of the celestial sphere. This latter fact is important because, if the star tracker that is aligned with the experiment

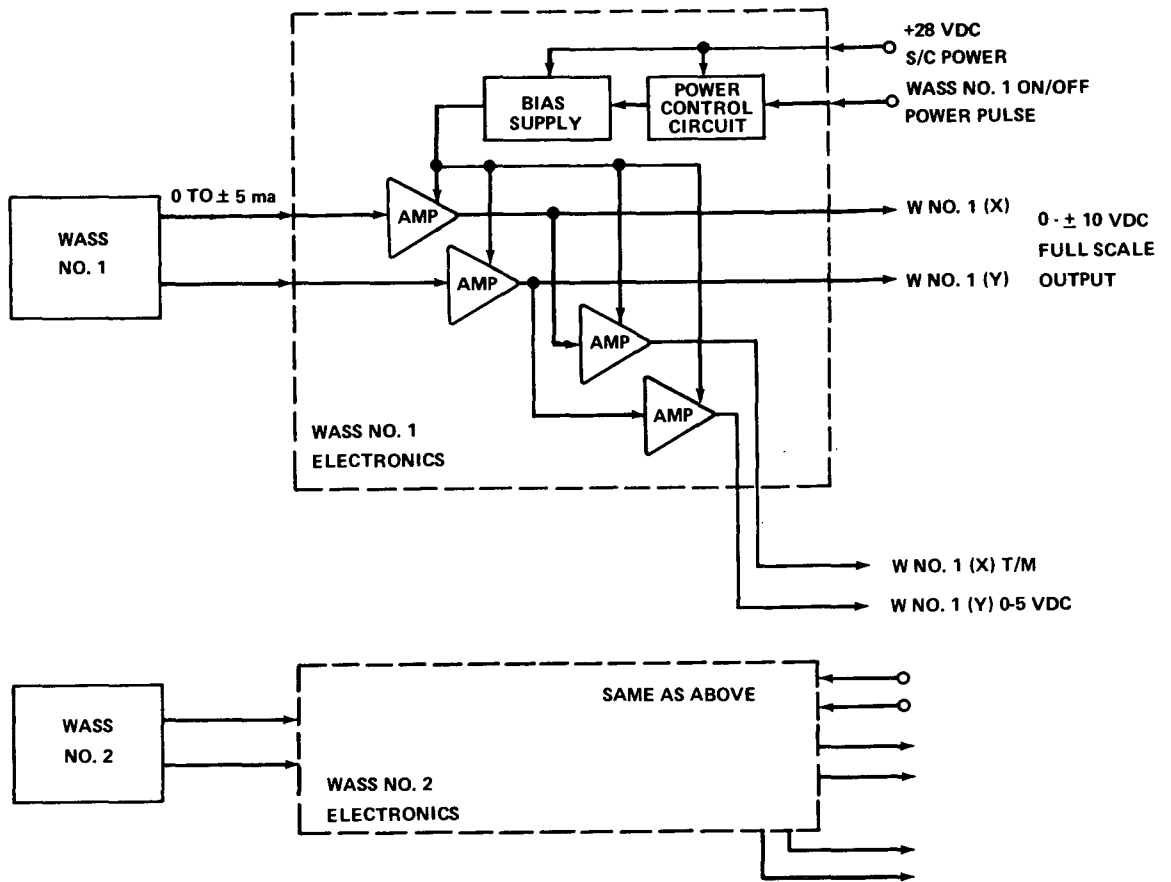


Figure VII-15. Simplified WASS electronics schematic.

optical axis has a reference star, the two-axis pointing accuracy can be maintained, with a slight degradation in the accuracy about the target line-of-sight, by using the digital sun sensor to determine the reference attitude about the target line-of-sight. Alternates to the baseline configuration are discussed in Appendix E.

Each tracker is a two-axis, dual mode star tracker that precisely measures the angle between its boresight axis and the line-of-sight to the target star. Star position information is provided in two axes mutually perpendicular to the boresight axis. The following are specific features of the star tracker:

- Electronic scanning of the FOV.
- Ability to scan a large FOV.

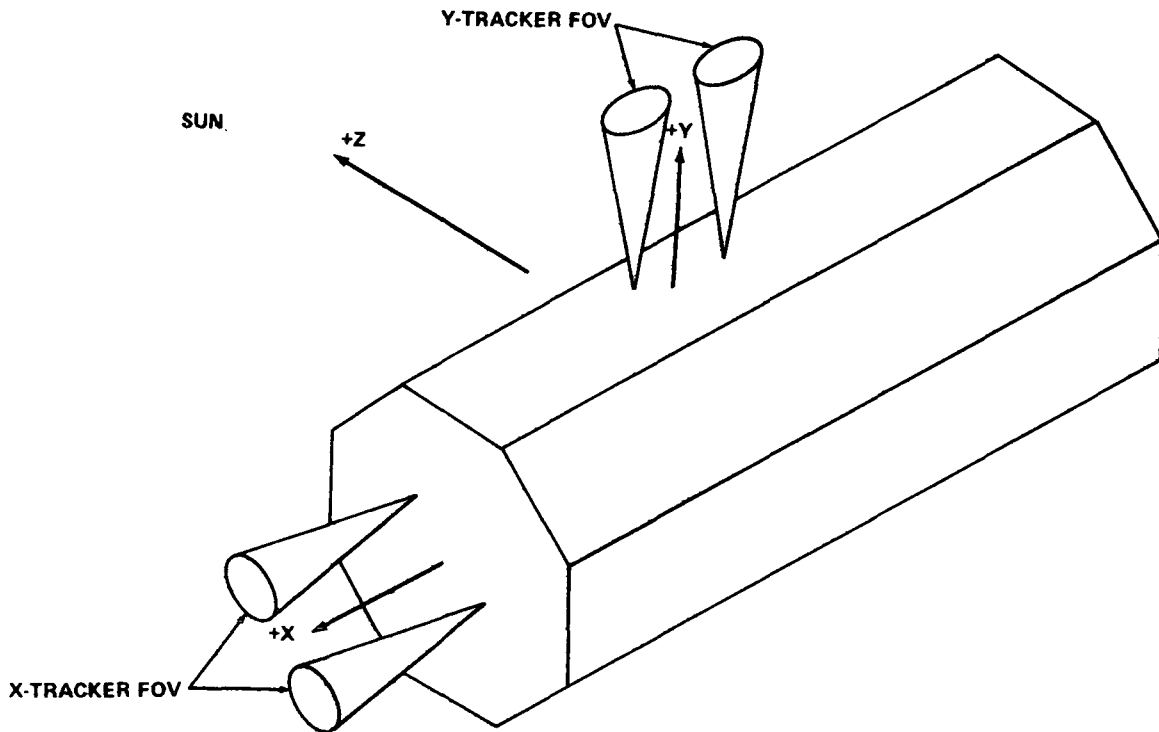


Figure VII-16. HEAO-C star tracker configuration.

- Selection of the brightest star in the FOV.
- Excellent position information resolution.
- Automatic switching between track and acquisition modes of operation.
- Linear star magnitude indication.
- Bright source protective shutter.
- Modular design permitting changes in FOV, accuracy and sensitivity by optics interchange.
- Magnetic shielding.

Figure VII-17 illustrates the modular design concept using Questar optics based on an ITT design. The image dissector, deflection coil, and magnetic shield assembly are located in a structural tube that protrudes from the rear of the housing. In this assembly, the image dissector and its associated focus/deflection coil are potted solidly into the triple-layered magnetic shield providing a lasting alignment between the optics and the image dissector. The principal characteristics of the tracker selected to meet the HEAO-C requirements are as follows:

Size:	15 in. long by 4 in. in diameter.
Optics:	3.5 inches in diameter
Sensor:	F4052 (Ruggedized and temperature compensated). Photocathode: S-20.
Total FOV:	6 degrees diameter.
Sensitivity:	+6 magnitude (acquisition and track)
Accuracy:	2.5 arc sec at boresight 30 arc sec at edge of FOV.
Outputs:	Track signals: X and Y Bandwidth: 0.1 Hz Star brightness: Proportional to log of star brightness.
Bright Object Protection:	Sun shield  Over-exposure detector  Shutter

The operation of the image dissector is the key to the operation of the star tracker. Figure VII-18 shows an image being focused on the photocathode to form an electron image of the target. Behind the photocathode are an aperture mask and secondary emission dynodes capable of amplifying a signal many thousand times. When an accelerating voltage is applied between the photocathode and a mechanical limiting aperture, only those electrons leaving

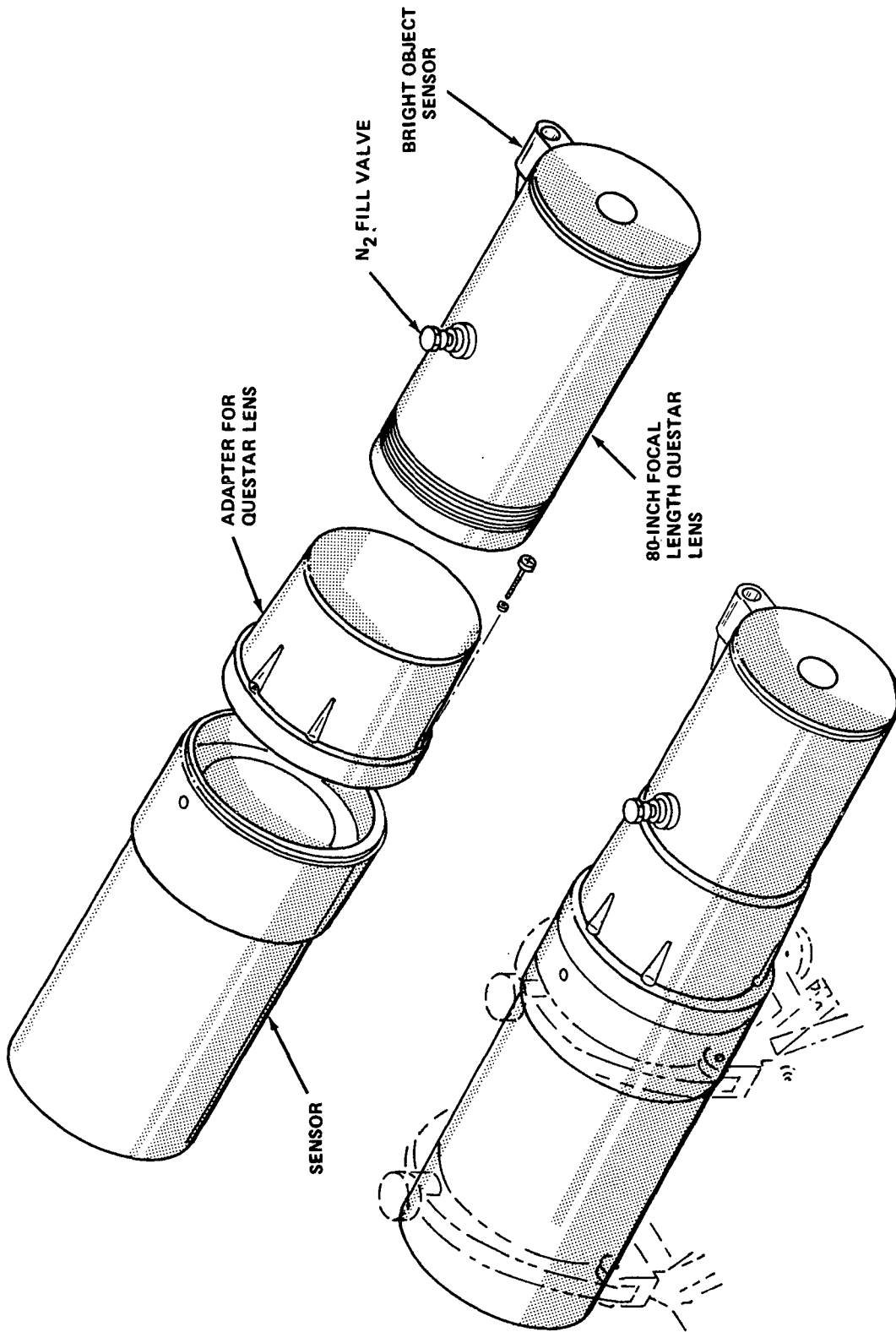


Figure VII-17. Optical data corrector (ODC) Questar configuration.

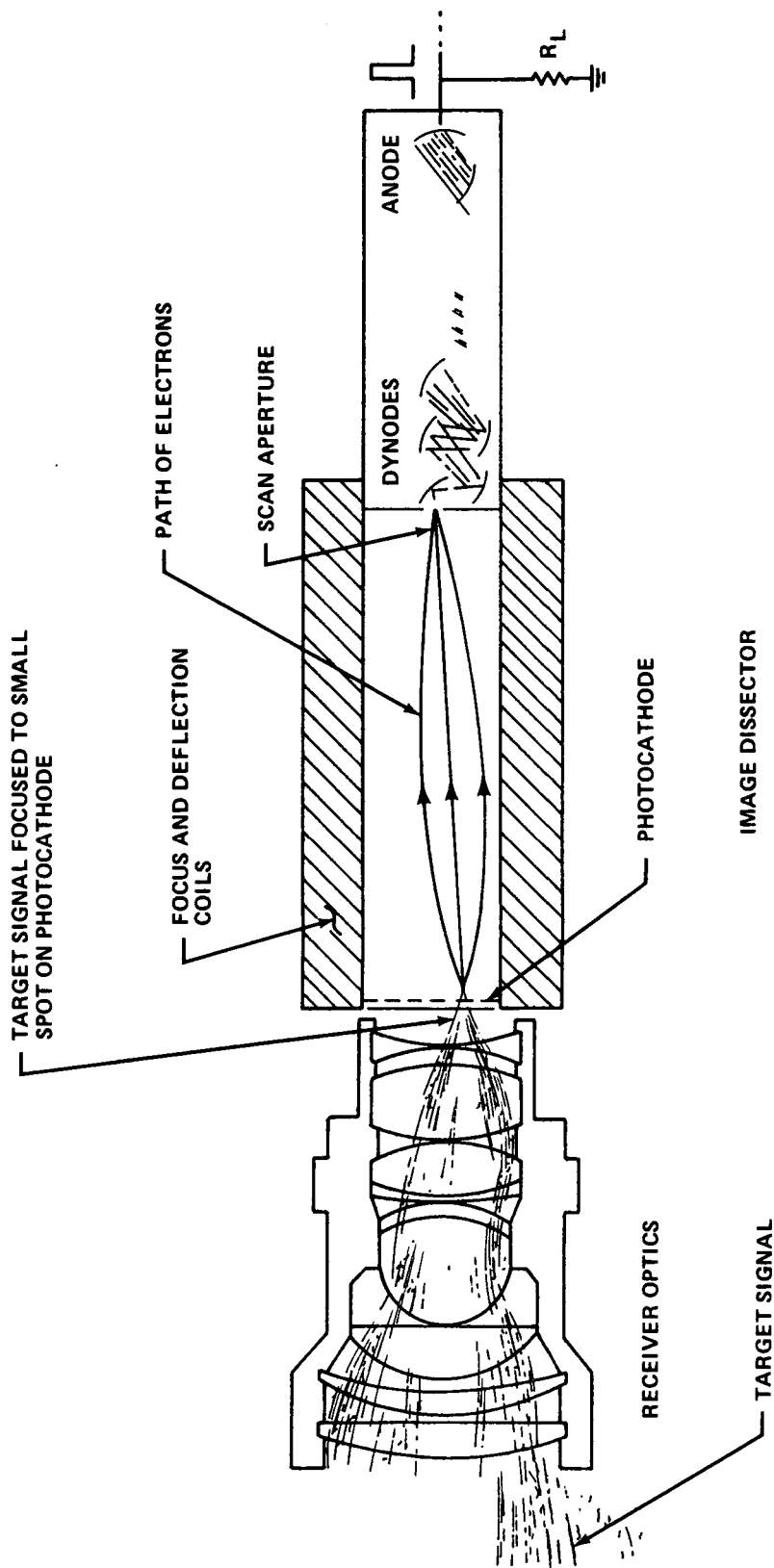


Figure VII-18. Optics and sensor.

a specific area on the photocathode will pass through the aperture. When a target image is positioned on the photocathode by the lens system, the electron optics of an electromagnetic focusing field forms a very small stream of electrons. A deflection coil positioned around the image section provides magnetic deflection of the target image electron beam. By applying proper deflection coil currents, the electron beam is made to sweep back and forth across the aperture resulting in a modulation of the electron beam. The resulting output signal is used in a closed loop system to keep the instantaneous photocathode dimension as defined by the limiting aperture centered on the target. In operation, the star tracker electronics drive the deflection coils in either a search mode scanning the 6 degree FOV or in the track mode scanning about a target. In the track mode, the modulated image dissector tube output is processed to produce internal two-axis error signals that are used as feedback signals to the deflection coils for the correction of target position and velocity errors. Target brightness, target presence, and two-axis position voltages are outputs generated by the star tracker electronics.

Initially, the star tracker is in the scan or search mode of operation where a cycle begins that selects the brightest star in the FOV. Upon completion of this cycle, a target pulse counter enables the mode control to switch from search to track and the digital search scan stops at the next target pulse which is the brightest in the FOV due to automatic gain control (AGC) adjustments that took place during the brightest star selection cycle. In the track mode, the pulse width modulated target video signal is amplified and AGCd to produce a square-wave output. Demodulator circuits develop error signals proportional to the distance between the center of the cross scan and the center of the target in two axes. Both signals are fed to summing amplifiers which generate the two-axis position signals. The preamp AGC level set during the initial bright star selection of the scan mode is a logarithmic function of target brightness and is used after amplification to provide a linear indication of brightness. If the background or any other light source becomes bright enough to damage the tracker, an over-exposure detector generates a signal that closes a mechanical shutter and removes power to the image dissector tube.

e. Digital Sun Sensors. The baseline ASCS uses two DSSs and electronic assemblies, one active and one standby, to provide complete redundancy. The sensors are mounted to the spacecraft structure in approximate alignment with the +Z-axis and with the reference aligned to the experiment optical axis. The sensors provide accurate two-axis attitude signals proportional to spacecraft +Z-axis deviations from the solar vector. Off-sunline operation permits offset pointing from the sun up to 15 degrees for continuous operation or up to 30 degrees for one orbit.

The baseline DSS, manufactured by the Adcole Corporation, provides sun position determination as angles of rotation about the two orthogonal X and Y Observatory axes. The FOV is 64 by 64 degrees; the resolution is 1/256 degree; and the accuracy on axis is better than one minute of arc. The output for each axis is a parallel natural binary number of 14 bits. An analog output is also provided; it is linear over  $\pm 30$  arc min from null and is saturated at angles greater than  $\pm 30$  arc min. The technique used by the DSS is illustrated in simplified form in Figure VII-19. A reticle containing an entrance slit on

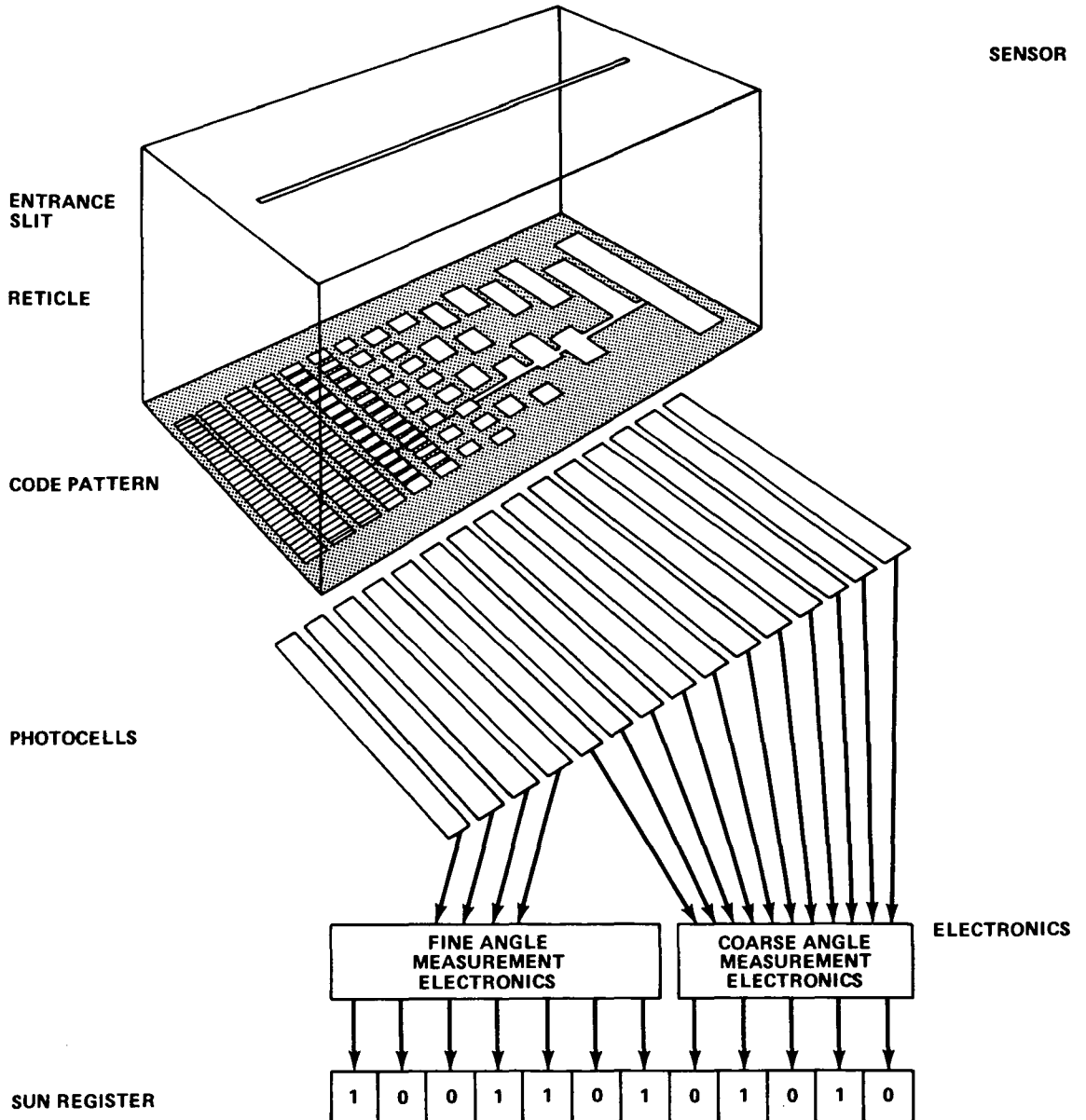


Figure VII-19. Digital sun sensor schematic.

one side and a binary coded pattern on the other side is mounted over an assembly of photocells in the sensor unit. A second reticle, mounted with its entrance slit at right angles to that of the first provides information about a second axis. The combination of reticles and photocells thus provides two-axis information. The outputs from the photocells are processed by the DSS electronics to provide the two-axis DSS outputs.

By sensor design, the five most significant bits representing 2, 4, 8, 16 and 32 degree increments are provided by one reticle and photocell pattern and the nine least significant bits (1, 1/2, 1/4, 1/8, 1/16, 1/32, 1/64, 1/128, 1/256 degree) are generated by a fine reticle photocell pattern. The two "coarse" angle slits (one for each axis) are provided on a single reticle (Fig. VII-20). The two additional slits are for automatic threshold adjust. To obtain the 2, 4, 8, 16, and 32 bits for coarse angle measurement, a coded mask is used. Ambiguity in reading the binary code when more than one transition is required at the same time is eliminated by the use of "V-brush" logic.

Figure VII-21 is a simplified block diagram of the DSS electronics circuitry required to read and store the sun angle on external command and to provide a parallel binary output. The outputs of the four "fine" photocells for each axis are chopped by four quadrature square waves derived from a chain of flip-flops counting down from a fixed-frequency oscillator. Their outputs are summed and passed through a bandpass filter to yield a sine wave whose phase is an indication of the sun angle. The phase angle is measured by counting the number of pulses at the oscillator frequency that occur between the zero crossing of the phase reference and the zero crossing of the sine wave. The count is initiated after synchronizing to an external command signal. The number counted is transferred into a buffer storage register and is held until receipt of another command.

Coarse angle determination is the function of the remaining photocells. The automatic threshold adjust (ATA) cell and associated amplifier serve to set the threshold for determination of zero or one from the other cells. If the output from a photocell exceeds the output of the ATA cell, the digit is one; if not, the digit is zero. The ATA cell is arranged to have the full field of view of the sensor, but its slit is half as long as the slits for the data cells. Use of the ATA cell compensates for the change of output with angle of incidence, compensates varying satellite-sun distance, and greatly simplifies ground calibration by eliminating the need for an accurate absolute level of illumination in the tests. The selection of the leading or lagging cell for each digit is initiated by the most significant digit in the counter. The exclusive OR gates then accomplish the selection and cause the correct number to be set into the storage register.

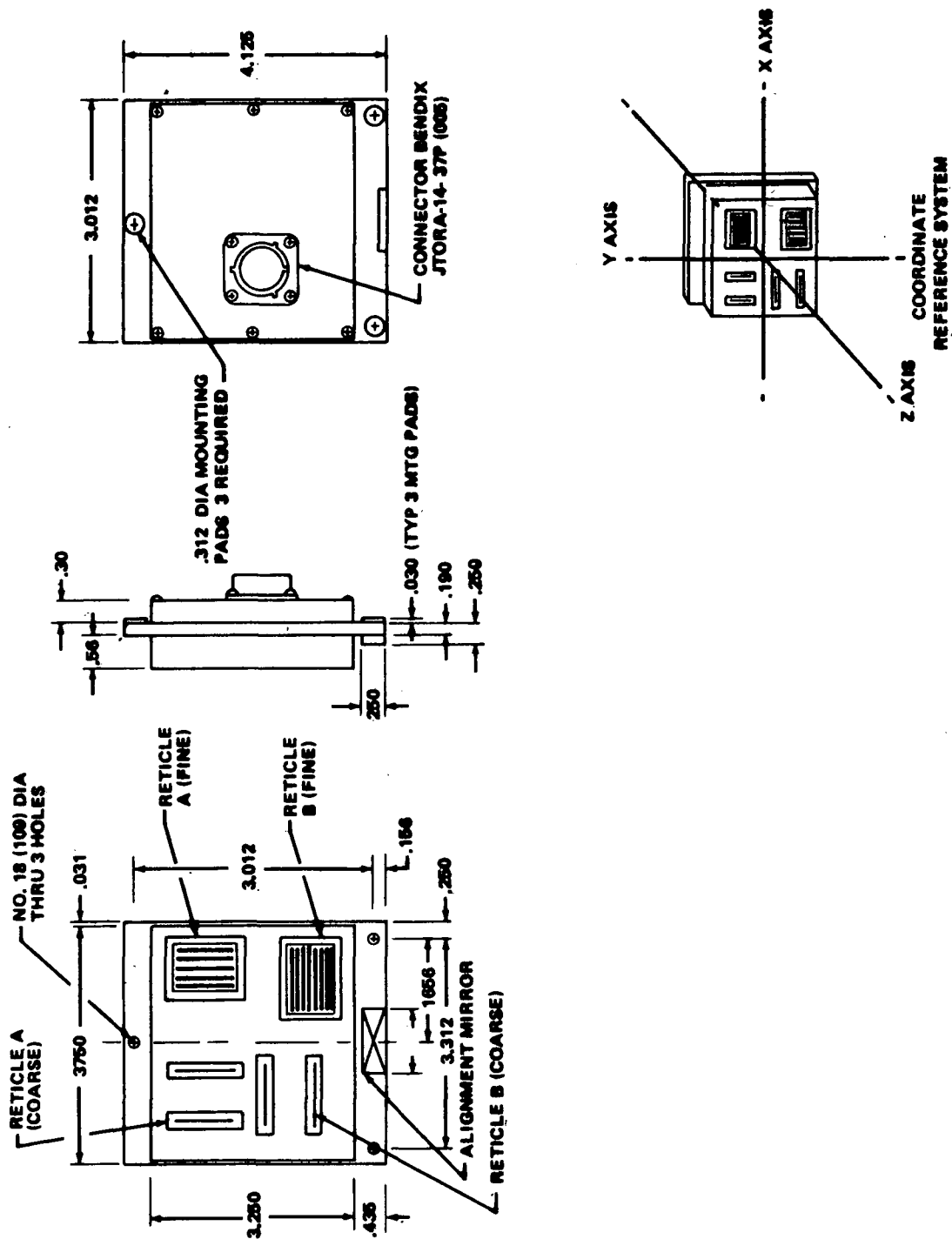


Figure VII-20. Digital sun sensor outline.

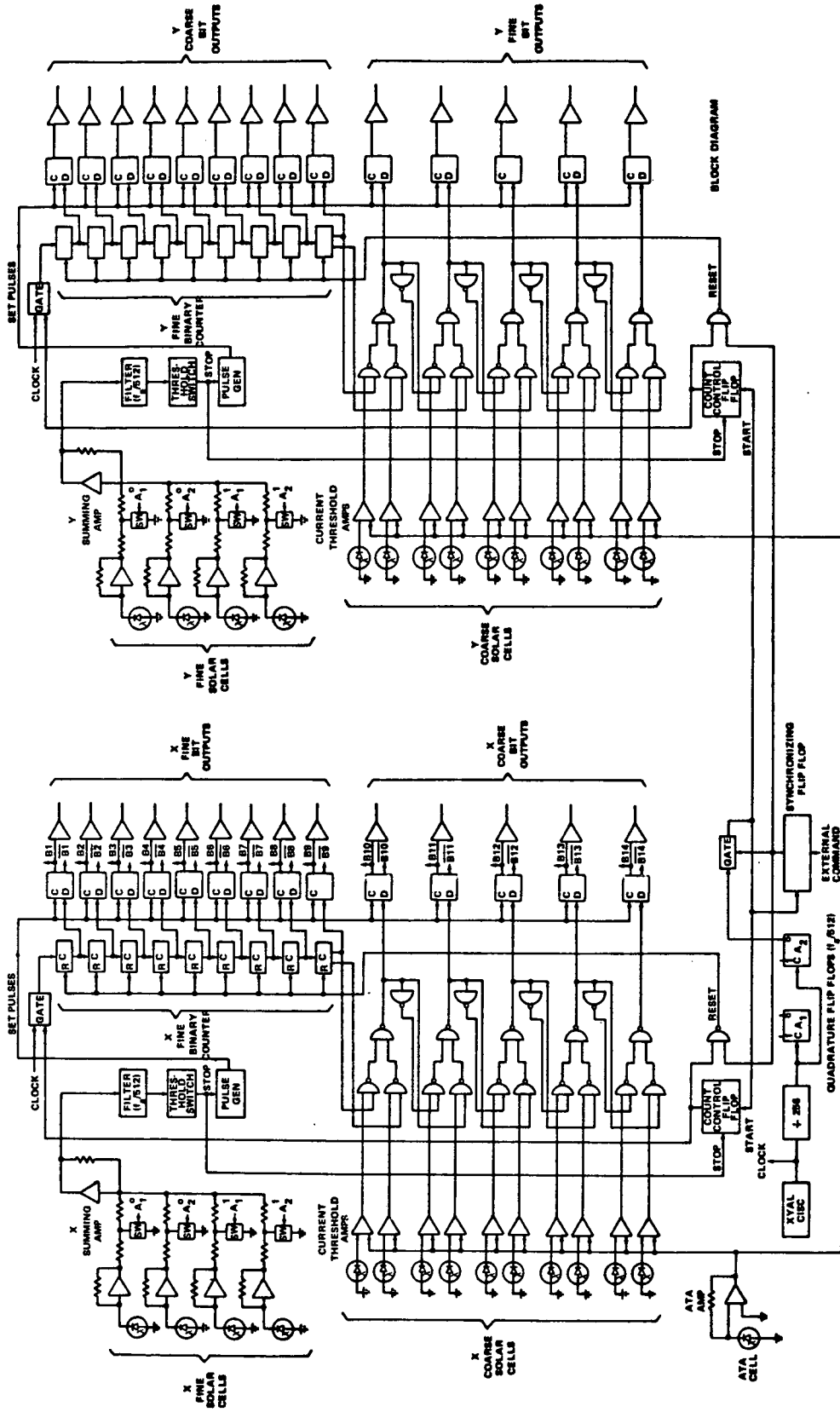


Figure VII-21. Digital sun sensor electronics.

The delay between the external command and the determination of sun angle has a maximum equal to twice the period of the chopping waveform. If a digital-to-analog conversion of the sun angle is made for control purposes, updating often may be desirable. The chopping frequency can be made as high as 25 kHz. However, a frequency of 10 kHz is used which, in the proposed baseline DSS, is generated by an oscillator contained in the electronics package.

Although not required in the HEAO ASCS mechanization, the DSS provides an analog error signal which is derived from the outputs of the buffer storage register. The outputs of the seven least significant bits are converted to derive a 128 step linear output as a function of angle. The more significant bits are decoded into signals that modify the analog output in such a manner as to bias the output for error angles of 0 to 30 minutes and to restrict the dynamic range to  $\pm 30$  minutes.

The physical envelope of the electronics measures approximately 7.8 by 2.5 inches. It weighs 2.5 pounds and requires approximately 1.7 watts of dc power.

### 3. Actuators

a. CMG Configuration. The baseline ASCS uses four Bendix MA-500 CMGs with minimum modification, arranged in a skewed configuration. This selection utilized phase B study results and was made to provide commonality between HEAO Missions A, B, and C. Use of the same CMG developed for Missions A and B should result in a developed and qualified item for HEAO-C at minimal cost.

Figure VII-22 shows the arrangement for the baseline skewed four-CMG configuration with the CMGs aligned in the zero angular momentum (reference) position. Each of the CMGs is gimballed in a manner that constrains the angular momentum vector  $\bar{H}$  of each CMG to lie in a plane. Geometrically, this is accomplished by orienting the gimbal axis of each CMG perpendicular to the plane containing its  $\bar{H}$  vector. By varying the angle  $\beta$  at installation, the momentum envelope of this configuration can be adjusted. For the HEAO-C, a near spherical momentum envelope is preferred so that momentum can be exchanged between axes during maneuvers. A  $\beta$  angle of 53.1 degrees provides approximately equal momentum capability for each of the vehicle control axes. Each CMG runs at only half the design speed to produce 250 ft-lb-sec per unit. A detailed description of the steering laws required to command the individual CMG gimbal rates for maneuvering and disturbance to torque counteraction is contained in Section E-2 and Appendix E.

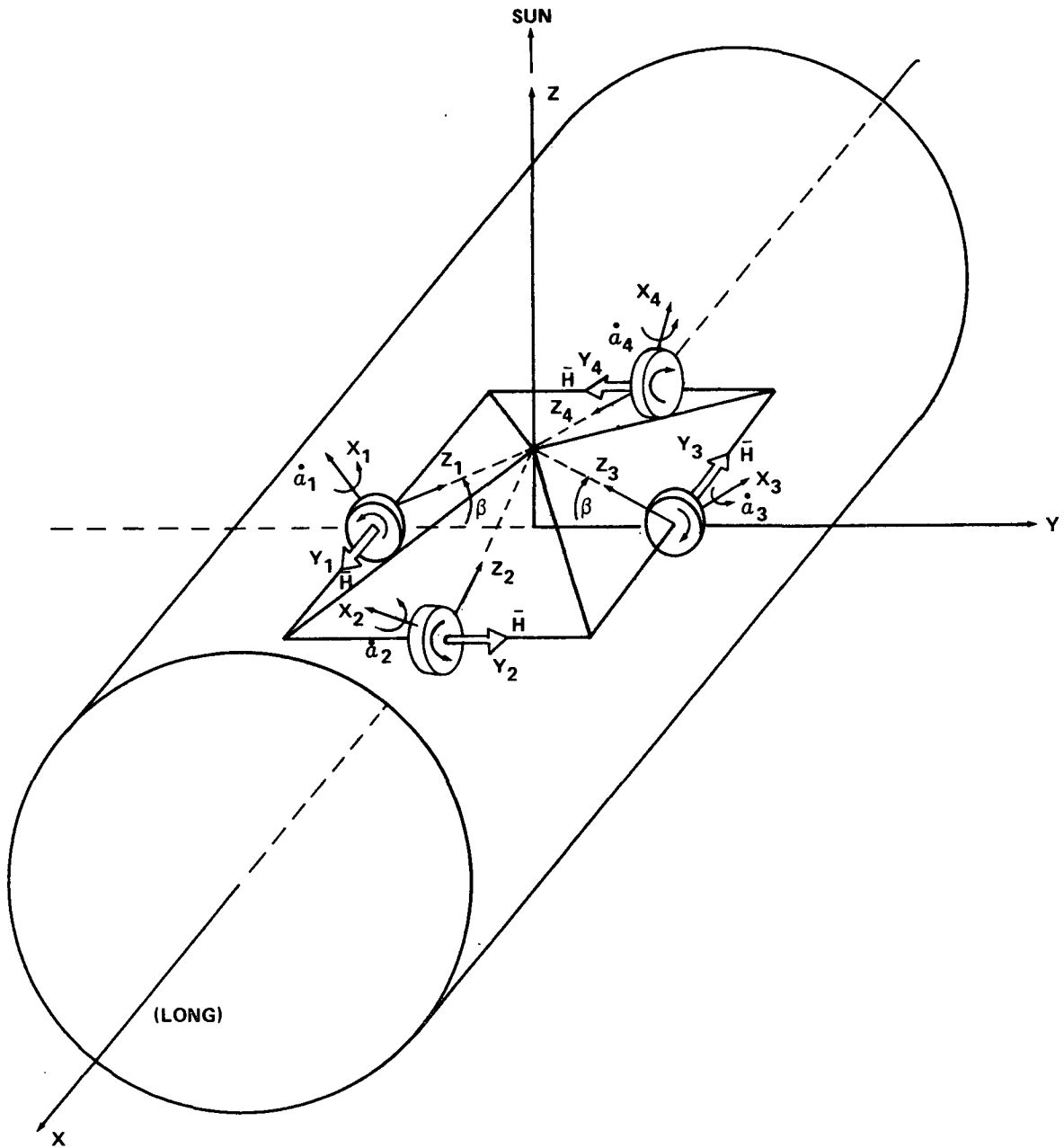


Figure VII-22. Four-CMG skewed configuration.

The baseline CMG unit selected for the HEAO-C is a modification of the MA-500 developed by Bendix for the Air Force. Reference VII-3 contains a detailed description of the minimum modified MA-500 CMG and its electronics.

A summary of this description is given here. Table VII-5 lists the basic characteristics of the minimum modified MA-500 CMG together with the basic MA-500 characteristics. The modified version selected for HEAO-C can also run at 8000 rpm if additional momentum capability is desired. This may be required if one of the configuration of four CMGs should fail. The primary modifications made are the use of a brushless dc spin motor, a direct torquing dc torque motor, and slip ring assemblies on the sensor pivots.

The CMG electronics provides the power and control functions necessary to operate one CMG. Four electronic sets are required, each being identical to and independent of the others. The three electronics functional areas are as follows:

- Spin motor electronics.
- Gimbal torquer electronics.
- Signal conditioning electronics.

Figure VII-23 is a block diagram for one channel. The following are some of the features that may be observed:

- Dual brushless dc motor and electronics for independent drive of the dual motors.
- Hall effect elements to transmit rotor position information to the drive input.
- Speed control circuit to bias the Hall devices to provide closed loop speed control.
- Brushless dc torquer design.
- Brushless dc tachometer using Hall elements and sensing windings.
- Signal conditioning electronics for wheel bearing temperature sensors, vibration sensors and resolver signal buffers.

Selection of the brushless dc spin motor type CMG with the other designated modifications provides reduced gimbal friction and deadzones with a potential increase in pointing stability (see Appendix E).

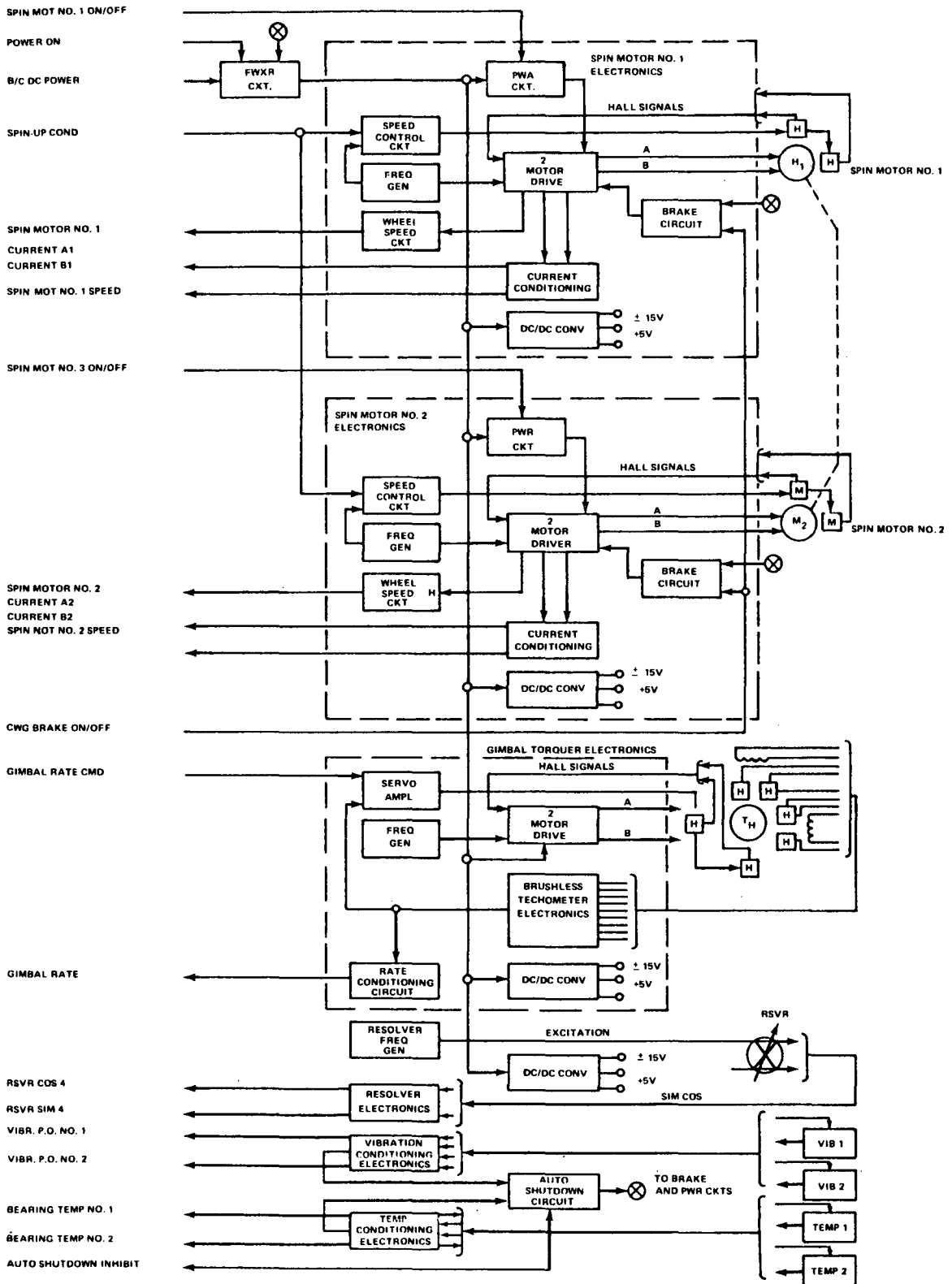


Figure VII-23. CMG electronics block diagram for one channel.

TABLE VII-5. MA-500 SINGLE GIMBAL CMG CHARACTERISTICS

CMG Assembly	Present	Minimum Modified For HEAO
Weight	160 lb	135 lb
Peak Output Torque	500 ft-lb	10 ft-lb
Peak Gimbal Rate	1 radian/sec	2.5 deg/sec
Gimbal Freedom	±170 deg	unlimited
Bandwidth (20:1 Rate Range)	60 to 80 radians/sec	Not Critical
Static Friction	3.5 ft-lb	1.5 ft-lb
Gimbal Control Power (Duty Cycle Dependent)	15	10 to 20 W
Heater Power	None	Thermal Interface Dependent
<u>Rotating Assembly</u>		
Wheel Diameter	18 in.	18 in.
Wheel Speed	8000 rpm	4000 rpm
Spin Motors	2 (ac or bdc <sup>a</sup> )	2 bdc
Wheel Support	ATM <sup>b</sup> Type	ATM Type
Spin Bearings and Lub System	ATM Type	ATM Type
Performance Monitors	Bearing Temp; Speed	Bearing Temp; Speed
Engineering Monitors	Bearing Vib; Vacuum	Bearing Vib; Vacuum
<u>Actuator Pivot</u>		
Drive	Geared 18:1 (ATM Type)	Direct (No Gearing)
Peak Torque	100 ft-lb	<10 ft-lb Required
Torquer	Brush Type or bdc	bdc
Tachometer	Brush Type (Motor Rate)	bdc (Motor and Gimbal Rate)

TABLE VII-5. (Concluded)

CMG Assembly	Present	Minimum Modified for HEAO
<u>Sensor Pivot</u>		
Data Transfer	Flex Leads	Slip Ring Assembly
Gimbal Position	Resolver	Resolver
Gimbal Rate	Brush Type Tach.	None Required
Stop Switches	±170 deg	None Required
bdc		

- a. bdc — brushless dc
- b. ATM — Apollo Telescope Mount

b. Reaction Control System.<sup>1</sup> A HEAO-C study guideline to maintain commonality with HEAO-A and -B was a primary driver in determining the type of RCS to use on HEAO-C. During the HEAO-A and -B Phase A study, a monopropellant hydrazine RCS was established as a baseline. This choice was further substantiated by the Grumman Aerospace Corporation and TRW in their Phase B studies on HEAO-A and -B. The Phase B studies also made effective use of off-the-shelf and flight-qualified hardware which results in a cost-effective RCS. The HEAO-C total impulse requirement, approximately 115 000 lb-sec, is essentially of the same magnitude as for Missions A and B; therefore, a monopropellant hydrazine RCS similar to that established in the Phase B studies is chosen. Inherent with this choice is a RCS that provides clean burning and good performance and is simple and safe.

The Lockheed OAS is equipped with a reaction control module (RCM) which can be used effectively by locating the HEAO-C RCS in that area. This arrangement also leaves more space in the spacecraft for other equipment. Since the telescope viewing area is opposite the OAS end of the spacecraft, the RCS cannot readily be placed at that location. This is fortuitous since it is desirable that the REMs be located as far away as possible from the telescope viewing area to reduce any possible contamination.

---

1. Special acknowledgement is made to the Lockheed Missiles and Space Company/Sunnyvale, Rocket Research Corporation, the Grumman Aerospace Corporation, and TRW for verbal and informal written data as well as basic data that contributed to the RCS portion of this report.

During the two year mission life of the HEAO-C, the RCS is used principally to desaturate the CMGs which are the primary actuators in the HEAO-C ASCS. Desaturation of the CMGs is expected to occur an average of once per orbit, and the burn time for any particular reaction engine assembly (REA) to perform part of this function is expected to be less than a couple of seconds. This RCS burn may be carried out in some type of pulse train mode or continuous firing as dictated by the ASCS control electronics.

For HEAO-C attitude control prior to spin-up of the CMGs, the RCS provides impulse, which is directed and regulated by the ASCS control electronics, to nullify external and internal disturbances and to maintain spacecraft attitude about three axes. The RCS impulse is also used to drive the spacecraft to a specific orientation at a predetermined angular rate. Use of a single type of engine permits a compromise in conflicting requirements of high thrust and low impulse bit for coarse and fine control of the spacecraft. The conflict is resolved by appropriate orientation of engines, combined with modulated pulse width and pulse frequency controlled firings, as effected by the ASCS control electronics.

The RCS for the HEAO-C is basically a modified version of the Lockheed satellite control section (SCS) RCS. (The OAS is a stripped-down version of the SCS.) The modification is necessary to meet the HEAO-C two year lifetime requirement and to provide maximum reliability.

The following paragraphs describe the baseline RCS.

(1) Configuration and Hardware Summary. A functional schematic of the baseline RCS for the HEAO-C is shown in Figure VII-24. The RCS is a blowdown, pressure-fed, hydrazine, monopropellant, propulsion system consisting of propellant tanks, REMs, REAs, and latching solenoid isolation valves as main elements. Auxiliary items are fill/drain valves for the hydrazine fuel ( $N_2H_4$ ) and the gaseous nitrogen ( $GN_2$ ) pressurant, interconnecting plumbing for the  $N_2H_4$  and  $GN_2$ , fuel line filters, heaters and thermostats, and pressure and temperature transducers. These elements are assembled in the RCM of the OAS as shown in Figure VII-25. A weight statement for the baseline RCS is shown in Table VII-6.

The RCS features of primary significance are as follows:

- 16 five-pound maximum thrust REAs are used.
- Fuel is contained in eight tanks.

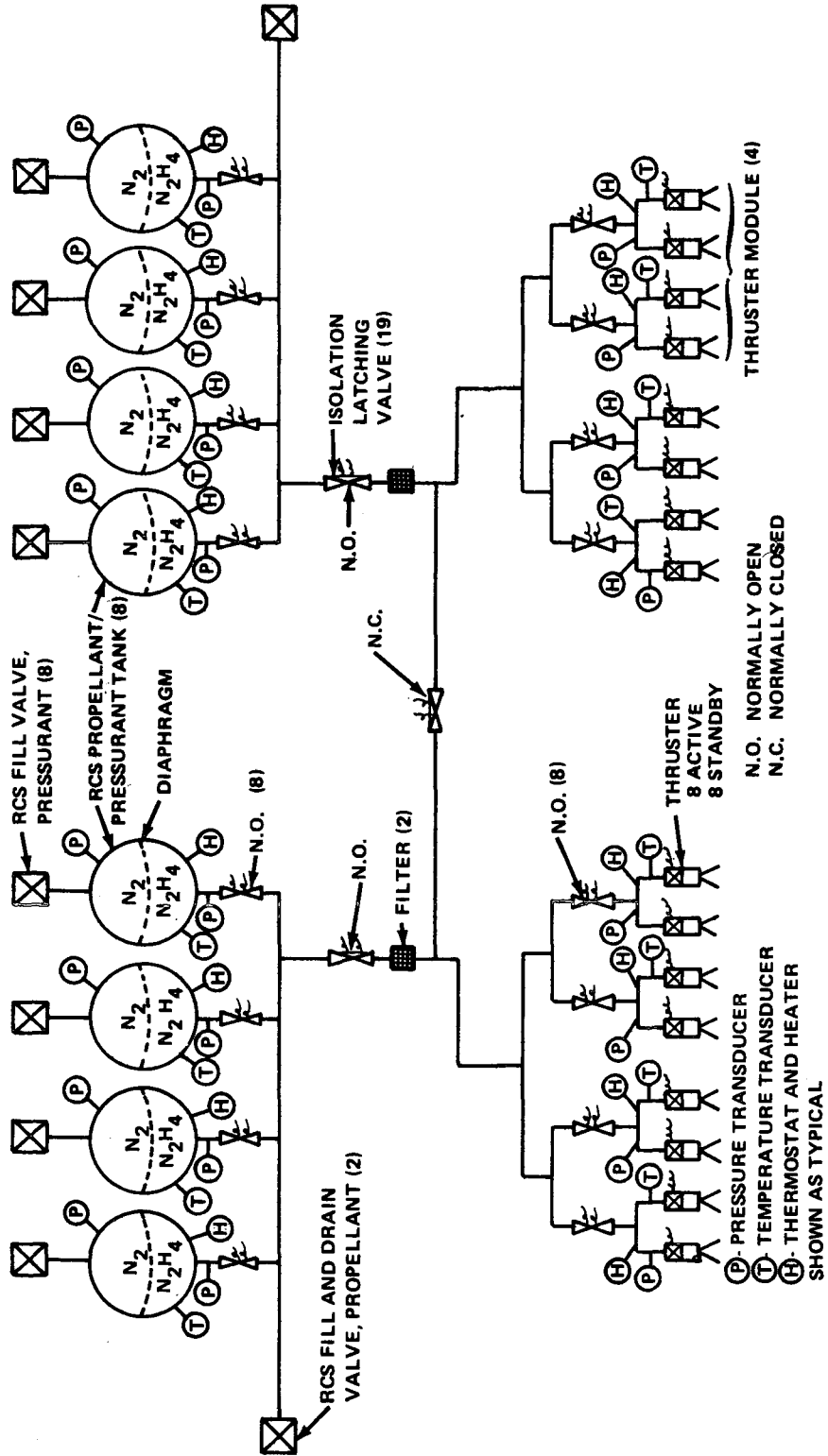


Figure VII-24. System schematic of the baseline HEAO-C RCS.

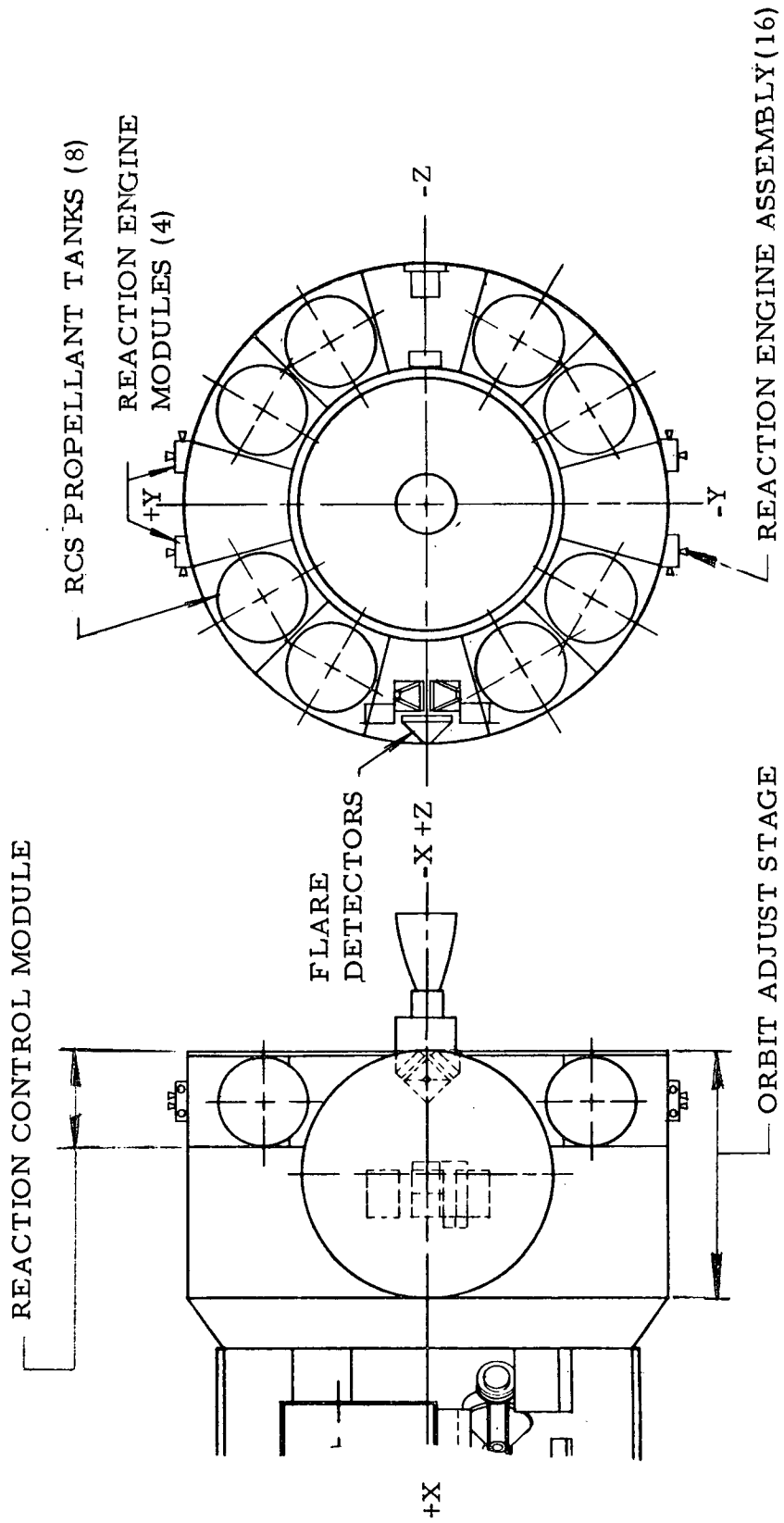


Figure VII-25. Layout of baseline RCS major component locations.

TABLE VII-6. REACTION CONTROL SYSTEM WEIGHT SUMMARY

Item	Component Weight (lb)
GN <sub>2</sub> Fill and Drain Valve (8)	2.00
Propellant Fill and Drain Valve (2)	0.60
Isolation/Shutoff Valve (19)	11.40
Tank, Including Thermostats and Heaters (8)	138.00
Pressure Transducer, Other Than REM (24)	7.20
Temperature Transducer, Other Than REM (8)	1.12
Filter (2)	0.50
REM, Including Thermostats and Heaters, Instrumentation, and Other Associated Equipment (4)	36.00
Plumbing	<u>10.00</u>
System Dry Weight	206.82
Propellant N <sub>2</sub> H <sub>4</sub>	829.00
Pressurant GN <sub>2</sub>	<u>19.00</u>
Total System Weight	1054.82

- Fuel pressurization is achieved by the simple tank pressure blowdown scheme.
- Subsystem isolation and propellant cross-strapping is provided by latching solenoid isolation valves.
- All components are off-the-shelf items.

Using the schematic shown in Figure VII-24, the operation of the baseline RCS is described as follows. The baseline RCS is made up of two identical units each consisting of a bank of four propellant tanks which supply  $N_2H_4$  to two REMs. However, the two units are cross-strapped and separated by a closed latching solenoid isolation valve. Cross-strapping provides the capability of either bank of tanks or a portion of either to supply  $N_2H_4$  to all four REMs, or both banks of tanks or portions of both can supply  $N_2H_4$  to the two REMs of one unit. Separating the RCS into two identical units and cross-strapping the two results in high reliability for the system. Details of the fuel line circuitry and failure mode effects will be discussed later. The reliability of the baseline RCS is discussed in Appendix G.

#### (a) Subsystem Operation and Hardware Description

1 Tanks. In determining the amount of RCS propellant needed for the HEAO-C mission, the REAs were assumed to provide an average specific impulse of 140 seconds. This value is believed to be a conservative estimate, and dividing this number into the HEAO-C total impulse requirement of 115 000 lb-sec for the two year mission results in 822 pounds of propellant needed. Eight tanks of the type used in this study are required to contain the propellant. Each tank is a 22.25 inch diameter sphere and has a diaphragm made of an elastomeric material designated EPT-10, which has very good long-term compatibility characteristics with  $N_2H_4$ . However, a two year life-time capability using this diaphragm has not been demonstrated. The four tanks in each unit are manifolded together on the propellant side of the diaphragm, and each unit has a common fill/drain valve for propellant loading. The tanks in each bank are filled to their normal maximum operating capability, i. e., 103 pounds of  $N_2H_4$  per tank. With this propellant loading, the tanks are approximately half full with  $N_2H_4$ . The remaining tank volume, on the gas side of the diaphragm, is pressurized with  $GN_2$  to a value in the range of 225 to 300 psia. The normal blowdown operating pressure ratio for the REAs is 2.0 to 1 (233 to 117 psia) with propellant temperature ranging from 40°F to 140°F; however, a range of blowdown pressure ratios are acceptable to the REAs. The  $GN_2$  pressurant positively expels  $N_2H_4$  from the tanks and, as the  $N_2H_4$  is used, the pressure level drops, ultimately reaching its minimum value when the tanks are empty.

Because of the large amount of RCS propellant required for the HEAO-C mission, complete propellant redundancy is not practical. However, if a maximum specific impulse of 200 seconds could be achieved by the REAs, 575 pounds of propellant would be needed for the two year mission, as opposed to 822 pounds required assuming 140 seconds of specific impulse. Thus, by assuming a conservative specific impulse, some propellant redundancy is provided. If a propellant tank were lost, as will be discussed later, the remaining RCS propellant would be sufficient to complete the two year mission provided the REA performance is high. Performance of the REA is a function of several parameters, which will be discussed later in this report as well as in Appendix E.

Each tank has a separate GN<sub>2</sub> fill/drain valve and line, as opposed to the common valve of the tanks manifolded together. This arrangement provides the capability to quickly trace a malfunction, such as a pressurant leak, to a given tank and to isolate that tank from the rest of the system. A latching solenoid isolation valve is contained in the N<sub>2</sub>H<sub>4</sub> feed line leading from each tank to the common manifold line in each bank of tanks. Under normal modes of operations, all of these valves are open. Should the tank control assembly associated with the onboard attitude control and malfunction detection system sense a failure, such as a pressurant leak in one of the tanks, then that tank can be isolated from the rest of the system by commanding its latching solenoid isolation valve to close. The fill valves for both the propellant and pressurant are manually operated and have caps which provide a redundant seal for long-term N<sub>2</sub>H<sub>4</sub> and GN<sub>2</sub> storage.

The desired temperature range to maintain the N<sub>2</sub>H<sub>4</sub> in each tank is between 40° F and 140° F. The temperature of the spacecraft's interior at the location of the RCM is not expected to go below 40° F, which is above the N<sub>2</sub>H<sub>4</sub> freezing point of approximately 36° F. However, since the normal orientation mode of the spacecraft is to maintain the entire length of one side pointing toward the sun at all times, about half of the propellant tanks will be on the warm side of the spacecraft and the other half will be on the cold side. This causes some uncertainty of the temperature distribution of the N<sub>2</sub>H<sub>4</sub> in each tank; therefore, as a contingency, a thermostatically controlled strip electrical heater system is attached to the outside of each tank. These heaters are also redundant. Each tank is then covered by multiple layers of aluminized mylar and glass insulation.

Each tank is instrumented with temperature and pressure transducers. Data from the instruments will be transmitted to ground stations to enable an assessment of the well-being of each tank in the propellant supply system. Should the temperature in a particular tank become too low, the heater

associated with that tank can be commanded "on" and operated under thermostatically controlled conditions. The heater can also be commanded "off." Since each heater requires about five watts for normal operation, electrical power is conserved by commanding each individual tank heater "on" as opposed to one command turning on all tank heaters.

The baseline propellant tank is a space-qualified component used in Lockheed's SCS RCS. The tank shell is made of Ti-6Al-4V, titanium, is spherical with a diameter of 22.25 inches, and weighs 17.10 pounds including a heater and thermostat assembly and the insulation cover. The tank contains a diaphragm made of ethylene propylene terpolymer, an elastomeric material designated EPT-10. This material has very good long-life compatibility with hydrazine and is sufficiently durable to withstand approximately 100 expulsion cycles. However, a two year lifetime capability using this diaphragm with hydrazine needs to be demonstrated. The diaphragm is ribbed to give good fuel expulsion efficiency. The diaphragm is retained in the tank by an internal ring which captures a bead at the diaphragm's edge. The ring is welded into the tank at the time the two tank halves are welded together. The tank volume is 5580 cubic inches and the maximum operating pressure is 350 psia. The tank has a proof pressure of 525 psia and a burst pressure of 700 psia. Pressure Systems Incorporated (PSI) manufactures and assembles the entire tank with the exception of the insulation cover which is provided by Lockheed. Table VII-7 summarizes the baseline propellant tank data and performance.

## 2 Reaction Engine Assembly/Reaction Engine Module.

Rocket Research Corporation, under contract to the Lockheed Missiles and Space Company (LMSC), has designed, developed, and flight-qualified a REM consisting of four REAs delivering, nominally, five pounds thrust each to provide spacecraft roll, yaw, and pitch attitude control. The REA is designated as MR-50A by the Rocket Research Corporation. Four of the REMs which employ monopropellant hydrazine as a fuel are used on each LMSC SCS, representing a total of sixteen engines. It is proposed that this REM be used as part of the HEAO-C RCS as it can meet most of the requirements.

Two REAs in each REM are an active set of thrusters and two are a standby set. Each of these sets in each REM is an independent subsystem (one active, one standby), independently controlled and manifolded. This arrangement results in a basic set of eight active REAs and a basic set of eight standby REAs. The REMs are installed at the 10 foot diameter in the RCM structure. The arrangement of the REAs in the REM and the location of the REMs on the RCM are shown in Figure VII-25. For further clarity, the distinction between the active set of REAs in each REM and the standby set is shown in Figure VII-26 with respect to the REM locations on the RCM. As shown in Figures

TABLE VII-7. PROPELLANT TANK DATA AND PERFORMANCE

Item	Data
Manufacturer	Pressure Systems Inc. (PSI)
Dimension	22.25 in. diameter sphere
Volume	5580 in. <sup>3</sup>
Weight	17.10 lb
Development Status	Qualified for SCS
Program Used on	Lockheed P-95
Operating Pressure	350 psia
Proof Pressure	525 psia
Burst Pressure	700 psia
Tank Shell Material	Ti-6Al-4V, Titanium
Diaphragm Material	Ethylene Propylene Terpolymer, EPT-10

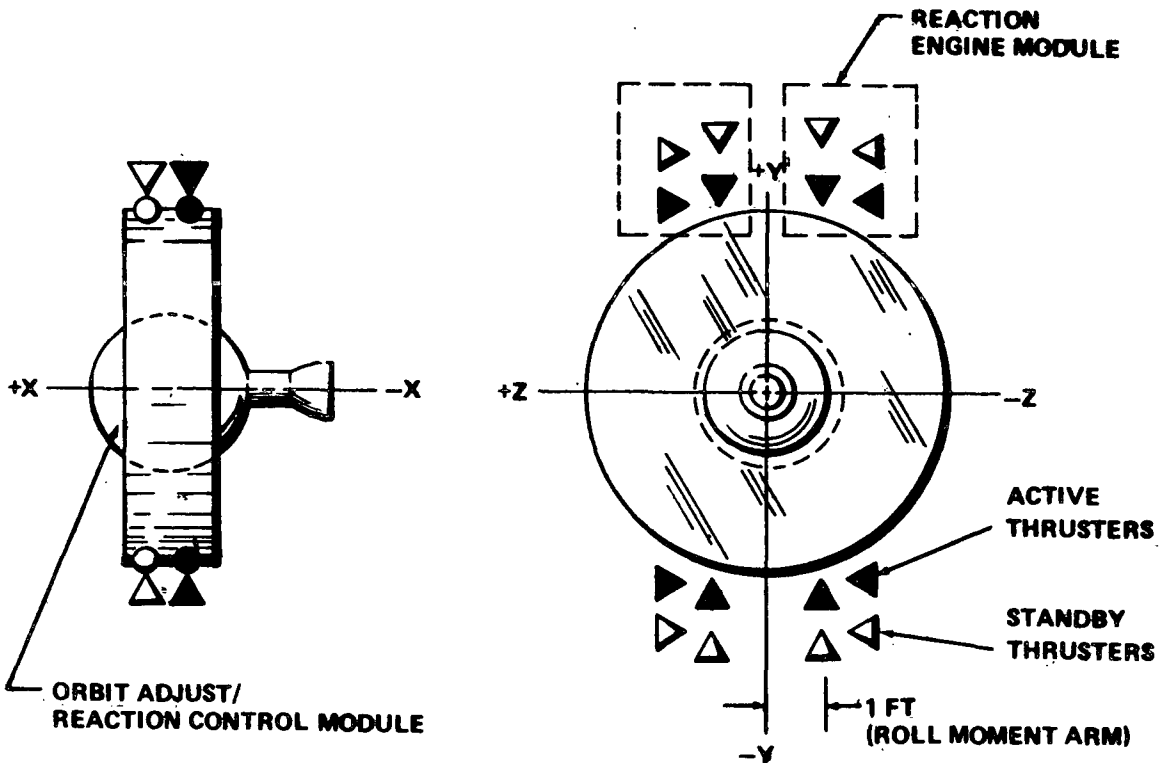


Figure VII-26. Reaction engine assembly/reaction engine module configuration.

VII-25 and VII-26, four of a basic set of eight engines are used for pitch/roll and the other four for yaw/roll. Fine roll control is provided by firing a given REA or a coupled pair of the four used for pitch/roll because each of these REAs when used for roll control has a one foot roll moment arm. Course roll control is provided by firing a given REA or a coupled pair of the four used for yaw/roll since each of these REAs when used for roll control has approximately a five foot roll moment arm.

The baseline location of the REMs on the RCM was determined primarily because this concept already exists on the Lockheed SCS and modifications such as placing the REMs at 90 degree intervals around the RCM would result in higher cost. When the method used in desaturating the CMGs is considered, it is found that the baseline configuration provides cleaner firing logic and, in most cases, one REA is pulsed to effect a combined pitch/roll or a yaw/roll maneuver. Firing one REA rather than a pair for a particular maneuver results in better performance and more efficient utilization of the REA due to longer firing times, and propellant is also conserved. In the case of the 90 degree configuration, which will be discussed in Appendix E, a roll component vector cannot be effected by firing a pitch or a yaw REA. However, from a propulsion efficiency point of view, especially considering the single REA performance, the 90 degree configuration appears to be best.

Hydrazine is supplied to two fuel inlets on each REM. One inlet supplies the active set of REAs and the other supplies the standby set. In operation,  $N_2H_4$  is supplied to all REAs in a REM, and the standby set of REAs are inoperative only because firing commands are not being directed to them. All REAs are controlled by a single channel of control electronics; however, for redundancy, another channel is provided as a standby. A normally open latching solenoid isolation valve is provided in each inlet fuel line leading to each REM. Should a REA failure necessitate a shutdown of that active set of REAs in a given REM, the REM control assembly associated with the onboard control and malfunction detection system can command closure of the isolation valve associated with that set of REAs. Once the active REAs are isolated, electrical firing commands are directed to the standby REAs in that particular REM. Firing commands to the other three REMs are unaffected. A discussion of the REA firing command logic for spacecraft control is presented in Section E-1 and Appendix E of this report.

Table VII-8 presents a summary of some of the REA/REM performance limits. Since the RCS will be desaturating the CMGs approximately once per orbit, the maximum number of pulses required of any one REA has been determined to be about 145 000 with a total impulse approaching 18 000 lb-sec.

This requirement is within the REA qualification limit. The minimum thrust of 2.5 pounds and the minimum impulse bit (MIB) of 0.15 lb-sec capability of this REA, while maintaining a pulsing specific impulse in the 125 to 205 second range, is an important characteristic that minimizes the fuel requirement during desaturation of the CMGs. The pressurization system blowdown ratio, electrical pulse width, and maximum and minimum operating pressures are all integrally related with such performance parameters as thrust level repeatability, impulse bit repeatability, and impulse bit response as summarized in Table VII-8. The data presented in this table refer to the REA/REM performance requirements necessary for the Lockheed SCS mission. Before applying the REM to the HEAO-C RCS, a REA/REM requalification is necessary.

The REM is designed as a completely integrated all-welded/brazed assembly and consists of two identical subsystems, an active and a standby, independently controlled and manifolded. Each subsystem consists of one pitch/roll REA and one yaw/roll REA oriented 90 degrees apart. Each REA consists of a thrust chamber and nozzle; a direct-actuated, electrically operated thrust chamber valve (TCV) which is normally closed; and a thermal shield assembly. Each REM contains two chamber pressure transducers, one on each of the active REAs. However, for application to the HEAO-C spacecraft, each REM will be modified to contain four chamber pressure transducers, one on each of the active REAs and one on each of the standby REAs. Each REM also contains one thermistor to monitor average valve temperature, four thermocouples to monitor chamber wall temperature, two REM plate heaters (REA valve heaters), two thermal short heaters (REA catalyst bed heaters), and two thermostats. The REM contains four separate electrical connectors—two for valve power, one for heater power, and one for instrumentation leads. In the event of failure, the standby subsystem can perform the functions of the failed active subsystem. The REM-RCM interface consists of an interface plate casting which provides a four-bolt hole pattern mechanical interface and a four-connector electrical interface. Shock mounts located between an interface plate and the REA mounting structure provide some thermal isolation to the vehicle as well as attenuation of vibration and shock loads imposed by the vehicle. The interface plate vehicle bolt hole pattern provides for left and right REMs for vehicle installation purposes, and all electrical connectors are individually keyed to insure proper electrical hookup. Once the REMs are attached to the RCM, an aerodynamic fairing is placed over them for protection during ascent through the atmosphere. This fairing is retained throughout the entire mission. Cutaways are provided in the fairing for the REA exhaust plume.

TABLE VII-8. REA/REM PERFORMANCE CAPABILITIES<sup>a</sup>

Item	Data
Thrust (min)	2.5 lbf
Minimum Impulse Bit (MIB) up to 1.0 cps (max)	0.15 lbf-sec
Total Pulses per REA	175 000
Total Impulse per REA	18 000 lbf-sec
REA Minimum Electrical Pulse Width	22 msec
Specific Impulse  Pulsing at 0.01 cps Steady-State	125 sec 205 sec
Steady-State Response  Time to 1.0 lb thrust (max)	100 msec
Response — MIB Pulsing  Percent in 50 msec Percent in 100 msec	33 60
Repeatability  Impulse Bit Between Two REAs Thrust Between Two REAs	±22% ±15%
Duty Cycle per REM  Maximum Activity  Minimum Activity	Two REAs firing steady-state for 5 minutes. 5 cps pulsing per REA.  One REA firing at 0.01 cps

TABLE VII-8. (Concluded)

Item	Data
Propellant	Hydrazine, MIL-P-26536
Environmental Temperature Range	0 to 140° F
Propellant Temperature Limits	+40 to +140° F
Operating Voltage	24.5 to 33 Vdc
Life	
Firing (min)	45 days
Calendar	42 months after acceptance test

a. Data were taken from Reference VII-4.

The design parameters of the REA are summarized in Table VII-9. Monopropellant hydrazine is injected from the TCV through the feed tube and through the injection element into the Shell 405 catalyst bed. Catalyst bed dimensions were determined by use of the monopropellant hydrazine design and scaling criteria developed by Rocket Research Corporation under contract to Jet Propulsion Laboratory, NAS-7-373 [VII-5a]. The granular Shell 405 ABSG catalyst, purchased to a Rocket Research Corporation material specification, is constrained between the catalyst bed plates and the injector face.

Prior to assembly, Haynes 25 screens are tack-welded to both sides of the bed plates to eliminate any migration of catalyst within and out of the catalyst bed. With the exception of the injector which is Inconel, all other parts of the thrust chamber assembly (TCA) are fabricated from Haynes 25 with the thrust chamber being machined from Haynes 25 bar including the 40:1 RAO expansion nozzle.

TABLE VII-9. REA DESIGN SUMMARY<sup>a</sup>

Parameter	Data
Catalyst	Shell 405
Nozzle	
Expansion Ratio	40:1 (RAO)
Throat Diameter, in.	0.197
Exit Diameter, in.	1.246
Material of Construction	
Thrust Chamber	Haynes 25 (L605)
Injector and Feed Tube	Inconel 600
Heat Shield Assembly	CRES 304 (flanges) Haynes 25 (shields)
Weight, lbm	
Heat Shield and Support	0.41
Thrust Chamber	0.39
Valve	<u>0.40</u>
Total REA	1.20
Dimensions, in.	
Thrust Chamber Diameter	1.18
Thrust Chamber Length	3.74
Thrust Chamber Valve Length	<u>1.59</u>
Total REA Length, in.	5.33

a. Data were taken from Reference VII-4.

Table VII-10 presents a detailed steady-state performance summary of a REA test data point over the nominal REM operating range.

The REM affords an extremely "clean" vehicle interface because roll, yaw, and pitch thrusters, associated instrumentation, structural mounts, and passive and active thermal control systems are contained in one package requiring minimum maintenance and providing essential direct plug-in capability to the vehicle [VII-4].

Appendix E contains a detailed discussion devoted to the development, design, and performance aspects of the REA and the REM.

3 Fuel Line Circuitry, Latching Solenoid Isolation Valves, Fuel Filters, and Failure Mode Analysis. As has been mentioned previously, the eight propellant tanks are divided into pairs such that each pair supplies  $N_2H_4$  to two REMs. The fuel line circuitry carrying fuel from the propellant tanks to the REAs incorporates 19 latching solenoid isolation valves. These valves are to facilitate isolation of malfunctioning tanks or engines and to interconnect the propellant tanks, or portions of them, of one unit with all four REMs, or all tanks can supply the two REMs of one unit. The fuel circuitry and valve arrangement allows much flexibility with respect to isolating a malfunctioning part of the RCS from the rest of the system and restoring satisfactory operation and maximum capability to the remaining good portion of the system.

Should a tank malfunction cause a pressurant or propellant leak, the tank control assembly associated with the onboard control and malfunction detection system can command closure of the isolation valve associated with that tank. Should the valve not close due to electronic failure, malfunction detection failure, or valve failure, the entire  $N_2H_4$  propellant associated with that particular unit of tanks can be lost because of the common propellant manifold. If the propellant in a bank of tanks is lost due to these two series of failures, then for all practical purposes the functional lifetime of the HEAO-C spacecraft from that point is cut in half. If the failure occurred early in the mission, as a worst case, the spacecraft would be good for approximately one year instead of two, assuming no other failures. Since the two units of the baseline RCS are cross-strapped with a propellant line and separated with a closed isolation valve in that line (see Figure VII-24), propellant can be supplied to the nonfunctioning REMs from the tanks in the functioning unit. This process is carried out in the following manner: A single main feed line leads from the common manifold of a bank of tanks in a unit to another common manifold in that unit associated with the two fuel inlets to the two REMs. Cross-strapping of the two units is provided by a feed line connected between the two main supply

TABLE VII-10. REA PERFORMANCE SUMMARY  
 NOMINAL OPERATING CONDITIONS<sup>a</sup>

Parameter	Initial	Final
Feed Pressure (psia)	233	117
Propellant Temperature (°F)	70	70
Chamber Pressure (psia)	103.6	59.8
Mass Flow Rate (lbm/sec)	0.02413	0.01403
Characteristic Exhaust Velocity (ft/sec)	4264	4228
Thrust Coefficient	1.753	1.725
Altitude Thrust (lbf)	5.61	3.18
Specific Impulse (lbf-sec/lbm)	232.5	226.7
Ammonia Dissociation (%)	63.5	65.3
Exhaust Gas Temperature (° F)	1623	1597

a. Data were taken from Reference VII-4.

lines in each unit. A latching isolation valve is located in the main supply line of each unit upstream of the point where the cross-strapping feed line connects (see Figure VII-24). This valve is commanded "closed," isolating the entire bank of tanks associated with the nonfunctioning unit. This prevents  $N_2H_4$  from entering the damaged tank area and being lost when the propellant is transferred. The closed isolation valve associated with the cross-strapping feed line is commanded "open," allowing propellant to flow to the two nonfunctioning REMs. Then normal spacecraft control can be continued.

Consider a case when the isolation valve associated with a malfunctioning tank closes upon command and isolates the tank from the RCS. This situation leaves three tanks in a unit to supply  $N_2H_4$  to two REMs. Under average conditions, the propellant in the bank of three tanks will be used faster than the propellant in the bank of four tanks. For a given time this condition will result in the feed pressure being lower in the three tanks as opposed to that in the four. Since the baseline RCS is a blowdown system, and thrust is dependent on feed pressure, the REAs connected with the three tanks will have a lower thrust than the REAs associated with the four tanks. This condition could cause some control problems with the spacecraft as a result of unequal torques. Each tank is instrumented with temperature and pressure transducers and, by observing data transmitted to the ground by these instruments, an assessment can be made as to the pressure differential in each bank of tanks. Should this pressure differential approach an intolerable limit, the closed isolation valve in the cross-strapping line can be commanded "open," causing propellant to flow from the set of tanks with the greater pressure to the set of tanks with the lower pressure. Then, the pressure in the two sets of tanks will be equal, and the isolation valve can be commanded "closed." Even in the normal mode of operation when all tanks are functioning, a pressure differential between the two sets of tanks could occur, and equalization of this pressure can be accomplished by the method just described.

Latching solenoid isolation valves are also provided in the two feed lines that lead to each REM. Should a REA of an active set of REAs in a given REM develop a leak due to a faulty valve seat, that set of REAs can be isolated by commanding its associated isolation valve to close. Then, electrical commands can be directed to the standby REAs in that REM. At a later time should the thrust chamber valve of one of these standby REAs (now active) stick open causing continuous thrust, the REM control assembly associated with the onboard malfunction detection system would command its associated isolation valve to close, cutting off the propellant supply. By accepting a leaky REA, that REM could, then, continue to operate in a possible degraded mode by commanding the isolation valve associated with the original active REAs to open.

All isolation valves associated with the fuel line circuitry are the latching solenoid type. With the exception of one, all of these valves are open in a normal mode of operation. The only time that any of these valves will be commanded "closed" is in the event a failure of a part of the RCS demands isolation of that part from the rest of the system. The normally closed isolation valve is associated with the propellant cross-strapping feed line. This valve is opened to transfer propellant from one unit to another in the event of a  $N_2H_4$  supply tank failure in either unit. This valve is also opened in a normal mode of operation if, at a given time, the pressure in the two banks of tanks needs equalizing. Squib valves are not utilized because they are "one shot" devices and the plumbing arrangement required to supply alternate feed paths to overcome this disadvantage complicates the feed line circuitry. However, squib valves are more reliable and are less expensive compared to the latching solenoid type. The latching solenoid valve can be closed or opened on command, providing the capability to troubleshoot an anomaly in the system, and if a "fix" is made, the system can be brought online again. For example, a REA valve could stick open causing the REA to thrust continuously. The REM control assembly associated with the onboard malfunction detection system would naturally shut down that REA by commanding the isolation valve associated with that REA set to close. Data transmitted to the ground may indicate that the REA valve was operating under an abnormally high temperature condition. After allowing a cool-off period, the isolation valve could be commanded "open," and the REA could start normal operation again. Should a latching solenoid isolation valve be inadvertently switched out of its normal position, a command can be given to switch it back.

The isolation valve used in the baseline RCS for HEAO-C is the same type used by the Lockheed SCS RCS. The valve is a magnetically-latched type, solenoid-driven, actuated open and closed by an electrical pulse. Switches inside the valve that open and close by the movement of the valve seat from one position to another indicate the position of the valve seat. An electrical power requirement of 108 watts is required to actuate the valve, and once the valve is latched in the appropriate position the power is removed.

A fuel filter is located in each main fuel line leading from each bank of tanks to the REM manifold. Its function is to protect the REA thrust chamber valve from any contaminants that might be present in the  $N_2H_4$ . The filters are located upstream of the point where the cross-strapping feed line connects with the main feed line. The filters are placed at this location such that if one became plugged, the result would be the loss of a bank of tanks rather than two REMs. A pressure transducer is located in each feed line leading to each REM. This instrument monitors the fuel pressure being supplied to the REAs, and it would provide information on unusual or excessive pressure drops such as could occur if the filters became plugged.

All feed line tubings are a stainless steel alloy with all connections being an all welded/brazed assembly. By integrating the entire RCS in a structure such as the RCM (see Figure VII-25), the distance between the REMs and the propellant tanks is minimized. Thus, the length of the feed lines is minimized reducing the probability of  $N_2H_4$  freezing in the lines. The REMs are attached to the RCM on the Y-axis such that they will receive an equal portion of the sun's radiation. The REMs could be attached on the Z-axis of the RCM as an alternate location, but this concept is undesirable from a thermal point of view since one set of REMs will always be in the sun and the other set in the shade.

Referring to Figure VII-25, the XY plane divides the two banks of tanks; however, the plumbing is arranged such that each bank of tanks supplies two REMs that are 180 degrees apart. Arranging the plumbing in this manner serves two purposes. First, the thermal environment is a little more evenly distributed between the REMs and the propellant tanks. Second, and most important, spacecraft control can be maintained, in a degraded mode, with one unit of the RCS completely lost and the other unit operating.

4 Reaction Control Module Structure. The RCM, shown in Figure VII-25 consists of two machined rings connected by chemically-milled, corrugation-stiffened, aluminum skins carrying primary loads. Internal secondary structure supporting the Orbit Adjust Subsystem and RCS tanks is an annulus of trapezoidal cross section, divided into 12 equal compartments by radial shear panels. Eight of these compartments are occupied by RCS tanks; two, 180 degrees apart, are occupied by REMs and associated plumbing and valves; and one is occupied by all the fill/drain valves, both propellant and pressurant, for the RCS and the OAS. Other ground support equipment connections are also located in this last compartment. One empty bay remains that could be used for an additional RCS tank, experiment, or other apparatus. After assembly of the RCM, access to the compartments is achieved through trapezoidal openings in the concave forward face of the annulus. The OAS skirt is secured to this module by a circle of bolts at the ring in the annulus forward face. After complete assembly of the OAS, the propellant tanks are completely enclosed and surrounded by sheet metal. The length of the RCM section is 23 inches, and the diameter is 120 inches. The weight of the RCM structure excluding all RCS and OAS components is 374 pounds.

(b) Hydrazine and Exhaust Contamination. The properties of monopropellant  $N_2H_4$  are presented in Table VII-11. When hydrazine comes in contact with Shell 405 catalyst, the hydrazine is spontaneously decomposed. Once the decomposition begins, the reaction is self-sustaining. The products of combustion are gaseous ammonia ( $NH_3$ ), nitrogen ( $N_2$ ), and hydrogen ( $H_2$ ).

TABLE VII-11. PHYSICAL, CHEMICAL, AND THERMODYNAMIC  
 PROPERTIES OF  $N_2H_4^a$

Item	Data
Mean Molecular Weight	32.0453
Density	62.8 lbm/ft <sup>3</sup> at 68° F
Freezing Point	34.8° F
Boiling Point	235.9° F
Critical Pressure	2132 psia
Critical Temperature	716° F
Vapor Pressure	0.28 psia at 68° F
Heat of Formation	+677 Btu/lbm at 77° F
Heat of Vaporization	602 Btu/lbm at 77° F
Specific Heat	0.736 Btu/lbm-° F at 68° F
Thermal Conductivity	0.205 Btu/hr-ft-° R at 68° F
Gas Constant	48.2 ft-lbf/lbm-° R
Gamma	1.197 at 76° F
Viscosity	0.972 centipoise-68° F
Cost	\$1.50/lbm

a. Data were taken from Reference VII-5b.

These exhaust products are very clean and tests thus far have indicated that they are not a serious contamination threat to a spacecraft. Small traces of hydrazine and bits of Shell 405 catalyst may be found in the exhaust of a hydrazine monopropellant engine, but with the engine operating under proper conditions, these constituents of the exhaust should be very small or nonexistent, minimizing the threat of contamination to the spacecraft. With the exception of a cold gas RCS such as N<sub>2</sub>, H<sub>2</sub>, He, or Freon, the exhaust of a monopropellant hydrazine RCS is about the cleanest available. Although with extremely sensitive surfaces and instruments such as the HEAO-C experiments and optical sensors, some contamination concern must still be maintained and further investigation into this area is recommended.

(2) RCS Electronics. The RCS electronics provides the power to operate the RCS and the signal processing necessary for the RCS status sensors. As shown by the functional block diagram, Figure VII-27, there are the following six basic types of circuitry:

- Thruster drive electronics.
- Heater control circuitry.
- Temperature and pressure sensor conditioning.
- Latching solenoid control and driver electronics.
- dc/dc power supply.
- Latching solenoid command logic.

These functions as related to the RCS thruster and tank configuration are discussed in detail in the RCS configuration description of this report.

#### 4. Signal Processing

a. Digital Computer. The DCU selected for the HEAO-C is the Bendix unit as baselined during the Phase B study effort. The Bendix DCU consists of the following subsystems:

- BDX-900 series central processor (CP).
- Input/output interface electronics (I/O).
- Memory.
- Power Supply.

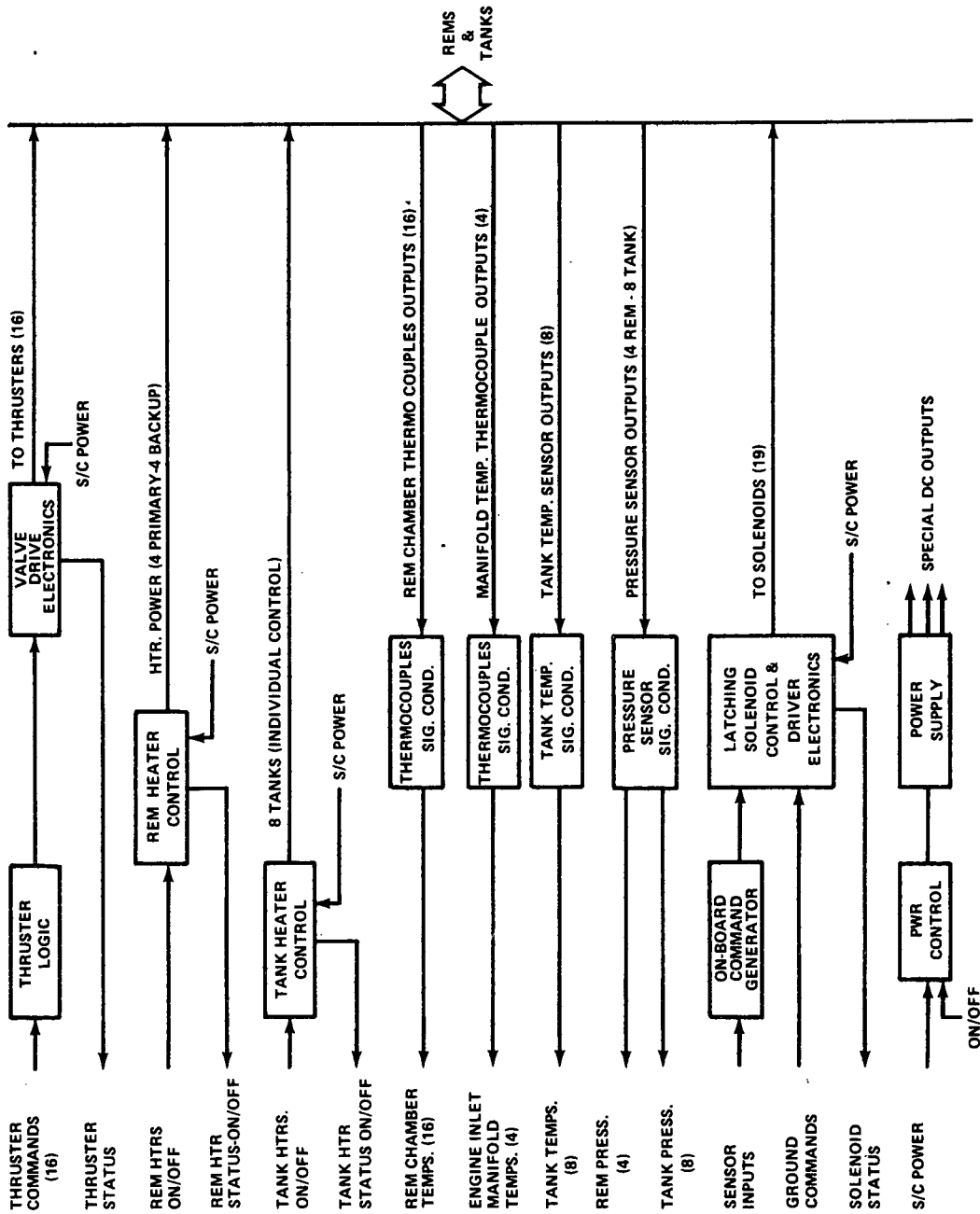


Figure VII-27. RCS electronics function diagram.

The DCU is assumed to be available from the Mission A and B Programs; therefore, only a summary description of the internal arrangement will be given.

(1) DCU I/O. The I/O interface electronics is the link between the CP of the DCU and the sensors and actuators. Routing of the input and output information of the I/O is through the transfer assembly.

The I/O uses three types of input and three types of output channels. Functionally, each type of channel can be described as follows:

- Analog Input Channel — Signals in analog form are coded in binary numbers suitable for the CP.
- Digital Input Channel — Signals that do not require binary coding are processed.
- Discrete Input Channel — Processes information that indicates process state and requires computer memory input.
- Analog Output Channel — Digital-to-analog (D/A) convert signals (voltage or current, dc or sinusoidal) that must be handled by an analog output channel.
- Digital Output Channel — Signals are processed that must be output to the process devices in digital form.
- Discrete Output Channel — Handles go/no go output signals to the process devices.

(2) Digital Signals

- Input Discrete — The CP will accept, under program control, two 16 bit discrete input words. While the CP issues a Data Input Strobe, a 16 bit word is put on the I/O bus and is sent to the CP for processing. The gates which accept the two input words have open collector outputs and, as such, can be "Or'd."
- Output Discrettes — The CP will issue a Data Output Strobe under program control and output one of three 16 bit output words to the I/O.

- Real-Time Clock — The primary function of the counter is to produce highly accurate ( $\pm 15$  ppm) real time interrupts which serve as a time base for the computer program. It is also used for generating timing for telemetry interrupts and strobes, and for time and control signals in the analog-to-digital (A/D) converter.
- Telemetry and Uplink — Tank buffer registers will be provided in the DCU I/O to accept data and instruction word from the uplink. Two buffer registers will be provided in the I/O to receive data from the CP and transmit it to the data handling system for telemetering.

(3) DCU Memory. The memory element of the HEAO/DCU will consist of a read only memory and a read-write memory. Sufficient variable or scratch pad memory will be provided to store data, results of computations, and any special programs that may require transmission from a ground station in emergencies.

(4) DCU Self-Test. The DCU is programmed to execute central processor self-check, I/O interface, and program memory check. On initial detection of a failure, the diagnostic programs will be repeated for verification of the malfunction. Confirmation of the malfunction will cause the DCU to be considered as failed. If the initial detected failure is a transient, the DCU will ignore this failure and continue to carry out its normal functions. If the on-line DCU is declared as a repetitive failure, it is automatically placed in a standby mode of operation and switchover procedures are initiated.

(5) DCU Switchover. The initial phase of the switchover procedure is to automatically place the failed DCU in a standby mode and to pass the control of the Observatory to an emergency backup control system. The emergency backup control system is mechanized by means of the transfer assembly where electronics are provided for commanding the RCS. The WASS, emergency RCS command electronics, and the RCS place the Observatory in the sun acquisition reference orientation.

Further ground station analysis will be conducted to confirm the status of the suspect DCU and ground control will be the final authority in judging the status. By ground control, a standby DCU will be activated and placed on line in the case of a confirmed failure, or the suspect DCU will be restored to operation.

... A typical simplified signal flow diagram for the HEAO-C ASCS including the DCU is given in Figure VII-28. This diagram identifies a provisional total of at least 47 signals received from the sensing devices; these include attitude data such as angular rate, and status data such as whether a sun sensor is on or off and whether a star tracker is in the track or search mode. In addition, there are input commands from the data system plus at least 23 signals giving torquer status, such as CMG gimbal rates and angles. Thus, the input bus of the CP must be connected in turn to each of more than 70 inputs supplied by the I/O interface electronics.

On the output side, 24 signals control the torquers but at least 15 additional signals are needed to turn the sensors on and off, to select sensor operating modes, and to perform similar functions. The CP output bus must be connected in turn to each of 39 or more output lines in the I/O interface electronics.

The number of inputs and outputs may increase considerably when the detailed requirements for specific sensors and actuators are examined.

A detailed specification of the DCU software cannot be given due to a number of contingencies that exist, the primary contingency being the desired commonality between the systems for all missions. However, the basic software functions for the DCU to be used on the HEAO-C can be functionally described. Figure VII-29 is a simplified functional diagram of typical HEAO-C DCU software required. The functions are considered typical for performing the tasks required for each operational mode. Additional functions will be required and a final mechanization of the subroutines required will group certain of these functions under individual subroutines. For each Observatory operating mode, a subroutine must be provided that used the appropriate equations to convert sensor signals into actuator commands. As depicted, the executive routine commands mode switching in response to sensor output and ground commands. The executive routine also controls the Data Input Strobe and the Data Output Strobe of the I/O so that in each operating mode, the subroutine of the CP being used receives the proper sensor outputs and supplies the proper actuator commands. Generally, the computer's time is divided between executing the subroutine in use and performing self-checking tests.

b. Transfer Assembly (TA). The transfer assembly serves as the interface between all ASCS sensors, actuators, and the DCU I/O interface. The TA or comparable device that was baselined for Missions A and B in the Phase B study has been selected for the HEAO-C.

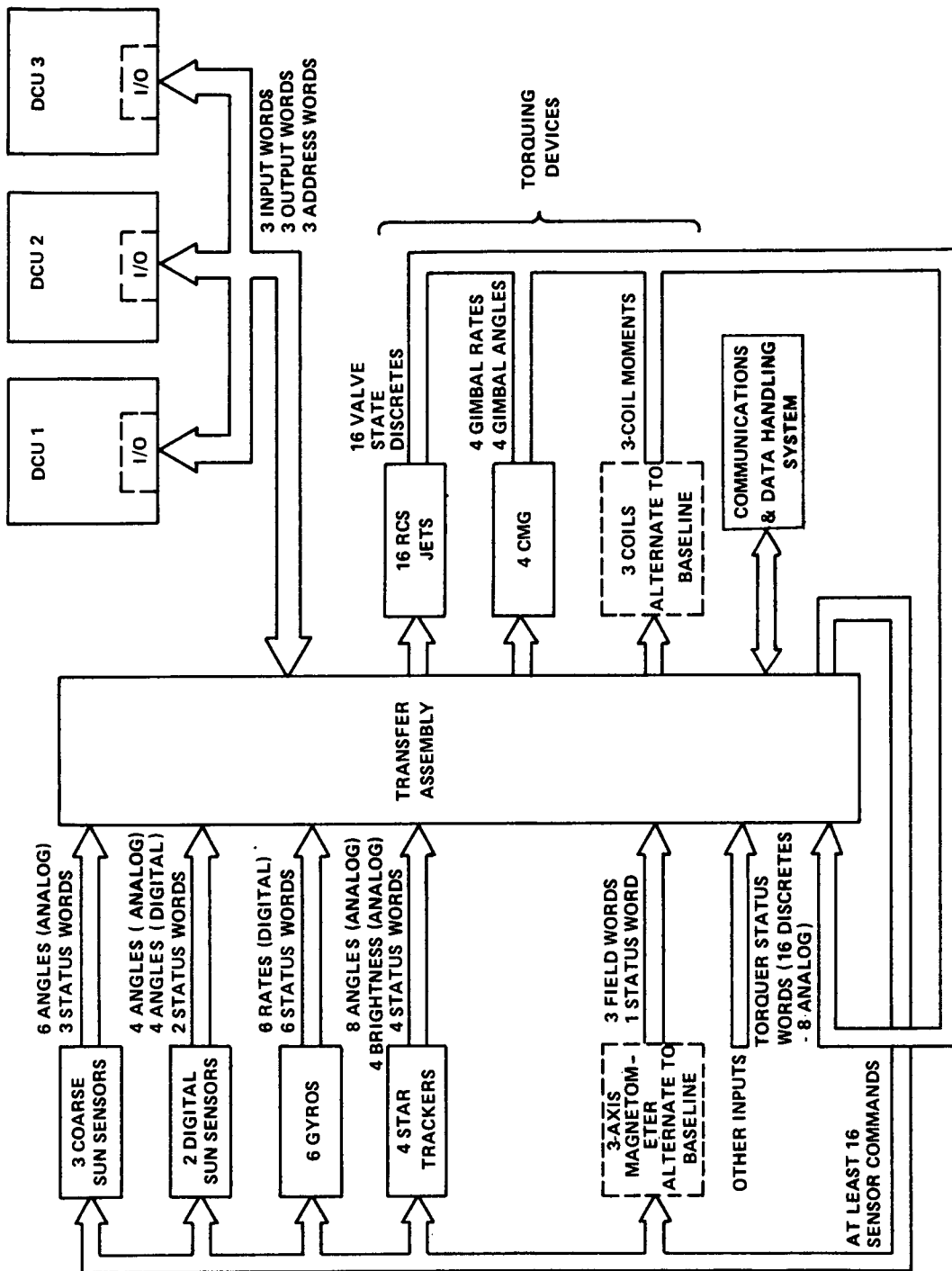


Figure VII-28. DCU simplified flow diagram.

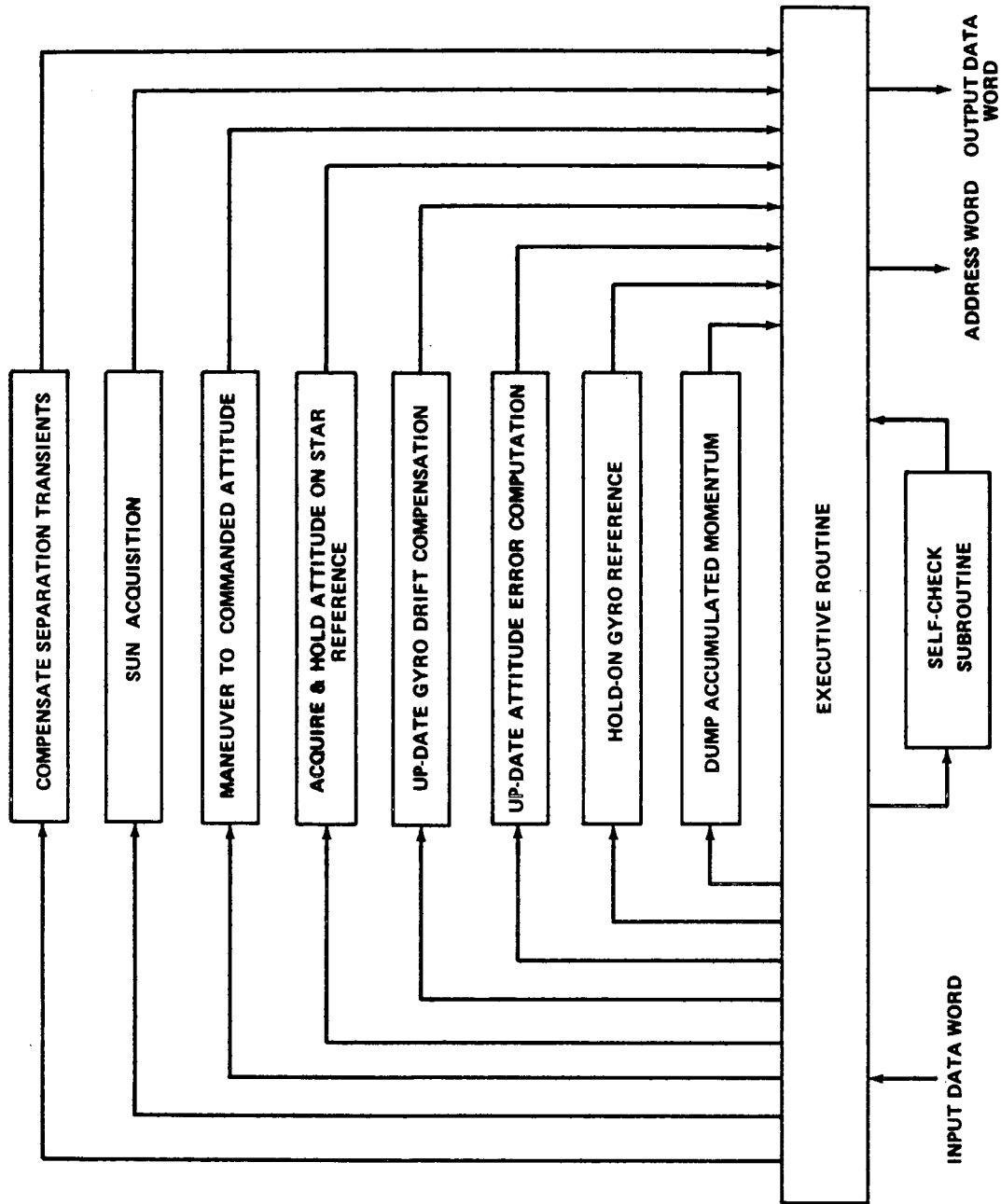


Figure VII-29. Computer software.

At the end of the Phase B study effort on HEAO-A and -B, a firm definition of the transfer assembly design was not available, primarily because of the design dependence on the final hardware selection. However, the design concepts and probable implementations have been defined and have been used in the HEAO-C conceptual transfer assembly design. Certain modifications for HEAO-C use are to be expected since Missions A and B are primarily celestial sphere surveying missions and HEAO-C is primarily a pointing mission. These modifications are expected to be mainly in the area of circuit routing between sensors, actuators, and the DCU. Some low level logic changes are to be expected but the changes should be minor.

The primary functions of the TA are as follows:

- Passive isolation of the redundant DCUs.
- Emergency mode vehicle and thruster control laws implementation.

To isolate the DCUs, the TA provides fan-in and fan-out capability so that any one of the DCUs can operate with any sensor input and can supply outputs to any actuator. The passive isolation concept used prevents a failed DCU from inhibiting operation of the standby DCUs. The isolation technique is applied to both analog and digital inputs to the DCU I/O where the specialized circuitry exists to accommodate the various signal requirements.

Any one of the three computers will be capable of providing the necessary system output signals when the other two are switched by means of isolation networks passed between the DCU output terminals and the utilizing system. The concept is based on a current sensing technique whereby three corresponding signals are fed to a common low impedance junction through isolation resistors. The technique utilizes the fact that only the operating computer is capable of generating an input current since input power is not being supplied to the standby units.

The primary problem area in the baseline TA concept occurs where high accuracy analog signals must be supplied to the DCU I/O. Conceptually, it was proposed in the HEAO-A Phase B study that this be overcome by the use of a differential arrangement that doubles the number of isolation components but has the advantage of virtually eliminating common mode noise.

An emergency mode is provided in the TA to place the Observatory in a sun oriented attitude when a critical abnormal condition occurs. The

emergency mode electronics in the TA consists of an analog implementation of the necessary electronics to provide commands to the RCS thrusters directly in response to the two axis outputs of the WASS and reference gyros. The WASS outputs command the thrusters to maintain the Observatory +Z-axis in sun alignment, and rate error signals are provided by the reference gyro assembly. In the acquired attitude, the Observatory can remain for the time necessary to perform diagnostic routines and to activate the standby units. During this mode the active DCU is placed in a standby mode and the capability of commanding CMG gimbal rates is removed.

Figure VII-30 is a simplified block diagram of an alternate conceptual design for the TA. This design has the advantages that high accuracy analog signals are A/D converted prior to being routed to the DCU and the TA can also serve as an I/O interface between sensors, actuators, and the central processor of the DCU.

The outputs of the sensors are applied to the input of the TA where signal conditioning, buffering, and conversion is supplied as required. The sensors include the basic ASCS sensors as well as any status sensor outputs (i. e. CMG gimbal angle encoders and rate sensors) required by the DCU central processor. A digital multiplexer converts each input in turn to the DCU input bus. Similarly, the output distributor B connects each output in turn to the output bus. Switching is controlled by the address word received from the computer on address bus B. A single 16 bit word is sufficient for handling up to 256 inputs and 256 outputs.

The input bus is connected, by the input distributor, to the input line of one of the three computers. Similarly, the output bus and address bus B are connected, by the output distributor A, to the output and address lines of the same computer. These two distributors are controlled by address bus A, which carries an address word from the input/output test unit. This unit is intended to detect failures in the input/output portions of the computers; it is assumed that other computer failures can be detected by their own internal self-test routines. The input/output unit is connected to all nine input, output, and address lines. This enables it both to carry out input/output tests and to receive any fault notifications generated by the computers' self-test routines.

In the alternate TA concept, the emergency mode electronics for commanding the thrusters would be implemented in a manner similar to that used with the baseline TA.

Selection of the transfer assembly final design will involve a number of trade-offs. The addition of switching and logic capability must be provided as required.

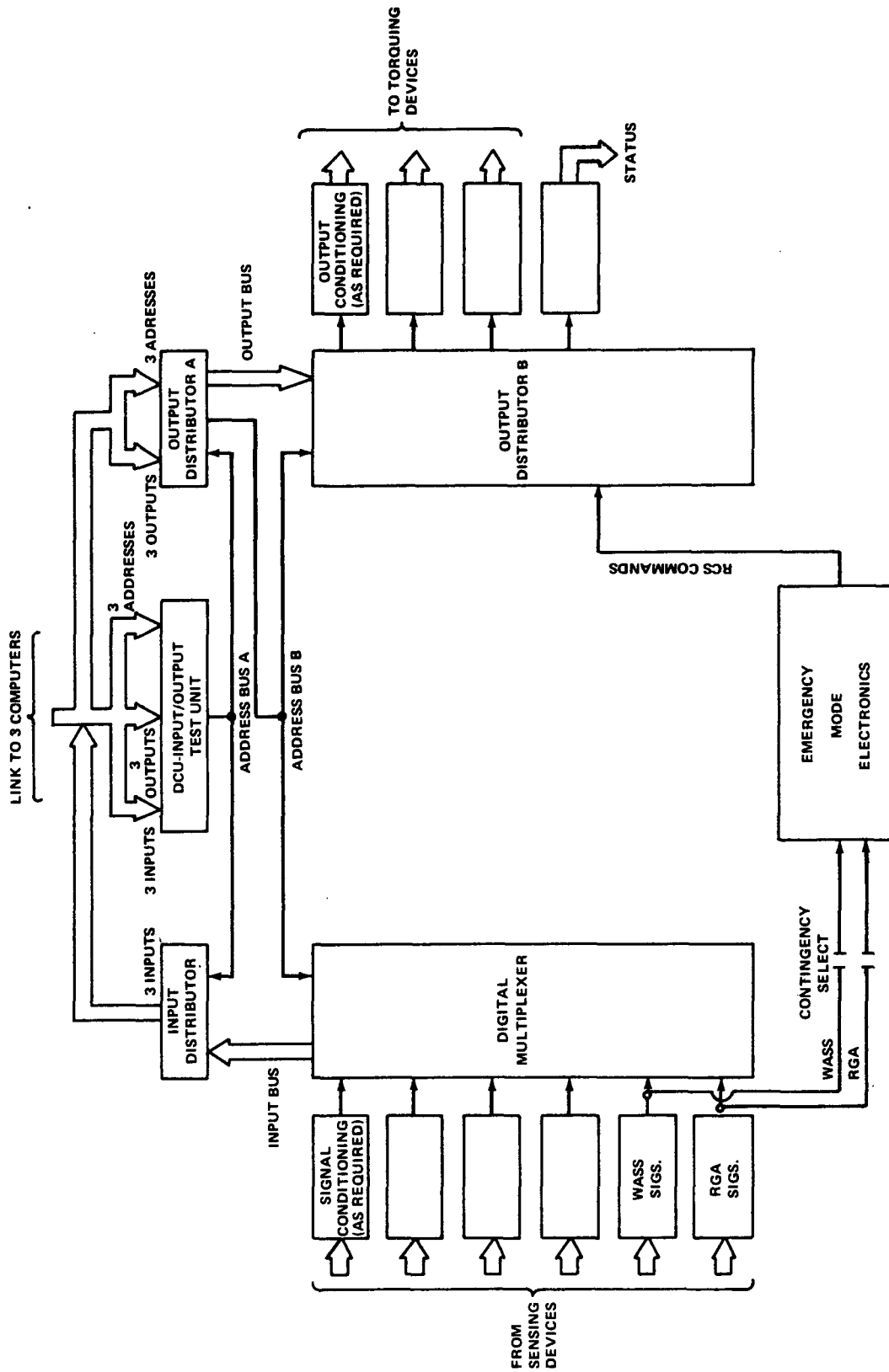


Figure VII-30. Transfer assembly.

## C. System Operation

### 1. Attitude Control Using RCS

a. **Initial Stabilization After Booster Separation.** Initial stabilization after booster separation is performed to reduce the spacecraft body rates caused by separation from the Titan booster to acceptable null values. These initial rates can be as high as 3 degrees per second.

Stored commands in the digital computer unit are initiated at booster separation to configure the ASCS to the sun acquisition mode (Fig. VII-31). The RGA, activated prior to launch, measures the body rates and routes this information via the transfer assembly and digital processor I/O unit to the vehicle control law where actuation commands are generated and transmitted to the RCS. Following rate stabilization, the sun alignment function of the sun acquisition mode will be performed.

b. **Sun Acquisition/Reacquisition.** The final operation in the sun acquisition mode is the alignment of the +Z HEAO axis to the sunline to provide maximum exposure of the solar panels to the sunlight. A WASS having a  $2\pi$  steradian field of view aligned with the +Z HEAO axis and an identical WASS aligned with the -Z HEAO axis provide  $4\pi$  steradian sun sensing capability. If the -Z HEAO axis WASS senses the sun, the control law provides commands to the RCS to torque the -Z HEAO away from the sun and to bring the sun into view of the +Z HEAO axis WASS. Error signals from the +Z WASS are now used in a null-seeking mode by the vehicle control law to command the RCS to align the +Z HEAO axis to the sun. During the alignment to the sun, the RGA provides rate stabilization signals to the control law. Once alignment has been attained, the vehicle is maintained in that attitude for orbit determination, subsystem actuation and checkout, and preparation for orbit adjustment.

A sun reacquisition function is provided primarily for emergency purposes and would be used in case of subsystem malfunctions, loss of vehicle attitude reference by acquisition of the wrong star reference, or similar occurrences. The ASCS functions as it does in the initial acquisition of the sun with the RCS as the baseline actuator. However, later in the mission after CMG activation, the CMGs can supply all control torques when the ASCS is functioning normally and for the reference alignment mode during attitude reference updating.

c. **Initial Orbit.** Special consideration must be given to this phase of the mission because of the additional ASCS load in maintaining attitude control

SUBSYSTEM	SUN ACQUISITION	REFERENCE ALIGN.	ORBIT ADJUST	CELESTIAL POINTING	OFFSET MANEUVER
WASS	X				
DSS		X		X	<input type="checkbox"/>
FHST		X		X	<input type="checkbox"/>
RCS	○	○	X	*	*
CMG	◇	◇		X	X
RGA, COMPUTER, & TRANSFER ASSY.	ALL MODES				

LEGEND:

- X USED
- INITIAL OPERATION
- ◇ AFTER INITIAL OPERATION
- USED IF DESIRED PER GROUND COMMAND
- \* CMG DESATURATION ONLY

NOTE: SPECIAL CONFIGURATIONS AVAILABLE UNDER GROUND CONTROL

Figure VII-31. HEAO-C ASCS configurations.

for the expected 140 by 250 nautical mile initial orbit. Figure VII-5 illustrates typical relations between the gravity gradient torques and the aerodynamic torques for various orbital attitudes. The aerodynamic torques increase greatly as the orbit altitude is decreased. As the 150 nautical mile altitude is reached, additional fuel and thruster firing are required to maintain vehicle attitude. Gravity gradient torques have an almost insignificant change in effect over the altitude range. Associated closely with the aerodynamic torques is the length of time the vehicle remains in the initial orbit, as this governs the fuel consumption and number of thruster firings. Table VII-12 presents the fuel consumption variations for the probable range of orbital staytimes along with the number of thruster firings. The ASCS will be in the sun acquisition mode configuration (Fig. VII-2) during the initial orbit. Thus no special sensors or actuators are required.

d. Reference Update. The initial attitude reference update is performed with the ASCS in the reference alignment control mode. Figure VII-31 indicates the complement of sensors and actuators used and Figure VII-32 is a functional block diagram of the ASCS in this mode. As indicated by the flow chart (Fig. VII-2), the reference alignment mode is always entered from the sun acquisition mode. The primary reason for the initial attitude reference update is to establish a three axis analytical reference attitude frame to be used by the digital computer unit in computing the maneuver to the orbit adjust vehicle attitude. The digital sun sensor, activated during the sun acquisition mode, provides error signals via the transfer assembly and DCU I/O unit to the vehicle control law where RCS commands are generated to align the +Z HEAO axis with the solar vector to an accuracy of one minute of arc. The remaining process necessary to complete the establishment of the three axis reference frame is to determine the vehicle attitude about the sunline.

Star sources of +6 magnitude or brighter are to be used to determine the vehicle attitude about the sunline initially and later are to be used to provide three axis attitude error information. Based on the earth-sun relation for the time of year and knowing that the spacecraft is aligned in two axes to the sun, the missions operations control center (MOCC) selects a swath of stars about the solar vector containing the candidate reference stars. The reference stars are selected from this swath primarily from a magnitude and angular separation that provide ready identification. Once this preferred pattern of reference stars has been selected, both the pattern in the form of a star catalog and the magnitude threshold command are provided to the spacecraft computer and star tracker subsystem at the next convenient ground command interval, thus eliminating the unused dimmer stars and simplifying identification.

TABLE VII-12. RCS IMPULSE AND ACTUATION BUDGET

Event	Total Impulse (lb/sec)	Fuel Required (lbm) at Isp = 140 sec	Worst Case Engine Cycling Per Engine	Comments
Null 3 deg/sec 3 axes	1043.8	7.45	30	Includes attitude control
Solar Acquisition (90 deg about x and y)	269.0	1.91	4	2 deg/sec max maneuver rate
Attitude Control in 140 × 250 n. mi. Orbit	153.6 or 16 032.0	1.09 at 4.5 Orbits 114.8 at 30 Days	319 or 31 500	0.244 lbm/orbit
OAS Thrust Vector Misalignment During Burn to 205 × 250 n. mi.	1079.5	7.71	150	7.5 min burn
Attitude Control in 205 × 250 n. mi. Orbit	33.49	0.239	70	0.239 lbm/orbit for 1 orbit
OAS Thrust Vector Misalignment During Burn to 205 × 270 n. mi.	804.1	5.74	112	5.58 min burn
Attitude Control in 250 × 270 n. mi.	51.0	0.364	106	0.242 lbm/orbit for 1.5 orbits
OAS Thrust Vector Misalignment During Burn to 270 n. mi. Circular	673.2	4.80	94	4.68 min burn
Attitude Control in 270 n. mi. Orbit Until CMGs are up to Speed, End of Checkout and Acquisition of X-Ray Reference	253.3	1.81	451	0.245 lbm/orbit for 7.4 orbits
CMG Momentum Dumping at 270 n. mi.	107 767	769.7	211 090	Only 53 572 actuations per engine are expected
TOTALS	112 126.99 or 128 055.39	795.647 or 909.357	212 426 or 243 607	

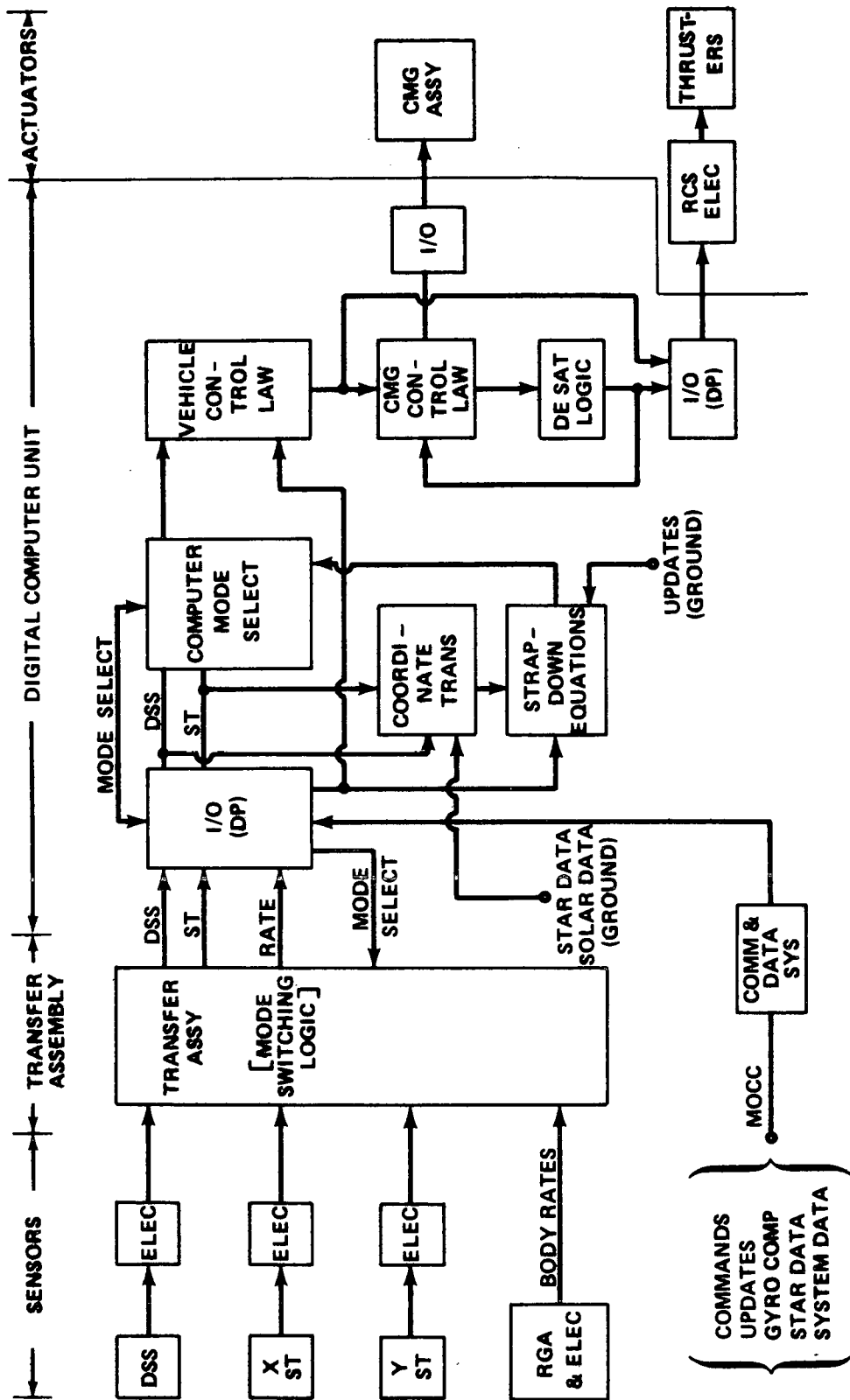


Figure VII-32. Celestial point and reference alignment mode-ASCS.

Initially, no knowledge of the spacecraft attitude about the sunline is available and a command is issued to perform a slow precise roll maneuver about the sunline. This command also can contain the information to set the star tracker magnitude sensitivity threshold. As the spacecraft rolls, the star trackers sense the stars and measure their elevations with respect to body axes. The azimuth separations are determined by integrating the vehicle maneuver rate and with the elevation measurements are used to establish a star pattern by computing star angular separations. This star pattern is compared with the onboard star catalog angular separation of the swath selected and when a match is obtained, the spacecraft attitude can be determined. An additional ground command rotates the spacecraft until the star trackers acquire two selected stars (one per tracker on each of two axes) and this attitude is maintained by the spacecraft while confirmation is obtained and the reference frame coordinates are stored in the memory of the digital computer. Maneuver parameters to attain the attitude for OAS burn are computed with respect to this reference frame.

e. Attitude Maneuvering. The first large angle maneuver to a specified attitude required in the mission is that for the first orbit adjust stage burn (see Figure VII-3). To accomplish this, the control system is commanded to the orbit adjust mode. This provides the functions to maneuver the spacecraft to the required attitude and to hold this attitude to  $\pm 2$  degrees for all three axes during this OAS burn. The method used to perform the maneuver uses the information from the reference gyro assembly in a strap-down calculation employing a four parameter quaternion transformation (Fig. VII-33). The orbit adjust control mode is entered from the reference alignment mode within which an analytical attitude reference frame has been established. The control errors necessary for maneuvering are generated with respect to this reference frame which is maintained in an updated state by the star tracker and digital sun sensor measurements. The elements of the strapdown calculation format are initialized and updated from these sensor outputs.

In effect, a single rotation about an eigenaxis is performed to rotate the vehicle coordinate frame, as computed from the reference alignment attitude, into the commanded orbit adjust coordinate frame. The commands are supplied in rates for use in the quaternion format for generating the errors for the large maneuver. The actual performance of the maneuver will be done in three parts, namely, an acceleration phase to reach a given rate about the eigenaxis, a coast phase until a certain angular rotation has been reached, and a deceleration phase in which the vehicle rate is reduced to zero and the desired rotation angle is attained. Figure VII-34 (a) presents a typical profile for performing the maneuver. Command shaping filters are generally used during the acceleration and deceleration phases to reduce vehicle structural stresses. During

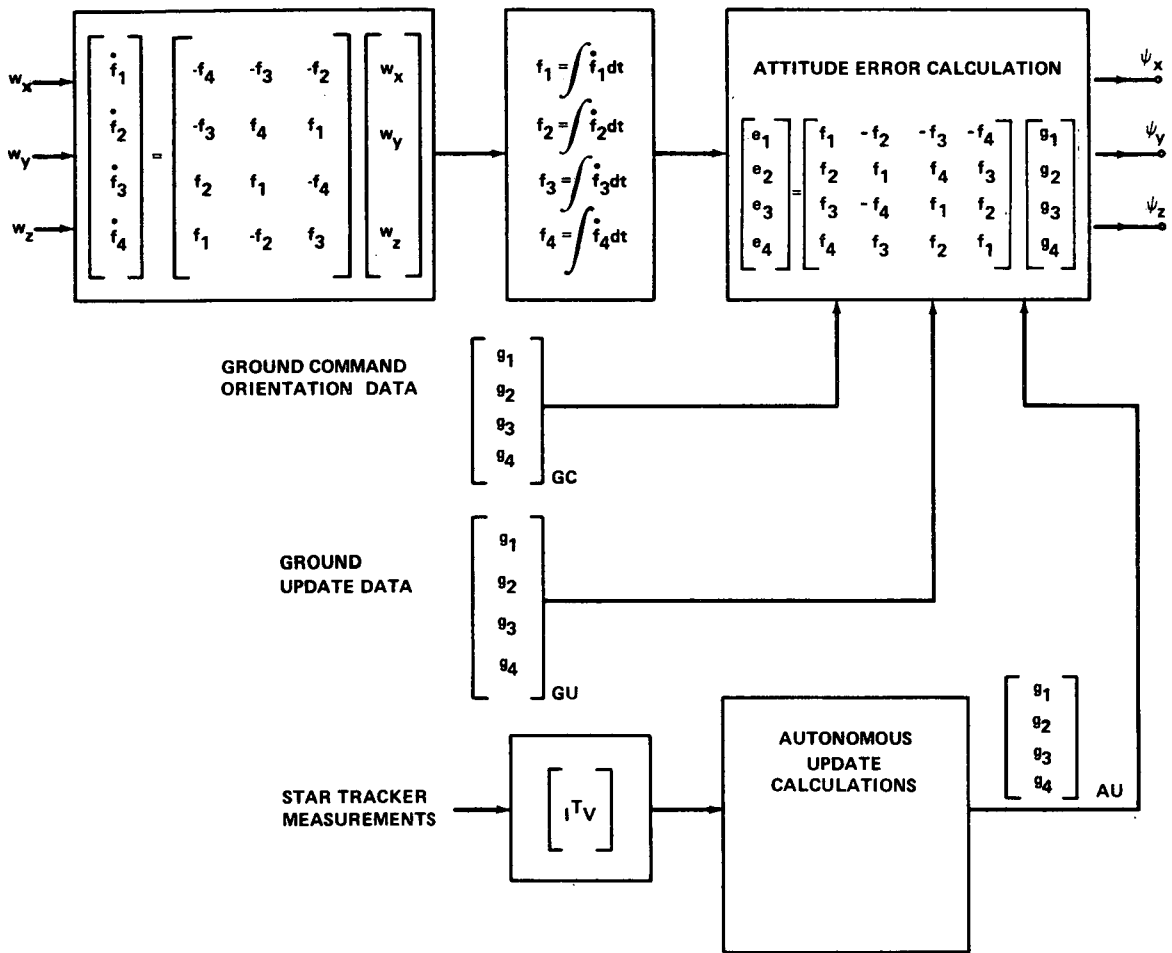


Figure VII-33. Strap down processing concept.

the maneuver, the rotational angle is computed continuously and when the rotation angle error is less than or equal to a predetermined value, the control system automatically maintains the vehicle at the desired attitude.

Figure VII-34(b) illustrates another candidate profile that can be implemented when large maneuver angles are required with minimum time constraints. Approximately equal acceleration and deceleration periods are provided using the maximum torque capability of the RCS. Command shaping filters and position error control switch-over will be required for this case.

f. Intermediate Orbit. To attain a 270 nautical mile circular orbit, the ASCS provides the capability to align the spacecraft and maintain its attitude during the specified OAS burns. From the nominally dispersed ascent

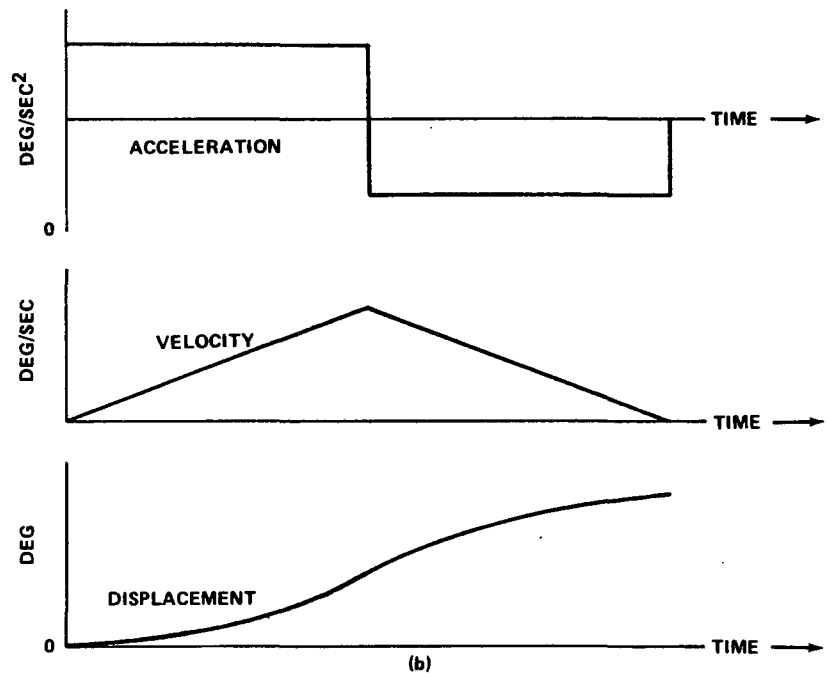
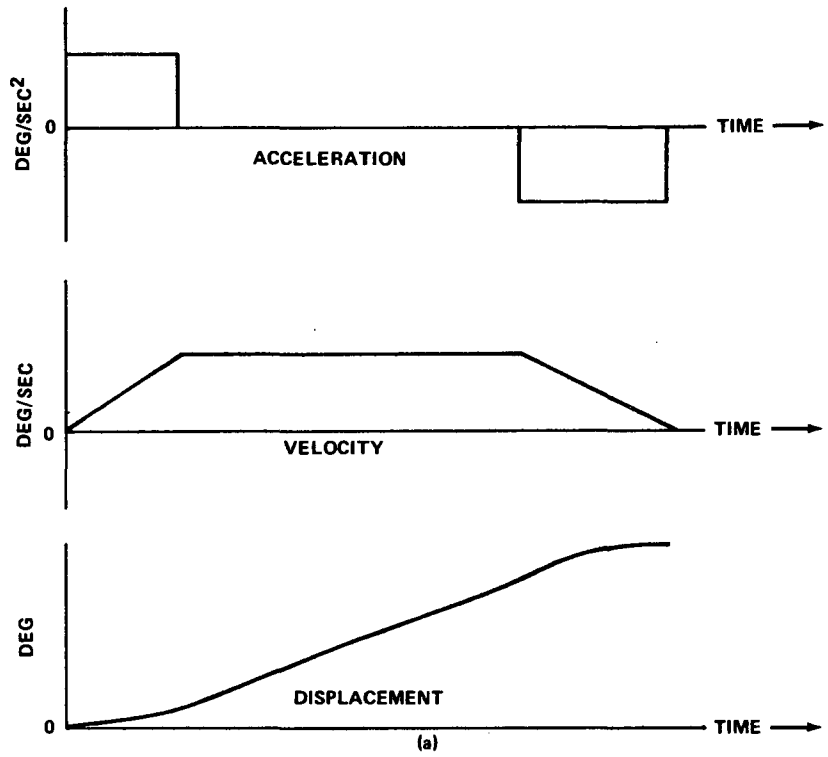


Figure VII-34. Maneuver profiles.

ellipse of 140 by 250 nautical miles provided by the launch vehicle, the first OAS burn places the spacecraft into an intermediate 140 by 270 nautical mile transfer orbit. After providing the required alignment, the ASCS maintains spacecraft attitude during the OAS burn by using the reference gyro assembly to generate attitude errors and the RCS to provide the control torques to overcome the disturbances generated by the OAS engine with the specified one-half degree maximum thrust misalignment. For a nominal launch profile, the OAS engine burn occurs near the orbit perigee point at which the OAS thrust vector is approximately aligned with the orbital velocity vector. This burn raises the apogee altitude to a nominal 270 nautical miles. The ASCS maintains the inertial attitude of the spacecraft to an accuracy of  $\pm 2$  degrees. Sufficient flexibility is provided by the ASCS to align and hold the spacecraft for orbit corrections other than the selected nominal profile through ground commands, once the initial orbit has been determined. Prime consideration was given to the speed with which the necessary maneuvers can be performed to provide ample orbit lifetime prior to final circularization.

g. Final Orbit. Following the first OAS burn to obtain the intermediate orbit, the ASCS uses the reference gyro assembly and the RCS thrusters to provide a 180 degree maneuver in less than one orbit to orient the OAS thrust vector so that it will be colinear with the orbital velocity vector at apogee (Fig. VII-3). The next OAS burn is performed in this attitude for final circularization approximately at apogee with the ASCS holding the inertial attitude during engine firing.

At the end of the second OAS burn, a nominal orbit of 250 by 270 nautical miles has been predicted. The ASCS has the capability to perform additional maneuvers and attitude holds to permit a more perfect circular orbit to be obtained using essentially the same procedure. In addition, there is the additional possibility of returning to the reference alignment mode to obtain an updated reference frame alignment for precisely computing the final orbit adjust attitude if required. Following the final OAS burn, the spacecraft is commanded to the sun acquisition mode where it remains, in preparation for the next mission phase.

h. CMG Spinup. Control torques to stabilize the HEAO during spinup are supplied by the RCS thrusters. For the skewed four-CMG configuration, present plans are to simultaneously spin up two rotors with oppositely directed momentum vectors to minimize spinup power as well as the accumulated vehicle momentum. The total spinup time is approximately 2 hours per CMG pair, or 4 hours total. The trade-offs which determine the spinup method are peak electrical power, RCS fuel consumption, and time. Starting the CMGs in pairs requires about 64 watts peak power, which is acceptable. Barring an

unusual mismatch between CMG run-up characteristics, the fuel required to counteract the CMGs should be negligible, and the RCS fuel consumption consists primarily of that required for gravity gradient and aerodynamic torques.

CMG activation will be accomplished in the sun acquisition mode.

## 2. Attitude Control Using CMGs

a. **Experiment Pointing.** The experiment pointing and data gathering phase of the mission will be performed with the ASCS in the celestial pointing mode. The following sensors and actuators are used:

- Star trackers.
- Digital sun sensors.
- Reference gyro assembly.
- Control moment gyros (primary actuators).
- Reaction control system (CMG desaturation).

The functions provided by the ASCS during experimentation are as follows:

- Maneuvering.
- Target acquisition.
- Inertial attitude hold.
- Attitude determination.

Initially, the celestial pointing mode must be entered from the reference alignment mode where a three axis analytical reference frame has been established. Subsequent maneuvers and target acquisition can be commanded directly in the celestial pointing mode since an updated attitude reference frame is maintained continuously in the DCU through both onboard updates using the star tracker outputs and attitude updates generated by the mission control center.

Figure VII-33 provides a simplified block diagram of the processing functions performed and the sources of the input data.

In the baseline concept, the transfer assembly and the DCU input/output unit (I/O) provide the interface between sensors, actuators, data processor and ground command link. The I/O provides command decoding and routing to the transfer assembly, analog-to-digital conversion for sensor inputs, digital-to-analog conversion of the processor outputs as required, and multiplexing of inputs and outputs. The transfer assembly provides the switching and switching logic necessary to configure the sensors and actuators for each control mode, provides for switching redundant sensors and digital processors per ground commands and digital processor malfunction detection commands.

Figure VII-33 illustrates the simplified strap down processing concept to be used in the generation of the attitude error signals required by the vehicle control law for vehicle attitude control. The measured body rates are continuously supplied by the reference gyro assembly as inputs to the f-parameter calculations that relate the body coordinate frame to the computational coordinate frame. The f-parameters are input to the attitude error calculation block containing the desired orientation of the body frame with respect to the computational frame where a matrix multiplication of the f and g parameters generates four error terms. Three of the error terms comprise the attitude errors about the three control axes and are routed to the vehicle control law to generate the vehicle torque commands for attitude corrections. The fourth error term is a measure of the angular rotation about the eigenaxis.

To maneuver the spacecraft to a new inertial orientation, the four parameters required for the attitude error calculation are generated by the mission operations control center and are transmitted to the spacecraft as updates to the g-parameters in the attitude error calculation. The resulting errors generated for each of the three control axes cause the spacecraft to rotate about an eigenaxis that rotates the body frame from its present orientation to the desired orientation. The error term representing the angular rotation about the eigenaxis provides continuous information of the difference between the desired rotation and the instantaneous angle and can be used to control the acceleration, coast, and deceleration phases of the maneuver as well as for its primary function of supplying the error in the desired rotation.

The reference gyro assembly is the primary source of information to the strapdown computations and due to the uncompensated gyro drift rates, errors in the computation occur because of the difference between the actual and measured rates. Terms in the attitude error calculation are updated by two methods to minimize the errors resulting from gyro drifts. The star tracker measurements provide the source of onboard or autonomous updates once the maneuver under gyro control has been completed and the reference

stars have been acquired. A vehicle-to-inertial-coordinate transformation of the star tracker measurements provides the inputs to the autonomous update calculations, and the update parameters are inserted into the attitude error calculation block. The digital sun sensor can provide two-axis information and one star tracker can provide one-axis information to obtain three-axis measurements to also supply the autonomous update inputs. The second update method is to use infrequent update parameters from the ground. Ground computation using the attitude determination data telemetered from the onboard sensors generates these parameters.

The reference gyro assembly provides the attitude error information during occultation of reference stars and during maneuvers. Drift corrections to obtain the highest accuracy from the RGA are, primarily, provided by ground generated commands that cause torquing signals to be inserted directly into the gyro torquing loops. In this manner, constant and g-sensitive gyro drifts are eliminated leaving only the random drift uncompensated. Computation capability is available onboard to do this drift correction autonomously using the star tracker outputs, or a combination of star trackers and digital sun sensors, during target acquisition.

b. Attitude Maneuvering. The maneuvering concept using CMGs is basically the same as that used with the RCS. A single rotation about an eigenaxis is performed to rotate the vehicle coordinate frame, as computed from the reference alignment attitude, into the desired frame established for the target. The actual maneuver will consist of an acceleration phase, a deceleration phase, and target acquisition phase. Command shaping filters will be used to reduce the vehicle structural stresses.

The maneuver commands are generated by the mission control center and transmitted to the spacecraft in a four-parameter format (Fig. VII-33). Multiple commands for use as required are permissible. The four-parameter command is routed to the attitude error calculation subroutine in the digital computer unit where the command parameters are used as updates to the error calculation. The position error signals generated are routed to the vehicle control law where CMG gimbal rate commands are issued. As the vehicle is torqued by the CMGs, the rates are measured by the reference gyro assembly and are applied through the four-parameter calculations into the error calculations. When the commanded maneuver has been completed, the four-parameter error term is such that the position error inputs to the vehicle control law are zero.

Once the CMGs have been activated and are available for vehicle control, there is no limitation on the number of allowable maneuvers. The CMGs may be used for all maneuvers, including sun reacquisition, except for the cases where critical component failures have occurred.

The vehicle response and maneuver capabilities using CMG control are described in Section E2 and Appendix E.

c. Experiment Calibration. The function of experiment calibration is accomplished by the use of internal energy sources and well-defined energy sources located in space. The use of the external sources provides the only impact to the ASCS.

The procedure for maneuvering to an attitude where the experiment optical axis is pointing at the calibration source is identical to that described in Section C.2.b. Storage of multiple commands in the digital computer unit for implementation as required is permissible.

The procedure for acquiring and holding the calibration attitude is identical to the procedure used in experiment pointing with the ASCS in the celestial pointing operational mode. No additional sensors or procedures to implement the experiment calibration function are required.

## D. System Errors

The two categories of error sources considered for a preliminary error analysis of the ASCS are as follows:

- Attitude sensor errors.
- Actuator contribution errors.

The first category considers the sensors, primarily, and the error contributions are based on estimates obtained from typical component specifications and literature supplied by potential component suppliers. The largest error contributor is the fixed star tracker (FST). A significant trade study was necessary to select the field of view, star magnitude sensitivity, and vehicle tracker configuration to assure enough navigation stars while retaining the specified accuracy. Appendix E provides a detailed discussion of the considerations used in the trade study.

The summary of the attitude determination error estimates given in Table VII-13 considers the two primary cases of target pointing: First, when the star trackers have acquired sufficient guide stars to provide continuous three-axis attitude updates and, second, during periods of guide star occultation with gyro sensing only. Also considered is an alternate mode of operation in which the digital sun sensors provide two-axis signals and a star tracker provides one-axis error signal.

For the baseline star tracker with a field of view of 6 degrees, the 30 arc second error represents a worst case error when the guide star is being tracked at the extreme edge of the FOV. In terms of the total FOV, the edge tracking error can, by design, be easily constrained to one part in 500 to one part in 750. The 30 arc second edge tracking error for the HEAO-C tracker represents one part in 720.

Experiment pointing stability capabilities are governed primarily by the star tracker noise equivalent angle (NEA) and the CMG nonlinearities. The NEA is a function of the bandwidth, field of view, instantaneous aperture, focal length, and lens diameter, all of which are to some extent under the designer's control. Star magnitude sensitivity is also a prime factor in determining the NEA but this is not necessarily under design control as navigation star availability for fixed head star trackers largely determines the required sensitivity. Manufacturer's data indicate that the HEAO-C star tracker NEA can be made to be approximately 1 arc second for the required +6 magnitude sensitivity.

To determine the effects on pointing stability of the nonlinearities of the modified Bendix MA-500 CMG that has been selected for the baseline ASCS, a single gimbal analog computer study was performed (Appendix E). The results of the study indicate that when the ASCS is in the pointing mode with acquired guide stars and the spacecraft is under the influence of the sinusoidally varying gravity gradient torques, the pointing stability is generally near 1 arc second. For short periods of time, when the disturbance torques pass through zero and the CMG gimbal torque motor must reverse direction, the stability is in the range of 2 to 3 arc seconds. Limit cycles of 2 to 3 arc seconds with a period near 100 seconds can also occur under certain conditions.

The general conclusion is that the ASCS can achieve 2 arc second stability with the predicted star tracker resolution and in the presence of the specified CMG friction and dead zone nonlinearities.

TABLE VII-13. ATTITUDE DETERMINATION ERROR SUMMARY

Sensors Mode and Error Source	Error (arc sec)
Star Tracker and RGA Star Tracker Computation Signal Conditioning RGA Drift  Total rss <sup>a</sup> Error = 31 arc sec	 30 6 6 0.15   
Guide Star Occultation (30 min) Initial Error RGA Drift Computation Signal Conditioning  Total rss Error = 45.5 arc sec	 31 32 6 6  
Digital Sun Sensor (2-axis) and Star Tracker (1-axis) Digital Sun Sensor Axes Digital Sun Sensor Computation Signal Conditioning RGA Drift  Total rss Error = 61 arc sec	  60 6 6 0.15  
Star Tracker Axis  Total rss Error = 31 arc sec	  

a. rss — root sum square

## E. Baseline Performance Simulation

1. RCS. The baseline RCS system was studied through the use of a digital computer simulation<sup>2</sup> (TACS, Appendix E) and through hand calculations where appropriate. Although initially, the baseline system was thought to be the better system, it is now questionable whether the alternate system might not be better from a CMG desaturation point of view as explained in Appendix E.

Several vehicle attitudes were tried for the HEAO study, but the one that continuously maintained the X body axis 45 degrees with respect to the orbital plane was found to ensure the largest fuel consumption and highest engine cycle rate. This vehicle attitude is the worst from an RCS attitude control viewpoint; it may not be the worst during the momentum dump mode which is by far the largest fuel consumer.

There are several control possibilities offered by the control law used (Appendix E and Figure VII-35). Pitch and yaw can have single or double engine firings, and roll (X-axis) can have one to four engines fire simultaneously. With the single engine firings in pitch or yaw, roll is unavoidably introduced. Roll has a vernier control in that the yaw/roll engines provide coarse roll control and the pitch/roll engines provide fine roll control, but the present law does make use of this. Since roll is somewhat overcontrolled, this vernier control will allow additional flexibility. Figure VII-36 shows the angular accelerations and rates about each axis due to single engine firings for the baseline and alternate systems.

Based on a limited number of computer runs,  $A_1/A_0$  (rate to position gain ratio) was selected to be a value of 5 and was found to work quite well. Since it was not optimized, more simulation runs will have to be made before a final value is chosen.

Fuel consumption and engine cycle rates were the two dominant parameters studied, and the results of the study are shown in the impulse and actuation budget in Table VII-12.

The single most important use of fuel occurs during CMG momentum dumping. Over 107 000 lb-sec of impulse will be required in the 2 year period the HEAO will be in orbit. At an Isp of 140 seconds, this is equivalent to 770

---

2. Brandon, Larry: A Description of the Thruster Attitude Control Simulation and Its Application to the HEAO-C Study. To be published as a NASA Technical Memorandum by Program Development, George C. Marshall Space Flight Center.

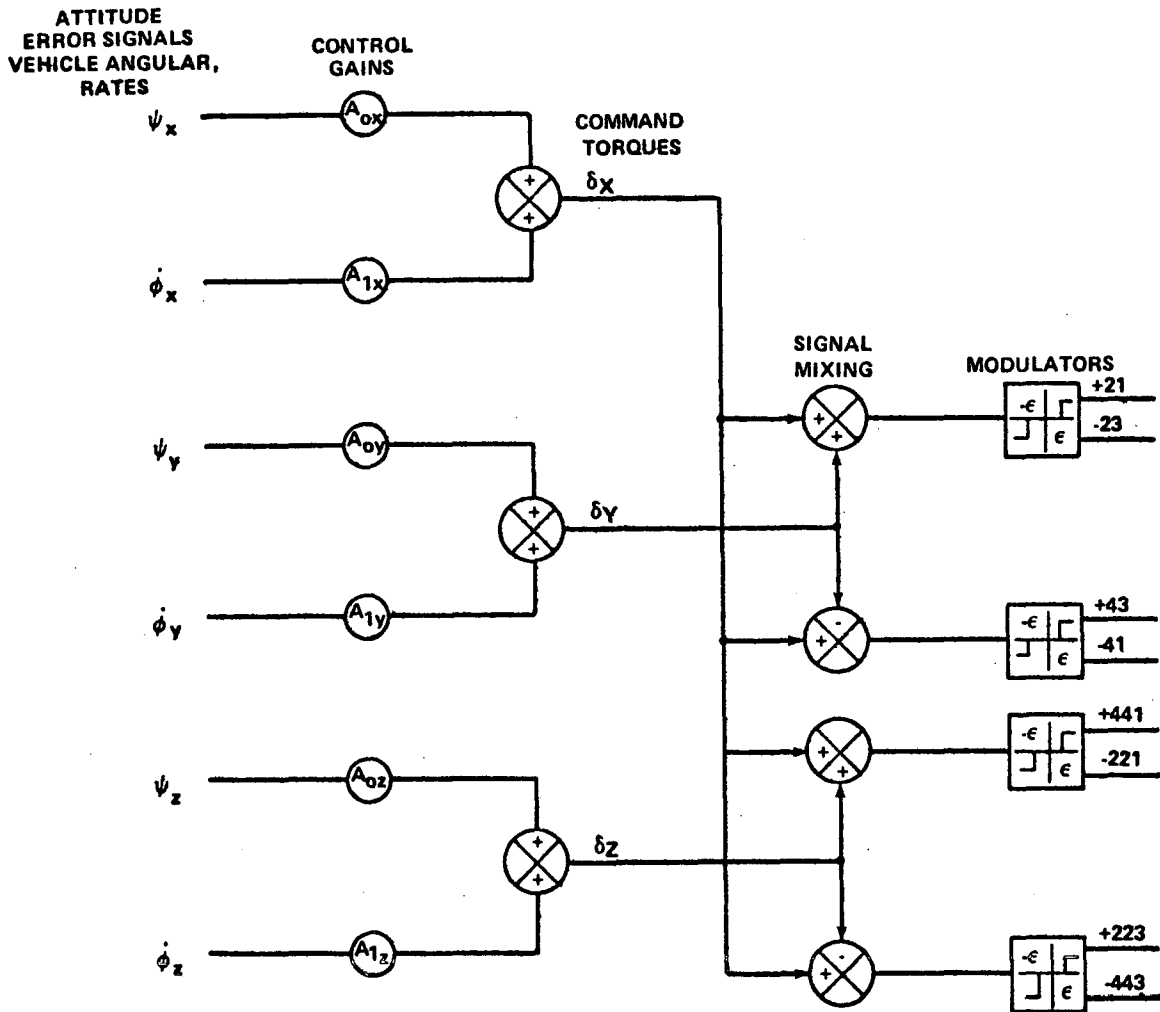


Figure VII-35. The RCS control law used in the baseline studies.

pounds. This assumes an average secular momentum accumulation of 210 ft-lb-sec per orbit (Table VII-2). The baseline will be very efficient at dumping momentum if a significant portion of the dumping is done about the roll axis (X-axis); however, this is not expected to be the case. This would allow long single engine burns (high Isp) as opposed to shorter two engine burns about pitch and/or yaw (see Appendix E).

The next most important use of fuel will occur, possibly, during the stay in the initial 140 by 250 nautical mile orbit. If it is for the nominal stay of 4.5 orbits, fuel consumption is almost negligible. However, if the vehicle

MIN. ON TIME = 0.025 sec THRUST = 5 lbf	ANGULAR ACCELERATION PER ENGINE ARC sec/ sec <sup>2</sup>			ANGULAR RATE PER ENGINE ARC sec/ sec			MOMENT OF INERTIA (SLUG - FT <sup>2</sup> )			
	$\ddot{\phi}_X$	$\ddot{\phi}_Y$	$\ddot{\phi}_Z$	$\dot{\phi}_X$	$\dot{\phi}_Y$	$\dot{\phi}_Z$				
HEAO-C WITH OAS	BASELINE			1764 OR 442.8	319.68	317.16	44.1 OR 11.07	7.99	7.92	$I_x = 2878$ $I_y = 69512$ $I_z = 70049$
	ALTERNATE			1785	319.68	317.16	44.6	7.99	7.92	

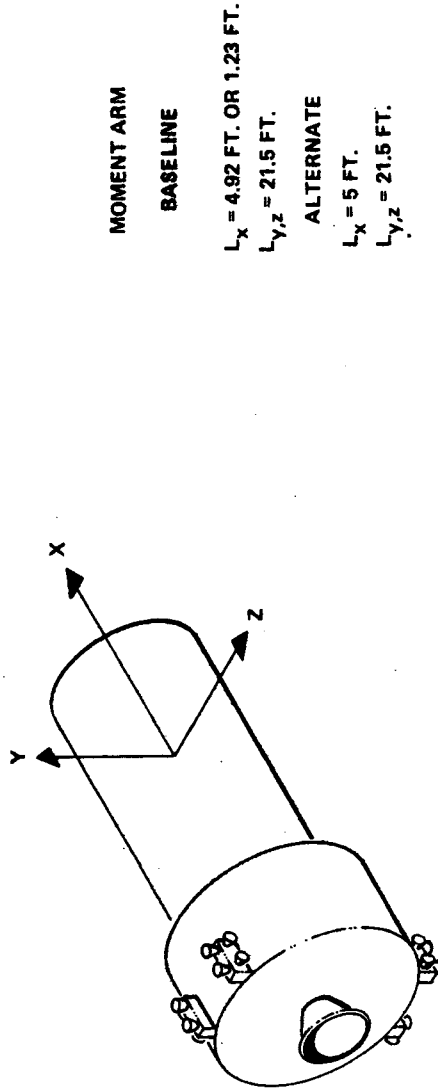


Figure VII-36. HEAO-C thruster characteristics.

is parked for 30 days, which is close to the maximum orbital staytime, and attitude reference is maintained within  $\pm 0.5$  degree, about 16 000 lb-sec impulse will be required. At an Isp of 140 seconds, this is equivalent to 115 pounds of fuel. It is felt that attitude hold during the stay in the initial orbit should not have as narrow a deadzone as the one used in the study.

It was found in the simulation that aerodynamic torques for the nominal air density profile in the 140 by 250 nautical mile orbit do not contribute significantly to the RCS performance. Because of high apogee, the vehicle does not remain low enough for a sufficiently long time for aerodynamics to play a significant role. If a lower insertion orbit is chosen, or if the two sigma density profile is used, aerodynamics will play a significant role, possibly exceeding the effects of gravity gradient.

Orbit Adjust Stage thrust vector management (due to OAS engine misalignment) requires about 2560 lb-sec impulse for all burns from the 140 by 250 nautical mile orbit to the 270 nautical mile circular orbit. This will be at most 15 to 18 pounds of fuel depending on the Isp of the RCS.

The 30 day stay (if used) in the 140 by 250 nautical mile orbit and the momentum dump mode will cause almost all of the engine cycling. Figure VII-37 (engine nomenclature is the same as shown in Figure E-55) shows the accumulated actuations every 100 seconds for the 270 nautical mile orbit but it is so close to the 140 by 250 nautical mile orbit that it is felt it would be appropriate here. This is for the worst case attitude control configuration. Two of the engines actuate about 70 times per orbit (60 times for the 270 nautical mile orbit); four of the engines fire about 20 to 40 times per orbit; and two have an insignificant number of actuations. It is easily seen that a maximum stay time of 30 days would significantly add to the number of actuations of an engine in this worst case. The 30 day stay in this worst case can cause an engine to cycle over 30 000 times. As mentioned above, an increase in the deadzone would help alleviate this problem.

Engine cycling during momentum dump is dependent on the method used, but for the two methods outlined in the appendix, the worst case in each is about 11 000 cycles or 211 000 cycles. It must be noted that these figures are for worst case and there is only a very remote chance that they will be reached. More realistic figures are 2800 cycles and 52 750 cycles. Both of the worst case figures assume that the same two engines always dump the accumulated momentum.

Figure VII-37 previously discussed with regard to the 140 by 250 nautical mile orbit shows the accumulated actuations for the worst case in the 270

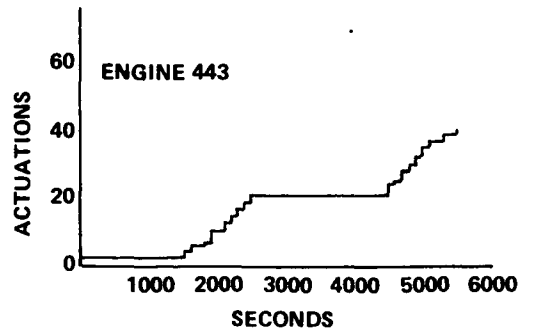
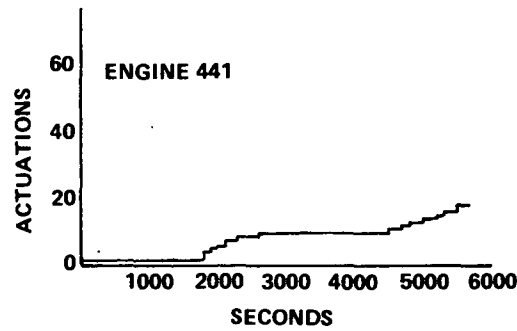
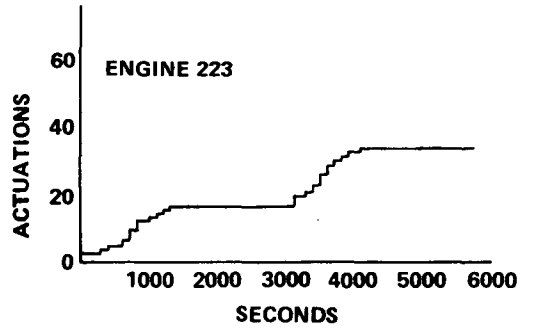
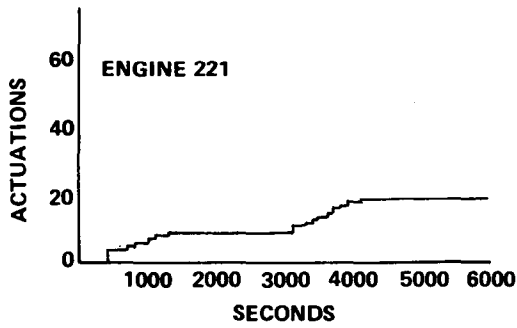
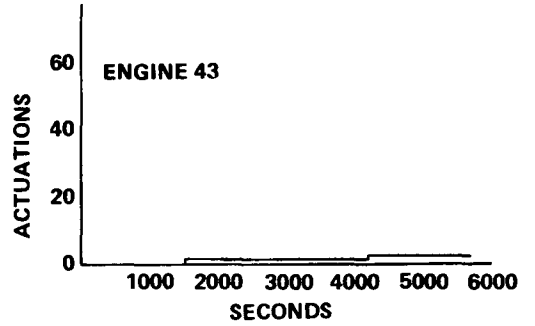
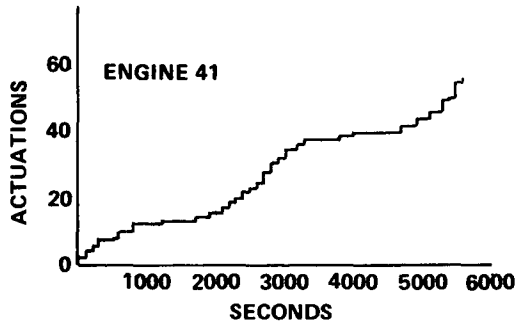
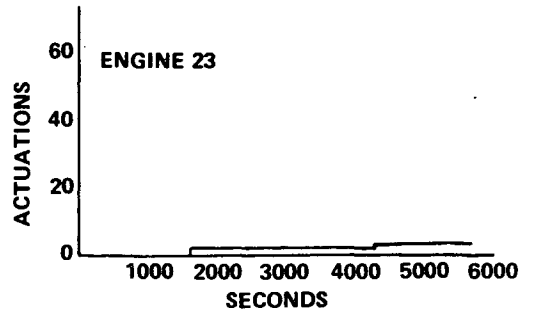
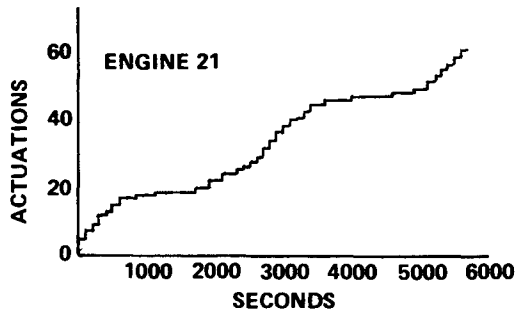


Figure VII-37. Engine actuation for the worst case in the 270 nautical mile circular orbit.

nautical mile circular orbit. Extrapolating these numbers in the case of failure of the CMG system shows that about 660 000 actuations could be expected in the worst case. A more typical number would be somewhat less than that although simulations were not run to determine the "better" number. It is felt that engine cycle life would be exceeded in any case. Using the numbers obtained from the simulations and present HEAO-C fuel capacities, it was found that the RCS system would be capable of performing in a degraded attitude control mode for one year or less if the CMGs fail.

Originally, it was felt that since a reaction control system was required on the HEAO during OAS burn, it should be considered for vehicle control during experiment pointing. Since a thrust of 2.4 pounds may be required during the OAS burn and since the RCS will degrade during its lifetime, a 5 pound thruster is required at the beginning of the HEAO mission. Using the lowest possible on time and still retaining a reasonable specific impulse, the jitter specification is exceeded by a large amount. Hence, a dual level RCS engine is required to meet the jitter specification, adding complexity and cost to the system. As shown in Figure VII-38, even this will not work for a 2 year mission since, as the impulse goes down, the actuation rate goes up rapidly. Only a very short mission would be possible using all RCS control before the cycle life of an engine would be exceeded. Hence it would be impossible to use an all-RCS configuration for the HEAO-C even if it did compare favorably in performance and cost with other systems under consideration.

## 2. CMG System

a. Description. A digital computer program was written to simulate the dynamic behavior of the HEAO-C spacecraft in a circular earth orbit. The program is basically a modification of the program [VII-6] used for HEAO-A with the addition of CMG dynamics and steering law. The equations programmed were Euler's equations for rotational motion about the principal Observatory axes, Euler's kinematical relations which relate the Observatory principal axes to the solar reference, transformational matrices which relate the environmental forces to the Observatory axes, control logic which relates the HEAO attitude errors and rates through appropriate feedback gains to applied torques about the Observatory axes, a spherical harmonic expansion of the earth's magnetic field, CMG dynamics, several selected steering laws, and magnetic control torque logic for CMG momentum management.

For added realism, the program included all natural movements which could affect the spacecraft's attitude motion. These movements include the earth's revolution about the sun (1 deg/day), regression of the ascending line of orbital node (6 deg/day) and the earth's rotation (360 deg/day). The environmental forces acting on the spacecraft were gravity gradient, aerodynamic, and magnetic.

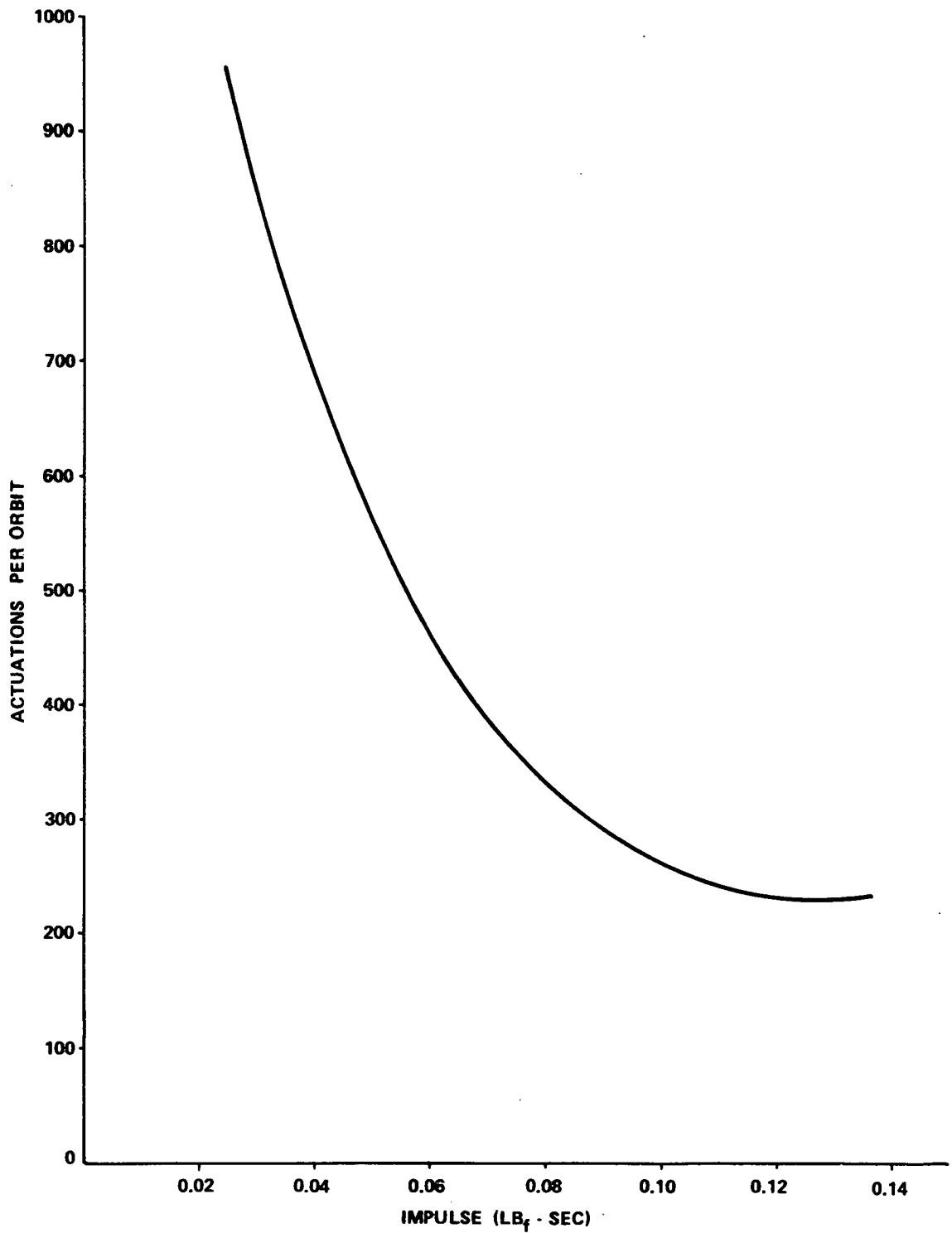


Figure VII-38. HEAO-C RCS, actuations per orbit versus impulse.

The dominant environmental torque is that caused by gravity gradient (g. g.) effects. To simulate the gravity torque, the vector components of the local radius vector must be projected into body coordinates. The effects of orbital position, orbital inclination, orbital regression, time of year, and position of the ascending line of nodes were considered in deriving the required transformational matrices. The magnitude of the g. g. torque also depends upon the vehicle inertia properties, in particular the difference between the inertia values. Both spacecraft inertia values and orbital conditions were selected such that the g. g. torque attained its maximum value.

Figure VII-39 is a simplified block diagram of the HEAO-C digital simulation. The simulation contains four nonlinearities: (1) limits on the CMG gimbal rates; (2) limits on the CMG gimbal positions, which are not shown; (3) limits on each position feedback channel (not shown); and (4) limits on the electromagnet dipole moments. The limits on the CMG gimbal position were deleted and the CMGs are assumed to have unlimited angular positions. Those blocks below the dashed line represent environmental torques acting on the spacecraft.

b. Parameters and Cases Simulated. The following parameters are utilized in the simulation for base runs:

$I_x$	=	2598 slug-ft <sup>2</sup> , long (pointing) axis inertia;
$I_y$	=	82 119 slug-ft <sup>2</sup> , intermediate inertia axis;
$I_z$	=	82 650 slug-ft <sup>2</sup> , maximum (sunward) inertia axis;
AA	=	270 n. mi., orbital altitude;
i	=	28.5 deg, orbital inclination;
$\lambda$	=	270 deg, winter solstice time of year;
$\Omega$	=	180 deg, morning terminator line of nodes;
$\Omega_e$	=	345 deg, position of Greenwich Meridian relative to Aries;
H	=	250 ft-lb-sec, momentum per CMG;
$M_L$	=	0.4 ft-lb/gauss, electromagnet dipole limit;

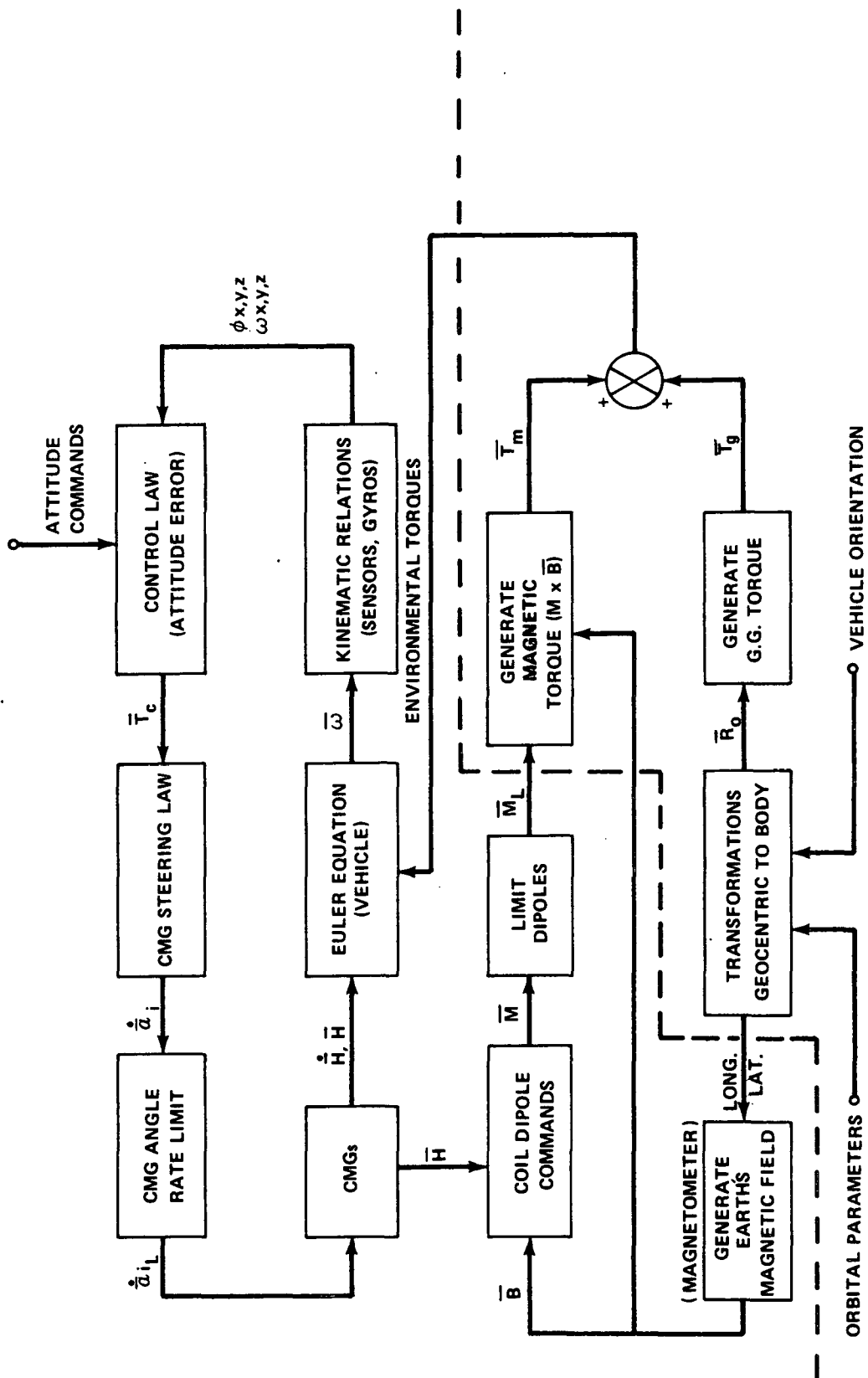


Figure VII-39. Simulation block diagram.

$L_{11}$	=	-256 X-axis position feedback gain;
$L_{21}$	=	-8097 Y-axis position feedback gain;
$L_{31}$	=	-8149 Z-axis position feedback gain;
$K_{11}$	=	-1142 X-axis rate feedback gain;
$K_{22}$	=	-36 100 Y-axis rate feedback gain;
$K_{33}$	=	-36 333 Z-axis rate feedback gain;
$L_{xm}$	=	15 ft-lb/rad, X-axis position feedback limit;
$L_{ym}$	=	478 ft-lb/rad, Y-axis position feedback limit;
$L_{zm}$	=	481 ft-lb/rad, Z-axis position feedback limit;
$L$	=	1 deg/sec, CMG gimbal rate limit;
$K_m$	=	0.01 magnet dipole gain; and
$\beta$	=	53.1 deg, CMG skew angle.

Well over 100 cases were simulated for various HEAO-C configurations, orbital conditions, and control gains. Utilizing the base run parameters, with the g. g. torque near its maximum value, several CMG steering laws were evaluated. On the basis of this evaluation, the pseudo inverse steering law is recommended for HEAO-C. All the simulation results shown in this section are based on the pseudo inverse CMG steering law and the base run parameters. Additional runs for other steering laws are shown in Appendix E.

During the study period, several configurations were evaluated. These were an HEAO configuration with distributed subsystems, a configuration with a subsystems module, and several configurations which had the OAS stage attached. The inertia values shown above represent a growth version of the HEAO with distributed subsystems and with the OAS stage attached.

The feedback control gains were selected to give a damping ratio of 0.7 and a natural frequency of 0.314. The corresponding time period is 20 sec and

the system time constant is 10 sec/rad. As shown in Appendix E [VII-7], the pointing error is proportional to the disturbance torque magnitude and inversely proportional to the position feedback gain. In essence, the greater the required pointing accuracy, the higher the feedback gains. Introduction of integral position feedback permits the use of lower position and rate gains. However, HEAO-C pointing performance can be obtained with only position and rate feedback terms in the attitude error signal. As an alternate, electromagnets are used to dump the accumulated momentum against the earth's magnetic field. In this case, the magnetic loop also provides integral feedback of the attitude error signal which improves vehicle pointing performance as an added bonus. The objective of the attitude error signal is to formulate some desired vehicle torque command.

The objective of the CMG steering law is to convert the torque commands into CMG gimbal rate commands. Whenever the CMG gimbal positions are moved, a corresponding change occurs in the CMG momentum vector, hence producing a control torque which acts on the vehicle to counteract the disturbing torque due to the environment. Ideally, the steering law should make the CMGs produce exactly that torque which is commanded. The problems in selecting a steering law are primarily caused by the fact that there are more unknowns than there are equations between the unknown variables. For example, the four-skewed-CMG configuration baselined for HEAO-C has four gimbal rate commands as unknowns. However, there are only three equations from which to obtain a gimbal rate solution. These equations are obtained by equating the three components of the torque command vector to the CMG torque vector. Although there are many solutions, an exact solution in the usual sense does not necessarily exist. At this point, each designer will devise his own scheme for obtaining a solution. What is needed, of course, is a constraint equation between variables so that an exact solution can be obtained. For each assumption or constraint, a different steering law will be obtained. Several candidate steering laws<sup>3</sup> have been derived for HEAO. These are a constant gain, maximum contribution, pseudo inverse, the Bendix three gimbal inverse, the BECO<sup>4</sup> momentum distribution, and the General Electric transpose with torque feedback. Each steering law was evaluated through digital simulations of vehicle pointing performance. Based on such factors as complexity, accuracy, CMG failure adaption, performance after failure, mathematical singularities and singularity avoidance, the pseudo inverse CMG steering law is

---

3. Davis, Billy G.: A Comparison of CMG Steering Laws for HEAO-C. To be published as a NASA Technical Memorandum by Program Development, George C. Marshall Space Flight Center.

4. Teledyne Brown Engineering Company.

recommended for HEAO-C and also for HEAO-A. As a specific comparison, the Bendix steering law introduces several singularities that are inherent to their law and make necessary a rather complex singularity detection and avoidance scheme. By far, the Bendix three gimbal inverse steering law [VII-3] is more complex than any of the other candidate steering laws without a corresponding increase in either accuracy or reliability. In contrast, the pseudo inverse is more accurate than any of the other laws, adapts to a failure mode without software modification, performs after a failure without any degradation, and does not seem to require either singularity detection or avoidance although gyro hangup avoidance may still be a problem. A brief description of the pseudo inverse of a matrix is given in Reference VII-8 and the general theory is given in Reference VII-9. For the four-skewed-CMG configurations, a 3 by 3 matrix must be inverted to obtain the pseudo inverse.

For any CMG configuration and steering law, there are certain conditions that can produce problems in either the performance of the system or in the ability to obtain the commanded torque. As defined in Appendix E, the CMG torque is related to the gimbal rates by a torque matrix whose columns are unit vectors along each CMG torque output axis. Since there are four CMGs, there are four columns in the torque matrix. Whenever any three columns are colinear, control capability is lost. Whenever all four columns are coplaner, no torque can be produced perpendicular to that plane. This condition is defined as "gyro-hang-up." That is, whenever the commanded torque is perpendicular to the total CMG torque vector, it cannot be produced. The ultimate in gyro-hang-up is CMG saturation. Obviously, if the CMGs have produced all the momentum possible in a given direction and the commanded torque vector asks for more in that direction, it is impossible to produce the required change in momentum and control is subsequently lost. For an inertially oriented spacecraft, a component of the g. g. torque is almost always offset from its zero reference, producing a momentum component that tends to saturate the CMGs over a period of time. Before the CMGs are saturated, the prevailing condition must be detected and stored CMG momentum must be interchanged with that produced by a second source such as RCS or electromagnets. In so doing, the CMG gimbal positions are returned to their reference position, usually a zero momentum state.

Figure VII-40 illustrates the g. g. torque vector components and total torque magnitude relative to the Observatory principal axes in ft-lb. Notice that the Y-component is biased negatively and attains a value of 0.14 ft-lb. Other orbital conditions, however, can cause the biased torque to appear on either the X- or Z-axis, or to be prorated between all axes simultaneously. The Observatory momentum components corresponding to the torques shown in Figure VII-40 are shown in Figure VII-41. Since the HEAO is almost

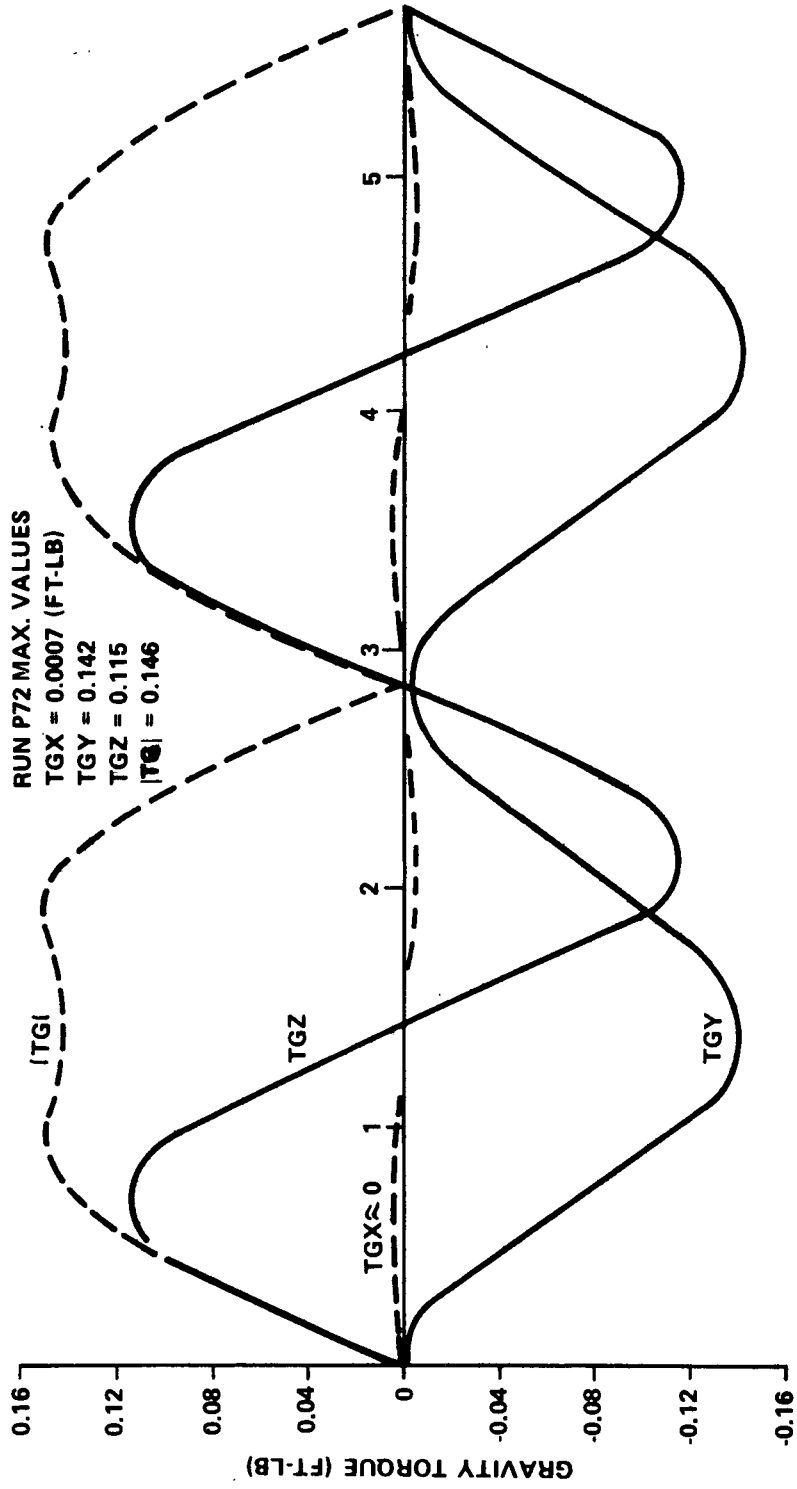


Figure VII-40. Gravity gradient torque versus orbital time (10<sup>3</sup> sec).

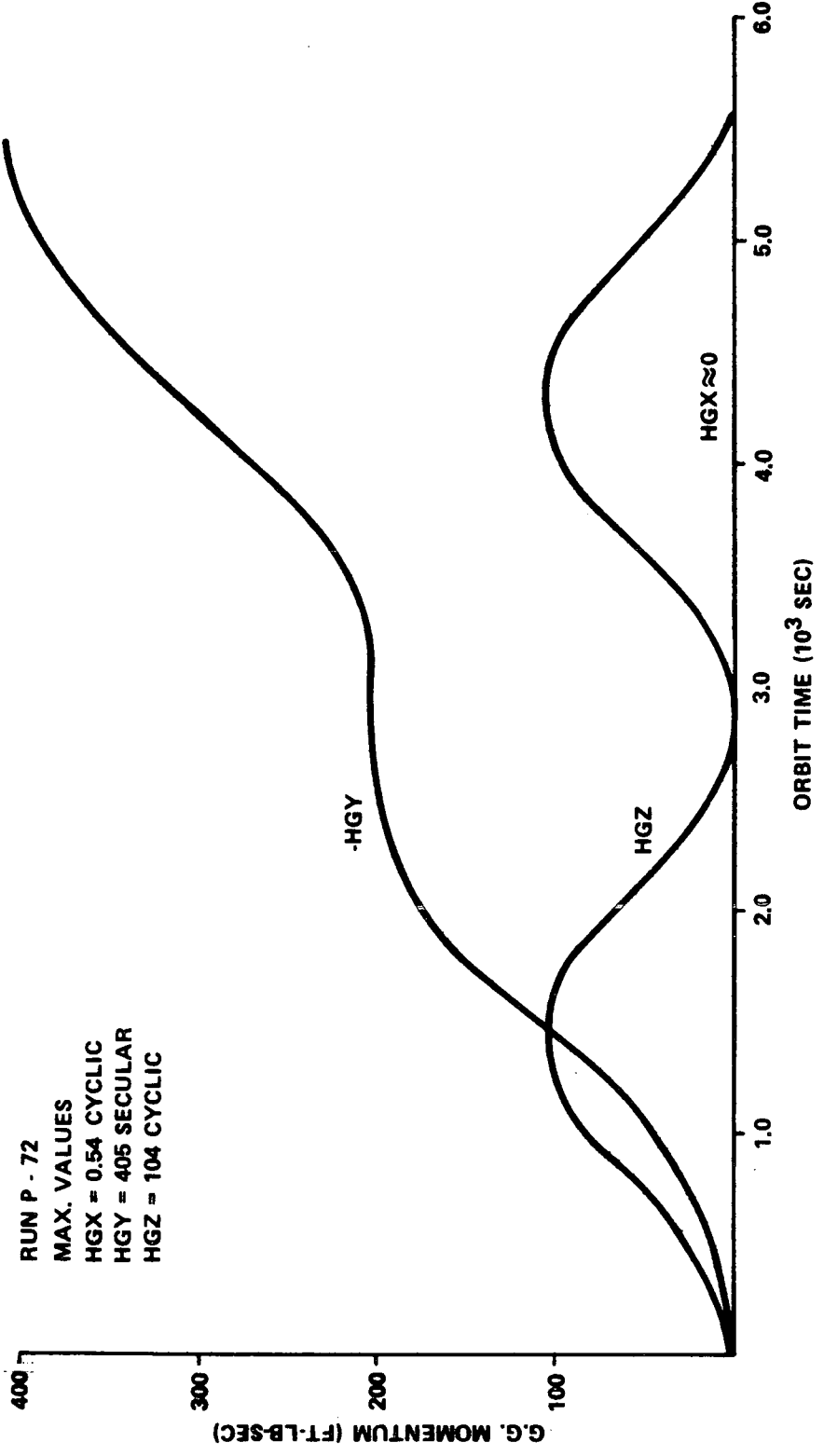


Figure VII-41. Gravity gradient momenta versus orbital time.

symmetric about the X-axis, both the g. g. torque and momentum is near zero on that axis. The cyclic Z-axis torque produces a biased but cyclic momentum. But the biased Y-axis torque produces a linear buildup of momentum with time that will eventually saturate the CMGs. This momentum buildup over a period of time is denoted as secular momentum and must be dumped to prevent CMG saturation. As shown, the secular momentum is 405 ft-lb-sec per orbit and as previously shown by the CMG momentum envelope, four 250 ft-lb-sec CMGs produce a maximum capability of about 800 ft-lb-sec in the Y-axis direction. Therefore, if momentum is not dumped, the CMGs will saturate in about two orbits. Computer run P-72 verified the CMG saturation time. If, however, the CMG momentum size were doubled to a value of 500 ft-lb-sec per CMG, then, under worse case conditions, about four orbits are required to reach saturation. One general problem area for future study is the technique for dumping only the secular momentum without dumping the cyclic portions. Starting with zero initial conditions, the CMG momentum components are identical to the g. g. momentum up to saturation, at which time the two diverge.

c. Simulation Results. Pointing performance of HEAO-C is measured by the angle between the long spacecraft axis and the desired X-ray target source. The pointing error is given by

$$\delta_p = \left[ (\phi - \phi_c)^2 + (\psi - \psi_c)^2 \right]^{\frac{1}{2}},$$

where  $\phi$  and  $\psi$  are rotations about the two transverse axes and  $\phi_c$  and  $\psi_c$  are the commanded rotations required to point to an X-ray source (see Appendix E). Pointing jitter rate is given by

$$\Delta = (w_x^2 + w_y^2 + w_z^2)^{\frac{1}{2}},$$

where  $w_x$ ,  $w_y$ , and  $w_z$  are the body angular rates. The attitude error must be less than 1 arc min and jitter rate less than 1 arc sec/sec. Figure VII-42 shows typical performance with all CMGs operating by the pseudo inverse steering law. The maximum deviations are 0.102 arc min pointing and 0.36 arc sec/sec jitter, which meets HEAO-C specifications. No momentum has been dumped. As a result of secular g. g. momentum, the CMG gimbal angles get rather large. As shown in Figure VII-43, gimbal angle number 3 attains a value of 142 degrees at the end of one orbit,  $T_0$ , while CMG gimbals

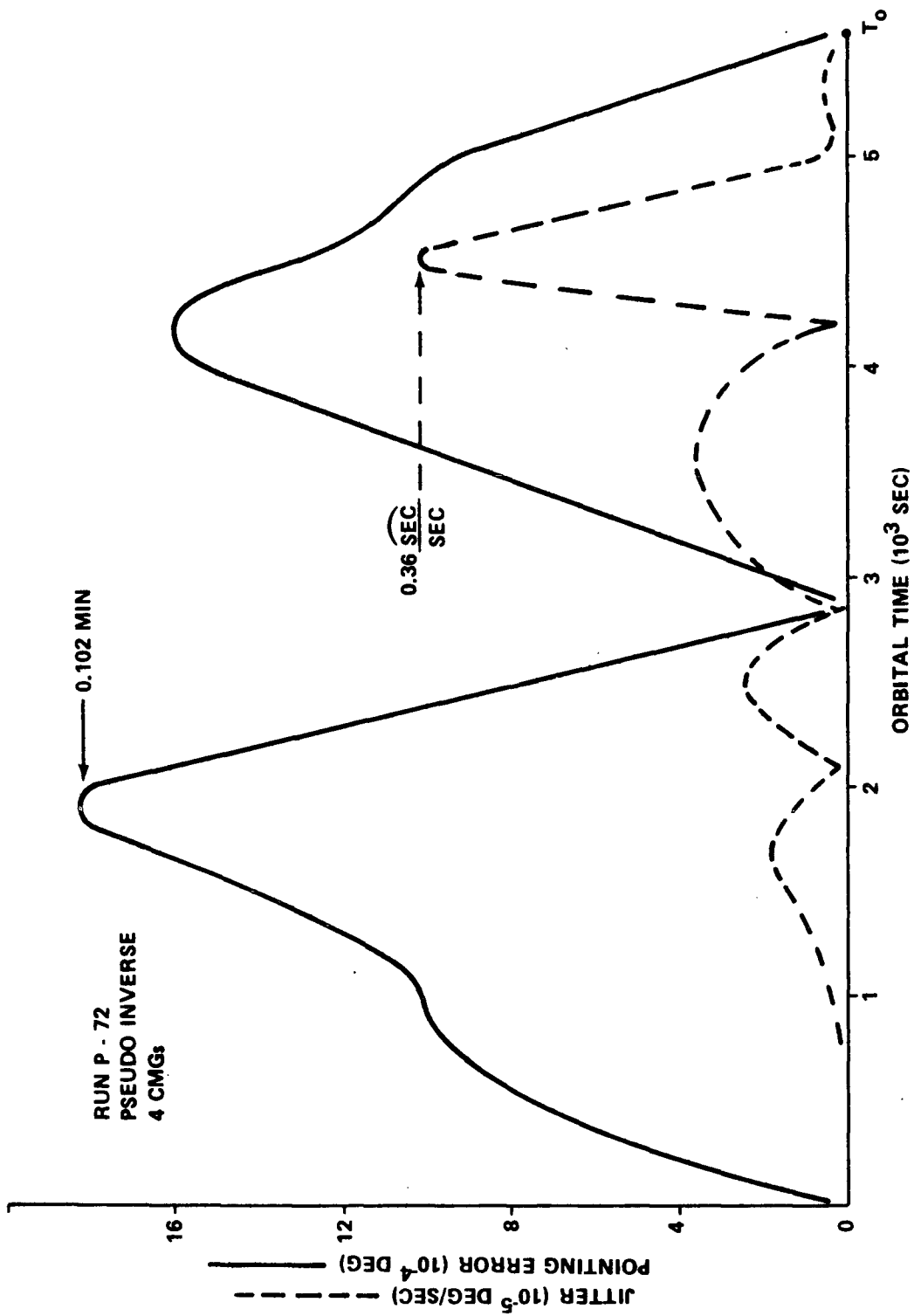


Figure VII 42. Pointing error and jitter versus orbital time.

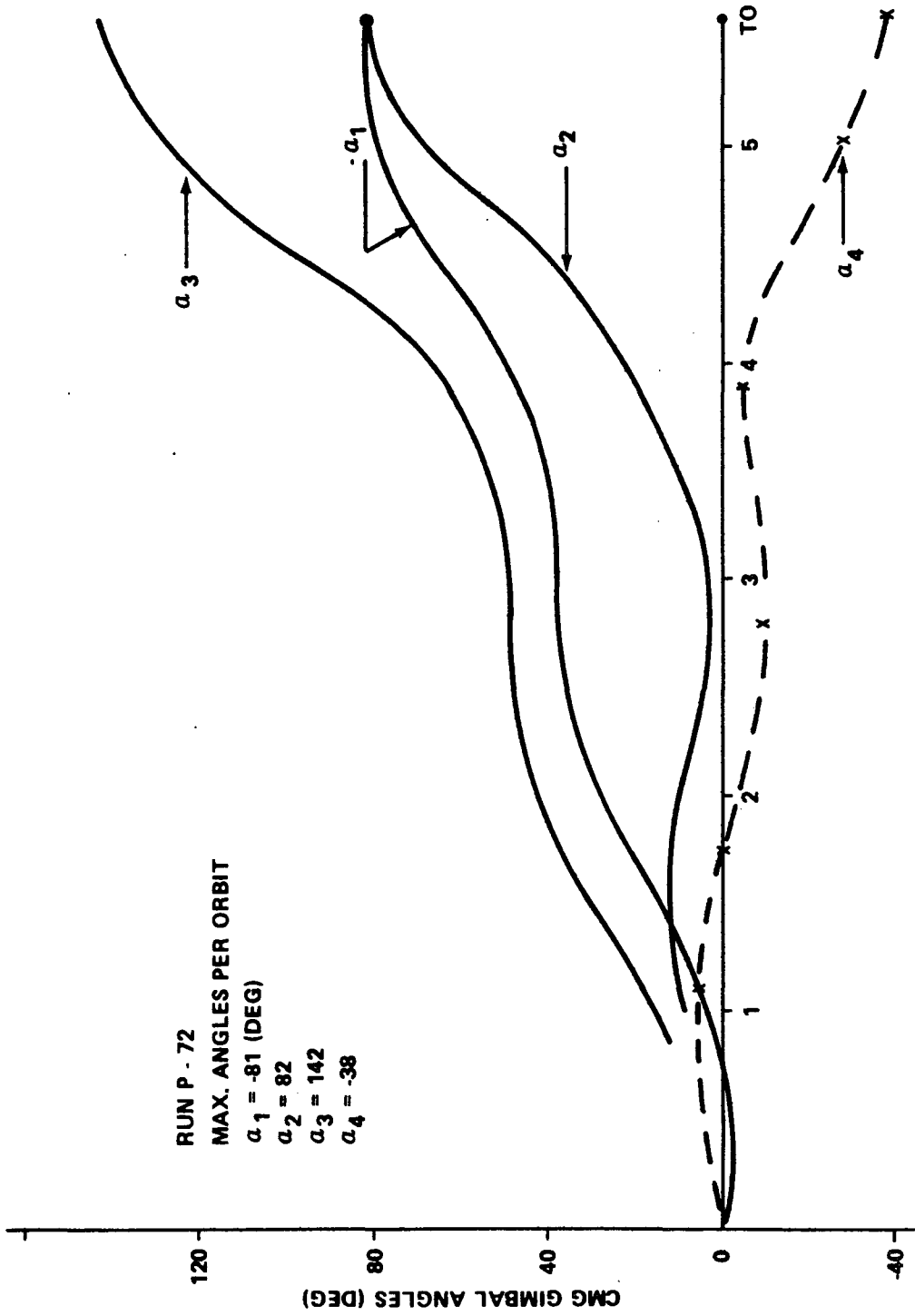


Figure VII-43. CMG gimbal angles versus orbital time ( $10^3$  sec).

1 and 2 reach a magnitude of 82 degrees. Although not shown, saturation is attained near two orbits with  $\alpha_1 = -90$ ,  $\alpha_2 = 180$ ,  $\alpha_3 = +90$ , and  $\alpha_4 = 0$  at which time control is lost. Up to one orbit, CMG number 3 appears to be doing the most work.

The number 3 CMG was failed by setting its momentum to zero. However, no change was made in computing the gimbal rate commands for the remaining CMGs and the elements of the column vector in the CMG torque matrix corresponding to CMG number 3 was not set to zero. The pointing performance is illustrated in Figure VII-44. At about 4000 sec, the three 250 ft-lb-sec CMGs saturate and control is lost. Before saturation, the peak pointing error is 0.072 minutes of arc and the jitter (not shown) is 0.417 arc sec/sec. Additional runs in which other CMGs were failed indicate that the HEAO performance specifications can be met using any three CMGs and the pseudo inverse steering law. However, if a full orbit under worst case g. g. torques must be attained before CMG desaturation, the CMG momentum must be increased to 500 ft-lb-sec per wheel. Figure VII-45 shows the corresponding gimbal angles. With CMG number 3 out, the remaining CMGs were initialized to a new zero momentum state with  $\alpha_1 = 0$ ,  $\alpha_2 = 56.4$ , and  $\alpha_4 = -56.4$ . At CMG saturation, gimbal 2 has moved about 80 degrees to attain 140 degrees in 4000 sec. Both the gravity gradient and CMG stored momentum are shown in Figure VII-46. Before saturation, the two profiles are identical, but differ once the CMGs have saturated. Notice that slightly less than 300 ft-lb-sec have been stored in the CMG system at saturation. The three CMGs, however, have a momentum potential of 750 ft-lb-sec. Hence, under worst case conditions less than one-half of the CMG momentum capacity is usable, a predictable event based on the maximum momentum envelopes shown in Appendix E, Figure E-48 with one CMG out.

With one CMG out, there are three remaining gimbal angles and three equations that relate them to the commanded torque, in which case an exact inverse can be used to obtain the CMG steering law. Additional cases (not shown) were programmed with exact inverses for three CMG configurations. Data from these cases were compared with that of the pseudo inverse with one CMG out; the results were identical. That is, with one CMG out, the pseudo inverse steering law reduces to an exact inverse. Again, the simulation data agree with theory of the pseudo inverse [VII-8 and VII-9].

A cold gas RCS system for control during OAS burn, three orthogonal electromagnets for CMG momentum dump against the earth's magnetic field, and four skewed CMGs for maneuvering and attitude control form an attractive

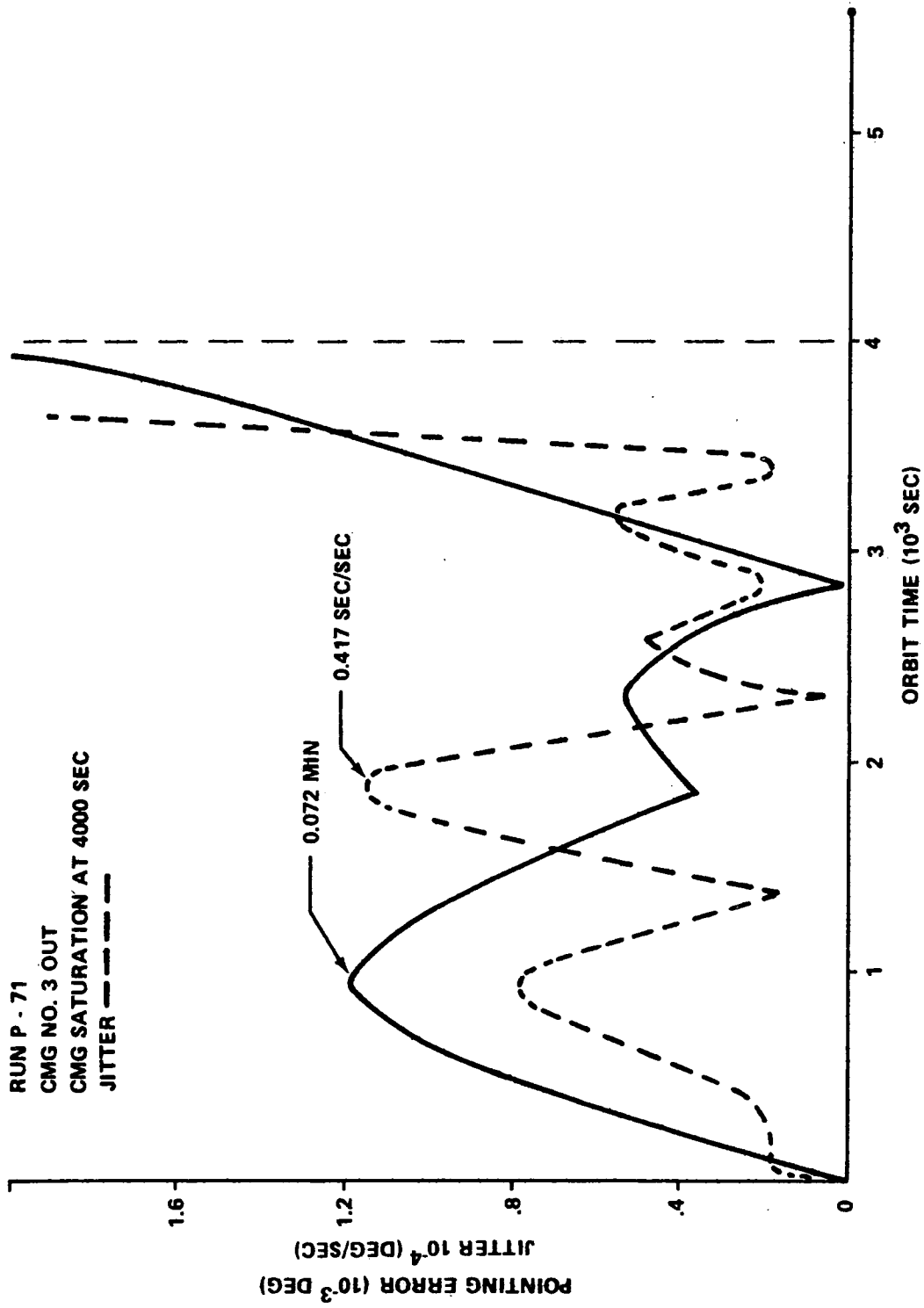


Figure VII-44. Vehicle performance with CMG number 3 failed.

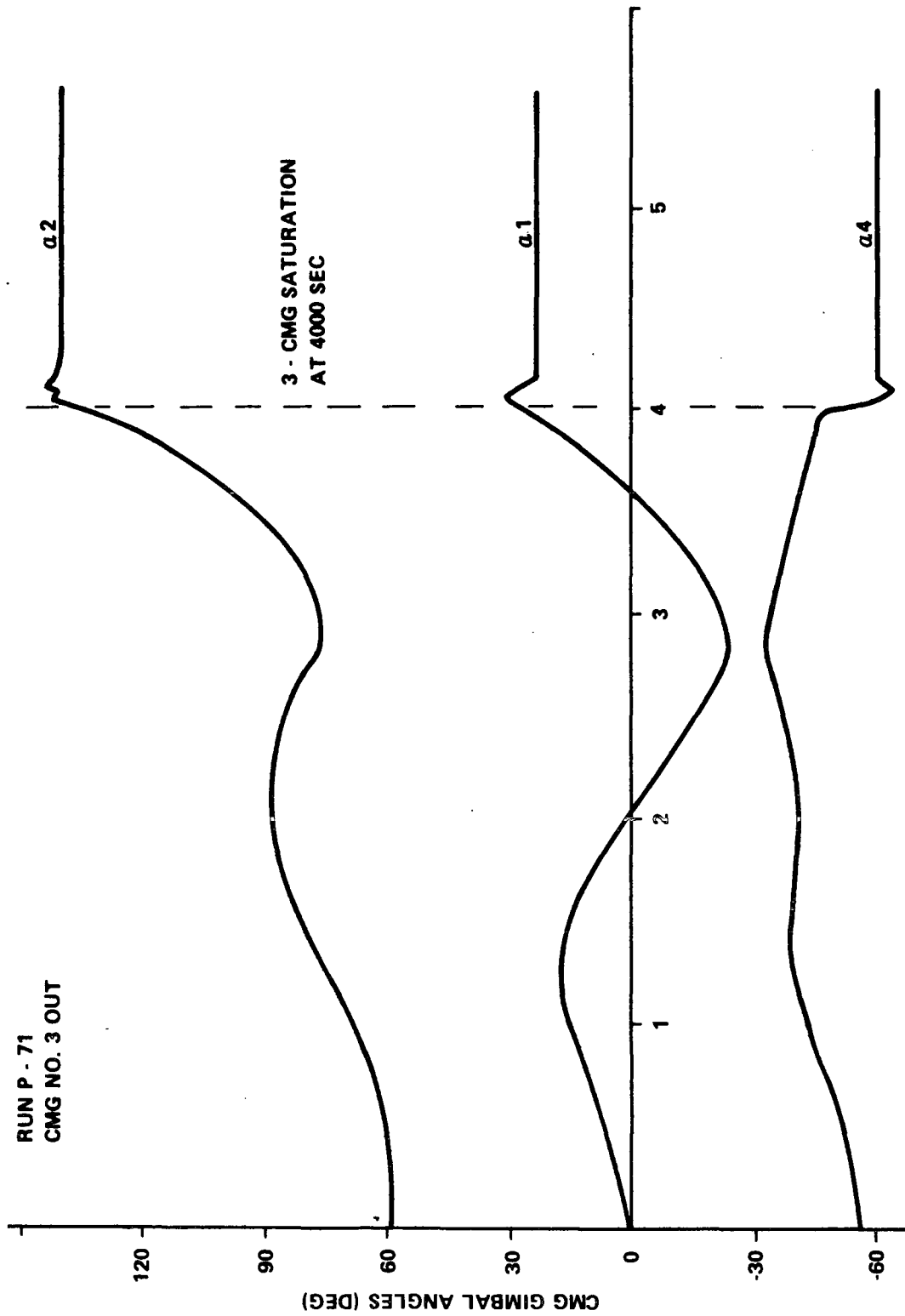


Figure VII-45. CMG gimbal angles (CMG number 3 out) versus orbital time (10<sup>3</sup> sec).

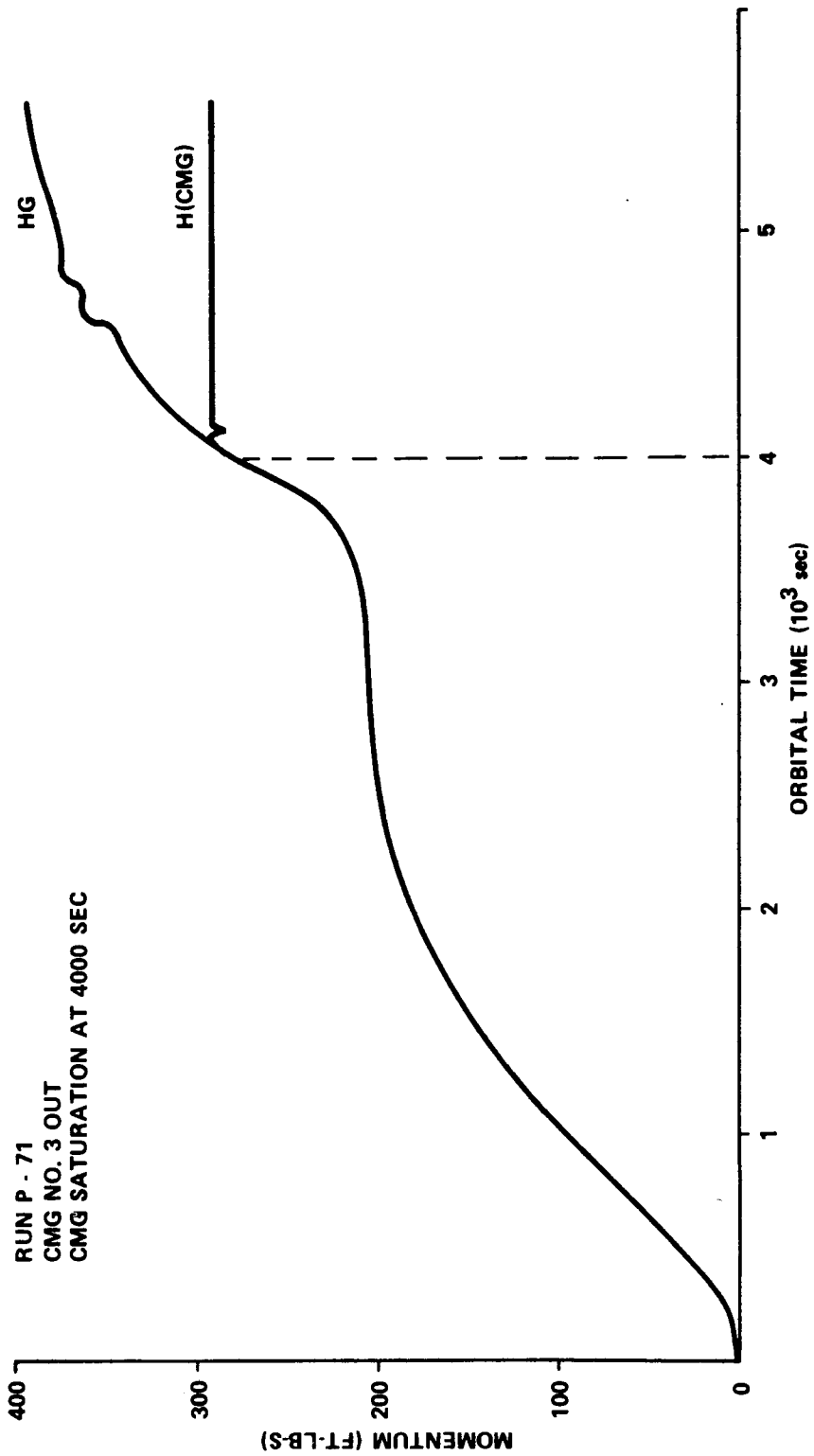


Figure VII-46. Gravity and CMG Momenta, CMG number 3 failed.

alternate for HEAO-C. A current proportional to the momentum stored in the CMGs is passed through three orthogonal electromagnets to produce a dipole moment which interacts with the earth's magnetic field. The result is a magnetic torque which is used to continuously dump CMG momentum [VII-10]. The components of the earth's field projected into the Observatory principal axes are shown in Figure VII-47. The maximum magnitude is about 0.4 gauss.

Several runs were made to find the appropriate coil size needed to dump the worst case accumulated momentum. With the power per coil limited to 10 watts, coils sized for 0.2 ft-lb/gauss weigh about 30 lbm each and can dump the expected secular momentum. However, for greater depth of failure, the coils were sized upward so that the torque produced would equal or exceed that due to gravity. With each coil sized for 0.4 ft-lb/gauss, enough torque is produced to provide direct control of HEAO-C, in which case pointing performance could be maintained with two CMGs failed. However, additional logic and direct torque commands to the coil current commands will be required. As simulation data were obtained using coils for CMG momentum dump, it became apparent that the Observatory performance improved. A linear analysis of the HEAO-C equations of motion [VII-7] proved that magnetic momentum dump introduced the integral of attitude error through the control loop, improving both pointing and jitter performance of HEAO-C. Moreover, since momentum is continuously dumped, the CMG gimbal angles stay very small, permitting the use of a constant gain steering law. Since the coil commands are based only on the CMG momentum state, when one CMG is failed, the remaining CMGs are automatically driven to a new null (zero momentum) state without reprogramming or software modification. Appendix E [VII-7] contains a summary of the following advantages of using electromagnets for continuous momentum management:

- (1) No fuel or RCS required for momentum dump.
- (2) Lifetime not limited by expendables.
- (3) Saturation detection not required.
- (4) Very small gimbal angles permit use of a constant gain

steering law.

- (5) One CMG fail operational capability.
- (6) Operation with two CMGs failed is possible.
- (7) Small size CMGs (50 ft-lb-sec each) could be used.
- (8) Improved pointing performance.

There are, however, some possible disadvantages to the use of electromagnets. These are possible magnetic contamination which may require shielding of certain components, such as photomultiplier tubes; or power usage which would be limited to 30 watts for the three coils. Overall, the system should be more reliable than one using RCS dump.

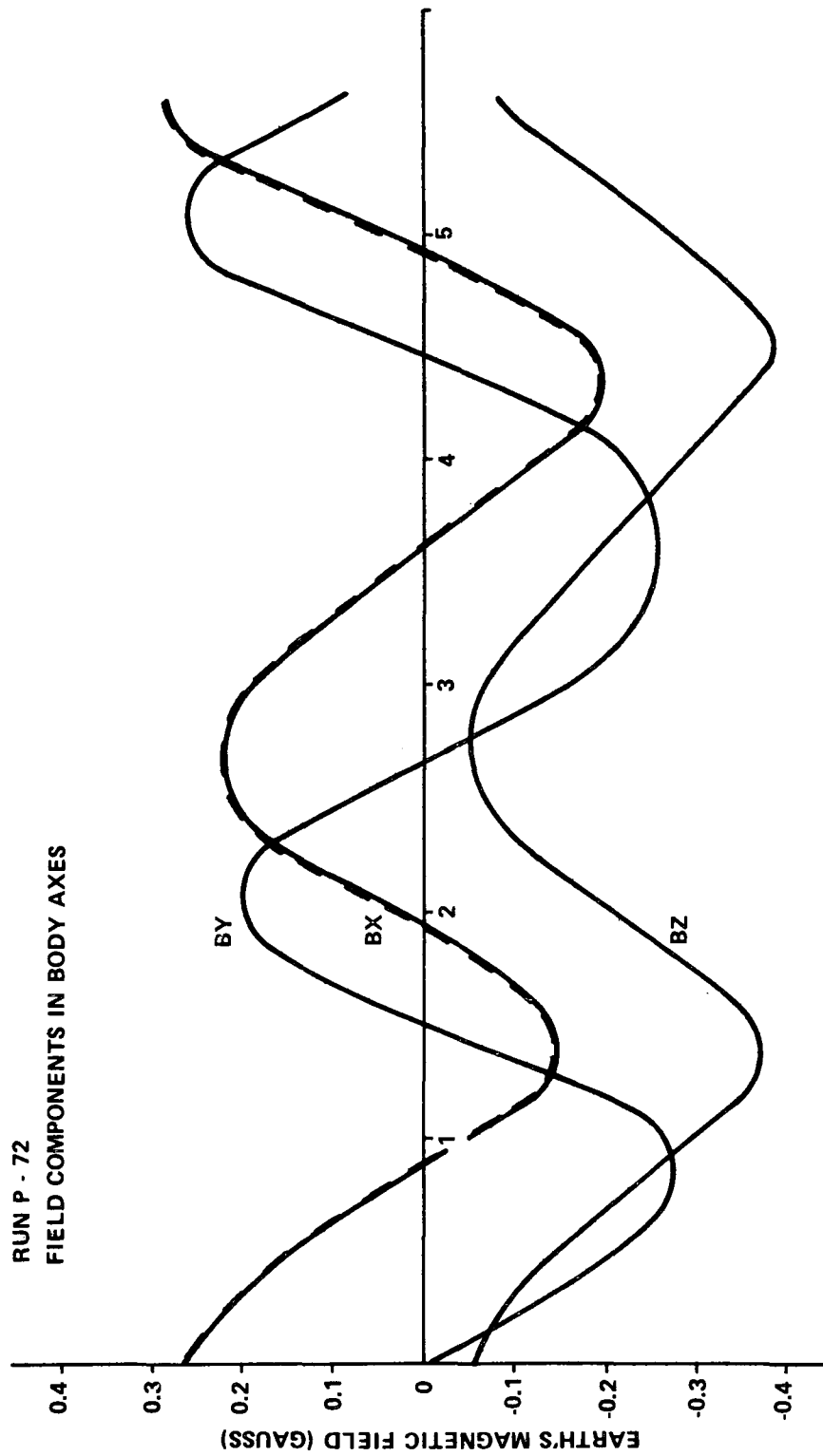


Figure VII-47. Earth's magnetic field versus orbital time ( $10^3$  sec).

Run number P-67 illustrates typical performance using electromagnets for CMG momentum dump. Figure VII-48 shows the peak pointing error to be 0.042 arc minutes with CMG number 3 failed. The peak jitter (not shown) is 0.086 arc sec/sec. The system performance shows a marked improvement compared to the standard runs as shown by Figure VII-42 or VII-44 without magnetics. The initial CMG angles were set (Fig. VII-49) to a null position for CMG number 3 out. As shown, the CMG gimbal angles do not deviate more than  $\pm 3$  degrees from their null position. Consequently, the CMG system does not store much momentum during normal operation. The momenta stored in the CMGs and that due to gravity are shown in Figure VII-50. Without continuous dump, the CMG momentum would have equaled that due to gravity. The maximum momentum accumulated in the CMG system is about 25 ft-lb-sec, indicating that very small CMG size could have been utilized for control. In a subsequent run (not shown) four 25 ft-lb-sec CMGs were used to maintain satisfactory performance. The vector components of the coil dipole moment are shown in Figure VII-51. Since each coil is orthogonally aligned with a spacecraft axis, the components are equivalent to current commands to each individual coil. As previously stated, the dipoles per coil were limited to 0.4 ft-lb/gauss. The X-axis coil saturates twice during the orbit and is doing more work than the other two. The X-axis coil was failed, as well as CMG number 3, in the next run (not shown) and the pointing performance was relatively unchanged. However, only about two-thirds of the accumulated gravity momentum was dumped. In other words, the system could saturate in about four orbits if a worst case attitude hold were maintained with one CMG and one coil failure. Figure VII-52 illustrates the vector components of the magnetic torque being applied to the spacecraft. The peak magnitudes (0.14 ft-lb on the Z-axis) are about equal to that of gravity gradient (Fig. VII-39), indicating that the coils are sized appropriately for direct control in the event of two CMG failures. Additional runs using electromagnets in combination with steering laws other than the pseudo inverse show that the use of magnets greatly improves the performance of any steering law, especially that of the constant gain, maximum contribution, or transpose in which cases the system bandwidth is a function of the gimbal angles. By keeping the gimbal angles small, all steering laws perform equally well.

In summary, system simulations have shown that four 250 ft-lb-sec skewed CMGs with the pseudo inverse steering law can provide the required pointing and jitter performance for HEAO-C, even with one CMG failed. Under worst conditions with one CMG failed, the CMGs saturate after about three-fourths of an orbit, necessitating either a more frequent RCS dump interval than the once per orbit baseline or an increase in the CMG spin rate to provide additional momentum capacity. Additional studies need to be made to determine the performance capability of two CMGs augmented by RCS control.

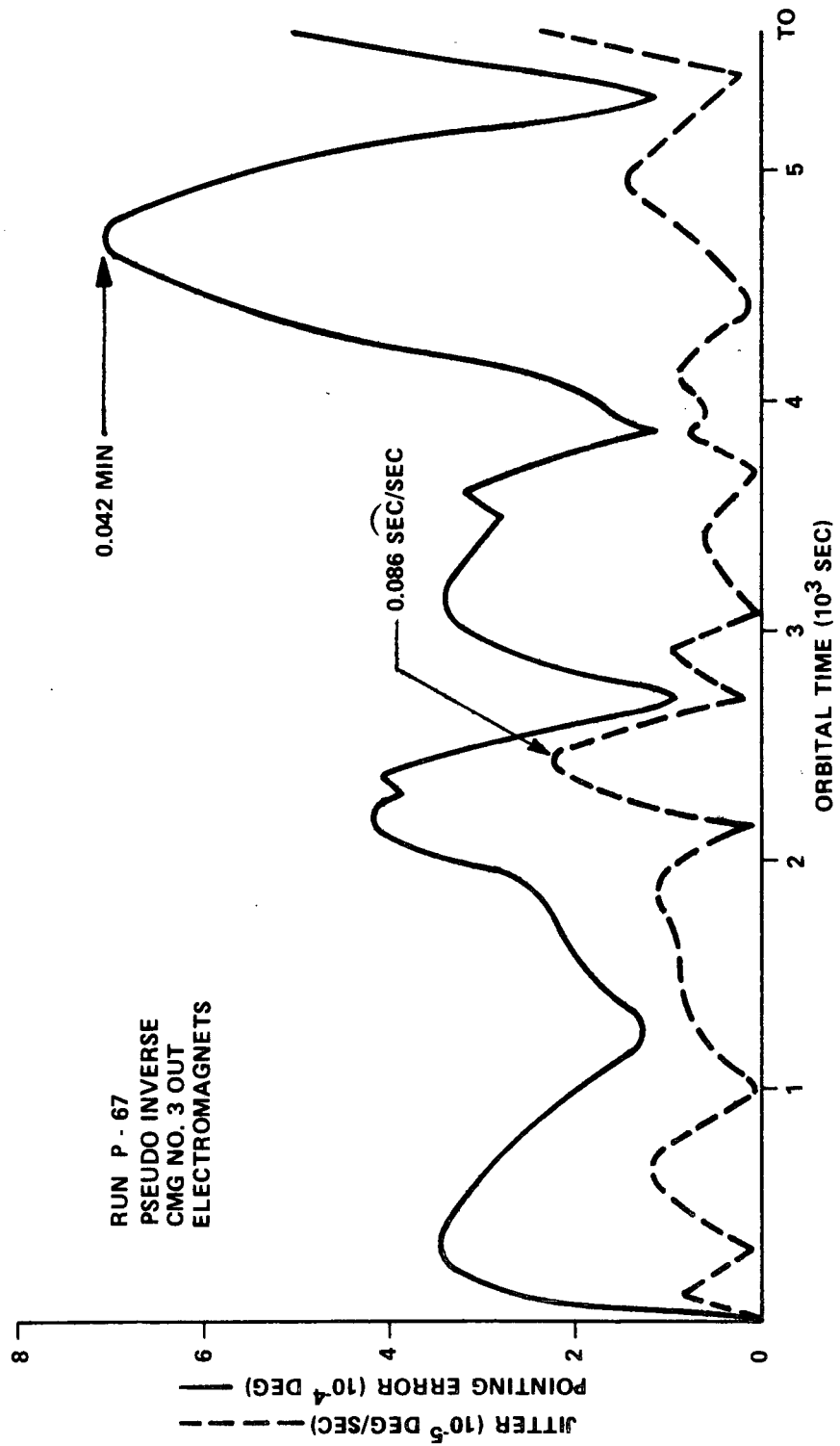


Figure VII-48. Alternate system performance.

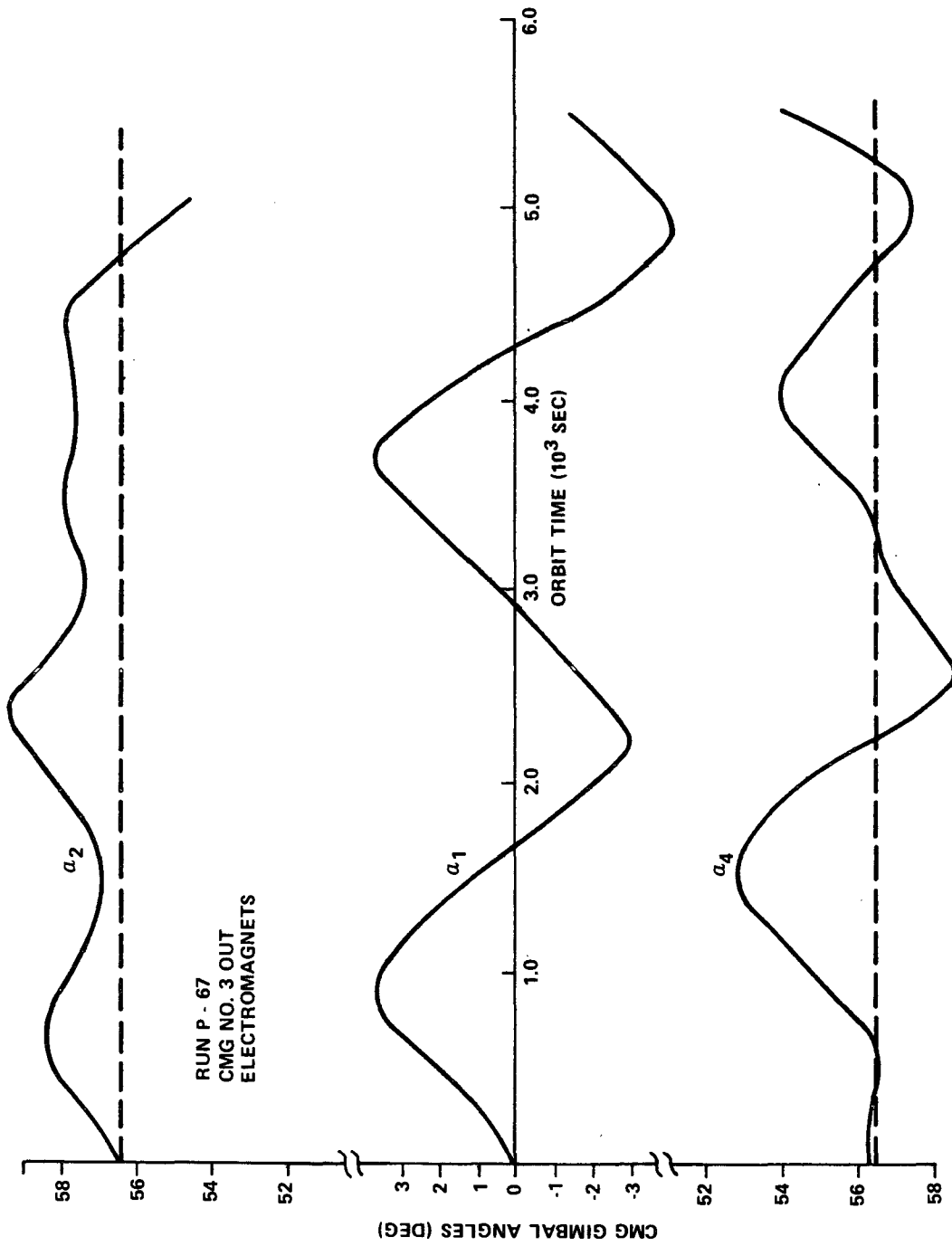


Figure VII-49. CMG gimbal angles with magnetic momenta dump.

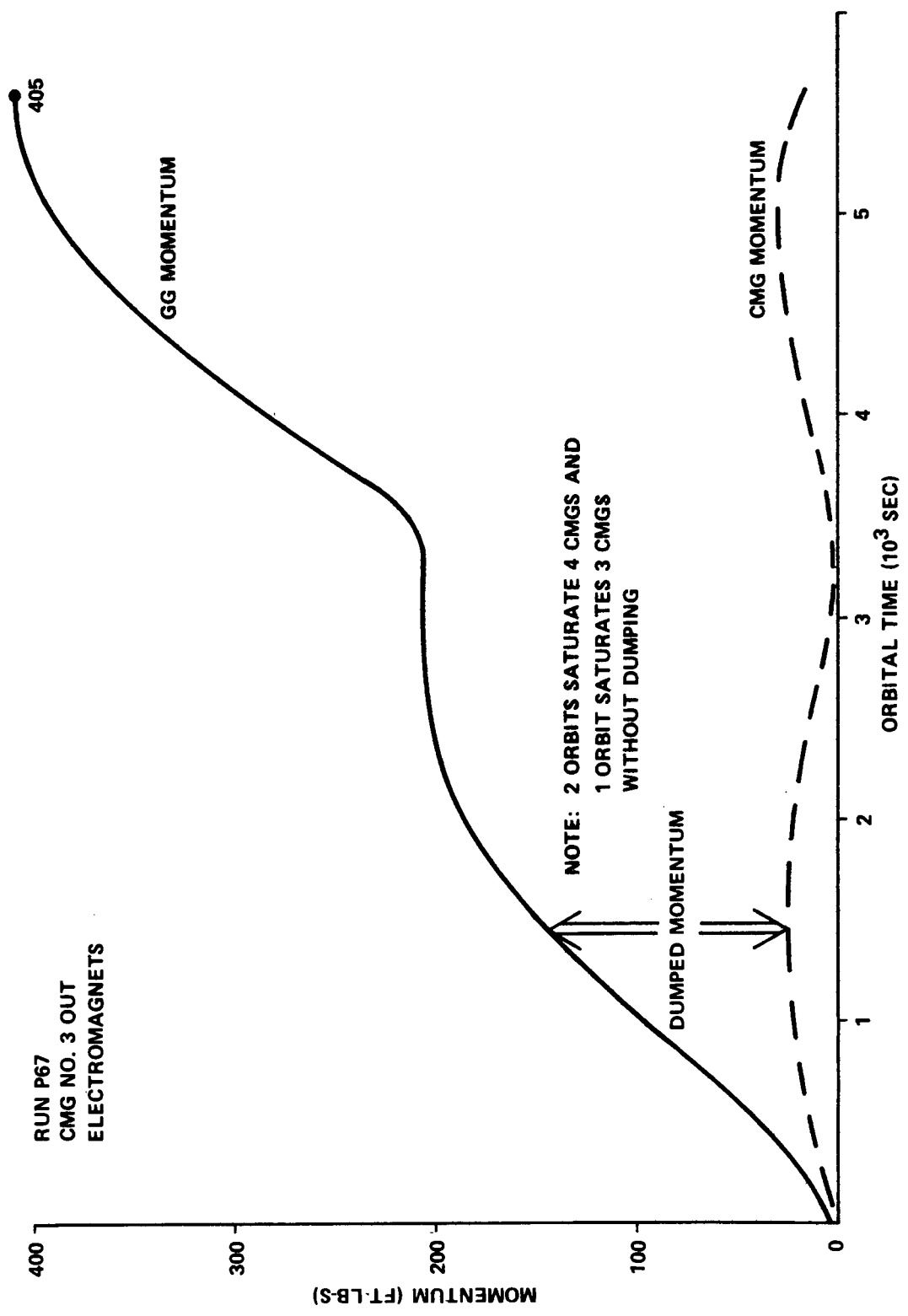


Figure VII-50. Gravity and CMG momentum with continuous dump.

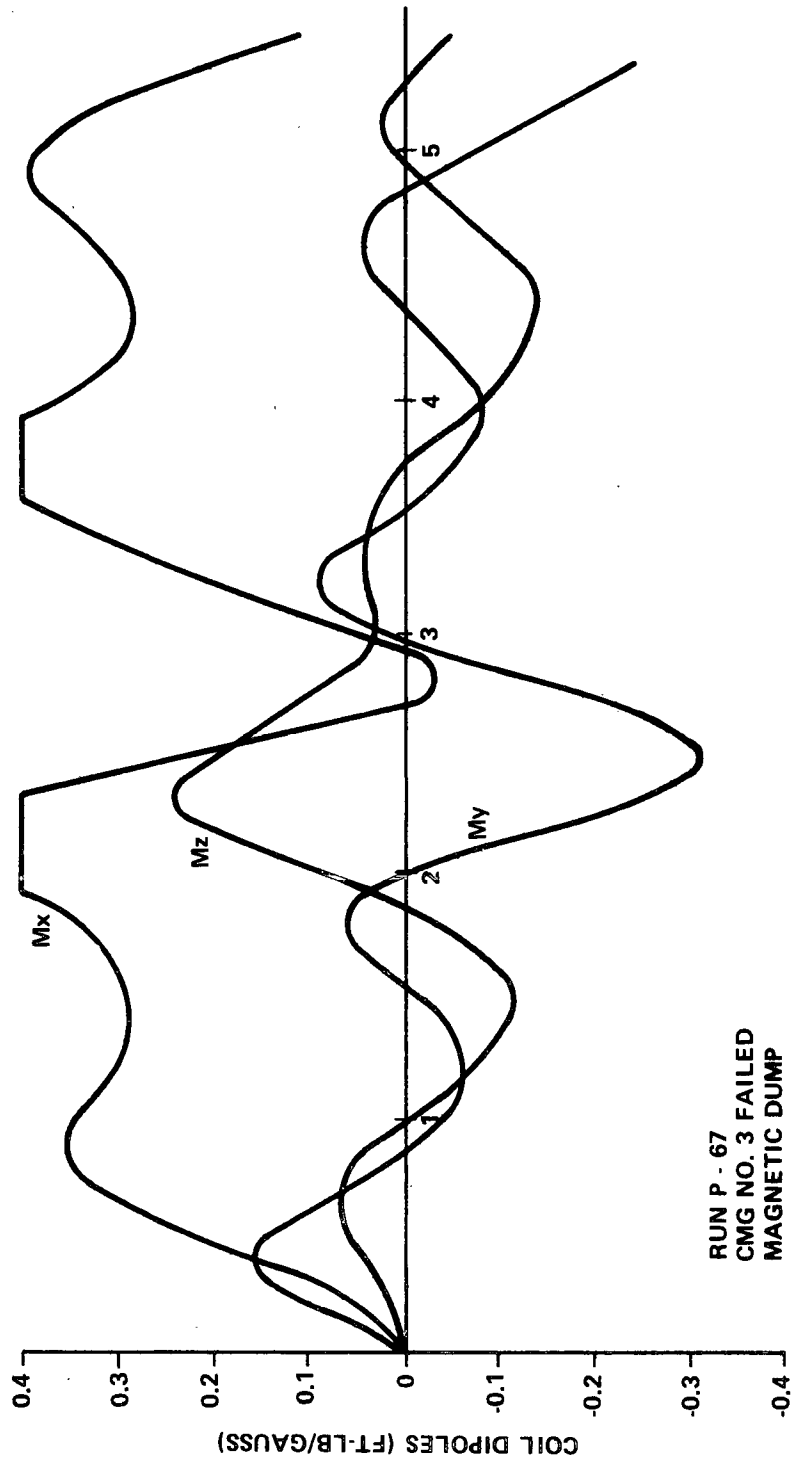


Figure VII-51. Electromagnet dipole moments versus orbital time ( $10^3$  sec).

RUN P - 67  
CMG NO. 3 FAILED  
MAGNETIC DUMP

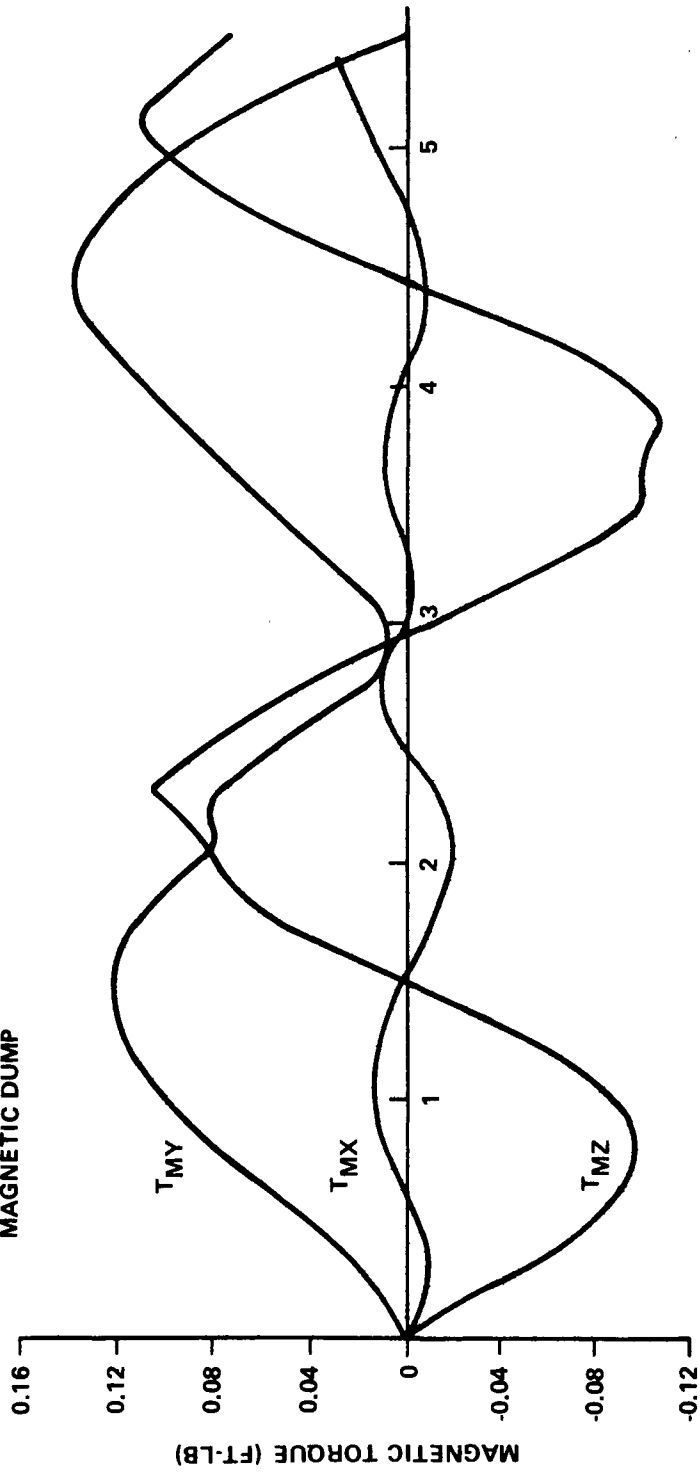


Figure VII-52. Magnetic torque to dump CMG momenta versus orbital time (10<sup>3</sup> sec).

d. **Response Capabilities.** The maximum vehicle maneuver capabilities are determined by both the CMG system torque and available momentum for making the maneuver. Assuming 250 ft-lb-sec per CMG with the gimbal rate limited to one degree per second, each CMG has a torque capability of 4.36 ft-lb. Utilizing a four-skewed-CMG configuration with a skew angle of 53.1 degrees, the maximum torque per vehicle axis is about 14 ft-lb on the sun pointing axis and 5 ft-lb on the two transverse axes, as shown in Figure VII-53. The maximum rotational rate imparted to the vehicle is 2.66 rpm about the axis of minimum inertia (X-axis). On the sun pointing (Z) axis, the momentum capacity of 800 ft-lb-sec allows the CMGs to spin up the vehicle to 0.109 rpm. Several runs were made with HEAO-C operating in a spinup mode similar to that required for HEAO-A. In all cases, HEAO-A performance requirements were attained with a wide margin. Maximum CMG torque on the Z-axis permits rapid movement about the sunline for initial spinup or for small maneuvers about that axis as in normal HEAO-C operation. In case of unusual maneuvers, as in solar flare viewing, the spacecraft could be rotated about the Y-axis by 90 degrees. If a time optimal maneuvering command were issued, the rotation for this antisolar viewing would take about 3 minutes plus another 3 minutes estimated for settling out time to attain HEAO-C pointing requirements. This gives a total time of about 6 minutes. However, a time optimal maneuver scheme was not incorporated into the HEAO simulation and this is an area for future study. Normal maneuvers of 90 degrees or less were satisfactorily conducted through the HEAO simulation by position commands only. Each position feedback channel was limited to 20 degrees per minute equivalent spacecraft rotation per axis. The time required to go from one X-ray source to another is short for small angle maneuvers and the CMGs do not have time to reach saturation. Normal pointing maneuvers can be made by position commands only, without utilizing a more complicated time optimal scheme.

## F. ASCS Reliability Summary

The ASCS reliability block diagram is given in Figure VII-54. Table VII-14 summarizes the ASCS reliability calculations of Appendix G.

Neither the transfer assembly nor the WASS assembly has been included in the baseline system reliability estimation. The first is not yet sufficiently well defined to permit a realistic estimate and the second is a convenience item. Both are discussed further in Appendix G.

	CMG MOMENTUM (b)	CMG TORQUE (c)	MAX. TURNING RATE	TIME FOR (a) 180 DEG. TURN
X-AXIS	800 FT-LB-S	5.235 FT-LB	2.66 RPM	2.18 MIN
Y-AXIS	800 FT-LB-S	5.235 L FT-LB	0.110 RPM	6.54 MIN
Z-AXIS	800 FT-LB-S	13.95 FT-LB	0.109 RPM	6.59 MIN

(a) POSITION FEEDBACK LIMIT OF 20 DEG/MIN ON EACH AXIS RESTRICTS 180 DEG TURN TO 9 MIN.

(b) SECULAR GRAVITY GRADIENT MOMENTUM CAN SATURATE CMGS AT ABOUT 2 ORBITS TIME. SKEW ANGLE OF 53.1 DEG GIVES EQUAL MOMENTUM PER AXIS.

(c) MAXIMUM TORQUE WITH GIMBALS AT THE CMG SYSTEM NULL POSITION.

Figure VII-53. Vehicle response capabilities.

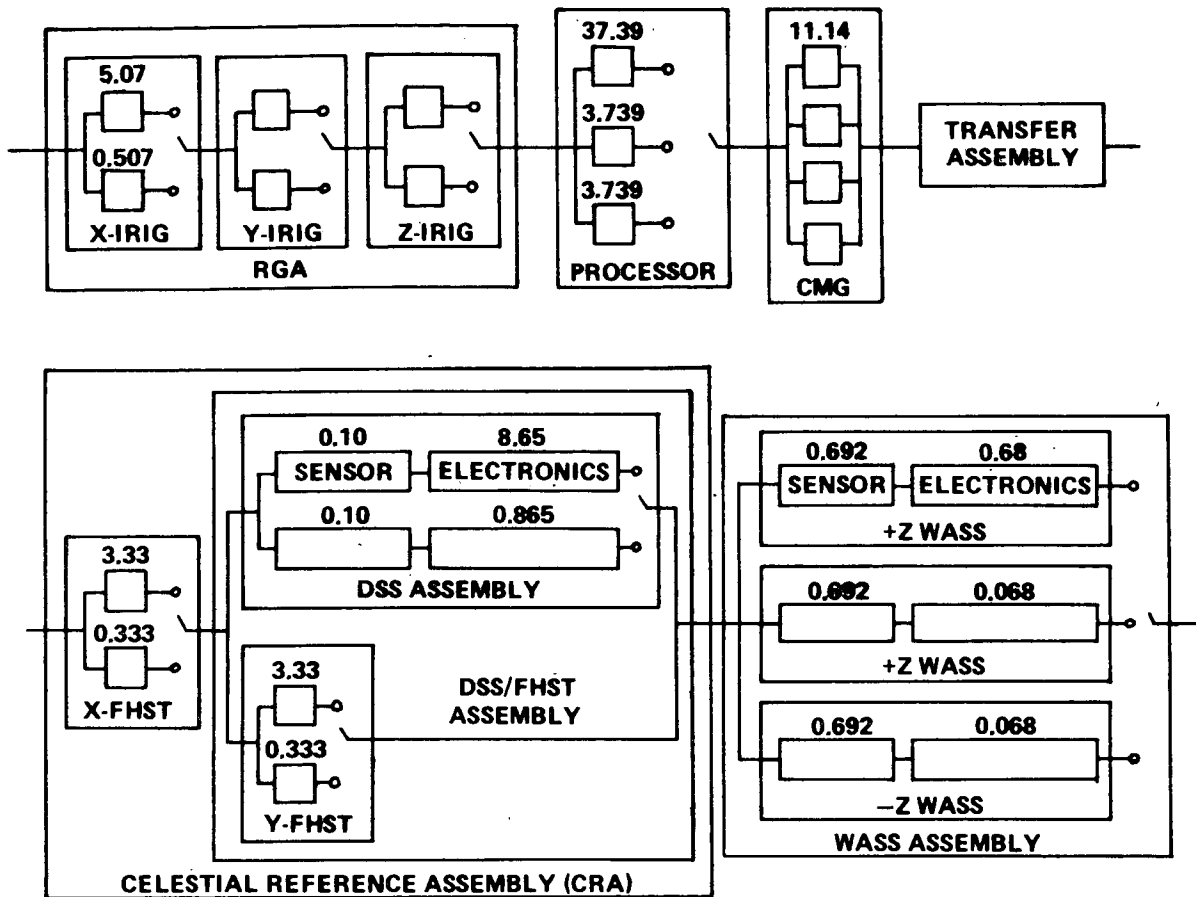


Figure VII-54. ASCS reliability block diagram.

The ASCS is the HEAO-C weak link, and its weak link is the CMG assembly. Some modification of the baseline will be necessary if the one year 0.95 reliability goal is to be met. The following alternates have been considered: Use of skewed configurations of five and six CMGs, six CMGs in an orthogonal scissored pair arrangement, and use of the baseline four-CMG assembly with a magnetic coil system for CMG momentum desaturation. These alternates, and their numerical reliability effects, are discussed in Appendix G.

Apart from the CMG assembly, the ASCS (with the exception of the transfer assembly) has reached the point where any reliability increases will be expensive. The transfer assembly is unique to HEAO-C so that a high reliability can be obtained by use of "hi-rel" parts and redundancy at the circuit level. There does exist a possibility of eliminating certain equipment without greatly decreasing reliability. A qualitative discussion of the possibility is given in Appendix G.

TABLE VII-14. ASCS RELIABILITY NUMERICS SUMMARY

Assembly	1 Yr	2 Yr
Transfer	0.98969	0.97949
WASS	1.00000	0.99999
Celestial Reference	0.99954	0.99818
X-FHST	0.99954	0.99820
DSS	0.99690	0.98826
FHST/DSS	1.0	0.99998
Processor	0.99407	0.96354
Gyro Reference	0.99684	0.98780
CMG	0.95428	0.85284
Baseline System	0.94520	0.81024

An RCS schematic is given in Figure VII-55; Table VII-15 summarizes the RCS reliability calculation of Appendix G.

TABLE VII-15. RCS RELIABILITY NUMERICS SUMMARY

Assembly	Reliability	
	1 Yr	2 Yr
Propellant	1.00000	0.93920
Thruster	0.99739	0.98966
RCS Electronics	1.00000	0.99999
Baseline RCS	0.99739	0.92948

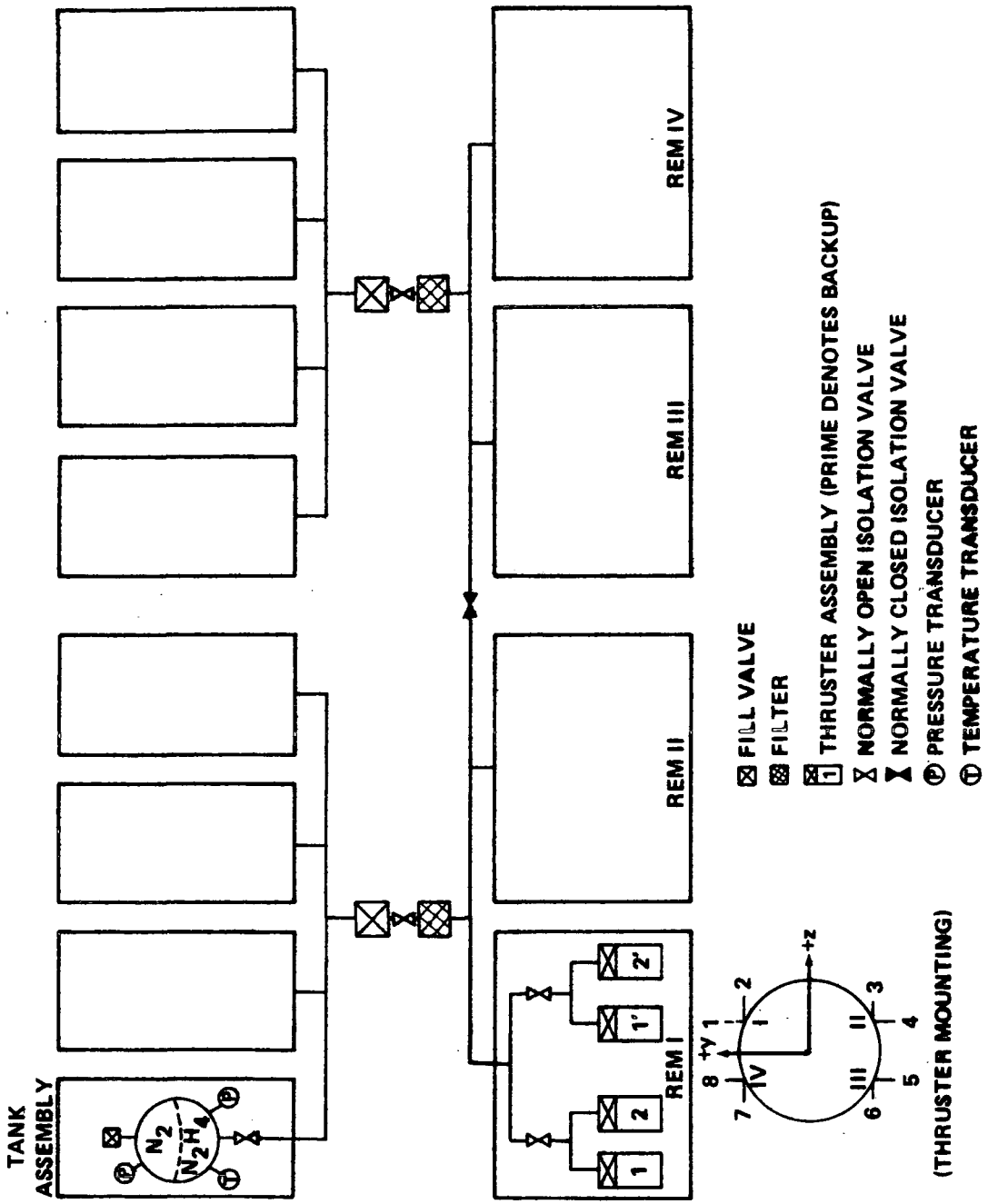


Figure VII-55. RCS schematic.

For reliability purposes, the RCS consists of the three blocks, or assemblies, as shown in Table VII-15. The RCS electronics, not shown in Figure VII-55, consists of a primary and standby channel. The propellant consists of the tanks, their bladders, heaters, pressure and temperature transducers, isolation valves, and plumbing. Due to the lack of a fuel margin at two years, the two year propellant block reliability is simply the probability that no failures occur in the propellant block. At any time less than two years, reliability is the probability that a positive amount of propellant remain in at least one tank, and that sufficient operational plumbing exists to deliver this to the thruster block. Should the engine specific impulse increase, redefinition of these reliabilities would probably be required.

It is noted that the reaction engine module (REM) isolation valves (two per REM) are potential single point failures when leakage is considered. However, there is no obvious means of eliminating these.

## G. Conclusions and Recommendations

By design, the baseline ASCS has a pointing capability that exceeds the basic specifications so that additional Observatory system errors due to thermal warpage, initial relative alignment errors, etc., do not cause the overall pointing specification to be exceeded.

The accuracy requirements for the HEAO-C are more stringent than for Missions A and B. However, the experiment requirements for A and B are leaning toward more rigid pointing stability. This indicates that a detailed trade-off analysis is required for all missions in determining the final ASCS selection. A significant increase in performance for Missions A and B appears feasible by letting the HEAO-C requirements be the driver in the final selection of the ASCS for all missions. This increase in performance would be obtained with a higher initial program cost, but the overall program cost for the multiple HEAO missions would receive essentially no impact.

The most critical items from an ASCS accuracy standpoint are the star trackers, control moment gyros, and the reference gyro assembly. For growth potential, there seems to be little advantage in considering the selection of more accurate reference gyros. The random drift rate ( $0.015 \text{ deg/hr.}$ ,  $3\sigma$ ) of the HEAO-C baseline gyros is pushing the technology despite the claims by some gyro manufacturers of at least an order of magnitude reduction. To reach a condition where the random drift only is present requires accurate drift compensation during system operation to eliminate the large non-g-sensitive and g-sensitive terms. Frequent drift compensation updates using onboard processing with occasional ground updates are recommended to realize the best gyro performance.

The baseline star tracker instruments and the configuration on the spacecraft were selected to provide the required accuracy, assure star availability, and provide redundancy. A star fix defined such that at least one star per axis is present simultaneously for the X- and Y-axes is assured 91 percent of the time. The most critical areas for star availability are near the galactic poles, but even in these regions the star-empty areas are widely separated and the probability is low that the experiment targets will coincide with these small regions. The star tracker trades are gimballed trackers versus fixed head trackers, a reconfiguration of the selected trackers, and the addition of at least one more fixed head tracker to the baseline selection.

An alternate operational mode using the digital sun sensors and one star tracker can serve as a backup mode after star tracker failures or for the rare occasions that could occur when the reference stars are not available for a desired pointing direction. The performance is slightly degraded but still provides the required pointing stability and absolute pointing accuracy requirements. However, under absolute worst case conditions, the performance is marginal.

A major source of pointing stability errors is the nonlinear friction and deadzone properties of the CMG gimbals. Preliminary studies using the nonlinear terms specified for the baseline CMGs have shown that a 2 to 5 arc second pointing direction change can occur when external disturbance torques require the gimbal torque motor to reverse direction. These periods of instability can occur about four times per orbit as a result of gravity gradient torques. The actual error magnitude is sensitive to system gains and compensations whose required values are sensitive to vehicle properties. A thorough design study, as the vehicle design becomes firm, will be required to establish the gains and compensations in final form.

A summary of the baseline ASCS capability is as follows:

Absolute Pointing Accuracy	30 arc sec
Pointing Stability	2 to 5 arc sec
Jitter Rate	Less than 1 arc/sec

The primary performance limitations are caused by the following:

- Control moment gyro nonlinearities
- Fixed head star trackers

Gyro drifts during star occultations

CMG desaturation techniques

The following are growth considerations:

Gimballed star trackers

CMG nonlinearity improvements

Gyro drift compensation techniques

Fine guidance system (i. e. , GEP fine guidance.)

Based on both analog and digital simulations of HEAO-C, four single-degree-of-freedom CMGs, skewed at an angle of 53.1 degrees to provide a near spherical momentum envelope, can meet both the pointing and jitter specifications. Assuming worst case environmental torques and having each CMG sized for 250 ft-lb-sec, about two orbits are required to saturate the system without dumping momentum. However, with one CMG failed, the remaining three CMGs can be saturated in slightly less than one orbit, requiring either a more frequent dump than the once per orbit baselined or spinning up the CMGs to the higher level of 8000 rpm to produce more momentum per wheel. With two CMGs failed, control authority is lost for the baseline design. However, if the CMG control torque were augmented with the RCS, degraded performance could be maintained with the total lifetime shortened accordingly. Partial RCS control to augment two CMGs is an area recommended for further study.

During the study, several CMG steering laws were evaluated. As long as the gimballed angles stay less than 90 degrees, almost any steering law can meet the HEAO requirements. With 250 ft-lb-sec CMGs, the gimballed angles get large within an orbit, thereby ruling out the use of a constant gain steering law. When one CMG has failed, the remaining CMGs must work harder. With several of the steering laws (the Bendix three gimbal inverse, for example) the failure must be identified and corrective software changes must be made. After making any required changes, the resulting steering law must be identical to the exact inverse of the 3 by 3 torque matrix to prevent degradation in pointing performance. Based on both simulation results and mathematical theory, the pseudo inverse steering law reduces to an exact inverse whenever any CMG is arbitrarily deactivated. With the pseudo inverse, system performance is not degraded by using only three CMGs for control. The pseudo inverse CMG steering law is recommended for HEAO-C.

To allow more than one CMG failure without affecting performance, consideration should be given to using more CMGs but with each sized to a lower momentum capacity. For the same total momentum capacity, six 125 ft-lb-sec CMGs would permit three failures without degrading performance. However, the momentum would have to be dumped about each half-orbit to prevent saturation under worst case environmental conditions.

Based on estimated impulse requirements for CMG momentum management, the fuel weights for an all-RCS dump could become prohibitive, especially for a growth version of HEAO, for which the inertia distribution becomes less favorable. The alternative system recommended for HEAO utilizes electromagnetic torquers reacting with the earth's magnetic field to dump accumulated momentum. In this case, a RCS is not needed after the OAS burn control period. Trade-offs show that the magnetic system is better than RCS from both a weight and reliability viewpoint. Moreover, the low torque levels of a magnetic system permit continuous momentum dumping without interfering with experiment pointing, not the case with RCS. Simulations show and analysis has proven that, as an added bonus, a magnetic CMG desaturation system improves pointing performance by providing integral control of the attitude error signal through the magnetic loop. Since CMG momentum is continuously dumped, the gimbal angles stay small (less than  $\pm 3$  deg for four 250-ft-lb-sec CMGs) and typically the stored momentum is less than 20 ft-lb-sec. Hence, with a magnetic CMG desaturation system, the CMG momentum per wheel should be reduced considerably from the present baseline size. Alternatively a greater depth of CMG failures could be tolerated without degrading performance. Additional studies need to be conducted to assess the performance capability of two CMGs augmented by direct magnetic control. Current results indicate that HEAO performance can be maintained with such a system.

A cold gas RCS is recommended for control during OAS burn if a magnetic CMG system were used for normal attitude control purposes. The cold gas system would also be used for initial stabilization and attitude hold before the CMG-magnetic system was operational. Additional studies are needed in these areas.

The RCS described herein is similar to an existing functioning system used in another program. Most of the components are the same; only the functional procedure has changed, and additional hardware is used to adapt the system for use on HEAO-C. An investigation of other monopropellant hydrazine systems has not revealed an adaptable unit as qualified as Rocket Research Corporation's REM for use in meeting the RCS requirements of the HEAO-C spacecraft. The utilization of these existing components will result in a low cost RCS for the HEAO-C spacecraft.

The RCS components described herein will have to be qualified to meet the HEAO-C two year lifetime requirement. Certain individual components will have to be modified and then quality-tested for application to HEAO-C. For example, the EPT-10 diaphragm used in the propellant tank will have to demonstrate either through test, analysis, or both, a two-year lifetime compatibility with hydrazine. Phase B and C studies may substantiate the idea that the REA should be adapted to and qualified with a dual series redundant TCV, rather than using the single valve the REA now employs. A dual redundant TCV which utilizes two solenoid coils in series (one active, one standby) and two poppets connected in series would provide redundancy in opening and closing as well as decrease the probability of propellant leakage. These assets would be most desirable for the REA used on the HEAO-C RCS.

Since the REAs will normally operate under a low duty cycle during the HEAO-C mission, a great demand will probably be made of the REM active thermal control system. This system will be required to maintain REA temperature within acceptable limits to provide peak performance, conserve fuel, and, most important, prolong catalyst bed lifetime. Therefore, it is important that the active thermal system of the REM be qualified for the two year lifetime.

Should the HEAO-C propellant budget grow or more propellant redundancy be required of the RCS, then the capability exists to manifold the RCS to the OAS tank. This tank is capable of holding approximately 3000 pounds of propellant when operating in a blow down mode. Part of this propellant would be used for orbit adjustment of the HEAO-C and the remainder could be used for RCS control. This system is discussed as an alternate in Appendix E. Other alternate RCS concepts studied for the HEAO-C spacecraft are also discussed in that Appendix.

During the initial study phases of the HEAO-C, considerable attention was placed on the attitude control capability of the RCS with the idea that CMG desaturation could be efficiently accomplished with the same configuration and control law. However, analysis soon indicated that CMG desaturation could require a different RCS configuration for efficient dumping and, in fact, the configuration most efficient for attitude control could be extremely inefficient from the CMG desaturation viewpoint. Since the momentum dumping mode will place by far the heaviest demand on the RCS, the RCS configuration should be chosen almost entirely on that basis. Hence, the alternate RCS configuration is beginning to emerge as a likely candidate since pure pitch and yaw control (momentum will be dumped primarily about these axes) can be obtained maintaining high engine burn efficiency and at the same time roll can be controlled

in a manner to aid dumping about pitch and yaw. The only drawback to the alternate system is that the cycle life of an engine may be exceeded (depending on the method of RCS desaturation used) since only four engines primarily will be used for dumping as opposed to eight for the baseline system, i. e. , four engines will be doing the work of eight.

## REFERENCES

- VII-1. Davis, Billy G.: A Discussion of Orbital Workshop Orientation and Gravitational Effects. NASA TMX-53829, May 5, 1969.
- VII-2. Weidner, D. K., ed.: Natural Environment Criteria for the NASA Space Station Program. NASA TMX-53865, 2nd Ed., October 31, 1969.
- VII-3. Bendix Corporation: HEAO Phase B Study Final Report, Volume I -- System Summary and Description. March 1971.
- VII-4. Smith, W. W., et al.: Development and Design Aspects of a Five-Pound-Thrust RCS Rocket Engine Module. AIAA Paper No. 70-654, June 15, 1970.
- VII-5a. Schmitz, B. W.; Williams, D. A.; Maybee, D.; and Smith, W. W.: Design and Sealing Criteria for Monopropellant Hydrazine Rocket Engines and Gas Generators Employing Shell 405 Catalysts. AIAA Paper No. 66-594, June 1966.
- VII-5b. Iwen, A. C.: Propellant Properties Data. Summary Report SMS-PVEL-078, Contract No. NAS8-20073, T. D. A2-AVB-3-057, Revised, Brown Engineering Company, Huntsville, Alabama, April 1969.
- VII-6. High Energy Astronomy Observatory Attitude Sensing and Control System. Job Number 301200, Computation Laboratory for Program Development, George C. Marshall Space Flight Center, May 1971.
- VII-7. Sperry Rand Corporation: Linear Analysis of Control Systems Applicable to the HEAO-C Satellite. SP-255-00528, Space Support Division, Huntsville, Alabama, August 1971.
- VII-8. Greensite, A. L.: Elements of Modern Control Theory. Vol. 1, Spartan Books, 1970.
- VII-9. Penrose, R.: On the General Inverse of a Matrix. Proc. Cambr. Phil. Soc., 1955, pp. 406-413.
- VII-10. Singer, Fred, ed.: Torques and Attitude Sensing in Earth Satellites. Academic Press, 1964.

PRECEDING PAGE BLANK NOT FILMED  
TABLE OF CONTENTS

	Page
A. Introduction . . . . .	VIII- 1
B. Requirements . . . . .	VIII- 2
1. Basis and Summary . . . . .	VIII- 2
2. General Mission and System Requirements . . . . .	VIII- 2
a. Function . . . . .	VIII- 2
b. Type of System . . . . .	VIII- 2
c. Performance . . . . .	VIII- 5
d. Life . . . . .	VIII- 5
e. Reliability . . . . .	VIII- 5
f. Technology . . . . .	VIII- 5
g. Environment . . . . .	VIII- 5
h. Configuration . . . . .	VIII- 5
i. Weight . . . . .	VIII- 5
j. Commonality . . . . .	VIII- 6
k. Orbital Parameters . . . . .	VIII- 6
l. Pointing . . . . .	VIII- 6
3. Electrical System and Load Requirements . . . . .	VIII- 7
a. General System . . . . .	VIII- 7
b. Spacecraft Subsystem Load Requirements . . . . .	VIII- 7
c. System Loads and Power Profiles . . . . .	VIII- 12
C. Baseline Electrical System Description . . . . .	VIII- 16
1. Electrical Power Subsystem . . . . .	VIII- 21
a. Solar Array Subsystem . . . . .	VIII- 24
b. Energy Storage Subsystem . . . . .	VIII- 43
c. Power Conditioning Subsystem . . . . .	VIII- 55
d. Equipment Location . . . . .	VIII- 61

## TABLE OF CONTENTS (Concluded)

	Page
2. Electrical Distribution and Control Subsystem . . . . .	VIII- 63
a. Transmission . . . . .	VIII- 63
b. Solar Power Distributors . . . . .	VIII- 64
c. Electrical Control Assemblies . . . . .	VIII- 69
d. Electrical Integration Assemblies . . . . .	VIII- 73
e. Pyrotechnic Subsystem . . . . .	VIII- 77
f. Cabling and Grounding . . . . .	VIII- 79
3. Electrical System Interfaces . . . . .	VIII- 80
a. Load and Functional Interfaces . . . . .	VIII- 82
b. Command Interfaces . . . . .	VIII- 82
c. Instrumentation Interfaces . . . . .	VIII- 82
d. Spacecraft/OAS Interface . . . . .	VIII- 84
e. ESE Interfaces . . . . .	VIII- 97
f. Physical Interfaces . . . . .	VIII-101
4. Electrical Support Equipment . . . . .	VIII-101
D. Electrical System Reliability . . . . .	VIII-105
1. General Assessment . . . . .	VIII-105
2. EPS Reliability Summary . . . . .	VIII-105
3. Design Philosophy and Reliability Provisions . . . . .	VIII-107
E. Conclusions and Recommendations . . . . .	VIII-109
References . . . . .	VIII-113
Bibliography . . . . .	VIII-113

## LIST OF ILLUSTRATIONS

Figure	Title	Page
VIII-1.	HEAO-C power profile . . . . .	VIII-15
VIII-2.	Electrical power system . . . . .	VIII-23
VIII-3.	Deployed baseline solar array . . . . .	VIII-25
VIII-4.	Baseline solar array configuration . . . . .	VIII-27
VIII-5.	Solar array I-V characteristics . . . . .	VIII-29
VIII-6.	Solar array power performance ratings . . . . .	VIII-30
VIII-7.	Solar array growth capability . . . . .	VIII-31
VIII-8.	Baseline solar panel dimensions . . . . .	VIII-34
VIII-9.	Solar cell flat lay-down mounting . . . . .	VIII-35
VIII-10.	Solar panel materials and weights . . . . .	VIII-36
VIII-11.	Solar panel electrical arrangement . . . . .	VIII-37
VIII-12.	Solar panel physical layout . . . . .	VIII-38
VIII-13.	Solar panel I-V characteristics . . . . .	VIII-39
VIII-14.	Solar array deployment mechanisms . . . . .	VIII-41
VIII-15.	Deployment damper . . . . .	VIII-42
VIII-16.	Battery assembly . . . . .	VIII-47
VIII-17.	Battery rated discharge characteristics . . . . .	VIII-49
VIII-18.	Battery schematic . . . . .	VIII-50
VIII-19.	Battery cell charge limits . . . . .	VIII-52

## LIST OF ILLUSTRATIONS (Concluded)

Figure	Title	Page
VIII-20.	Battery charger simplified diagram . . . . .	VIII-53
VIII-21.	Battery charger operational modes . . . . .	VIII-54
VIII-22.	Regulator simplified diagram . . . . .	VIII-59
VIII-23.	Regulator output characteristics . . . . .	VIII-60
VIII-24.	Electrical system assembly locations . . . . .	VIII-62
VIII-25.	Electrical system simplified diagram . . . . .	VIII-67
VIII-26.	Solar power distributor simplified diagram . . . . .	VIII-68
VIII-27.	Solar power distributor assembly . . . . .	VIII-70
VIII-28.	Electrical control assembly . . . . .	VIII-74
VIII-29.	Fault protection in EIA . . . . .	VIII-76
VIII-30.	Electrical integration assembly . . . . .	VIII-78
VIII-31.	Grounding configurations for loads with secondary power supplies . . . . .	VIII-80
VIII-32.	RF shield grounding configurations . . . . .	VIII-81
VIII-33.	Modified OAS cable interconnect drawing . . . . .	VIII-91
VIII-34.	Electrical support equipment for solar array checkout . . . . .	VIII-104
VIII-35.	EPS reliability block diagram . . . . .	VIII-106

## LIST OF TABLES

Table	Title	Page
VIII-1.	Summary of Mission Related Requirements for the HEAO-C Electrical System . . . . .	VIII - 3
VIII-2.	Electrical System Requirements Comparison of HEAO-A, -B, and -C . . . . .	VIII - 4
VIII-3.	Experiment Power Load Summary. . . . .	VIII - 8
VIII-4.	Summary of Power Requirements for Communications and Data Handling Systems. . . . .	VIII - 9
VIII-5.	Summary of Power Requirements for Attitude Sensing and Control System. . . . .	VIII-10
VIII-6.	RCS/OAS Electrical Load Requirements. . . . .	VIII-11
VIII-7.	HEAO-C Experiment Average Power Summary . . . . .	VIII-13
VIII-8.	HEAO-C Experiment Peak Power Summary . . . . .	VIII-14
VIII-9.	HEAO-C Spacecraft System Average Power Requirements During Various Mission Phases . . . . .	VIII-17
VIII-10.	Summary of Power Requirements for Mission C Operation in Low Orbit and High Orbit. . . . .	VIII-18
VIII-11.	HEAO-C Electrical System Characteristics and Performance Ratings . . . . .	VIII-22
VIII-12.	Baseline Solar Array Summary . . . . .	VIII-33
VIII-13.	Solar Array Deployment Mechanism Weight Breakdown. . . . .	VIII-43
VIII-14.	Energy Storage Subsystem Battery Assembly Characteristics . . . . .	VIII-46
VIII-15.	Characteristics and Ratings for Ni-Cd Battery Assembly . . . . .	VIII-48

## LIST OF TABLES (Concluded)

Table	Title	Page
VIII-16.	Battery Charger Characteristics . . . . .	VIII- 55
VIII-17.	Baseline Regulator Assembly Characteristics and Rating . . . . .	VIII- 61
VIII-18.	Solar Power Distributor Characteristics and Ratings . .	VIII- 71
VIII-19.	Electrical System/Command Interface . . . . .	VIII- 83
VIII-20.	Analog Instrumentation List, Electrical System Interface . . . . .	VIII- 85
VIII-21.	Discrete Instrumentation List, Electrical System Interface . . . . .	VIII- 87
VIII-22.	Spacecraft/OAS Electrical Interface Commands Via CIU . . . . .	VIII- 92
VIII-23.	OAS to Spacecraft Interface Instrumentation . . . . .	VIII- 93
VIII-24.	Spacecraft/OAS Interface Controls and Electrical Power . . . . .	VIII- 96
VIII-25.	Preliminary ESE/Umbilical Interfaces . . . . .	VIII- 97
VIII-26.	Preliminary ESE/CIU Interfaces for Carry-on Cables . . . . .	VIII-100
VIII-27.	HEAO-C Electrical System Equipment . . . . .	VIII-102
VIII-28.	EPS Reliability Numeric Summary . . . . .	VIII-105

## CHAPTER VIII. ELECTRICAL SYSTEM

### A. Introduction

This chapter presents the MSFC Phase A study of the HEAO-C electrical system. Previous MSFC studies and the Phase B HEAO A/B studies performed by TRW and Grumman formed the base data upon which this study began.

The HEAO-C electrical system requirements and the selected baseline system conceptual design are defined. A comparison of the HEAO-C requirements with those for the HEAO A/B electrical system designs is made. Alternate approaches for HEAO-C and tradeoff analyses are given in Appendix F. The analyses and tradeoffs performed in References VIII-1 and VIII-2 influenced the selection of the baseline design.

The electrical system contains two major parts or subsystems – the electrical power subsystem (EPS) and the electrical distribution and control subsystem (EDCS). Each of these subsystems are further subdivided into lesser subsystems. The EDCS, as described herein, does not include network cabling and interfaces of the communications and data handling system.

Although alternate types of power sources were not candidates within guidelines, preliminary considerations were given to the use of radioisotope thermoelectric generator (RTG) power system. Although this study was not extensive, it did indicate feasibility from an electrical system and schedule standpoint. However, it imposed major configuration changes, extendable booms, and launch safety constraints that were not attractive. The approach offered several system and operational advantages such as elimination of complex battery-charger subsystem, continuous day-night power, and freedom from solar pointing constraints. cursory cost estimates indicated that the program costs would exceed that of a solar-array battery system. The cost difference could be reduced if cost sharing with other programs could be established for the RTG and fuel source development. Application feasibility from a radiation interference standpoint was indicated in a HEAO-RTG radiation environment study performed by Teledyne Brown Engineering in Summary Report SE-PD-1323. However, programmatic desires to maintain commonality of design between HEAO A/B and HEAO-C eliminated further consideration of an RTG source during this study.

## B. Requirements

1. Basis and Summary. The mission and general system requirements defined herein were based on those determined by preliminary studies of the HEAO-C mission and the requirements established during Phase B studies of the HEAO A/B missions. Since commonality of spacecraft systems for all missions was a strong desire, the specific electrical requirements (derived from general requirements) and system concepts also were established to be as consistent as possible with the requirements for Missions A and B. Because of the commonality driver, frequent references to and comparisons with HEAO A/B are made.

The requirements established for the electrical system are discussed in two parts – the general requirements (ground rules for this study) imposed by the mission of spacecraft system, and the specific electrical systems requirements. The specific requirements, discussed in Section B. 3. , are detailed or unique requirements established for the electrical system to meet the general requirements. General mission requirements are discussed in Section B. 2.

A summary of some of the major requirements which determined the design concepts of the electrical system baseline is given by Tables VIII-1 and VIII-2. The tables also compare requirements of the HEAO-A, -B, and -C Missions.

### 2. General Mission and System Requirements

a. Function. The electrical system must provide the following for the HEAO system:

- (1) A primary electrical power source.
- (2) Energy storage and/or secondary power capabilities.
- (3) Power conversion and conditioning.
- (4) Power distribution, control, and protection.
- (5) Electrical integration of systems and spacecraft subsystems.
- (6) Interfaces for test and launch support.

b. Type of System. Technology and economy constraints require the electrical system to provide 28 volt, regulated, dc service. Special

TABLE VIII-1. SUMMARY OF MISSION RELATED  
REQUIREMENTS FOR THE HEAO-C ELECTRICAL SYSTEM

	Low Altitude Elliptical Orbit	High Altitude Circular Orbit
Orbital Altitude	140 × 250 n. mi.	270 n. mi.
Orbital Inclination	28.5 deg	28.5 deg
Solar Vector/Z- Axis Angles	1 deg continuous	15 deg continuous 30 deg one orbit/ day
Minimum Orbital Lifetime	30 days	2 years
Orbital Period	~ 91-93 <sup>a</sup> min	94.8 min
Minimum/Maximum Occultation	~ 28/36.2 <sup>a</sup> min	27.4/35.7 min
Minimum/Maximum Sunlight	~ 56/65 <sup>a</sup> min	59.1/67.1 min
Number of Orbits	480 max	11 080 min

a. Values vary with altitude and eccentricity of orbit.

**TABLE VIII-2. ELECTRICAL SYSTEM  
REQUIREMENTS COMPARISON OF HEAO-A, -B, AND -C**

Parameter	A/B Spacecraft	C Spacecraft
Load Requirements (Avg.)	534 W	633 W
Contingency Allowance	107 W	89 W
Design Power	641 W	722 W
Orbit (Altitude/Inclination)	200 n. mi. /28.5 deg	270 n. mi. /28.5 deg
Off-Sun Pointing Requirement	30 deg (Cont.)	15 deg (Cont.)
Off-Sun Capability	40 deg (Cont.)	40 to 45 deg (Cont.) (depends on orientation)
Normal Voltage	28 Vdc	28 Vdc
Voltage Regulation	±5 V	±2%
Design Life	2 Years	2 Years
Predicted Reliability at 2 years	0.997 <sup>a</sup>	0.944
Battery Depth of Discharge	15%	15%

a. A/B prediction did not include distribution and control and is given for one year only.

requirements must be accommodated, if needed, to satisfy mission requirements. The EPS shall be a conventional, solar array-battery type.

c. Performance. The performance requirements are specified in Section B. 3, herein. In general, the electrical system must be capable of delivering, continuously throughout the mission, an average power of 722 watts. It must be capable of delivering the maximum power and short term peaks, as determined high performance and reliable service throughout the mission is essential.

d. Life. The system design and hardware concepts shall assure that the power and functional requirements are satisfied throughout the two year mission.

e. Reliability. The system design shall be based on highly reliable principles and data having high confidence factors. The electrical system shall conform to the reliability requirements of 0.95 for one year set for the HEAO spacecraft. As a minimum, the predicted reliability for the electrical system shall be 0.99 for one year. Adequate redundancy and back-up modes shall be included in the design to assure that no single point failure modes exist

f. Technology. Maximum use of flight proven concepts and components is ground-ruled for low cost and development risk. Unnecessary innovations are to be avoided. This requires that the system be based on a nominal 28 Vdc standard.

g. Environment. The electrical system shall be compatible with environmental conditions specified for the mission. The maximum solar array temperature shall be limited to 93° C by design.

h. Configuration. The electrical system shall conform to the HEAO spacecraft configuration and maximum envelope constraints. The solar array shall mount on a regular octagon configuration, 30 feet long, and with a maximum structural diameter of 102 inches. The maximum envelope diameter is 105 inches.

i. Weight. The system weight must be compatible with the spacecraft limits and allocations. A self imposed weight limit for the HEAO-C electrical system is 1100 pounds.

j. Commonality. Commonality of electrical systems and hardware to perform HEAO missions A, B, and C is a primary objective.

k. Orbital Parameters. The electrical system shall be capable of satisfactory performance in the specified circular orbits about the earth, as follows:

Inclination	28.5 degrees
Altitude	200 to 270 nautical miles (includes Missions A/B)
Launch Date	System design shall accommodate possible variations in launch date

These requirements translate into time and energy balance requirements on which the electrical system depends. Derived from the orbital analyses of the HEAO Mission, the following parameters are specified:

- Orbital Period Range 92.5 to 94.8 min
- Maximum Dark Period (Occultation) 36.6 to 35.8 min
- Minimum Dark Period 27.4 min
- Range of Sunlight Time 55.5 to 67.2 min
- Average Dark Period (yearly) 34.3 min
- Sun Angle to Orbital Plane 0 to 52 deg

l. Pointing. The solar array shall supply the primary power required by the system for the following orientation conditions:

- Vehicle Z-axis continuously pointed 15 degrees off-sun line.
- Vehicle Z-axis pointed 30 degrees off-sun line for several orbits per day.

### 3. Electrical System and Load Requirements

#### a. General System

(1) The HEAO electrical system shall provide the power generation, conditioning, control, and distribution for the HEAO payload, spacecraft systems, and the Orbit Adjust Stage (OAS). These capabilities are to be provided from prelaunch operations throughout the two year lifetime of the spacecraft.

(2) The system shall be designed so that single point failures will not degrade the system performance or jeopardize the mission objectives.

(3) The electrical system shall incorporate reliable features or devices for protection against internal or external overloads or faults, over-voltage and under-voltage reverse currents; and for fault isolation.

(4) In general, dc power shall be delivered to the loads. The minimum average rating shall be 722 watts.

(5) Power shall be distributed to the loads at  $28 \pm 2$  percent volts, steady state. Transients shall not exceed  $\pm 50$  volts for pulse widths of 10 microseconds.

(6) Additional electrical systems requirements are specified in detail in Appendix F-8.

b. Spacecraft Subsystem Load Requirements. The load requirements have fluctuated considerably during the course of the study due to the preliminary nature of the information. The results of the final iteration of the load analysis is shown by Tables VIII-3 through VIII-6. These tables give the peak and average power required by the various equipment within a given subsystem or experiment group. The peak values do not necessarily reflect total connected load nor short term transient startup. The peaks are given for steady state conditions with maximum power complement of the line items to be operating during any single orbit.

The average power levels given were based on typical operating combinations of equipment for typical operational orbits. In conjunction with various subsystem designers, duty cycles were determined for the noncontinuous loads. These were used to derive average power conditions for each of the subsystems. All average loads shown were determined on the basis that the nominal system voltage of 28 Vdc existed at the load.

TABLE VIII-3. EXPERIMENT POWER LOAD SUMMARY

Load	Power		Highest Load Configuration	
	Average (W)	Peak (W)	Average (W)	Peak (W)
High Resolution Image Detector	32.5	38.5	32.5	38.5
High Resolution Crystal Spectrometer	21.0	27.0		
Proportional Counter Mode	19.5	25.5		
Spiraltron Array Mode	0.0	6.0		
High Resolution Transport Mechanism				
Large Area Image Detector	14.5	20.5	14.5	20.5
Large Area Solid State Detector	8.2	8.2	2.0a	2.0a
Large Area Transport Mechanism	0.0	6.0		
Flare Detectors	40.0	50.0	40.0	50.0
Monitor Proportional Counter	9.0	9.0	9.0	9.0
Flat Crystal Spectrometers	17.0	29.0	17.0	29.0
Aspect Detector	14.0	14.0	14.0	14.0
Low Energy (LE) Telescope	24.0	50.0	24.0	50.0
Data Management System	81.0	81.0	<u>81.0</u>	<u>81.0</u>
Totals			<u>234.0</u>	<u>294.0</u>

a. Standby During Image Detector Operation

TABLE VIII-4. SUMMARY OF POWER REQUIREMENTS  
FOR COMMUNICATIONS AND DATA HANDLING SYSTEMS

Load	Average Power (W)	Peak Power (W)
<b>Communications</b>		
Dual Transponder		
RCVR (4)	14.0	14.0
XMTR (2)	2.0	42.0
Command Phase Shift Keyed (PSK) Demodulator (2)	0.8	0.8
Frequency Multiplexer (2)	4.0	4.0
Subtotal	20.8	60.8
<b>Data Handling</b>		
Pulse Code Modulator (PCM) Encoders (2)	6.4	6.4
Format Generators (2)	4.2	4.2
Command Processor (2)	15.6	15.6
Command Memory (2)	3.7	7.0
Remote Acquisition Units (40)	1.2	1.2
Remote Command Units (8)	1.4	1.4
Data Storage Control Unit (1)	1.0	1.0
Tape Recorders (4)	11.0	30.0
Clock (1)	14.0	14.0
Subtotal	58.5	80.8
Total	79.3	141.6

TABLE VIII-5. SUMMARY OF POWER  
REQUIREMENTS FOR ATTITUDE SENSING AND CONTROL SYSTEM

Load	Average Power (W)	Peak Power (W)
Star Trackers	16.0	16.0
Reference Gyros	45.0	45.0
Sun Sensor Electronics	2.1	2.1
Control Moment Gyros (CMG)	36.0	128.0
Control Moment Gyro Electronics	72.0	72.0
Transfer Assembly	5.0	5.0
Computer	65.0	65.0
Reaction Control System (RCS) Electronics	11.0	20.0
Totals	252.1	353.1

TABLE VIII-6. RCS/OAS ELECTRICAL LOAD REQUIREMENTS

Cyclic Loads	Duty Cycle <sup>a</sup> (%)	Power Peak (W)	Average Power (W)
Tank Heaters (8) (5 W Ea.)	12	40	5.2
Catalyst Heaters (8) 4 Units at 3 W Ea.	20	12	2.6
Valve Heaters (8) 4 Units at 21 W Ea.	20	84	17.9
REM Valves (16) 4 Valves at 29 W Ea.	0.04	116	0.1
Isolation Valves (19) <sup>b</sup> 1 Valve at 108 W	0.04	108 <sup>c</sup>	0.1
Subtotal		279	25.9
Continuous Load			
Instrumentation		16.0	16.0
Total		295	41.9

a. Worst Orbital Duty Cycle

b. Used only for Failure Mode or Off-Nominal Performance Compensation

c. Not likely to occur with other peaks — apply 25% demand factor

c. System Loads and Power Profiles. System load analyses indicated that the majority of the requirements are satisfied by a 28 Vdc system. Special voltage sources are normally included in the experiments. Although the details of each load device were not analyzed, it is recognized that special sources such as inverters for ac devices, etc. , are required. It is not expected that such a requirement will materially affect the system requirements if conversion losses have not been accounted.

The individual subsystem loads were considered with respect to the various mission phases and the expected ranges of operational conditions to assure that conservative load requirements were established for the baseline system. Using the mission time sequence information derived in Chapter III, power summaries of the various subsystems and experiments were compiled for the major mission phases and events. For each phase, several possible load combinations were studied to assure that the highest/power operating mode was accounted. Tables VIII-7 and VIII-8 are typical examples of experiment load combinations that could occur during high altitude orbital operations. The highest average peak power of 234 watts and 294 watts, respectively, are presented in Tables VIII-7 and VIII-8. The variation in average power required was only 21 watts.

Similar data for subsystems and experiment load combinations were used to construct the power profile shown by Figure VIII-1. The highest probable load configuration is shown for each major event which affects electrical power. The figure does not reflect abnormal or maximum worst case conditions in general.

Referring to Figure VIII-1, the spacecraft is switched to internal power between 15 minutes and 5 minutes prior to launch<sup>1</sup>. The umbilical on the OAS allows the system to be powered from electrical support equipment (ESE) up to this time. Batteries may be charged until this time for maximum stored energy at launch time. Although injection occurs approximately 10 minutes after launch, a period of one orbit was considered the nominal maximum time for sun acquisition and solar array deployment. Array deployment is scheduled to occur within 5 minutes after injection. The electrical system will have the capability of sustaining the spacecraft for several orbits to allow for abnormal launch performance.

---

1. Launch site provisions for mating with the OAS umbilical plate were assumed to be available. HEAO connections to ESE after T-2 hours must be investigated. Electrical access through the Titan stage is considered a very remote possibility. Should umbilical provisions not be available, the battery capacity must be sized for a least two additional hours and RF links must be established to monitor and control spacecraft functions subsequent to T-2 hours.

TABLE VIII-7. HEAO-C EXPERIMENT AVERAGE POWER SUMMARY

Experiment	1	2	3	4	5	6
High Resolution Image Detector	32.5	32.5				
High Resolution Crystal Spectrometer			21.0		21.0	
Proportional Counter Mode				19.5		19.5
Spiraltron Mode						
High Resolution Transport Mechanism <sup>a</sup>						
Large Area Image Detector	14.5		14.5	14.5		
Large Area Solid State Detector	2.0	8.2	2.0	2.0	8.2	8.2
Large Area Transport Mechanism <sup>a</sup>						
Flare Detectors	40.0	40.0	40.0	40.0	40.0	40.0
Monitor Proportional Counter	9.0	9.0	9.0	9.0	9.0	9.0
Flat Crystal Spectrometers	17.0	17.0	17.0	17.0	17.0	17.0
Aspect Detector	14.0	14.0	14.0	14.0	14.0	14.0
Data Management System	81.0	81.0	81.0	81.0	81.0	81.0
Low Energy X-Ray Experiments	24.0	24.0	24.0	24.0	24.0	24.0
Total Average Experiment Power	234.0	225.7	222.5	221.0	214.2	212.7

a. Average power consumption is negligible because of small duty cycle.

TABLE VIII-8. HEAO-C EXPERIMENT PEAK POWER SUMMARY

Experiment	1	2	3	4	5	6
High Resolution Image Detector	38.5	38.5				
High Resolution Crystal Spectrometer						
Proportional Counter Mode			27.0		27.0	
Spiraltron Mode				25.5		25.5
High Resolution Transport Mechanism <sup>a</sup>	6.0	6.0	6.0	6.0	6.0	6.0
Large Area Image Detector	20.5		20.5	20.5		
Large Area Solid State Detector	2.0	8.2	2.0	2.0	8.2	8.2
Large Area Transport Mechanism <sup>a</sup>	6.0	6.0	6.0	6.0	6.0	6.0
Flare Detectors	50.0	50.0	50.0	50.0	50.0	50.0
Monitor Proportional Counter	9.0	9.0	9.0	9.0	9.0	9.0
Flat Crystal Spectrometers	29.0	29.0	29.0	29.0	29.0	29.0
Aspect Detector	14.0	14.0	14.0	14.0	14.0	14.0
Data Management System	81.0	81.0	81.0	81.0	81.0	81.0
Low Energy X-Ray Experiments	50.0	50.0	50.0	50.0	50.0	50.0
Total Peak Experiment Power	294.0	279.7	282.5	281.0	268.2	266.7

a. Mechanisms do not operate simultaneously with experiment

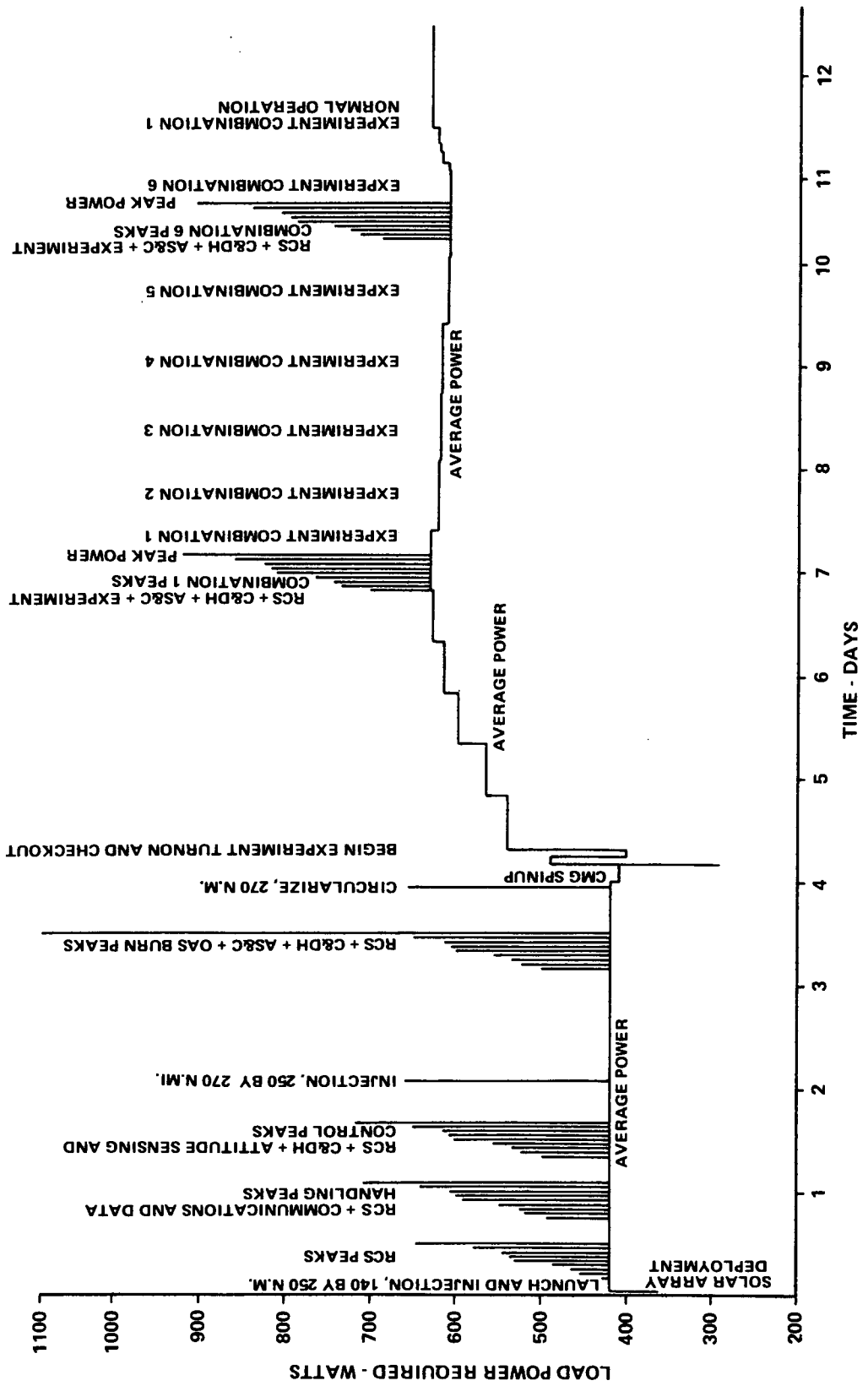


Figure VIII-1. HEAO-C power profile

After injection and during orbital coast the array will be deployed automatically or, as a backup, from ground command. Since the OAS thrust will be coplanar with the array panels and because accelerations will be very low, no problems or mission hazards will be incurred by deploying the array prior to the OAS engine burns. The nominal case of three OAS burns is within 4 days after initial injection.

The period from day 4 to day 11 is nominally devoted to experiment turn-on and checkout operations. After day 11, the spacecraft is considered to be in normal operation, and the experiments operate in the various combinations shown in Table VIII-7. These combinations occur as required for the remainder of the mission.

Peak power loads consist of thermal control, RCS, communications, and attitude sensing and control operations. Actual peak load depends on the coincidence of the peaks. Typical possibilities shown in Figure VIII-1 indicate that the peak during normal operation is approximately 930 watts. If additional power should be required, such as abnormal CMG spinup, etc., the peak could be somewhat higher. Note that Figure VIII-1 also shows the average power requirements by mission phase and that normal, average power requirements are indicated from 7 days 4 hours to 10 days 6 hours. The power profile is summarized by Tables VIII-9 and VIII-10. During launch and orbital adjustment phases of the mission, the propulsion, communication, and spacecraft subsystems consume the major portion of the power. The major peaking and cyclic loads are expected during the orbit adjust phases. The battery subsystem must be capable of furnishing the system power from prelaunch to the time when the spacecraft is oriented to the sun and the array is deployed.

The system load requirements for typical high and low orbital operations are summarized by subsystems in Table VIII-10. The electrical system loads have been added to establish the total requirements. Although the initial contingency allowance was 20 percent, it was reduced to the 14 percent shown when late increases in subsystem power requirements were received. The high orbit requirements of 722 watts average, and 1238 watts peak primarily determine the power characteristics needed in the baseline system design. When the mission timeline is considered, it is seen that the actual expected peak power demand is substantially lower.

### C. Baseline Electrical System Description

The electrical system consists of two major subsystems — the EPS and the EDCS — which are functionally interdependent, and each is composed of the lesser subsystems and assemblies described.

TABLE VIII-9. HEAO-C SPACECRAFT SYSTEM AVERAGE  
POWER REQUIREMENTS DURING VARIOUS MISSION PHASES

	Launch	Low Orbit Operation	OAS Burn	Solar Alignment	Operational Checkout	Normal Operation
Attitude Sensing and Control	110.0	139.1	144.1	353.1	252.1	252.1
Communications	20.8	20.8	20.8	20.8	20.8	20.8
Data Handling	58.5	58.5	58.5	58.5	58.5	58.5
Thermal Control	10.0	10.0	10.0	10.0	10.0	10.0
RCS	41.9	41.9	41.9	41.9	41.9	41.9
OAS	103.0	133.0	367.0	0.0	0.0	0.0
Electrical System	16.0	16.0	16.0	16.0	16.0	16.0
Total Average Power Required	360.2	419.3	658.3	500.3	399.3	399.3

TABLE VIII-10. SUMMARY OF POWER REQUIREMENTS FOR MISSION C  
OPERATION IN LOW ORBIT AND HIGH ORBIT

Load	Operation in Low Orbit		Operation in High Orbit	
	Average Power (W)	Peak Power (W)	Average Power (W)	Peak Power (W)
Experiments	a	a	234.0	294.0
Communications and Data Handling	79.3	141.6	79.3	141.6
Attitude Sensing and Control	139.1	144.1	252.1	353.1 <sup>b</sup>
Thermal Control	10.0	40.0	10.0	40.0
RCS	41.9	295.0	41.9	295.0
OAS	133.0	367.0	c	c
Electrical System	16.0	25.0	16.0	25.0
Baseline Subtotal	419.3	1012.7	633.3	1148.7
Contingency (≈14%)	59.0	59.0	89.0	89.0
Total	478.3	1071.7	722.3	1237.7

- a. Not used in low orbit
- b. Assumes simultaneous spinup of all CMG's
- c. Not used in final high orbit

The EPS subsystems, assemblies, and their functions are:

- Solar Array Subsystem – Generates primary power for the spacecraft - Consists of solar cell panels, release and deployment mechanisms, sensor and controls, and transmission links to EDCS.
- Energy Storage Subsystem – Stores electrochemical energy, delivers secondary power during sun occultation periods, conditions and controls primary power for energy storage – Consists of battery charger assemblies, secondary batteries, sensors and battery control networks.
- Power Conditioning Subsystem – Conditions and regulates primary and secondary power, provides load fault isolation, and delivers regulated power to EDCS for distribution – Consists of regulator assemblies, sensors, load sharing and control networks.
- Special Power Supplies – Provide primary power for pyrotechnic devices, furnishes isolated excitation voltages, precision 5 volt supplies for measuring, and if needed, special voltages for loads – Consist of a primary pyro-battery and small supplies and regulators distributed throughout the system.

The EDCS subsystems and assembly functions are:

- Transmission Networks – Transmit and control primary power between sources, primary junction boxes and buses, and power assemblies – Consist of cabling connectors, controls, and primary junction assemblies.

- Solar Power Distributors — Accumulate array outputs into primary buses, protects and controls primary distribution — Consist of primary buses, switches, protective devices, and controls.
- Electrical Control Assemblies — House, protect, and control main distribution buses; control distribution to major loads and to secondary distribution; provide instrumentation and command interfaces; furnishes common ground for system — Consist of switches, controls, interlocks, connector and junction assemblies, sensors, and protective devices.
- Distribution Networks — Provide interconnection of main and secondary distribution assemblies, route power, control signals, and hardware sensor lines among various electrical assemblies and loads; provide hardware test access for subsystems, experiments and OAS — Consist of cabling connectors and junction assemblies.
- Electrical Integration Assemblies — Provide local distribution interfaces for experiment and subsystem equipment, house secondary buses and special power supplies, provide load control and protection — Consist of cabling connectors, junction assemblies, protection devices, sensors, and regulation components.
- Cable Integration Unit — Provides cable interfaces between OAS and spacecraft, provides access to ESE and OAS umbilical.
- Pyro-Subsystem — Provides pyro buses, distribution networks, safety interlock, sensors, controls and interfaces for initiating pyrotechnic functions — Consists of pyro junction box, special cabling, sensors, and switch controls.

The baseline electrical system, derived during the study, meets or exceeds the requirements set forth in Part B of this chapter, except that the late load changes which occurred were absorbed by reducing the load contingency from the specified 20 percent to approximately 14 percent. This could be adjusted if time permitted because no limitations were approached and no marginal performance cases were evident.

In Part B, an average load requirement of 722 watts was established. Continuous power is to be delivered at  $28 \pm 2$  percent Vdc. This includes the 14 per cent contingency added to compensate for inaccuracy of preliminary load determinations. The preliminary load analysis indicated a possible peak loading of 1238 watts for certain combinations of load operations. More detail will be required to accurately assess peak conditions.

The system is designed to furnish power continuously during the two year mission. Power is drawn from batteries during the dark periods of each orbit. The design load requires 502 watt hours of energy during the maximum, 35.8 minute, dark period. When operating from stored energy the system has an efficiency of 85.5 percent. The solar array furnishes the load power and recharges batteries during the sunlight periods of the orbit. In this mode, the system furnishes load power at an efficiency of 84.7 percent. The orbital average efficiency of the overall system is 75.3 percent. The performance factor for the system, indicating the ratio of power required from the solar array to that delivered to the loads, is 2.14 for the orbits having a 35.8 minute dark period.

The characteristics and performance ratings for the baseline electrical system are given in Table VIII-11 for beginning-of-life (BOL) and end-of-mission (EOM) conditions.

1. Electrical Power Subsystem. The EPS has essentially the same output requirements and rating as the electrical system, except that it must also supply power for transmission and distribution losses and for energy storage. The elementary block diagram of Figure VIII-2 shows bus interconnections and the major assemblies comprising the baseline EPS. The subsystem delivers conditioned, regulated power to the main distribution buses for distribution to the spacecraft subsystems. During the sunlight portion of the orbit, primary power for the load and for battery charging is generated by the solar array subsystem.

TABLE VIII-11. HEAO-C ELECTRICAL SYSTEM  
CHARACTERISTICS AND PERFORMANCE RATINGS

Characteristic	Mission Time					
	BOL			EOM		
	0	15	30	0	15	30
Pointing Condition (deg)						
Avg. Load Requirement (W)	722	722	722	722	722	722
Rated Avg. Power (W)	963	941	871	879	857	792
Design Margin (Avg. W)	241	219	149	157	135	70
Peak Load Required (W)		1238			1238	
Peak Output Power Rating		1800			1800	
Continuous Off-Sun Pointing Capability (deg)		48			40	
Nominal Output Voltage	28 Vdc					
Regulation	± 2%					
System Efficiency	75.3%					
Performance Factor	2.14					
Minimum Life	2 yr					
Predicted Reliability	0.992 at 1 yr, 0.944 at 2 yr					

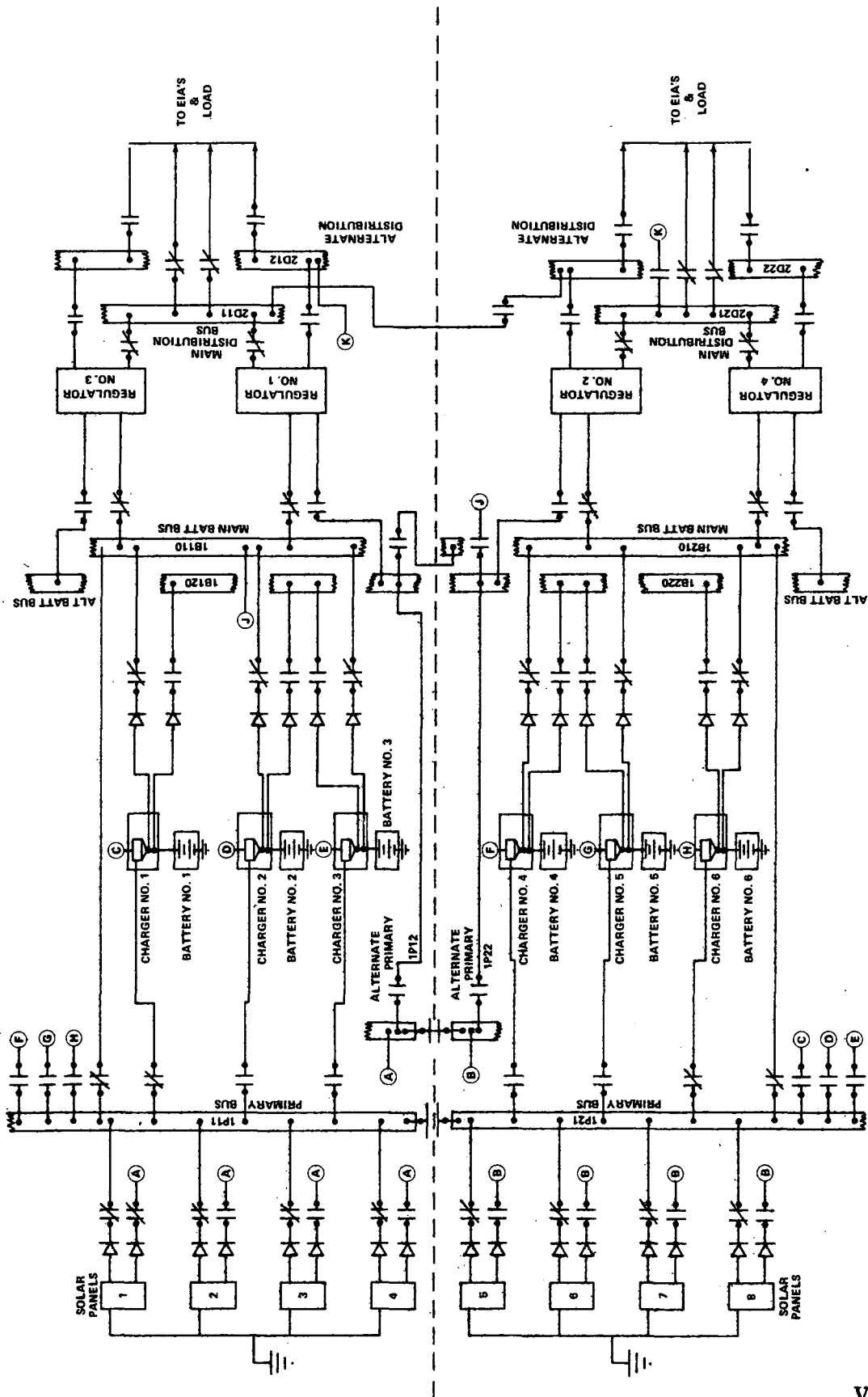


Figure VIII-2. Electrical power system.

## a. Solar Array Subsystem

(1) **Baseline Description.** The baseline solar array is physically divided into four sections — two wings and two body sections. Each wing has three separate solar panels, and each body has one panel; thus, the array consists of eight solar panels. The stacking factor (solar cell density on panels) is 90 percent for the wing panels and 42 percent for the body panels (equivalent to  $\approx 15$  percent on a section basis). Low stacking factors on the body panels keep the temperatures low to give better efficiency and to avoid undue thermal stresses on the cell assemblies. The array is pictured with the wings deployed in Figure VIII-3. Note that only one-third of each body section is covered with a solar panel; the uncovered area is available for load growth if needed.

Deployment of the array wings is initiated automatically following injection into the prescribed low altitude orbit. A completely redundant system that can be initiated by ground command is provided to assure that the array wings are deployed. All deployment mechanisms except the panels themselves are redundant. Power to initiate deployment is furnished primarily from the pyro battery in the OAS; the spacecraft batteries serve as a redundant power source for this purpose.

The array has been sized to satisfy the continuous, average, 722 watt load requirement and to supply system loss and battery recharge needs. It must furnish at least 1549 watts average power. A continuous off-sun pointing capability of approximately 40 degrees (15/30 degrees required) is permitted. For the very remote, abnormal case, one panel not deployed, the array will still satisfy the requirements at the EOM.

The baseline solar array is rated, for the 15 degrees pointing, EOM conditions at  $\approx 1830$  watts. It has a BOL rating of 2015 watts at 15 degrees orientation off sun line. A degradation allowance of 4 percent per year was used for the array design. Ratings are given for the design temperature of approximately 70° C for the wings. Maximum temperatures will not exceed 83° C, 10° C below specifications. This provides an adequate margin for possible "hot spots" and for temperature gradients across the panels. Thermal effects on array performance are analyzed in Appendix F.

Solar array panels were designed for commonality with the HEAO-A and -B configurations. The panels are 38.2 by 119.2 inch aluminum honeycomb assemblies. The solar cell assemblies are mounted on the panels with qualified, low outgassing materials. A reliable flat-laydown technique is specified for fabrication.

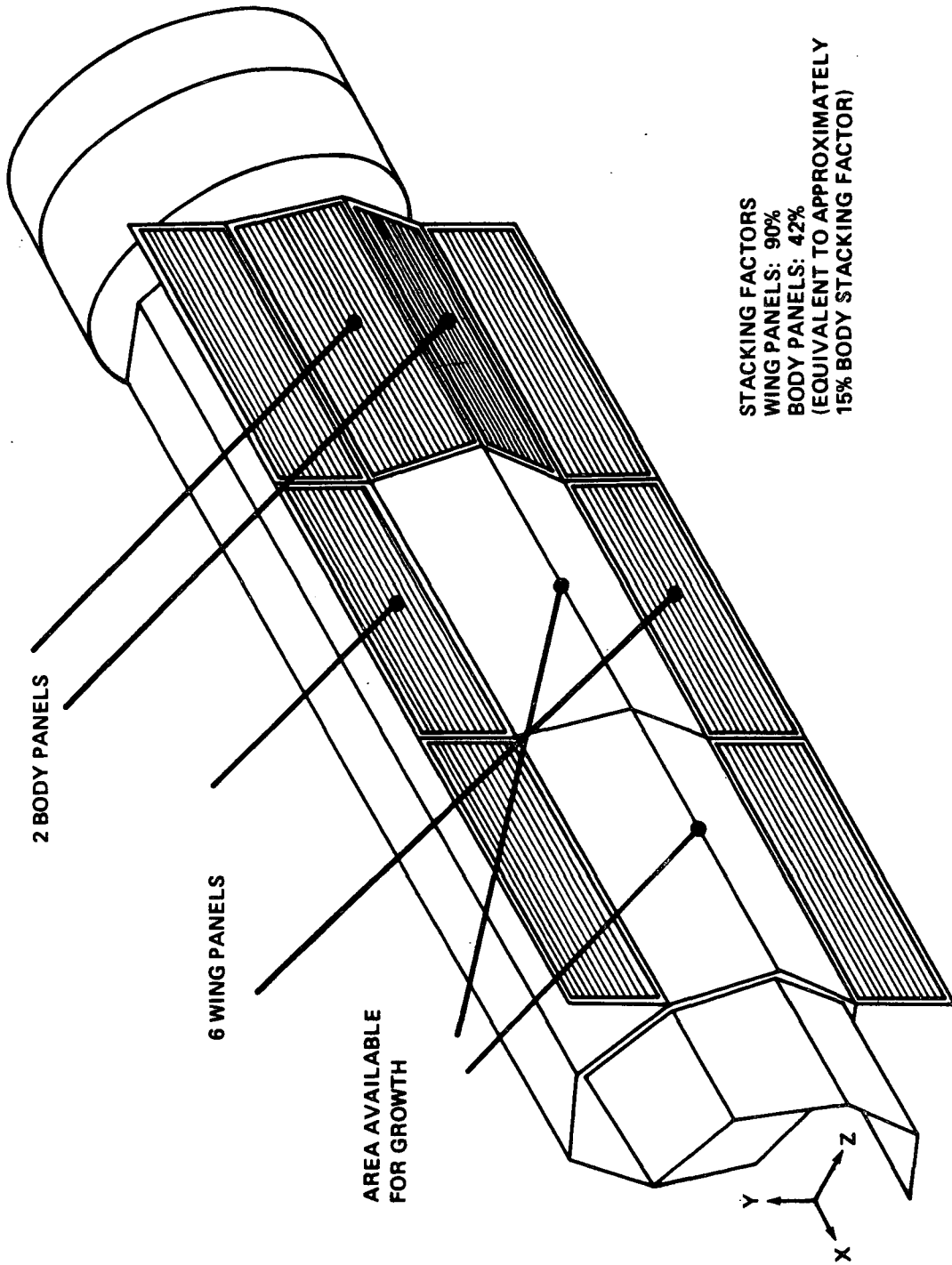


Figure VIII-3. Deployed baseline solar array.

Silicon, N/P solar cells, with a base resistivity of 2 ohm-cm and a 2 by 4 cm size have been baselined. Their initial rating, bare, will provide 11 percent efficiency. Six mil, coated coverslides are used for radiation protection and improved thermal characteristics. The entire array has 70 individual solar cells assemblies with 110 cells in series. A total of 22,220 solar cells are required for the array.

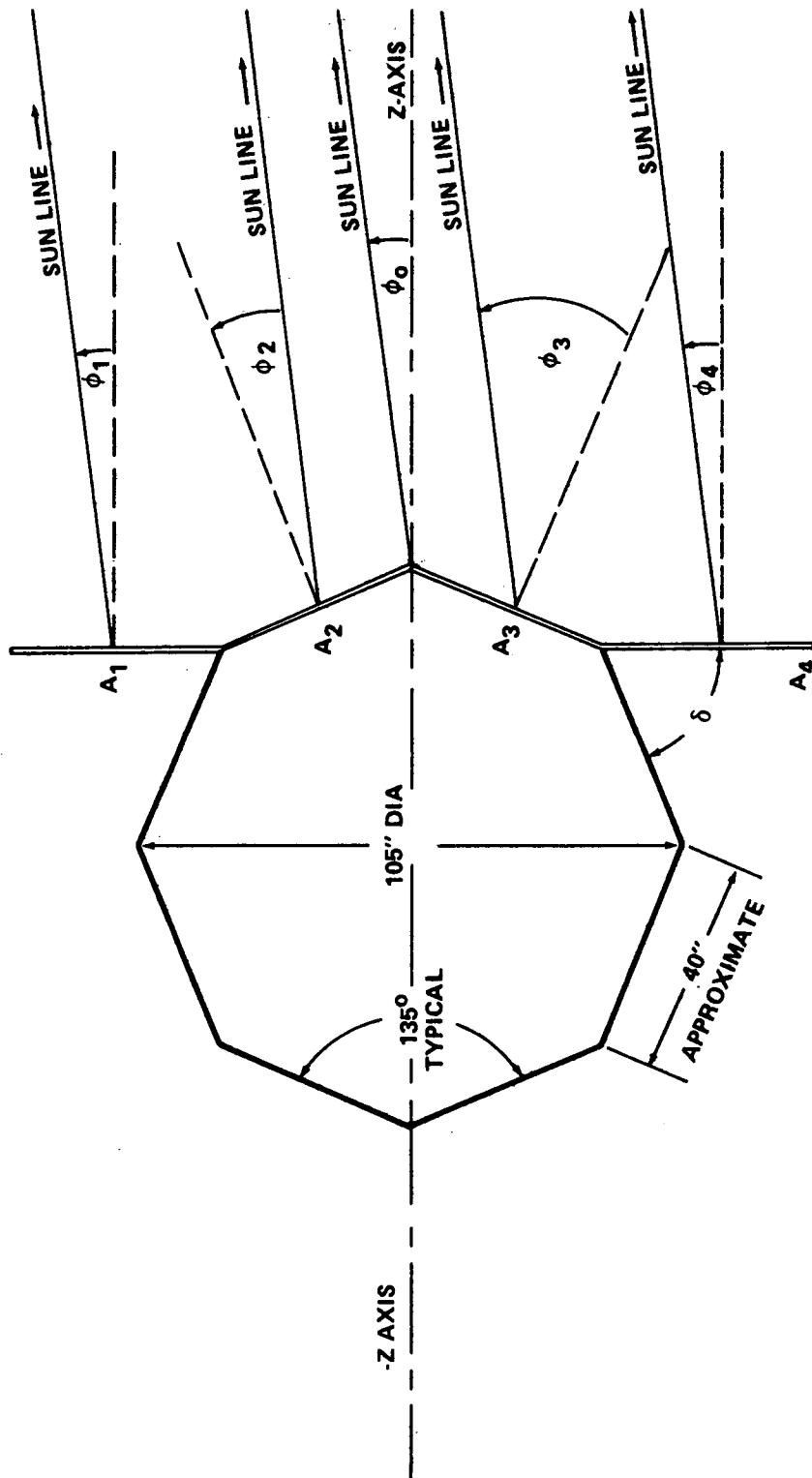
Should mission operational considerations defer the deployment of the array, the undeployed array will furnish enough power to support between 350 and 400 watts. With power management by command, the spacecraft can be powered down to this level during coast intervals for most of the time spent in low altitude orbits. Therefore, without over-discharge of spacecraft batteries, it is feasible to operate the spacecraft during the entire one month contingency period allowed for worst case booster performance without deploying the solar array wings. This capability assumes that the spacecraft maintains sun orientation during low altitude operations.

The baseline solar array provides a considerable growth potential since four panels of the body are unused. The design is conservative and consistent with the reliability and redundancy ground rules. Should further studies indicate that load growth is not needed, the solar array alternate number 1 (Appendix F) is a feasible and desirable array configuration.

The preliminary weight analysis indicates that the array panels will weigh 275 pounds. The deployment, restraint, and mounting hardware for the array wings will weigh approximately 50 pounds.

(2) Performance Characteristics. The solar array performance studies reported in Appendix F were based on detailed solar cell and coverslide characteristics derived from test data. Following conceptual design calculations, mathematical models of the array were made from cell data for computer analysis of array performance. The effects of variations in temperature, vehicle orientation, stacking factors (cell density), deployment angles, and time in orbit were analyzed.

The array configuration was primarily determined by the spacecraft shape and dimensions. Figure VIII-4 illustrates the basic configuration of the baseline array with the wings deployed. During launch each wing, consisting of three panels, is restrained against one side of the octagon shaped spacecraft. In orbit, the wings are deployed 67.5 degrees from their launch position to make them perpendicular to the Z-axis of the spacecraft. Since the vehicle orientation with respect to the sun is specified by



- $\phi_0$  = ORIENTATION ANGLE
- $\phi_1 - \phi_4$  = WING INCIDENCE ANGLE
- $\phi_2$  = BODY PANEL INCIDENCE ANGLE
- $\phi_3$  = OTHER BODY PANEL INCIDENCE ANGLE
- $\delta$  = WING DEPLOYMENT ANGLE

Figure VIII-4. Baseline solar array configuration.

the angle between the Z-axis and the sun line, the angle of incidence for the wings is equal to off-sun pointing angles for the spacecraft. The angle of incidence for the panels mounted on the body, however, it is a function of the angles between the sun line and the X and Y axes as well as the Z pointing angle. When the vehicle is sun-oriented, the angle of incidence on the body panels is 22.5 degrees. For other orientations, the degree of "roll" about the X-axis and "tilt" about the Z-axis determines the body panel incidence angles.

Solar panel temperature is a function of orientation, stacking factor, cell/coverslide characteristics, and panel radiation properties. The temperature of the wings is also a function of the deployment angle. Orientation and temperature significantly affect array performance. A stacking factor of 90 percent, typical of panel construction, was used throughout the study for the wings. Thermal re-radiation from the rear of the body panels is obstructed by the spacecraft insulation. This results in higher temperature for a given panel configuration. Therefore, low stacking factors were used for the body section. To stay within the temperature limit, the stacking factor cannot exceed 65 percent. The stacking factor for the body panels of the baseline array was selected from parametric performance curves to suit the load and orientation requirements. On the basis of total body section area, a stacking factor of 15 percent was selected. However, for fabrication convenience and to reduce the number of panels required, only two body section panels have been baselined. Each panel has a stacking factor of 42 percent; this is equivalent to the 15 percent on a section basis.

The array was analyzed for BOL and EOM conditions, for orbital occultation variations, for off-sun pointing limits as a function of seasonal changes, and for abnormal deployment conditions. The rated voltage-current characteristics are given for typical BOL and EOM conditions in Figure VIII-5. The average power performance as a function of orientation to the sun is given for the baseline array in Figure VIII-6. Both the BOL and EOM curves are for an orbit having a maximum 35.8 min occultation period.

The growth potential for load increases was also investigated. By increasing the number of body panels to six and increasing the stacking factor, the average power rating of the baseline array can be increased from 1830 watts to about 2575 watts for the EOM design condition at 15 degrees off-sun pointing. Figure VIII-7 depicts the power growth potential of the solar array as a function of the stacking factor of the body section. At 2575 watts the maximum temperature limit is reached.

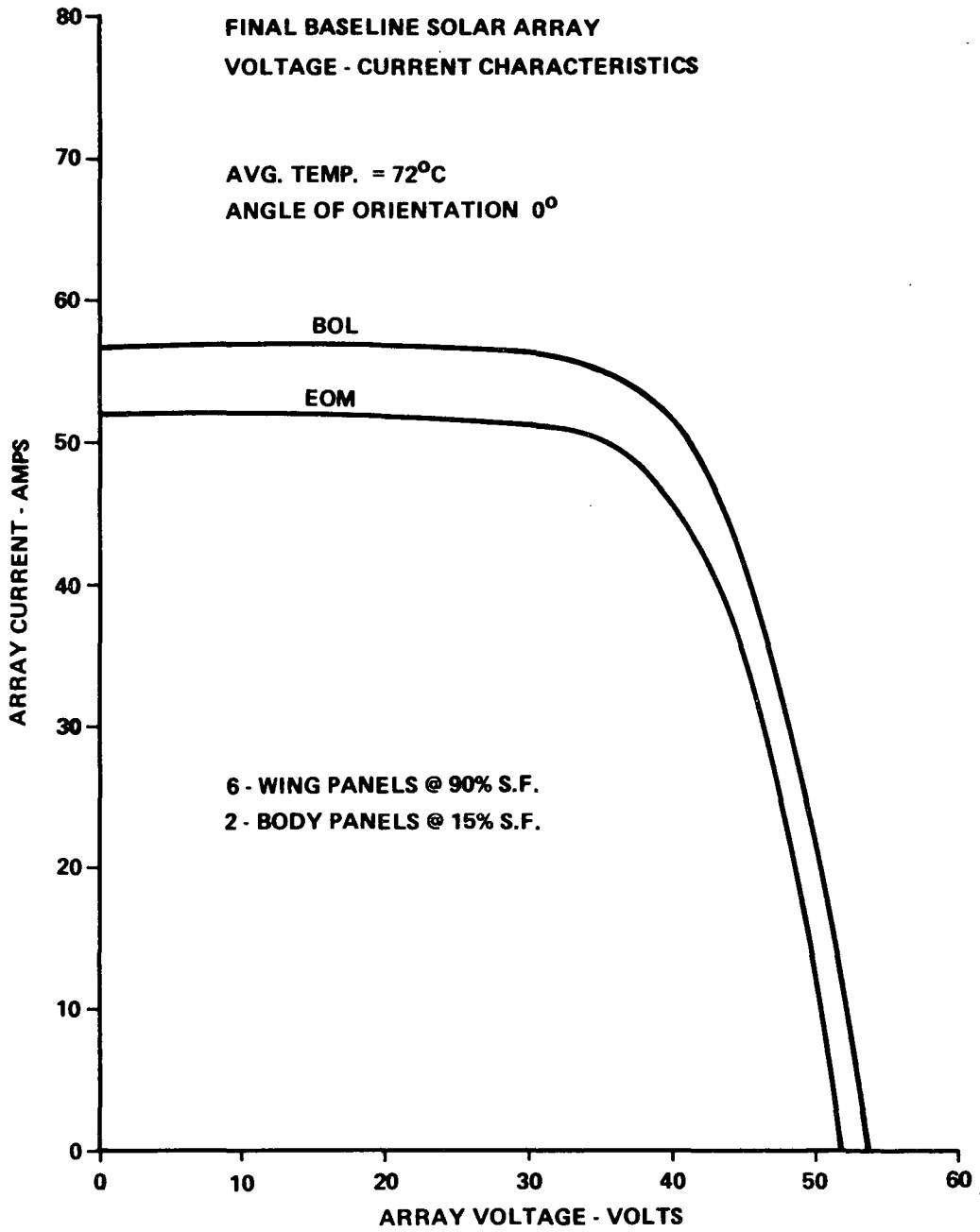


Figure VIII-5. Solar array I-V characteristics.

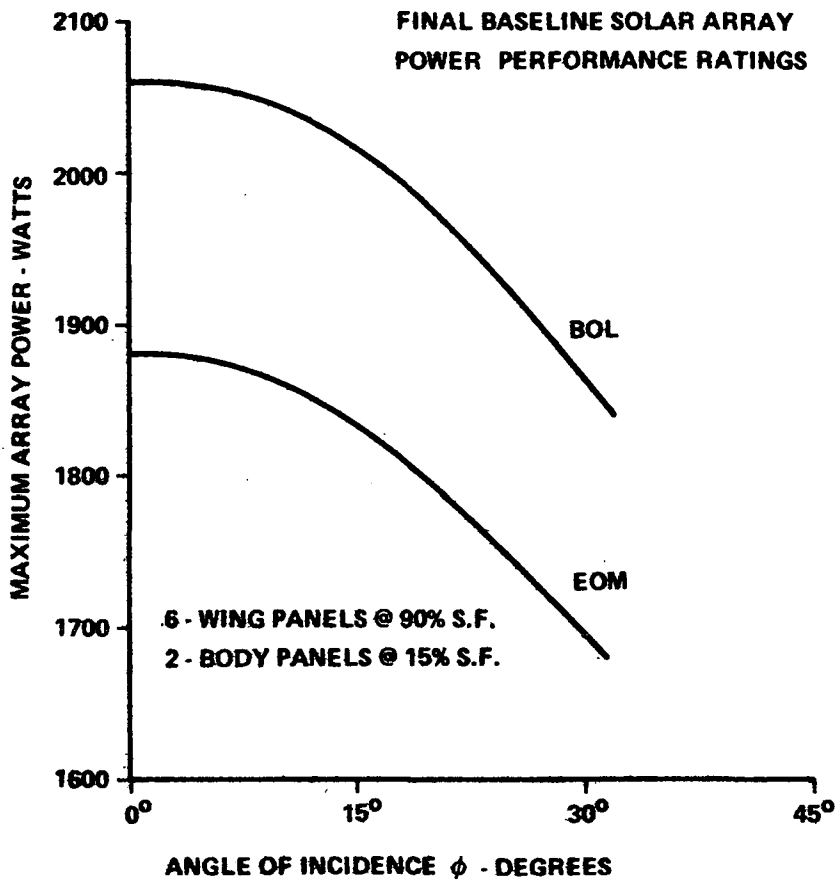


Figure VIII-6. Solar array power performance ratings.

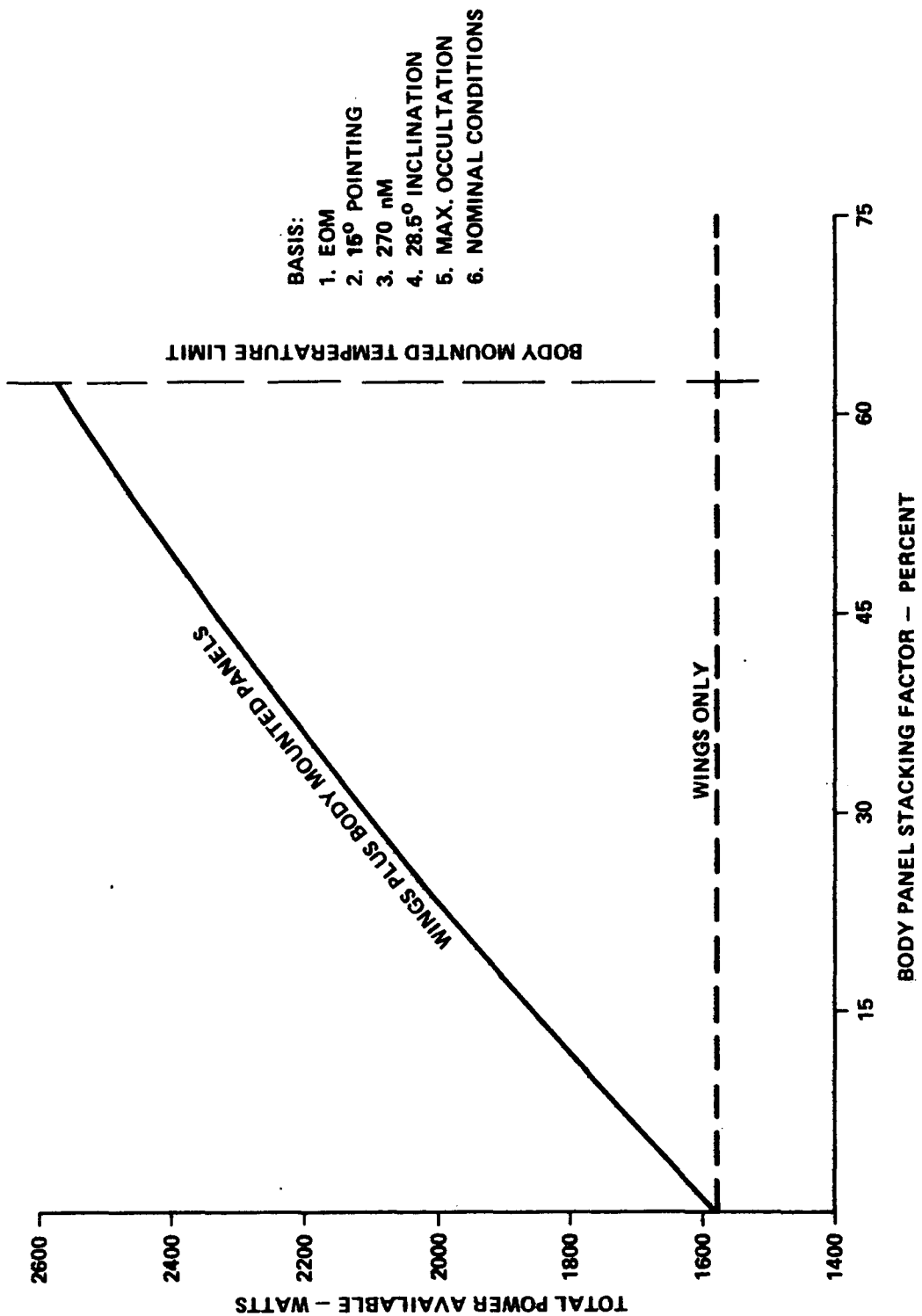


Figure VIII-7. Solar array growth capability.

A summary of the characteristics and ratings for the baseline solar array is presented in Table VIII-12.

### (3) Solar Panels

(a) Substrate and Configuration. Eight solar panels are required for the baseline solar array. The baseline solar panel is compatible with the spacecraft configuration and constraints and was adapted for commonality with the HEAO-A and -B applications.

A solar panel consists of solar cell modules, connections and wiring, adhesive and insulation materials, and attachment hardware mounted on a 0.7 inch thick aluminum honeycomb substrate. Each panel is 119.2 inches long and 38.2 inches wide as illustrated by Figure VIII-8. The maximum area considered practical for mounting solar cells provided by the panel is 4350 square inches (28 170 cm<sup>2</sup>). Except for the number of solar cells mounted (stacking factor), the wing panels and body panels are identical.

The honeycomb substrate construction was derived from structural and dynamic analyses as indicated in Chapter V. Ten mil aluminum face sheets are bonded to 2.3 lb/in.<sup>3</sup> core material with HT424 adhesive to give the 0.7 inch thickness. Aluminum channels inserted in the honeycomb to frame the panel provide smooth edges and additional rigidity.

(b) Adhesive and Paint. Adhesive used for solar panel fabrication must have special characteristics (e. g., hardness, expansion, and contraction coefficients, curing time and temperature, etc.) to permit practical, quality construction. It must also be durable in a vacuum and resistant to the space environment.

The adhesives selected were Sylgard 182, SiLastic-140, and Epi-Bond-101. These have good use and test history and also conform to MSFC SPEC-50M02442 which is considered a prime requirement for such materials to be used on astronomy missions, where outgassing must be avoided.

The back and void areas of the panels are to be coated with S-13-G paint, selected for its excellent thermal characteristics. This paint also shows relatively low deterioration with exposure to space environments.

TABLE VIII-12. BASELINE SOLAR ARRAY SUMMARY

Electrical Ratings						
Mission Time Orientation Off Sun (deg)	BOL			EOM		
	0	15	30	0	15	30
Rated Avg. Power (for 59 min) (W)	2060	2014	1864	1881	1834	1695
Required Avg. Power (W)	1549	1549	1549	1549	1549	1549
Design Margin (W)	511	465	315	332	285	146
Max Power (W)	1915	1850	1660	1760	1700	1525
Peak Voltage (Open Circuit)	78			75		
Operating Point Min Design Voltage	38			38		
Continuous Off-Sun Pointing Capability (deg)	48			40		
Physical Characteristics						
No. Array Panels (Total)	8					
Wings (Foldout)	2					
Panels per Wing at 90% Stacking Factor	3					
Body Panels at 42% Stacking Factor	2					
Total Array Panel Area	253 ft <sup>2</sup>					
Total Panel Weight	275 lb					
Substrates	0.7 in. Al honeycomb					
No. Cell Assemblies (With 110 series cells)	70					
Cell Type	N/P Silicon - 2 ohm - cm					
Cell Size	2 x 4 cm					
Cell Thickness	14 mils					
Rated Cell Efficiency	11%					
Total No. Cells	22 220					
Cover Slides (Coated)	6 mils					
Temperature Rating	-40° C to + 100° C					
Operating Temperature Range	-25° C to + 83° C					
Deployment Mechanism	Torsion Rods/Dampers					
Restraint Release (Wings)	Redundant Pyro Bolts					
Deployment Hardware Weight	50 lb					

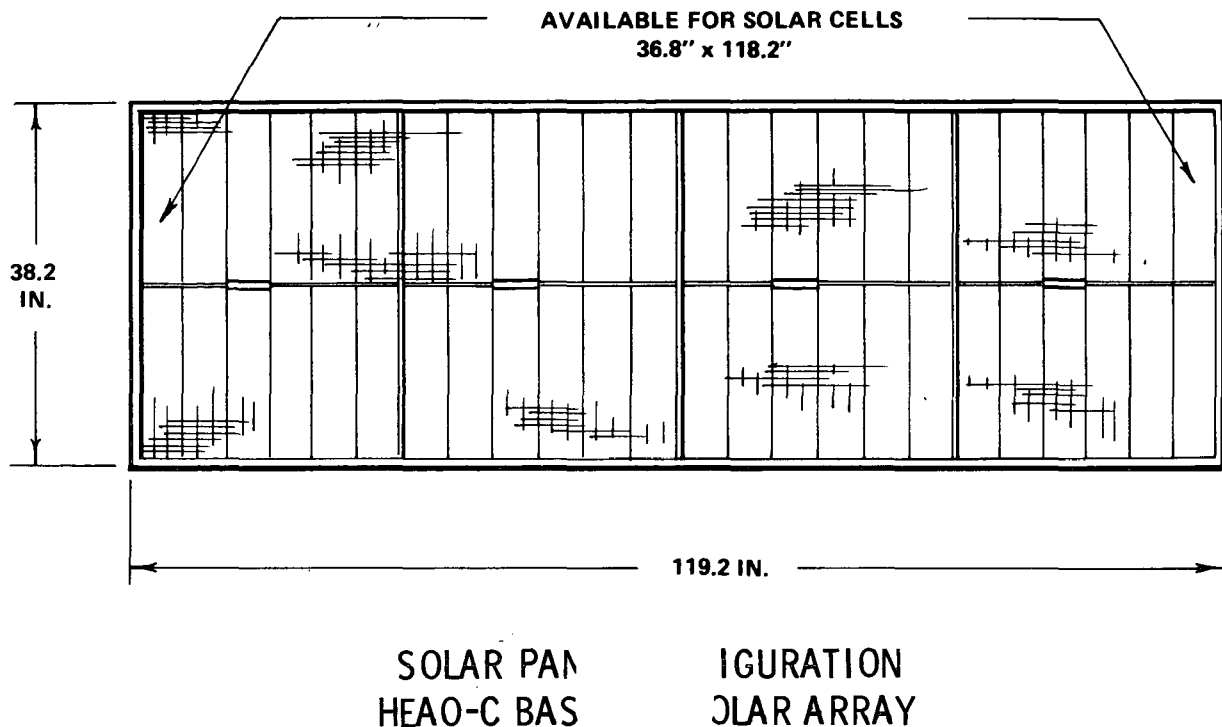


Figure VIII-8. Baseline solar panel dimensions.

(c) Solar Cell Mounting. The solar cells and coverslides used on the solar panels are described in Appendix F. These cells and coverslides will be fabricated into modules and assembled on the solar panel substrates using the materials described. A flat lay-down technique is used for this assembly as shown by Figure VIII-9. Special attention to the thermal expansion characteristics of the various parts is required. As shown by the figure, all interconnects require a stress relief configuration.

The baseline solar panel for the array wings will weigh 36.1 pounds. A detailed weight breakdown of the materials used in panel fabrication is shown in Figure VIII-10. Body panels with a 42 percent stacking factor will weigh 32.0 pounds.

(d) Electrical Arrangement. When a 90 per cent stacking factor is applied to the area available for cells on the panel, the permissible cell area becomes 25 520 cm<sup>2</sup>. The total number of cells equivalent to this area is 3190 which is the number used on a wing panel. With adequate spacing, 73 rows of 4 cm cells can be mounted along the panel length. Each row may have 44 cells, allowing for spacing and terminations.

The system requires a minimum array voltage of at least 38 volts. To meet this requirement within the panel configuration constraints, the number of series cells selected was 110. Consideration of panel dimensions and thermal conditions led to a cell arrangement with the

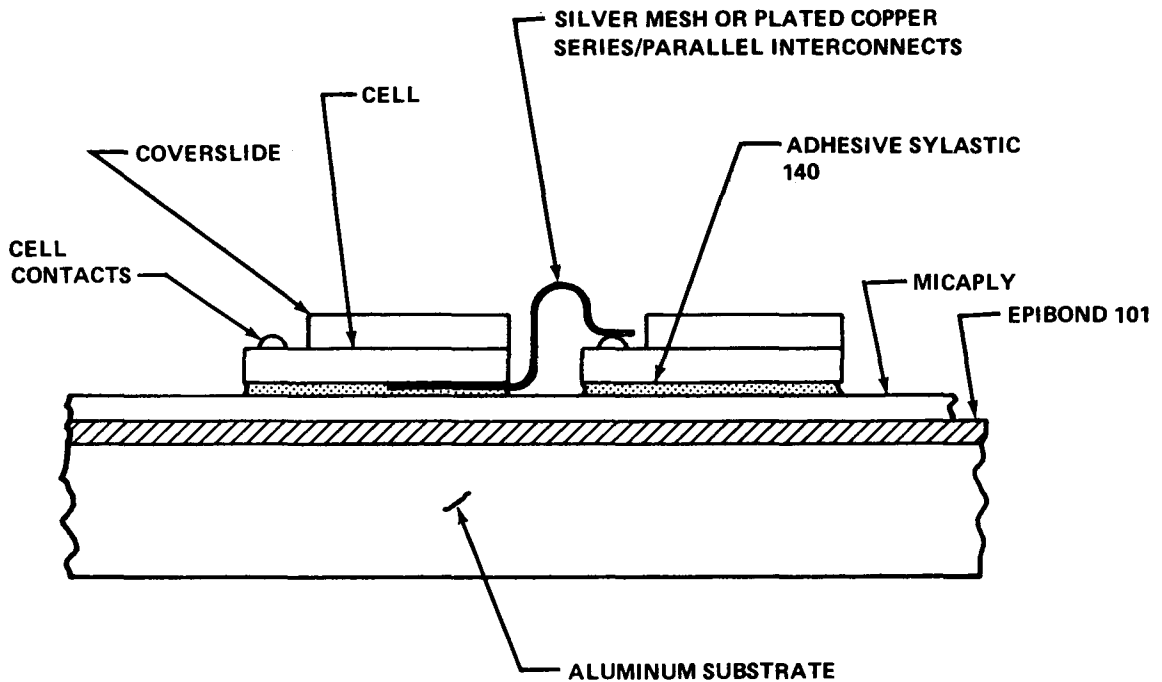


Figure VIII-9. Solar cell flat low-down mounting.

cells connected in series across the width of the panel. This minimized the detrimental effects of temperature gradients across the panel.

Since fabrication techniques, handling, and adhesive curing time limit the size of practical cell modules, the maximum submodule baselined is 3 cells in parallel. The maximum module consists of 22 submodules connected in series (or 66 cells.) The number of parallel cells is also consistent with blocking diode ratings. Modules are separately mounted on the panel and, then are connected to provide the required electrical arrangement.

The schematic diagram shown in Figure VIII-11 illustrates the electrical arrangement of cells, submodules, and modules required to complete one solar cell assembly. Two modules connected in series occupy three rows on the panel. Five modules in series are required to attain 110 series cells. Thus, one solar cell assembly occupies six complete rows and half of the next three rows. The figure also lists the total complement of cells, assemblies, modules, and submodules required on the baseline panel.

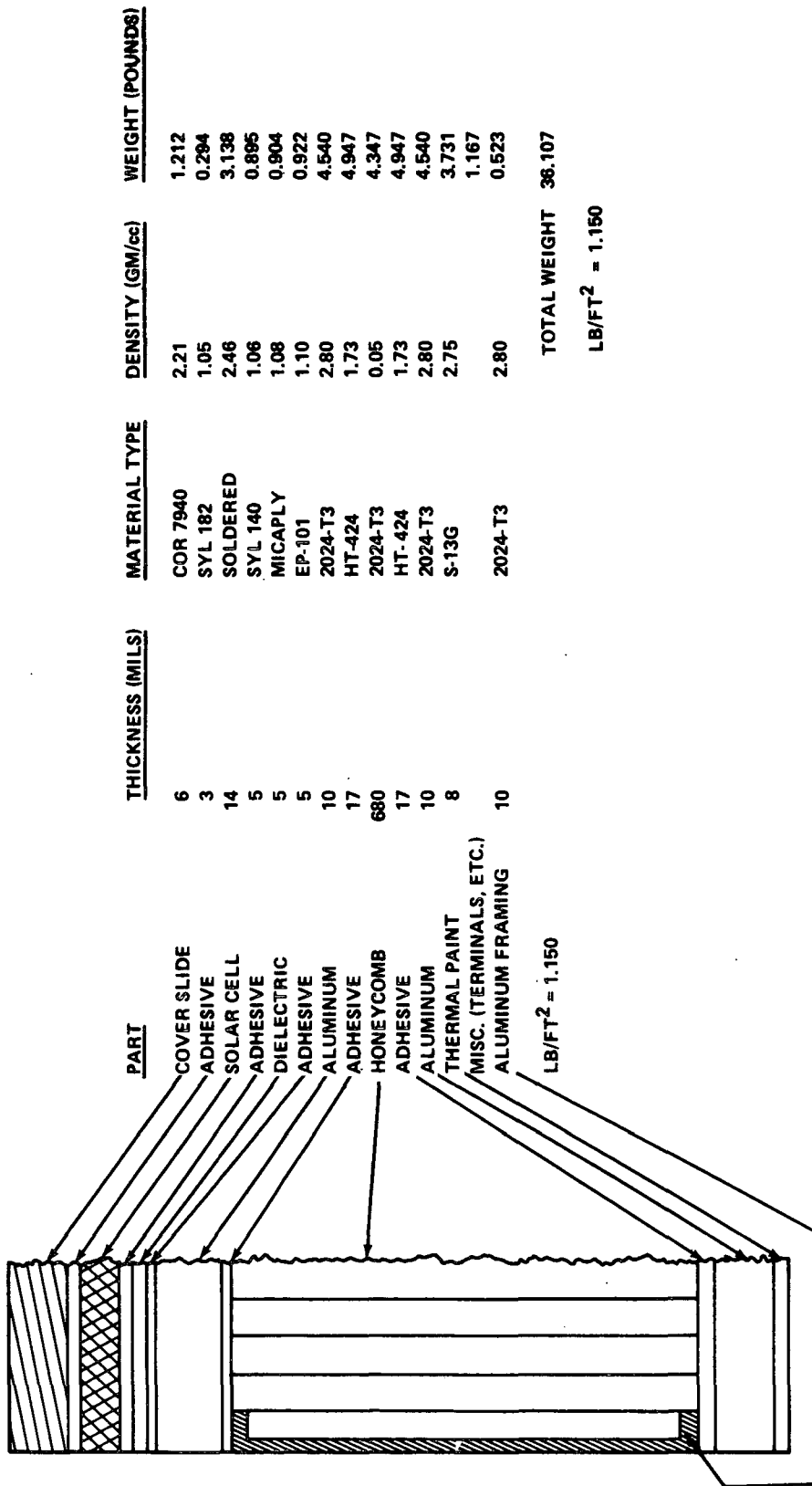
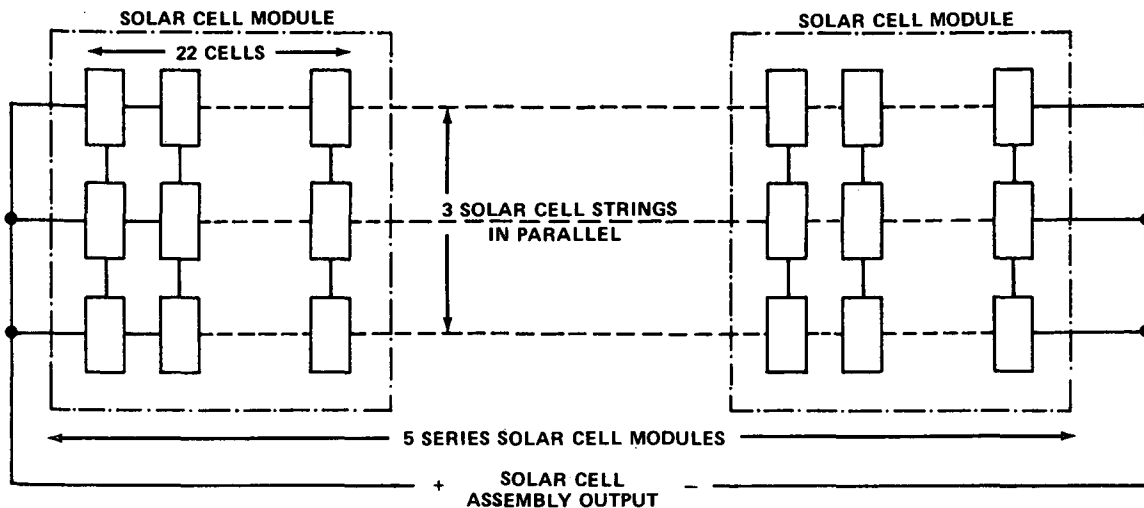


Figure VIII-10. Solar panel materials and weights.



1 SOLAR CELL ASSEMBLY = 5 SERIES SOLAR CELL MODULES  
 1 SOLAR CELL MODULE = 22 SERIES SOLAR CELL SUB MODULES  
 1 SOLAR CELL SUB MODULE = 33 SOLAR CELLS IN PARALLEL FOR 9 ASSEMBLIES, 2 IN PARALLEL FOR 1 ASSEMBLY  
  
 1 SOLAR PANEL CONSISTS OF:  
 9 ASSEMBLIES = 45 MODULES = 990 SUB MODULES (3 PARALLEL CELLS)  
 1 ASSEMBLY = 5 MODULES = 110 SUB MODULES (2 PARALLEL CELLS)  
 TOTAL 10 ASSEMBLIES = 50 MODULES = 1100 SUB MODULES

990 SUB MODULES x 3 CELLS = 2970 CELLS  
 110 SUB MODULES x 2 CELLS = 220 CELLS  
 PANEL TOTAL 3190 CELLS

Figure VIII-11. Solar panel electrical arrangement.

Figure VIII-12 shows the physical arrangement of the modules and solar cell assemblies on the baseline panel. Details of the provisions for termination of each assembly and for turnaround buses are also given.

The 10 solar cell assemblies are separated electrically; each assembly is separately wired to the spacecraft. Redundant termination of cell assemblies is provided. Feedthrough turret terminals would be used for thin panels; however, for the 0.7 inch thickness baseline, slotted terminals with a feedthrough hole are used. These are mounted on terminal boards placed over filled holes through the panels provided for wiring to the backside of the panel. A connector bracketed to the rear of the panel provides the electrical interface for spacecraft cabling, allowing each panel to

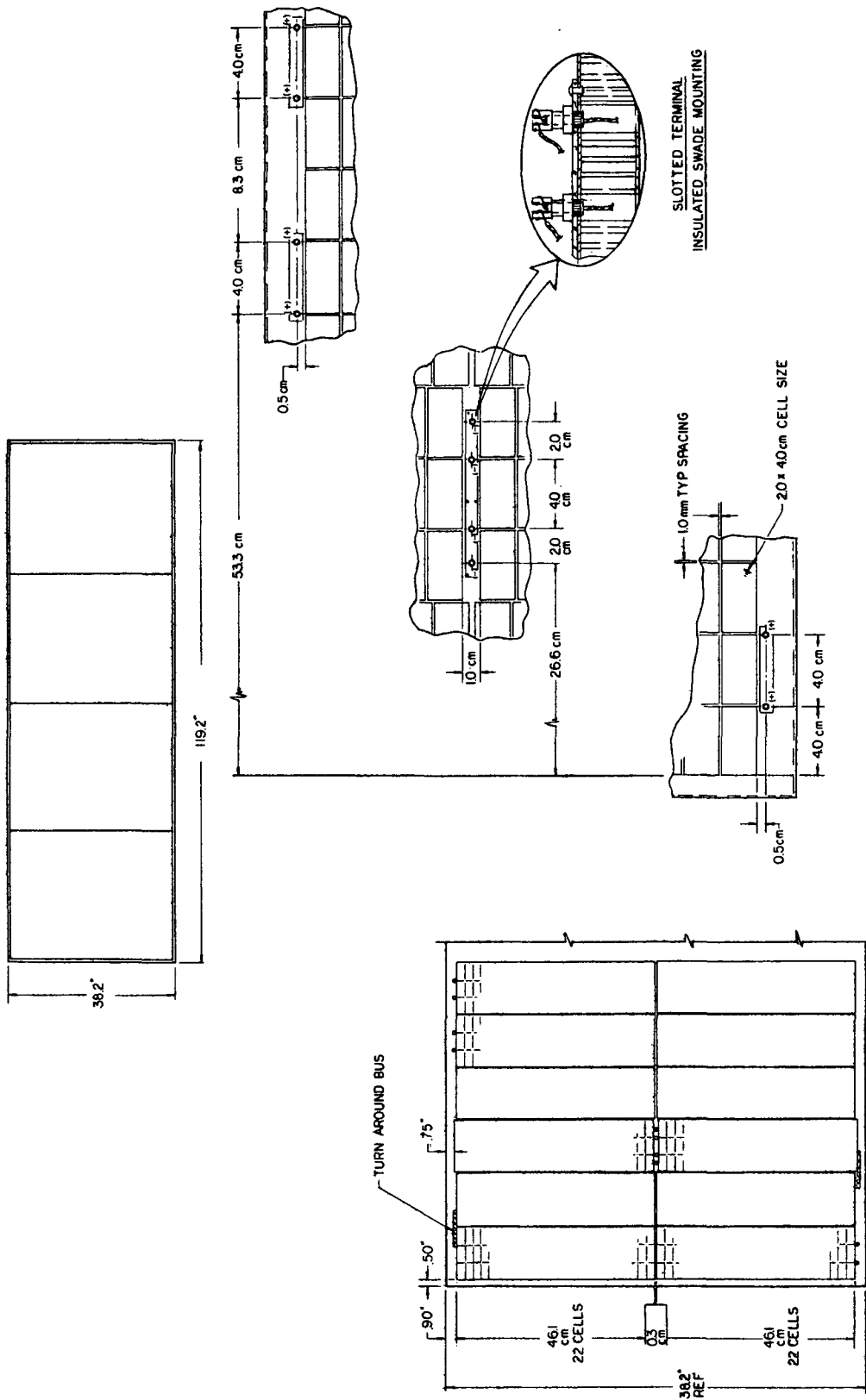


Figure VIII-12. Solar panel physical layout.

be separately installed (or removed, if necessary) during construction and testing of the spacecraft.

The BOL rating (at 28° C) and the EOM design performance for the baseline solar panel are indicated by the I-V curves of Figure VIII-13.

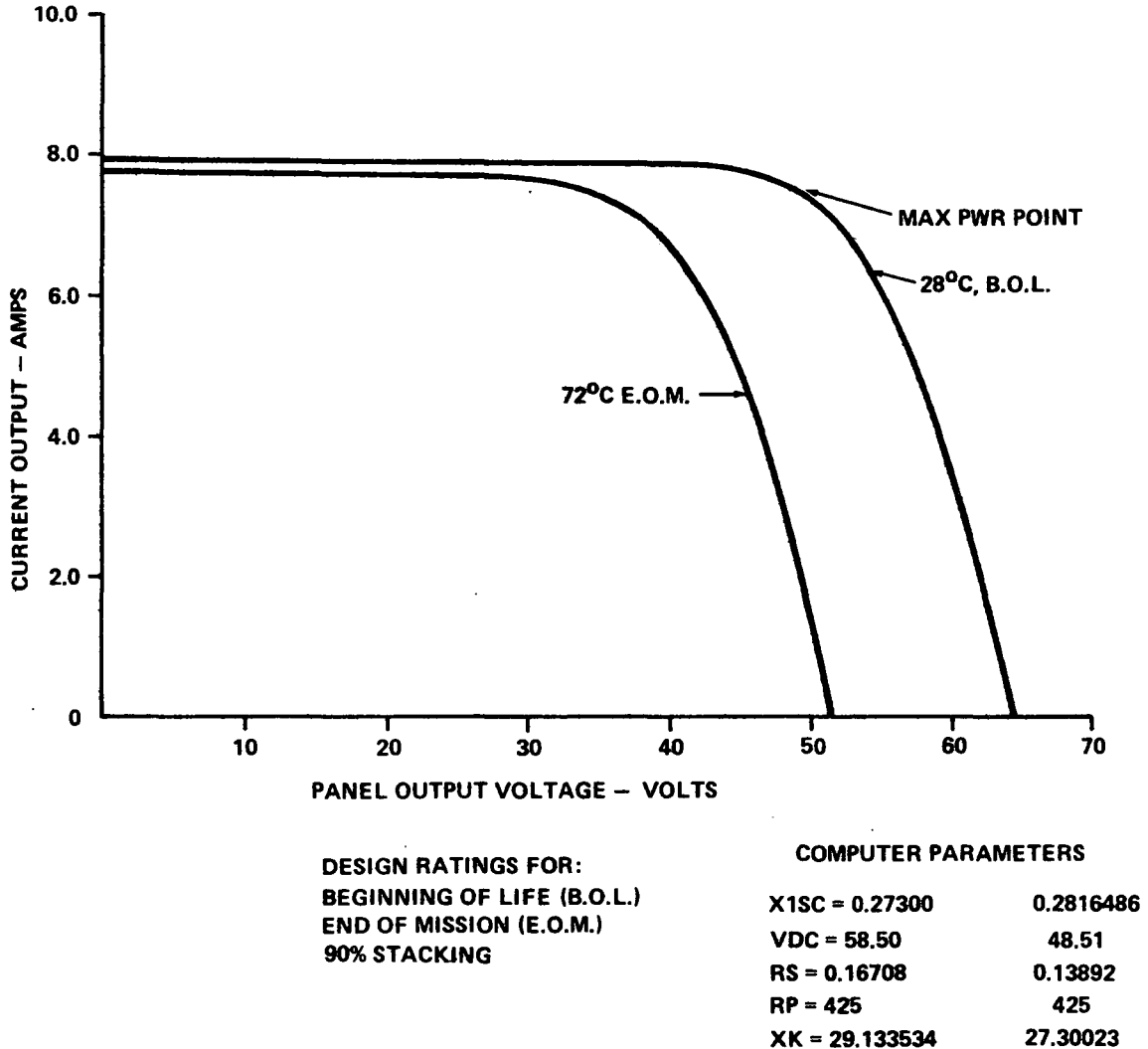


Figure VIII-13. Solar panel I-V characteristics.

(4) Deployment Mechanisms. The maximum power from the solar array will be available only if the foldout panels are deployed to the proper position when the spacecraft has been placed into orbit. There is substantial power (over 900 watts) developed by the body-mounted panels and

the undeployed foldout panels when the spacecraft is sun-oriented; however, it is not sufficient to meet the load requirements. A reliable, effective deployment mechanism is necessary to assure adequate array performance.

A recommended technique for deployment of the foldout panels is shown in Figure VIII-14. In this design the panels are firmly mounted to the spacecraft prior to deployment. Detail A of the figure shows the position of the panels in their retained configuration. As can be seen in this view, the panels and the deployment mechanism lie within the maximum allowable envelope of the spacecraft (105.0 inch diameter.) Four locking dogs, which are secured with two latches, retain each panel prior to deployment, as shown in Details B and C. Each of the two latches has two redundant explosive bolts; the design is such that a latch will be released when either of the bolts is fired. A preload is applied to the panels prior to deployment by means of coil springs which are located beneath the corners of each panel. These springs, which are shown in Detail B of the figure, reduce the vibration levels experienced by the panels during the launch phase of the vehicle.

When the spacecraft has been placed in the proper orbit and has acquired the sun, the foldout panels are deployed by firing the explosive bolts. It should be noted here that these bolts are equipped with a capture nut and bolt catcher so that little, if any, debris and contaminant is released into space when the devices are fired. This also reduces the likelihood of a high energy scrap from the explosion causing damage to the array or other elements of the spacecraft.

The energy for the deployment of the panels is supplied by two preloaded torsion bars which are located at the inner edge of each panel and secured at one end to the panel and at the other end to the spacecraft. The panels rotate on hinges which are designed to carry the loads imposed when the vehicle is launched. The deployment of the panels is gradual so that no sudden shock is incurred when they reach the limit of their travel. Damping for the deployment motion is provided by two rotary type dampers which are located at the ends of each panel (see Details D and E). The dampers are positioned concentric with the torsion bars and provide a viscous friction to the bars during the release of their energy during deployment. A detailed drawing of the damper is shown in Figure VIII-15. One feature of this type of damper which is not obvious from the figure is that, in the unlikely event that the bleed orifice becomes clogged with a foreign particle, there is sufficient clearance between the shaft wiper plate and the housing to allow the damping fluid to flow by, thus, providing normal operation.

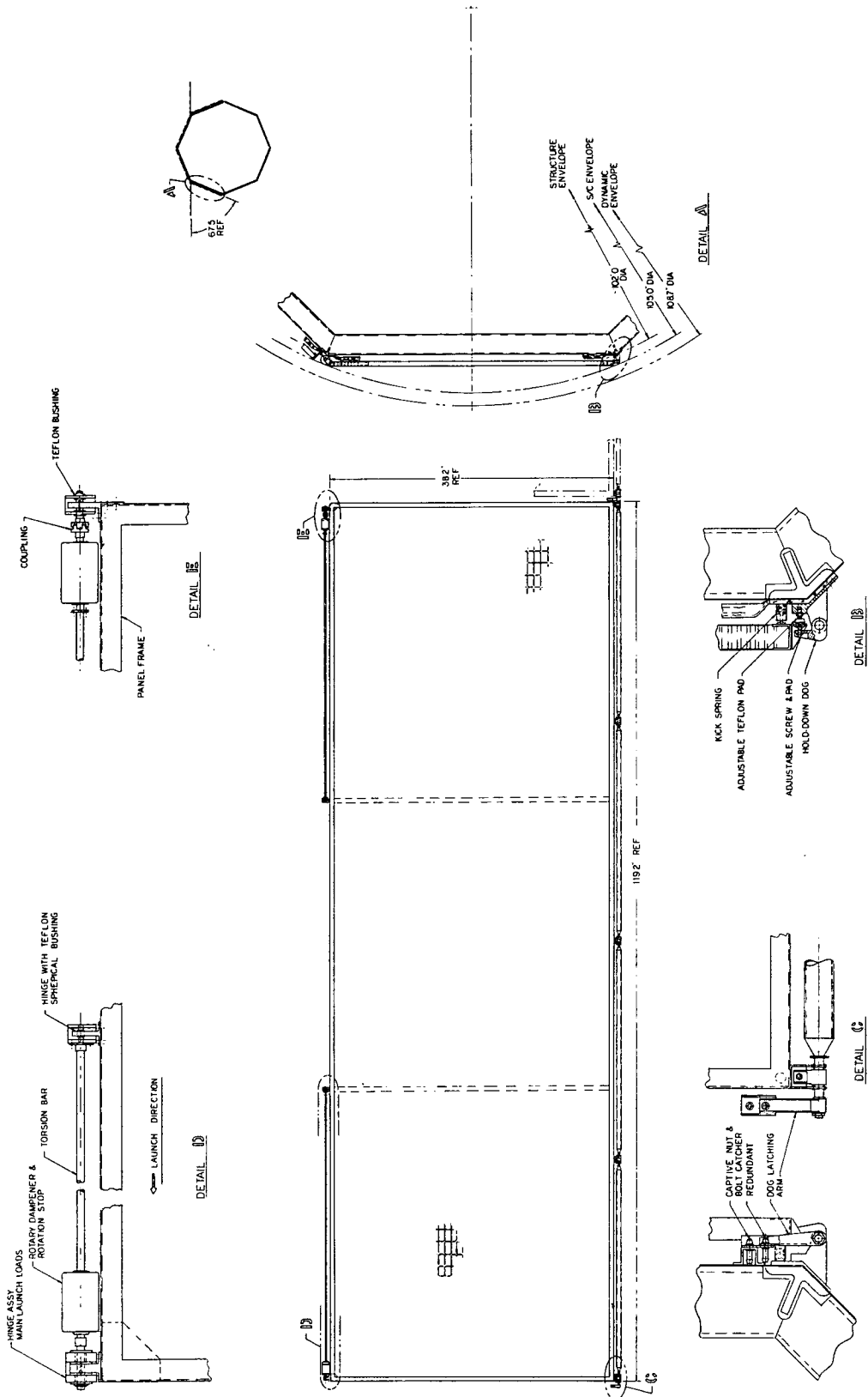


Figure VIII-14. Solar array deployment mechanisms.

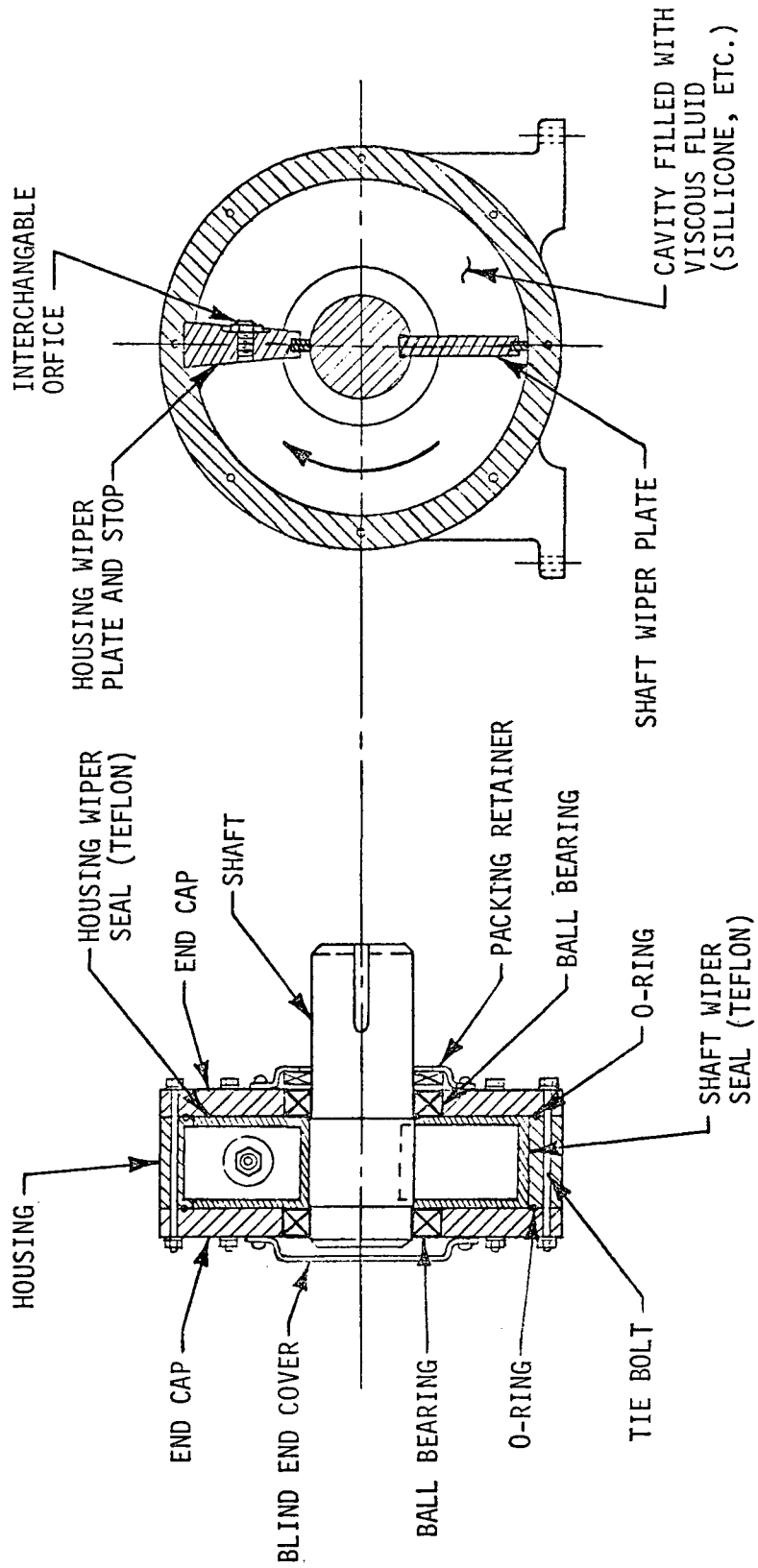


Figure VIII-15. Deployment damper.

When the panels are deployed to the proper position, a simple locking mechanism will secure them in place. This concept provides for a positive, nonreturnable type of latch when it is secured, and as such, it will not allow the foldout panels to be returned to their folded positions. This is not seen to be a shortcoming of the design.

The components required for the deployment of the six foldout panels weigh 50.4 pounds. A listing of the components and their individual weights is shown in Table VIII-13.

TABLE VIII-13. SOLAR ARRAY  
DEPLOYMENT MECHANISM WEIGHT BREAKDOWN

Item	No.	Unit Weight (lb)	Total Weight (lb)
Rotary Damper and Rotary Stop	12	1.0	12.0
Torsion Bar	12	0.7	8.4
Support Hold-Down Assembly	6	4.0	24.0
Load-Carrying Hinge	6	0.3	1.8
Secondary Load-Carrying Hinge	9	0.2	1.8
Kick Spring	12	0.2	2.4
Total			50.4

b. Energy Storage Subsystem. Operation of the spacecraft while it is in the earth's shadow requires that the EPS have a means of storing energy. This energy must be converted to electrical power and delivered to the spacecraft loads during the occultation periods of the orbit when primary power is not available. Rechargeable electrochemical batteries are utilized for this purpose. During the portion of the orbit when the spacecraft is

illuminated by the sun, the batteries will be charged with energy from the solar panels.

(1) Battery Section. The baseline EPS employs six battery assemblies. Each battery has its own charger to assure reliable charge control. The battery assemblies are composed of secondary, nickel-cadmium (Ni-Cd) cells that are hermetically sealed for space applications. Temperature sensors and third electrode cells are also included in the assemblies for charge control.

These type batteries were selected for HEAO-C because they are the only type with the cycle life, proven reliability, and charge characteristics applicable to low earth orbital missions similar to the HEAO mission.

In normal operation, the spacecraft is furnished power by redundant, separate distribution buses, each receiving power from one or two regulators. The secondary power from the batteries to the regulators is routed through the chargers and the electrical control assemblies (ECAs). Three batteries supply power to one ECA and the other three furnish the second ECA so that all six batteries simultaneously support the system. Alternate operational modes are discussed later. For nominal design conditions, the average depth of discharge will be about 14 percent of rated capacity which will assure reliable performance and long life. At this level the batteries have a minimum life of 16 000 cycles where only 11 000 are required. The batteries have sufficient capacity and rating so that less than three could operate the system, thereby, giving more than 100 percent redundancy.

The overall efficiency of the system when operating from energy storage is 85.5 percent. The average load requirement of 722 watts translated to the battery outputs requires 845 watts for an average period of 34.3 minutes and a maximum period of 35.7 minutes. The average and maximum energy requirements are 482 and 502 watt-hours, respectively. The batteries are the chief source of peak power and must be rated to supply the 1375 watt peak requirements.

The battery section of the EPS will adequately meet the systems demands provided the spacecraft thermal control maintains the battery temperature reasonably close to the requested limits of  $10 \pm 5^\circ$  C. Very high or low temperatures are detrimental to performance and life. Within the given range, the batteries will have an efficiency slightly over 80 percent.

The characteristics and ratings for the battery section of the energy storage subsystem are summarized in Table VIII-14.

Baseline Battery Assembly. The baseline battery assembly was selected from tradeoffs discussed in Appendix F. Proven designs and hardware were considered for the application. Three manufacturers are able to deliver satisfactory cells if sufficient care is taken in the specification, acceptance testing, and matching. Of the three sizes considered, the performance differences were small. More use and test data were available for the 20 ampere-hour size and, since this size was more easily adapted to the baseline scheme, it was selected. The assembly dimensions were based on the cell configuration of one manufacturer. Different cell configuration standards for the other manufacturers would change the assembly dimensions; however, the volumes and weights would remain almost the same.

The battery assembly for the EPS baseline, shown by Figure VIII-16, has the dimensions 13 by 6.6 by 7.25 inches and will weigh 52 pounds. It consists of a magnesium alloy (stainless steel alternate) housing, 22 series connected cells, connectors, sensors, insulators, and thermal shims. All the cells are hermetically sealed in rectangular, stainless steel containers.

As illustrated, two rows of cells are used. The back row has 12 cells; the forward row has 10 to allow space for connectors. Three to five mils of Kapton or H-Film is bonded to the sides and bottom of the cells for electrical insulation. The assembly is designed for maintaining close temperature control,  $10 \pm 5^\circ \text{C}$ , and will satisfy all other environmental requirements. Copper foil shims separate each cell and are connected to the housing to assure good thermal conduction.

Each cell has a minimum rating of 20 ampere-hours and is qualified and space proven. Typical discharge characteristics for the cells, given by Figure VIII-17, indicate the minimum voltage rating permitted as a function of capacity and temperature. All curves are given for a one hour discharge rate. Three of the cells in each assembly are third electrode types that can supply signals to stop charge when fully recharged.

Special strap assemblies with a stress relief configuration interconnect the cells. The straps are welded to the cell terminals. Redundant connections and temperature sensors for control and instrumentation are provided. The schematic diagrams for an assembly is given by Figure VIII-18 showing the cell connection, sensors, and the operational test connectors.

TABLE VIII-14. ENERGY STORAGE  
SUBSYSTEM BATTERY SECTION CHARACTERISTICS

Characteristic	Subsystem Total	
<u>General</u>		
Battery Assemblies	6	
Cells	132	
Type	Secondary Ni-Cd	
Style	Hermetically Sealed	
Nominal Rating Class	20 Ah	
Electrical Interface	MS Connectors	
<u>Physical</u>		
Weight	312 lb	
Volume	3870 in. <sup>3</sup>	
Temperature	10 ±5° C	
Thermal Dissipation	123 Wh	
<u>Electrical</u>	<u>Required</u>	<u>Rated</u>
Avg. Energy	482 Wh	3360 Wh
Max Energy	502 Wh	3804 Wh
Discharge Voltage	22 to 33 Vdc Permitted	24 to 29 Vdc
Charge Voltage	29 to 33 Vdc	29 to 33 Vdc
Peak Load	1375 W	3300 W
Max Current	56 A	120 A
Cycle Life	11 080	16 000
<u>Performance Factors</u>		
Depth-of-Discharge (DOD)	≤ 15%	14%

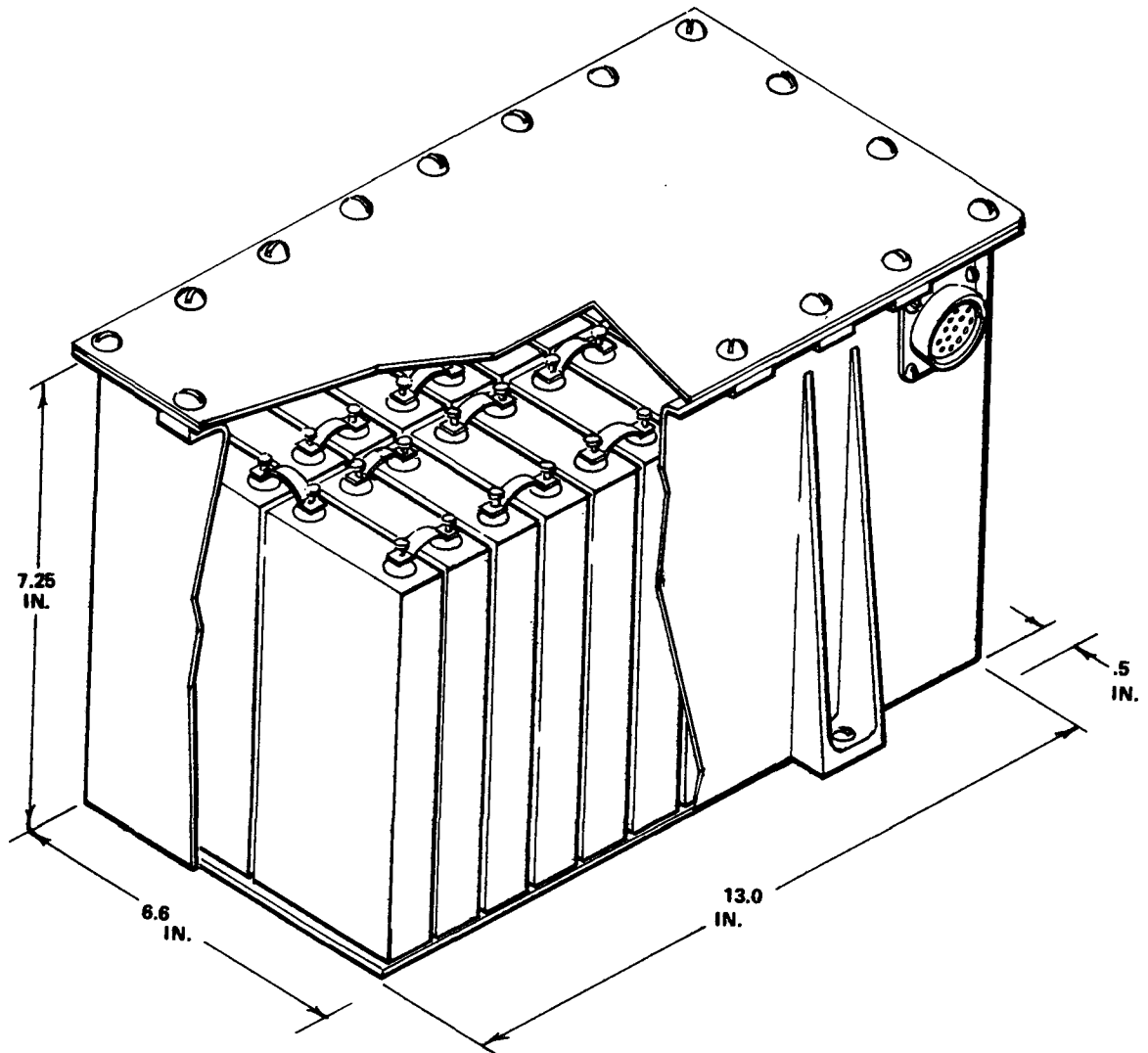


Figure VIII-16. Battery assembly.

The baseline battery assembly is nominally rated for 20 amperes, 24 to 29 Vdc output at the one hour discharge rate. The minimum capacity rating will be 560 watt-hours. Recharge will be strictly controlled. The maximum charge rate and voltage will be limited to 15 amperes and 33 Vdc, respectively. The characteristics and ratings of the baseline battery assembly are given in Table VIII-15.

(2) Charge Control Section. Although the system design permits the battery assemblies to discharge in parallel, each of the six battery

**TABLE VIII-15. CHARACTERISTICS AND RATINGS FOR Ni-Cd BATTERY ASSEMBLY**

<p><u>Physical</u></p> <p>Assembly Size</p> <p>Assembly Weight</p> <p>Assembly Volume</p> <p>Cell Type</p> <p>Cell Size</p> <p>Configuration</p> <p>No. Cells</p> <p>Max Thermal Dissipation</p>	<p>13 × 6.6 × 7.25 in.</p> <p>52 lb</p> <p>622 in.<sup>3</sup></p> <p>Secondary Ni-Cd</p> <p>20 Ah</p> <p>Rectangular-Hermetic Seal</p> <p>22 Series</p> <p>21 Wh/Orbit</p>
<p><u>Electrical</u></p> <p>Capacity</p> <p>Rated Power (1 hr)</p> <p>Current</p> <p>Voltage</p> <p>Efficiency</p> <p>Specific Energy</p> <p>Energy Density</p>	<p>560 Wh</p> <p>560 W</p> <p>20 A</p> <p>28 Vdc</p> <p>80%</p> <p>10.8 Wh/lb</p> <p>0.865 Wh/in.<sup>3</sup></p>
<p><u>Miscellaneous</u></p> <p>Connectors</p> <p>Sensors</p>	<p>MS Type</p> <p>1 Operation</p> <p>1 Test</p> <p>3 Third Electrode Cells</p> <p>4 Thermistor (Temp)</p>

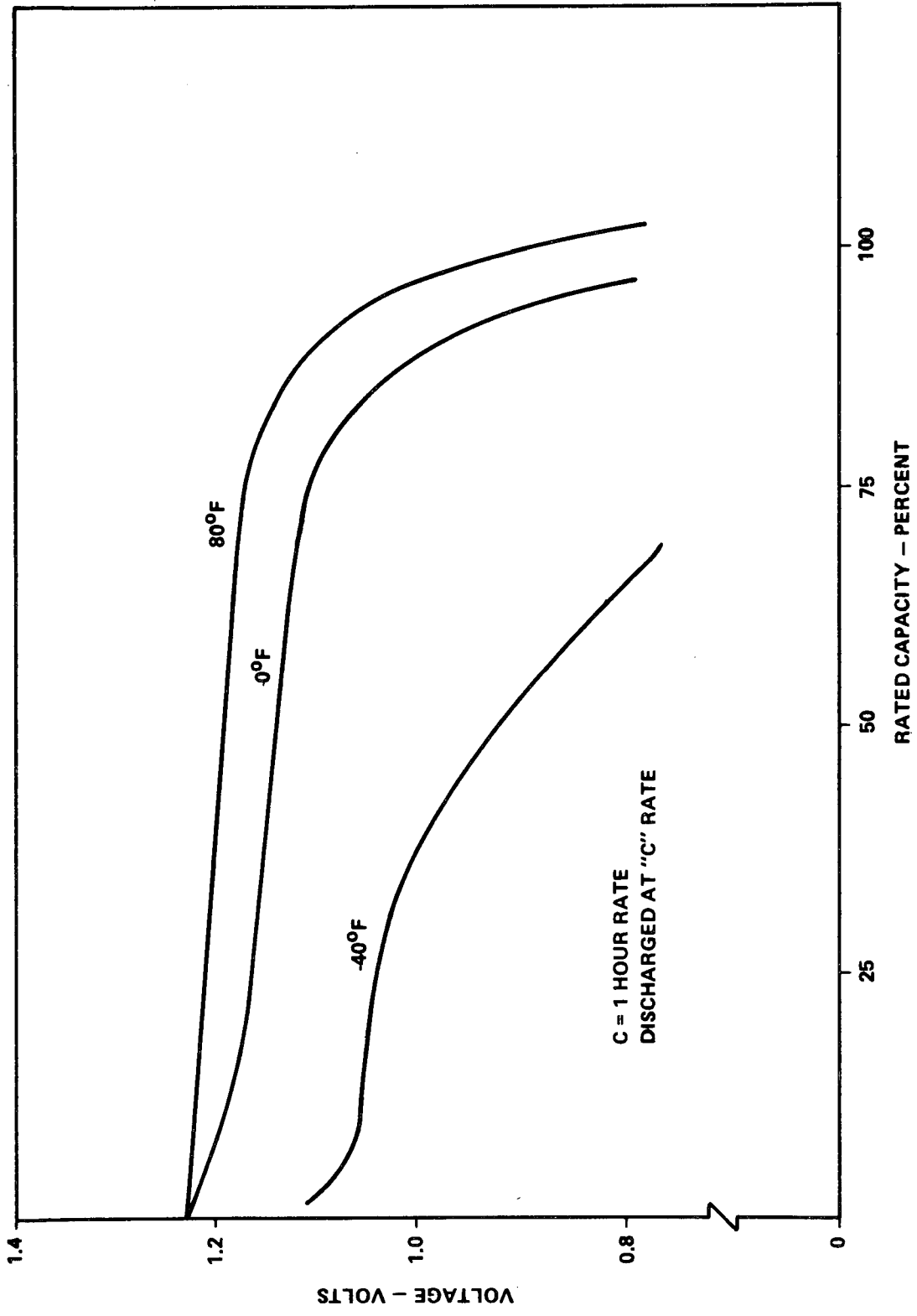


Figure VIII-17. Battery rated discharge characteristics.

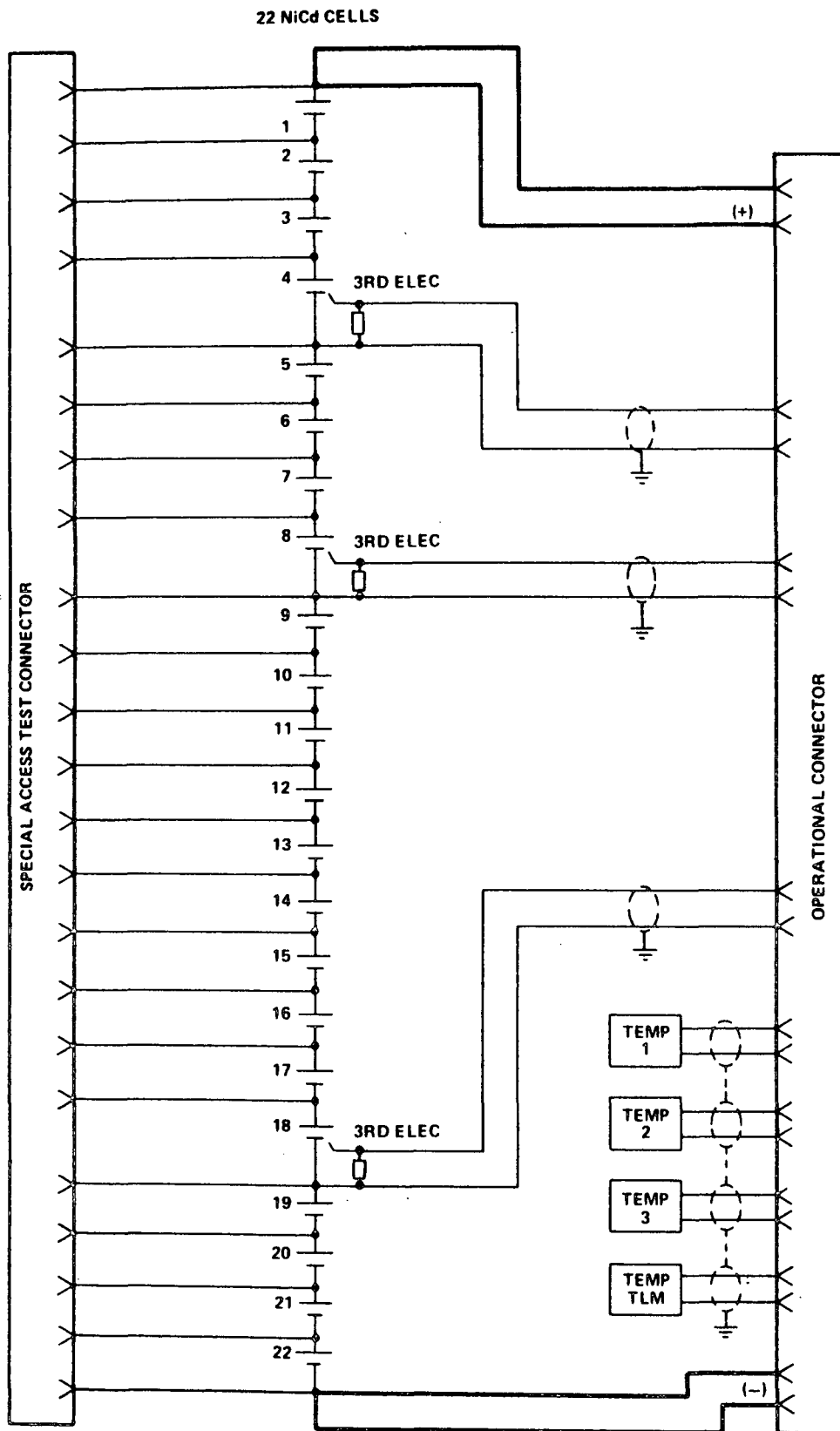


Figure VIII-18. Battery schematic.

assemblies has its own dedicated charge control located in the six charger assemblies. For a large power system and to meet the reliability and long life specified for the mission, well designed charge control specifically adapted to the battery characteristics is needed. Because of their capacity and high energy density, batteries represent one of the most critical parts of the system. Their chemical nature makes them very sensitive to loading, charging, and temperature conditions. The chargers are designed to compensate for such variations. This not only enhances battery performance but also protects the system against catastrophic malfunction should the batteries be abused. Most of the satellite failures attributed to the power system have occurred because charge controls were inadequate.

The charger assemblies included in the EPS baseline will meet the HEAO requirements and can be constructed from modules and subassemblies qualified for other NASA programs. These assemblies must operate from an unregulated solar array source having voltage variations between 38 and 80 volts. Solar array power is received from the two solar power distributors or via the redundant, alternate route through the ECAs. The units in total must be able to deliver at least 628 watt-hours to the batteries. For the maximum occultation orbits, 35.8 minutes, the required average power is 640 watts. The charger assembly ratings must be higher than the average because the batteries receive most of their recharge in the initial part of the sunlight period when the solar array output is high. A rating allowance is also required for the cases where less than six batteries are active.

The output power of the chargers must be delivered at available voltage and current matched to the battery's charge characteristics. The output voltage range is 22 to 33 volts. Output characteristics are a function of battery current, voltage, state-of-charge, and all are function of temperature. Typical of the battery characteristics which must be accommodated by the charger assemblies are the overcharge voltage and current limits shown in Figure VIII-19 for a single cell. These limits change with temperature. Charge control is complicated by the fact that there are variations in cells which must be compensated. The larger the number of cells, the greater the difficulty because individual characteristics are masked by the cell grouping. Other battery characteristics that the chargers must recognize are discussed in Appendix F.

Another important system function provided by the charger control section is the assurance that the loads are satisfied before taking power from the array for the batteries. Should the array become power-limited because of abnormal orientation or degradation of a section, sensors

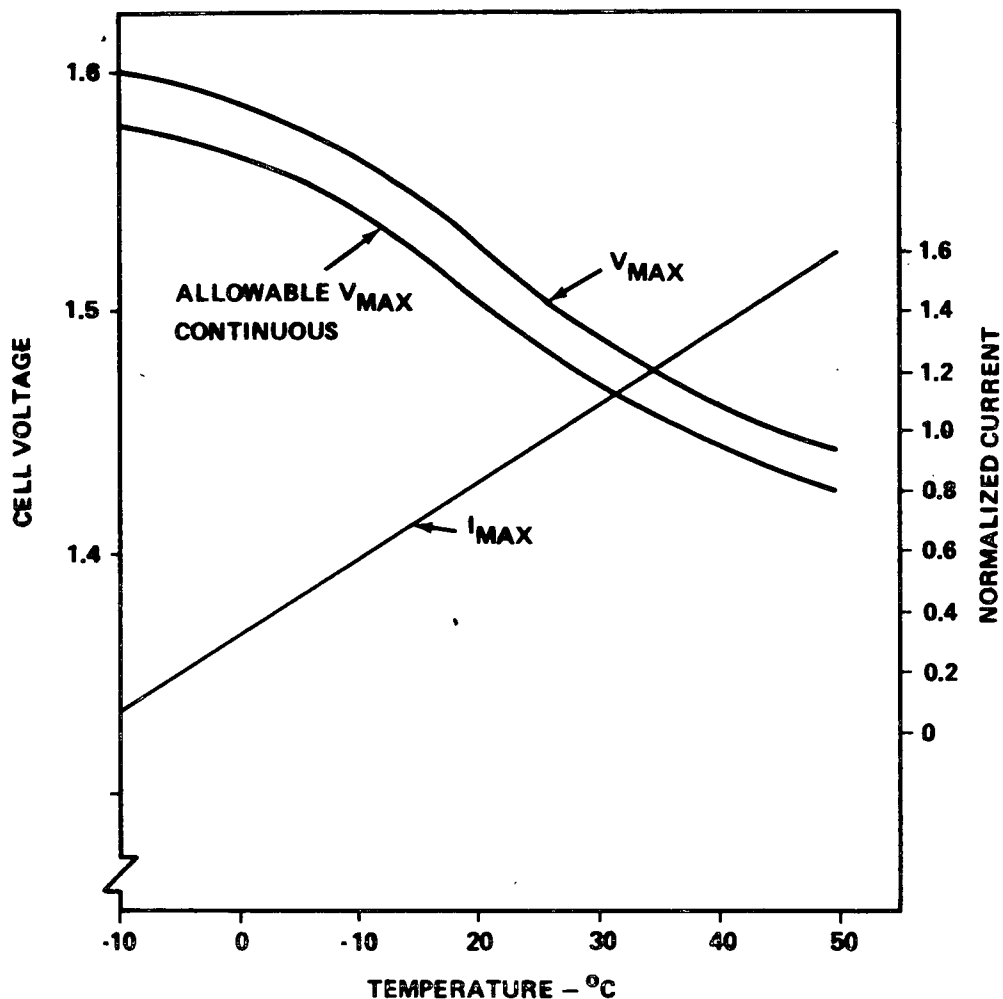


Figure VIII-19. Battery cell charge limits.

in the solar power distributors will indicate the available power to the chargers by charging only to the extent that loads are not "starved." Charge controls will also prorate the available energy to the batteries in accordance with their needs. Sensors are provided to relay unbalanced energy conditions to the ground via the telemetry link. Chargers also permit the use of the high power available from the array when it first emerges from darkness in a cold condition.

Baseline Charger Assembly. The baseline charger assembly incorporates circuitry and controls which provide a temperature modified constant current-constant voltage characteristic at the output. The charger accepts redundant charge reduction or termination-signals from third electrode cells or from the ampere-hour meter installed. Peak power tracking networks

provide controls for avoiding overloads on a limited array. The power handling section of the charger is a nonisolated step-down switching regulator with redundant critical components.

A simplified schematic of the battery charger is shown in Figure VIII-20. A low pass filter section is included in the front of the charger to prevent radio frequency interference (RFI) problems. An output filter capacitor is not necessary since the battery acts as a good output filter; however, the output cables are shielded.

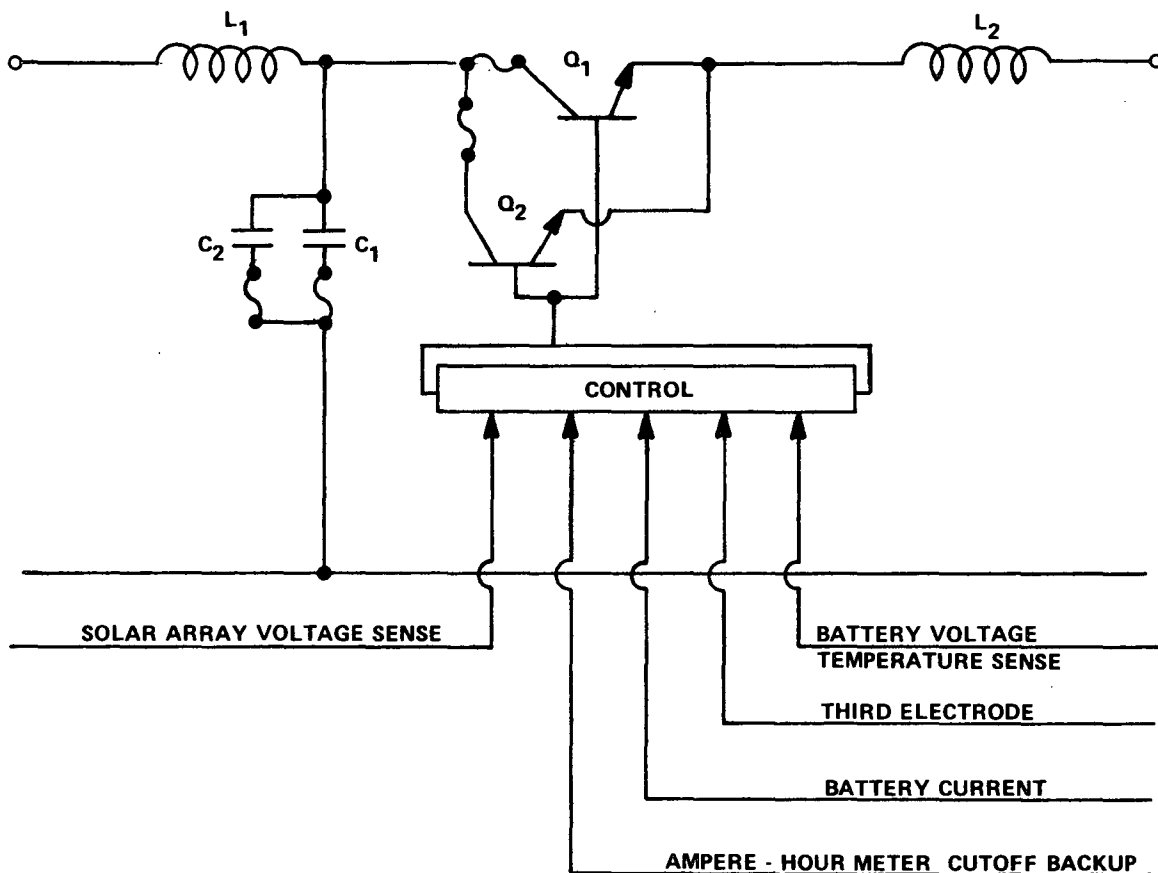


Figure VIII-20. Battery charger simplified diagram.

In Figure VIII-21, the output characteristics of the charger assembly are shown as a function of the control mode in effect. Initial charging is accomplished in a constant current mode. The charger limits the current to a pre-set level less than the 20 ampere rating of a battery. It will continue to operate in this mode unless temperature and third electrode signals modify the charge rate or until battery demands are fulfilled, which is indicated

by voltage and temperature and finally by the third electrode cells. For the case illustrated, where the solar array power becomes limited, peak power tracking information causes the charger to reduce the charge rate in accordance with the available power. Charging continues until voltage-temperature limits are indicated by the battery sensors. The charger then reduces the output by one-half volt which tapers the charge current to a low level. Third electrodes or ampere-hour meters signal charge termination when the battery is fully recharged.

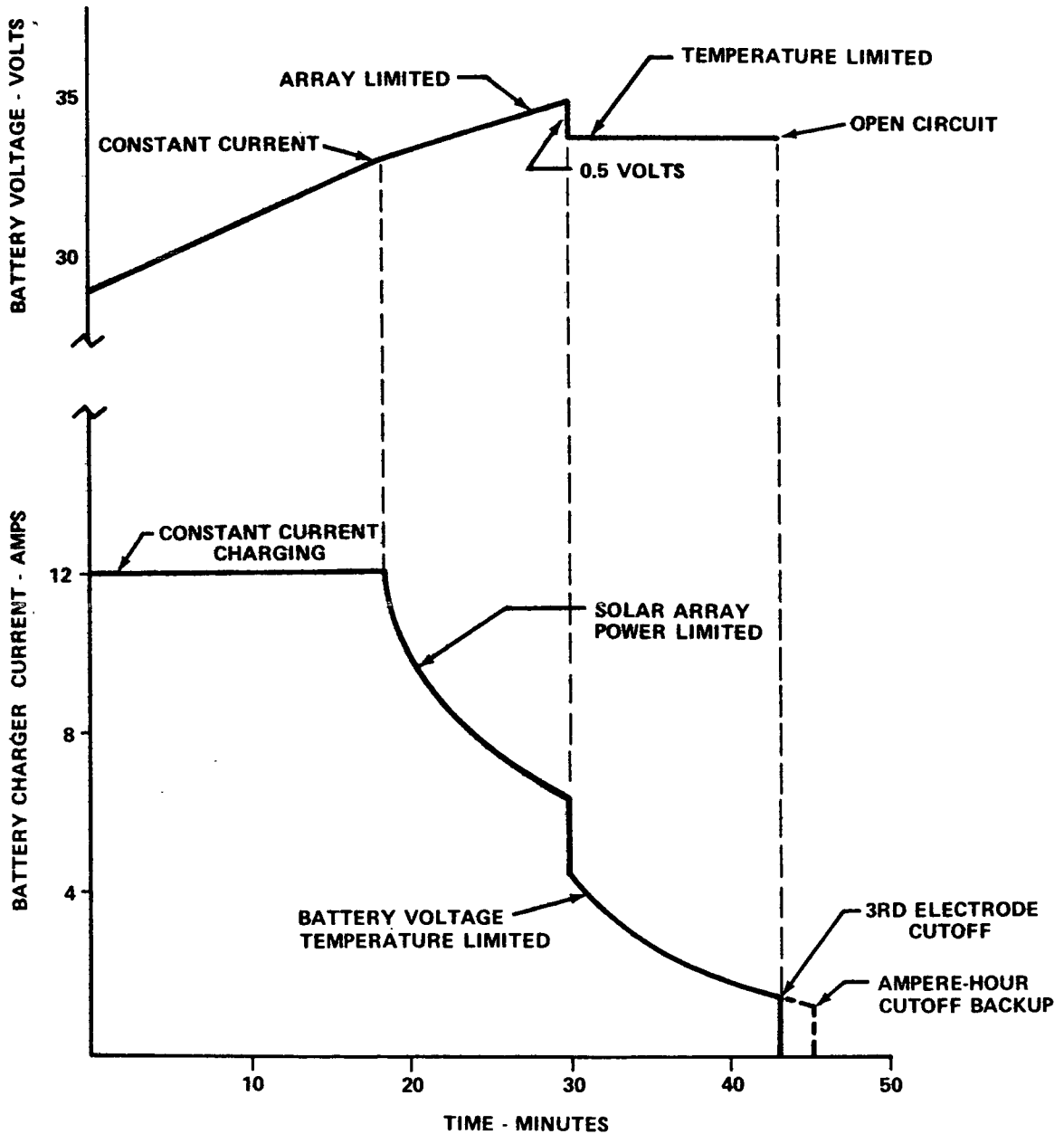


Figure VIII-21. Battery charger operational modes.

Except for the input controls, the isolation, and the filtering, the charger operation is very similar to that of the regulators described under Power Conditioning. Details of circuitry and alternates considered are given in Appendix F.

A summary of the baseline battery charger characteristics is presented in Table VIII-16.

TABLE VIII-16. BATTERY CHARGER CHARACTERISTICS

Input Voltage	
Equipment Rated (Open Circuit)	125 Vdc
Normal from Solar Array	38 to 80 Vdc
Output Current	
Equipment Rated (Short Circuit)	25 A
Normal Operation (Max)	12 A
Input Power (Max)	500 W
Output Voltage	22 to 33 Vdc
Efficiency	95% at Full Load
Thermal Dissipation	25 W Max
Size	11 × 8 × 6 in.
Weight	14 lb
Ambient Temperature Range	-25° C to 100° C

c. Power Conditioning Subsystem

(1) General Description. The electrical system delivers regulated power to the spacecraft loads. The regulation and control of the raw power, between 38 and 80 volts, from the solar array is performed by the power

conditioning subsystem in the EPS. Four converter-regulators, rated at 1800 watts total, will be used in the baseline design: Two are active and two provide redundant backup, or both sets can operate and share the load.

Regulated power is delivered to buses in the (ECAs) for distribution to the various load centers. In normal operation the spacecraft loads are divided between the two regulators. In some modes of operation it may be necessary for the regulators to operate in parallel, with the outputs of several units connected to a common bus. To achieve this type of operation the regulators are designed to share the load, approximately equally with those operating in parallel. Sharing signals, as needed, are derived from bus sensors within the ECA.

Regulated power is delivered to the loads at a 28 Vdc nominal, which is standard in many previous space applications. Regulation is maintained at  $\pm 1$  percent of nominal at the regulator output terminals and  $\pm 2$  percent at the loads. The difference is due to voltage drops in the distribution system.

The power conditioning subsystem is designed to receive power from various combinations of batteries for dark period operations. The input voltage from energy storage will be 24 to 29 Vdc, normally.

The primary and secondary buses which supply input power are located in the two ECAs of the electrical distribution and control subsystem.

The use of output regulators for the HEAO system may be questioned on the basis of efficiency and cost. Accurate, conclusive tradeoff data have not been generated to date; however, it appears that coarsely regulated, shunt controlled approaches will not be much better on an overall system basis. Rationale for selecting the output regulator approach is listed below:

- The regulator is a power matching device, which divorces the design and operational problems of the solar array and battery subsystems from those of distribution and load control. This offers a high degree of flexibility needed early in the program and could actually be a cost saver.

- Regulators provide an inherent overload protection for the critical primary buses.
- The filtered outputs significantly reduce the probability of electromagnetic interference (EMI) problems within the system. Such problems, if discovered late, can incur expensive delays.
- Regulators permit earlier design and fabrication of solar panels. They also allow the use of the high power generated at the beginning of a sunlight period when the array is cold. If this is shunted off it could easily represent a 10 percent loss in the array power available, depending on the array thermal characteristics. For the body-mounted array proposed for HEAO this appears to compensate for the efficiency gained by eliminating regulators.
- Regulators provide better conditions for charge control and eliminate the possibility of large thermal excursions within the spacecraft that could occur from the large voltage swings incurred by the shunt-coarse regulation approach.
- Cost investigations have shown that power conditioning represents only 5 percent to 10 percent of the EPS cost. The arrays are the most expensive hardware. Regulation hardware is probably 1 percent of the cost. Programmatic and contract cost are the biggest ones. Integration costs are next, followed by subsystem design and development. Fabrication and hardware costs are last.

The output rating of the power conditioning subsystem must be equivalent to that given by Table VIII-11, since most of the system power will be channeled through this subsystem.

(2) Baseline Regulator Assembly. Several candidate power regulators which have been developed for space programs have been considered for their ability to meet the Mission C requirements. All units reviewed would require modification to adapt to the design for HEAO-C. The latest designs that appear best suited for HEAO-C were those for the Skylab and for the Apollo Telescope Mount (ATM). The HEAO-C regulators combine subassemblies and basic modules, qualified for both programs, to achieve the characteristics and performance required. These assemblies will have a high, 90 percent, efficiency.

The baseline regulator assembly output rating is 450 watts at 28 Vdc. It is rated and connected into the system so that any two are capable of powering the spacecraft without performance degradation. About 62 percent of the system requirements can be supplied by one regulator assembly. Each regulator assembly has redundant input and outputs so that from one to four may be paralleled, upon command, to redundant primary bus and/or to redundant distribution buses. Since the regulators must be capable of operation from the batteries down to 23 volts and from the solar array up to 78 volts, the baseline equipment has an input rating of 22 to 100 Vdc.

A simplified schematic diagram of the regulator is shown in Figure VIII-22. It consists of power transistors, diodes, capacitors, filters, and control circuits. The fuses indicate redundant, critical components that are protected and self-clearing. Each assembly is current-limiting and provides inherent overload protection for itself and for the power source. Internal and external voltage sensing provisions provide redundancy and permit adaptable regulation characteristics. Voltage-current sensitive controls afford an energized standby capability, i. e., one regulator supplies power, the parallel unit operates unloaded, ready to take over or to absorb unusual peaks. By selection, the same features can accomplish load sharing between regulators, if needed. Heavy filtering of the input and output is provided to assure a "noiseless" system.

Output characteristics of the regulator assembly are illustrated in Figure VIII-23. As the load requires the output power to increase, the voltage gradually decreases from 28.0 volts to 27.5 volts. More precise voltage regulation is easy to obtain; however, some slope to the output voltage characteristic is desirable for stability and load sharing. At a point slightly above 450 watts the output current becomes limited to 16.4 amperes. If an abnormal condition should further increase the load demand, the output current remains constant but the regulator reduces the voltage sharply; thus, in turn it decreases the power delivered. Although not shown, the input current or



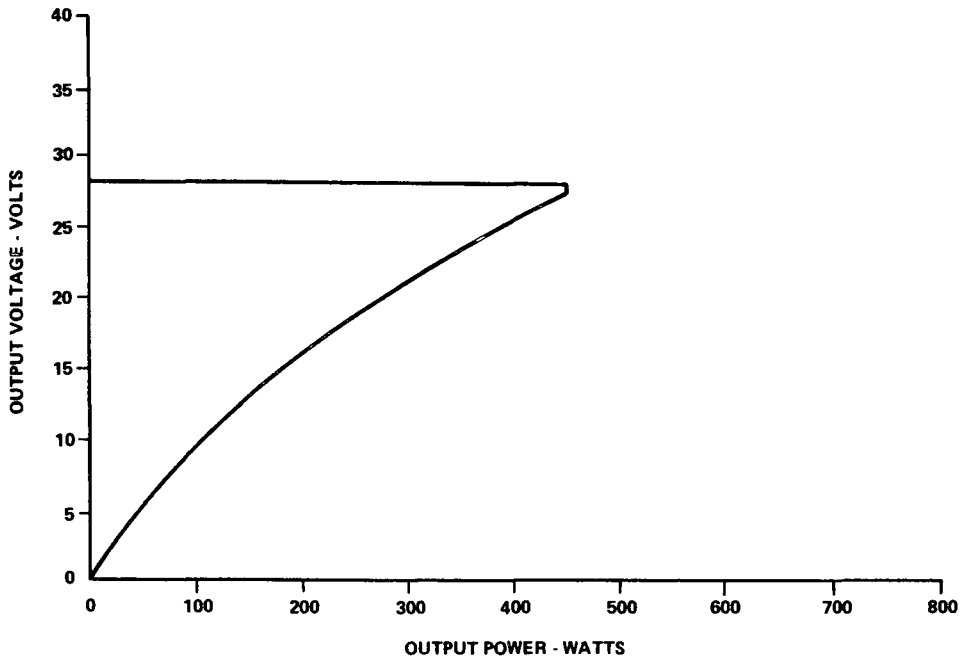
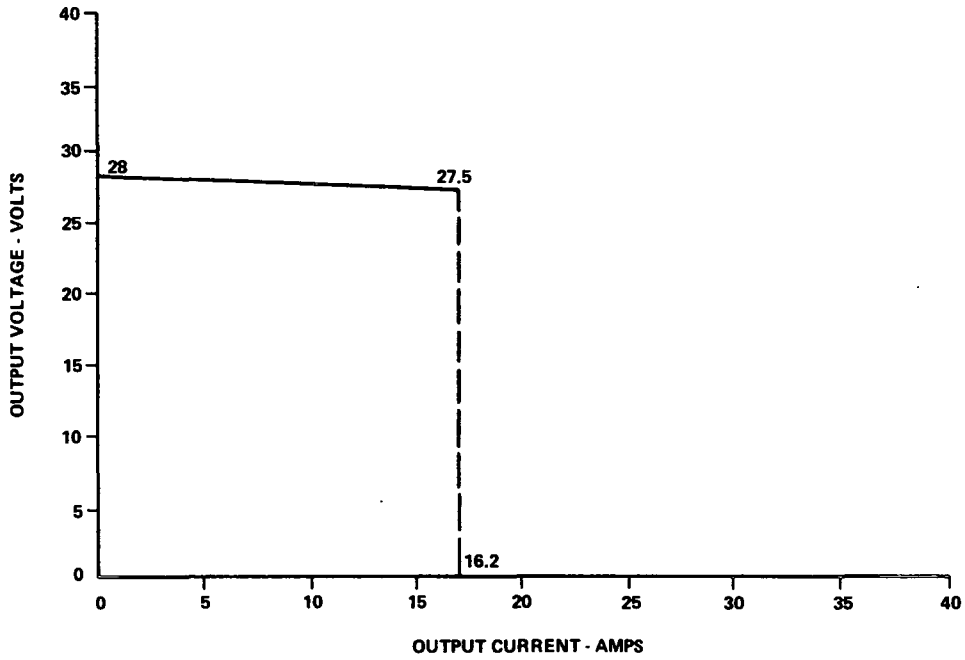


Figure VIII-23. Regulator output characteristics.  
 a. Current-voltage.  
 b. Power-voltage.

TABLE VIII-17. BASELINE REGULATOR  
ASSEMBLY CHARACTERISTICS AND RATING

Input Voltage (Equipment Rating)	22-100 Vdc
Normal From Batteries	24-29 Vdc
From Solar Array	38-80 Vdc
Voltage Slope	0.03 V/A
Output Power	0 to 450 W
Efficiency	90% Min at Full load
Assembly Size	11 × 8 × 5 in.
Assembly Weight	8 lb
Thermal Dissipation	
Maximum Ambient Temperature	100° C

d. Equipment Location. Thermal characteristics, equipment relationships, and cable lengths and weights have been considered in locating EPS equipment within the spacecraft. The location of all the major electrical system assemblies is shown by the isometric illustration of the spacecraft in Figure VIII-24. Thermal dissipation requirements for power handling assemblies are accommodated by locating them on the side of the spacecraft normally pointed away from the sun. To avoid thermal interaction with scientific equipment and to provide the close ( $10 \pm 5^\circ$ ) temperature control for the batteries, the battery chargers, and regulator assemblies are located in a temperature controlled compartment isolated from the rest of the spacecraft.

The equipment is centrally located for easy access and short cable runs to the solar array and to the various parts of the spacecraft requiring electrical service. The EPS assemblies are located close to subsystem electronics and to major loads. Charger and battery assemblies are closely located, as illustrated. Since the batteries and regulators deliver power to

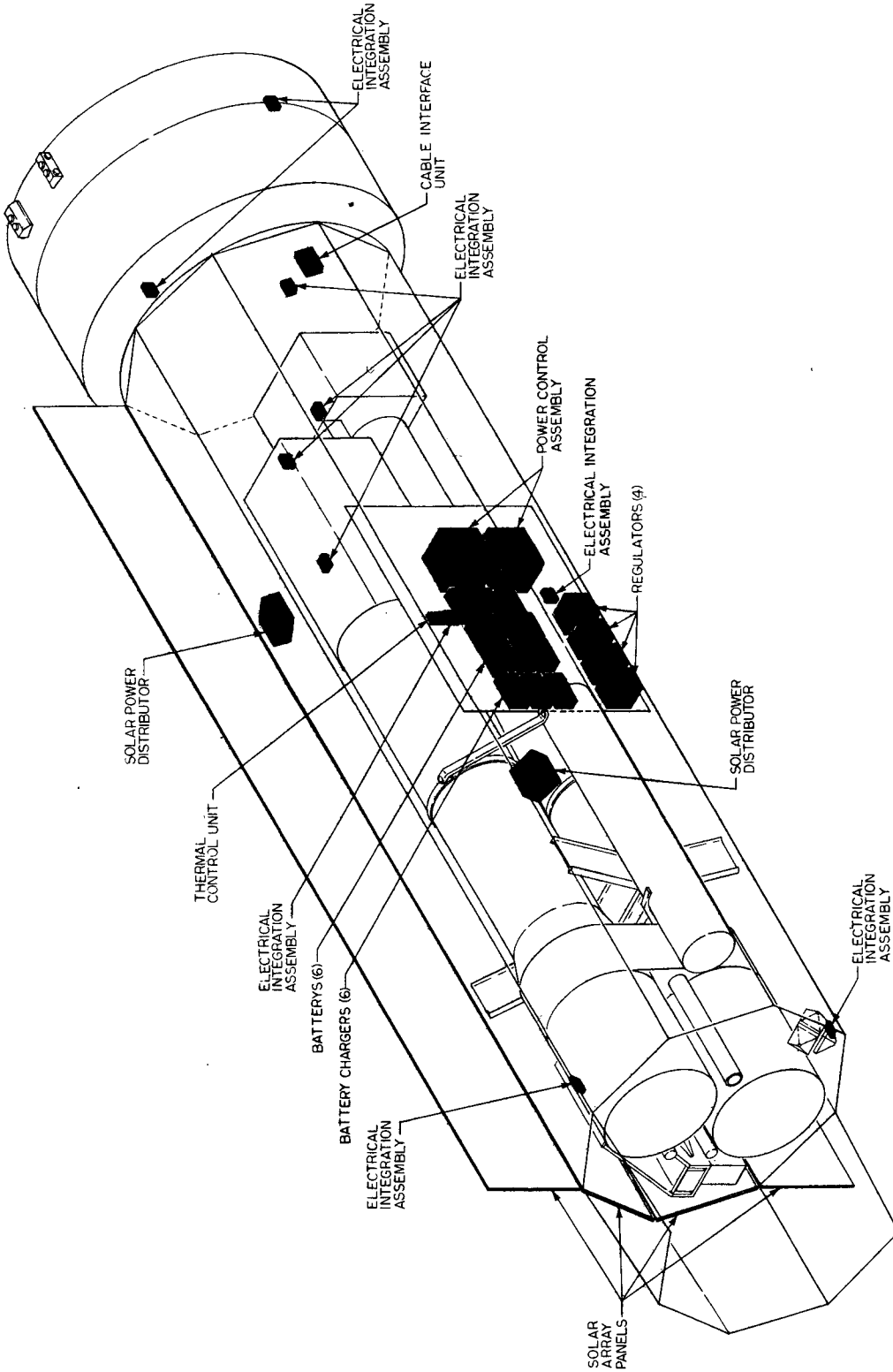


Figure VIII-24. Electrical system assembly locations.

the electrical control assemblies of the EDCS, these assemblies are near each other.

2. Electrical Distribution and Control Subsystem. Electrical integration of the various components and systems in the spacecraft is accomplished by the EDCS. This subsystem provides the means for controlling and distributing the power to the loads, monitoring and protecting the operation of the EPS, and interfacing the payload with the Orbit Adjust Stage (OAS) and the ground electrical support equipment. It specifies all cabling within the system and implements, automatically or from command, pyrotechnic operations.

The elementary electrical system schematic, Figure VIII-25, shows detailed concepts for electrical control, switching, and distribution within the spacecraft. This schematic is condensed to exclude repetitious detail but illustrates unique functional schemes employed in the baseline. The electrical system has 100 percent redundancy of major assemblies except for the solar panels and the battery capacity for 15 percent DOD. Solar panel and battery designs are conservatively designed for two year mission reliability. Additional redundancy and derating of critical components within the assemblies are also provided to insure highly reliable system performance. Modularization, assembly arrangement, and cable routing provide physical redundancy as well as electrical. Thus, propagation of a given fault into the backup system is avoided.

The system is divided into two major parts — each part (except solar array) is capable of operating the spacecraft. Further subdivision of power buses and equipment together with the cross coupling provided at essential points allow for fault isolation and bypasses at the subassembly level and provide more than parallel redundancy for essential secondary and critical primary power access. System operation and features are also described in Figure VIII-25 and the functions of the major assemblies are explained.

a. Transmission. The power generated by the solar array is brought into the spacecraft by eight separate transmission cables, one for each of the array panels. The cables are connected to the two redundant solar power distributors within the spacecraft. Within each cable are separate positive and negative power conductors for each of the 10 solar cell assemblies located on each panel. Additional conductors are provided within each cable to allow for four 3-wire temperature sensors on a panel. To avoid long transmission cable runs to provide easy access, the solar power distributors are located on the solar array side of the vehicle as indicated by Figure VIII-24. They are

about 90 degrees apart (about x-axis) and are centrally located to provide short cable routes (about 10 feet) for further transmission of primary power to the ECAs and to the battery charger assemblies that are centrally located on the opposite side of the spacecraft. For the equipment locations shown, the typical length of the solar array cables is 15 feet. Conductors were sized to limit voltage drops to 0.4 volt maximum. Qualified cables and connectors rated for 600 volts and 200° C temperature are used for transmission.

b. Solar Power Distributors. Each of the two solar power distributors receives power from four solar panels — three wing panels and one body-mounted panel. However, each is designed to handle full spacecraft power and has growth capacity to service six array panels. The major functions performed by the solar power distributors are the following:

- Combine the outputs of the solar panel modules into common primary power buses.
- Route solar power to the battery chargers and to the power regulators. (Also may be used to distribute unregulated power if it is utilized in the spacecraft.)
- Distribute power from electrical support equipment to the battery chargers during ground checkout.
- Perform the switching functions necessary for routing power around a fault in the solar panels or the distributors themselves.
- Provide a means of monitoring solar array voltages and currents for telemetry and fault detection.
- Provide a convenient access point for testing and checkout of the solar array using Dark I-V test methods.
- Provide pyrotechnic firing circuits for the solar wing deployment squibs.
- Provide for interconnection of pyro buses with those in the OAS pyro junction box.

Because the solar power distributors have not been defined in previous HEAO studies, details of the assembly concepts and circuitry are shown by the solar power distributor schematic diagram of Figure VIII-26. The diagram has been simplified for explanation purposes; for instance, the inputs from diode modules 2, 3, and 4 are shown as single lines although they are equivalent to module No. 1.

Each solar panel cable interfaces with a blocking diode module which is a subassembly of the distributor. The number of blocking diode modules used will equal the number of solar panels serviced. Although printed cabling would be preferred for reasons of size, configuration, and decreased contacts needed, the input module design was selected to be consistent with the requirement to use proven standard cable connectors. Like all connectors selected for the solar distributor, the input connector conforms to MSFC SPEC-40M39569.

Each diode module accommodates 20 power conductors (equivalent to the 10 solar assemblies per panel) and 12 pins are provided for array temperature instrumentation. The modular design permits easy adaptation to solar array size and also provides a good thermal package for the 20 blocking diodes housed in the module. It may be noted that the blocking diodes are parallel redundant and that they are located in the negative leg of the solar cell assembly. This arrangement was chosen to enhance the reliability. Since the diode voltage is less than 1 volt the voltage stress and insulation requirements are very low. Several diodes would have to be shorted before noticeable performance changes would occur and this would not be catastrophic. As they are placed, even a short to ground at the diode changes the voltage on that particular solar cell assembly by only about 0.8 volt. Most of that string's power is still available. Comparing the same failure mode for an arrangement where the diodes were located in the positive leg would show a drastic difference. A diode short to ground in that case could wipe out an entire panel or even a primary bus if the fault was not cleared.

Power switches and relays, designated by the letter "K" on the diagram, are in general the magnetic latching type to conserve control power. Bifilar wound types were selected to minimize system switching transients. All relays are qualified and conform to MSFC SPEC-40M37496.

Solar array power received through the blocking diodes is accumulated at the primary buses in the solar power distributors. Switches K-1 through K-4 permit the selection of the primary bus, 1P11 or 1P12, to which a given panel input is to be applied. This allows half of the system to

operate from two isolated buses or from one bus with the other in standby. These switches also serve as backup fault protection for the sources, the current being reduced to levels that are more easily cleared than at the full bus level. The inputs to K-1 through K-4 are segmented into two parts to assure that the contacts operate at conservative current, about 3.5 amperes maximum compared to the 10 ampere rating. All contacts will be redundant.

K-5 provides a bus tie permitting half the system to operate in a single bus mode. This switch controls power channeled to the second solar power distributor via 1P12 should the loads be unbalanced, or in the event that a source failure occurs. Should the situation be reversed, K-6 is closed to take power from the other distributor. Normally K-5 and K-6 will be open and bus 1P12 will serve as a backup or transfer bus.

Redundant contacts are used to furnish power to the distribution buses located in the ECAs. Switches K-7 and K-8 permit the ECA No. 1 to be powered from either of the primary buses. Alternate primary outputs, controlled by K-9 and K-10 will sustain the loads through ECA No. 2 should both of the primary outputs of solar distributor No. 2, or should ECA No. 1, become faulty.

Relays K-11, K-12, and K-13 control power to battery chargers 1 through 3. Redundant charger outputs are controlled by K-14, K-15, and K-16. In addition, a third primary power channel is provided for battery chargers by K-5 or K-6 which couple the buses between distributors.

The primary output channels to ECA No. 1 and to chargers 1, 2, and 3 have automatic overload protection. Signals derived from command inputs are required to switch buses and operational modes. Sufficient protection and redundancy is provided throughout the system to assure primary bus integrity. Thus, overload protection of the redundant outputs to the prime loads is not provided to avoid possible malfunction of protection devices. Similarly, backup buses for the alternate loads, such as ECA No. 2, are not overload protected. Protection within the ECAs is adequate for the alternate primary sources.

Input cables for control are separate from power cables. Each solar distributor may receive control signals from either of the electrical control assemblies. Automatic and commanded signals originating in the ECAs perform fault isolation, operating mode selection, and power management functions.

FOLDOUT FRAME 1

FOLDOUT FRAME 2

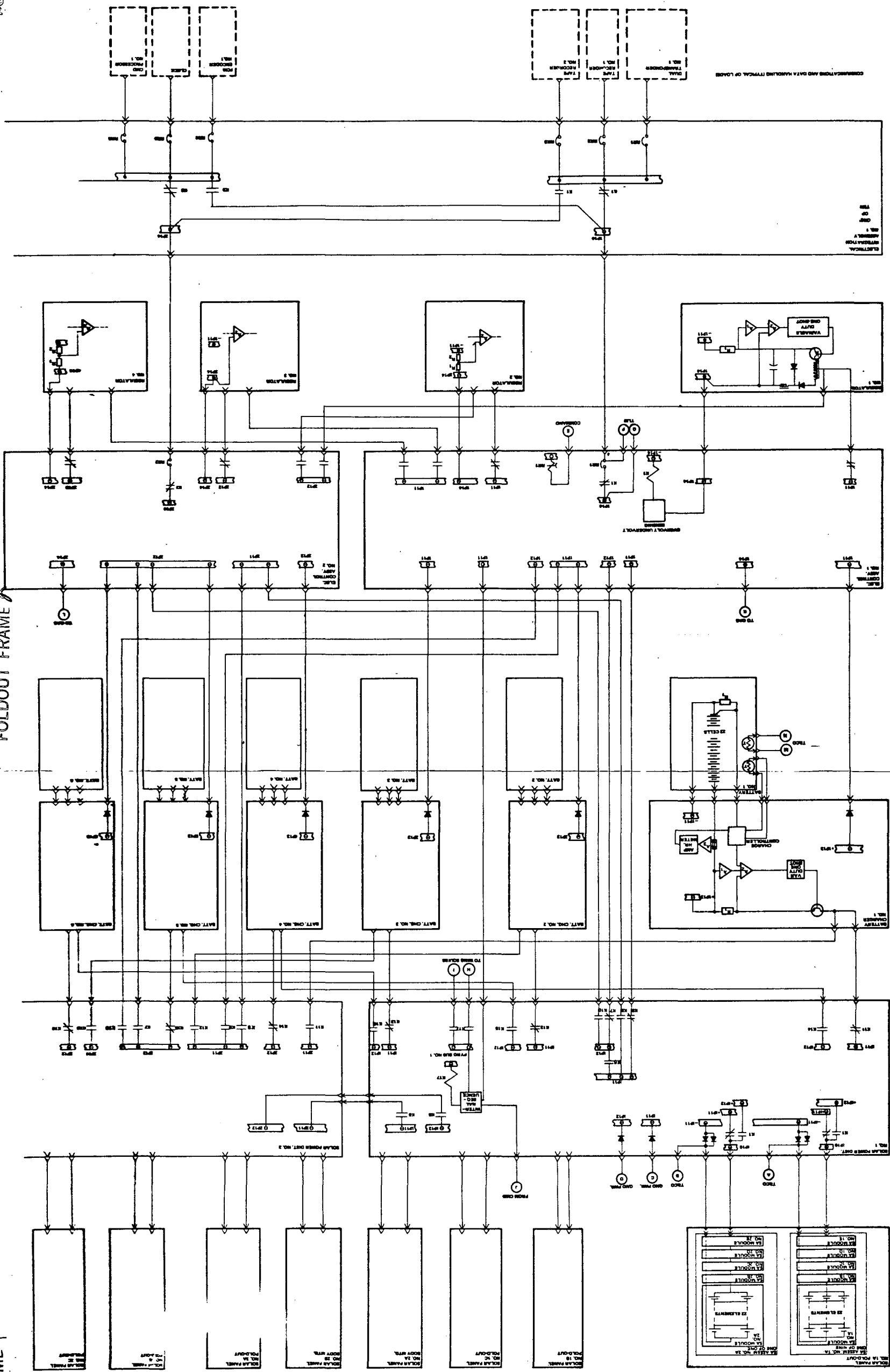


Figure VIII-25. Electrical system simplified diagram.

FOLDOUT FRAME 1

FOLDOUT FRAME 2

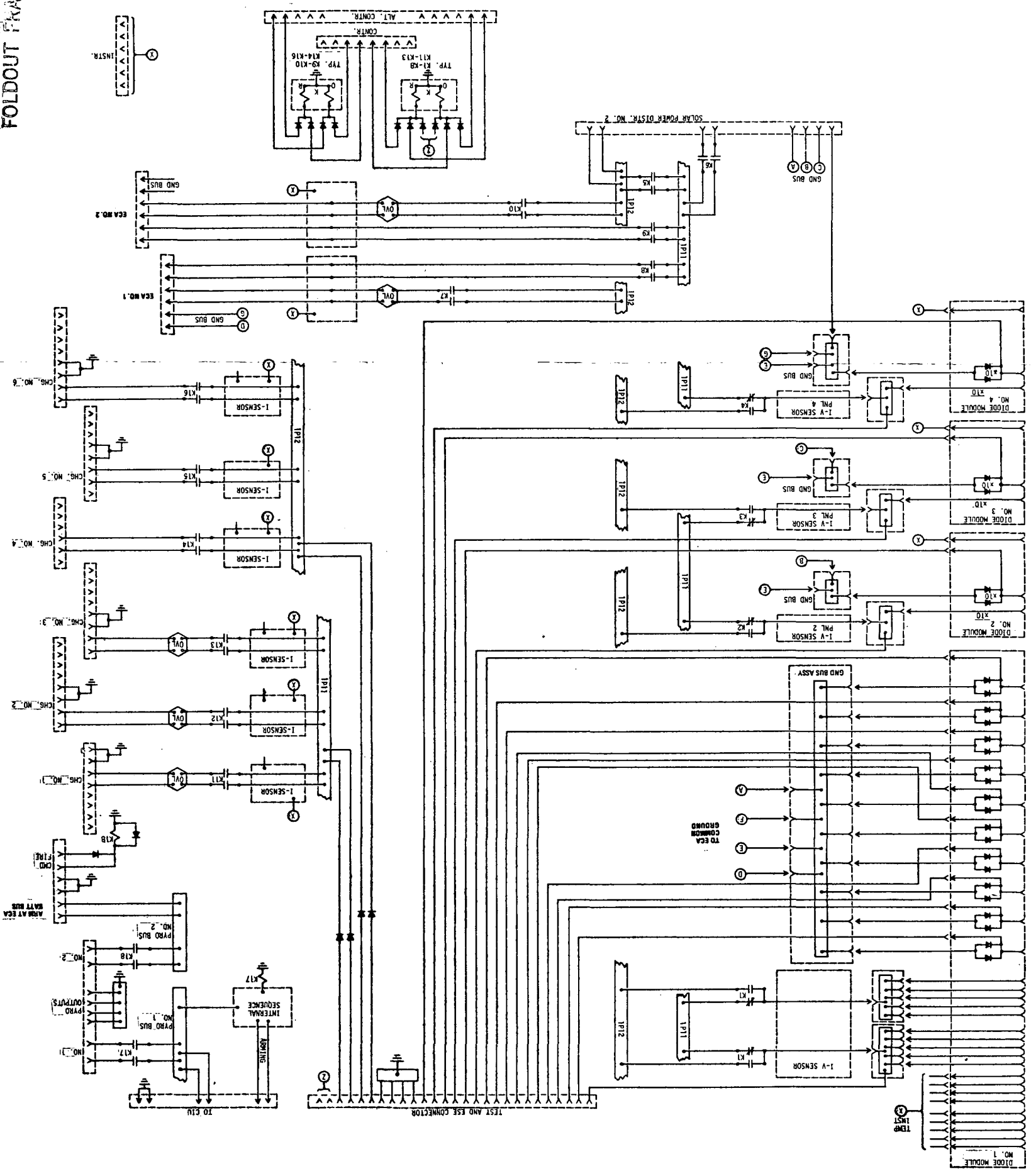


Figure VIII-26. Solar power distributor simplified diagram.

Command signals for critical functions, such a pyrotechnic operation or fault protection overrides, are routed directly to each of the solar power distributors, separately. Instrumentation outputs are routed to the ECAs or to ESE channels as required.

The ESE and test connector shown is cabled to the cable interface unit (CIU) provided on the spacecraft for system testing and for control and checkout from the launch site ESE. Ground power which simulates the solar array is furnished to operate the EPS or to charge batteries while on the ground. This connector accommodates hardwire control signals to operate the power bus switches and the critical power control sensors required for power management.

The test connector, in conjunction with switches K-1 through K-5, provide the capability for testing the solar array integrity and approximate performance while the spacecraft is on the launch vehicle. The Dark I-V Method, discussed in Section C. 4, is used to perform such tests. Voltage from ground power supplies, having characteristics similar to the solar array, is supplied to the terminals of each solar cell assembly on the solar panels. In sequence, connections are made to the terminals by-passing the blocking diodes. This permits the reverse current characteristics of each solar cell assembly on each panel to be recorded. Switches must be operated to isolate all system loads from the solar panel during these tests. Otherwise, erroneous data would be obtained due to load drain.

The pyrotechnic bus provisions are discussed in Section C. 2. e.

The conceptual design of the solar power distributor is illustrated in Figure VIII-27. Separate input and output subassemblies are used for thermal and modularization reasons. The subassemblies are constructed from component modules, printed circuit cards, terminal junction assemblies, and connectors. Connectors, printed boards, and junction assemblies within the baseplate provide interconnections for subassemblies and modules. The characteristics and ratings of the solar power distributor are summarized in Table VIII-18.

c. Electrical Control Assemblies. The ECAs are the heart of the electrical system since they control the major electrical interfaces internally and with other subsystems. The ECAs control operational and power outputs and provide the location for common grounding of the systems.

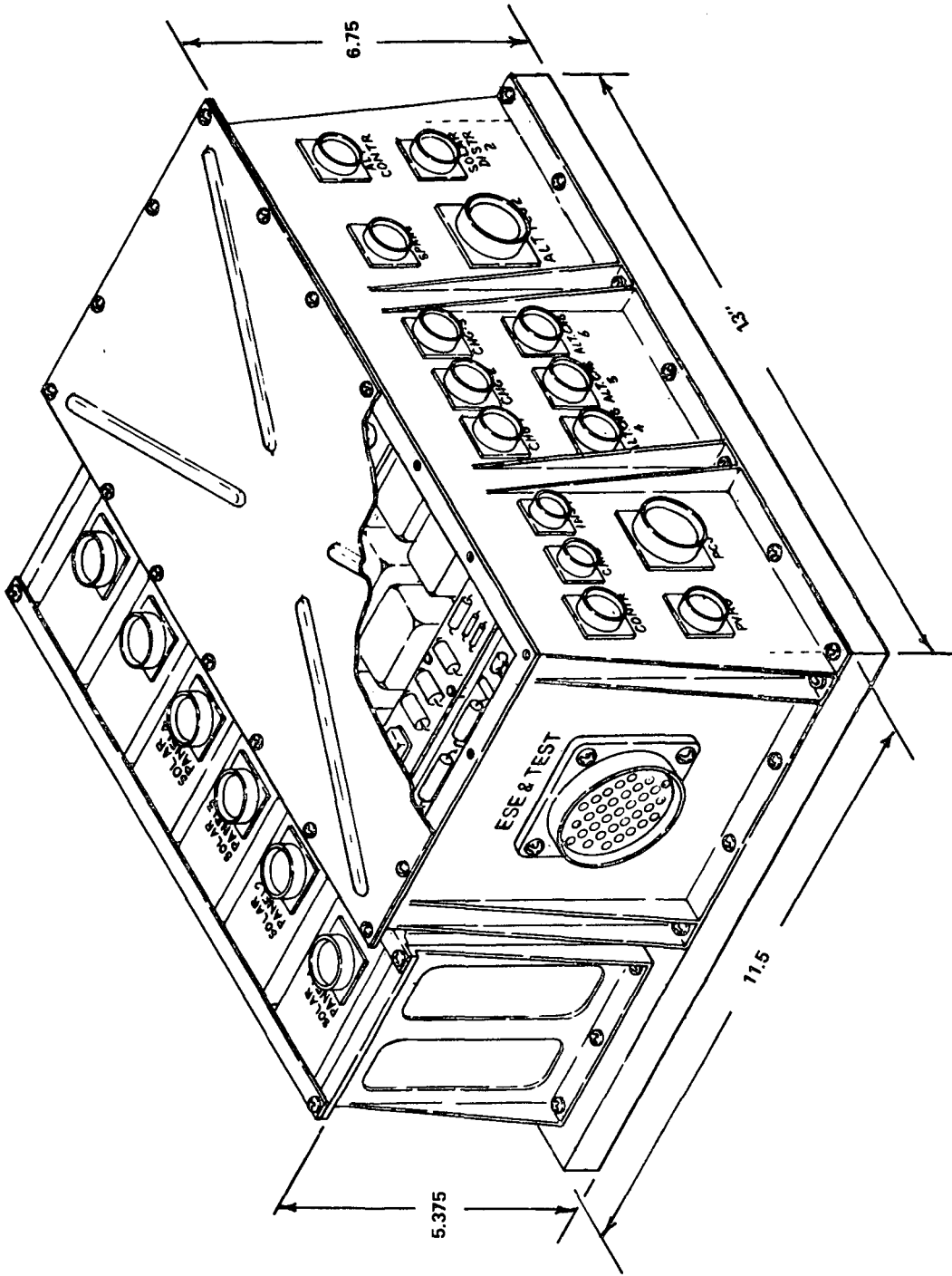


Figure VIII-27. Solar power distributor assembly.

TABLE VIII-18. SOLAR POWER  
DISTRIBUTOR CHARACTERISTICS AND RATINGS

<u>Physical</u>	
Weight	18 lb
Max Dimensions	13 × 11.5 × 6.75 in.
Volume	794 in. <sup>3</sup>
Thermal Dissipation	
Sunlight Period	34.1 W
Dark Period	2 W
Orbit Avg.	21 W
Operation Temp.	-65° to 85° C
Max Vibration	30 g to 2 KH <sub>z</sub>
<u>Electrical</u>	
Baseline Ratings:	
Inputs	34
Power (Ea.)	27.2 W
Max Current (Ea.)	0.75 A
Max Voltage	78 Vdc
Total Power	925 W
Outputs	4 Redundant
Total Power	925 W
Nom. Voltage	40 Vdc
Min Insulation	250 V at 200° C
Maximum Ratings	
Capacity	60 Inputs
Power	2400 W
Voltage	125 Vdc

Reference to Figure VIII-25 indicates that the distribution and management of regulated and secondary power in the spacecraft is performed at a subsystem level by the electrical control assemblies. These units incorporate the regulated power buses and switching devices that are necessary to interface the power system with the distribution subsystems and the using loads in the spacecraft. Each of the assemblies has provisions for receiving primary power from either of the solar power distributors. Redundant primary buses within each ECA are sources for two of the four regulators. The backup bus may receive power from the alternate solar distributor primary bus or may be used to transfer power to the other two regulators via ECA No. 2.

Redundant battery buses are also included in each ECA to receive power from three of the six batteries. Power from each battery is routed through its respective charger to the ECAs. The second bus permits one or all batteries connected to ECA No. 1 to be crosscoupled to the regulators and loads on ECA No. 2. The redundant battery bus is also used to obtain the necessary parallel configuration to supply the backup pyro bus.

Each ECA provides redundant sources of unregulated, primary power and battery power for two voltage regulators and possibly some unregulated loads. The regulated outputs of the regulators are routed back to the main or backup regulated bus within each ECA.

In the normal operating mode, each ECA supports half of the system from its main regulated bus. One regulator per ECA is operating; the other is in standby. Unregulated, primary power from one solar distributor and power from three batteries in parallel are provided from one of the redundant buses to the operating regulator. In the event of a system or load fault the faulty equipment will be automatically isolated. The redundant features permit alternate operating modes to bypass uncleared faults. For example, any two of the regulators, operating separately or in parallel, will support the spacecraft loads. Switching of battery outputs and regulator inputs allows any regulator to be powered from any battery or various parallel combinations of batteries. The bus to which a given battery is connected is selected within the ECA.

The signal condition, logic networks, and implementation devices required for most of the electrical system operations are located in the ECAs. The primary interface between the electrical system and the command and instrumentation subsystems is also accommodated through the ECAs. Diagnosis of the system performance and status may be accomplished on the ground and selection of operating modes for power management can be initiated

through the command link. Critical switching is resettable so that automatic functions may be overridden by ground command.

Output power from each ECA is normally directed to five remote electrical integration assemblies (EIAs) where secondary distribution buses are established for the various subsystems and experiments. The main distribution is controlled and protected within the ECA. Provisions are made to supply certain special loads or equipment critical to mission success directly from the ECAs. Examples of such loads are (1) back-up pyro bus, (2) command receivers, and (3) transmitters.

Major protection features incorporated in the ECAs are over-voltage protection of loads, protection of power sources from overloads or short circuits in distribution, low voltage protection of batteries, and reverse current protection for primary and secondary power equipment. The detectors and isolation switching associated with these protective features, as well as the instrumentation that informs the ground of operational status, is located in the ECAs.

Additional interfaces and functions are accomplished by the ECA. The battery and regulator instrumentation for operational monitoring in orbit is routed through the ECA to the telemetry subsystem. Similar sensors required for prelaunch operation is routed through the ECA to spacecraft provisions for ESE connection. Ground power and control signals from ESE are directed into the ECAs to permit operation and checkout of the spacecraft during prelaunch.

The ECA assembly concept is illustrated by Figure VIII-28. Standard network connectors are used for external cable interfaces. Protective devices, sensors, logic circuitry, and small distribution switches are mounted on printed circuit cards; this provides a versatile, modular assembly. Modular power switch and junction subassemblies provide flexible interconnection, busing, and grounding arrangements within the assembly.

d. Electrical Integration Assemblies. Ten EIAs have been estimated for the electrical system baseline. As shown by the layout diagram, Figure VIII-24, these assemblies are strategically distributed throughout the spacecraft so that each is located at the load equipment which it primarily services.

Design for specific interfaces and secondary distribution is beyond the scope of Phase A studies; therefore, the specific functions and interfaces of each EIA were not defined. However, to size and conceptually complete the



alternate ECA, are provided for each subsystem or experiment group having redundant equipment or input power channels.

Each EIA provides a local interface with the command and data handling subsystems for operational control of the individual loads and for redundancy mode switching. Control and instrumentation lines are routed from the ECAs to the EIAs for those loads requiring hardware control and monitoring from the electrical support equipment. The EIA design provides for incorporation of small special power supplies, such as measuring voltage or isolated precise regulators, as required.

Sensors and logic contained within each EIA provide load fault isolation for distribution protection. Low voltage at the load enables the alternate power input from the same EIA. Should a load fault and low voltage persist, the load will be isolated and telemetry information generated to indicate the situation to the ground. Redundant loads and the redundant EIA may, then, be enabled via the command link. The simplified schematic shown in Figure VIII-29 illustrates the protection and fault isolation concept using latching relays for control (some of these may be replaced with semiconductor switches.) The operate command energizes K-1<sub>(0)</sub> and switch K-1 latches in the closed position shown. Power from Bus No. 1 is furnished to the load over one of the redundant lines and the voltage detector is energized by switch K-3. The voltage detector senses the voltage of the load over the alternate line connected to the load. Low voltage at the load will cause the detector to operate K-2, thereby, providing power from the backup source, Bus No. 2.

Starting with the load operating from Bus No. 1 and the switches in the position shown, assume that an overload fault occurs in the load. The overload detector will signal the reset coil of K-1 to open the switch and isolate the load. Since the voltage detector remains energized because K-3 is latched closed, the low voltage will be detected. The input of the detector will close K-2 providing power again to the load. If the fault has not cleared, after a short delay the fuse will isolate the load. The status of the switching can be relayed to the ground by detecting the proper combinations of switch positions. An "OFF" command opens switches K-1, K-2, and K-3. Switch K-4 is provided only in the backup EIA. It permits overriding the overload device by commands from ground. This provision also guards against a faulty overload device. Only one override command signal and one reset is needed for a given subsystem.

Local access to the system common ground, cable shield grounding, and the capability for adding filter modules are provided by the EIA to assure that conducted and radiated EMI problems are avoided. All power switches

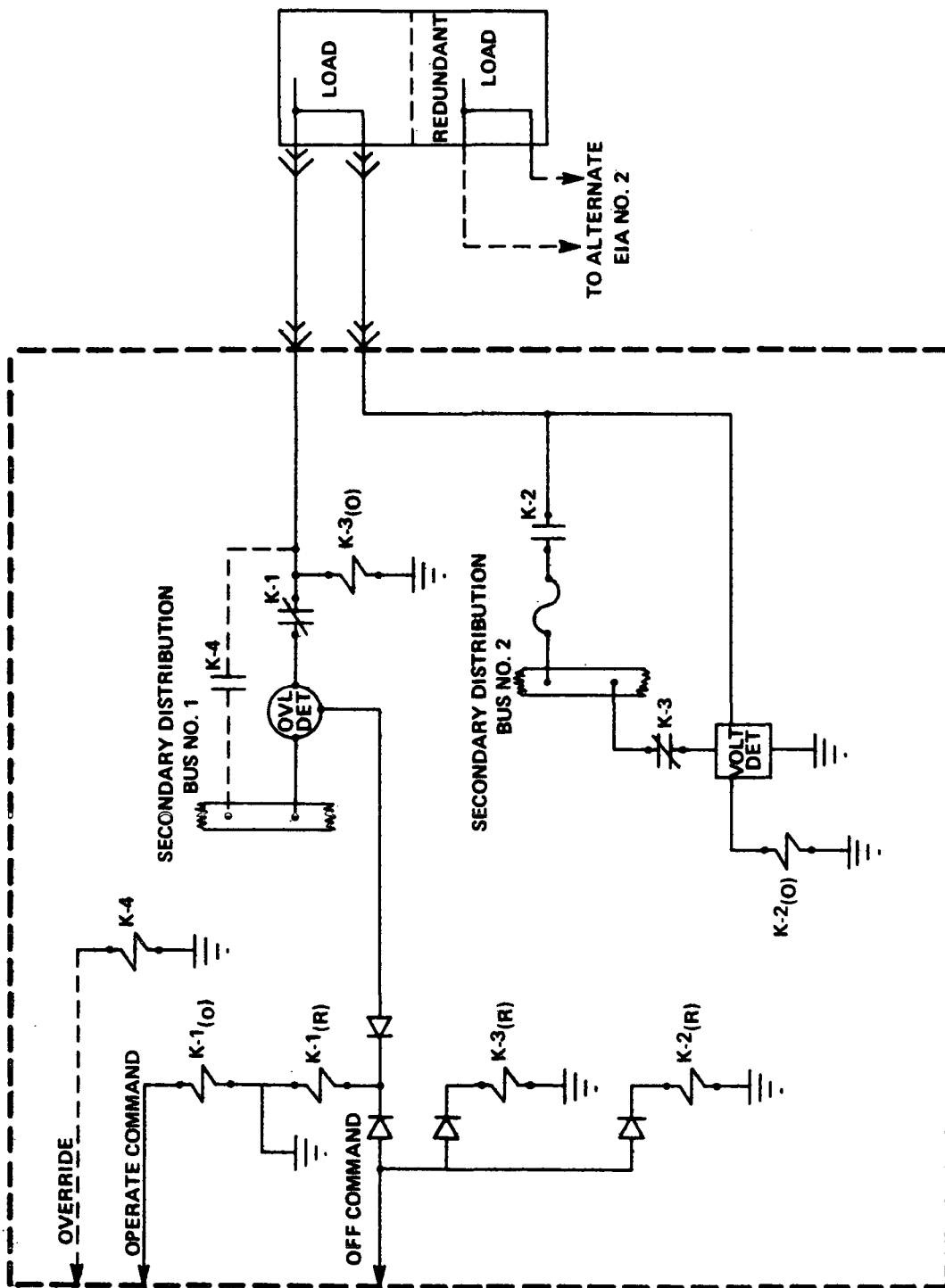


Figure VIII-29. Fault protection in EIA.

will have transient suppression features on the inputs. Arc suppression on the outputs is provided only as needed.

The electrical integration assemblies are composed of an input subassembly and an output subassembly as illustrated in Figure VIII-30. Each subassembly is modularly constructed to provide the necessary electrical flexibility without changing the physical design of the subassemblies. Input assemblies are designed to present a common interface to the main distribution subsystem. With several subassembly models, all the system interfaces can be accommodated. The adaptations are made within these subassemblies, thereby, not imposing system changes.

Additional versatility is provided by the baseline system. Each ECA has spare capacity to service several additional EIAs if needed. Should it be advantageous for a given subsystem to interface with only one assembly, the same redundancy features can be offered by providing the necessary physical isolation of subassemblies upon assembly. Thus, a dual EIA can be provided that has two input subassemblies and two or more output subassemblies. Standard miniature, circular connectors are used on the input subassemblies. Various types of qualified circular and rectangular connectors are available for the output subassemblies to satisfy specific equipment interfaces.

e. Pyrotechnic Subsystem. The mission success is critically dependent on several, high energy mechanical operations — ejection of the vehicle shrouds, separation of the OAS and spacecraft from the booster, deployment of the solar array, and possibly, enablement of spacecraft propulsion. These operations are initiated by pyrotechnic devices designed for redundancy and protection against hazardous conditions. High surge power for short time intervals is required to initiate the pyrotechnic functions.

The electrical system has special redundancy and safety features to maintain the integrity and to assure successful operation of pyrotechnic mechanisms. Redundant pyrotechnic devices are used to implement each function. Each device has redundant, electrically isolated, initiators or squibs that can ignite the power train. The system provides two isolated power sources for initiating pyro devices. One initiator of each device will receive power from the primary pyro source, the redundant initiators are powered from the backup pyro source.

The shroud ejection and separation from booster functions (also propulsion functions if required) are implemented by the pyro junction box

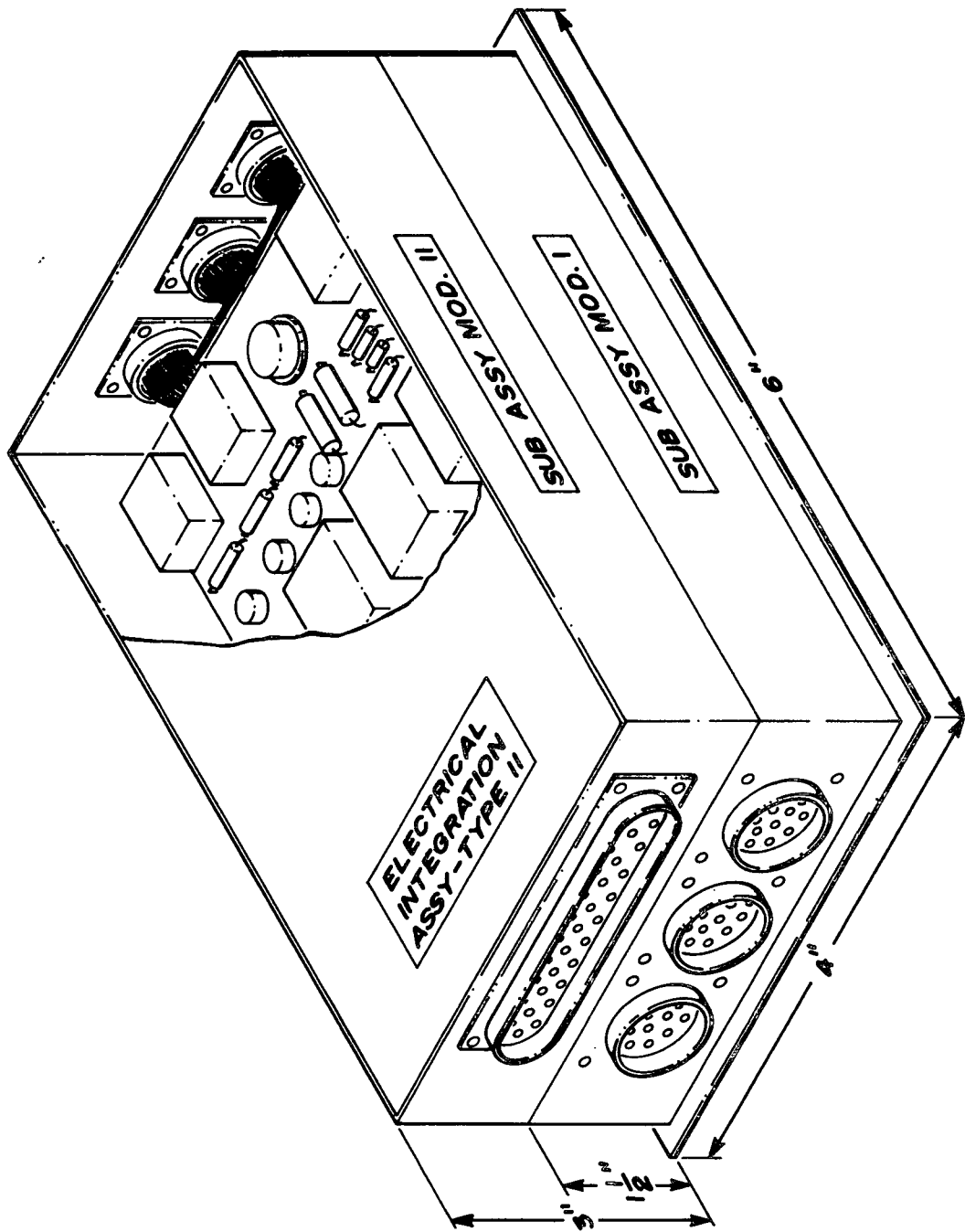


Figure VIII-30. Electrical integration assembly.

provided in the OAS. This assembly has been designed specifically for Titan-OAS operations and interfaces. It contains the required protection, interlocks, and arming features as well as redundant buses for pyro power. Arming and firing signals are received from the booster for the ejection and separation functions. Redundant arming and firing commands are provided from the HEAO spacecraft.

The primary power source is a silver-zinc battery, Type 31, designed for OAS pyrotechnic requirements. The spacecraft batteries are the backup source. Separate, shielded cables are used to interconnect the two pyro buses in the OAS pyro junction box with the redundant pyro buses located in each of the solar power distributors (see Figure VIII-26). The cabling is redundant because there are two solar power distributors. The primary pyro buses in the solar power distributors are energized by the primary battery in the OAS. Upon command, the backup pyro buses in both distributors and in the pyro junction box are energized from the secondary, spacecraft batteries via the special bus switching provided in the ECAs.

Solar array deployment is armed by separation. Firing is initiated by onboard timers. The redundant system is completely separate. It is armed and initiated by signals from the spacecraft command subsystem.

f. Cabling and Grounding. To meet the reliability and system requirements, the baseline electrical system provides physically and electrically redundant cabling. The application requires various types of conductor arrangements and cabling assemblies. Both shielded and unshielded conductors and cable assemblies will be needed. Twisted pairs are anticipated for various EPS cables; coaxial cables are required for radio frequency (RF) signals. The system requirements given in Appendix F specify shielding and grounding requirements necessary to avoid EMI and to assure reliable system performance.

Briefly, a single point grounding scheme has been established for the distribution of power and associated signals. Therefore, a negative return line is required for every load receiving 28 Vdc power. Return lines will be routed through EIAs to the ECAs where common point grounding is accomplished. To avoid undue hardships on experiment and equipment designers and to eliminate unnecessary ground wires, local structure grounding and shielding schemes have been devised for equipment operating from dc, isolated power supplies at their input. Figure VIII-31 shows shows three configurations of subsystems where structure grounding to vehicle ground points (VGPs) satisfy system requirements. With proper bonding techniques, all equipment enclosures are grounded to the vehicle structure at the point of mounting.

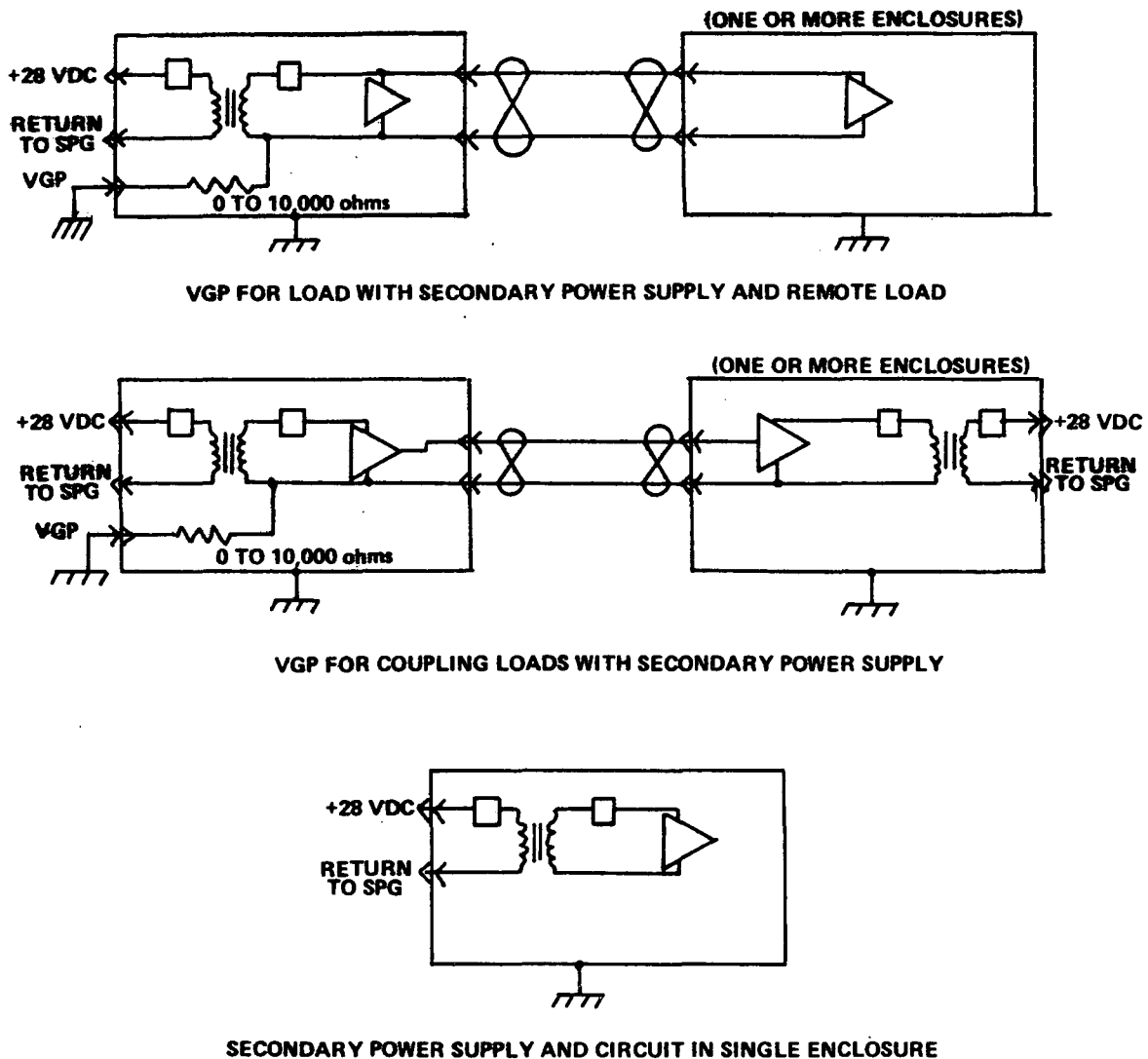
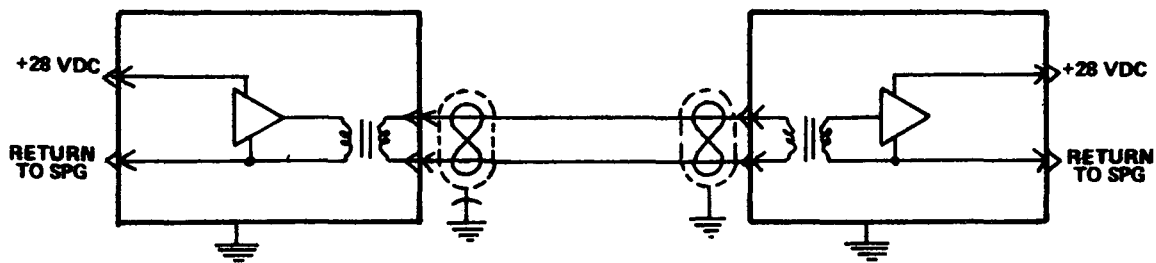


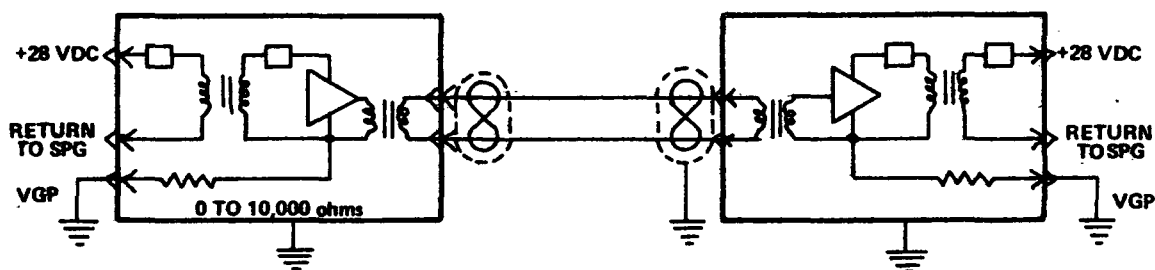
Figure VIII-31. Grounding configurations for loads with secondary power supplies.

To eliminate the interference between subsystems that may be caused by coupling, cable and equipment shielding requirements will be strictly enforced. Again considering possible equipment electrical configurations, Figure VIII-32 depicts three RF shielding and grounding techniques that will satisfy system requirements.

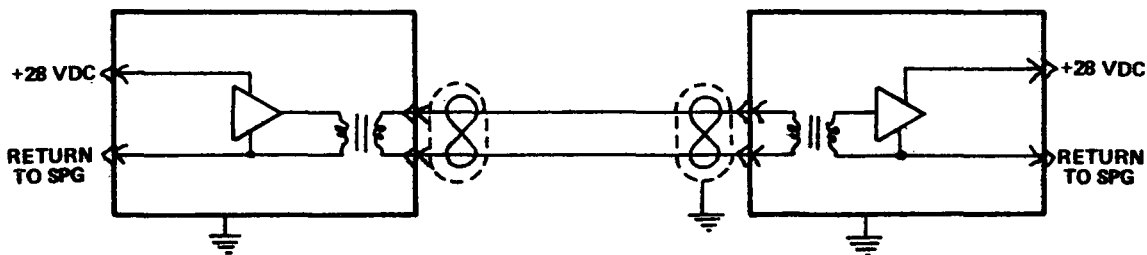
3. Electrical System Interfaces. The data and iteration time available did not permit complete definition of all the interface requirements for the



MINIMUM REQUIREMENT



TO EXCLUDE RF NOISE AT RECEIVER WITH VGP



TO EXCLUDE RF NOISE AT RECEIVER WITH ISOLATED CIRCUITS

Figure VIII-32. RF shield grounding configurations.

HEAO-C electrical system; however, those defined are considered quite adequate for a Phase A study. The following categories of interfaces are established for the electrical system:

- Load and Functional
- Operational Command
- Operational Diagnostic (Instrumentation)
- Spacecraft/OAS
- Ground ESE
- Physical

Each of these interfaces are generally described and summaries of the major interfaces are defined in the tables that follow.

a. Load and Functional Interfaces. Load and functional interfaces and the OAS interfaces are those imposed on the electrical system by other spacecraft subsystems. The other interface categories represent requirements established by the electrical system to be satisfied by the spacecraft and other subsystems.

The load and functional requirements are discussed in Section B. The functional requirements within the system and the electrical interfaces between system assemblies have been discussed in Sections C. 1 and C. 2.

b. Command Interfaces. Interfaces with the command subsystem are required to operate various experiment and subsystem equipment from ground command. The baseline system has provisions for power management and system diagnostics from the ground. The command subsystem provides stimuli to control operation of system assemblies and major switching functions. Various operational modes and redundant channels may be selected upon command. The operation of the pyrotechnic subsystem, critical to mission success, is also possible via the command link.

The overall command subsystem requirements are given in Chapter IX. The commands required for operation of the electrical system are summarized in Table VIII-19.

c. Instrumentation Interfaces. Transmission of information to the ground is required to assess the performance and status of the electrical system and to effect the necessary operational controls and selection of redundant modes.

TABLE VIII-19. ELECTRICAL SYSTEM/COMMAND INTERFACE<sup>a</sup>

Command	Number of Functions	Point of Interface
Transfer Solar Panels/Buses	8	SPD <sup>b</sup> #1/#2
Open/Close Primary Bus Ties	2	SPD #1/#2
Enable/Disable ECAs — Primary	4	SPD #1/#2
Enable/Disable ECAs — Redundant	4	SPD #1/#2
Charger Enable/Disable — Primary	6	SPD #1/#2
Charger Enable/Disable — Backup	6	SPD #1/#2
Battery Enable/Disable — Primary	6	ECA #1/#2
Battery Enable/Disable — Backup	6	ECA #1/#2
Open/Close Battery Bus Tie	2	ECA #1/#2
Open/Close Distribution Bus Tie	2	ECA #1/#2
Regulator Enable/Disable	4	ECA #1/#2
Regulator Redundant Enable/Disable	4	ECA #1/#2
Enable/Disable Primary EIAs	5	ECA #1/#2
Enable/Disable B/U EIAs	5	ECA #1/#2
Regulator Control Modes	2	ECA #1/#2
ECA Protection Override	2	ECA #1/#2
SPD Protection Override	2	ECA #1/#2
EIA Protection Override	5	EIA #2/4/6/8/10
Energy Pyro Buses	2	ECA/CIU
Arm Pyro Switches	1	SPD/CIU
Separate Backup — Redundant	1	CIU
Eject Fairing — Redundant	1	CIU
Deploy Arrays — Redundant	1	SPD #1/#2

a. Individual load controls presently included in experiment and sub-system requirements.

b. Solar power distributor.

Instrumentation within the electrical system generates both analog and discrete signals. The analog signals provide information on such parameters as voltage, current, power, and equipment temperature. Operational modes and switch positions are indicated by discrete signals. The interfaces established with the data handling subsystem accommodate the instrumentation requirements of the electrical system. The data handling subsystem processes and relays the signals to the communication subsystem for transmission to the ground.

Table VIII-20 lists the analog instrumentation interface requirements established for the electrical system. The discrete signal instrumentation requirements are given in Table VIII-21.

d. Spacecraft/OAS Interface. One of the major electrical interfaces is between the spacecraft and the OAS — Two major hardware elements of the HEAO-C program. Since the OAS was designed for other programs, modified hardware is required for the HEAO missions; therefore, the interfaces must be negotiated with the supplier of OAS hardware.

Reference VIII-3 and Appendix B define the OAS interface for the requirements established for Phase B studies of the HEAO-A and -B missions. The Mission C requirements for reliability and a two year mission life incurred extensive additions and changes in the RCS which require further modification of the OAS. Such changes are expected to be effective on the A and B Missions but, compared to Reference VIII-3, require modification on existing interfaces.

Although the hardware concept may be changed by existing OAS configurations, CIU has been defined as part of the spacecraft electrical system to localize and control the spacecraft/OAS interface. The CIU is a junction box assembly located at the extreme aft end of the spacecraft. All spacecraft electrical functions (power, controls, commands, and instrumentation) which cross the interface are routed to the CIU for interconnection with the OAS cabling network. All subsystems will have access to the CIU as required.

The cable interface unit serves other functions. It provides spacecraft access to the umbilical located on the OAS required to operate, control, and check out the system from the electrical support equipment during the prelaunch phase.<sup>2</sup> In addition, the CIU permits direct connection to test equipment used for preliminary performance testing of the systems prior to mating with the OAS. Some of the EPS interfaces with the CIU are indicated on the system schematic, Figure VIII-25, by "bubble" terminations A, B, C, D, K, and L.

---

2. *ibid.*

**TABLE VIII-20. ANALOG INSTRUMENTATION  
LIST, ELECTRICAL SYSTEM INTERFACE**

<b>Instrument Function</b>	<b>Number of Signals</b>	<b>Sensor Location</b>	<b>Point of Interface</b>
Solar Panel Currents	8	SPD #1/#2	SPD #1/#2
Solar Panel Temperature	8	Array	SPD #1/#2
Array/Primary Bus Voltage	2	SPD #1/#2	SPD #1/#2
Alternate Primary Bus Voltage	2	SPD #1/#2	SPD #1/#2
Battery Currents	6	Chargers	ECA #1/#2
Battery Voltage	6	Chargers	ECA #1/#2
Battery Internal Temperature	6	Battery Assembly	ECA #1/#2
Battery Sink Temperature	6	Battery Assembly	ECA #1/#2
Charger Assembly Temperature	6	Charger	ECA #1/#2
Ampere Hour Meters	6	Charger	ECA #1/#2
Regulator Input Voltage	4	ECA #1/ #2	ECA #1/#2
Regulator Input Current	4	Regulator	ECA #1/#2
Regulator Assembly Temperature	4	Regulator	ECA #1/#2
Experiment/EIA Group #1 Load Current	2	ECA	ECA #1/#2
Experiment/EIA Group #2 Load Current	2	ECA	ECA #1/#2
Subsystem/EIA Loads	4	ECA	ECA #1/#2

TABLE VIII-20. (Concluded)

Instrument Function	Number of Signals	Sensor Location	Point of Interface
5 Volt Supplies	2	EIA (3 & 5)	EIA #3/#5
OAS Load Currents	2	EIA #1/#2	ECA #1/#2
Secondary Distribution Voltage	8	EIA (1-8)	EIA #1-#8
OAS Primary Voltage	2	EIA (9&10)	CIU
OAS Excitation Supply	2	EIA (9&10)	CIU
HEAO Pyro Bus #1 Voltage	1	SPD #1	SPD #1
HEAO Pyro Bus #2 Voltage	1	SPD #2	SPD #2
Pyro Battery Temperature	1	OAS/ Battery	OAS J-Box
OAS Pyro Bus #1 and #2 Voltage	2	Pyro J-Box	OAS J-Box
OAS Pyro Currents #1 and #2	2	Pyro J-Box	OAS J-Box

**TABLE VIII-21. DISCRETE INSTRUMENTATION  
LIST, ELECTRICAL SYSTEM INTERFACE**

Instrument Function	Number of Signals	Sensor Location	Point of Interface
Solar Panel/Primary Bus Selected Status	8	SPD #1/#2	SPD #1/#2
Primary Bus Tie Position	2	SPD #1/#2	SPD #1/#2
Battery Bus Tie Position	2	ECA #1/#2	ECA #1/#2
Main Distribution Tie Position	2	ECA #1/#2	ECA #1/#2
Battery Enabled/Disabled Main Battery Bus	6	ECA #1/#2	ECA #1/#2
Battery Enabled/Disabled Redundant Battery Bus	6	ECA #1/#2	ECA #1/#2
Regulator Enabled/Disabled Main Bus	4	ECA #1/#2	ECA #1/#2
Regulator Enabled/Disabled Redundant Bus	4	ECA #1/#2	ECA #1/#2
Regulator on Main Distribution Bus	4	ECA #1/#2	ECA #1/#2
Regulator on Redundant Distribution Bus	4	ECA #1/#2	ECA #1/#2
High-Low Voltage Detected Distribution	2	ECA #1/#2	ECA #1/#2
Low Battery Voltage Detected	6	Chargers	ECA #1/#2
Charger Enabled/Disabled Primary Channel	6	SPD #1/#2	SPD #1/#2
Charger Enabled/Disabled Redundant Channel	6	SPD #1/#2	SPD #1/#2

TABLE VIII-21. (Continued)

Instrument Function	Number of Signals	Sensor Location	Point of Interface
Primary Bus Overload Detected	4	SPD #1/#2	SPD #1/#2
Secondary Distribution Bus Overload Detected	10	ECA #1/#2	ECA #1/#2
ECA Enabled to Primary Bus 1P11	2	SPD #1	SPD #1
ECA Enabled to Primary Bus 1P12	2	SPD #1	SPD #1
ECA Enabled to Primary Bus 1P21	2	SPD #2	SPD #2
ECA Enabled to Primary Bus 1P22	2	SPD #2	SPD #2
Array Pyrotechnics Armed	2	SPD #1/#2	SPD #1/#2
Array Pyrotechnics Enabled	2	SPD #1/#2	SPD #1/#2
Array Wings Deployed	2	Array	SPD #1/#2
Booster Separation	1	OAS	CIU
Fairing Separation #1 & #2	2	OAS	CIU
Booster Separation Primary — Backup Command Received	2	OAS	OAS J-Box
Fairing Eject Primary and Backup Command Received	2	OAS	OAS J-Box
Enable Separation Buses 1 and 2	2	OAS Pyro Box	CIU
Enable Ejection Buses 1 and 2	2	OAS Pyro Box	CIU

TABLE VIII-21. (Concluded)

Instrument Function	Number of Signals	Sensor Location	Point of Interface
Separation MDF <sup>a</sup> Detectors	4	OAS	OAS J-Box
Fairing Eject Event Monitor	12	OAS	OAS J-Box

a. Mild detonating fuse.

A cable interconnection diagram, Figure VIII-33, is given for the OAS modified for HEAO-C. The following changes are to be noted in comparison to Reference VIII-3:

- A Type 31, primary pyro battery is added to assure adequate mission reliability and to assure adequate surge current rating for the pyrotechnic buses.
- Reaction engine module (REM) control assemblies were added to accommodate RCS redundancy scheme.
- Tank control assemblies (TCAs) were added to accommodate addition of the RCS tanks, addition of heaters and latching solenoid valves, and the redundant controls required.
- Two EIAs were added to account for modifications, to compensate for stripping electrical distribution and junction boxes from the reference OAS, and to be consistent with the spacecraft redundancy schemes for distribution.
- Access to ESE is provided by cabling between CIU and the umbilical.
- An instrumentation junction box and a remote data acquisition unit were added to simplify the interface and to be consistent with data handling subsystem design for the spacecraft. The OAS instrumentation is transferred to the spacecraft over RF cables.
- Not obvious on the diagram, modifications to the OAM/RCS junction box were assumed to accommodate the RCS additions and changes. Two OAM/RCS junction boxes may be required.

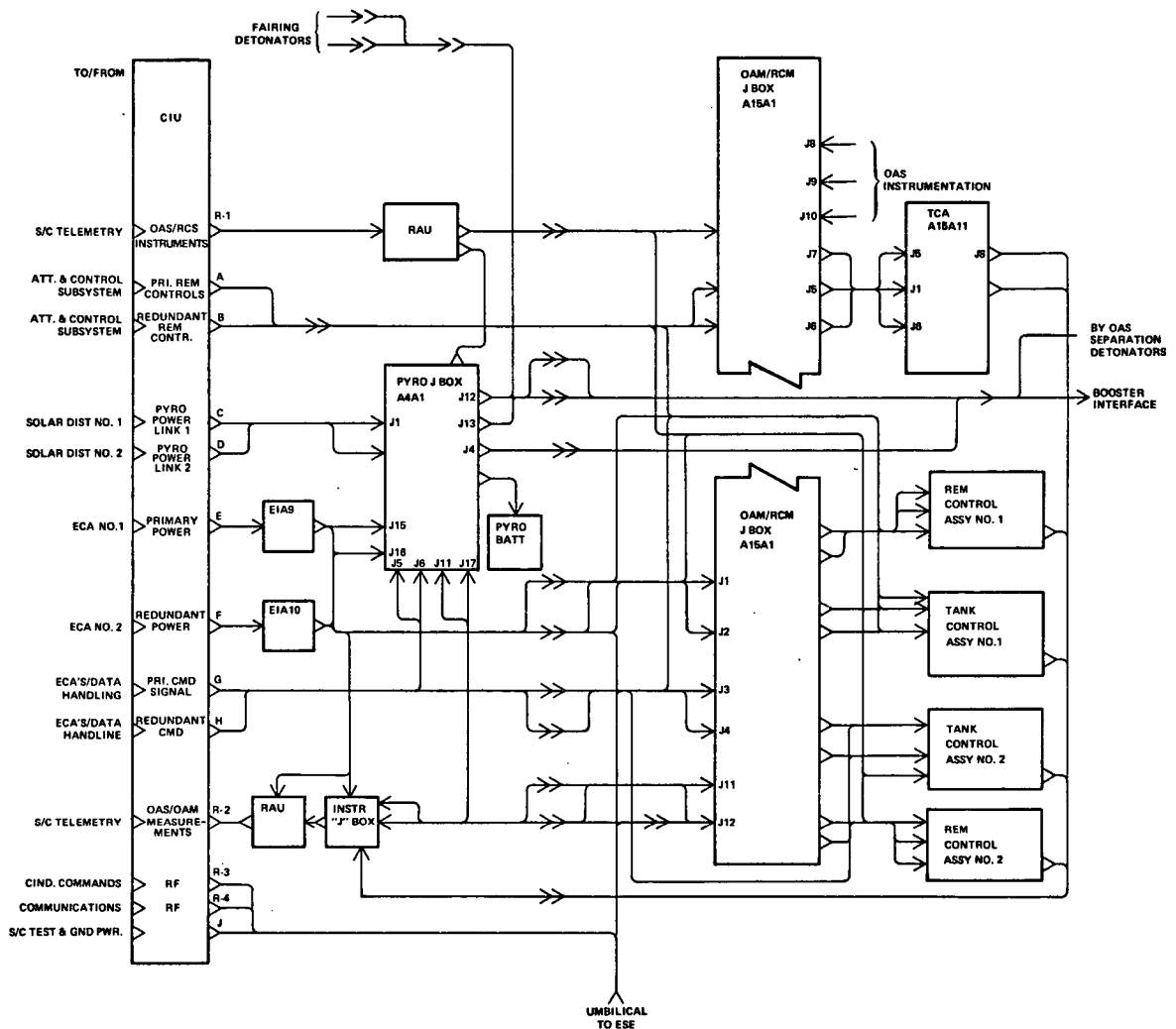


Figure VIII-33. Modified OAS cable interconnect drawing.

The CIU cable interfaces with the OAS are indicated in Figure VIII-33. The preliminary listing of the functions crossing the interface, given in Tables VIII-22 through VIII-24, indicates the cable connectors identified by letters on Figure VIII-33. Table VIII-22 identifies spacecraft/OAS command functions. The instrumentation functions, handled by RF cables crossing the OAS/spacecraft interface, are given in Table VIII-23. The controls, power, and ESE functions to be accommodated are listed in Table VIII-24.

TABLE VIII-22. SPACECRAFT/OAS  
ELECTRICAL INTERFACE/COMMANDS VIA CIU

Function	Connector Sign	Number of Signals
BU/OAS Separation Pyro Enable	G/H	2
Fairing Pyro Enable	G/H	2
Stop OAS Burn (L2 + L4)	G/H	2
Start OAS Burn (L2 + L4)	G/H	2
Stop OAS Burn (L1 + L3)	G/H	2
Start OAS Burn (L1 + L3)	G/H	2
Enable/Disable OAS (L1 + L3)	G/H	4
Enable/Disable OAS (L2 + L4)	G/H	4
TCA Inject Manifold Heater #1 On/Off	G/H	4
TCA Inject Manifold Heater #2 On/Off	G/H	4
TCA Propellant Valve Heaters On/Off	G/H	4
Primary -- Backup OAS Tank Heaters On/Off	G/H	4
REM Valve and Catalyst Bed Heaters On/Off	E/F	8
REA <sup>a</sup> Ground Command Operate	A/B	16
RCS Tank Heaters On/Off	E/F	8
RCS Tank Isolate Valves On/Off	E/F	8
Tank Manifold Isolate Vales On/Off	E/F	2
Cross Feed Valve On/Off	E/F	1
REM Feedline Isolate Valves On/Off	E/F	8

a. Reaction engine assembly.

TABLE VIII-23. OAS TO SPACECRAFT  
INTERFACE/INSTRUMENTATION

Instrument Description	Number of Signals	Signal Type	Connector
TCA Chamber Pressure	1	Analog/RF	R2
TCA Quad Valve Temperature	1	Analog/RF	R2
TCA Bed Pressure	1	Analog/RF	R2
OAM Tank Temperature	4	Analog/RF	R2
OAM Tank Pressure	1	Analog/RF	R2
OAM Feedline Pressure	1	Analog/RF	R2
OAS Pyro Bus #1 Voltage	1	Analog/RF	R2
OAS Pyro Bus #2 Voltage	1	Analog/RF	R2
OAS Pyro #1 and #2 Current	2	Analog/RF	R2
TCA Wall Temperature	1	Thermo/ RF	R2
TCA Nozzle Temperature	1	Thermo/ RF	R2
TCA Manifold Temperature	2	Thermo/ RF	R2
TCA Catalyst Bed Temperature	2	Thermo/ RF	R2
OAS Main Power Bus #1	1	Analog	E
OAS Main Power Bus #2	1	Analog	F
Pyro Battery Voltage	1	Analog/RF	R1
Pyro Battery Temperature	1	Analog/RF	R1
REA Chamber Wall Temperature	16	Thermo/ RF	R2
RCS Tank Temperature	8	Analog/RF	R2
REM Average Temperature	4	Analog/RF	R2
RCS Valve Temperature	8	Analog/RF	R2
RCS Tank Pressure	8	Analog/RF	R1

TABLE VIII-23. (Continued)

Instrument Description	Number of Signal	Signal Type	Connector
Tank Pneumatic Pressure	8	Analog/RF	R1
REM Propellant Feed Pressure	8	Analog/RF	R1
REA Chamber Pressure	16	Analog/RF	R1
RCS Tank Isolation Valve Position	8	Discrete/RF	R1
Tank Manifold Valve Position	2	Discrete/RF	R1
Cross Feed Valve Position	1	Discrete/RF	R1
REM Feedline Valve Position	8	Discrete/RF	R1
OAS Propellant Valves Open	4	Discrete/RF	R2
OAS Propellant Valves Closed	4	Discrete/RF	R2
OAS Start/Stop (L1 + L3)	1	Discrete/RF	R2
OAS Start/Stop (L2 + L4)	1	Discrete/RF	R2
OAS (L1 + L3) (L2 + L4) Enable/Disable	2	Discrete/RF	R2
OAS Valves On	4	Discrete/RF	R2
TCA Manifold Heater On	2	Discrete/RF	R2
TCA Propellant Valve Heater Primary and Redundant	1	Discrete/RF	R2
OAS Tank Heaters On	2	Discrete/RF	R2
Backup/OAS Separation	1	Discrete	C/D

TABLE VIII-23 (Concluded)

Instrument Description	Number of Signal	Signal Type	Connector
Fairing Separation #1 and #2	2	Discrete	C/D
Backup Separate Command Received	2	Discrete/ RF	R2
Fairing Eject Command Received	2	Discrete/ RF	R2
Enabled Separation Buses	2	Discrete	C/D
Enabled Fairing Eject Buses	2	Discrete	C/D
MDF Separation Detonator #1 & #2	4	Discrete	R2
Fairing Eject Events (1 - 12)	12	Discrete/ RF	R2

TABLE VIII-24. SPACECRAFT/OAS  
INTERFACE/CONTROLS AND ELECTRICAL POWER

Description	Number of Signals	Connectors
Primary Power to OAS	2	E
Redundant Power to OAS	2	F
Power From Pyro Bus #1	2	C
Power to Pyro Bus #2	2	D
Arm Pyro Buses	4	C/D
Eject Arm Array Pyros	2	C/D
EIA 9 Load Control	5	E
EIA 10 Load Control	5	F
Primary REA Controls	8	A
Redundant REA Controls	8	B
Control Sensors Primary	12	A
Control Sensors Backup	12	B
<b>SPACECRAFT TO UMBILICAL (ESE CHECKOUT)</b>		
Communication/Telemetry Spacecraft	1 - RF Coax	R4
Ground Command Link	1 - RF Coax	R3
Ground Power/Control/ Monitor	1 - 60 Pin	J

e. ESE Interfaces. The orbital vehicle baselined for HEAO-C requires the establishment of several electrical interfaces with ESE. The data available on experiment and subsystem performance testing requirements, prior to mating the spacecraft with the OAS, were not sufficient to define system simulator and test equipment requirements and the interfaces required for test operations. A brief analysis of system and operational requirements was performed to define vehicle/ESE interfaces for prelaunch operations.

Requirements for ESE intercommunication with the OAS umbilical and with carry-on cables were considered to define the preliminary interfaces given. Lack of definition concerning launch facilities, OAS modifications, and umbilical constraints permitted only estimates of umbilical allocations. Where subsystem information was not available, ESE requirements were estimated.

Equipment requiring control, monitoring, or power until launch require access to the ESE through the umbilical. Prelaunch operations and checkout which can be completed prior to approximately T-2 hours are considered carry-on cable requirements. Orbit Adjust Stage cabling provides direct connection of equipment located in the OAS with the umbilical. Test and checkout cabling within the HEAO spacecraft terminates at the CIU located at the aft end of the spacecraft. The OAS cabling must interconnect the CIU with the umbilical to provide spacecraft access to ESE. Carry-on cables connect directly to the CIU and are removed prior to T-2 hours.

A functional listing of the preliminary ESE interfaces with the electrical connectors on the umbilical is given by Table VIII-25, and Table VIII-26 lists test functions and connectors at the CIU for system testing with carry-on cables.

TABLE VIII-25. PRELIMINARY  
ESE/UMBILICAL INTERFACES

Function Description	Number of Functions
Ground Power (28 Vdc)	2
Buses in Solar Distributors	(-)
Primary Bus Switch Controls	8
Battery Charger Controls	6
Battery Output Controls	6

TABLE VIII-25. (Continued)

Function Description	Number of Functions
Battery Current Monitor	6
Battery Voltage Monitor	6
Battery Temperature Monitor	6
Distribution Bus Controls	2
Regulator Input Controls	4
Regulator Output Controls	4
Primary Bus Voltage Monitor	2
Main Distribution Voltage Monitor	4
Power Transfer Control	2
Command Subsystem Operate Control	4
Command Subsystem Monitors	2
Communication Operate Controls	2
Data Handling Subsystem Controls	2
Data Handling Monitor	2
Attitude and Control Subsystem Controls	5
Attitude and Control Monitoring	5
Launch Readiness Indicators	3
Ground Power to Pyro Buses	2
Pyro Bus Transfer Switch	1
Pyro Bus Arming Control	2

TABLE VIII-25. (Concluded)

Function Description	Number of Functions
Pyro Voltage Detectors	2
Pyro Interlocks Ready	1
Pyro Battery Voltage	1
Pyro Battery Temperature	1
OAM Tank Pressure	1
OAM Feedline Pressure	1
OAM Tank Temperature	4
OAM Propellant Valve Position	2
OAS Subsystem Power Control	2
Instrumentation Voltage Monitor	1
OAM Valve Controls	3
RCS Tank Pressure	8
RCS Tank Monitor Pressure	8
RCS Tank Temperature	8
RCS Propellant Valve Controls	9
RCS Propellant Valve Positions	9
Calibration Voltage	1
Access to Command Subsystem	1 Coax Cable
Access to Communication/Data	1 Coax Cable

11A

TABLE VIII-26. PRELIMINARY ESE/CIU  
INTERFACES FOR CARRY-ON CABLES

Function Description	Number of Functions
Primary Ground Power	2
Secondary Ground Power	2
Solar Panel Switch Controls	8
Scan Solar Modules/Dark I-V Test	70
Regulator Sensors	8
Charger Sensors	18
Battery Sensors	12
Redundant Switch Controls	33
Test Protective Devices	12
Test Voltage Detectors	8
Redundant Bus Voltage Monitor	4
Bus Current Monitor	8
Load Current Monitor	10
Switch Position Monitors	24
Experiment Test Points	2 - 60 Pin Connectors
Communication Subsystem Test	1 - 29 Pin Connector
Attitude and Control Subsystem Test	1 - 60 Pin Connector
RCS Test	1 - 60 Pin Connector
Data Handling Test Points	1 - 60 Pin Connector
Pyro Subsystem Interlock and Test Points (Interface not at CIU)	Various Connectors

f. **Physical Interfaces.** Preliminary designs to the assembly level were made for baseline electrical subsystems. Each of the major assemblies required have been described in Section C. Subsequent to functional definition, spacecraft standards, qualified components, approved assembly techniques and installation practices were considered to define the ratings, physical characteristics, and configurations of the assemblies. The physical interfaces for the electrical equipment were coordinated with the structural/mechanical and thermal designs baselined for HEAO-C.

The primary physical interfaces (i. e. , the number of assemblies, assembly weight, assembly dimensions, and thermal characteristics) are summarized by the electrical system equipment list given in Table VIII-27.

4. **Electrical Support Equipment.** The electrical support equipment proposed for the HEAO-A and -B Missions will satisfy most (over 90 percent) of the HEAO-C spacecraft requirements. The exceptions anticipated are the equipment normally modified to adapt to specific spacecraft interfaces and the equipment peculiar to Mission C experiments. Data on the final configuration of ESE for HEAO-A and -B and on the test and checkout requirements for the C Mission experiments is insufficient to assess specific differences that may be needed. Most of the differences will probably occur in the equipment needed for acceptance and design verification testing of the system prior to prelaunch operations. It is expected that relatively small modification and additions will be needed for prelaunch checkout and launch operations.

A cursory analysis of studies made to date for HEAO-A and -B indicates that the ESE proposed in Reference VIII-1 would be the most compatible with the HEAO-C baseline due to basic system similarities. For instance, CMGs were baselined; the power requirements and the EPS configuration are closer to the HEAO-C requirements. It should be noted that changes in the ESE proposed in Phase B studies will be required because the system requirements specified for Phase C differ from those used to date. HEAO-C concepts are quite consistent with the later specifications.

It is expected that the automatic ground equipment (AGE) defined in Reference VIII-3 will be tailored to meet the HEAO mission requirements and will be delivered with the OAS. The two year mission requirement and associated modifications to RCS requirements will require additions and modifications to the OAS and its AGE not shown in Reference VIII-3. These changes are expected for the A and B Missions, as well as for HEAO-C. A few additional changes have been recommended for the OAS electrical system to enhance mission reliability and to simplify some of the interfaces. The effect of these modifications on the ESE will be relatively small since basic

TABLE VIII-27. HEAO-C ELECTRICAL SYSTEM EQUIPMENT

	No. of Assemblies	Unit Weight (lb)	Unit Size (In.)	Thermal/Orbit Dissipation (Avg. Wh)	Total Weight (lb)
<b>Spacecraft Equipment</b>					
Solar Distributors	2	18	13 x 11.5 x 6.75	35 <sup>a</sup>	36
Electrical Control Assembly	2	16	14 x 8 x 8	30	32
Electrical Integration Assembly	8	2.5	6 x 4 x 3	7	20
Regulator Assembly	4	8	11 x 8 x 5	125	32
Charger Assembly	6	14	11 x 8 x 6	30 <sup>a</sup>	84
Battery	6	52	13.1 x 6.7 x 7.4	123	312
Cable Interface Unit	1	8	9 x 6 x 2	0	8
Solar Array					
Wing Panels	6	36.1	119 x 38.2 x 0.7	N/A	217
Body Panels	2	32.2	119 x 38.2 x 0.7	N/A	65
Deployment Hardware	6	8.4		N/A <sup>b</sup>	50
Cabling				25 <sup>b</sup>	125
Spacecraft Subtotal					981
<b>OAS Equipment</b>					
Electrical Integration Assembly	2	2.5	6 x 4 x 3	1	5
Pyro Battery (Primary Type 31)	1	16	LMSC <sup>c</sup> Item	N/A	Weights are
Pyro Junction Box	1	6	LMSC Item	N/A	
OAS/RCS Junction Box	1	12	LMSC Item	14	Included in
Instrument Junction Box	1	4	LMSC Item	2	
Umbilical Cabling	1	9	LMSC Item	N/A	OAS Weight
		50		2	

a. Dissipation average for sunlight period only.

b. Internal cabling dissipation is 15 Wh.

c. Lockheed Missiles and Space Company.

functions and types of equipment are not changed. For instance, additional tanks, instrumentation, and controls are needed.

The OAS umbilical will be used to operate and control the spacecraft system from the ESE during prelaunch checkout. Operation from ground power and battery charging is permitted up to 15 minutes prior to launch by the use of the OAS umbilical. This greatly enhances energy storage capacity and mission reliability.

A requirement to check out the solar arrays during prelaunch operations has been established for Missions A, B, and C to assure that the array has not been damaged during handling and assembly of the spacecraft on the booster. Testing is to be accomplished using the Dark I-V Method developed by MSFC.

The Dark I-V test measures the forward diode characteristics (I-V curve) of the solar cell assemblies on the panels. The Dark I-V curve will be obtained for each panel and each solar cell assembly by using specialized equipment for forward biasing of solar panels, and by using suitable hardware for associated data collection. The test will be performed during different phases of the spacecraft test program from assembly to launch. Comparison of the test data with reference to I-V curves determines the condition of the array and its performance capabilities.

The tests provide data to check for major degradation of the solar panels such as:

- a. Two or more solar cell modules electrically disconnected.
- b. Excessive series line impedance.
- c. Small shunt resistance.

Interface with the solar array for Dark I-V testing will be at the CIU on the spacecraft. The interface between the spacecraft and ESE will be essentially the same as for the A and B Missions. The interface will be made through carry-on cables available up to T-2 hours. Since it is not necessary to conduct these tests beyond T-2 hours, it is not necessary to burden the umbilical connector located on the OAS.

A block diagram of the ESE Dark I-V Equipment used for the Skylab-ATM solar arrays is shown in Figure VIII-34. The equipment shown can very easily be adapted to the HEAO interface. Present schedules indicate that the ATM equipment can be made available for the HEAO-C.

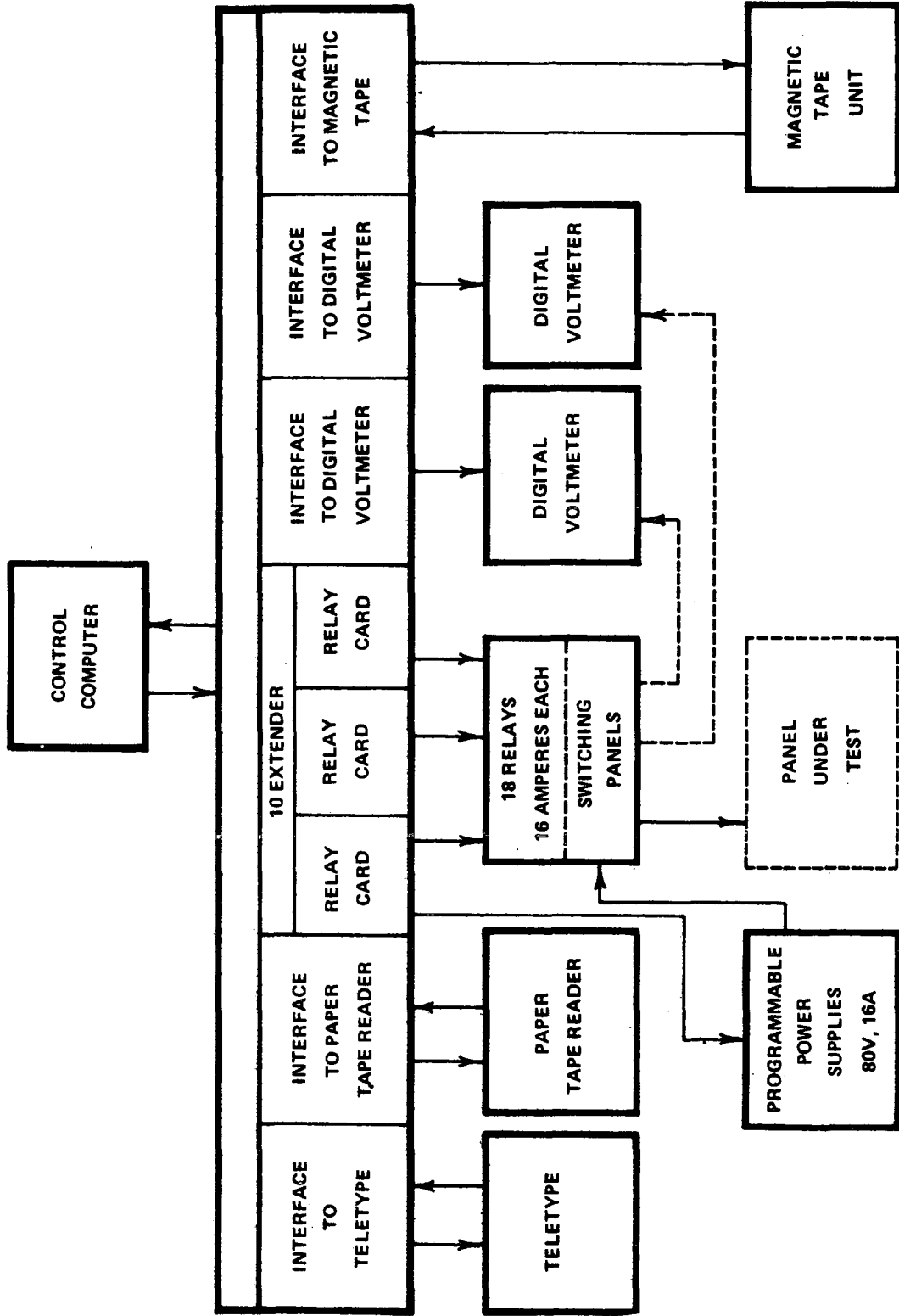


Figure VIII-34. Electrical support equipment for solar array checkout.

## D. Electrical System Reliability

1. General Assessment. An extensive reliability analysis (Appendix G, Section 3) was conducted to guide design approaches toward the high reliability goals set for HEAO-C. The electrical system design concepts were iterated with these studies to attain the high reliability predictions of 0.992 for one year and 0.944 for two years. Assuming that all the input data made available for the reliability study were applicable and accurate, it is evident that considerable improvement in the spacecraft systems is needed to achieve the two year goal of 0.90. Although the electrical system reliability of 0.944 exceeds the spacecraft goal, it is not likely that it would be adequate, when combined with other subsystems, to attain this very high overall goal. On the other hand, there is sufficient design and development experience with space vehicle electrical systems to confidently assure that conceptual EPS system, hereof, can be developed to exceed the two year mission requirements.

2. EPS Reliability Summary. The results of the reliability analysis of the EPS is summarized in Table VIII-28. Analyses were based on the EPS reliability block diagram given in Figure VIII-35.

TABLE VIII-28. EPS RELIABILITY NUMERIC SUMMARY

Assembly	Reliability	
	1 Yr	2 Yr
Solar Array	0.99983	0.99983
Power Regulator	0.99703	0.98081
Power Control	0.99888	0.99568
Electrical Integration	0.99915	0.99664
Battery/Charger	0.99708	0.97010
Baseline EPS	0.99199	0.94403

The solar array reliabilities were computed using a conservative cell failure rate. The solar array itself has a two-year reliability indistinguishable from unity. By a careful calculation it was determined that the unreliability is due to the panel deployment mechanism (the probability that one of the six panels will fail to deploy is approximately 0.0002).

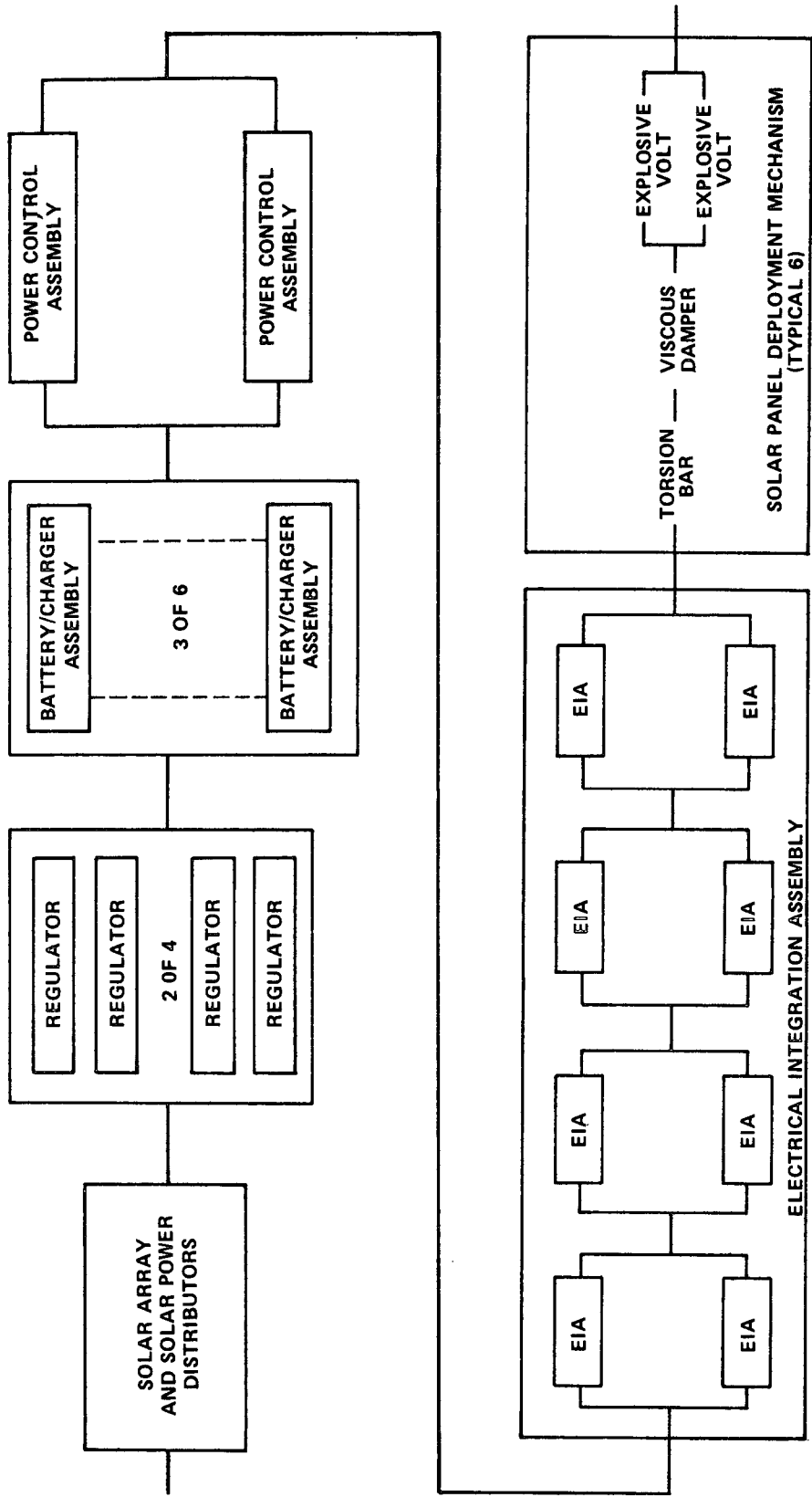


Figure VIII-35. EPS reliability block diagram.

A simple, approximate battery/charger assembly reliability model has been used with pessimistic failure rate data. Thus, while it is thought that the battery/charger assembly reliabilities exceed the values given in Table VIII-28, not too much credence should be granted the listed numbers. Further battery reliability studies will be required to establish credible reliability estimates.

Detailed discussions of the assumptions, procedures, and results of the EPS reliability analysis are given in Appendix G, Section 3.

3. Design Philosophy and Reliability Provisions. Although the preliminary analysis was rigorous, considerably more attention to reliable design and hardware is required to assure mission success with a high degree of confidence. Initial predictions are more useful to compare design concepts and to establish reliability policies than they are accurate on an absolute basis. This is due to the difficulty of obtaining sufficient, verified reliability data to the detail needed to insure applicability to the system designs being considered. Such studies, however, are invaluable to eliminate potential system weaknesses, to focus attention on "problem" equipment, and to establish procedures to obtain the necessary reliability in detailed design and equipment implementation.

To the extent possible in the study period, reliability information was used to select equipment capacities and to incorporate redundancy and protective features to obtain the high reliability rating for the EPS. The details of many of the reliability features are described in Section C and in the sub-system and assembly technical discussion of Appendix F. In addition, based on previous experience, subtle provisions and detailed requirements were established that are not evident in the reliability data. These provisions also can make the difference between system success and failure because they compensate for equipment weaknesses, component limitations, and more than single failure modes possible within the system.

Notable examples of reliability features incorporated in the baseline electrical system are:

a. A minimum of 100 percent redundancy is provided for all assemblies and power channels except for the solar panels and total battery capacity with cycle life.

(1) The design margin allowed and the modular redundancy within the array provides a very high reliability at two years.

(2) The number of battery assemblies, their current and power capacity are more than 100 percent redundant. About 50 percent excess cycle life/capacity is provided.

b. Power sources are protected against internal and external faults, overloads, reverse currents, and over- and under-voltage.

c. Spacecraft loads are assured redundant sources of power and are protected from over-voltage and interference between loads.

d. Both open and short faults can be isolated.

e. Where possible, different devices and circuitry are used in redundant channels to avoid common failure modes. For instance, array deployment may be initiated by automatic sequencing or by completely isolated command signals initiated from the ground. The primary pyro battery is backed up by secondary spacecraft batteries.

f. In most cases, additional, partial, or dual redundancy of critical components and controls within EPS assemblies is provided. For instance, battery charge termination is controllable from third electrode cells and from ampere-hour meter signals.

g. Conservative ratings and possible failure modes of critical components were considered in configuring systems and subsystems. For instance, the following conditions were considered:

(1) Power contacts will operate at about 40 percent of rating. These are backed up with redundant contacts. Arc suppression is provided for critical or high peak load switching.

(2) Semiconductors and capacitors will operate at 50 percent of rating. Thermal characteristics and derating for temperature and peak voltage have been considered in the assembly designs.

(3) Detail characteristics of battery cells, variations, and reliable assembly techniques have been accounted (see Appendix F).

h. Physical and location redundancy as well as electrical redundancy have been provided for electrical equipment and cabling.

## E. Conclusions and Recommendations

HEAO Mission C, from an electrical equipment standpoint, is very similar to Missions A and B, the largest differences being the scan mode and the load requirements. HEAO-C loads are about 20 percent (100 watts) larger than the A and B loads. This is due, primarily, to the equipment redundancy used to meet the two year life and high reliability requirements. Because of the preliminary nature of the information, conservative estimates account for some of the differences.

The similarity of the experiments, the spacecraft configuration, and the guideline for subsystem commonality permitted an electrical system design for HEAO-C that will exceed the requirements of HEAO-A and -B. The assembly complement of the system and the modularization incorporated provide a high degree of flexibility for optimization with lesser requirements or for adaptation to mission changes.

The baseline electrical system is based on highly reliable concepts. The predicted reliability of 0.944 for two years exceeded its allocation. The subsystem designs were based on mature assembly and component concepts and were analyzed to a depth that permits predicting a successful two year performance with a high degree of confidence. Both electrical and physical redundancy of assemblies and cabling have been provided. Where possible, different types of controls and protection have been provided for the redundant channels of the system to assure that common failure modes are avoided. The system automatically protects loads and power sources and affords redundant power routes for devices isolated by the protective features. Loads are protected against high voltage failures of power equipment and overloads in other equipment. The power source is protected against short circuits in loads and against low voltage and high temperature battery conditions. Redundancy of critical subassemblies and components within the assemblies assures reliable performance. Subassembly and component designs were selected to operate at less than 50 percent of their rating without the assistance of redundant items.

Additional study of distribution and controls are recommended to investigate whether or not simplification of protection and switching can be made without degrading reliability. To fully assess distribution networks, additional details of the ratings, characteristics, and functional sequences are needed for the various assemblies and equipment within the experiments and subsystems.

It was concluded from the solar array study, that a foldout array is required for the HEAO-A, -B, and -C mission requirements with the established spacecraft configuration and commonalty constraints. The solar array panels can be designed for physical and constructional commonality between missions.

The baseline solar array configuration described in Section C is conservative and exceeds the minimum pointing requirements. It provides the maximum power growth potential for the given spacecraft because it is the maximum area possible for mounting solar cells within the constraint that only a single fold is allowed for the wing panels. The baseline provides adequate capacity to satisfy the average 722 watt design load at the end of the two year mission even if one solar wing panel failed to deploy. Continuous 40 degree off-sun pointing is permissible if all panels are properly deployed.

The Alternate No. 1 solar array configuration described in Appendix F, meets HEAO-C requirements and provides some load growth capability. It, too, can be recommended for present requirements. Because the body and wing panels are co-planar, its design analysis is simpler; however, from a panel and deployment hardware standpoint, the baseline and Alternate No. 1 are equivalent. Alternate No. 2 does not meet the load requirements and is not recommended.

Although two configurations can be recommended for HEAO-C, this may not apply to the A and B missions because array selection is also dependent on experiment packaging, external sensors, and viewing angles. Considering the A and B loads and possible configurations and arrangements, it is feasible to design common panels and deployment hardware for all three missions. Further study is recommended to assure that the modularization selected for the array permits near optimum adaptation to each mission.

Central power regulation is recommended for performance reliability, for the versatility provided for requirement changes, and the EPS design and development flexibility afforded. Compared to coarsely regulated approaches, the regulated approach should reduce thermal and EMI problems within the spacecraft. It is more easily adapted to reliable battery charge controls. The study indicated that overall cost and weight penalties for using regulators are insignificant.

Six battery assemblies using twenty-two 20 ampere-hour cells were required to meet the load and reliability allocations. Redundant charge control sensors having different operating modes are provided to assure reliable, two year performance. Because they are considered essential to mission success, the following battery provisions are recommended:

- The average depth of discharge should not exceed 15 percent.
- Battery temperature should be maintained between 5° and 15° C.
- A charger dedicated to each battery should be provided.
- Protection against low voltage and overloads should be provided.
- The spacecraft batteries should be used only as a backup source for firing pyrotechnics. Pyros have high surge current and short circuit failure mode characteristics that could prematurely terminate the mission.

The stripped down version of the OAS, defined in Reference VIII-3, was based on a one year mission and the requirement to separate the spacecraft from the OAS in orbit. Therefore, all RCS equipment was eliminated from the stage as well as the power, control, and electronic provisions that were in the original OAS.

The HEAO-C baseline requires considerable electrical system changes to the OAS defined in Reference VIII-3 and Appendix B. It is expected that many of the changes discussed will be incorporated in the OAS to be baselined for HEAO-A and -B; however, this baseline has not been documented.

Reinstallation of a primary pyro battery in the OAS is necessary to assure that pyrotechnic surge current and reliability requirements are met. Electrical integration assemblies have been incorporated to compensate for the removal of such equipment from the original OAS and to provide distribution and controls consistent with the spacecraft system. Electrical access through the OAS umbilical was assumed for prelaunch operation of the spacecraft. A need for coax links, for ground power, controls and monitoring has been established on the basis that umbilical mating provisions exist at the launch site.

The addition of RCS tanks, engines valves, etc., requires additional interfaces, distribution equipment, and cabling. The HEAO-C RCS incorporates additional tanks, latching solenoid valves, and redundancy schemes not included in the original OAS definition. Such concepts require additional network and equipment modification.

Although preliminary electrical interfaces and concepts have been defined in Section C, additional studies are recommended to accommodate the OAS requirements established for HEAO-C. Detailed consideration of the OAS and interfaces to be baselined for HEAO-A and -B is needed to specify adequate requirements to avoid major, expensive design changes for later missions.

The baseline electrical system definition is quite adequate for initiating Phase B studies of the HEAO-C mission. Except for the distribution and interface subjects, where additional study is recommended, most of the sub-systems and major assemblies have been defined to a level that would permit early initiation of Phase C design. The preliminary specification of detailed requirements given in Appendix F is quite adequate for initiating Phase C efforts.

## REFERENCES

- VIII-1. Grumman Aerospace Corporation: High Energy Astronomy Observatory. Vol. II, NASA Contract No. NAS8-26272, April, 1971.
- VIII-2. TRW, Systems Group: HEAO Phase B Final Report. Vol. II, NASA Contract No. NAS8-26273, April, 1971.
- VIII-3. Lockheed Missiles and Space Co.: HEAO Orbit Adjust Stage and Associated Hardware Definition. LMSC Report A989276, NASA Contract NAS8-26492, May 21, 1971.

## BIBLIOGRAPHY

Space Environment Criteria Guidelines for Use in Space Vehicle Development. NASA TMX-53957, 2nd Ed., August 26, 1970.

# TABLE OF CONTENTS

	Page
A. Mission Guidelines . . . . .	IX- 1
B. Constraints . . . . .	IX- 1
1. Tracking Network . . . . .	IX- 1
2. Experiments . . . . .	IX- 6
C. Functional Requirements . . . . .	IX- 9
D. Baseline Description . . . . .	IX-10
1. Antennas . . . . .	IX-14
2. Transponder . . . . .	IX-17
3. Command Storage . . . . .	IX-17
4. Remote Multiplexer . . . . .	IX-23
5. Clock . . . . .	IX-23
E. Performance Analysis . . . . .	IX-24
1. Antennas . . . . .	IX-24
2. Command Equipment . . . . .	IX-26
3. RF Equipment . . . . .	IX-29
4. Spacecraft Clock . . . . .	IX-29
5. Tape Recorders . . . . .	IX-36
a. Saturn Recording . . . . .	IX-38
b. Modulation Recording . . . . .	IX-40
c. Channel Analysis . . . . .	IX-41
d. Heads . . . . .	IX-44
e. Bearings . . . . .	IX-48
F. Spacecraft Operational Modes and Telemetry Format . . . . .	IX-50
1. Telemetry Requirements . . . . .	IX-50
a. Spacecraft . . . . .	IX-50
b. Experiments . . . . .	IX-50

## TABLE OF CONTENTS (Concluded)

	Page
2. Format . . . . .	IX-55
3. Command Structure . . . . .	IX-60
G. RF Spectrum Usage . . . . .	IX-60
1. Analytical Procedure . . . . .	IX-65
2. Overall Effect . . . . .	IX-68
H. Reliability . . . . .	IX-69
1. RF Equipment . . . . .	IX-70
2. Data Handling Equipment . . . . .	IX-70
I. Future Studies . . . . .	IX-74
J. Summary and Conclusion . . . . .	IX-74
References . . . . .	IX-75

## LIST OF ILLUSTRATIONS

Figure	Title	Page
IX- 1.	Baseband codes . . . . .	IX- 3
IX- 2.	Carrier tracking circuits. . . . .	IX- 3
IX- 3.	Baseband circuits. . . . .	IX- 4
IX- 4.	Subcarrier demodulator. . . . .	IX- 5
IX- 5.	Baseline C & DH system block diagram. . . . .	IX-10
IX- 6.	Comparison of central and remote decoders . . . . .	IX-15
IX- 7.	Comparison of central multiplexer and remotes. . . . .	IX-15
IX- 8.	Cavity-backed spiral antenna . . . . .	IX-16
IX- 9.	Conical antenna . . . . .	IX-16
IX-10.	Antenna location and deployment scheme . . . . .	IX-18
IX-11.	Transponder . . . . .	IX-19
IX-12.	Command storage unit. . . . .	IX-20
IX-13.	2 1/2D memory organization . . . . .	IX-21
IX-14.	Command processor . . . . .	IX-22
IX-15.	Spacecraft clock. . . . .	IX-23
IX-16.	Experimental plot of gain of an S-band, cavity-backed, spiral antenna . . . . .	IX-25
IX-17.	Experimental data of cavity-backed, spiral antennas . . . .	IX-26
IX-18.	Composite antenna patterns . . . . .	IX-27

## LIST OF ILLUSTRATIONS (Continued)

Figure	Title	Page
IX-19.	Bit error rate . . . . .	IX-28
IX-20.	Temperature-controlled oven . . . . .	IX-34
IX-21.	Oscillator frequency change with temperature . . . . .	IX-35
IX-22.	Curves of mismatch oven temperature and the crystal turning point . . . . .	IX-37
IX-23.	RZ recording wave forms . . . . .	IX-39
IX-24.	NRZ recording wave form . . . . .	IX-39
IX-25.	Comparison of NRZ and S $\Phi$ M . . . . .	IX-40
IX-26.	Power spectral density . . . . .	IX-41
IX-27.	Block diagram of tape recorder electronics . . . . .	IX-41
IX-28.	Output of tape recorder . . . . .	IX-42
IX-29.	AC bias . . . . .	IX-44
IX-30.	Tape recorder . . . . .	IX-46
IX-31.	Tape recorder transport schematic . . . . .	IX-48
IX-32.	Preloading of bearings . . . . .	IX-49
IX-33.	Format for experiment checkout telemetry . . . . .	IX-55
IX-34.	Block diagram format generator . . . . .	IX-56
IX-35.	Format for launch and OAS telemetry . . . . .	IX-56
IX-36.	Format for fixed experiment telemetry . . . . .	IX-58

## LIST OF ILLUSTRATIONS (Concluded)

Figure	Title	Page
IX-37.	Generalized format control loop . . . . .	IX-59
IX-38.	MSFC command format . . . . .	IX-60
IX-39.	Modified command format . . . . .	IX-60
IX-40.	Autocorrelation function of an NRZ of a random signal . . .	IX-65
IX-41.	Split phase signal autocorrelation function . . . . .	IX-66
IX-42.	Power spectral density of downlink signal . . . . .	IX-66
IX-43.	Signal combined with noise from tape and channel . . . . .	IX-69
IX-44.	Communications system block diagram . . . . .	IX-71
IX-45.	Data handling system reliability block diagram . . . . .	IX-73

## LIST OF TABLES

Table	Title	Page
IX- 1.	Summary Timing Requirements . . . . .	IX- 7
IX- 2.	Accuracy of Epoch Time Synchronization . . . . .	IX- 8
IX- 3.	C & DH Components in the Equipment Compartment. . . . .	IX-12
IX- 4.	Baseline Remote Multiplexers . . . . .	IX-13
IX- 5.	Ranging Mode Performance Analysis . . . . .	IX-30
IX- 6.	Performance Analysis of Recorded and Real-Time Data Mode . . . . .	IX-32
IX- 7.	Comparison Frequency Sources . . . . .	IX-34
IX- 8.	Spacecraft Telemetry Requirements . . . . .	IX-51
IX- 9.	Experiment Telemetry Requirements. . . . .	IX-52
IX-10.	Telemetry Data Summary . . . . .	IX-53
IX-11.	Spacecraft Modes of Operation . . . . .	IX-53
IX-12.	Worst-Case Telemetry Mode . . . . .	IX-54
IX-13.	Words Per Frame (Based on Worst-Case Frame) . . . . .	IX-57
IX-14.	Data Requirements for Fixed-Experiments-Only Mode (One Frame). . . . .	IX-57
IX-15.	Spacecraft Command List . . . . .	IX-61
IX-16.	Experiment Command Summary . . . . .	IX-64
IX-17.	Command Requirements Summary. . . . .	IX-64

## LIST OF TABLES (Concluded)

Table	Title	Page
IX-18.	Communications System Reliability Numerics Summary . .	IX-72
IX-19.	Data Handling Numerics Reliability Summary . . . . .	IX-72

## CHAPTER IX. COMMUNICATION AND DATA HANDLING SYSTEM

### A. Mission Guidelines

The following guidelines are directly related to the communication and data handling (C & DH) systems for the HEAO-C mission:

- Manned Space Flight Network (MSFN) tracking stations shall be used; Stadan may be used to supplement MSFN.
- The spacecraft shall provide clock signals which must be accurate to at least 0.1 millisecond per day.
- Experimental data rate shall not exceed 25 kbs and total spacecraft data rate shall not exceed 27.5 kbs.

Other guidelines that affected the design were the following:

- Mission life time of 2 years.
- No single point failures.
- Reliability goal of 0.95 for 1 year.

### B. Constraints

The requirements of the communication and data handling systems for HEAO missions A, B, and C are very similar even though the missions are quite different. The scanning maneuvers of Missions A and B had a decided impact on the antenna coverage requirement. The fact that Mission C is a pointing mission, however, does not relax these requirements since the spacecraft must be capable of pointing to any position in the celestial sphere. The fact that one surface of the spacecraft is oriented toward the sun for electrical power may have some bearing on the location of the antennas on the spacecraft.

1. Tracking Network. The constraint that most greatly influenced the system design was the requirement of being compatible with MSFN. Since this network was conceived and configured to meet the requirements of the manned lunar landing, several technical aspects are not optimum to support

the unmanned scientific satellite type mission. These details are pointed out under the sections where they occur.

The two year life time and no single point failures requirements were used throughout the design of the spacecraft to insure a high probability of completing the long-duration mission. In most instances the concept and hardware selected for Missions A and B could be used with only additional redundancy for critical units. This commonality should provide for a speedy and economical transition from Mission A to Mission B to Mission C. The following tracking stations were considered available even though the status may change considerably between the time of this study and the operational date of Mission C:

Canary Islands (CYI)	(MSFN)
Santiago (SAN)	(MSFN/STADAN)
Ascension (ACN)	(MSFN)
Hawaii (HAW)	(MSFN)
Guam (GWM)	(MSFN)
Carnarvon (CRO)	(MSFN)
Texas (TEX)	(MSFN)
Johannesburg	(STADAN)
Quito	(STADAN)

The baseline uses only 4 of the 10 stations except when special support is required. The requirement for at least one orbit per day of near-real-time experimental data at the control center may necessitate the inclusion of a station such as Rosman which has a high data rate link to Goddard Space Flight Center (GSFC).

A few of the requirements from Missions A and B must be enumerated to complete the overall communication and data handling system considerations. The quality of the data as received at the ground station should have a bit error rate not in excess of one error in  $10^5$  bits. This should be for both tape recorded data and real-time data. The command uplink should provide for signal above noise to preclude erroneous commands being received and acted upon by the spacecraft. In addition to the command encoding security, the transmitted bit error rate should have a signal to noise ratio commensurate with one error in  $10^9$  bits. The downlink bit rate was established at

approximately 500 kbs due to ground station limitations. The subcarrier data rate was limited to 200 kbs by the demodulator circuit. The tracking stations, as presently configured, track and transmit with a single polarization right-hand circular polarization (RHCP) or left-hand circular polarization (LHCP). The transmitter is connected by a diplexer to the same antenna feed system that drives the receiver. The pulse code modulator (PCM) decommutators in the various ground stations are capable of accepting five different types of PCM codes [IX-1]. All five codes are two levels as shown in Figure IX-1.

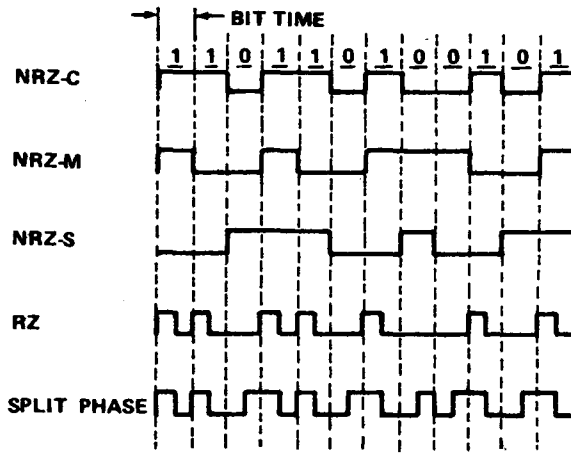


Figure IX-1. Baseband codes.

Related to these codes is the requirement that at least 10 percent of the output power of the transponder remain in the carrier. This is to allow for autotracking wideband signals. The 30 foot antenna stations are considered ideal for the earth orbital mission since the signal is quite strong. The gain of these antennas at S-band is 44 dB and system noise temperature is 170° K. The carrier tracking, as it is presently configured, is shown in Figure IX-2. The loop bandwidth is 700 Hz

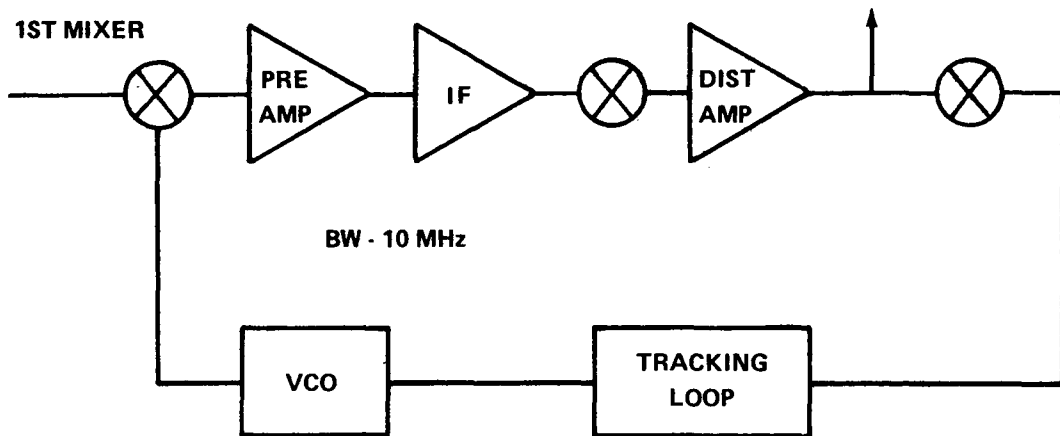


Figure IX-2. Carrier tracking circuits.

for the high doppler rates and strong signals. The threshold of the loop is 6.0 dB. Only a small amount of power is required to lock up this loop. The distribution amplifier drives the FM demodulator and the phase detector. To be compatible with the results of the Mission A and B Phase B studies, only phase modulation is considered. In this mode the composite baseband is recovered using a product detector that has four selectable bandpass filters preceding the detector and output amplifier. The high data rate of the tape recorder plus the subcarrier requires the wideband filter. The subcarrier is biphase modulated by the real-time data. The tape recorder data can be separated from the subcarrier by a low pass filter. The subcarrier will require a demodulator circuit (Figure IX-3). The Apollo telemetry used 1.024 MHz for a subcarrier.

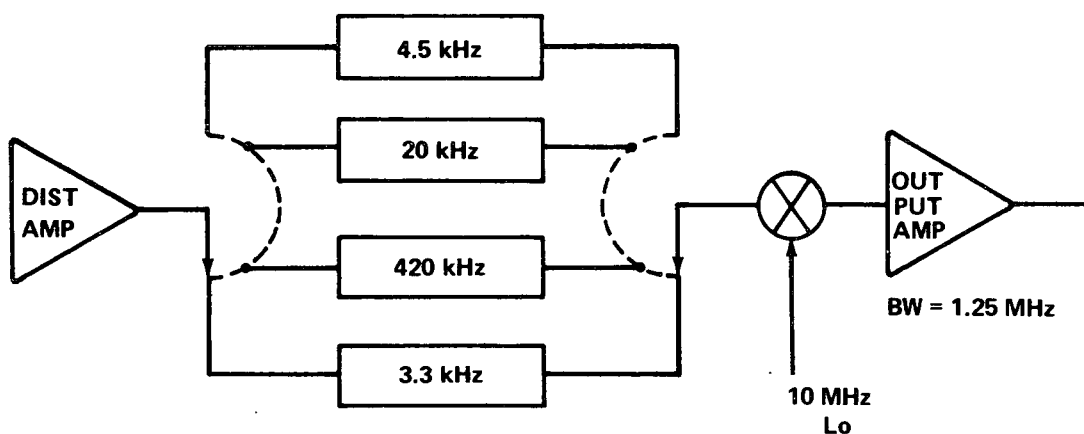
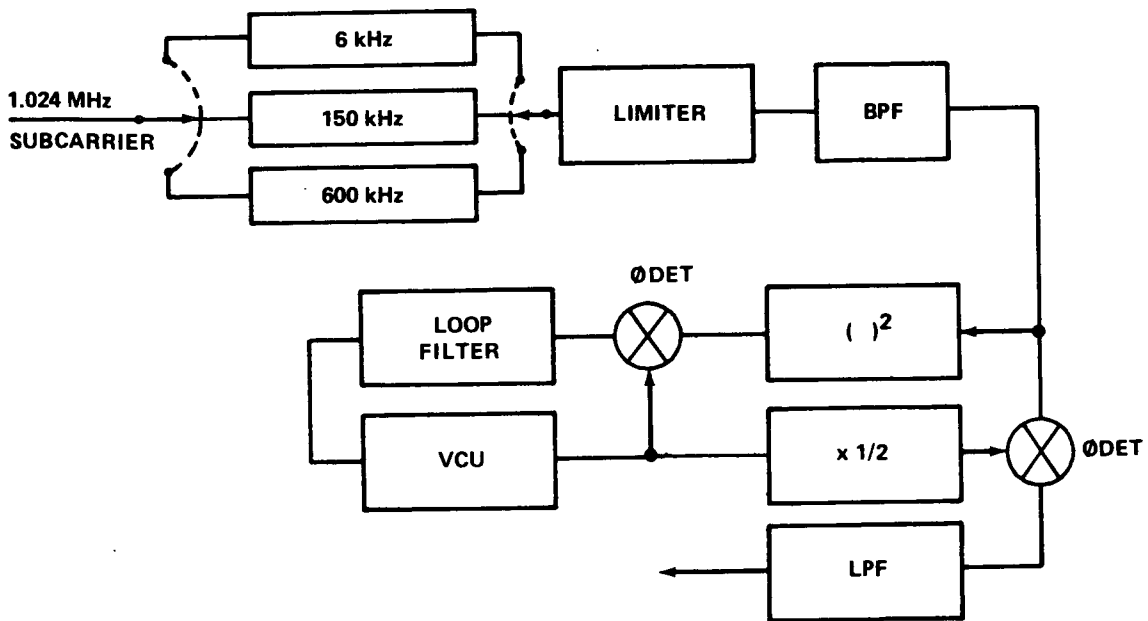


Figure IX-3. Baseband circuits.

The spacecraft had the capability of transmitting 200, 51.2, or 1.6 kbs biphase modulated on the 1.024 MHz subcarrier; it was necessary to provide the demodulator with three different predetection bandwidths. These bandwidths are obtained using a variable bandwidth filter, shown in Figure IX-4, and their values are 600, 150, and 6 kHz, respectively. These bandwidths are equal to three times the bit rate and are selected by a front panel control. When the proper bandwidth is selected for the particular bit rate transmitted from the spacecraft, the 1.024 MHz biphase modulated subcarrier is routed to a limiter, a filter, and a phase detector. In the case of the HEAO-C mission, with 27.5 kbs data on the subcarrier, the 150 kHz filter will have to be used even though it is five times the data rate. The other output to the phase detector is obtained by squaring the 1.024 MHz biphase modulated subcarrier, thus eliminating the modulation and obtaining a 2.048 MHz stable component which is locked on using a modulation restrictive phase-locked loop. The output of the loop is then routed



**BASEBAND INFORMATION**

Figure IX-4. Subcarrier demodulator.

to the phase detector via an  $\times 1/2$  multiplier. The output of the multiplier is the PCM information which is routed to the bit synchronizer. Although a 150 kHz filter is not optimum for the HEAO-C mission, this off-optimum would be reflected in a higher spacecraft transmitter power requirement.

The ground station timing system plays an important role in the tracking and telemetry data by providing reliable and accurate time tags or reference scalars. The system consists of three different types of precision frequency sources, redundant time standards, a receiver for comparison with WWV or LORAN-C (depending on location), and a signal distribution patch panel. The three frequency sources are ultraprecise cesium beam frequency standard, rubidium atomic frequency standard, and quartz crystal oscillator in a double oven having proportional control. The three sources are slaved together by the combiner and remain within  $\pm 12$  degrees of each other. Each of the sources provides a 5 MHz output that is operated on by the various elements to derive 5 MHz, 1 MHz, and 100 kHz for distribution. A binary code digital (BCD) to binary converter provides time of the year down to one millisecond. This signal can be recorded on one of the tracks parallel to the spacecraft data.

The magnetic tape recorders at the ground stations can be functionally divided into three categories depending on their application: (1) wideband (video), (2) narrowband and (3) voice. The wideband recorders are capable of recording signals from 400 Hz to 1.5 MHz in direct mode and from dc to 500 kHz in the FM mode. The narrowband machines are used to record tracking data and verification signals. These machines operate from dc to 250 kHz on 14 channels. Wideband FM signal processing is used for data from 300 Hz to 250 kHz. The voice recorders are not of interest to the HEAO-C mission.

2. Experiments. The large area (LA) and high resolution (HR) experiments generate the majority of the experiment data, and the following requirements will be discussed first:

- a. Data rate of 20 kbs maximum.
- b. Clock accuracy of 0.1 msec.
- c. Command capability of 300 commands with time execution accuracy of 1 second in 24 hours.
- d. Computer synchronous signal of approximately 17 kHz.

The data rates from the LA, HR, and miscellaneous experiments are exceptionally high. The high resolution position detector and the aspect sensor are the largest contributors. The fact that the position of each source in a field of view must be very accurately located with respect to the entire field requires a rather long data word. The spacecraft movement establishes the word rate. The clock accuracy requirement is brought about by the desire to observe X-ray pulsars with several of the instruments. The accuracy as stated does not mean that the spacecraft clock must be synchronized with radio station WWV or the Naval Observatory; rather, it means that time tags can be corrected and correlated with earth based visual observation to within 0.1 msec. This certainly requires a very good frequency source on the spacecraft, but is also places a very demanding requirement on tracking station time standard and operating procedures. The clock input for the experiments' computer must be supplied from the spacecraft. The exact frequency of this signal will have an impact on the frequency selected for crystal in the spacecraft clock; they should be related by some whole number. This in turn will have an influence, to a certain degree, on the time resolution of the spacecraft clock. The low energy (LE) telescope has similar requirements in the area of timing. These are given in Table IX-1.

TABLE IX-1. SUMMARY TIMING REQUIREMENTS

	Large Area and High Resolution	Low Energy
Resolution	1 msec	0.1 msec
Accuracy	0.1 msec	0.1 msec
Long-term Stability	$\pm 5 \times 10^{-9} / 24 \text{ hr}$	1 msec/orbit
Short-term Stability	$\pm 2 \times 10^{-10} / \text{sec}$	No spec.

The low energy experiments require the better time resolution of 0.1 msec. This implies a square wave frequency of pulse duration of 0.1 msec. This would require a frequency of at least

$$f_s = \frac{1}{T} = 2 \times 10^4 \quad \text{or} \quad 20 \text{ kHz.}$$

Accuracy requirements of more than 0.1 msec may place a constraint on which tracking stations may be used. Remote tracking stations less than 1500 statute miles from a LORAN-C transmitter can be synchronized with the U. S. Naval Observatory Master Oscillator to within 1 microsecond. However, for ranges where sky wave is used (greater than 1500 and less than 10 000 statute miles), a 25 microsecond capability exists. It is doubtful that all MSFN tracking stations can routinely obtain and maintain 1 to 25 microseconds without detailed post pass analysis. A value of less than 100 microseconds was demonstrated during Apollo missions using portable clocks and the Jet Propulsion Laboratory (JPL) moon bounce technique. Listed in Table IX-2 are MSFN stations proposed for Mission C and the present measured accuracy and projected future capability. Data on the Stadan stations were not available but would be worse than MSFN. The time correlation technique used an Apollo spacecraft and one station as a reference station. On command from the reference station, a counter at each station in view of the Command and Service Module (CSM) was activated. The counter was driven by a 1 MHz signal from the primary precision frequency source at the station. The counter was stopped in the same manner. The timing accuracy was determined by the following equation:

$$\text{Time bias} = \frac{C_r - C_i}{K} - \frac{R_r - R_i}{C}$$

TABLE IX-2. ACCURACY OF EPOCH TIME SYNCHRONIZATION

Station	Measured Accuracy of Sync (Microsec)	Method	Future (Microsec)
Ascension	± 50	Time Corr.	±25
Hawaii <sup>a</sup>	± 30	Time Corr.	±10
Santiago	±100	Port. Clock	±25
Canary Island	± 20	Time Corr.	±10
Guam <sup>a</sup>	± 15	Time Corr.	±10
Texas <sup>a</sup>	± 10	Time Corr.	±10
Carnarvon	± 25	GEOS-B	±25

a. Synchronized by LORAN-C station.

where  $C_i$  is the counter reading from  $i$ th station;  $C_r$  is the counter reading reference station;  $K$  is the counter frequency (1 MHz);  $R_i$  is the slant range from CSM to  $i$ th station;  $R_r$  is the slant range to reference station; and  $c$  is the speed of light. The results of the Apollo 14 time correlation test indicated that precision network synchronization using LORAN-C techniques can provide accuracies to within 100 microseconds. The MSFN Network specification is ±200 microseconds.

The low energy experiment method of determining the presence of an X-ray pulsar requires a stable clock during the measurement. It is stated as 1 millisecond per orbit. Since the orbital period of a spacecraft at 270 n. mi. is 5730 seconds, this is about  $1.5 \times 10^{-2}$  which is well within the requirements of the large area and high resolution experiments. The  $\pm 2 \times 10^{-10}$ /sec short-term stability of the LA and HR does not seem to present a problem. These requirements are well within the present state-of-the-art for crystals in a controlled oven environment.

The 300 commands required for LA and HR experiments will require some changes in the basic Apollo command format. To have 300 commands in a repertoire, at least 9 bits must be available; at present there are only 6 in the information portion of the command message. This would provide for only 64 commands per decoder address. It is evident that some change will be required; however, the message length must remain 30 bits or less. The internal message structure can be changed by changes in the software. The sum of the experiment data does not exceed the ground rule of 25 kbs. The arithmetic sum is only 22 kbs with synchronization, frame, subframe, etc., causing a slight increase.

### C. Functional Requirements

Many of the functional requirements of the C & DH system have been covered in other sections, but are specifically addressed here to indicate clearly what is expected of the system for Mission C. This system can, from the functional point of view, be characterized as a four-element system, comprised of the RF system, commands, data acquisition, and data storage equipment. The RF system provides a means for sending data to the spacecraft and receiving data from the spacecraft through the tracking stations distributed along the path of the spacecraft. The uplink and downlink carrier frequencies are coherently related to permit determination of range and range rate by comparison of the uplink and downlink range code. The unified S-band system is a single carrier for all uplinks and downlinks. Channels for the various types of data are provided by a subcarrier superimposed on either the uplink or downlink carrier. The command element provides a means for controlling the spacecraft systems and experiments. The commands are encoded for security and are modulated on a subcarrier for combining with the range code and for transmission to the spacecraft. The spacecraft must demodulate, decode, and distribute these commands to the various subsystems of the spacecraft. The data handling equipment acts as an interface between the C & DH system and the other subsystems and experiments of the spacecraft. It acquires, organizes, encodes, and transfers data from these elements to either the RF equipment for transmission to the ground or to data storage equipment for storage until a contact is made with the ground station. The nature of the mission requires that the system be capable of multiple formats depending on the mode of operation and the complement of instrument being used at a given time. The system must be flexible enough to allow changes in the measurement and location equipment. The system provides internal control for various formats, bit rates, synchronization words, channel address, and subchannel addresses. The remote multipliers can accept analog, bilevel, discreets, and low-level

analog signals. The data handling equipment also provides timing for those elements directly under its control and supplies timing signals and time from start of mission for other subsystems in the spacecraft. The data storage equipment provides a means of storing the experimental and spacecraft engineering data until the spacecraft is in contact with a ground station. It also provides for rotation of the tape recorders to divide the operating time evenly among operative machines.

## D. Baseline Description

The baseline communication and data handling system can best be described by referring to a block diagram of the system. A simplified one is shown in Figure IX-5 for this purpose.

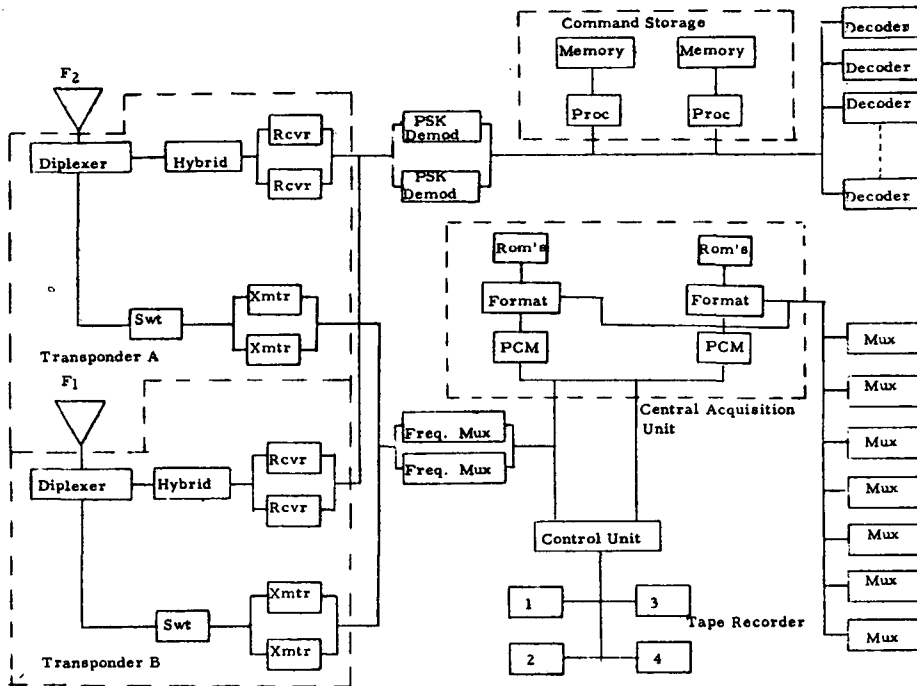


Figure IX-5. Baseline C & DH system block diagram.

Two antennas are used to provide omnidirectional coverage. Each antenna operates on a different frequency to preclude interference nulls and lobes. One antenna is mounted on a boom to ensure a slight overlap of the two antenna patterns so that selection diversity combining on the spacecraft is

possible. The diplexer, hybrid, receiver, and transmitter are all part of the transponder. Two transponders are required since each must operate on a different frequency. The transponder contains redundant receivers and transmitters. This provides a higher probability of completing a two year mission and precludes a single failure from completely aborting the mission. The phase shift keyed (PSK) demodulator and frequency multiplexer are considered a part of the RF equipment even though they are not contained within the transponder. The PSK demodulator performs the dual function of combining the output signal of the two transponders and detecting and decoding the uplink command subcarrier. The command is reduced to its original information bits (5 sub-bits per information bit) and outputted to the command processor and the remote decoders. If the message contains a time tag (message length exceeds 13 bits), the total message less vehicle address is stored randomly in the command memory. If the command message is for real-time execution, the remote decoder, whose address appears in the subsystem location, acts upon the command. The messages that are stored in the memory are called up periodically and compared with the spacecraft clock. When the time tag matches the spacecraft clock, the subsystem address and the text are shifted out of the register onto the command lines. The remote decoder recognizes the command as real-time command and acts upon it as if it had just been received from the ground station.

The data acquisition portion of the data handling system has many remote multiplexers throughout the spacecraft at the major electronic assemblies and subsystems to provide entry for the data into the system. The central acquisition element is comprised of the format generator, read only memory, and PCM encoder. The PCM encoder addresses the multiplexer based on the information contained in the memory. The format generator provides various formats, bit rates, synchronization words, channel addresses, and subchannel addresses. The PCM encoder is a misnomer in the sense that analog to digital conversion takes place at the remote units. The encoder takes PCM data and encodes them into a telemetry frame for either transmission or storage in the tape recorder, or both.

The data storage system contains a control unit and four reel-to-reel magnetic tape recorders to provide sufficient storage capacity so that no information will be lost even when ground stations are "down" and less than four stations are available. In the normal mode of operation, one recorder is operated while another is being played back. Also, the data being generated on board are provided to the frequency multiplexer for combining with output of the tape recorder. The recorders are sequenced so that the operating time is divided evenly among the four units.

The frequency multiplexer phase shift keys a 1.024 MHz subcarrier with real-time data and combines it with the tape recorder data. The modulation indices are controlled by the proper mix of the two signals. At times, the tape recorder data are replaced by the pseudo random noise (PRN) code for tracking. This will require a change in the indices to optimize the division of power between the carrier and the subcarrier.

Table IX-3 characterizes the weight, volume, and power of the baseline C & DH system.

TABLE IX-3. C & DH COMPONENTS IN THE EQUIPMENT COMPARTMENT

Item	Weight (lb)	Power (W)	Dimensions (in.)
Transponder (2)	48.0	56.0	8 × 6 × 13
Frequency Mux (2)	2.0	4.0	7.25 × 5 × 1.6
PSK Demodulator (2)	2.0	0.8	1.3 × 2.8 × 6
PCM Encoder (2)	8.0	6.4	6 × 9 × 2.8
Format Gen. (2)	7.6	4.2	6 × 9 × 2.8
Command Processor (2)	4.0	15.6	6 × 9 × 2.8
Command Memory (2)	12.0	7.0	6.2 × 7.0 × 4.8
Remote Mux (40)	12.0	1.2	2.8 × 2.8 × 1.0
Remote Decoder (8)	8.0	1.4	6 × 9 × 2.8
Data Storage Control (1)	3.0	1.0	6 × 7.3 × 1.6
Tape Recorder (4)	60.0	30.0	9 × 7.25 × 5.75
Clock (1)	<u>3.0</u>	<u>14.0</u>	6 × 9 × 1.4
Total	169.6	141.6	

The remote multiplexers are placed at locations of the major electronic assemblies and at central points within the various subsystems among the telemetry sensors. These locations are listed in Table IX-4 for the baseline to show the magnitude of the data handling system.

TABLE IX-4. BASELINE REMOTE MULTIPLEXERS

Subsystem or Assembly	Quantity	Redundant	Total
Reference Gyro Assembly (RGA)	3	Yes	6
Control Moment Gyro (CMG)	4	Yes	8
Star Tracker	2	Yes	4
Digital Sun Sensor (DSS)	1	No	1
Wide Angle Sun Sensor (WASS)	3	No	3
Reaction Control System (RCS)	1	Yes	2
Experiments	7	No	7
Thermal Control System	1	No	1
Orbit Adjust Stage (OAS)	1	No	1
Power Control Assembly	2	No	2
Format Generator	1	No	1
Clock	1	No	1
Tape Recorder Control Assembly	1	No	1
Transponder	1	Yes	2

The Phase B study contractors ascertained that remote decoding was the most feasible for Missions A and B. This was based on such factors as flexibility, cost, growth capability, reliability, and weight. The weight for a command system with a capability to handle the maximum number of commands

that the Apollo command message structure will allow is quite significant. It is assumed that each command must be sent at least 10 feet from the central decoder. Figure IX-6 indicates that if 20 feet (two conductors) of #22 AWG wire were used, the weight would be about 0.06 pound per command. The message format for Apollo will allow as many as 512 commands. This could amount to about 31 pounds in harness weight and 1 pound for the central decoder. However, if 8 remote decoders are used with 10 feet of wire per decoder (20 ft with return) and fanning of 3 feet per command, the weight would be 13.5 pounds as shown below:

	<u>Weight (lb)</u>
8 decoders (1 lb each)	8.0
(5 ft × 20 ft × 8 ft) (0.003)	0.9
512 × 3 × 0.003	$\frac{4.6}{13.5}$

This would not be a significant weight savings on a large spacecraft like HEAO; however, if one additional bit is added to the information portion of the message format (which is contemplated) the weight would grow to 61.5 pounds and the weight savings becomes attractive. The weight of remote decoders for twice the capacity would only increase by 4.6 pounds for fanning out the additional commands at each remote decoder (see Figure IX-6).

It is interesting to note that the remote acquisition of telemetry data is not quite as straightforward as the command system. Figure IX-7 shows that the remote multiplexers must handle more than 4 digital channels to realize any saving. If the device can multiplex 8 channels, a savings can be realized only if the average distance from central unit exceeds 10 feet. For analog, slightly over 32 channels greater than 2.5 feet were required.

The versatility, reliability, growth, and efficient means of interfacing with the various and continually changing experiments overrides the meager cost savings.

1. Antennas. The baseline antenna system consists of two right-hand, circularly polarized, S-band antennas. One antenna is a cavity-backed, four-arm spiral (Fig. IX-8), while the other is a conical log-spiral on a 6 foot boom (Fig. IX-9). The coverage pattern, based on tests of the individual elements, indicates a very nearly perfect omnidirectional coverage; however, the spacecraft and its solar panels will be certain to cause some nulls due to reflection.

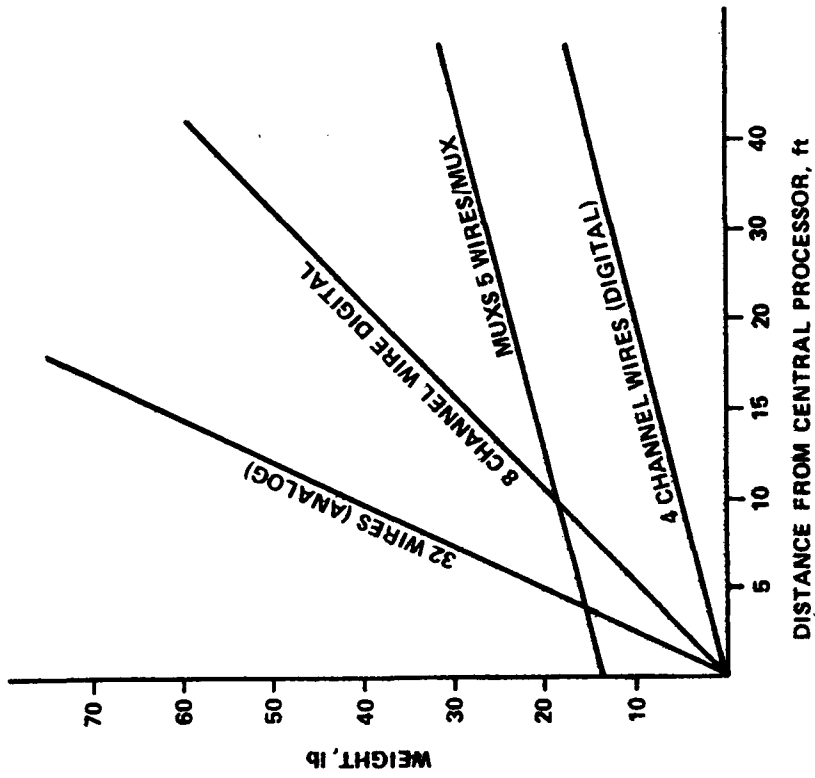


Figure IX-7. Comparison of central multiplexer and remotes.

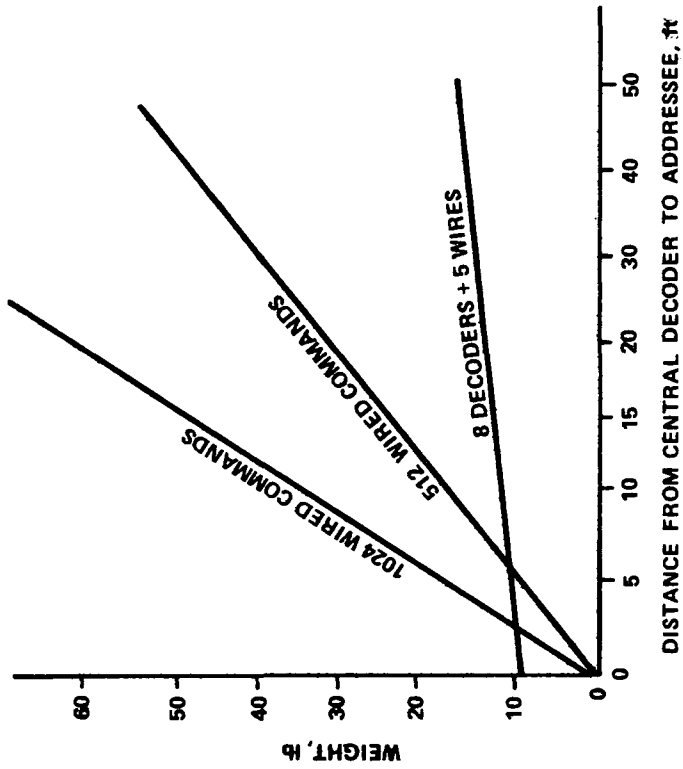


Figure IX-6. Comparison of central and remote decoders.

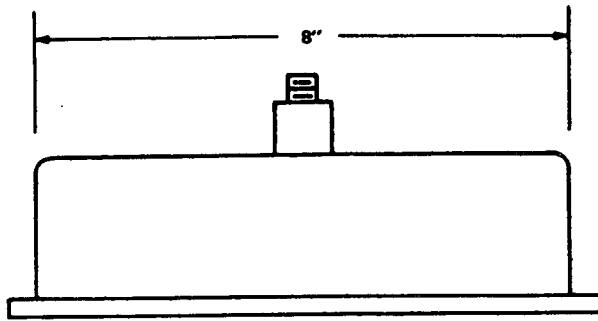


Figure IX-8. Cavity-backed spiral antenna.

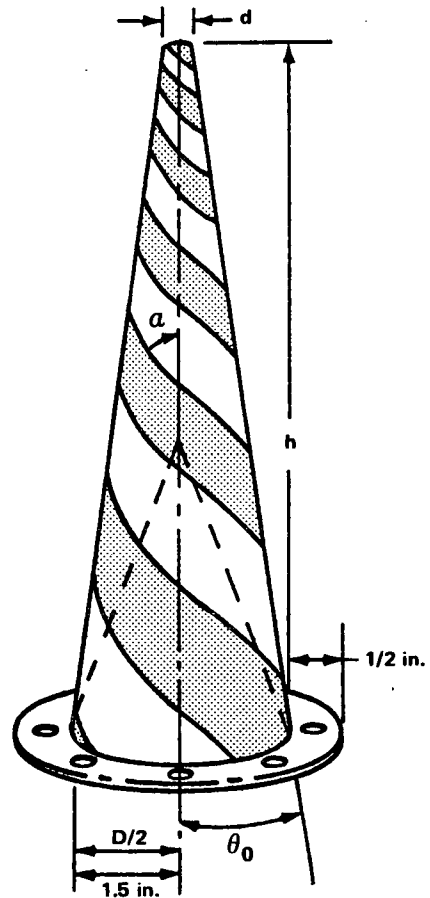


Figure IX-9. Conical antenna.

The physical dimensions of the conical antenna had an influence on the deployment scheme. It would be highly desirable to have the apex of the cone of the conical antenna always pointed away from the spacecraft, even in the launch configuration. Then in the event of a malfunction of the deployment mechanism, the pattern would be symmetrical. The usual design of the conical antenna minimizes back lobes; however, here it is desired to have a cardioid pattern. Figure IX-9 [IX-1] shows the parameters in the following equations:

$$d = \frac{1}{4} \lambda_1 \quad \text{and} \quad D = \frac{3}{8} \lambda_2 \quad ,$$

where  $\lambda_1$  is the highest frequency that must be radiated and  $\lambda_2$  is the lowest. The height of the truncated cone is found by trigonometric relationships of the

cone. Normally the half-angle of the cone is about 10 degrees; however, for the baseline an angle of 7 degrees was selected based on experimental measurements made at the Marshall Space Flight Center (MSFC) antenna range. The height of this antenna was approximately 10 inches. This would exceed the available space if the antenna was folded so that it was at a right angle with the boom for launch. Since the reliability of a simple deployment scheme as used here is so high, the antenna is mounted coaxial with the boom.

The cavity-backed spiral is located on the surface of the spacecraft normal to the sun vector. It is about one wavelength (lowest frequency) in diameter and the cavity is a quarter of a wavelength deep. The physical location and deployment scheme is shown in Figure IX-10.

2. Transponder. The transponder (Fig. IX-11) is a unified S-band type developed for the Earth Resources Technology Satellite (ERTS). "Unified" may be explained as a single carrier for the uplink and a single carrier for the downlink. This transponder was designed to be compatible with the MSFN. The baseline contains two units because of the frequency diversity scheme. The unit is all solid state packaged in a sealed housing, and thermally coupled to the spacecraft's cold plate. Each transponder is redundant within the package. The unit includes a built-in diplexer and single antenna port. The unit operates between 2200 and 2300 MHz at an output power of 1 watt minimum. The modulation bandwidth is from 300 Hz to 3 MHz. It is capable of phase modulation of +4 radians, with a deviation sensitivity of 1 radian per volt.

The receiver operates between 2020 and 2120 MHz and has a noise figure of 8 dB and a sensitivity of -46 to -126 dBm. The transmitter requires 21 watts and the receiver 7 watts. The cold plate must be between +32° F and 118° F for operation. The unit is modified slightly from the ERTS configuration to provide an automatic gain control (AGC) signal for use in the frequency diversity selection in the PSK demodulator. The uplink frequency and the downlink frequency are related by the MSFN ratio of 240:221.

3. Command Storage. The command storage system (Fig. IX-12) consists of two elements: a low-power, high-reliability, plated-wire memory and a customized processor. The memory has a capacity of 4096 words of 30 bit length. The data are transferred between the processor in parallel. The speed of the memory has 2.50 nanoseconds read time and requires 500 nanoseconds write time. The memory is organized on a 2 1/2D basis. A 2 1/2D memory represents a compromise between bit-organized and word-organized core memories. The 2 1/2D memories use a coincident current and a wire select. In Figure IX-13, the X drive line is common to cores in

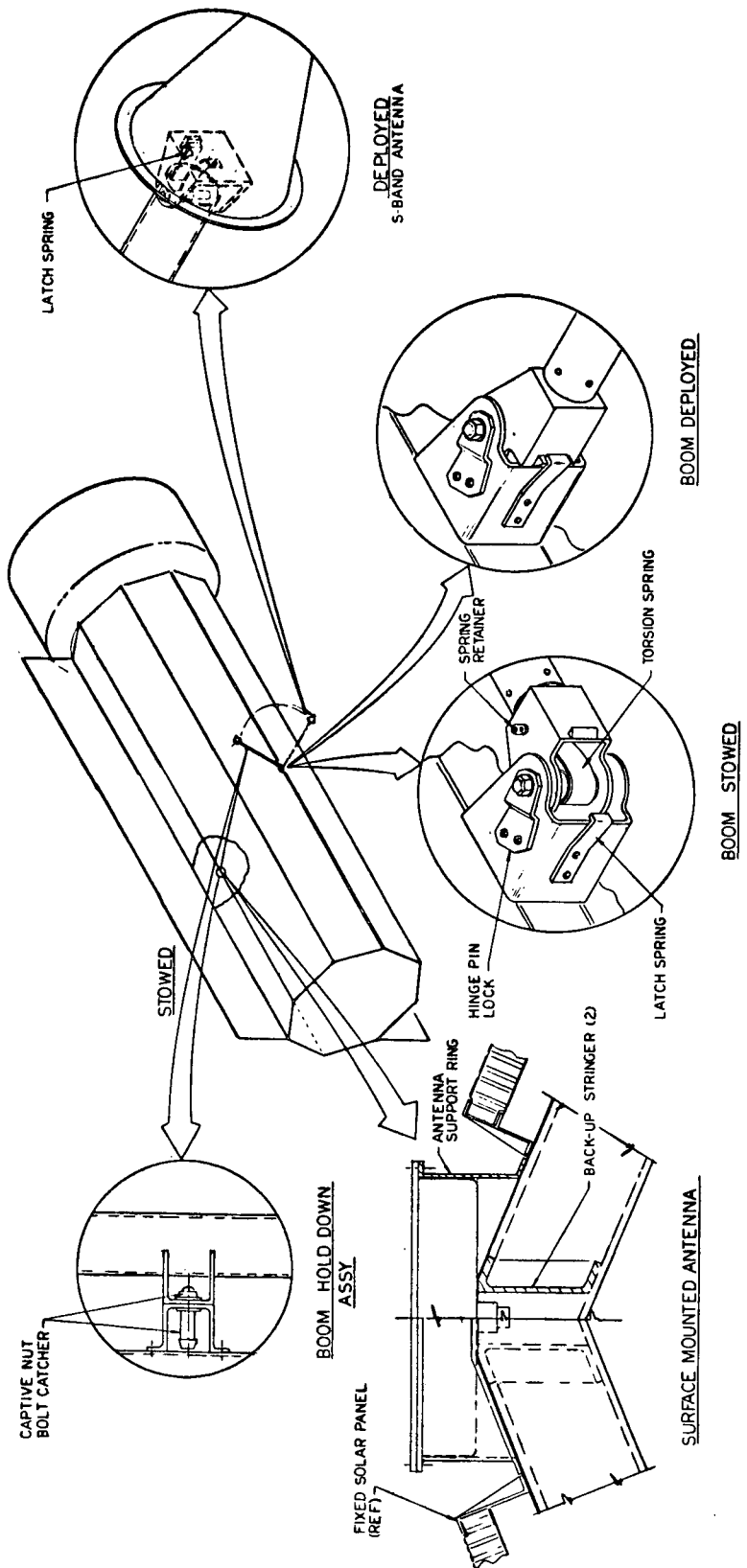


Figure IX-10. Antenna location and deployment scheme.

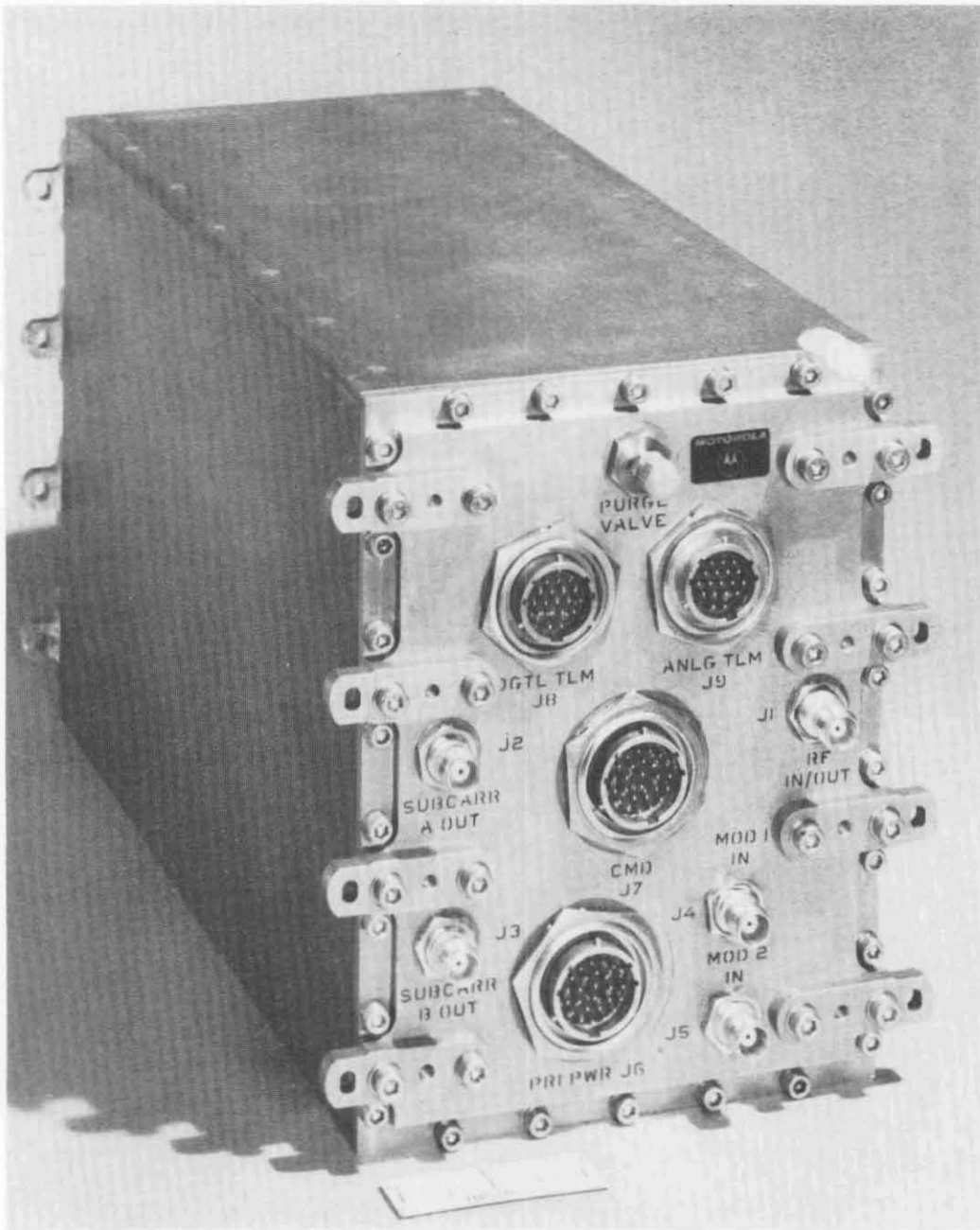


Figure IX-11. Transponder.

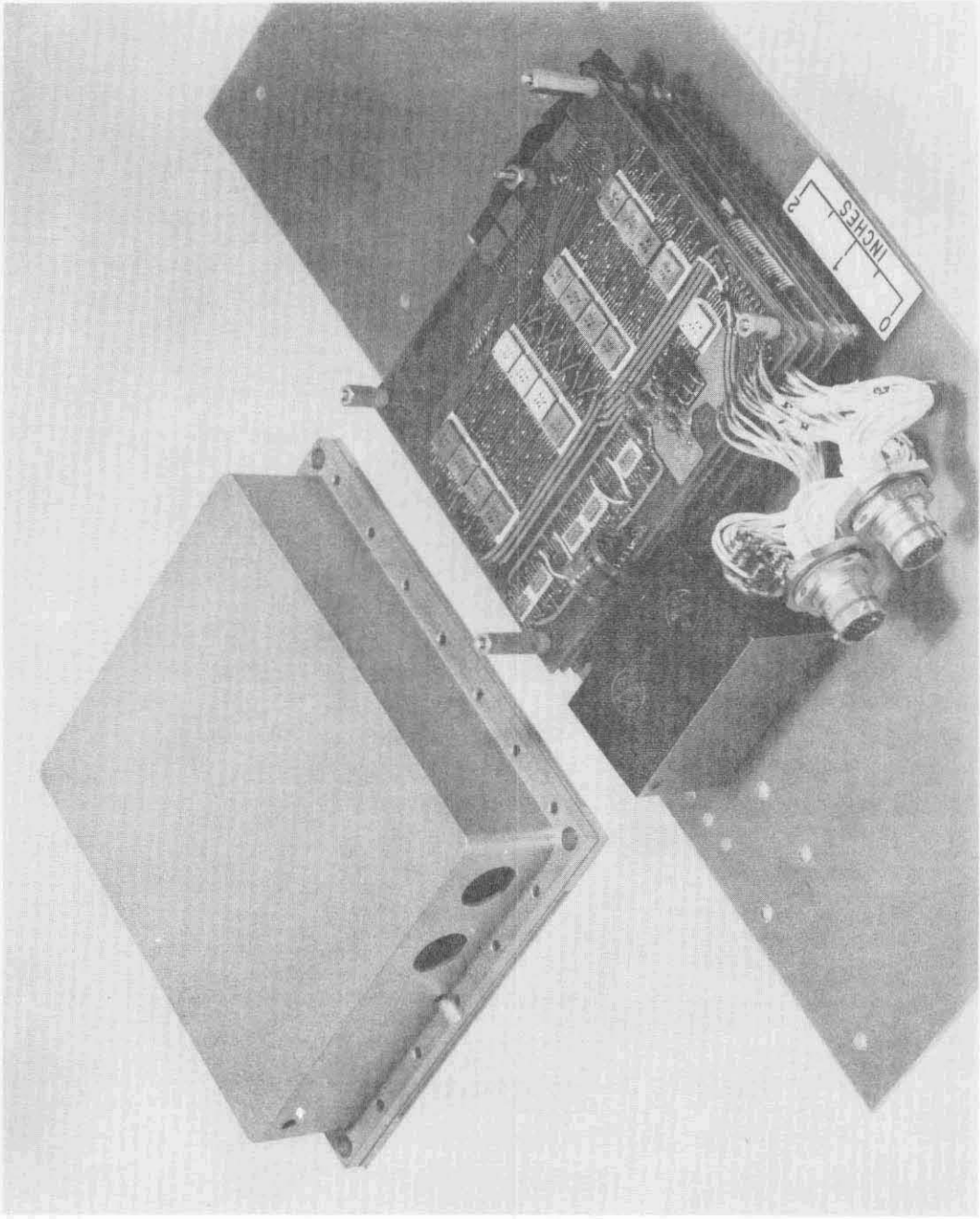


Figure IX-12. Command storage unit.

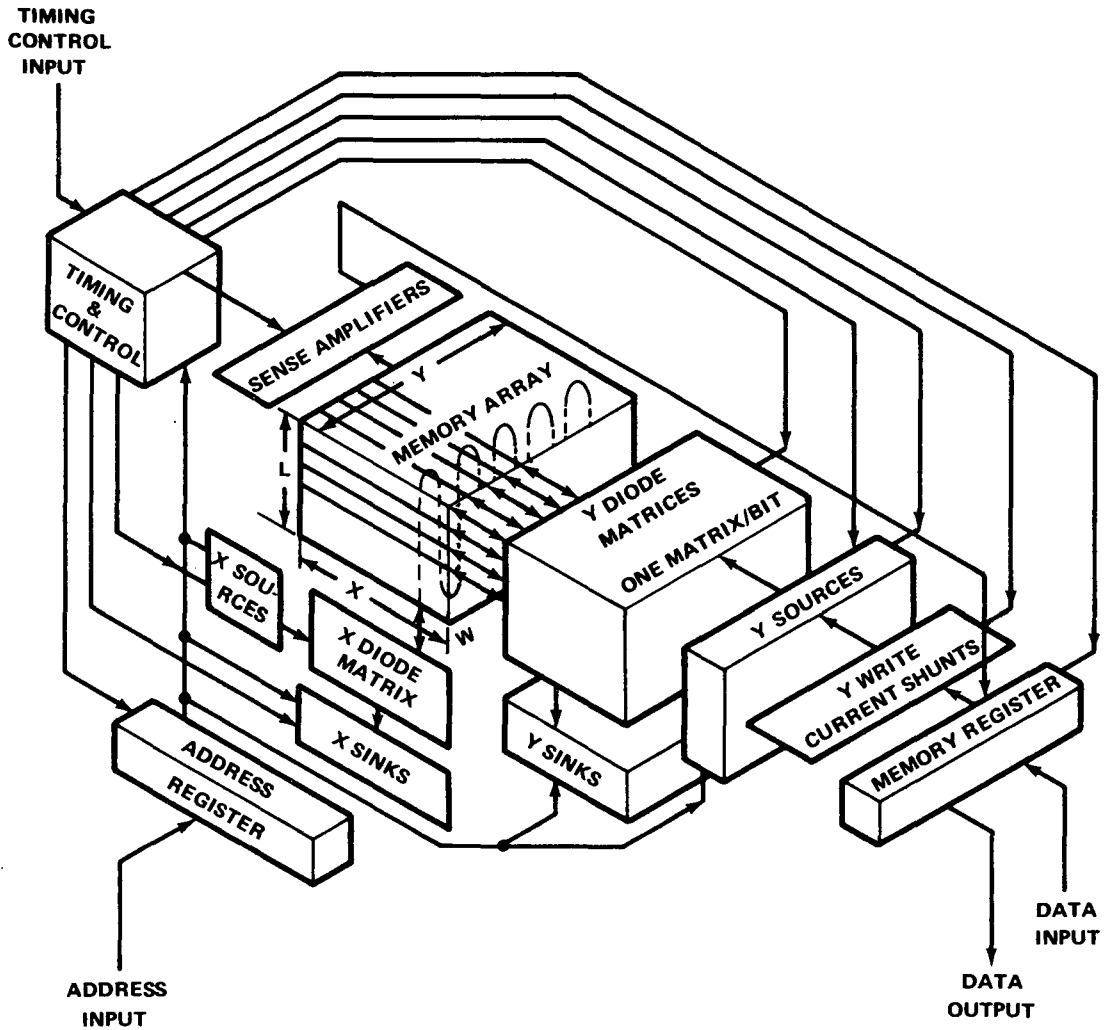


Figure IX-13. 2 1/2D memory organization.

various levels. A single word select circuit consists of X diode matrix, and X source and sink switching circuits are required for word selection. There is a Y drive for each of the locations in the L-Y plane.

The command processor (Fig. IX-14) contains certain logic circuits that are needed to operate the system. Since the spacecraft can be used for real-time and stored commands, the processor must be able to distinguish between the two. Since the stored command is always 30 bits and vehicle

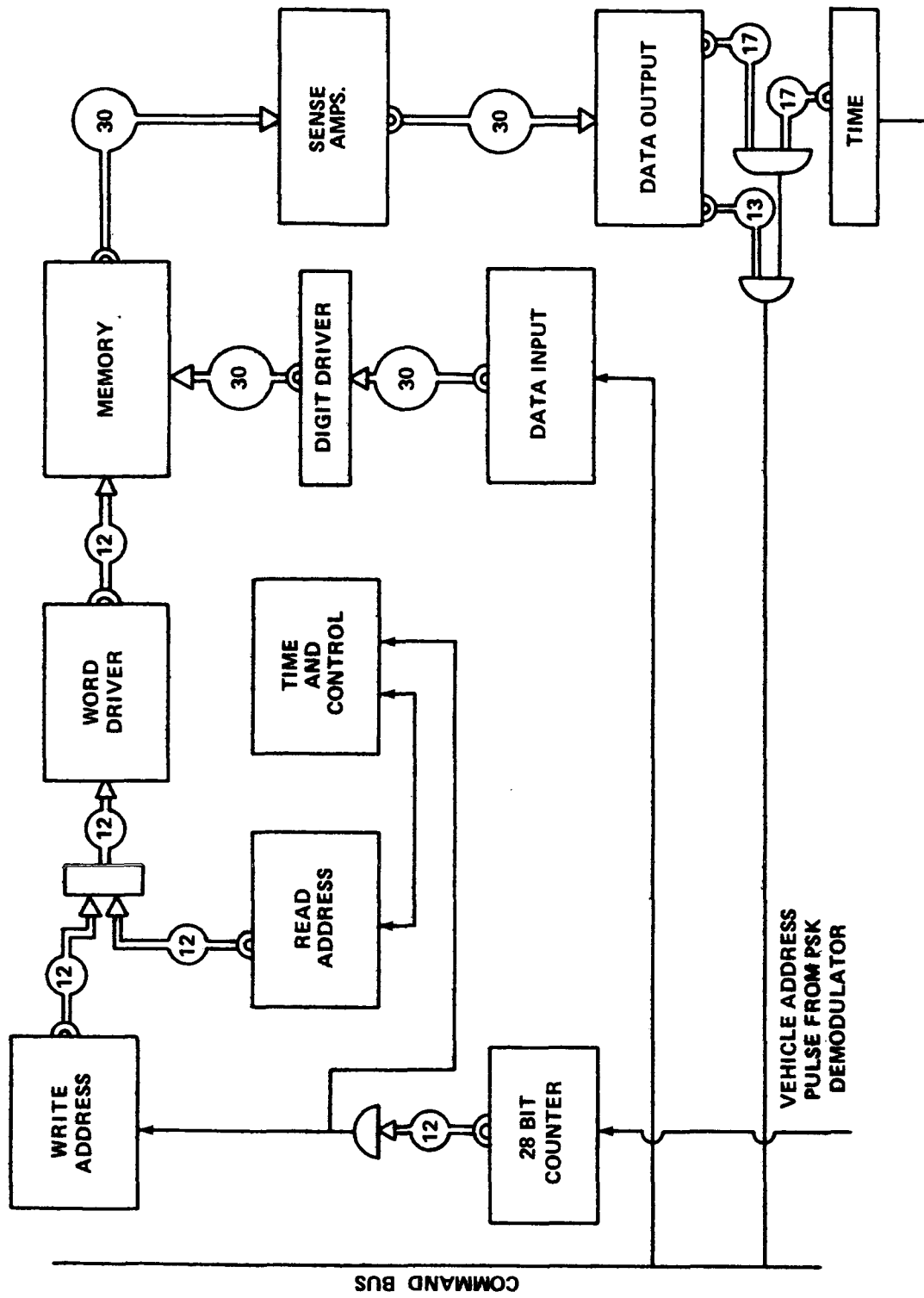


Figure IX-14. Command processor.

address is 2 bits, if the number of bits between two vehicles' addresses is 28 bits, the processor transfers the contents to storage. The storage location is determined by a word counter; it is incremented each time a word is stored. The telemetry system receives verification that a command has been stored. All commands are stored in the sequence in which they are received. When the word counter reaches the capacity of the memory, it recycles to one. The contents of the memory are continually cycled through a register for comparison with the clock, and, when the time tag and clock agree, the register is clocked out onto the command bus and acted upon by the remote decoder whose address is contained in the message.

4. Remote Multiplexer. The 40 remote multiplexer units act as a cable reducer as well as a flexible interface. Each unit is rectangular in shape and all identical except for the jumpers on the program connector. This connector provides a flexible interface that allows changes to be made until the vehicle is placed on the launch pad. The unit is capable of accepting all types of inputs. The capacity is 64 analog or 8 digital inputs per unit. Analog inputs are converted to digital at the remote unit for ease of operation. The address of channel is generated in proper sequence in the central control elements and transmitted to all units; only the channel addressed responds with an 8 bit word.

5. Clock. The spacecraft clock consists of three crystal-controlled oscillators, shown as OSC #1, OSC #2, and OSC #3 in Figure IX-15. Each

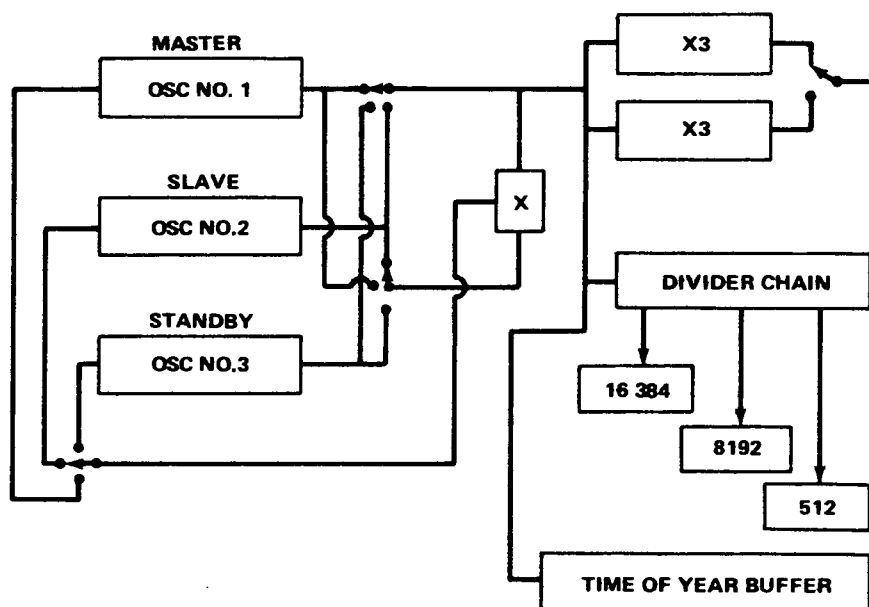


Figure IX-15. Spacecraft clock.

oscillator is located in an oven whose temperature is proportional-controlled to assure freedom from frequency shift due to thermostat cycling. All units are run continuously although only the master and slave are phase-locked at any given instance. The reason for this is that it takes several hours for a crystal to stabilize after the heat has been turned on. The master and slave can be maintained within phase on the order of a few radians. If either oscillator fails, the standby unit becomes the slave and its phase is locked to the surviving oscillator. In this manner, the counters and frequency dividers that provide all the spacecraft timing functions are not affected should an oscillator malfunction.

## E. Performance Analysis

1. Antennas. Obtaining omnidirectional antenna coverage at S-band on a spacecraft as large as HEAO is a formidable problem. The baseline system employs two antennas located on opposite sides of the spacecraft. Both antennas are circularly polarized to preclude losses due to cross polarization. The antennas were selected to give low angle coverage and small aperture. The surface-mounted antenna that was selected is a cavity-backed, four-arm, planar log-spiral. This antenna has good coverage for surface-mounted antennas as can be seen by the polar plot of its gain (Fig. IX-16). These data were determined experimentally by The Boeing Company for another program, but are representative of what could be expected on a HEAO-size spacecraft. This type antenna is usually very efficient and can be matched to the transmitter so that the voltage standing wave ratio (VSWR) does not exceed 1.5:1. This would amount to about 0.2 dB mismatch loss. When coupled with ohmic losses it would not exceed 1.2 dB. This does not include a short length of coax cable to feed the antenna. Since the transponder is located just behind the surface-mounted antenna, the cable loss can be neglected. Figure IX-16 is an experimental plot of the gain of an S-band, cavity-backed, spiral antenna. This antenna can be surface-mounted. While its pattern can be affected by objects in its immediate vicinity, the comparison of experimental and actual application is usually very favorable.

The spiral antenna is ideally suited for the solar array side of the spacecraft since it must be flush-mounted, have a large bandwidth, have circular polarization, and be of small size. The log-spiral meets all these requirements. The power handling capability is limited by its ability to dissipate heat due to power losses in the elements. The dielectric material that supports the elements is usually a poor thermal conductor; however, since the output power is only one watt, this does not seem to be a problem for HEAO. The gain of this

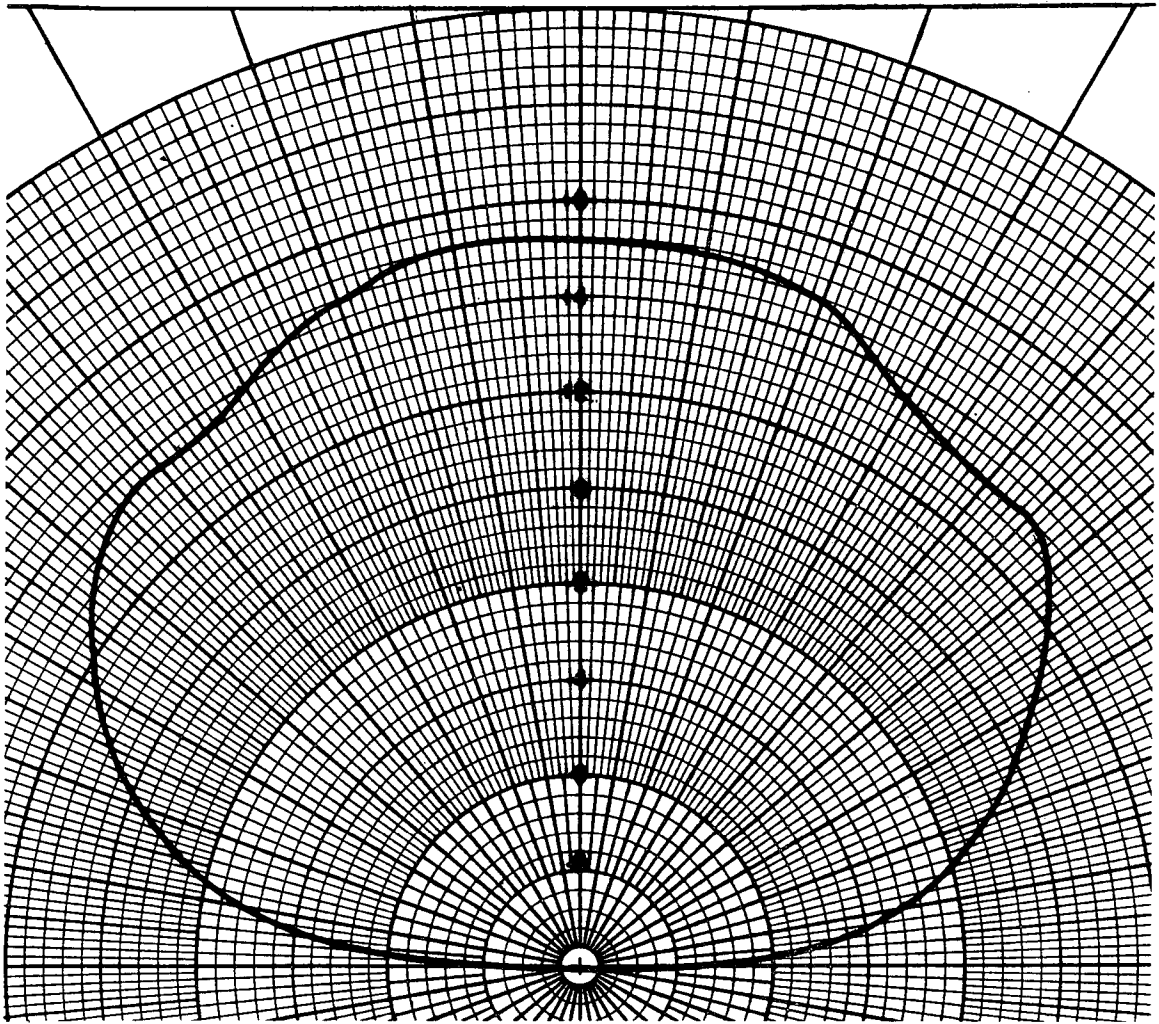


Figure IX-16. Experimental plot of gain of an S-band, cavity-backed, spiral antenna.

type of an antenna is determined by the diameter of the cavity. A curve of gain as a function of cavity diameter in wavelength is depicted in Figure IX-17. The diameter of the cavity in this particular case was selected to be 0.9 wavelength. From the curve this would be about +5 dB gain at the maximum. Very good agreement between measured and theoretical gain was obtained by The Boeing Company. This results in a high degree of confidence that the antenna will work as desired on the HEAO-C. This of course still must be verified on an antenna range.

The antenna on the antisolar side of the spacecraft must be similar to the antenna described above, but it must provide an overlap of coverage of

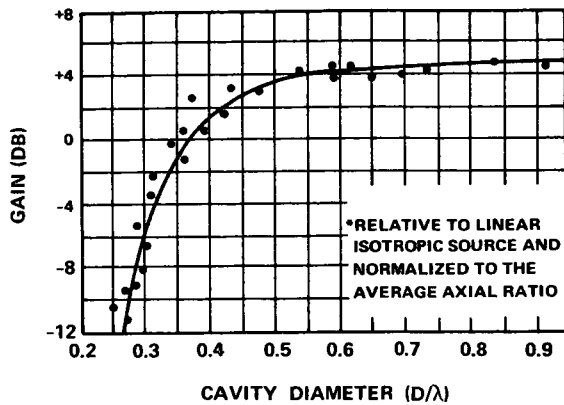


Figure IX-17. Experimental data of cavity-backed, spiral antennas.

the surface-mounted antenna. The only way of providing this with the solar panels extended is to mount the antenna on a boom. A spiral antenna can be wrapped around the surface of a cone. Unlike the planar spiral discussed above, the pattern is unidirectional without a cavity backing. This is desirable for the boom-mounted antenna. A noticeable improvement in bandwidth over the planar can be realized by using a log conical spiral. This can be done since it is not dependent on the cavity depth. The polarization can be made circular by properly

feeding the antenna. A scale model of a conical spiral was tested by the MSFC Antenna Lab. The 1/5-scale-model test results are shown in Figure IX-18. The pattern shows a rather large overlap. The diversity combiner would not be designed to switch until there was a considerable improvement in one antenna over the other, for example 3 dB, then the switch would occur at -5 dBi. This should be the stated gain of the antenna system for worst case conditions.

2. Command Equipment. Sub-bit error is based on the signal-to-noise ratio in the channel. This is illustrated by the curve in Figure IX-19. The sub-bit is coherently phase shift keyed on the 1 kHz clock. For a +8 dB theoretical energy-to-noise spectral density in a 20 kHz bandwidth, the bit error rate (BER)  $10^{-4}$ , therefore  $P_e(\text{SB}) = 10^{-4}$ . The probability of an information bit being in error requires that a "0" was sent but a "1" was decoded, or vice versa. For this to occur, five successive sub-bits must be in error:

$$\begin{aligned}
 P_e(\text{IB}) &= P_e(\text{SB})_1 \cdot P_e(\text{SB})_2 \cdot \dots \cdot P_e(\text{SB})_5 \\
 &= (10^{-4})^5 \\
 &= 10^{-20}
 \end{aligned}$$

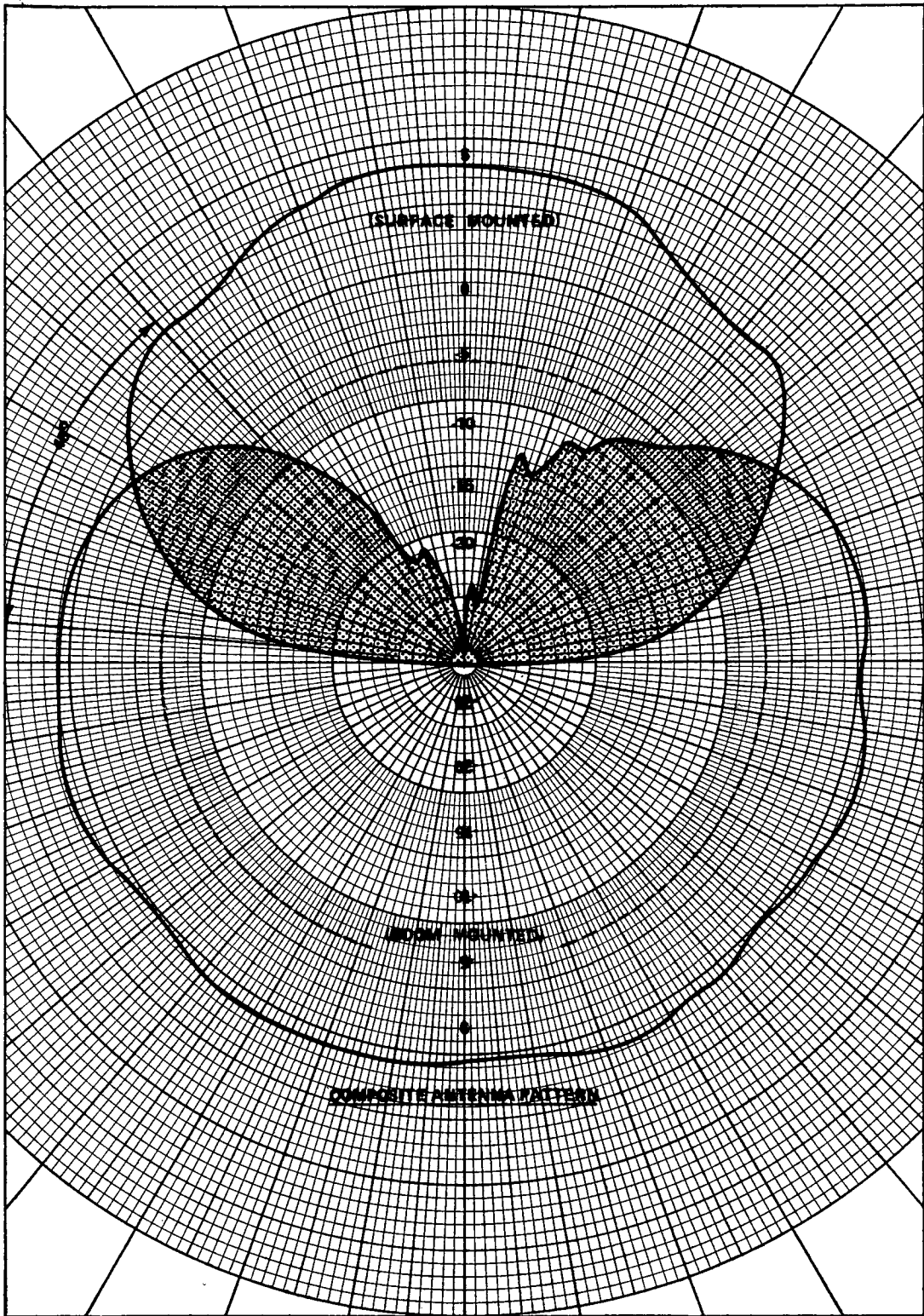


Figure IX-18. Composite antenna patterns.

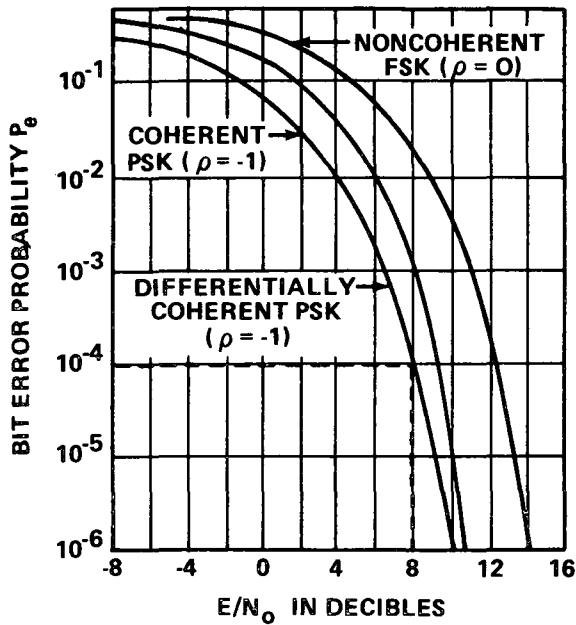


Figure IX-19. Bit error rate.

$$\begin{aligned}
 R(\text{IB}) &= 5P_e(\text{SB}) \\
 &= 5 \times 10^{-4} .
 \end{aligned}$$

However, when nine information bits per command are required, the probability of rejecting the entire command is

$$\begin{aligned}
 R(\text{C}) &= 9R(\text{IB}) \\
 &= 4.5 \times 10^{-3} .
 \end{aligned}$$

The probability of getting a real time command through the spacecraft decoder on the first try is

$$\begin{aligned}
 Q &= 1 - R(\text{C}) \\
 &= 0.9955 .
 \end{aligned}$$

The probability of a stored command being decoded is slightly less:

$$\begin{aligned}
 Q(\text{SC}) &= 1 - 30R(\text{IB}) \\
 &= 0.985 .
 \end{aligned}$$

If it is assumed that all nine-bit commands are valid, that is if any one information bit is in error, a command error occurs:

$$P_e(\text{C}) = 9 \times 10^{-20} .$$

In the case of stored commands, the message is 30 bits long and the probability of a false command would be  $3 \times 10^{-19}$ .

If the sub-bit code is designed such that if one sub-bit of the five-bit group is in error, the complete command will be rejected. The probability that a group of sub-bits will be rejected is

The maximum information bit rate is 200 bps, and with a word length of 30 bits, the word rate is 66.6 words per second or 3996 words in one minute. During a five minute tracking station contact it would be possible to completely reload the command memory (4096 words), assuming that each word is sent only five times before verification is received by the ground station command computer.

3. RF Equipment. Performance analyses of the RF equipment were made to determine the size of the onboard transmitter. The values used for the various elements of both spacecraft and ground stations were selected to ensure a worst-case condition. The values, however, were realistic, based on measured data or contractor's advertised specifications. The output power of 1 watt was adequate for all downlink modes. Data from the ranging mode performance analysis are presented in Table IX-5. Data derived from the performance analysis of the recorded and real-time data modes are presented in Table IX-6.

4. Spacecraft Clock. One of the most interesting observations that will be possible with HEAO will be X-ray pulsars. In the past three years, considerable attention has been given to pulsars in the optical, radio, and X-ray portions of the spectrum. Astronomers have been able to correlate the accuracy of the radio and optical pulsars from the Crab Nebula to a high degree. Since X rays do not penetrate the earth's atmosphere, observations of the X-ray pulsars have been limited to sounding rocket flights. Most of the X-ray experiments on the HEAO Mission C Spacecraft will have the capability to observe pulsars. In general it is believed that pulsars are neutron stars and that the pulsar's period is associated with the spin period. Therefore, the characteristics that appear to be of the most interest are the pulse width and period. All of the experiments, either directly or through the sampling process of the time division multiplexing telemetry depend on the spacecraft clock. In the process of measuring the pulsar period and the pulse width, the stability of the clock during the observation is the most important factor. In the correlation between optical and radio observation on the ground, the long-term stability and accuracy of the updating or calibration with terrestrial standards become the prime considerations.

A very precise timekeeping device is based on a stable frequency standard. In the past three decades, considerable advancements have been made in the timekeeping art. The atomic hydrogen maser is no doubt the most exacting of the primary standards; however, it has not found a practical application because of its size and cost. The atomic clock, like the cesium beam-controlled oscillator, can be built and aligned without reference to any other standard. This is termed a primary standard. A cesium beam standard is

TABLE IX-5. RANGING MODE PERFORMANCE ANALYSIS

<u>Uplink Characteristics</u>	
Ground Station (2 kW)	63.0 dBm
Ground Antenna Gain (30 ft)	44.0 dB
Atmospheric Attenuation (5 deg elevation)	- 0.3 dB
Space Loss (1122 n. mi.)	-166.0 dB
Spacecraft Antenna Gain	- 5.0 dB
Circuit Loss	- 1.2 dB
Input Receiver Power	- 65.5 dB
Spacecraft System Temperature	2110° K (8 dB noise figure)
Noise Spectral Density	-165.4 dBm-Hz
<u>Carrier</u>	MOD INDEX = 1.84 rad.
	10% power in carrier
Modulation Loss	11.5 dB
Loop Noise Bandwidth	28.5 dB
	(700 Hz)
Required Signal-to-Noise Ratio	6.0 dB
Input Signal to Carrier	-177.0 dB
Noise in Loop	-136.9 dB
Signal-to-Noise Ratio	59.9 dB
Performance Margin	53.9 dB
<u>Ranging Channel</u>	33.8%
Modulation Loss	- 1.23 dB
Noise (Bandwidth)	63.0 dB
	(2 MHz)
Noise Power	102.4 dBm
Received PRN Signal	- 65.5 dBm
Signal-to-Noise Ratio	35.6 dB
<u>Downlink</u>	
Spacecraft Transponder Power (1 W)	30.0 dBm
Circuit Losses	- 1.2 dB
Spacecraft Antenna Gain	- 5.0 dB
Space Loss	-166.0 dB
Atmospheric Attenuation	- 0.3 dB
Ground Antenna Gain	44.0 dB
Received Signal	- 98.5 dB
Ground Station Noise Spectral Density	-176.3 dB

TABLE IX-5. (Concluded)

<u>Carrier</u>	
Modulation Loss	- 9.4 dB
Noise Loop BW (700 Hz)	28.5 dB
Noise in Loop	-147.8 dBm
Input Signal	-107.9 dBm
Signal-to-Noise Ratio	39.9 dB
Required Threshold	6.0 dB
Performance Margin	33.9 dB
<u>Square Wave Subcarrier</u>	
Modulation Loss	- 28.05 dB
Noise Loop BW (250 Hz)	23.98 dB
Noise in Loop	-152.32 dBm
Input Signal	-126.55 dBm
Signal-to-Noise Ratio	25.77 dB
Required Threshold	10.00 dB
Performance Margin	15.77 dB
<u>Sine Wave Subcarrier</u>	
Modulation Loss	- 1.77 dB
Noise Loop BW (150 kHz)	51.76 dB
Noise in Loop	-124.54 dBm
Input Signal	-100.27 dBm
Signal-to-Noise Ratio	24.27 dB
Required Threshold	8.5 dB

TABLE IX-6. PERFORMANCE ANALYSIS OF RECORDED  
AND REAL-TIME DATA MODE

<u>Downlink Characteristics</u>	
Spacecraft Transmitter	30.0 dBm
Circuit Losses	- 1.2 dB
Antenna Loss	- 5.0 dB
Space Loss	- 166 dB
Atmosphere Absorption	- 0.3 dB
Ground Antenna G2m	+ 44 dB
Received Signal	- 98.5 dBm
Noise Spectral Density (System Temp., 170° K)	-176.3 dBm - Hz
<u>Carrier</u>	
Modulation Loss	- 6.9 dB
Carrier Signal (BW = 700 Hz)	-105.4 dBm 28.45 dB
Noise in Carrier Loop	-147.85 dBm
Carrier-to-Noise Ratio	42.45 dB
Threshold	10 dB
Margin	32.45 dB
<u>500 kbs Data</u>	
Modulation Loss	- 3.54 dB ( $\Delta\theta_1 = 1.025$ )
Subcarrier Signal (BW = 716 kHz)	-102.04 dBm 58.55 dB
Noise in Loop	-117.75 dBm
Carrier-to-Noise Ratio	15.71 dB
Margin	5.71 dB
Modulation Improvement	3.28 dB
$S_0/N_0$	18.99 dB
<u>27.5 kbs Data</u>	
Modulation Loss	- 11.82 dB ( $\Delta\theta_2 = 0.75$ )
Subcarrier Signal (BW = 150 kHz)	-110.32 dBm 51.76 dB
Noise in Loop	-124.54 dBm
Carrier-to-Noise Ratio	14.22 dB
Margin	5.72 dB

used by the National Bureau of Standards. The cesium beam is an atomic resonance device. It can, however, be made into a portable unit with the same level of accuracy and stability usually achieved by large-scale laboratory models. A cesium standard consists of a crystal oscillator and a cesium beam tube linked by a servocontrol loop so that the output of the crystal oscillator is compared to the atomic resonator. The circuit contains elements to compensate for aging or drift of the crystal.

The rubidium gas cell is similar to cesium except that atomic resonant frequency is dependent upon the gas mixture and pressure. It is not considered to be a primary standard because of the small drift that must be periodically calibrated out. This drift is typically 100 times less than the best quartz crystal. Over the years the quartz crystal oscillator has proven to be a relatively inexpensive frequency source of small size when the stability and accuracy requirement is not too demanding, when a quartz crystal is stressed, and when electrical potential is induced in any nearby conductor. When an electric field is present, deformation of the crystal takes place; this is called the piezoelectric effect. An inherent characteristic of the crystal is that the resonant frequency changes with age. This is almost a constant after the initial few days to months. The long-term stability or instability is also influenced by such factors as external load changes, temperature fluctuation, and acceleration. The short-term stability refers to changes in average frequency of such a short time that long-term effects can be neglected. This is usually one second or less.

In Table IX-7 a comparison is made of the characteristics of the three frequency sources. These are the characteristics that would have the most influence on the selection of the spacecraft clock.

The figures for weight and volume for the rubidium standards were extrapolated from a laboratory-type instrument since there has never been a flight of the instrument. The estimates of weight and volume for the cesium atomic beam were based on the Hewlett Packard engineering prototype of an airborne cesium standard.

It does not appear that for a general-purpose spacecraft clock either of the atomic standards has progressed to the point where it can be considered as a contender. The quartz crystal has been used on Apollo and several unmanned missions and must be considered a prime candidate for the HEAO spacecraft. The long-term stability shown in Table IX-7 indicates a range from parts in  $10^{12}$  to parts in  $10^7$ . This wide range is due to the degree of

TABLE IX-7. COMPARISON FREQUENCY SOURCES

Parameters	Type of Source		
	Cesium Atomic Beam	Rubidium Vapor Cell	Crystal Oscillator
Long-term Stability	$5 \times 10^{-12} / 3 \text{ yr}$	$2 \times 10^{-11} / \text{mo}$	$1 \times 10^{-7} / \text{day}$ $5 \times 10^{-10} / \text{day}$
Short-term Stability	$<1 \times 10^{-13}$	$<7 \times 10^{-12}$	$5 \times 10^{-12}$
Weight (lb)	40	37	1 to 0.02
Volume (ft <sup>3</sup> )	0.43	0.93	0.029 to 0.001
Power (W)	27	35	4 to 0.25

temperature stability of the critical elements. A precision oscillator in a double-temperature-controlled oven can have an ambient temperature coefficient as low as 2.5 parts in  $10^{12}$  per °C. Designs using a network which contains thermistors, voltage variable capacitors, or temperature sensitive capacitors are referred to as temperature compensated oscillators. This technique results in an oscillator with 1 part in  $10^7$  over the temperature range from -30° C to 50° C. The precision oscillator in a double-temperature-controlled oven is shown in Figure IX-20. This seems to be a rather involved means of maintaining a constant temperature; it certainly is less reliable than the temperature compensated oscillator. However, to appreciate the job that ovens must do in maintaining the temperature, the variation in frequency with temperature is shown in Figure IX-21. This is one of a family of curves related to angles at which the AT cut crystal is obtained with respect to lattice structure of the crystal.

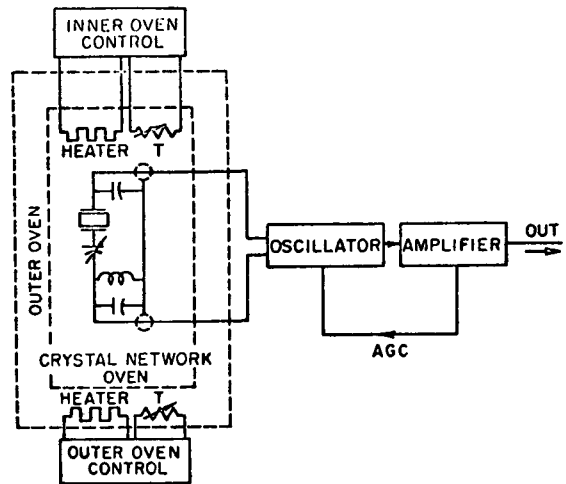


Figure IX-20. Temperature-controlled oven.

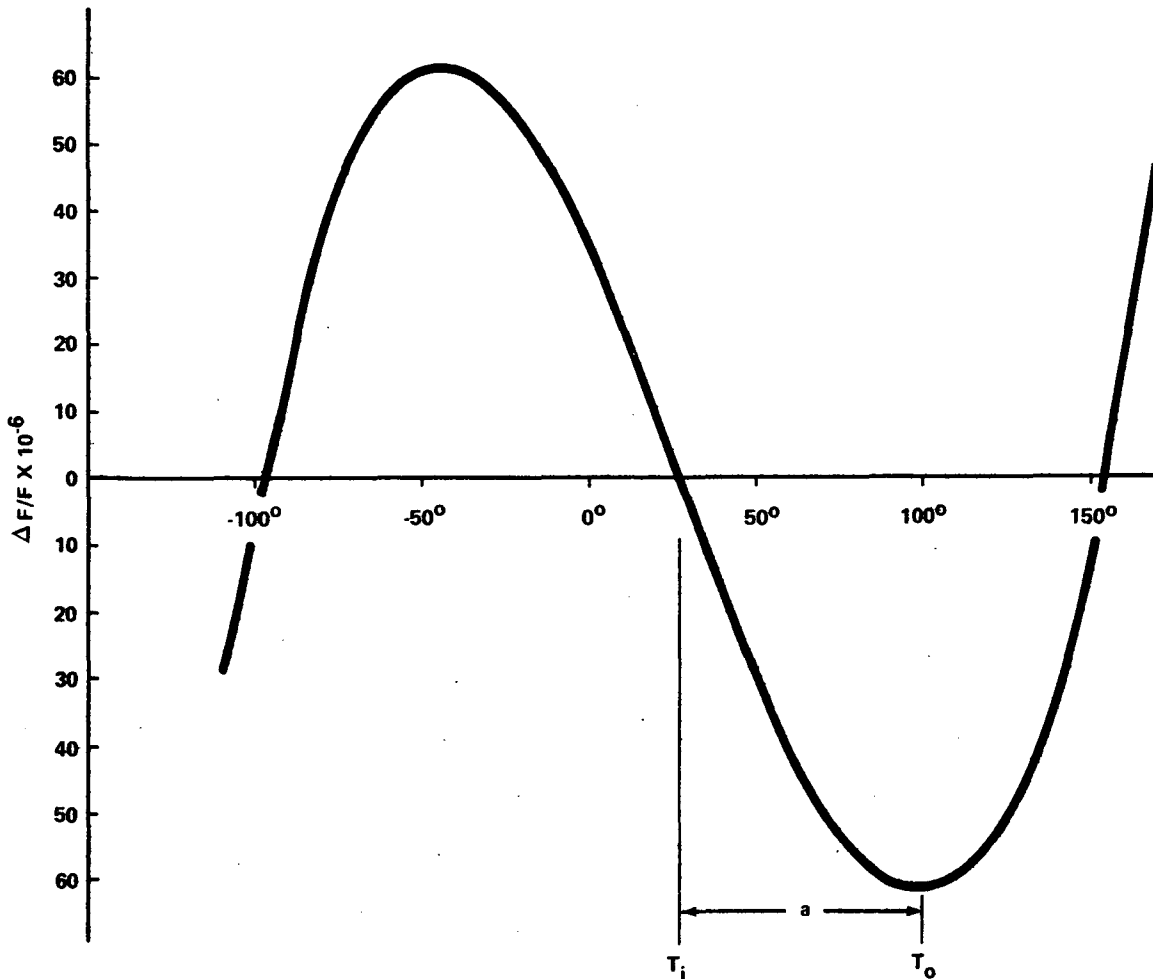


Figure IX-21. Oscillator frequency change with temperature.

Of course, the operating temperature of the oven must be above the highest ambient expected, but below maximum for the oscillator components such as transistors, resistors, and capacitors. The equipment compartment in the HEAO-C mission should not exceed  $80^\circ$  F ( $25^\circ$  C) from the standpoint of the telescope. The turning points ( $t_0$ ) of the curves are the best suited for oscillator operation. This particular curve has a turning point at  $100^\circ$  C, well above the highest temperature ever expected by the equipment compartment. The relationships of the oscillator frequencies due to changes in the crystal as a function of oven temperature are so small that it is difficult to see graphically (Fig. IX-21). The equation of curve is a cubic of the following form:

$$\frac{f - f_i}{f_i} = 8 \times 10^{-11} (t - t_i)^3 - 24 \times 10^{-11} (t_0 - t_i)^2 (t - t_i) \quad ,$$

where  $f_i$  is the frequency at inflection temperature;  $t_i$  is the temperature of inflection point, (27° C);  $t_0$  is the turning point temperature (100° C). The equation has zero slope points (turning points) located symmetrically about the inflection point (27° C). In the immediate vicinity of these zero slope points, the curve may be considered a second-degree equation approximated by

$$f = C (2\Delta T \Delta t + \bar{\Delta t}^2) \quad .$$

The notations are as follow:

- C     coefficient of approximate temperature curve
- T     difference in the turning point temperature and the nominal oven temperature (mismatch)
- t     allowable limits in oven temperature control system.

A curve has been developed to show how the temperature limits and mismatch of the oven to the turning point temperature of the crystal affects the frequency of the oscillation. The curves in Figure IX-22 indicate that, if the oven could be exactly matched to the crystal turning point, a temperature stability of  $1 \times 10^{-9}$  frequency stability could be realized with a rather large temperature limit; however, for as little as a 0.5° C to 2° C mismatch, it is extremely difficult. The  $5 \times 10^{-9}$  required for this HEAO-C mission is indicated by the dotted line. These bounds are well within the present state-of-the-art.

5. Tape Recorders. In the past, the spaceborne recorder has posed special reliability problems for spacecraft designers. Bearings, belts, and heads have historically been the weak links in the recorder. Various techniques have been tried to improve these areas over the past several years. The primary thrust has been toward reducing the number of bearings and belts. The bearing count in most machines is still high; however, the number of belts can be reduced to one in some designs where dc motors, rather than ac motors, are used. Studies have indicated certain precautions in design which will aid

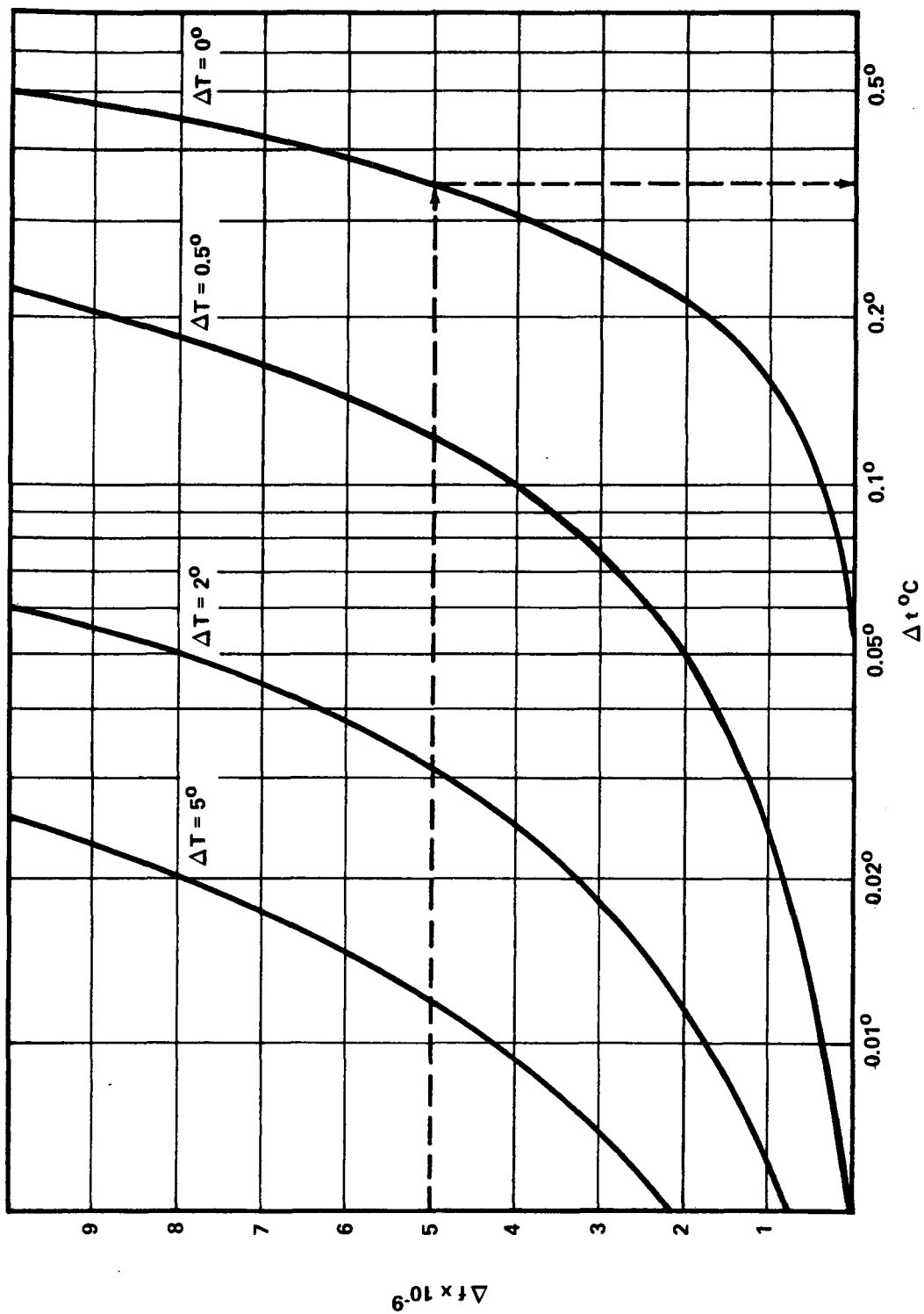


Figure IX-22. Curves of mismatch over temperature and the crystal turning point.

12 ⊕

in long-term reliability; but instead of trying to force the recorder state-of-art, the mission should be constrained to tape recorder capabilities. In the following paragraphs the mission constraints that impact the tape recorder are examined and wherever possible the requirements are relaxed in favor of the recorder.

In Chapter III, station contact data indicates that for any of the three network configurations there is at least one contact of nine minutes or more. The maximum interval of time without a contact is 89.28 minutes. The average gap time, of course, was smaller for the 10-station configuration than for the 4-station configuration. The simulation indicated that the maximum data storage required was approximately 165.1 megabits for all three. This is not surprising, since the maximum out-of-contact time was nearly the same. These data define several of the parameters that are important to the tape recorder design and will be discussed in more detail later. There seems to be very little difference in the support provided by either of the four station configurations. The only factor that seems to distinguish between configurations was the possibility of one of the four stations being out of operation. In either configuration, if any station other than Canary Island is closed at the time it would normally be tracking, only two revolutions without a contact result. In the configuration consisting of CYI, ACN, GWM, and HAW, if CYI is not operative, then during 4 orbits out of 14 orbits no tracking station would be available for recorder dump. This would mean that the total capacity should be four times the data gathered on a single revolution. These configurations depend heavily on stations that are in remote locations. This will result in a delay of information reaching the operation center if the medium for transfer is magnetic tape through the nominal mail system. Rosman, North Carolina, is the only tracking station at the present time capable of transmitting 500 kbs (max 1 magbit) in real time to the operations center assumed to be located at GSFC for this study. However, Rosman is located so far north that the contact with a spacecraft in a 28.5 degree inclination orbit is a very short (less than 5 minutes) interval, about 4 times in 20 revolutions. Hence, Rosman should not be considered as a prime tracking station, but it could obtain at least one orbit of experimental data per day.

a. Saturation Recording. There are basically two techniques for magnetic tape recording: pulse recording and carrier modulation recording. In pulse recording there are one or more flux transitions to either positive or negative saturation of the tape. Carrier modulation is usually angle modulation of a carrier that may or may not be coherent with the data. In the section concerning constraints, the ground stations were shown to be capable of handling return-to-zero (RZ), non-return-to-zero (NRZ), and split phase. The

RZ and NRZ are primary means of pulse recording. In Figure IX-23, the RZ record current is depicted along with the reproduce head voltage. A pulse is produced for each bit. The polarity indicates the numerical value (1 or 0). The pulse per bit has the advantage that a lack of signal is obviously an error. In addition, a dropout which lifts the tape away from the head does not result in error as to location of the bit along the tape.

In the case of NRZ (Fig. IX-24), the tape is saturated to one or the other polarity at all times. The reversal of polarity is used to indicate information. A reversal may be used to indicate a "1" while the absence may indicate a "0."

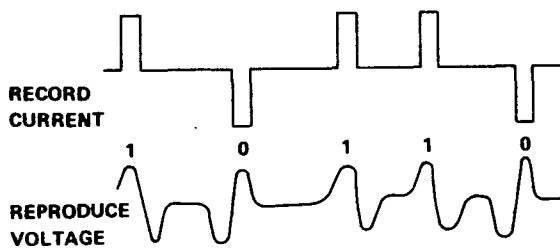


Figure IX-23. RZ recording wave forms.

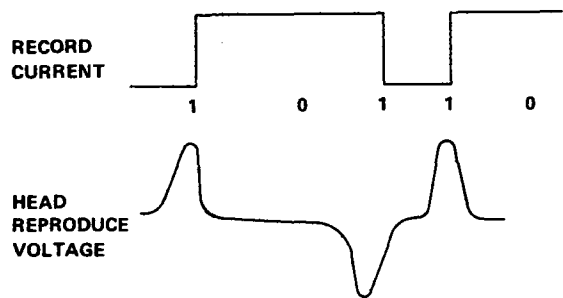


Figure IX-24. NRZ recording wave form.

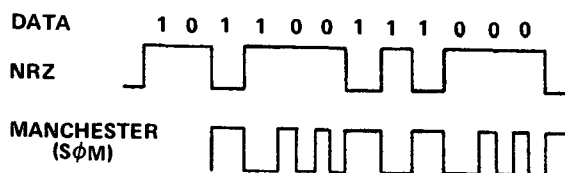
In comparison with RZ, the dropout in NRZ recording will produce less amplitude drop because the effective wavelengths are longer. A dropout will not only cause an error in one bit but can cause a loss in information until sync can be restored. In most application of NRZ, bit rate is assumed to be half the rate of RZ since only one change in state for a "1" is required. It would appear in recording that NRZ would have twice the packing density of RZ since from the two sketches the head current is switched only once per bit for NRZ and twice per bit for RZ. The reproduced pulse widths are very nearly the same for either case and, therefore, the packing densities are approximately the same. The NRZ usually requires a clock to determine when to sample for the presence or absence of a pulse. If this takes the form of an additional track on the tape, it would result in an effective reduction in the overall packing density. Another difficulty arises because in the NRZ scheme the tape is saturated in the intervals between pulses. Tape noise is at a maximum when the tape is saturated. The power required to cause full saturation must flow in the head at all times.

In the straightforward RZ or NRZ recording, the maximum packing density is usually defined as the density where adjacent pulses start to overlap at some arbitrary base point. Pulse amplitude up to 30 percent of peak is not unusual. In actual practice, sophisticated coding and decoding devices are used to increase the packing density. Chapman [IX-2] has shown that the maximum density possible for straight recording is a function of the tape oxide thickness. For 0.5 mil red oxide film the maximum density is 840 bits per inch. The density varies inversely with oxide thickness and at 0.3 mil the density is up to 1400 bits per inch. Experimentally, the oxide thickness has been reduced to a few microns with packing density increase up to 10 kilobits per inch; however, this would not be practical for a long-life machine. It is obvious that straight pulse saturation technique is not suitable for the HEAO-C mission.

b. Modulation Recording. When the digital data are applied to the tape by means of a modulated carrier, the tape need not be saturated. Therefore, the tape thickness is not a critical factor in the packing density limitations. In the case of a modulated carrier, the recorder can be treated as a communication channel. The packing density (bit per inch) is analogous to the channel capacity (bit per second). Flutter and dropout correspond to impulsive perturbation. The recorder has certain characteristics that must be taken into account. The recorder has no dc response, and dropouts can result in a 10 to 15 dB reduction in signal noise over time period corresponding to several hundred bits. Communication techniques have shown that coherent phase shift keying is the most efficient carrier transmission scheme. It is very fortunate that split-phase mark baseband encoding can be classified as a coherent phase modulated carrier. The modulation is obtained by operating on binary data (d) with clock (CL) that was used to generate data stream:

$$M = \overline{CL \oplus d}$$

where the " $\oplus$ " means "exclusive or" and the results are inverted. This is sometimes referred to as Manchester coding. Figure IX-25 compares the NRZ and the resulting split phase mark (S $\Phi$ M) after encoding.



Inspection of the two wave forms indicates that the Manchester would have higher frequency components than the NRZ. This observation is further confirmed by comparing the power spectrums (Fig. IX-26).

Figure IX-25. Comparison of NRZ and S $\Phi$ M.

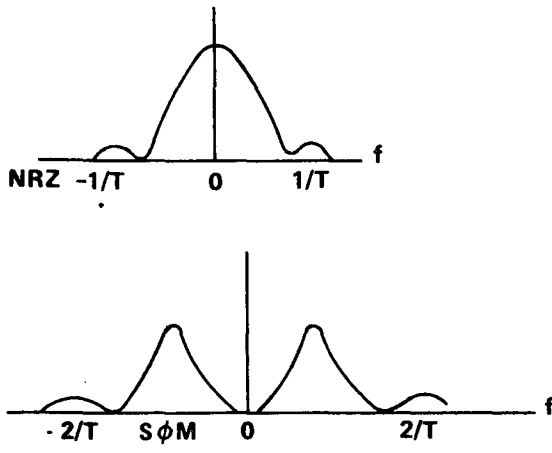


Figure IX-26. Power spectral density.

These figures indicate that SφM requires twice as much bandwidth but has no dc components. The absence of dc makes this code ideal for the magnetic circuit of the recorder. Also, nearly all the energy is concentrated in the data.

Even more significant is the fact that there is a transition at each bit; therefore bit sync can easily be obtained from the data. The block diagram in Figure IX-27 shows the SφM signal passing through a low pass filter to eliminate all but the first order lower side bands. The filtered

signal is mixed with a bias to linearize the recording process for minimum harmonic distortion. This is necessary to preserve the time relationship of the zero crossing of the phase modulated carrier. The tape is modulated using conventional direct recording techniques.

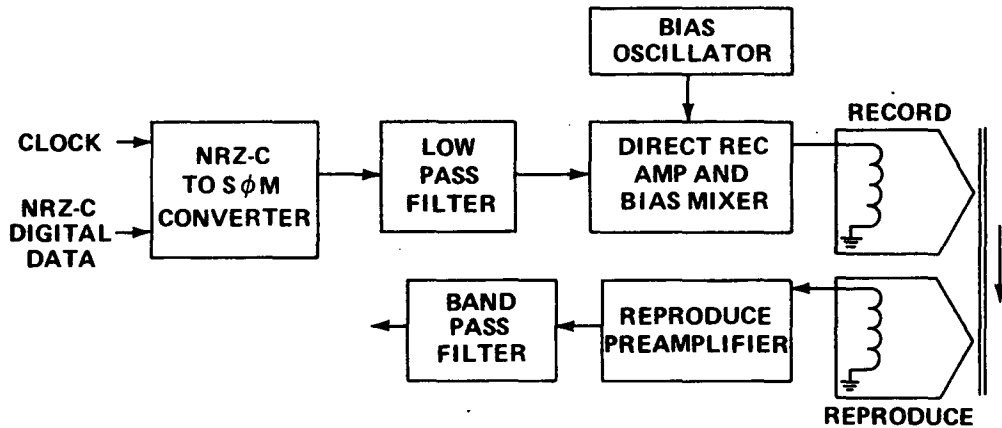


Figure IX-27. Block diagram of tape recorder electronics [ IX-3 ] .

c. Channel Analysis. In the analogy of a communication channel, the reproduce head and amplifier are the antenna and receiver, respectively. The signal into the amplifier is of the order of a few hundred microvolts. Just as in a radio receiver there is a certain amount of noise that accompanies the signal. The curves in Figure IX-28 indicate that at 76 IPS and with a head-to-tape separation between 1 mil and 1.25 mil, the signal-to-noise ratio is about

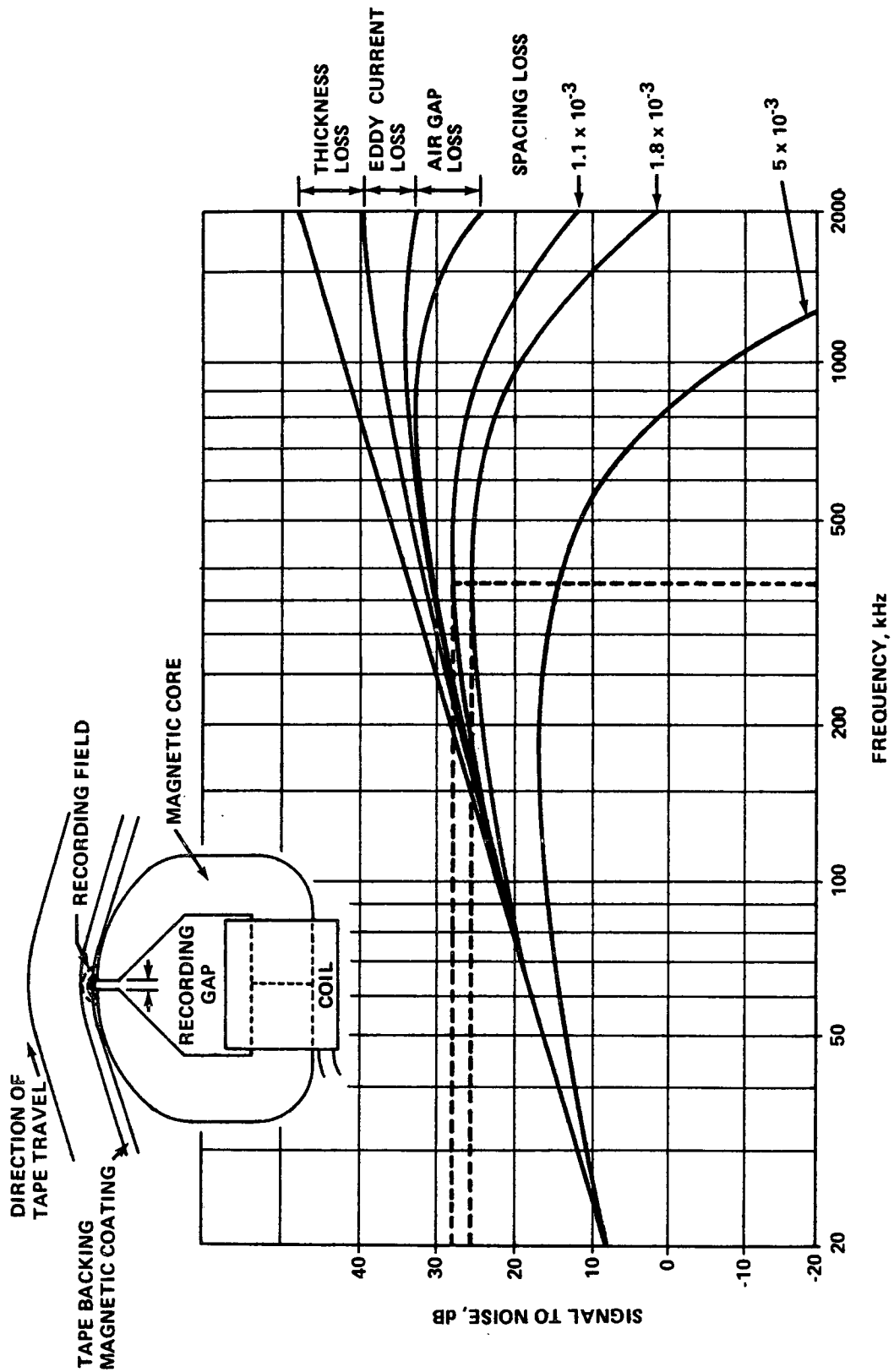


Figure IX-28. Output of tape recorder.

24 to 26 dB. These curves assume the use of a precision head and high resolution tapes, which actually would be the case. The bandpass filter is used to limit the spectrum to only that necessary to pass the signal and can be expected to improve the signal-to-noise ratio to approximately 32 dB. Since the ground station is capable of handling split phase data and it is desired to have some of the downlink RF carrier remaining for autotrack, the data will not be converted from SΦM to NRZ until it is received on the ground. In the curves showing the output of the tape recorder there is one curve where the spacing loss is indicated for 5 mil separation. This is the worst case condition and is caused either by windage or a small particle lifting the tape off the head. The signal-to-noise ratio output would drop to about 17 dB, which would be acceptable except for the fact that the signal will be further corrupted by noise in the process of transmitting it to the ground. In the downlink calculations for the tape recorder channel, using a perfect signal at the input to the transmitter, the signal-to-noise ratio was found to be 19 dB. If the noise due to the RF channel and the tape recorder noise are added on a power basis the following result is obtained:

$$\begin{aligned}
 \frac{S_0}{N_0} &= \frac{(S_1/N_1) (S_2/N_2)}{(S_1/N_1) + (S_2/N_2)} \\
 &= \frac{(50.12) (79.43)}{(50.12) + (79.43)} \\
 &= 30.72 \\
 &= 10 \log 30.72 \\
 &= 14.87 \text{ dB}
 \end{aligned}$$

This is a reduction of only about 2 dB. Manchester code (SΦM) is considered to be coherent PSK and consists of carrier pulses of constant amplitude but different phase relationships. The equation for BER when differential coherent detection is used is as follows:

$$P_e = \frac{1}{2} e^{-S/2N}$$

where  $P_e$  is the probability of error and  $S/N$  is the signal-to-noise ratio into the decision device ( $1.07 \times 10^{-7}$ ). This would be the worst conceivable condition of a dropout occurring just as the spacecraft appeared above the ground

station antenna mask. The fact that at this point the system requirement of BER of  $1 \times 10^{-5}$  is met gives a degree of confidence that the design is feasible.

The block diagram in Figure IX-29 indicates that ac bias is mixed with the encoded data prior to recording. Recording on magnetic tape is impractical without proper bias for the same reason that vacuum tube must

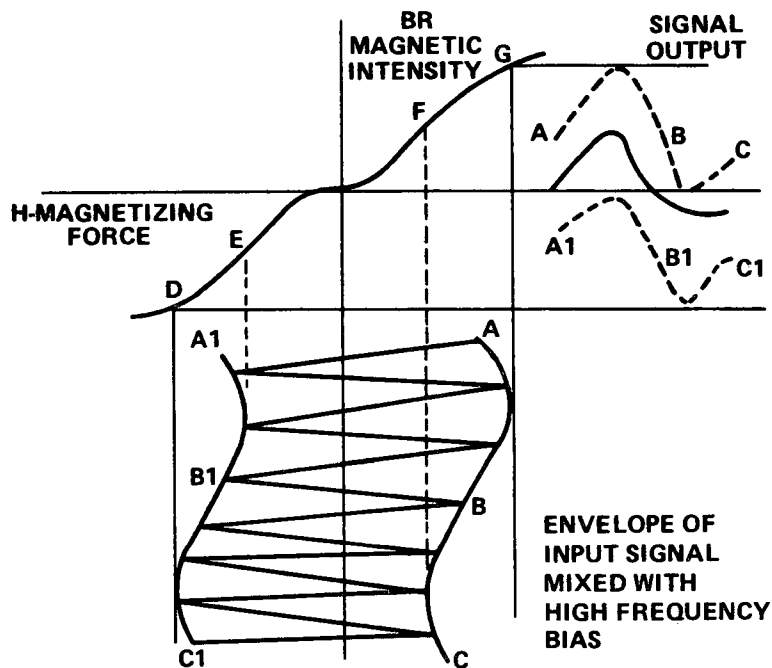


Figure IX-29. AC bias.

be biased because of nonlinearity performance characteristics. The ac bias is usually four to five times higher in frequency than the signal and greater in amplitude. In certain types of encoding, such as Manchester and Miller coding, the maximum bit rate is limited by the recorder bias frequency. The effect of the ac bias is demonstrated in Figure IX-29 where point ABC denotes the basic signal prior to bias mixing and FG is the segment of the curve where it is desired to operate.

d. Heads. Ferrite core heads, with alpha-sil, nonmagnetic pole tips, are used because of their increased sensitivity, extremely low wear rate, and their relative immunity to stiction problems as compared with laminated heads.

The heads are apexed to reduce the air-bearing effect and produce a better wear pattern. Actual contact between these laminated poles and the tape is prevented by the use of two sapphire rods on which the tape rides. This is done to prevent tape stiction on the large flat surface of the laminated face.

There are as many tape transport designs as there are companies who make airborne recorders. Basically the transport must move the tape past the head at a constant speed with sufficient tension to cause the tape to remain a constant distance from the head. At first glance this seems like a rather straightforward and extremely simple design problem; however, the inherent problem of maintaining a constant distance can be easily understood from the equation relating head and tape separation:

$$\text{Signal Loss (dB)} = \frac{55d}{\lambda}$$

where  $d$  is the tape-to-head separation and  $\lambda$  is the wavelength (tape speed = frequency  $\times$  wavelength).

This is sometimes referred to as the 55d over lambda loss which says that for each wavelength the tape is displaced from the head there is a 55 dB loss in signal.

The curves in Figure IX-28 show the division of playback losses. The upper limit of the bandwidth can be extended by increasing the tapespeed; however, at the point where the recorded wavelength equals the gap width, the output of the reproduce head falls to zero. The record head has to handle the high frequency bias which is essential for low-distortion direct recording. This frequency is normally at least three times the upper recorded bandwidth. In the case of the Manchester code, this would be 1.4 times the bit rate or 700 kHz. A 2 MHz, or higher, bias would be required. At 76 IPS, the air gap required would be 38 microinches. Present technology is capable of providing gap widths of 20 microinches or better. This would allow a record signal up to 3.8 MHz at this tape speed.

It was pointed out earlier that bearings, belts, and heads have presented reliability problems in previous designs. These components are integral parts of the tape transport module. This module is best discussed in conjunction with the sketch in Figure IX-30. The capstan pulls the tape past the head at a uniform speed and constant tension. The guide rollers maintain the tape at a constant distance from the head and guide the tape from one reel

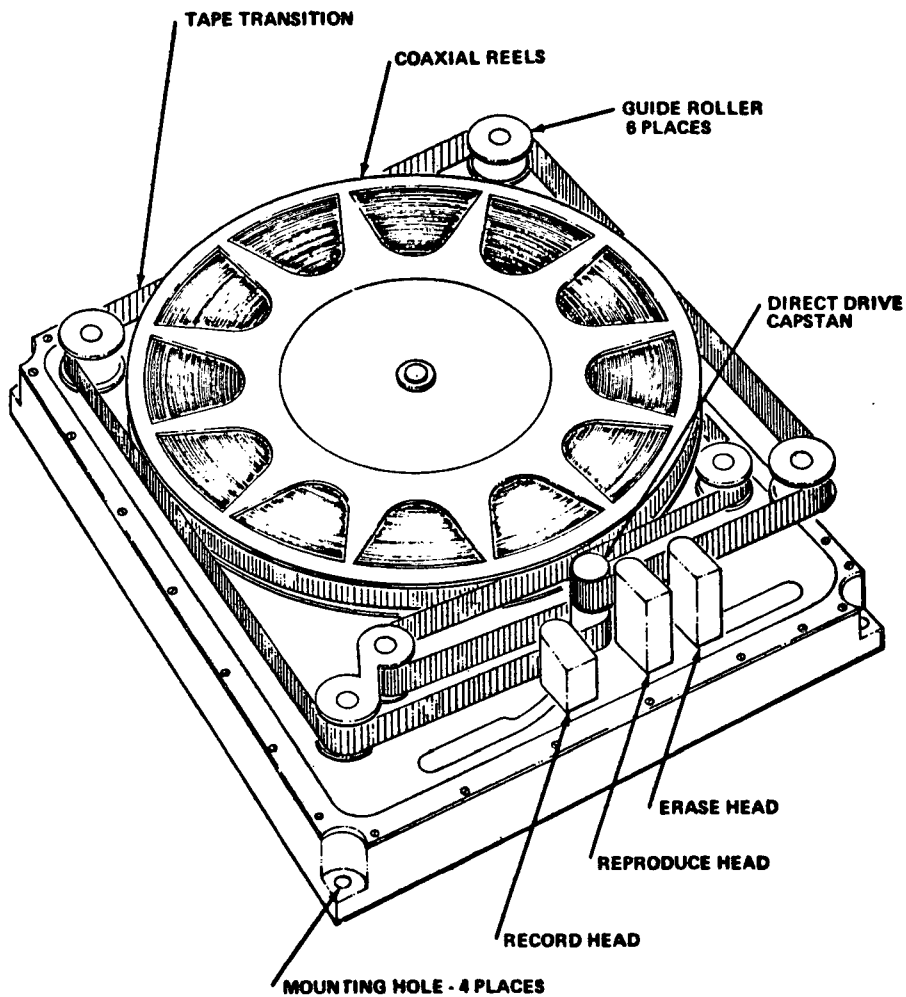


Figure IX-30. Tape recorder.

to the other. The supply reel must be torqued in the opposite direction to the rotation caused by the tape being paid out. This is necessary to maintain a constant tension in the tape that is vital to proper relationship of the tape-head separation. The takeup reel must be driven at a variable speed that provides constant tension so that the tape is packed very tightly on the reel. When tape is being wound on or off a reel at a constant linear velocity, the rotational velocity of the reel must be inversely proportional to the diameter at which the tape is being wound. At the same time, the torque applied to the shaft turning the reel must be proportional to the diameter of tape on the reel if the tension in the tape is to remain constant. In other words, the constant tension requires the product of the speed and torque of the reeling motors to remain a constant. In Figure IX-30 the supporting structure has been removed to give

a clear view of the "tape pulling" mechanism. Only one motor is used to reduce the number of belts and bearings. This motor drives the capstan which in turn pulls the tape from the supply reel. The negator spring provides the torque to maintain tension in the tape.

Pulling of the tape causes the supply reel to rotate at a speed proportional to the tape diameter. Torque to drive the takeup reel is provided by the rotation of the supply reel through the differential gear arrangement. The negator differential is widely used for space applications where power conservation is an important consideration. The reels are 6.5 inches in diameter and are attached to the end gears of the differential. The center shaft is coupled to a negator spring mechanism which provides tape tension. This tension is equal to torque reflected to the reel from the negator divided by the radius of tape pack at that instant. Since the tape moves at a constant velocity, the angular velocity of the reels varies as the tape builds up or unwinds from reels. When the supply reel is completely filled, it rotates slower than the takeup reel. This must be compensated for by winding the spring off the differential shaft and onto the negator supply hub. This continues until the amount of tape on each reel becomes equal; then, the negator begins to wind again on the differential. At the end of the tape, the negator spring is completely wound on the shaft as it was at the beginning of the cycle.

The schematic in Figure IX-31 shows a single motor and belt driving the capstan that provides all the mechanical energy to the system. A dc motor was baselined because of the reliability analysis, although most other spaceborne recorders have used ac hysteresis synchronous motors. The prime consideration has been the brushes associated with dc motors. These brushes cause arcing and radio frequency interference (RFI) as well as particle contamination. A second disadvantage that was considered was the lower inertia of the rotor of the ac motor. The ac motor has less torque than the dc motor, but usually only 0.2 in.-oz. is required. These considerations usually carry the design in favor of the ac motor but in this instance the ac motor configuration contained a clutch and three additional belts over the dc servo design. The size of the HEAO-C spacecraft eliminates many of the considerations that are paramount on the smaller spacecraft, such as RFI, inertia of the rotor, etc. Brushless dc motors would take care of brush contamination. The estimated mean time before failure (MTBF) for the recorder using a dc motor was 99 251 hours as compared to 49 000 hours for the ac motor. While these are estimates, a factor of two is significant.

The single capstan belt is made of 2 mil thick Kapton (polymide) and is about 0.125 inch wide. The belt is seamless and has a minimum life of

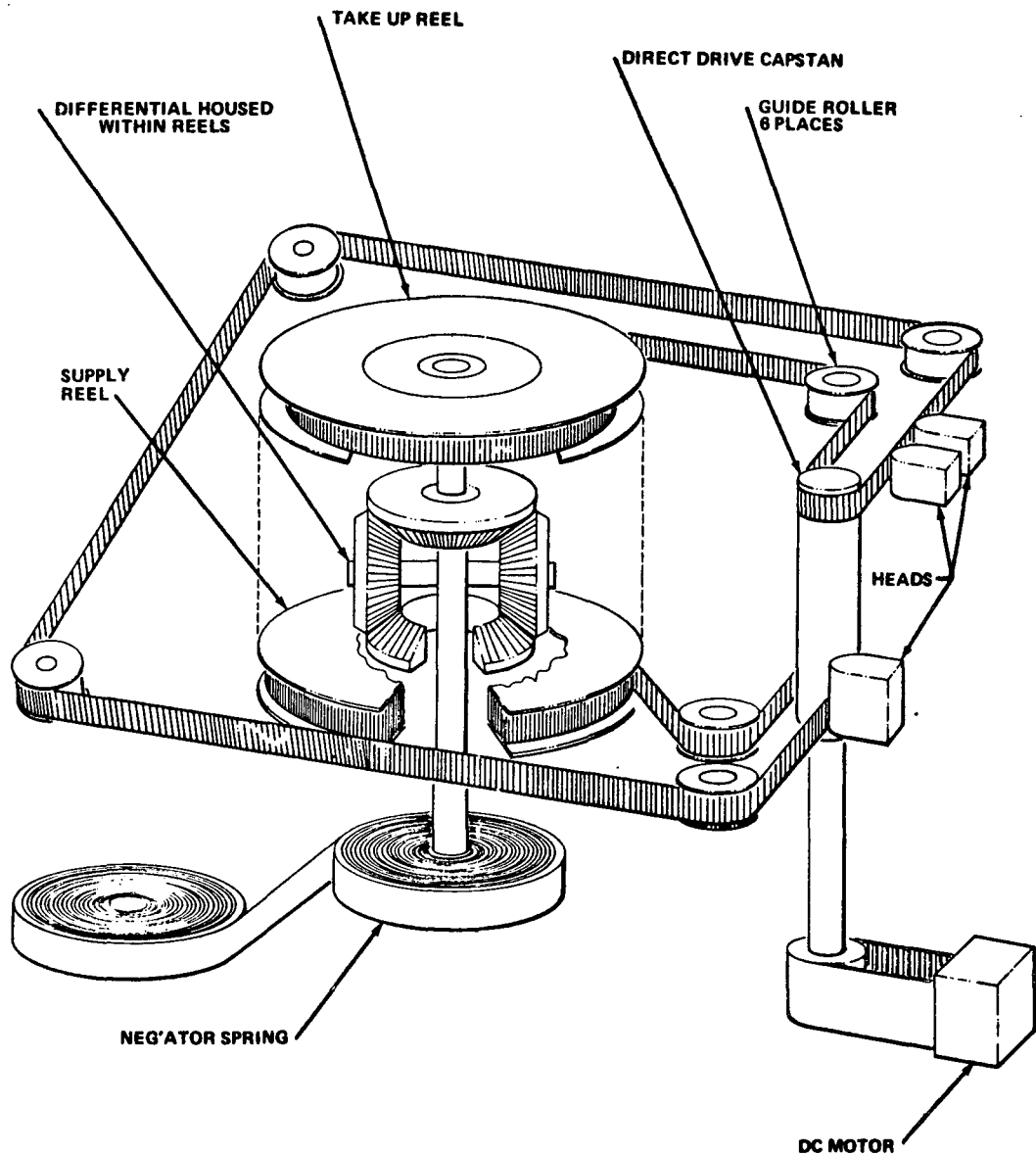


Figure IX-31. Tape recorder transport schematic.

$2 \times 10^9$  cycles. The design will restrict the stress in the belts to one-third of the yield point stress. The yield point stress for Kapton at 3 percent elongation is 10 000 psi.

e. Bearings. The motor, tape guides, differential, and capstans all require bearings. The type of bearing that best fits the particular application must be determined. The differential and reel drive would use angular

contact, full ball complement, flanged bearings because of their high load capability. These bearings could not be used in tape guides or the capstan because they are noisy. The other components would use ball bearings, but a type that is less noisy.

The following equation is sometimes used to estimate the load life of a bearing. This formula gives an evaluation of the effective damage from cyclic fatigue of the materials of the bearing.

$$L_h = \frac{16\,667}{N} \left( \frac{C}{R} \right)^3$$

where  $L_h$  is the life in hours;  $N$  is the speed in rpm;  $C$  is the dynamic load rating in pounds; and  $R$  is the equivalent radial load in pounds. The problem with this equation is that the manufacturer establishes the dynamic rating based on optimum lubrication conditions and an ultraclean environment. He also uses his own method of determining the dynamic rating which varies from one manufacturer to another. In the tape recorder, the lubrication usually fails after extended use because of contamination from material outside the bearing. To further the complication of using this equation, the preloads and external loads from pulls, belts, and tape must be known accurately to determine the load life of the bearing. The point contact principle of the ball bearing causes it to be very sensitive to shock. Bearings are preloaded to eliminate high initial deflection and to achieve a constant deflection rate (i.e., makes deflections verses load relationships linear). This can provide some degree of shock protection. Figure IX-32 shows the axial forces on the races of the bearing.

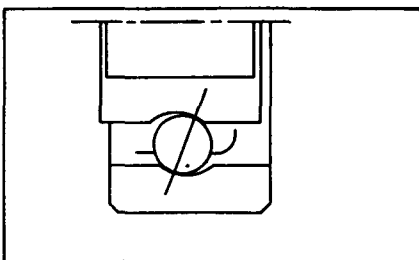


Figure IX-32. Preloading of bearings.

Spacing washers are used to force the races axially closer together and to use the elastic properties of the races as the restoring force. Preloads must be carefully designed. Of course, a preload bearing requires more torque to rotate than does an unloaded bearing. In the case of 0.25 pound axial force, the results could be an increase of 0.005 ounce-inch. With as many as 36 bearings in the recorder, this could amount to a sizeable part of the motor output

torque. It is evident that bearings will either directly or indirectly affect the reliability of the recorder. Every effort must be made to reduce the number of bearings needed, improve the lubrication scheme, and protect the bearing from shock.

## F. Spacecraft Operational Modes and Telemetry Format

### 1. Telemetry Requirements

a. Spacecraft. Before any telemetry formats can be developed, the modes of operation of all spacecraft systems must be defined. In addition, the data rates and telemetry requirements for each operational subsystem must be developed and tabulated. These data are presented in Tables IX-8 and IX-9, and are summarized in Table IX-10.

A preliminary list of spacecraft modes of operation is shown in Table IX-11. When these modes are compared with the data summarized in Table IX-10, it is obvious that the worst case mode occurs when all experiments are operating and the high-energy solid state detector is being used in conjunction with the high resolution imaging detector. This then will serve as the baseline for development of a telemetry format.

b. Experiments. At first examination it would appear that other formats might be developed for use with experiment combinations using a lower data rate; however, closer examination reveals that the word rate from the HR and LA telescope experiment is quite close despite a significant discrepancy in the bit rates. Therefore, it will be assumed that only one format will be used whenever the HR and LA telescopes are being used.

A summary of the worst case mode is presented in Table IX-12. If a telemetry frame size of 16 by 16 words is chosen, then a reasonable frame rate of 12 frames per second can be established. This table also shows the number of words that each experiment will contribute to each frame and indicates those data sources which can be best combined to give a submultiplexed channel. The only channel requiring super multiplexing will be the clock whose least significant bits must be output at least once every 0.04 second. To accomplish this and maintain a reasonable symmetry, the clock is being output 4 times per frame or 48 times per second.

A preliminary telemetry format is shown in Figure IX-33. Those words labeled "A" are to be super multiplexed, those labeled "B" run at the main frame rate, and those labeled "S" denote submultiplexing. All letters are referenced to the telemetry mode in Table IX-8.

Page intentionally left blank

TABLE IX-10. TELEMETRY DATA SUMMARY

	Data Rates		
	Bit Rate Per		
	0.04 sec	1 sec	5 sec
Spacecraft Data			
Digital	7 × 25	184	217
Analog		128	<u>1424</u>
		175	1641 ÷ 5
		<u>328</u>	
		815	
Miscellaneous Experiments			
Flare Detector		40	
Monitor Proportional Counter		552	
Flat Crystal Spectrometer		108	
Aspect Detector		<u>286</u>	
		986	
HR Telescope			
HR Image Detector (Mode A)		9296	
(Mode B)		7168	
Focal Plane Spectrometer		7763	
High-energy Telescope			
Solid State Detector		8406	
Image Proportional Counter		8288	
LE Telescope		795	

TABLE IX-11. SPACECRAFT MODES OF OPERATION

Operational Mode	Data Requirements	
	Spacecraft Housekeeping	Experiment
Launch	*	
OAS	*	
Checkout	*	*
Fixed Experiment Only	*	*
Telescope Combinations	*	*
Large Telescopes Only	*	*

TABLE IX-12. WORST CASE TELEMETRY MODE

Description	Samples Per Sec	Bits Per Sample	Words Per Sample	Words Per Sec	Words Per Frame at 12 Frames Per Sec	Frame Location
High Resolution Imaging Detector						
Position	512	18	2.5	1280	108	B <sub>1</sub>
Events Scaler	8	8	1	8	1	S <sub>2</sub>
Housekeeping	2	8	1	2		
Large Area Solid State Detector						
PHA	16	8	1	16		
Anticoincidence	3/8	16	2	1	2	S <sub>4</sub>
Housekeeping	2	8	1	2		
Total Events	4	16	2	8	1	B <sub>6</sub>
Event Rate	2048	4	0.5	1024	86	B <sub>2</sub>
Flare Detector						
PSD Rejects	1/2	8	1	1		
Antirejects	8	1	1	1	1	S <sub>5</sub>
Memory	2	8	1	2		
Housekeeping	2	8	1	2		
Monitor Proportional Counter						
PHA	64	8	1	64		
PSD Rejects	1	8	1	2		
Antirate	1	8	1	1	6	S <sub>6</sub>
Housekeeping	2	8	1	2		
Flat Crystal Spectrometer						
Anticoincidence	1	8	1	1		
PSD Rejects	1	8	1	1		
PHA	8	8	1	8	2	S <sub>7</sub>
Shaft Position	1	12	1.5	1.5		
Housekeeping	2	8	1	2		
Aspect Detector						
Position	10	24	3	30	3	B <sub>5</sub>
Amplitude	10	3	0.5	5		
Housekeeping	2	8	1	2	1	S <sub>8</sub>
LE Telescope	96	8	1	96	8	B <sub>3</sub>
Spacecraft						
Time	48	7	1	48	4	A <sub>1</sub>
Discretes	24	8	1	24	2	B <sub>4a</sub>
Analog	16	8	1	16	2	B <sub>4b</sub>
Submultiplexers	44	8	1	44	4	S <sub>1</sub>

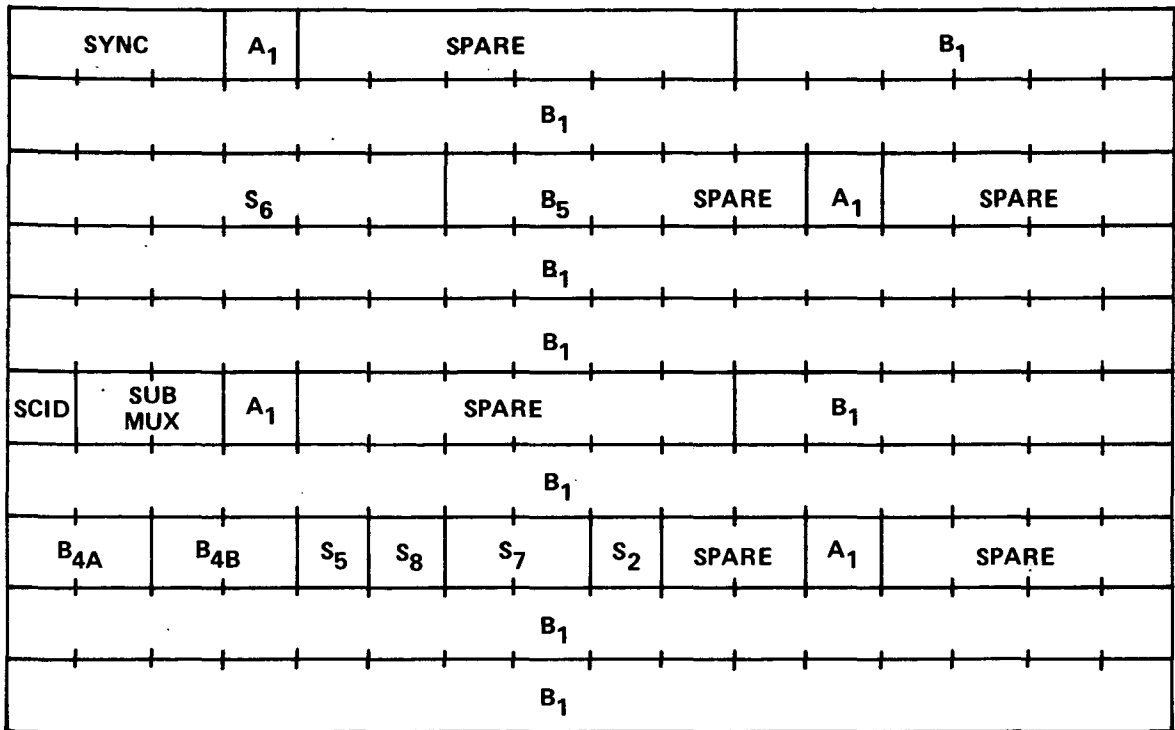


Figure IX-33. Format for experiment checkout telemetry.

By using this worst case format as a guide, one can develop formats for other modes of operation which use the same submultiplexed elements, thereby reducing the complexity of each format generator. A simplified block diagram of this concept is shown in Figure IX-34. Read-only memories (ROM) will be used for each distinct segment of the formats (e.g., data from the aspect system would have their own ROMs, as would the fixed experiments).

2. Format. Using this concept, a format can be developed for the launch and OAS modes. First, it will be assumed that spacecraft data will be desired at a higher rate during launch than during normal orbit operations. Using this assumption, the data from the spacecraft will be gathered on a 1 second basis as opposed to 1 and 5 second intervals. Also, since no spacecraft data need the timing accuracy required by the experiments, the time will be inserted only once per frame. These requirements are as presented in Table IX-13.

The format designations are the same as those used in developing the worst-case format. The closest standard format to the required 30 words

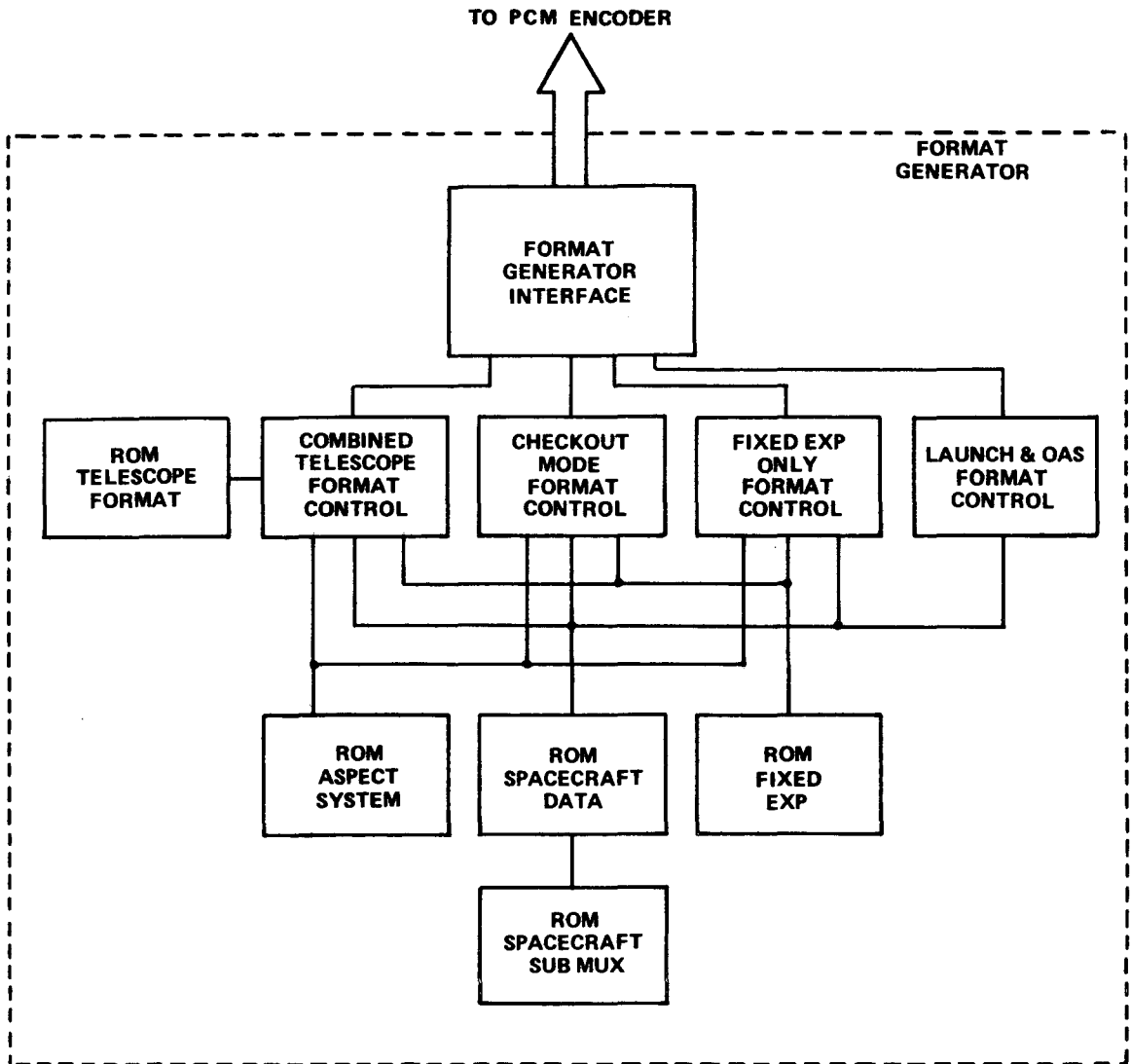


Figure IX-34. Block diagram format generator.

is a 4 by 8 format. A possible layout for this format is shown in Figure IX-35; it would be run at 12 samples per second just as the worst-case format.

In a similar fashion, a format for the fixed-experiment-only mode can be developed. Data requirements for one frame are given in Table IX-14.

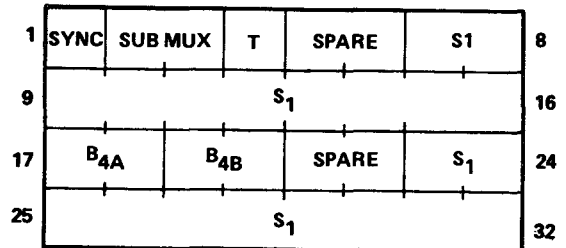


Figure IX-35. Format for launch and OAS telemetry.

TABLE IX-13. WORDS PER FRAME (BASED ON WORST CASE FRAME)

	No. of Words	Format Designation
5 sec Spacecraft Data Run at 1 sec Rate	20	S <sub>1</sub>
1 sec Analog Data Run at 1 sec Rate	2	B <sub>4A</sub>
1 sec Digital Data Run at 1 sec Rate	2	B <sub>4B</sub>
Time	1	T
Sync	1	Sync
Submultiplexer Definition	<u>2</u>	Submultiplexer
	30	

TABLE IX-14. DATA REQUIREMENTS FOR FIXED-EXPERIMENTS-ONLY MODE (ONE FRAME)

Words/Frame	No. of Words	Format Designation
Flare Detector	1	S <sub>5</sub>
Monitor Proportional Counter	6	S <sub>6</sub>
Flat Crystal Spectrometer	2	S <sub>7</sub>
Aspect Detector (Position)	3	B <sub>5</sub>
Housekeeping	1	S <sub>8</sub>
Spacecraft 5 Sec Data	4	S <sub>1</sub>
Spacecraft Analog Data	2	B <sub>4B</sub>
Spacecraft Digital Data	2	B <sub>4A</sub>
Time	1	T
Sync	1	Sync
Submultiplexer Definition	<u>2</u>	Submultiplexer
	28	

Again, the closest format matrix is 4 by 8. A possible format to implement this is shown in Figure IX-36. This format would be run at 12 frames per second.

1	SYNC	SUB MUX	SPARE	S <sub>7</sub>	T	8
9	S <sub>6</sub>			S <sub>5</sub>	T	16
17	S <sub>1</sub>		SPARE	S <sub>8</sub>	T	24
25	B <sub>4A</sub>	B <sub>4B</sub>	B <sub>5</sub>		T	32

Figure IX-36. Format for fixed experiment telemetry.

A similar analysis can be made of the requirements for a uniform checkout format that would be operated for the checkout of all experiments. If the assumption is made that only one experiment would be operated at a time, the driving requirement on the format becomes the worst-case experiment data rate. If this is added to the 12 words of spacecraft data, 4 words of aspect

data, and 8 words from the fixed experiments, then a requirement for 133 words of data per frame is established. Assuming the number of columns in the format matrix to be fixed at 8 or 16, the task is to establish the required number of rows. If symmetry is to be maintained, an even number of rows is required. Then, this yields a matrix of 10 rows, as shown in Figure IX-33. If a 10 by 16 matrix is not compatible with MSFN, alternatives must be considered.

The first alternative would be to remove the requirement for spacecraft data or miscellaneous experiments and aspect during checkout. This would reduce the data rate sufficiently to fit into an 8 by 16 matrix. Alternatively, if all these data are required, the format could revert to the 16 by 16 matrix.

Based on the above formats a generalized format control loop can be developed. This loop will describe the function of the format generator, whether a software or hardware generator is used. This generalized format loop is shown in Figure IX-37. Abbreviations used in the format are listed below:

- CNTA            The index counter for the main frame format
- TOTAL A        The total number of words on the main format
- CNTM            The index counter for the particular submultiplexer being accessed.
- TOTAL M        The total number of words in the particular submultiplexer

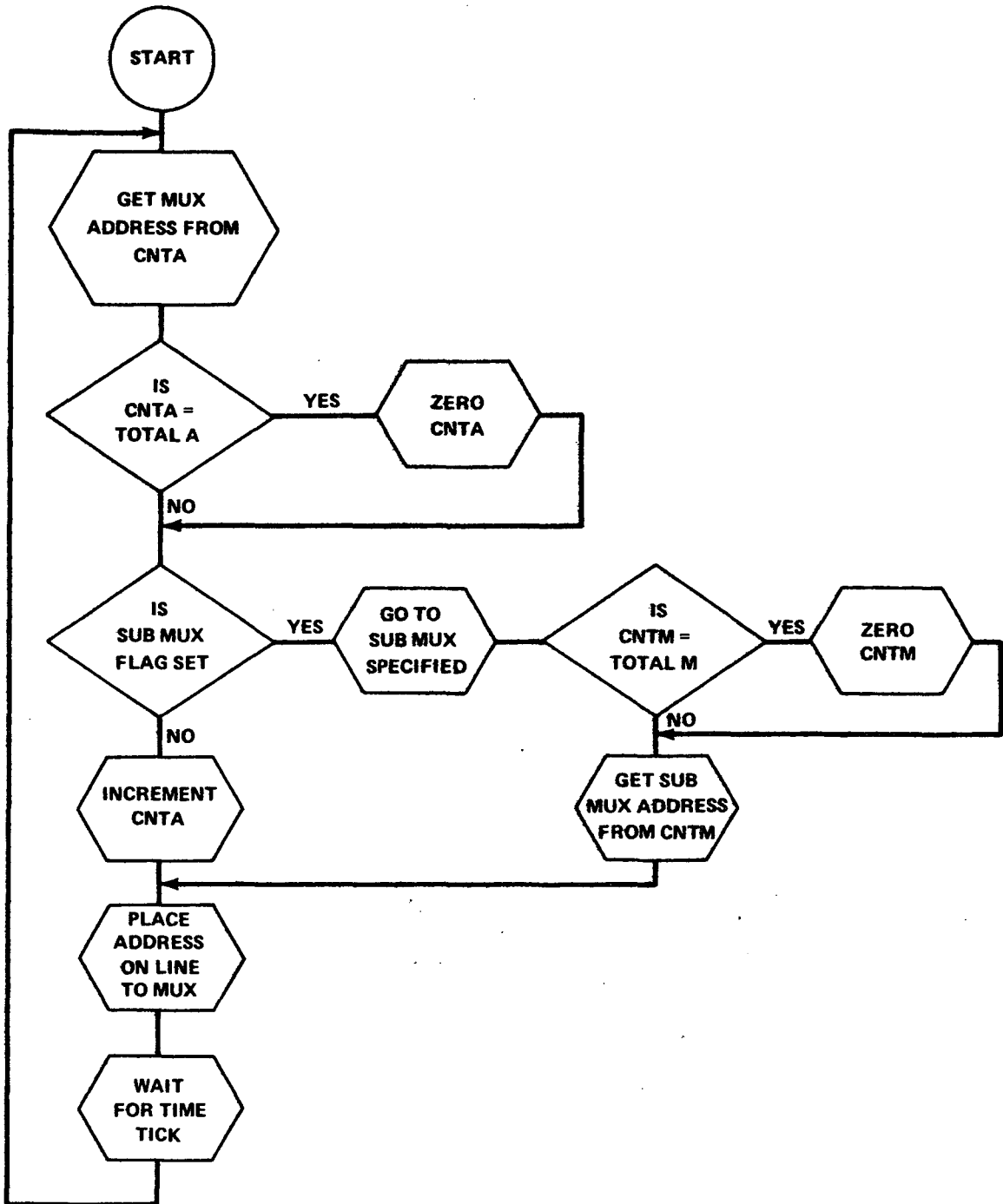
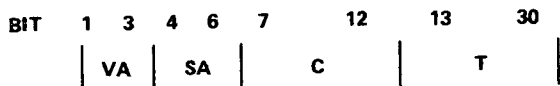


Figure IX-37. Generalized format control loop.

3. Command Structure. The command structure prescribed by MSFN requires the format presented in Figure IX-38 for all commands transmitted from ground stations to spacecraft. This, then, allows 8 subsystems to be



VA - VEHICLE ADDRESS

SA - SYSTEM

C - COMMAND

T - TIME TAG

Figure IX-38. MSFN command format.

defined, with each subsystem having a capacity of 64 commands. Examination of the command list given in Tables IX-15 and IX-16 reflects that the data and communications system and all the attitude sensing and control system both exceed this capacity. Therefore, a minor modification of this format should be considered. Since it is anticipated that no more than 4 spacecraft will be active at any one time, the vehicle address can be reduced from 3 bits to 2 bits, thereby allowing the command to

expand from 6 bits to 7 bits. This gives a capacity of 128 commands per subsystem. A modified command format is presented in Figure IX-39. A preliminary grouping of subsystems is listed in Table IX-17.

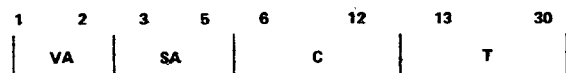


Figure IX-39. Modified command format.

## G. RF Spectrum Usage

The Apollo unified S-band system was designed with ranging signals on the baseband; telemetry data at 51.2 kbs are on a 1.024 MHz subcarrier and voice data are on a 1.25 MHz subcarrier. The HEAO-C uses a PRN ranging in one of the three modes, but the prime mode is with the tape recorded data on the baseband and 27.5 kbs real-time data on a subcarrier. The split phase coding from the tape recorded data has rather broad spectral nulls at 2 and 4 times the clock frequency. With subcarrier frequency of 1.024 MHz, the ideal baseband data rate should be 512 kHz of 256 kHz. This would place the subcarrier exactly in the center of the broad null. The real-time data are in the form of NRZ.

The ground station might require some modification for this optimum condition developed above; therefore, an analysis was conducted to compare the optimum to slightly off-optimum.

TABLE IX-15. SPACECRAFT COMMAND LIST

	No. of Commands
<b>Power System</b>	
Battery Charge Enable	8
Battery Charge Disable	8
Solar Power Distributor On/Off	2
Power Regulator On/Off	2
Power Control Assembly On/Off	2
Electrical Integration Assembly (EIA) On/Off	4
EIA Redundant On/Off	4
<b>Communication and Data Handling System</b>	
Spacecraft Clock On/Off	2
PCM Encoder On/Off	2
Format Generator On/Off	2
Format Select	7
Data Storage Control Unit On/Off	2
Tape Recorder Record	4
Tape Recorder-Reproduce	4
Tape Recorder Fast Forward	4
Tape Recorder Stop	4
Tape Recorder Select	4
Special Commands	4
Transmitter On/Off	4
Enable Auxiliary Oscillator	2
Bypass Auxiliary Oscillator	2
Ranging On/Off	4
Transmitter-PMP Input	4
Diversity Switch State	4
Receiver On/Off	4

TABLE IX-15. (Continued)

	No. of Commands
Frequency Multiplexer Enable/Inhibit	2
PSK Demodulator Enable/Inhibit	2
<b>Attitude Sensing and Control System</b>	
Wide Angle Sun Sensor Enable/Disable	2
Input Disabled	1
On/Off	2
Precision Digital Sun Sensor Enable/Disable	2
Input Disabled	1
On/Off	2
<b>Rate Gyro System</b>	
Pitch On/Off	4
Yaw On/Off	4
Roll On/Off	4
Drift Compensation Pitch (6 bits)	2
Drift Compensation Yaw (6 bits)	2
Drift Compensation Roll (6 bits)	2
Gyro Pitch Input Enable/Disable	2
Gyro Yaw Input Enable/Disable	2
Gyro Roll Input Enable/Disable	2
Drift Compensation Pitch Reset	2
Drift Compensation Yaw Reset	2
Drift Compensation Roll Reset	2
Pitch Gyro Enable/Disable	2
Roll Gyro Enable/Disable	2
Yaw Gyro Enable/Disable	2
Electronics On/Off	4
<b>Star Tracker</b>	
On/Off	8
Sun Shutter Automatic	4
Sun Shutter Open	4
Command Scan Mode	4

TABLE IX-15. (Concluded)

	No. of Commands
<b>Reaction Control System</b>	
Jet Pitch ( $\pm$ ) System Auto (A, B)	4
Jet Yaw ( $\pm$ ) System Auto (A, B)	4
Jet Roll ( $\pm$ ) System Auto (A, B)	4
Jet Pitch ( $\pm$ ) System Disable (A, B)	4
Jet Yaw ( $\pm$ ) System Disable (A, B)	4
Jet Roll ( $\pm$ ) System Disable (A, B)	4
Fire Jet Pitch ( $\pm$ ) System (A, B)	4
Fire Jet Yaw ( $\pm$ ) System (A, B)	4
Fire Jet Roll ( $\pm$ ) System (A, B)	4
<b>Control Moment Gyro</b>	
Spin Motor On (A, B)	8
Break On/Off	8
Electronics On/Off	8
<b>Computer</b>	
On/Off	6
Spacecraft Control Computer Select	3
Computer Interrupt Word	1
Computer Data Word	3
<b>Thermal System</b>	
Heater Group Enable/Disable	20
<b>Pyro Commands</b>	
Enable	1
Safe	1
ARM Squib Valves	2
Fire Squib Valve (Prime, Redundant)	16
ARM OAS Jettison	1
Jettison OAS	1
<b>OAS Commands</b>	
Prime Voltage Enable/Reset	2
Redundant Voltage Enable/Reset	2

TABLE IX-16. EXPERIMENT COMMAND SUMMARY

	No. of Bits
HR Telescope	16
HR Imaging Detector	24
HR Focal Plane Spectrometer	24
LA Telescope	16
Solid State Detector	42
Imaging Proportional Counter	8
Miscellaneous Experiments	
Flare Detector	20
Aspect Detector	8
Monitor Proportional Counter	20
Flat Crystal Spectrometer 2 ea. at 21	42
LE Telescope	24

TABLE IX-17. COMMAND REQUIREMENTS SUMMARY

System Address	System	Command Requirements
0 (000)	Attitude Sensing and Control	127
1 (001)	Power and Spacecraft (Thermal, Pyro, OAS)	30 44
2 (010)	Data Handling and Communications	67
3 (011)	HR Telescope	64
4 (100)	High Energy Telescope	66
5 (101)	Fixed Experiments	90
6 (110)	LE Telescope	64
7 (111)	Spare	135

The power spectral density of the tape recorded data and real-time data can be determined from the autocorrelation functions.

1. Analytical Procedure. The analytical procedure is to obtain the power spectral density of the Fourier transform of the autocorrelation function. The autocorrelation function of an NRZ of a random signal is shown in Figure IX-40. The power spectrum of a signal having this autocorrelation function is given by the following equation [IX-4]:

$$\begin{aligned}
 S(F) &= \int_0^T R(\tau) \cos(2\pi F)\tau \, d\tau \\
 &= 2 \int_0^T \left(1 - \frac{\tau}{T}\right) \cos(2\pi F)\tau \, d\tau \\
 &= T \frac{\sin^2(\pi FT)}{(\pi FT)^2}
 \end{aligned}$$

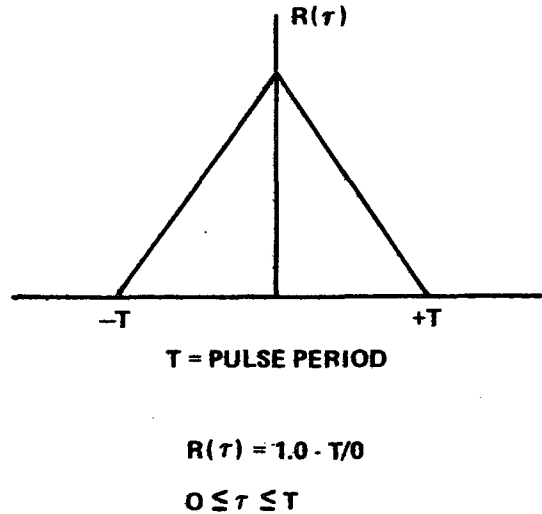


Figure IX-40. Autocorrelation function of an NRZ of a random signal.

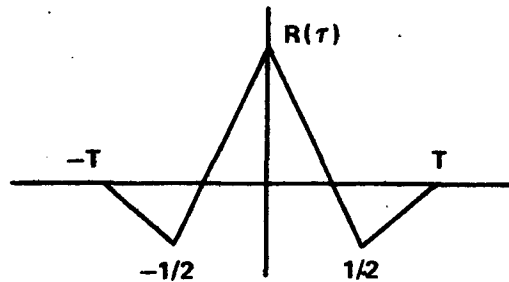
The split phase signal has an autocorrelation function as shown in Figure IX-41. In this case, the power spectral density is

$$\begin{aligned}
 S_s(F) &= \int_0^T R(\tau) R'(F) \cos(2\pi F)\tau \, d\tau \\
 &= \int_0^T \left(1 - 3\frac{\tau}{T}\right) \cos(2\pi F)\tau \, d\tau + \left(\frac{\tau}{T} - 1\right) \cos(2\pi F)\tau \, d\tau \\
 &= T \frac{\sin^2 \frac{\pi FT}{2}}{\frac{\pi FT}{2}} - \frac{\sin^2(\pi FT)}{(\pi FT)^2}
 \end{aligned}$$

Figure IX-42 gives a very good indication of the interference between the baseband signal and subcarrier. This figure ignores the fact that energy in the two signals is not equal. Therefore, the figure should not be used for quantitative estimates.

The real test is the amount of the real-time signal input to the recorded detector and vice versa. The ground station was shown with the phase locked loop and matched filter as means of demodulating the signals. The ratio of the wanted signal to the unwanted signal can be found based on the power spectrum of the two signals:

$$\frac{S_0}{N_0} = \frac{\int S_d(F) dF}{\frac{1}{T} \int S_d(F) S_u(F) dF}$$



WHERE

$$R(\tau) = 1 - 3\tau/T$$

FROM

$$0 \leq \tau \leq T/2$$

AND

$$R'(\tau) = \tau/T - 1$$

FROM

$$T/2 \leq \tau \leq T$$

Figure IX-41. Split phase signal autocorrelation function.

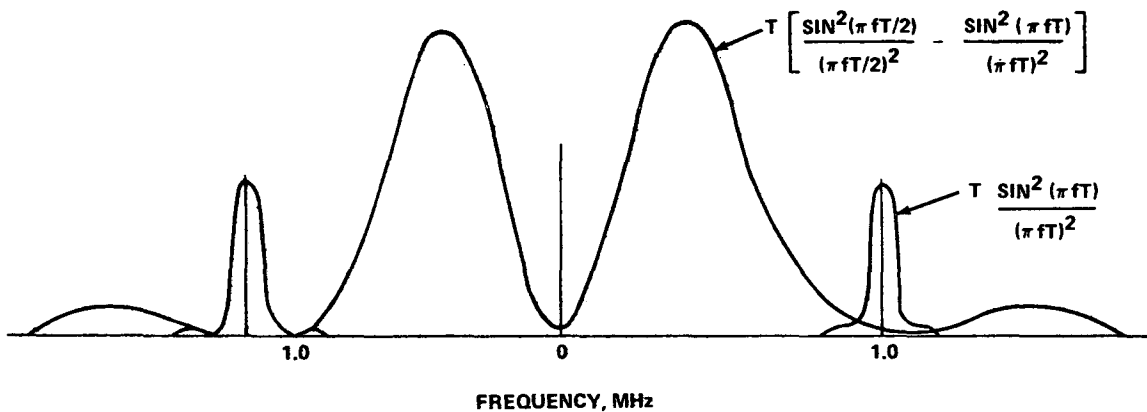


Figure IX-42. Power spectral density of downlink signal.

The  $1/T$  normalizes the output of the matched filter to 1.0 when the desired signal is present. Then,

$$\text{Signal Power} = R_d(0) = 1.0$$

$$\text{Noise Power} = \frac{1}{T} \int_{-\infty}^{\infty} R_d(\tau) R_u(\tau) d\tau,$$

where  $R$  denotes the autocorrelation function. In the case of the real-time data (1.024 MHz subcarriers) interference with the baseband signal (500 kbs tape recorded data), the above equation is treated as noise:

$$\text{Noise power} = \frac{1}{T} R_s(\tau) R_z(\tau) \cos(2\pi F_c \tau) d\tau.$$

In this instance  $F_c$  is the subcarrier frequency and  $T = 1/500$  kbs; therefore

$$\text{Noise power} = \frac{1}{T} \left[ \begin{aligned} & \frac{T}{2} \int_0^T \left(1 - \frac{3}{T}\tau\right) \left(1 - \frac{\tau}{T}\right) \cos(2\pi F_c \tau) d\tau \\ & + \frac{T}{2} \int_{\frac{T}{2}}^T \left(\frac{\tau}{T} - 1\right) \left(1 - \frac{\tau}{T}\right) \cos(2\pi F_c \tau) d\tau \end{aligned} \right].$$

To simplify the above equation, it is assumed that bit rate of the tape recorded data is 512 rather than 500 kbs. Then, the subcarrier frequency and baseband data become even integers of each other and the complex expression reduces by dropping out the sine terms:

$$\text{Noise Power} = \left(\frac{1}{\pi F_c}\right)^2 \left(\frac{1}{2T^2} + \frac{3}{2T_D T}\right).$$

Evaluating the equations above results in  $-31.1$  dBW<sup>1</sup> as the power level of the noise.

1. Decibels referred to 1 watt.

The direct interference of the tape data with the real-time data is found in a similar manner:

$$\text{Noise} = \frac{1}{T_D} \int_{-T}^T R_s(\tau) R_z(\tau) \cos(2\pi F_c \tau) d\tau \quad .$$

Since the only change is  $T_D = 1/2.75 \text{ kHz}$ ,

$$\text{Noise} = \left( \frac{1}{\pi F_c} \right)^2 \left( \frac{1}{2T_D} + \frac{3}{2T_D^2} \right) \quad .$$

As might be expected, the real-time data are affected more by taped data than the taped data are affected by the real-time data; this is the desired condition. When numerical data are substituted in the above, the result is -18.5 dBW. These values do not account for the fact that the energy in the two signals is not equal. The modulation losses [IX-5] for indices of 1.025 radians and 0.75 radian are given by

$$2J_1^2(\Delta\theta_1) \cos^2(\Delta\theta_2) = 11.7 \text{ dB}$$

and for the subcarrier signal (real-time data) are given by

$$\frac{8 \sin^2(\Delta\theta_2) J_0^2(\Delta\theta_1)}{\pi^2 \cos^2(\Delta\theta_2)} = 3.6 \text{ dB} \quad .$$

The difference in the energy in the tape data signal and the real-time data is -8.1 dB, or the tape recorded signal is nearly five times stronger than the real-time signal. The interference ratio is  $31.1 - 8.1 = 23.0 \text{ dB}$  for the tape data (wanted signal) to the real-time data (unwanted signal). The interference ratio for the real-time data to the taped data is  $18.5 + 8.1 = 26.6 \text{ dB}$ .

The harmonics' beating with the signal would occur, but the magnitude would be small enough to be neglected at this point in the development.

2. Overall Effect. The link calculations for the baseband resulted in a signal-to-noise ratio of 14.87 dB due to thermal effect combined with tape

noise. When the direct interference is combined with the thermal effect and tape noise, the signal-to-noise ratio is

$$\frac{S_0}{N_0} = 10 \log \left( \frac{1}{\frac{1}{N_t} + 1N_m} \right) = 10 \log \frac{(N_t) (N_{1m})}{N_t + N_{2m}} .$$

The above equation was derived from the model depicted in Figure IX-43. It results in a very small additional degradation of approximately 0.4 dB for the tape link. The real-time data link reduction is only about 0.63 dB. In either case, the resulting signal-to-noise ratio is still a high quality. The tape link has a 1.3 dB margin, while the real-time data has a 3.2 dB margin. If another iteration of the study were possible, the modulation indices would be selected to provide a larger margin in the tape link since these data are more critical.

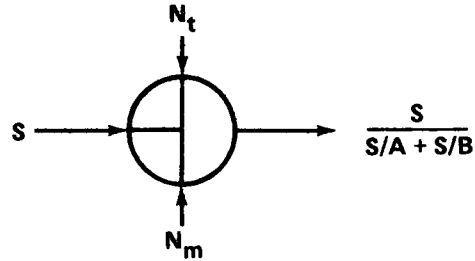


Figure IX-43. Signal combined with noise from tape and channel.

## H. Reliability

The philosophy that was followed throughout the communication and data handling system analyses was to use tried and proven techniques and qualified components wherever possible. Every effort was made to produce a design that was not pushing the current state-of-the-art but, at the same time, would not be obsolete by the operational readiness date. This was a very difficult task since technology has a tendency to evolve on a five year basis. The elements selected must be those that have progressed to the point where the design is firm and qualification is just beginning. These designs should mature while the details of the missions are being developed and they should be fully accepted by the time of the design freeze for flight hardware. The most effective means of insuring intrinsic reliability in a design is to strive for no single-point failures. Also, there should be several alternate modes of operation that would provide only slightly degraded performance in the event of a failure. In many instances dual redundancy was resorted to if the function was critical and alternates were not technically feasible or practicable.

The RF portion of the system exemplifies the philosophy set forth in the preceding paragraph. The frequency diversity RF system, using selection combining, allows for a single frequency operation in the event one of the two transponders should fail. The degradation in performance would be the operational delay while waiting until the spacecraft passes over a ground tracking station where it can be oriented properly with respect to the ground for the antenna that functions on the second frequency. Within the transponder, both the receiver and the transmitter are circuit redundant. This precludes the possibility of a single-point failure preventing the spacecraft from receiving commands. A dual redundant PSK demodulator automatically selects one of the two transponders based on the "signal present" indication from the individual transponder. If both transponders have an acceptable automatic gain control (AGC) level, then the outputs are summed and used to drive the 70 kHz phase lock loop.

The sub-bit decoder is located remotely from the central command unit. This is to allow each of the eight command decoders to operate independently of the central unit and, thus, improve the overall data handling reliability. These units are made up primarily of logic gates and can be made redundant at circuit element level, thus providing extremely high probability of performing for two years. The central command processor functions only on stored commands and, thus, does not represent a possible catastrophic failure. The loss of the command storage would only mean that all commands would have to be executed over a tracking station, but the mission would not be lost.

1. RF Equipment. The communications system block diagram is given in Figure IX-44. Table IX-18 summarizes the results of the reliability analysis given in Appendix G.

Of the two antennas, one is deployable; the antenna deployment mechanism was assumed similar to that of the solar panels, with redundant bolt-cutters as actuators releasing a spring-loaded boom. The communications system is the most reliable of the baseline astronics systems. A detailed discussion of the reliability estimation procedures is given in Appendix G.

2. Data Handling Equipment. The data handling system reliability block diagram is given in Figure IX-45. Table IX-19 summarizes the results of the data handling system reliability analysis of Appendix G.

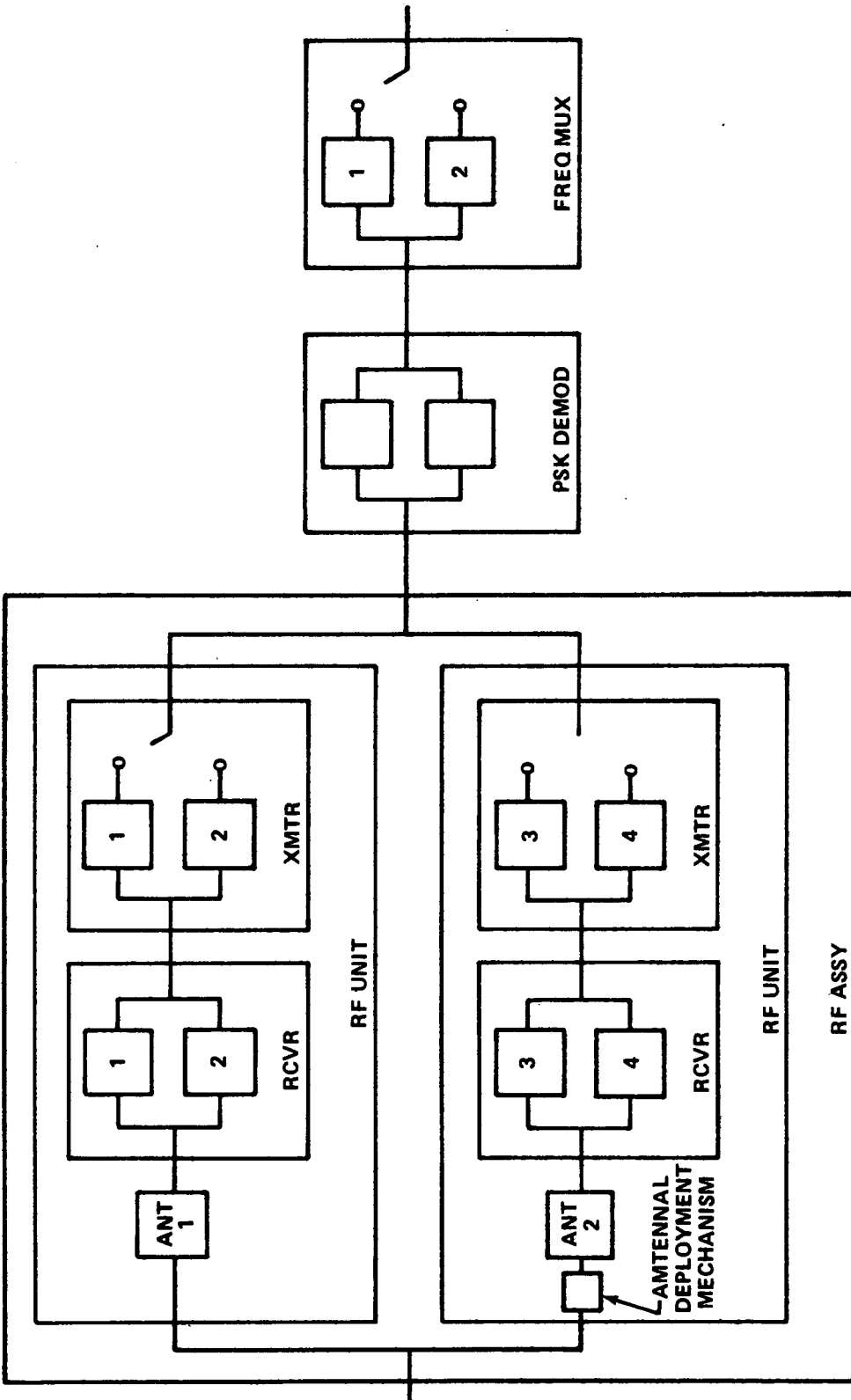


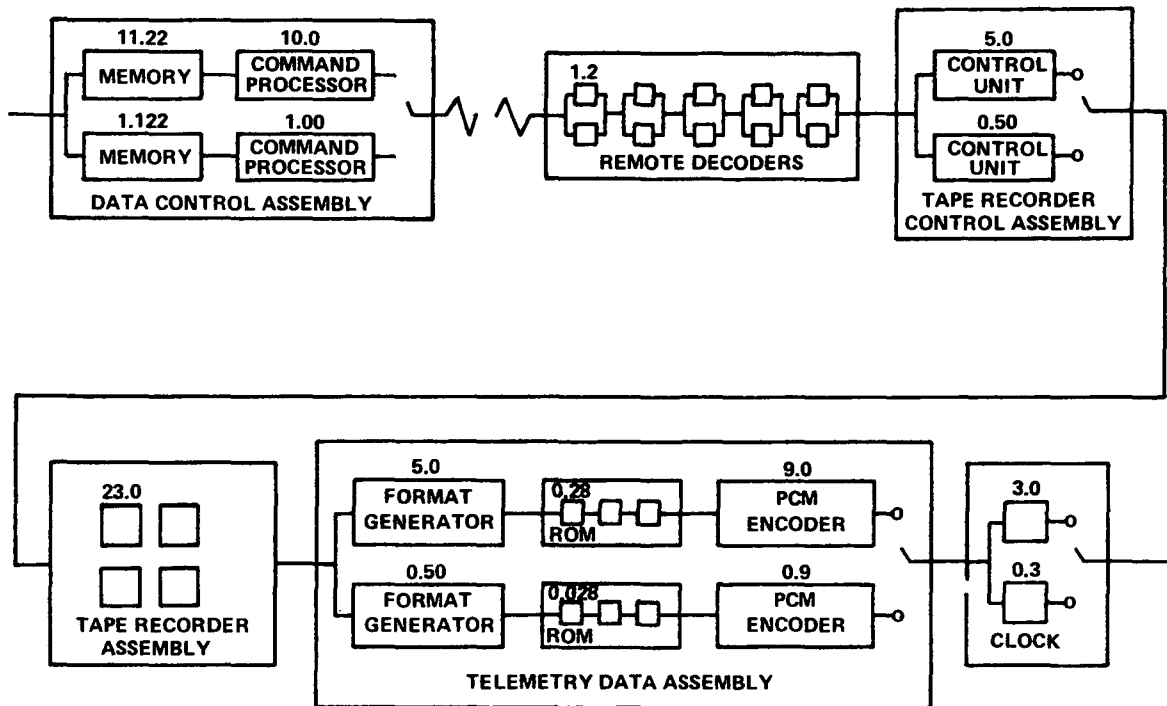
Figure IX-44. Communications system block diagram.

TABLE IX-18. COMMUNICATIONS SYSTEM RELIABILITY  
NUMERICS SUMMARY

Assembly	Reliability	
	1 Yr	2 Yr
RF	0.99992	0.99909
Antenna Deployment	0.99997	0.99997
Antenna	0.99886	0.99772
Receiver	0.99240	0.97221
Transmitter	0.99996	0.99985
PSK Demodulator	0.99976	0.99905
Frequency Multiplexer	<u>0.99994</u>	<u>0.99978</u>
Baseline Communications System	0.99963	0.99792

TABLE IX-19. DATA HANDLING NUMERICS  
RELIABILITY SUMMARY

Assembly	Reliability	
	1 Yr	2 Yr
Data Control	0.98264	0.93899
Tape Recorder Control	0.99897	0.99602
Tape Recorder	1.00000	0.99996
Telemetry Data	0.99150	0.96890
Remote Decoder	0.99877	0.99518
Clock	<u>0.99963</u>	<u>0.99853</u>
Baseline Data Handling System	0.98890	0.95895



**NOTES:**

1. REMOTE DECODERS FOR ASCS, GEP, EXPERIMENTER'S COMPUTER OMITTED.
2. ROM FOR LAUNCH FORMAT OMITTED.
3. TAPE RECORDER ASSEMBLY ANALYZED BY LOAD-SHARING MODEL WITH VARYING FAILURE RATES.
4. RELIABILITY OF DATA CONTROL ASSEMBLY DOES NOT AFFECT SYSTEM RELIABILITY.
5. APPROXIMATE CLOCK MODEL USED.

Figure IX-45. Data handling system reliability block diagram.

The reliability of the data control assembly is not included in the system reliability estimate; the purpose of this assembly is to provide a stored command capability, the loss of which entails some loss of operational efficiency. The net effect, however, is not considered to produce a severe reduction in the total amount of experimental data gathered. An approximate clock model was used. The proposed clock is a new design for which adequate reliability data could not be determined [IX-6]. The model used corresponds to the Grumman design for HEAO-A and -B. A detailed tape recorder analysis is given in Appendix G, whose principal result is a recommendation that the number of tape recorders be reduced from the four of the baseline to three.

## I. Future Studies

Several elements of the design, while only developed to the conceptual stage in this study, do exist to some degree at the present time and are available from various manufacturers. The next phase of the study should be directed at specific circuit design and, where practical, selection of the manufacturer whose design most closely agrees with the baseline. This is particularly true for the tape recorder. It should undergo prototype design and qualification testing. Scale modeling of the antenna system should be undertaken as soon as the physical envelope of the spacecraft has been defined. Alternate arrangements and locations may be justified in the spacecraft physical shape should change.

The transponder, command memory, and remote multiplexer designs already exist but may require qualification to the HEAO-C environment. The clock, command processor, and central data acquisition elements should have prototypes for qualification, fabrication, and testing.

The detailed reliability analysis indicated a requirement for three tape recorders; however, down time of the tracking stations was not included in this analysis, because it was beyond the scope of the study. A fourth tape recorder would provide additional storage of data for possible down time of tracking stations. Additional studies could clarify this aspect of the analysis.

## J. Summary and Conclusion

The basic requirements have been met and in some instances exceeded. The overall design is certainly well within the current technology available, and any advances made prior to the design freeze would provide growth capability. It does not appear that any area is overdesigned. Some of the margins in the communications channel are rather large, but the trade-off studies did not show significant savings in power or weight by reducing these margins. The communication and data handling design described in this report is very similar to the HEAO-A and -B designs. The principal difference is in the command storage capability included in the HEAO-C design.

## REFERENCES

- IX-1. Oliver, A.A. and Malech, R.G.: Radiating Elements and Mutual Coupling. Academic Press, New York, 1966.
- IX-2. Chapman, D.W.: Theoretical Limits on Digital Magnetic Recording Density. IEEE Transactions, February 1963.
- IX-3. Norris, K.A.: A Technique for High Density Digital Magnetic Recording. Western Electronic Show and Convention, August 24, 1967.
- IX-4. TRW: HEAO Briefing Brochure. NASA Contract No. NAS8-26273.
- IX-5. Foley, T.K.; Gaumont, B.J.; and Witherspoon, J.T.: Optimum Power Division for Phase Modulated Deep Space Communications Links. IEEE Transactions on Aerospace and Electronic Systems, Vol. AES-3, No. 3, May 1967.
- IX-6. Grumman Aerospace Corporation: HEAO Experiment Developer's Handbook, NASA Contract No. NAS8-26272 (Prime), March 25, 1971.

## TABLE OF CONTENTS

	Page
A. General Considerations . . . . .	X- 1
B. Assessment . . . . .	X- 1
1. Design for Shuttle-Only Launch . . . . .	X- 1
2. Design for Titan IIID/OAS-Only Launch . . . . .	X- 5
3. Design for Either Titan IIID/OAS or Shuttle Launch . . . . .	X- 5
a. Similarity of Launch Environment . . . . .	X- 5
b. Utilization of the Orbit Adjust Stage (OAS) . . . . .	X- 6
c. Launch Economy . . . . .	X- 6
4. Design for Shuttle Retrieval . . . . .	X- 7
a. Concept 1 (Dock to Front of HEAO) . . . . .	X- 9
b. Concepts 2 and 3 (Dock to Side of HEAO) . . . . .	X- 9
c. Concept 4 (Dock to Aft End of HEAO) . . . . .	X- 9
C. Concluding Remarks . . . . .	X-15
References . . . . .	X-16

## LIST OF ILLUSTRATIONS

Figure	Title	Page
X-1.	Shuttle payload envelope (typical) . . . . .	X- 3
X-2.	Launch vehicle performance capability. . . . .	X- 4
X-3.	Docking/retrieval Concept 1. . . . .	X-11
X-4.	Docking/retrieval Concept 2. . . . .	X-12
X-5.	Docking/retrieval Concept 3. . . . .	X-13
X-6.	Docking/retrieval Concept 4. . . . .	X-14

## LIST OF TABLES

Table	Title	Page
X-1.	HEAO-C/Shuttle/Titan Compatibility . . . . .	X- 2
X-2.	Shuttle Cargo Bay Uninsulated Interior Wall Temperatures . . . . .	X- 5
X-3.	Shuttle Payload Load Factors . . . . .	X-10

# CHAPTER X. SPACE SHUTTLE LAUNCH AND RETRIEVAL OF HEAO-C

## A. General Considerations

Although the Titan IIID/OAS was used as the baseline launch vehicle for the study, the impact of possible shuttle launch and retrieval on the HEAO-C design was assessed. This assessment was not performed in as much depth as the assessment of the baseline, but several key impacts were identified and are discussed herein. The shuttle design is still very "soft," and design data change frequently. For the purpose of this assessment, the shuttle design and interface requirements specified in Reference X-1 were used as a starting point and updated where possible.

## B. Assessment

The assessment was performed from four different standpoints, since each could have a significantly different effect on the design:

1. Design for Shuttle-only launch.
2. Design for Titan IIID/OAS-only launch.
3. Design for either Titan IIID/OAS or Shuttle launch.
4. Design for Shuttle retrieval.

The HEAO-C requirements, Shuttle capability, and Titan IIID/OAS capability are shown in Table X-1 for a few key items of consideration.

1. Design for Shuttle-Only Launch. If the HEAO-C spacecraft was designed for Shuttle launch rather than Titan launch, and if divergence from commonality with HEAO-A and -B was proven cost-effective, the following advantages might accrue to the design:

a. Lower launch acceleration levels, lower acoustic pressure levels, and greater allowable dynamic envelope would permit easier shock-mounting, lighter structures, possibly lower qualification testing limits, and more easily held alignment tolerances.

b. Larger payload compartment and greater payload capability would accommodate increased payload growth (Figs. X-1 and X-2); telescope

TABLE X-1. HEAO-C/SHUTTLE/TITAN COMPATIBILITY

	Payload Bay Size (~ft)	Payload	Launch Acceleration	Allowable Dynamic Envelope	Payload Ejection Dynamics	Initial Payload Orbital Orientation	Max Acoustic Pressure Level
HEAO-C Requirements	9 x 30	19 000 lb to 270 n. mi. 28.5 deg inclination	Not specified	Not specified	Not specified	Not specified (solar vector desired)	Not specified
Estimated Shuttle Capability	15 x 60	30 000 <sup>a</sup> lb to 270 n. mi. 28.5 deg inclination	1 g lat. max, 3.3 g long. max	±3 ft	Close to Zero	Anything desired	155 dB
Titan IIID/OAS Capability	≈ 9 x 47	24 000 lb to 270 n. mi. 28.5 deg inclination	1.5 g lat. max, 6 g long. max	Several inches	Approx. 3 deg/sec	Depends on ejection dynamics	165 dB

a. Orbiter maneuvering system (OMS)  $\Delta V = 1000$  fps.

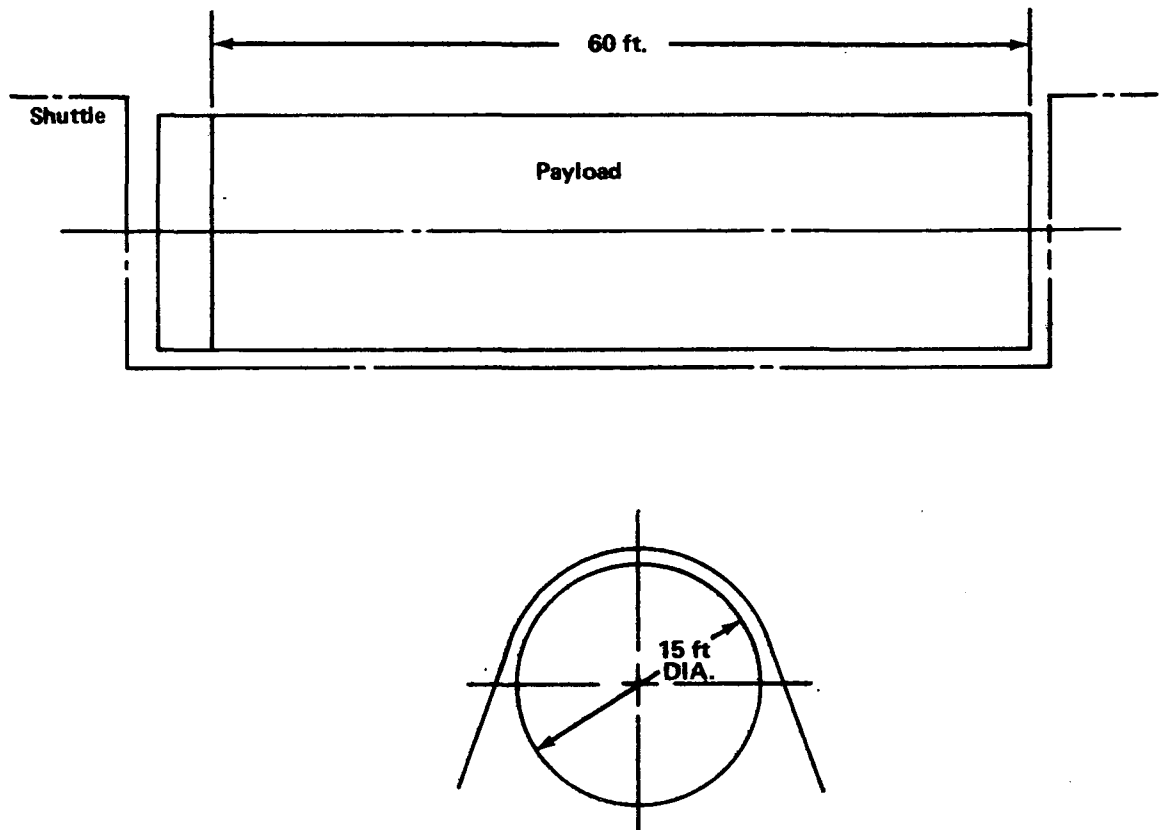


Figure X-1. Shuttle payload envelope (typical).

diameters could be larger and focal length longer, or more telescopes could be added to the payload package. The longer payloads for the Shuttle launch would not be constrained to the cantilevered designs required for the Titan launch.

c. Spacecraft RCS propellant could be reduced since initial tumble would be less and initial solar orientation could be accomplished before Shuttle release; the entire reaction control system (RCS) could be eliminated in favor of a magnetic system for control moment gyro (CMG) unloading.

d. The OAS could be eliminated; this would permit a shorter spacecraft and lighter structure.

e. If deployable solar arrays were used, confidence could approach that of fixed arrays due to man's presence. The same would be true for the deployable antenna.

WITHOUT AIR-BREATHING ENGINE SYSTEM (ABES)  
 ORBITER INERT WEIGHT,  $W_{NO} = 160,385$  LBS  
 $ISP_{OMS} = 309$  SEC  
 $i = 28.5^\circ$

ORBITER MANEUVERING SYSTEM  
 (OMS)  $\Delta V$  REQUIREMENTS  
 BASED ON:  
 ENTRY ANGLE =  $-1^\circ$   
 10%  $\Delta V$  CONTINGENCY  
 7 DAYS STATION KEEPING

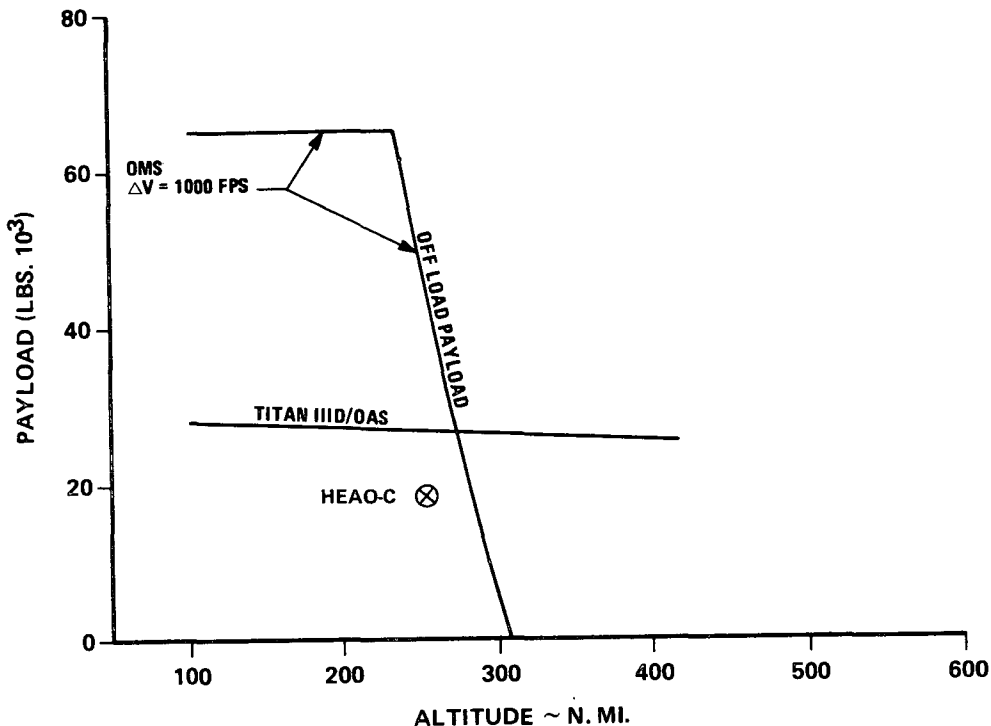


Figure X-2. Launch vehicle performance capability.

f. The sunshade could be deployable or detachable to shorten payload size; yet confidence could approach that of fixed sunshade, due to man's presence.

Should the HEAO-C be designed for a Shuttle-only launch and a later decision be made to fly on the Titan, considerable redesign and retest would be required. The degree of impact depends on how many of the above features were incorporated into the design initially.

2. Design for Titan IIID/OAS-Only Launch. From Table X-1, it can be seen that designing for a Titan launch generally imposes more severe constraints than designing for a Shuttle launch. Hence, if HEAO-C is designed for the Titan launch, no major changes would be required for accommodation to the Shuttle launch provided the number and location of attach points is maintained. Most probably, some local structural modifications at the attach points would be required. There are some second-order considerations, however, (mentioned in subsequent paragraphs) which would have to be evaluated to determine the impact of having to launch such a design on the Shuttle.

3. Design for Either Titan IIID/OAS or Shuttle Launch. Although current planning for the HEAO-C shows a launch date several years earlier than the planned operational availability for the Space Shuttle, changes might occur which would make this option programmatically attractive. However, from a technical standpoint, numerous considerations must be assessed before the total design impact can be defined and the cost-effectiveness of diverging from HEAO-A and -B commonality evaluated. A few typical areas requiring careful consideration are discussed in the following paragraphs.

a. Similarity of Launch Environment. Aside from acceleration loads and structural attach points, many other environmental factors must be considered such as contamination control, venting provisions, thermal control, etc. For example, the Shuttle payload bay wall temperature limits, updated since publication of Reference X-1, are given in Table X-2. The acceptability of these temperatures depends primarily on the required environment for the experiments during the prelaunch/ascent period of the mission. That is, the principal investigators and experiment manufacturers must specify the allowable experiment temperature limits to prevent undesirable effects (e.g., permanent deformation).

TABLE X-2. SHUTTLE CARGO BAY UNINSULATED INTERIOR WALL TEMPERATURES

Prelaunch	40° F to +120° F
Launch	40° F to +150° F
On-Orbit (doors closed)	-100° F to +150° F
On-Orbit (doors open) Payload Provided	
Reentry and Post-Landing	-100° F to +200° F

Although detailed analysis of the Observatory transient temperature history during launch was not undertaken for either Titan or Shuttle during the Phase A analysis, these uninsulated wall temperatures for the Shuttle appear unacceptable. As frequently done with the Titan nose cones, multilayer or fibrous insulation will probably have to be attached to the payload side of the Shuttle bay walls to reduce transverse temperature gradients. Other corrective actions might include the following:

- The Observatory can be maintained at a constant acceptable environment up to launch by, for example, a continuous dry air or nitrogen purge (at 70° F) of the cargo bay. This capability is supplied by ground support equipment and caution is exercised to prevent contamination.
- The X-ray mirror assembly thermostatically controlled heaters are turned on just prior to launch.
- The elapsed time from lift-off to orbit insertion will be less than 10 minutes. Consequently, although the controlled environment (purge) has been removed, the Observatory will not respond significantly due to its large thermal mass (analysis needed to verify this).
- Should the time from orbit insertion to deployment be too long, the orientation of the Shuttle can be altered to compensate.

The HEAO-C thermal control system design would probably be compatible with either launch vehicle after implementation of the above actions.

b. Utilization of the Orbit Adjust Stage (OAS). For a Shuttle-only launch, the OAS would not be required, but since it is required for Titan launch some spacecraft components, primarily the RCS systems, have been located in this area. A trade study will be required to ascertain the most cost-effective design approach to implement, e.g., strip out the main propulsion system and retain the OAS shell for RCS mounting or relocate the RCS within the spacecraft.

c. Launch Economy. Maximum efficiency of Shuttle launch might dictate simultaneous launch with a companion spacecraft. The following provisions might be made to shorten and lighten the HEAO-C should this become necessary:

- Remove the OAS and relocate the RCS subsystem into the basic spacecraft structure (propellant quantity can be reduced since no OAS burn is required).
- Redesign the sunshade to be deployable rather than fixed.

4. Design for Shuttle Retrieval. The HEAO-C is a candidate for Shuttle retrieval regardless of which launch vehicle places it into orbit. Clearly, if it has been designed for Shuttle-only launch, or possible Shuttle launch, many of the launch vehicle/spacecraft interfaces will have already been established and retrieval will be facilitated.

Three principal advantages accrue from designing for and implementing HEAO-C retrieval:

- Confidence in mission success is significantly enhanced. Should a major Observatory malfunction occur which degrades operational capability to such a low level that it is no longer cost-effective to continue orbital operations, the Shuttle makes it possible to retrieve, repair, and relaunch. Also, if Shuttle launched, on-orbit checkout during Observatory system activation is possible, and immediate retrieval can be implemented should a malfunction be detected during this critical period.
- Laboratory analysis of the effects of long lifetime in space environment will be possible. Subsequent to retrieval, HEAO-C experiments, materials, and subsystem components can be subjected to detailed laboratory testing to establish degradation levels and improve future lifetime and reliability estimates.
- Finally, retrieval opens up the possibility for refurbishment, replacement of focal plane detectors with different and newer instruments, and launching a second HEAO-C mission.

The capability for checkout of the payload after it undergoes the rigors of launch and flight should not be underestimated. From a Goddard Space Flight Center (GSFC) analysis of flight failure data on 24 spacecraft, 46 percent of the spacecraft experienced first-day failures. Moreover, 20 percent of all failures occurred during the first day [X-2]. Provided the

impact on the HEAO-C design can be kept to a reasonable level, it would seem desirable to incorporate this capability into the HEAO-C design for either Titan or Shuttle launch, even though it would be operative only if launched on the Shuttle. The capability for return of the HEAO-C to the ground if a malfunction is detected is the key to on-orbit checkout since HEAO-C is not designed for on-orbit maintenance.

A high level systems check could be performed before releasing the HEAO-C from the Shuttle. It appears that two coax connectors and one large conventional connector located on the HEAO will satisfy checkout requirements. A kit of HEAO-peculiar checkout equipment would be supplied with the spacecraft. It is assumed that the Shuttle will have some basic onboard capability for payload checkout, possibly furnished by a manned payload support module in the cargo bay, as this would normally be required for any payload. Cockpit monitoring of mission critical or hazardous items would be via the module or directly through the Shuttle interface.

The HEAO system and its electrical support equipment (ESE) are to be designed to verify mission readiness and to locate malfunctions to a black box level. The on-orbit checkout equipment will be similar to the ESE except it should be smaller and less complex. Detailed requirements and the degree to which malfunction detection is worthwhile in orbit needs to be determined. The primary method of checkout with the HEAO still in the cargo bay would be through use of a coax link to the transponders. After release of the HEAO, an open loop RF check should be made using a ground station before the Shuttle returns to earth. It should be noted that checkout of the HEAO while in the payload bay could also be done from a ground station, by using a parasitic antenna outside the Shuttle, or by opening the cargo bay doors; this would even further minimize requirements for onboard checkout equipment, but would limit operations to the times when the Shuttle was over a ground station.

The design impacts associated with docking, retrieval, and return of the HEAO-C to earth will probably be greater than those associated with launch. This is true particularly of the docking design concept and the structural support concept for the lateral g-loading during reentry and landing. Table X-3 shows a 4 g maximum lateral acceleration during orbiter entry, a higher lateral acceleration than for either Titan IID/OAS or Shuttle launch.

Four docking concepts are presented in the following paragraphs. A cooperative HEAO-C was assumed throughout this study; much additional study effort is required to establish the operational and design impacts associated with an uncooperative (tumbling) satellite, e.g., design for passive stabilization or active, redundant backup systems.

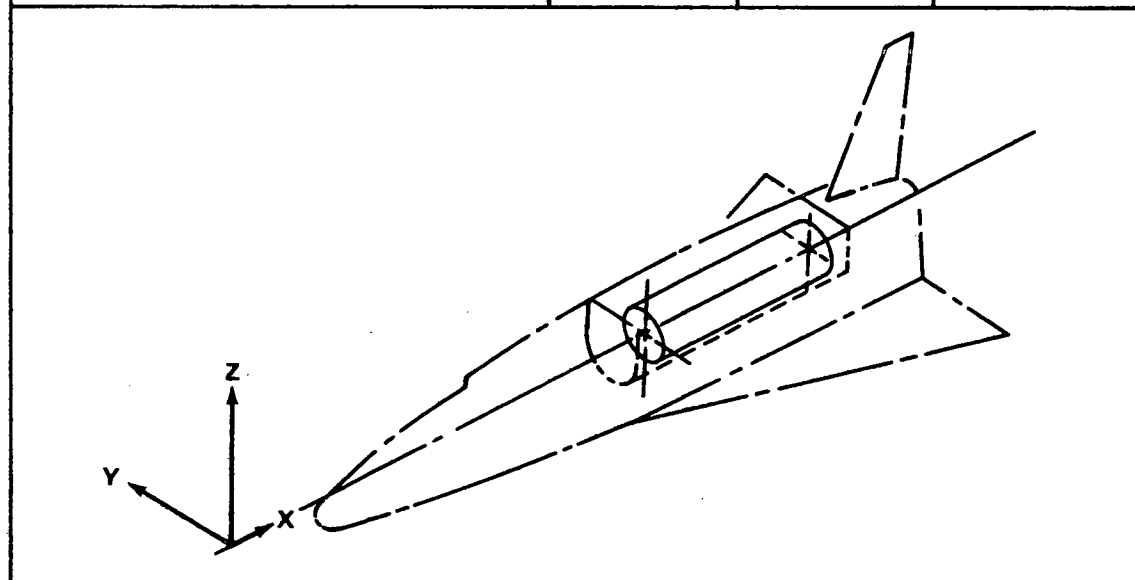
a. Concept 1 (Dock to Front of HEAO). This concept is shown in Figure X-3. It requires that the sunshade be collapsible (for docking and for Shuttle launch) and requires the docking mechanism to be an outboard concept (to prevent obscuring the experiment fields of view during Observatory operations). The drogues and ring must be collapsible for Titan launch, and possibly so for Shuttle launch. The most sensitive surfaces of the Observatory (experiment apertures and attitude sensors) would probably receive maximum exposure to potential contamination from the Shuttle RCS during docking, with this concept. For this reason and the obvious complexities associated with the collapsible mechanisms, this docking concept is undesirable. Figure X-3 also shows one feasible concept of supporting the HEAO in the Shuttle bay (docking adapter and aft cradle support concept).

b. Concepts 2 and 3 (Dock to Side of HEAO). These concepts are shown in Figures X-4 and X-5. Both concepts require the aft docking drogues to be retractable for Titan launch but not for Shuttle launch; after a Titan launch, they must be deployed for retrieval (approximately 45 degrees rotation). The only difference in concepts 2 and 3 is the location of the aft drogues (on OAS versus spacecraft body). The main disadvantage of this docking concept is the small "clock angle" misalignment, which could be tolerated during docking. The pallet used as the support structure for the HEAO during retrieval and return to earth would be a standard structure used for other Shuttle missions. Docking could be accomplished with the pallet inside the cargo bay or partially deployed (preferred for clearance and possible visibility improvement).

c. Concept 4 (Dock to Aft End of HEAO). This concept is shown in Figure X-6. It requires that a portion or all of the OAS be jettisoned to

TABLE X-3. SHUTTLE PAYLOAD LOAD FACTORS

Condition	X(g)	Y(g)	Z(g)
Launch	1.4 ±1.6	±1.0	±1.0
High Q Booster Thrust	1.9 ±0.3	±1.0	0.8 ±0.2
End Boost (Booster Thrust) <sup>a</sup>	3.0 ±0.3	±0.6	±0.6
End Burn (Orbiter Thrust)	3.0 ±0.3	±0.5	±0.5
Orbiter Entry	-0.5	±1.0	-3.0 ±1.0
Orbiter Flyback	-0.5	±1.0	+1.0 -2.5 ±1.0
Landing	-1.3	±0.5	-2.7 ±0.5
Crash (Nonintact Equipment Survival) <sup>b</sup>	-8 +1.5	±1.5	-4.5 +2.0



a. Excludes Booster-Orbiter separation loads which are to be determined.

b. Nonsimultaneous or -8.0 in 20 degree cone from  $N_x$ .

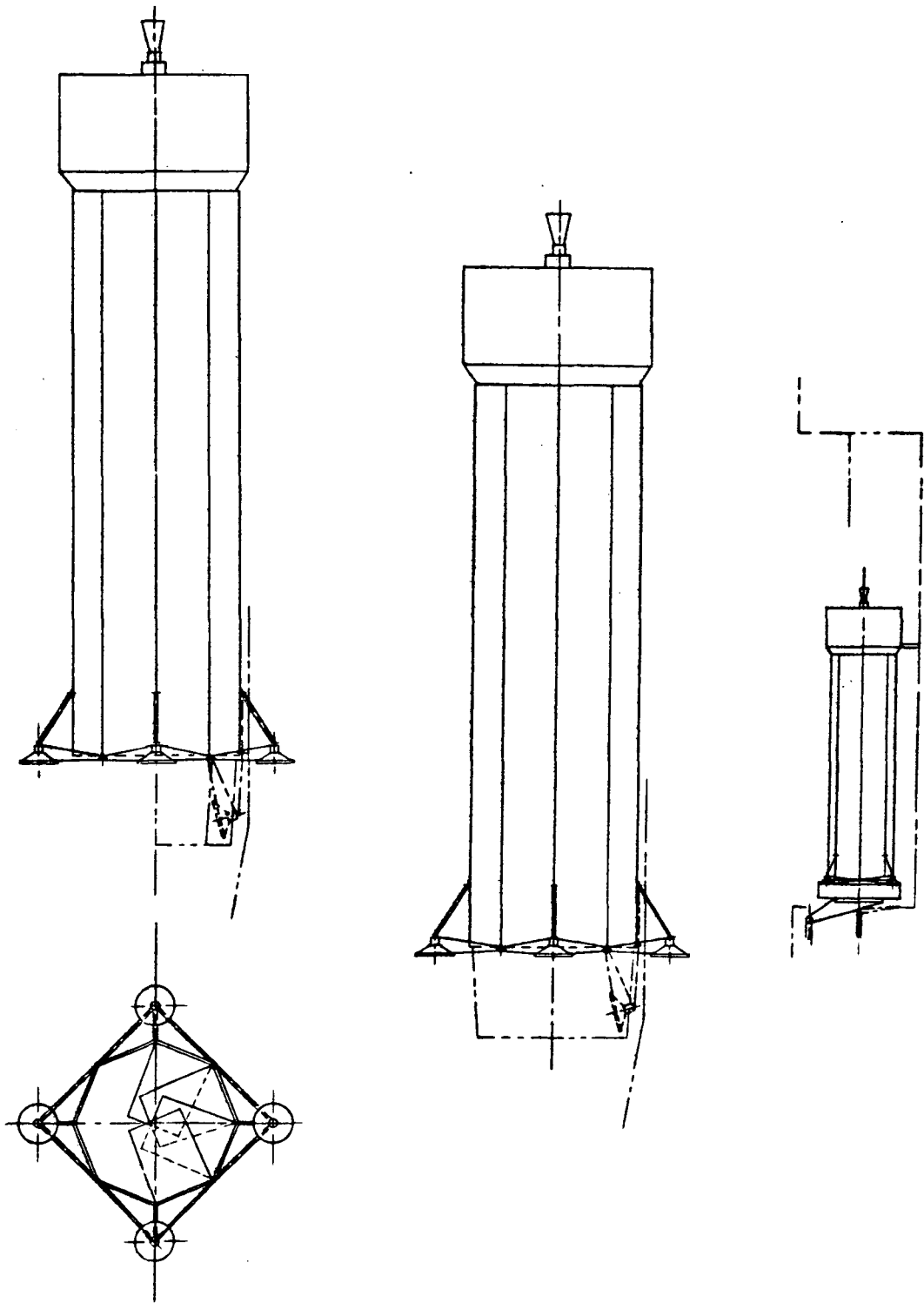
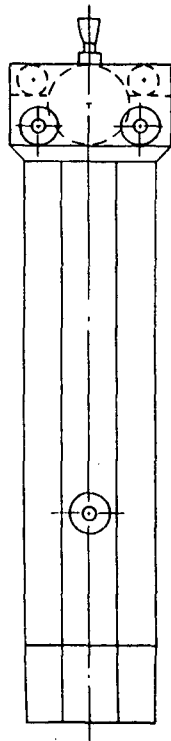


Figure X-3. Docking/retrieval Concept 1.



VIEW B-B

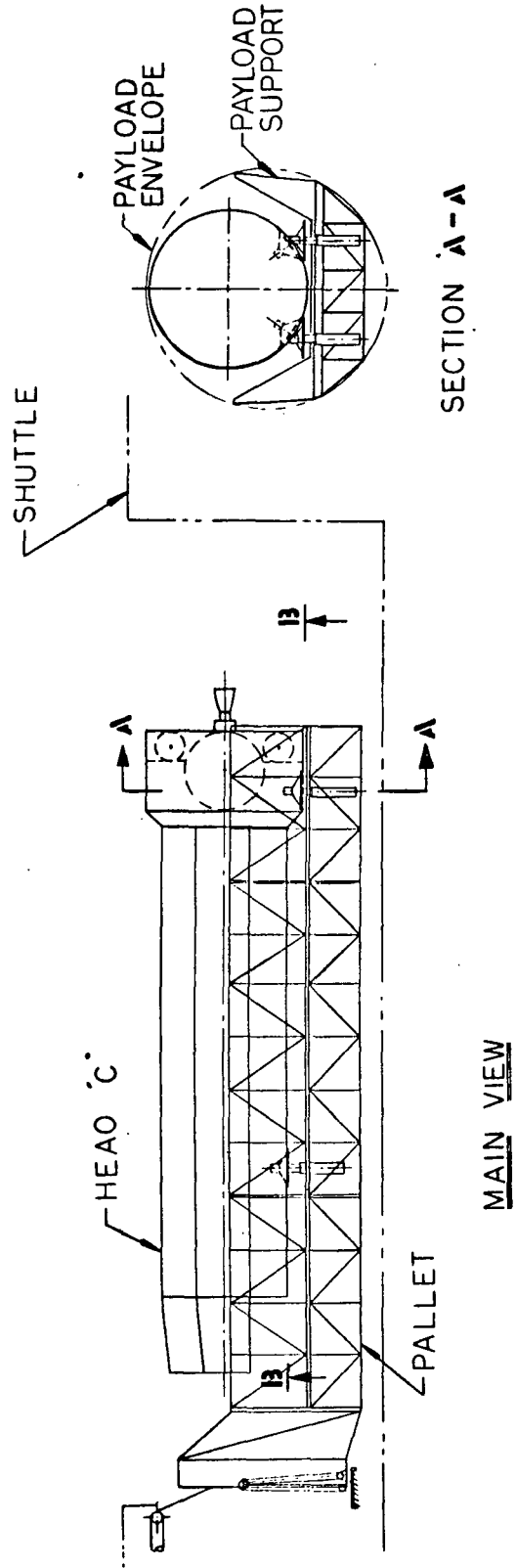
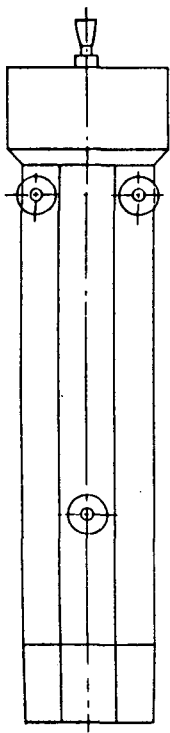
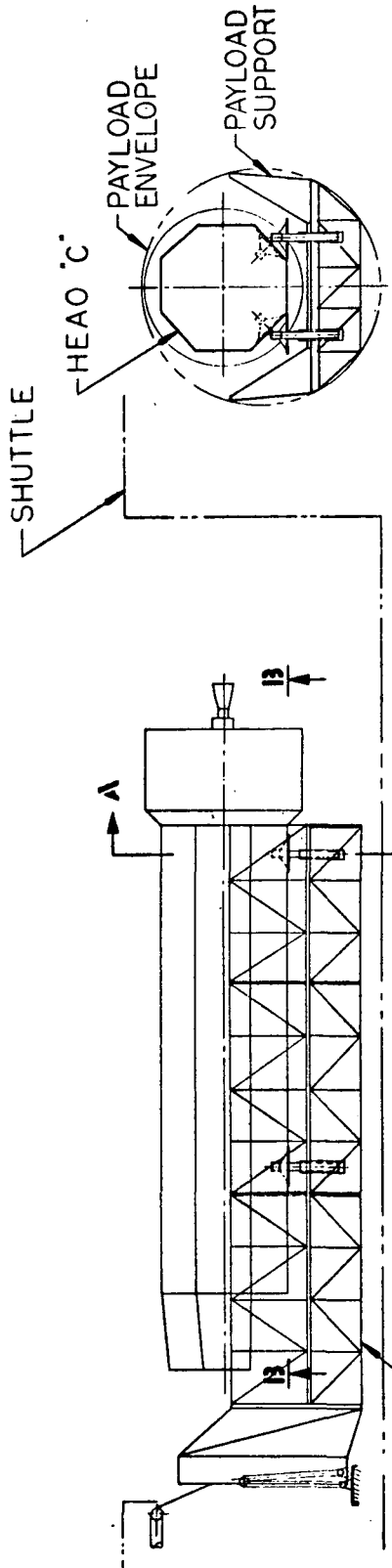


Figure X-4. Docking/retrieval Concept 2.



VIEW B-B



SECTION A-A

MAIN VIEW

Figure X-5. Docking/retrieval Concept 3.

13 ④

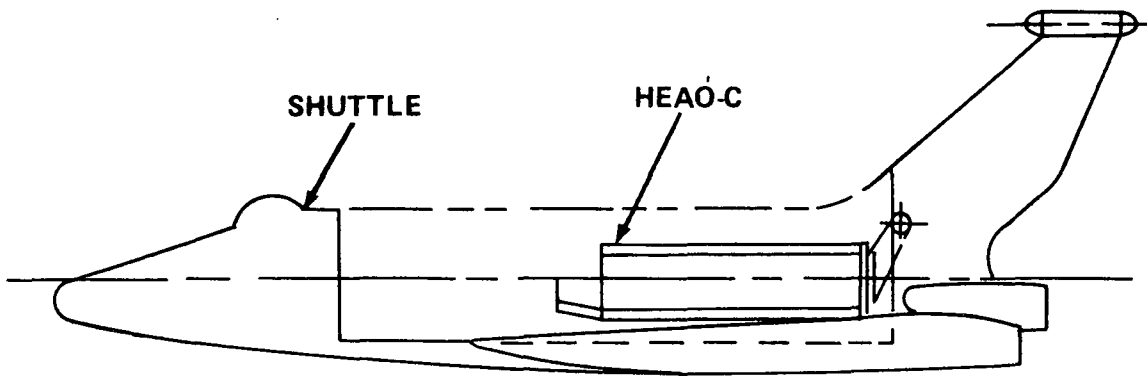


Figure X-6. Docking/retrieval Concept 4.

expose a docking adapter on the aft end of the HEAO. The separation mechanism could be identical to that at the OAS-to-Titan interface. The RCS thrusters and bottles (or another set) would have to be retained on the spacecraft to stabilize it during docking. This docking orientation provides the maximum probability of not contaminating experiment surfaces with the Shuttle RCS and eliminates deployable mechanisms and clock angle limitations. Retrieval mechanism concepts and concepts of Shuttle bay support devices must be investigated further.

It is expected that the greatest impact of Shuttle return on the structural design of the baseline HEAO-C design would be in the miscellaneous experiments which are cantilevered off the forward end of the optical bench. The experiment structures themselves must be able to withstand the 4-g lateral load shown in Table X-2, or there must be supplementary supporting structures provided as part of the spacecraft. There would probably be sufficient clearance in the Shuttle bay to stow the HEAO with solar array deployed (depends on HEAO structural support concept — pallet, etc.); the antenna boom could be designed to fold automatically as the HEAO is retracted into the bay. These possibilities may eliminate the necessity for design of active retracting devices for these appendages. An extravehicular activity (EVA) into the Shuttle bay could be used to secure arrays and booms to prevent reentry g-loading damage.

The Shuttle RCS thrusters should be located as far from the payload bay as possible and should be canted away from the docking approach direction to minimize probability of contamination of the HEAO. It is assumed that the HEAO must stabilize itself and that the Shuttle would perform the docking maneuvers.

Safety requirements may necessitate passivation of the RCS before reentry. Burning the propellant would provide less probability of contamination than dumping and would not require design changes but would require the Shuttle to counter the resulting torques.

## C. Concluding Remarks

The HEAO-C concept developed in this Phase A study has emphasized commonality with the earlier HEAO spacecraft; as such, it is not designed for in-orbit servicing and maintenance. Incorporation of the in-orbit servicing and maintenance philosophy into the design would have far-reaching programmatic as well as technical impacts:

- To a large extent, the fundamental commonality chain with the HEAO-A and -B spacecraft would be broken, although many of the subsystems and components might still be utilized.
- Redefinition of the HEAO-C mission would be required. Current experiment candidates and associated scientific objectives can be satisfied with a 2 year, high reliability mission; adequate expendables are incorporated in the current design; state-of-the-art components are employed; and the cost of additional redundancy and component life testing is much less than the cost of planned periodic servicing.

The primary advantage of planned, periodic servicing and maintenance is the achievement of very long orbital lifetimes and the updating, recalibration, and replacement of the scientific instruments. Should the HEAO-C mission be redefined to be compatible with this operational mode, then the spacecraft should become a precursor in a new family of spacecraft, perhaps an astronomy-dedicated Research Applications Module (RAM), rather than a follow-on in the current HEAO family.

## REFERENCES

- X-1. Preliminary Payload Interface Design Control Document for Space Shuttle Payloads. Compiled by the Preliminary Design Office, Program Development, Marshall Space Flight Center, June 16, 1971.
  
- X-2. Boeckel, J.H.; Timmins, A.R.; and Mercy, K.R.: GSFC Test Philosophy and Resultant Record. Proc. of the Symposium on Long Life Hardware for Space, Vol. I, held at Marshall Space Flight Center Mar. 17-19, 1969.

HIGH ENERGY ASTRONOMY OBSERVATORY  
MISSION C  
PHASE A FINAL REPORT

Volume II – Preliminary Analyses and Conceptual Design

By Program Development

The information in this report has been reviewed for security classification. Review of any information concerning Department of Defense or Atomic Energy Commission programs has been made by the MSFC Security Classification Officer. This report, in its entirety, has been determined to be unclassified.

This document has also been reviewed and approved for technical accuracy.

APPROVAL:

CONCURRENCE:

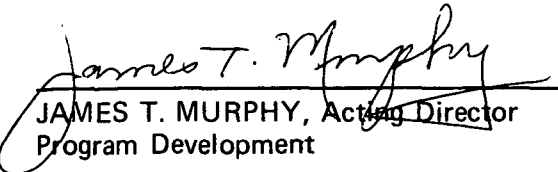
  
\_\_\_\_\_  
JAMES W. HEYER, Assistant Director  
Preliminary Design Office  
Program Development

  
\_\_\_\_\_  
CARROLL C. DAILEY, Manager  
HEAO Experiments Office  
Program Management

  
\_\_\_\_\_  
HERMAN P. GIEROW, Acting Director  
Mission and Payload Planning Office  
Program Development

  
\_\_\_\_\_  
F. A. SPEER, Manager  
HEAO Office  
Program Management

  
\_\_\_\_\_  
ERICH E. GOERNER, Director  
Preliminary Design Office  
Program Development

  
\_\_\_\_\_  
JAMES T. MURPHY, Acting Director  
Program Development

# DISTRIBUTION

TM X-64652

## INTERNAL

DIR

Dr. Rees

DEP-T

Dr. Lucas

DEP-M

Mr. Foster

AD-S

Dr. Stuhlinger

PD-DIR

Mr. Murphy/Mr. Downey  
Dr. Mrazek

PD-RV-MGR

Mr. Godfrey

PD-RAM-MGR

Mr. Zoller

PD-PT-DIR

Mr. Sneed (2)

PD-SA-DIR

Mr. Huber (2)

PD-PS-DIR

Mr. Goodrum

PD-MP-DIR

Mr. Gierow (3)

PD-DO-DIR

Mr. Goerner (50 + 10 of Vol. 1)

S&E-DIR

Dr. Weidner (2)

S&E-CSE

Dr. Haeussermann (3)

S&E-ASTR

Mr. Moore (10)

S&E-QUAL

Mr. Grau (3)

S&E-AERO

Dr. Geissler (5)

S&E-ASTN

Mr. Heimburg (8)

S&E-COMP

Dr. Hoelzer (2)

S&E-PE

Dr. Siebel (2)

S&E-SSL

Mr. Heller (6)

PM-DIR

Mr. Shepherd (2)

PM-MO-DIR

Mr. Kurtz

PM-HE-DIR

Dr. Speer (20 + 10 of Vol. 1)

PM-PR-M

Mr. Stevens